#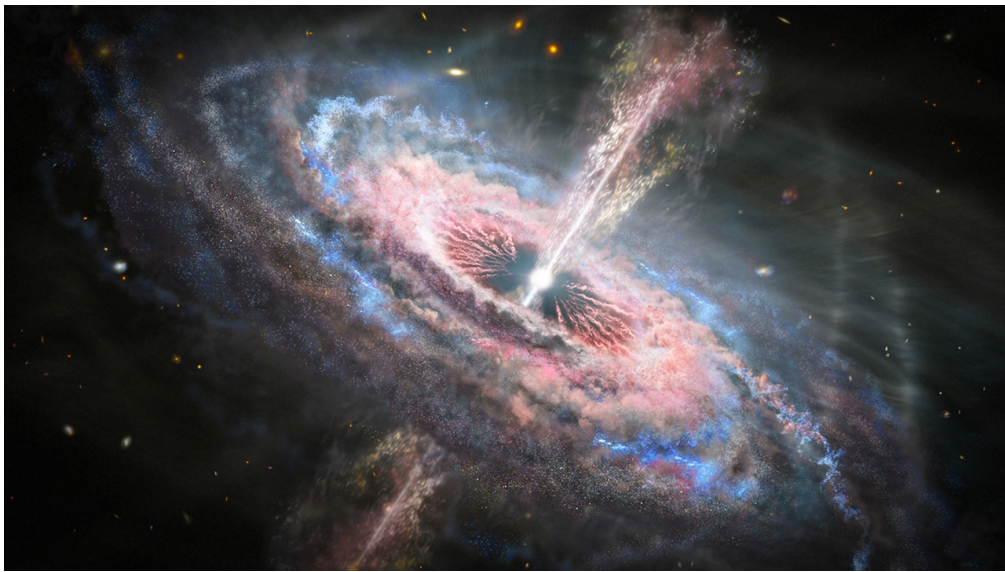 Clues to the inner workings of active galactic nuclei from spectral energy distributions, photoionization modeling and the rare subset of FeLoBAL quasars.

Daniel Lawther

Dark Cosmology Centre, Niels Bohr Institutet
University of Copenhagen

This dissertation is submitted for the degree of
PhD

August 2020

This thesis is dedicated to Mulder and Scully.

Acknowledgements

First and foremost I would like to thank my PhD supervisor, Marianne Vestergaard, who got me interested in active galactic nuclei in the first place, and who has been extremely supportive throughout this project. I have benefited greatly from your expertise in the field of AGN studies, your detailed feedback on early drafts of all the papers presented here, and your proposal-writing zeal regarding Mrk 590!

I owe a great deal of thanks to Mike Goad, who made me feel at home during a productive stay at Leicester University, and who was very constructive and responsive throughout the subsequent paper-writing period. I really enjoyed working on the BLR model, which was quite different to my previous projects - without your knowledge of photoionization physics and modeling advice, I wouldn't have known where to start.

Thanks to all my wonderful colleagues at DARK. In particular, Sandra Raimundo provided invaluable assistance with regards to theoretical models of accretion disks, and Daniele Malesani provided local support with Swift observation planning and data analysis. Thanks to the super-helpful DARK administrative staff, who shielded me from the worst excesses of academic bureaucracy, and to my fellow PhD and MSc students at NBI, who provided large quantities of fun throughout.

Finally, I'd like to thank my parents, who consistently encourage me to do whatever makes me happy :)

Cover art: Artist's impression of a quasar. NASA, ESA, and J. Olmsted (STScI).

Abstract

We find supermassive black holes in the central nucleus of all massive galaxies. They are thought to have grown to their present-day masses through accretion episodes. We observe these accretion episodes as Active Galactic Nuclei (AGN), including luminous quasars. AGN emit strongly across the entire electromagnetic spectrum, from radio waves to Gamma radiation. AGN represent natural laboratories for high-energy and strong-gravity physics, are believed to influence the evolution of their host galaxies, and provide high-redshift cosmological probes. To make the most of these opportunities requires a detailed understanding of the physics and geometry of their central engines. In this thesis I present four different studies relating to AGN accretion.

Our current model of AGN accretion involves an optically thick, geometrically thin accretion disk around the central black hole, which (in some cases) responds to illumination from a variable X-ray emitting region. The disk sizes inferred from UV-optical continuum reverberation mapping of local-Universe AGN are a factor ~ 3 larger than those predicted by the thin-disk model. In Chapter 2 I explore the effects of diffuse continuum emission from the broad-line region on reverberation-based disk size estimates. I find that, to first order, diffuse continuum contamination can explain the observed excess delays relative to the thin-disk model.

Observations of changing-look AGN suggest that the accretion flow can be highly variable, such that a given AGN can lose and/or regain its broad line and continuum emission on timescales of $\sim$years. In Chapter 3 I present evidence that the changing-look AGN Mrk 590, which lost its broad-line emission between 2003-2006, has re-ignited and now displays an ultraviolet to X-ray spectral energy distribution consistent with those of typical Type 1 AGN. The X-ray luminosity has returned to roughly half of its historic maximum, while the UV continuum emission has reappeared. The soft X-ray component is not detected in *Swift* XRT and *NuSTAR* observations, and has not returned to its previous bright state. I also present a reverberation mapping analysis during a recent X-ray flare, finding that the UV emission is correlated with the X-ray component and lags it by $\sim 2 - 3$ days.

A subset of quasars display strong, heavily blueshifted UV absorption lines with velocity dispersions $\Delta V \geq 2000 \text{ km s}^{-1}$. These broad absorption line (BAL) quasars may represent 'ordinary' quasars observed at a certain angle relative to the central engine. Alternatively, they may represent an early stage in a quasar's lifetime, during which a 'cocoon' of gas and dust is expelled from the central region. Both these scenarios have implications for the BAL host galaxies. If we observe BAL absorption depending on the inclination of the central engine, the properties of BAL and non-BAL host galaxies at a given AGN luminosity should be statistically indistinguishable. If BAL sources represent young quasars, we may expect to see signs of recent mergers or on-going star formation in

their host galaxies, depending on the triggering mechanism for AGN activity. In Chapter 4 I present a study of the host galaxies of four FeLoBAL quasars. I find no evidence for starburst activity in their hosts, and demonstrate that our data are consistent with quiescent elliptical hosts or dust-obscured starburst galaxies.

In Chapters 5 and 6 I present UV-optical and X-ray SEDs for a sample of $z \sim 2$ quasars, of which roughly half are radio-loud, as part of an ongoing effort to *i)* study the dependence of the observational properties of quasars on the SED shape, and *ii)* to investigate the origin of radio-loudness in quasars. I demonstrate that our sample is representative of the broader quasar population, in terms of UV-optical SEDs, X-ray emission properties, and inferred black hole masses. The radio-loud and radio-quiet sources in our sample are matched in terms of redshift and V-band apparent magnitude. I demonstrate that their optical-UV SEDs are statistically indistinguishable. I also present an exploratory study of the opportunities to investigate accretion disk physics for our $z \sim 2$ sample. I find that observed-frame infrared observations are required in order to adequately constrain the accretion disk properties and to test the thin-disk approximation for these quasars.

In Chapter 7 I offer some closing remarks on future prospects for each of these research projects.

Table of contents

Chapter 1

Introduction: Active Galactic Nuclei

At the heart of most - perhaps all - massive galaxies, we find a supermassive black hole (SMBH). These black holes are the most massive compact objects in the observed Universe, and are themselves found in dense environments, i.e., the nuclei of massive galaxies. Until very recently, the existence of SMBHs was only inferred indirectly, through their gravitational influence on their immediate surroundings and through the radiation emitted due to accretion of mass onto them. The recent sub-millimeter imaging observations of the SMBH in the galaxy M87, which resolve the 'shadow' (i.e., the photon capture region) near the event horizon of a black hole, provides direct evidence for the existence of supermassive black holes for the first time (Event Horizon Telescope Collaboration, 2019).

Most SMBHs appear as sleeping giants: they accrete mass at very low rates, and emit only insignificant amounts of electromagnetic energy. The black hole at the center of our own Galaxy, Sgr A*, is a typical quiescent SMBH (e.g., Boehle et al., 2016, and references therein). Meanwhile, a subset of SMBHs are very much awake, accreting nearby gas and emitting electromagnetic radiation. SMBHs that produce sufficient electromagnetic radiation that they are detectable at cosmological distances are referred to as Active Galactic Nuclei (AGN). They emit copious amounts of radiation across the entire electromagnetic spectrum, from radio waves to Gamma rays. The most luminous AGN are known as quasars; these can outshine the integrated stellar luminosities of their host galaxies, and are observable out to redshifts $z \sim 7$ (e.g., Bañados et al., 2016, 2018; Fan et al., 2019; Wang et al., 2017).

What can AGN teach us about the Universe?

Firstly, given their large luminosities and distances, quasars are useful probes of the high-redshift Universe. For example, their spectra provide excellent probes of the intervening medium, revealing intervening galaxies through hydrogen and metal absorption. Thus, quasars allow us to study galaxies in absorption (e.g., Fynbo et al., 2013; Mackenzie et al., 2019; Rafelski et al., 2016), including their metallicities and star formation rates (e.g., Berg et al., 2016), and to test models of large-scale structure (e.g., Padmanabhan and Refregier, 2017), as a function of cosmic time. The most distant quasars also probe the reionization epoch. Sources at $z \gtrsim 6$ display strong, redshifted H I absorption, the so-called Gunn-Peterson trough (e.g., Becker et al., 2001), due to the presence

of neutral hydrogen prior to the reionization of the Universe. McGreer et al. (2015) use this to demonstrate that reionization was complete by $z \sim 6$. Greig et al. (2019) use the absorption profile of the Lyα emission line to argue that the Universe was partially reionized even at $z \sim 7$.

Recently, several studies have demonstrated that quasars are potentially *standardizable candles*, suitable for cosmological distance measurement. One promising method uses the redshift-independent relationship between the rest-frame UV and X-ray luminosities as a luminosity indicator from which the distance can be inferred (Lusso et al., 2019; Risaliti and Lusso, 2015). Alternatively, relationships between the luminosities and the size scales of AGN (as measured using reverberation mapping methods) yield redshift-independent luminosity estimates. These size-luminosity relationships have been used as cosmological distance indicators for both the broad-line emitting region (Loli Martínez-Aldama et al., 2019; Watson et al., 2011), and the dust reprocessing region (e.g., Hönig et al., 2017). (Cackett et al., 2007) also explore the possibility of using the accretion disk size as a luminosity indicator. As quasars are observed out to redshifts $\gtrsim 7.5$, these techniques can extend our distance versus redshift measurements to higher redshifts than those attainable using Type 1a supernovae, and will valuable constraints on a potentially non-linear dark energy equation of state (e.g., King et al., 2014). They will also provide a valuable complementary test of the distance-redshift relationship already obtained at $z \lesssim 1.4$ using supernovae (e.g., Perlmutter et al., 1999; Riess et al., 1998) and of the cosmological constraints obtained out to $z \lesssim 3.5$ using baryon acoustic oscillations (e.g., eBOSS Collaboration et al., 2020; Eisenstein et al., 2005).

Since the advent of large telescopes with CCD detectors, and especially since the launch of the *Hubble Space Telescope*, the evidence for the ubiquitous presence of SMBHs in the centers of massive galaxies has been mounting (e.g., Kormendy and Ho, 2013). Thus, the processes that build galaxies must also produce a SMBH, which grow through accretion episodes to reach their present masses (e.g., Soltan, 1982). We observe correlations between SMBH masses and host galaxy bulge luminosities or stellar velocity dispersions (e.g., Ferrarese and Merritt, 2000; Gültekin et al., 2009; Magorrian et al., 1998; Marconi and Hunt, 2003; Tremaine et al., 2002). These correlations are somewhat unexpected, as the mass of the SMBH dominates the gravitational potential only in the very central regions of the host galaxy, whereas the bulge kinematics are governed by the stellar and dark matter potentials. The observed empirical SMBH-bulge correlations may be due to AGN activity expelling gas via radiation pressure or kinetic feedback, which would quench star formation (e.g., Barnes and Hernquist, 1991; Hopkins et al., 2005; Sanders et al., 1988).[1] The study of such relationships, and their redshift evolution, requires accurate determinations of the SMBH masses at both low and high redshift. For high-redshift galaxies, the only currently feasible way to obtain mass estimates is based on the kinematics of AGN broad-line regions (§1.4.2).

In summary: quasars are useful cosmological probes, may supplement Type 1a supernovae as standarizable candles for precision cosmology, and are an important piece of the puzzle of galaxy formation and evolution. In order to fully exploit their potential, we must understand the central

---

[1]Alternatively, the correlations may be caused by the stochastic effects of mergers, with no feedback mechanism in individual galaxies necessary (Hirschmann et al., 2010; Jahnke and Macciò, 2011; Peng, 2007). In the latter case, the scatter in the relationships is expected to increase with redshift, as the convergence with a linear relationship between black hole and bulge mass increases with the number of mergers a given host galaxy has undergone.

engine that generates the AGN emission. We also require methods to accurately estimate the SMBH masses, in order to understand the observed SMBH - host galaxy correlations.

Some efforts to understand the central engines of AGN

It is generally acknowledged that AGN activity is ultimately powered by the energy unleashed through accretion of matter onto a black hole (e.g., Lynden-Bell, 1978; Lynden-Bell and Rees, 1971). However, the detailed physical processes at play are still a puzzle. The accreting gas is expected to form a disk in parts of the accretion flow. The physical processes in these accretion disks (§1.2) are a vital ingredient in any AGN model.

Quasar spectra in the UV-optical are dominated by a continuum component, usually attributed to the accretion disk itself. The continuum-emitting regions have radii of at most a few light-days, as constrained observationally by variability timescales (e.g., Peterson, 2001), and confirmed by microlensing of the continuum (e.g., Mosquera et al., 2013, and references therein). These size scales are not yet accessible to UV–optical imaging for any AGN. We must therefore turn to alternative techniques in order to study the central engine. One approach is to study the spectral energy distribution (SED) emitted by the AGN, and isolate the component(s) due to direct emission from the accretion disk. For the standard geometrically thin accretion disk models, the accretion disk SED shape depends on the mass and spin of the central black hole, along with the mass accretion rate onto it (§1.2). By studying AGN SEDs, we can test these thin-disk models. The integrated accretion luminosity of the AGN also constrains the total power output of the disk, and thus places upper limits on the mass accretion rate. In practice this analysis requires some model-dependent assumptions, as a substantial part of the accretion power is emitted in the extreme-UV and therefore suffers strong Galactic and extragalactic Hydrogen absorption. Nevertheless, SED studies provide vital clues as to the nature of AGN central engines. The X-ray to radio SED is strongly inconsistent with a single emission component (e.g., Elvis et al., 1994; Fiore et al., 1995), indicating that AGN must have multiple emission and reprocessing regions (§1.1). The SEDs also reveal an important dichotomy in the AGN population, where roughly 10% of sources are radio-loud (§1.1.8) and emit a kpc-scale jet (e.g., Jiang et al., 2007; Kellermann et al., 1989).

Another way to probe the central regions of AGN is to quantify the response of various reprocessed emission components to variations in the driving continuum luminosity, in order to determine their size scales and geometry. This *reverberation mapping* approach (§1.4) is used to measure the size of the region that emits the broad emission lines (§1.1.4) seen in Type 1 AGN (e.g., Bentz et al., 2010a; Blandford and Payne, 1982; Clavel et al., 1991). This allows for estimation of the black hole mass via dynamical arguments. Recently, the same technique has also been used to make size estimates of the accretion disk itself (e.g., Edelson et al., 2015; Fausnaugh et al., 2016, ; see Chapter 2).

Outline of this Thesis

This Thesis is comprised of four separate projects, all ultimately aimed at improving our understanding of AGN accretion and of the resulting electromagnetic emission.

In Chapter 2 I investigate how diffuse continuum emission from the broad-line region biases disk reverberation mapping results. Accretion disk sizes measured using reverberation mapping are somewhat larger than those predicted for the standard thin-disk model (e.g., Edelson et al., 2017). Using a forward modeling approach, I demonstrate that diffuse continuum emission from the Broad-line emitting region itself leads to an overestimation of inferred disk sizes. This effect is important to consider when interpreting reverberation mapping data in the context of accretion disk modeling.

In Chapter 3 I present an analysis of *Swift* XRT and UVOT monitoring observations of the changing-look (§1.5) AGN Mrk 590 during 2013–2020. These changing-look objects display disappearing and/or reappearing UV–optical continua and broad emission lines on timescales of months to years. This behavior is not explained by simple thin-disk models for AGN accretion flows, which predict significant continuum flux variations only on timescales of ∼thousands of years. I find that Mrk 590 has returned to a brighter X-ray and UV luminosity than its historic low state, and currently has the observational appearance of a bona fide (albeit highly variable) Type 1 AGN. I also present an analysis of its hard X-ray spectrum observed by *NuSTAR*, which is dominated by a power-law continuum but also displays faint X-ray reflection features.

In Chapter 4, I study the properties of the host galaxies of four FeLoBAL quasars. This rare subset of quasars may represent an early stage of AGN activity, in which the young quasar expels gas and dust from its vicinity (e.g., Voit et al., 1993). Alternatively, they may represent 'ordinary' quasars observed at a certain narrow range of viewing angles. In the latter scenario, we expect their host galaxies to have statistically identical properties to the broader population of quasar host galaxies. I find that the host galaxies of the four FeLoBAL quasars are consistent with being massive quiescent galaxies, but I cannot exclude the possibility that they are dust-obscured starbursting hosts. I also quantify the uncertainties on host galaxy brightness and morphological measurements for *Hubble Space Telescope* imaging of bright quasars at $0.8 < z < 2$, via an extensive series of simulations.

In Chapters 5 and 6 I present the observed optical–UV–X-ray SEDs of 143 quasars at redshift $z \sim 2$. Using the *Swift* satellite, we have obtained simultaneous observations of the optical to X-ray wavelength regime. This minimizes the uncertainty in the SED shape measurements due to quasar variability, which is otherwise a significant source of uncertainty when different wavelength regimes are observed at different times. I characterize the UV and X-ray luminosities and UV to X-ray SED shapes for this sample, and establish to which extent these quasars are representative of the broader quasar population at $z \sim 2$. This catalog is selected to contain pairs of radio-loud and radio-quiet sources matched in terms of redshift and V-band apparent magnitude, allowing a robust comparison of their SED properties. I find no difference in the UV SED shape for radio-loud and radio-quiet quasars.

In the remainder of this Introduction, I give a brief review of our current understanding of AGN, concentrating on areas relevant to my thesis work. I outline our current model of the structure of AGN in §1.1; introduce the predictions of standard thin-disk models that are relevant to my work in §1.2; discuss AGN spectral energy distributions from an observational standpoint in §1.3; describe
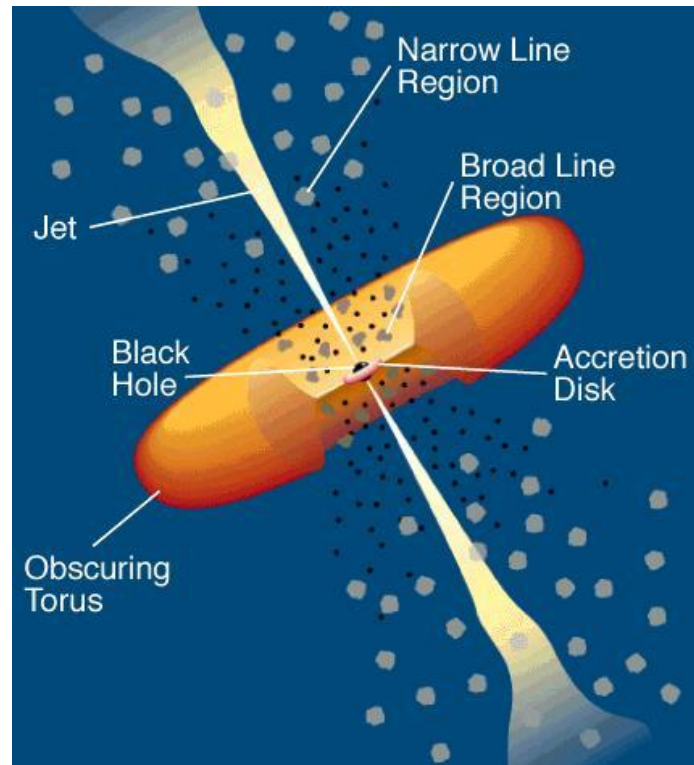
Fig. 1.1 Illustration of the standard model for AGN structure. Here, the smaller brown clouds represent the broad-line emitting regions close to the central accretion disk, which produces the ionizing continuum. The pale clouds further out from the accretion disk represent the narrow-line emitting region. The dusty torus obscures the continuum, broad line, and X-ray emitting regions along some viewing angles. Only the radio-loud AGN emit the jet depicted here. This image is provided by NASA, and is adapted from the illustration presented by Urry and Padovani (1995).

reverberation mapping methods to estimate black hole masses and accretion disk sizes in §1.4; and introduce changing-look AGN in §1.5.

1.1 The Current Model of AGN Structure

In this Section I outline our current best understanding of the structure of AGN, starting with the central black hole, and moving outwards to larger size scales. The detailed geometry and physics of each component described here are active research topics. However, the overall schematic layout displayed in Figure 1.1 is consistent with various observational characteristics of AGN, including their overall spectral energy distributions and their emission line variability behavior. In short, an accretion disk (§1.1.2) around a central black hole (§1.1.1) provides an ionizing continuum that is reprocessed in high-velocity broad-line emitting gas (§1.1.4) within light-days of the black hole, and in the slower-moving, narrow-line emitting gas further out (§1.1.7). X-ray emission components (§1.1.3) are produced in a compact, poorly understood region near the black hole. A dust structure (§1.1.5) preferentially obscures the central engine at certain viewing angles, and emits a thermal spectrum in the infrared. A subset of AGN launch collimated, relativistic jets from their central

regions (§1.1.8), which emit radio, X-ray and γ-ray radiation. Each AGN resides in the nucleus of its host galaxy (§1.1.9).

1.1.1 The Central Black Hole

The emission from AGN is ultimately powered by release of gravitational energy as mass accretes onto a supermassive black hole. Here, I outline some of the properties of black holes that are relevant to the study of AGN accretion flows.

Intrinsic properties of black holes: The concept of a black hole was originally suggested in the framework of Newtonian gravity, requiring only that light has a finite speed and is affected by gravitational acceleration (e.g., Michell, 1784). Today, we understand black holes in the theoretical context of Einstein's general relativity (Einstein, 1916). In particular, Schwarzschild (1916) and Kerr (1963) derived vacuum solutions for the spacetime around a non-rotating and a rotating massive body, respectively. These solutions provide excellent descriptions of the behavior of test masses around massive objects, and reduce to the Newtonian case in the limits of weak gravity and slow-moving test masses. They also allow for black holes, i.e., objects with sufficiently high density that their escape velocity exceeds the speed of light at some radius. The imaginary surface for which the escape velocity exceeds c is known as the *event horizon* of the black hole. It is located at the Schwarszschild radius, r_s, which scales with mass M as

$$r_s = \frac{2GM}{c^2}, \tag{1.1}$$

where G is Newton's gravitational constant. For low-density objects such as planets and stars, r_s is much smaller than their physical radius. In that case, the Schwarzschild radius corresponds to the radius that a black hole with the equivalent mass would have. For black holes, the Schwarzschild radius represents the ultimate limiting radius beyond which light cannot escape.

The gas and dust in galaxies has a net charge of zero, as the electromagnetic force is much stronger than the gravitational force and will tend to break up any net accumulation of charge. Thus, astrophysical black holes that grow through accretion of gas and dust will have zero net charge, but can have non-zero mass and angular momentum (Kerr, 1963). The black hole spin is usually parameterized by the dimensionless parameter $a_* = cJ(GM_{\mathrm{BH}}^2)$, where J denotes the angular momentum of the black hole (e.g., Porquet et al., 2019). The spin of an accreting black hole is thought to be related to its accretion history (e.g., King, 2008), and to interactions between the black hole and accretion disk which may extract angular momentum from the black hole (Blandford and Znajek, 1977).

Stable orbits around a black hole: An important concept for the study of accretion onto black holes is the *innermost stable circular orbit* (ISCO), which occurs at a distance r_{ISCO} from the black hole. This quantity corresponds to the innermost radius for which which circular Keplerian orbits are stable to perturbations. The gas in accretion disks is thought to move in near-Keplerian orbits, primarily supported by rotation (at least for standard thin disks; §1.2). The importance of rotational

support suggests that the accretion disk cannot emit much radiation within r_{ISCO}, as the gas within this radius will rapidly spiral in towards the event horizon. The innermost stable orbit scales with black hole mass as

$$r_{ISCO} = f(a_*) \frac{GM_{BH}}{c^2}, \tag{1.2}$$

where the factor $f(a_*)$ depends on the black hole spin (King, 2016). For a non-spinning black hole, $r_{ISCO} = 3r_s$. The innermost stable orbit asymptotically approaches r_s for a positively rotating black hole (with regards to the spin direction of the accretion disk), and increases up to $\sim 5.8r_s$ for a retrograde black hole spin (Bardeen et al., 1972). The size of r_{ISCO} has a profound effect on the emitted disk SED, as it determines the strength of the gravitational potential to which an inner accretion disk can extend.

Supermassive black holes: Astrophysical black holes are categorized according to their mass. Stellar-mass black holes are thought to be formed by the collapsing cores of dying massive stars ('collapsar supernovae'). The detection of black hole mergers in gravitational waves provides strong evidence for the existence of stellar-mass black holes with $M_{BH} \sim 25M_\odot$ (Abbott et al., 2016). AGN are powered by accretion onto *supermassive black holes* (SMBHs), with masses of $\sim 10^6 M_\odot$ or greater in massive galaxies, and masses as low as $\sim 5 \times 10^4 M_\odot$ in dwarf galaxies (Baldassare et al., 2015). SMBHs have only been observed in the nuclei of massive galaxies. Stellar-dynamical measurements indicate that SMBHs are ubiquitous in the centers of galaxies (e.g., Ferrarese and Ford, 2005; Kormendy and Ho, 2013), including our own Milky Way galaxy (e.g., Boehle et al., 2016; Reid and Brunthaler, 2004). The imaging of M87 obtained by the Event Horizon Telescope basically settles the debate as to the existence of SMBHs, although previous indirect evidence of compact dark objects at the centers of galaxies from stellar and gas dynamics were consistent with them being black holes. In any case, accretion onto a black hole is required to produce the observed AGN luminosities (e.g., Lynden-Bell, 1978; Lynden-Bell and Rees, 1971). SMBHs are therefore an essential ingredient in our current model for AGN activity. The formation processes of SMBHs detected as early as redshifts $z > 6$ (e.g., Fiore et al., 1995) are not currently well understood (e.g., Ardaneh et al., 2018; Bromm and Loeb, 2003; Pacucci et al., 2017; Sugimura et al., 2018).

The black hole sphere of influence: For SMBHs residing in the nuclei of galaxies, it is useful to define a region within which the total gravitational potential is dominated by that of the black hole. We refer to this region as the *sphere of influence*, r_h, of the black hole (e.g., Kormendy and Ho, 2013), where

$$r_h = \frac{GM_{BH}}{\sigma^2}. \tag{1.3}$$

Here, M_{BH} is the black hole mass, and σ denotes the velocity dispersion of stars near enough to the black hole that its gravity dominates the gravitational potential. The sphere of influence is important when estimating M_{BH} using stellar dynamics, as these estimates require the stellar motions to be influenced by the black hole potential. Gültekin et al. (2009) demonstrate that it is
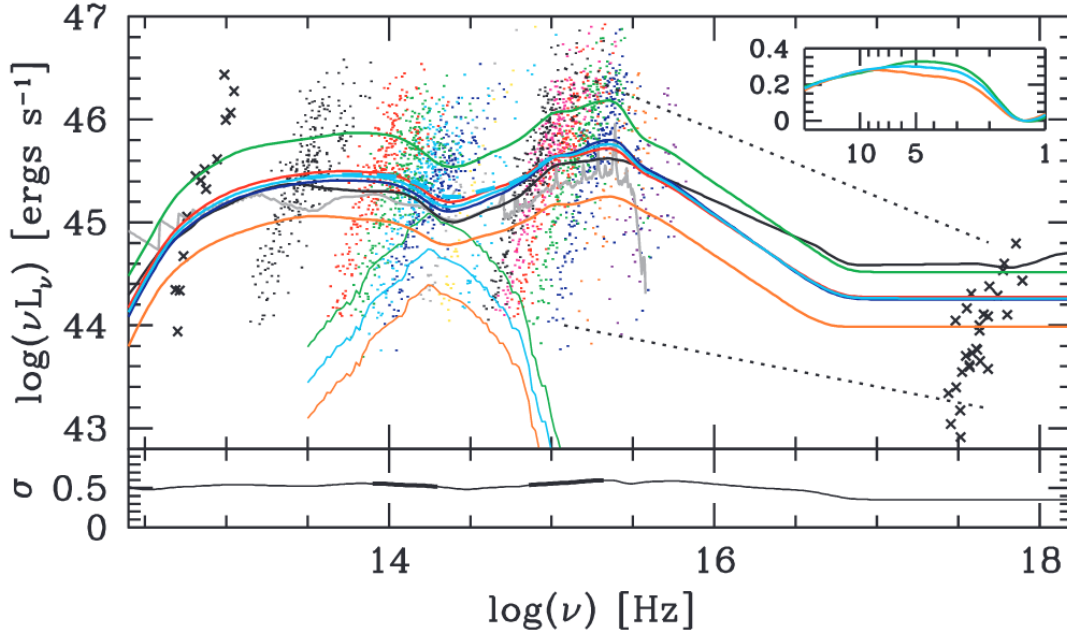
Fig. 1.2 The mean infrared to X-ray spectral energy distribution (SED) for 259 quasars, and subsamples thereof, as compiled by Richards et al. (2006). The spectral energy distributions are color coded as follows. *Cyan curve:* mean SED for the full sample. *Red:* optically red subsample, as defined by Richards et al. (2006). *Blue curve:* optically blue subsample. *Green curve*: optically luminous subsample. *Orange curve:* optically dim subsample. *Black curve:* mean SED for the quasar sample presented by Elvis et al. (1994). The broad infrared emission feature at frequencies below $\log \nu \sim 14.5$ is due to dust reprocessing. The broad 'big blue bump' peaking at $\log \nu \sim 15.3$ is attributed to the accretion disk emission. Both these features are prominent in the mean SED for the full sample, and also in the mean SEDs for the various luminosity and color subsamples. This Figure is taken from the quasar SED catalog presented by Richards et al. (2006).

not necessary to fully resolve r_h in the stellar observations, however, the uncertanties on M_{BH} are increased for lower spatial resolutions. The continuum, X-ray and broad line emitting regions are located within the sphere of influence, and their dynamics are therefore largely governed by the gravitational attraction of the black hole. However, r_h is of order tens of parsecs for SMBHs (e.g., Kormendy and Ho, 2013), and thus much smaller than the host galaxy bulge itself. This implies that the direct influence of the black hole on the host galaxy dynamics is negligible. The direct gravitational influence of the black hole can therefore not explain the observed relationships between SMBHs and their host galaxy bulge properties (e.g., the $M_{BH} - \sigma$ relationship, Ferrarese and Merritt, 2000; Gültekin et al., 2009; Onken et al., 2004).

1.1.2   The Accretion Disk

Figure 1.2 displays the mean spectral energy distribution (SED) for a sample of 259 spectroscopically identified Type 1 quasars, selected from the Sloane Digital Sky Survey quasar catalog (Schneider et al., 2005), and compiled by Richards et al. (2006). These authors also derive mean SEDs for subsamples based on luminosity and on reddening (1.2). Two prominent, broad 'bump' features are commonly observed in quasar SEDs, irrespective of their optical luminosities. The broad UV–

optical bump is attributed to thermal emission from an accretion disk around the central SMBH. This primary emission source is thought to power many of the other emission features observed in AGN SEDs. In particular, the prominent infrared emission feature displayed in Figure 1.2 is due to reprocessed disk emission in hot dust (§1.1.5); the broad emission lines (§1.1.4) and narrow emission lines (§1.1.7) are photoionized by the extreme-ultraviolet disk emission; and the X-ray emitting regions are thought to be due to Comptonized disk photons (§1.1.3).

The accretion disk emission is commonly modeled (e.g., Capellupo et al., 2016; Davis and Laor, 2011; Raimundo et al., 2012) as a geometrically thin, optically thick accretion flow (Novikov and Thorne, 1973; Shakura and Sunyaev, 1973). For these models, the accreting gas is thermalized, and emits a multiple-temperature blackbody spectrum. The overall shape of this spectrum is roughly consistent with the observed 'big blue bump' feature. However, the detailed SED shapes, extreme UV–optical variability, and observed accretion disk sizes for AGN are not fully consistent with the thin-disk predictions.

In this Thesis, I investigate AGN accretion disk emission using disk reverberation mapping techniques (Chapters 2 and 3), and via modeling of observed quasar SEDs (Chapter 6). To provide the reader with a context for these investigations, I describe the observational characteristics expected for geometrically thin disks in more detail later in this Introduction (§1.2). I also review previous observational tests of the thin disk model via SED studies in §1.3 and via disk reverberation mapping in §1.4.3.

1.1.3   The X-ray Emitting Region

Significant X-ray emission is nearly ubiquitous in optically selected quasars (Gibson et al., 2008). The size of the X-ray emitting region is observationally constrained by variability timescales (e.g., Barr, 1986; Zamorani et al., 1984), hard-band to soft-band reverberation mapping (e.g., Chainakun et al., 2019) and gravitational micro-lensing observations (e.g., Chartas et al., 2016; Dai et al., 2010; Mosquera et al., 2013) to be of order 10 times the Schwarzschild radius. The main emission features in the X-ray SED are the hard continuum, the soft excess, and the X-ray reflection features. My work on the changing-look AGN Mrk 590 (Chapter 3) includes an analysis of the 0.3-79 keV X-ray spectrum, including modeling of X-ray reflection features and constraints on the soft X-ray excess. I also study the 0.3-10 keV spectra for a statistical sample of $z \sim 2$ quasars in Chapters 5 and 6.

The Hard X-ray Continuum

To first order, the X-ray emission is characterized as a power-law continuum extending from ~ 1 keV to several hundred keV (e.g., Nandra and Pounds, 1994). Hard X-ray observations reveal a high-energy cutoff of this continuum emission at between ~ 50 keV–250 keV (e.g., Brenneman et al., 2014; Fabian et al., 2015). Thermal accretion disk models do not in themselves produce hard X-ray emission for black holes in the SMBH mass range. Instead, the hard X-ray continuum is commonly attributed to a hot corona above and below the disk, in which seed photons from the disk are inverse-Compton scattered to X-ray energies (Ghosh et al., 2016; Haardt and Maraschi, 1993; Zdziarski et al., 1996). For a thermal distribution of hot electrons with temperature T_e and optical

depth $\tau_e < 1$, a seed photon with initial frequency ν_i will on average obtain the final frequency ν_f after traveling through the corona:

$$\nu_f = \nu_i \exp\left(\frac{4k\tau_i^2 T_e}{m_e c^2}\right). \tag{1.4}$$

Thus, a hotter corona will produce a harder X-ray spectrum (i.e., one with a larger proportion of high-energy photons). Measurements of the X-ray SED turnover constrain the electron temperature to $kT_e \sim 150$ keV (e.g., Fabian et al., 2015). The illumination provided by the X-ray corona may in turn heat the accretion disk (Haardt and Maraschi, 1993), which would cause deviations from the predicted thin-disk temperature profile (Equation 1.12). Inverse-Compton scattering also cools the corona, which must then be reheated using some fraction of the energy released in the accretion flow. Observationally, the X-ray luminosity at 2 keV (thought to be produced in the corona) is correlated with the UV luminosity (Miller et al., 2011; Steffen et al., 2006; Strateva et al., 2005; Vignali et al., 2003). The non-linear nature of this relation, where brighter AGN produce relatively less X-ray emission, may be an important clue towards understanding how accretion energy is reprocessed into the X-ray emitting region (e.g., Lusso and Risaliti, 2017). It also provides a promising method for cosmological distance measurements (Lusso and Risaliti, 2016). I examine the correlation between UV and X-ray luminosities for our $z \sim 2$ quasar sample in Chapter 6.

The Soft X-ray Excess

Many AGN display excess X-ray emission at rest-frame energies below ~ 2 keV, relative to the extrapolated X-ray continuum. Soft X-ray excess is detected in $\sim 90\%$ of sources that have sufficiently low redshifts that the rest-frame soft X-ray regime is observationally accessible (e.g., Crummy et al., 2006; Walter and Fink, 1993). Phenomenologically, the soft excess resembles a blackbody component with temperatures ~ 0.1 keV– 1 keV; the physical interpretation of this result is ambiguous. Models where the soft excess represents the high-energy end of the thermal accretion disk spectrum are disfavored due to its consistent temperature independent of black hole mass (Done et al., 2012; Miniutti et al., 2009; Porquet et al., 2004). Instead, there may be a second inverse-Compton scattering region with a cooler electron temperature ($kT_e \sim 0.3$ keV), such that a fraction of seed photons from the inner disk are scattered to hard X-ray energies, while the remainder are only scattered in the cooler region (Done et al., 2012; Jin et al., 2012; Porquet et al., 2004). This second Compton scattering region is required to be optically thick and to cover much of the UV disk (Petrucci et al., 2018); it may correspond to the disk atmosphere. Two alternative mechanisms to produce soft excess are also suggested: relativistically blurred reflection in ionized gas (Crummy et al., 2006; Ross and Fabian, 2005; Walton et al., 2013), or relativistically blurred absorption (Gierliński and Done, 2004). I discuss the variability of the soft excess component in the Changing-look AGN Mrk 590 in Chapter 3.

X-ray Reflection Features

Superimposed on the power-law X-ray continuum are emission features thought to be due to reflection in an optically thick medium. These include a Fe K emission complex at rest-frame ~ 7 keV and a broad Compton reflection hump at rest-frame energies $\gtrsim 20$ keV (e.g., Nandra and Pounds, 1994). These reflection features can occur in the ionized gas of the inner accretion disk, in which case they will be relativistically broadened and smeared due to the high rotational velocities, or in cool gas further from the black hole, which will produce only a narrow Fe K core (Nandra et al., 2007). A relativistically broadened Fe K line is observed for a few AGN, and can be used to estimate the radius of the ISCO, and thus the black hole spin (e.g., Brenneman and Reynolds, 2006; Brenneman et al., 2011; Lohfink et al., 2012; Tanaka et al., 1995; Walton et al., 2013).

The Jet Contribution to X-ray Emission

Radio-loud quasars, which emit kpc-scale radio jets (§1.1.8), have brighter X-ray continua than radio-quiet sources by a factor ~ 3 at a given UV luminosity (Miller et al., 2011; Zamorani et al., 1981). There is evidence that the radio jet itself emits X-rays (e.g., Marshall et al., 2018), which may explain this excess X-ray brightness. Indeed, Miller et al. (2011) find that the excess X-ray emission strength correlates with the radio loudness. I confirm the excess X-ray emission for radio-loud quasars in our $z \sim 2$ sample (Chapter 6). For X-ray binaries (i.e., accreting stellar-mass black holes), Markoff et al. (2005) demonstrate that the X-ray SED can be fully explained by emission from the jet and reflection in the disk, without requiring an X-ray corona. It therefore seems plausible that there is a significant contribution to the X-ray SED from the inner regions of the jet, for radio-loud quasars.

1.1.4   The Broad Line Region

Figure 1.3 shows a composite, median-combined UV-optical spectrum based on over 2200 quasar spectra at redshifts $0.04 < z < 4.8$ observed by the Sloan Digital Sky Survey (Vanden Berk et al., 2001). Most of the emission between ~ 1200 Å - 4000 Å consists of continuum emission, which is attributed to the accretion disk (§1.2). Superimposed on the UV-optical continuum, we see several emission lines, e.g., Ly-α, hydrogen Balmer lines, C IV and Mg II. This distinctive emission line spectrum is typical of Type 1 AGN. Several transitions, e.g. the hydrogen Balmer lines, display both a broad and a narrow component, while other emission lines such as [O III] display strong narrow-line emission and have only a weak broad component; I address the narrow lines in §1.1.7. In this Thesis, I model the response of the broad line emitting region (BLR) for NGC 5548 in Chapter §2. I construct these models using *1)* photoionization modeling techniques (as described below), and *2)* BLR size estimates derived from reverberation mapping (§1.4). Here, I outline our current picture of the BLR, emphasizing the photoionization physics and BLR geometrical constraints relevant to my BLR modeling work.

The broad emission lines have linewidths in excess of ~ 1200 km s^{-1} (Hao et al., 2005), and up to 25000 km s^{-1} (e.g., Peterson et al., 2004). These large velocity dispersions are likely due to bulk
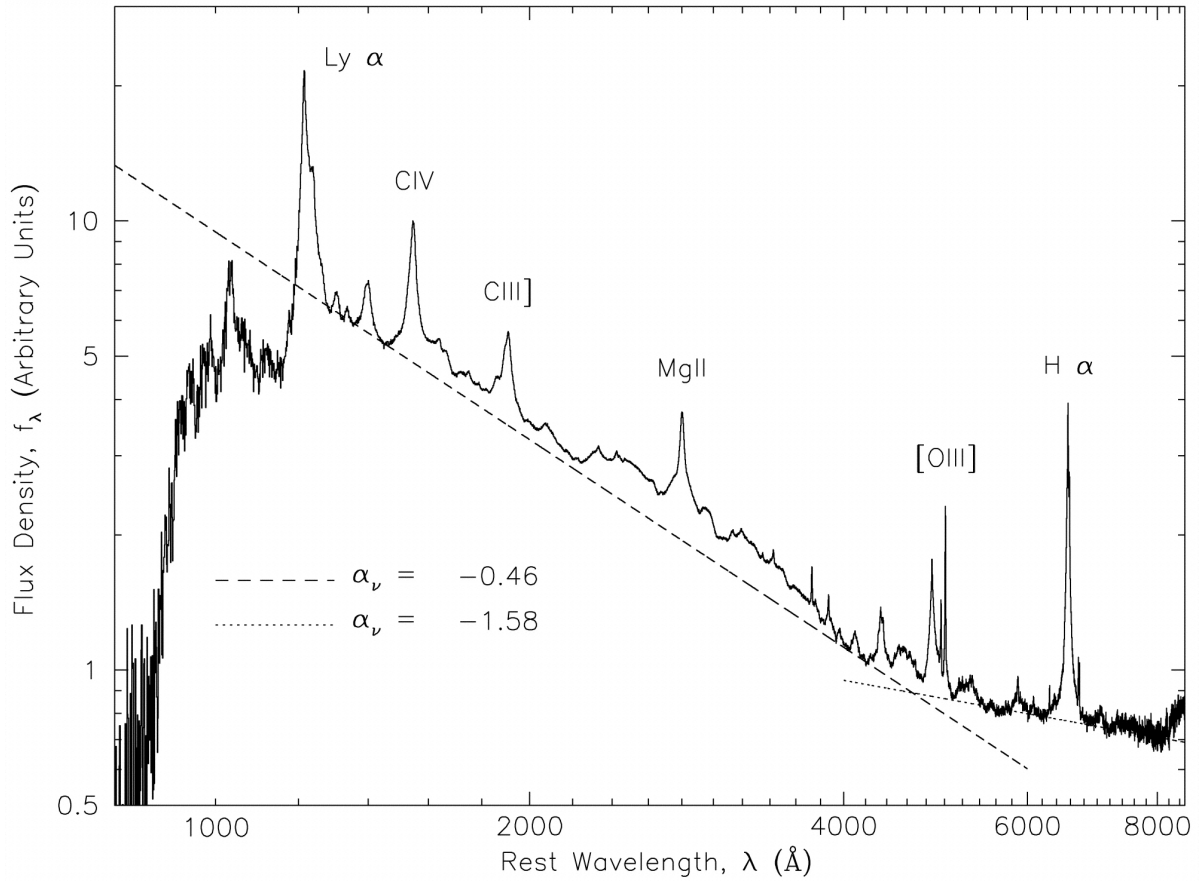
Fig. 1.3 Composite UV–optical spectrum based on over 2200 quasar spectra in the *Sloan* Digital Sky Survey (Vanden Berk et al., 2001). They fit the UV to optical continuum as a broken power-law, using 'continuum-dominated' windows assumed to be largely free of broad-line emission. The inflection at ~ 5000 Å is likely due to host galaxy stellar emission, which will be relatively stronger for the fainter AGN included in their sample. In the extreme-UV, the AGN emission is absorbed by intrinsic, intervening and Galactic neutral hydrogen. The broad emission lines are thought to be reprocessed extreme-UV continuum emission in gas clouds at distances of a few light-days (up to a few light-weeks) from the continuum source, based on reverberation mapping results. The narrow emission lines, of which [OIII] is the most prominent, are produced in a more extended region on ~ 100 pc to kpc scales. The drop-off beyond ~ 1100 Å is due to Galactic and intergalactic Hydrogen absorption.

motion in the gravitational potential close to the black hole. The broad line emitting region (BLR) is too compact to be imaged using conventional imaging techniques, and its detailed geometry is thus not well understood. Much of our understanding of the BLR is derived from reverberation mapping techniques. The BLR is stratified, with high-ionization lines generally being produced closer to the continuum source (e.g., Fausnaugh et al., 2017). The velocity field in the BLR is dominated by virial motion (e.g., Wandel et al., 1999), and often shows the kinematic signature of a thick disk (e.g., Grier et al., 2017, 2013; Horne et al., 2020). In support of this thick-disk BLR geometry, Gravity Collaboration et al. (2018) use infrared interferometry techniques to marginally resolve the hydrogen Paschen BLR for the nearby quasar 3C 273. They find that the broad line-emitting gas is undergoing ordered rotation perpendicular to the radio jet axis, with a mean radius broadly consistent with previous reverberation mapping results. Thick BLR disks might be produced by a line-driven wind (Murray and Chiang, 1995; Proga and Kallman, 2004) or dust-driven wind (Baskin and Laor, 2018; Czerny et al., 2017) arising from the outer accretion disk. The presence of a large quantity of virialized BLR gas is important, as it allows us to estimate the SMBH mass, if the radial distance of the BLR is known (§1.4.2). However, there is increasing evidence for a variety of BLR kinematics, e.g., outflowing disk winds (e.g., Dehghanian et al., 2020; Denney, 2012) and infall (e.g., De Rosa et al., 2018; Denney et al., 2009; Grier et al., 2017).

Photoionization of BLR 'clouds':   Forbidden transitions such as the [O III] line cannot be produced at densities above $n_e \approx 10^8$ cm^{-3}, due to collisional de-excitations. These forbidden lines generally produce only a weak broad component, which is usually blueshifted and may be attributed to outflowing gas (e.g., Mullaney et al., 2013). On the other hand, we see strong broad emission from permitted transitions such as e.g., the Hydrogen Balmer lines and CIV, which can be produced in high-density gas. As we do not observe strong broad forbidden-line emission, the density of the broad emission line region (BLR) must be above $n_e \approx 10^8$ cm^{-3}. The BLR is often conceived of as an ensemble of high-density 'clouds', with a covering fraction of roughly 0.3 as seen from the central source (e.g., Baldwin et al., 1995; Goad et al., 1993). Assuming discrete BEL clouds, the smoothness of the observed line profiles implies that the total number of individual clouds in the BLR is $\geq 10^6$, after taking their thermal broadening into account (e.g., Laor, 2004). These dense clouds require pressure confinement if they are not to expand and be destroyed by rotational shear in the black hole gravitational potential. Baskin and Laor (2018) demonstrate that radiation pressure confinement due to the continuum source is achieved at cloud densities of $n_e \sim 10^{10}$ cm^{-3}, consistent with the lower limit due to collisional suppression, and with the densities required to roughly reproduce the observed emission line flux for NGC 5548 (Chapter 2). Alternatively, dense clouds in the BLR may be confined by magnetic pressure (e.g., Netzer, 2020; Rees, 1987). Instead of discrete clouds, several authors suggest high-density regions in a continuous outflow as the source of BLR emission (e.g., Elvis, 2000, 2017; Matthews et al., 2020; Murray and Chiang, 1995). Unfortunately, it is more difficult to quantitatively predict the density distribution for continuous-flow models and to calculate BLR emission spectra based thereon (e.g., Matthews et al., 2020; Netzer, 2020).

The ionization parameter, $U(r)$, is an important concept for photoionization modeling of the BLR. It is defined as

$$U(r) = \frac{Q(\mathrm{H})}{4\pi r^2 c N_{\mathrm{H}}}. \tag{1.5}$$

Here, $Q(\mathrm{H})$ is the number of hydrogen-ionizing photons produced per second by the continuum source. To ionize neutral hydrogen, a photon must have an energy exceeding 13.6 eV. Thus, the ionization parameter is a unitless quantity describing the relative numbers of ionizing photons and neutral hydrogen atoms at radius r. Broadly, clouds with column densities $\sim 10^{23}$ cm^{-2} emit lines efficiently at $U \sim 0.01$, although the optimal ionization parameter depends on the particular emission line transition, and it is not possible to reproduce the observed BLR using a single value of U. At large U, the gas becomes overionized and emits weakly; if U is too low, the gas is insufficiently ionized to produce significant line emission. Thus, for any specified radial distribution of the cloud density N_{H} in the BLR, a given emission line will be produced efficiently only for a certain range of radii relative to the ionizing source. This is the idea behind the Locally Optimally-emitting Cloud model (Baldwin et al., 1995): given a broad distribution of BLR cloud densities at each radius, the observed line emission is dominated by those clouds for which the ionization parameter allows efficient line emission.

The ionization parameter provides a direct prediction of the minimum inner radius for broad line emission. At small radii, the ionization parameter exceeds $U \sim 0.1$ due to proximity to the continuum source. The BLR gas then becomes overionized and emits weakly. At the dust sublimation radius, $r_{\mathrm{sub}} \approx 0.2 \times (L/10^{46}\mathrm{erg\,s}^{-1})^{1/2}$, the continuum flux falls sufficiently to allow dust to survive. This dust absorbs UV radiation efficiently, reducing the ionization parameter such that the gas is under-ionized. The presence of embedded dust also suppresses line emission locally (Laor and Draine, 1993). Thus, while the BLR does not necessarily extend to the dust sublimation radius, it cannot extend far beyond it.

Photoionization modeling provides detailed predictions of the emission line strength generated in the BLR, for a given ionizing continuum SED. For this purpose, photoionization codes such as *Cloudy* (Ferland et al., 2013) are first used to calculate the emission spectrum from individual BLR clouds, spanning a range of densities and ionization parameters. The clouds have a fully ionized zone near the surface facing the continuum source, which shields a partially ionized zone (an excited HI zone). Thus, a single cloud can potentially produce both high-ionization lines such as Lyα, CIV and HeII, and low-ionization lines such as MgII and FeII. By assuming a BLR geometry and cloud density distribution, the integrated BLR emission can then be calculated and compared to observations. The response of the model BLR to variations in the ionizing continuum can also be studied. I perform such an analysis for NGC 5548 in Chapter 2. An important result of my analysis is that the BLR clouds also emit a significant diffuse continuum at all UV–optical wavelengths, as previously suggested by Goad et al. (1993). I demonstrate that this effect produces systematically longer observed inter-band continuum reverberation delays relative to those of the accretion disk continuum itself.

Another advantage of photoionization modeling of 'dense cloud' BLR models is that it provides valuable constraints on the unobservable extreme-UV continuum necessary to reproduce the observed line ratios and luminosities (e.g., Dietrich et al., 2002; Korista et al., 1997; Moloney and Shull, 2014).

In particular, sufficient high-energy photons are required in order to produce strong high-ionization lines. In Chapter 3 I make a rough estimate of the extreme-UV continuum in Mrk 590 using a very simple power-law model. However, for this extremely variable source, an accurate determination of the accretion luminosity would be valuable in order to investigate potential transitions in accretion state (§1.2) during the observed changing-look events. In future work, I hope to use constraints from the observed broad-line luminosities in the high-flux and low-flux states to derive a more accurate model of the extreme-UV continuum, which is an important contribution to the bolometric luminosity.

1.1.5   The Dusty Obscuring Structure

Dust grains cannot survive in the immediate vicinity of the accretion disk. The sublimation temperature for a given dust grain depends on its size and chemical composition, with graphite dust surviving at temperatures below ~ 1750 K and silicate dust surviving below ~ 1400 K (Laor and Draine, 1993). The dust sublimation radius is expected to depend on continuum luminosity as $r_{\rm sub} \propto L^{1/2}$, as supported by dust reverberation mapping (Suganuma et al., 2006, e.g.,). Beyond the dust sublimation radius, any dust structure that forms will absorb continuum and BLR emission from the inner regions. It will also suppress local BLR emission due to the photoionization considerations described above. As the dust is heated by the continuum source, it will emit blackbody radiation, which is identified with the observed AGN infrared emission bump (e.g., Barvainis, 1987). A torus-like AGN dust structure (Antonucci, 1993) explains the lack of broad emission lines in many Type 2 AGN, but can not explain the changing look AGN phenomenon discussed in §1.5 and Chapter 3. While I do not work with AGN dust emission in this Thesis, I outline the dust unification model here, in order to provide context to my work on changing-look AGN.

Type 1 and Type 2 unification via a dusty torus: Some AGN display both broad and narrow emission lines, with a bright UV-optical continuum, while others display no broad lines in direct emission, and only a weak or negligible continuum. Throughout this Thesis, I refer to sources with broad lines in their spectra as Type 1 AGN, while those without broad lines are Type 2 AGN. For historical reasons, lower-luminosity AGN are sometimes instead classed as Seyfert 1 and Seyfert 2 galaxies. Both types emit high-energy X-rays and and high-ionization narrow lines, indicating the presence of an accretion flow. Antonucci (1993) suggests a unification scheme for Type 1 and Type 2 AGN, where an optically thick (in the UV-optical) dust structure in a toroidal geometry obscures the accretion disk and BLR along sight-lines near the plane of the torus. The more extended narrow line emitting region (§1.1.7) and the dust-penetrating high-energy hard X-rays are then visible at any viewing angle. Thus, Type 1 and Type 2 sources are proposed to be intrinsically identical. Antonucci and Miller (1985) see a typical Seyfert 1-type optical spectrum, with broad Balmer line emission, in polarized, scattered light for the Seyfert 2 galaxy NGC 1068. Subsequent observations confirm that the BLR is present, but obscured, for some Type 2 AGN (e.g., Cai et al., 2010; Inglis et al., 1995; Moran et al., 2000; Young et al., 1998). The existence of so-called 'True Type 2 sources', i.e.,

sources which actually lack broad-line emitting gas, is debated (Antonucci, 2012; Elitzur, 2012; Elitzur and Netzer, 2016; Miniutti et al., 2013; Tran, 2003).

Recently, anisotropic AGN dust structures have been identified in infrared interferometry (e.g., Burtscher et al., 2016; Hönig and Kishimoto, 2017). These studies find a thin, hot dust disk in the AGN equatorial plane, along with an elongated polar dust structure that produces the bulk of the IR emission. Similarly, Alonso-Herrero et al. (2018) find evidence that the near infrared-emitting dust and the anisotropic obscuration may be due to two distinct structures, with the polar dust structure providing much of the infrared emission. Thus, the dust geometry in real AGN appears to be more complicated than the usual 'dusty torus' cartoon (e.g., Figure 1.1).

For a homogenous obscuring torus, the dust unification scheme predicts that individual objects should not transition between Type 1 and Type 2. This requirement is softened in the case of a 'clumpy' dust torus (e.g., García-Burillo et al., 2019) or a clumpy, dusty wind from the outer accretion disk (e.g., Gallimore et al., 2016). In these cases, individual dust clumps may move in or out of our line of sight, producing changes in the observed obscuration. Transitions between Type 1 and Type 2 AGN due to motion of dust clumps should display corresponding changes in the absorbing column density measured in, e.g., soft X-ray observations. Several type transitions on timescales of months to years have now been observed: the so-called changing-look AGN (§1.5. Many of these changing look events do not show evidence for variable obscuration (Denney et al., 2014; LaMassa et al., 2015), and are thus not due to the motion of clumps in the dust structure. Given that the narrow emission line region is extended (§1.1.7; Chapter 3) and will respond to continuum variations only slowly, the lack of continuum and broad-line emission in 'turn-off' changing-look AGN instead suggests the disappearance of the ionizing continuum emission (e.g., Denney et al., 2014).

In summary, while there is clear evidence for an obscuring dust structure in some Type 2 AGN, the changing-look events I work with in Chapter 3 are likely due to dramatic variations in the underlying continuum, and are not linked to changes in the dust structure.

1.1.6 Broad Absorption Lines and FeLoBAL Quasars

Approximately 15-25% of quasars display so-called broad absorption lines (BALs, Allen et al., 2011; Guo and Martini, 2019). BALs have large velocity dispersions ($\Delta v > 2000$ km s^{-1} by definition), and are highly blueshifted relative to the systemic velocity, implying high-velocity outflows. All BALs display broad absorption in high-ionization lines such as C IV. The rarer low-ionization BAL quasars (LoBALs) also display broad absorption in low-ionization lines such as Mg II. A subset of these also display strong iron absorption, and are known as FeLoBALs. The reason only a small subset of quasars display LoBAL absorption is not well understood. One suggestion is that LoBALs represent an early stage of quasar evolution, as a young quasar expels a 'cocoon' of gas and dust (e.g., Green et al., 2001; Lansbury et al., 2020; Martocchia et al., 2017; Voit et al., 1993). The onset of quasar activity may be triggered by a major galaxy merger, which would also cause intense star formation (e.g., Hopkins et al., 2005; Wethers et al., 2020). In Chapter 4 I test this evolutionary

scenario for FeLoBAL quasars, via a comparison of the star formation properties of FeLoBAL host galaxies with those of non-BAL quasar hosts.

Elvis (2000) present a disk-wind model for the broad line region, which offers an alternative explanation for BAL absorption features. In this scenario, the appearance of BAL absorption for a given quasar depends on our viewing angle: we observe broad absorption when our line of sight to the continuum source lies along the outflowing wind. Indeed, many of the observed features of BAL absorption lines are reproduced in simulations of a clumpy biconical disk wind (Matthews et al., 2016; Murray and Chiang, 1995). Models where BAL and non-BAL quasars are intrinsically identical are supported by the similarity of their mid-infrared SEDs (Gallagher et al., 2007; Schulze et al., 2017) and emission line properties (Weymann et al., 1991). Observations of strongly variable BAL absorption on timescales of a few years (e.g., Gibson et al., 2010; Vivek et al., 2014; Yi et al., 2019; Zhang et al., 2015) are currently not well understood, but may imply a clumpy BAL-absorbing region rotating with the disk, or may be due to changes in the ionization state of the absorbing gas (De Cicco et al., 2018; Wang et al., 2015).

The evolutionary and orientation-dependent explanations for BAL absorption make different predictions for their host galaxy morphologies and star formation rates. If FeLoBAL absorption depends only on the orientation of the central engine relative to our line of sight, their host galaxy star formation rates should be statistically indistinguishable from those of non-BAL host galaxies. If instead the BAL quasars represent the merger-triggered onset of quasar activity in a 'blowout phase', we expect to see evidence of merger-triggered star formation activity. We do not find enhanced starburst activity for the FeLoBAL host galaxies relative to a comparison sample of non-BAL quasars at similar luminosities (Chapter 4). However, the available *Hubble Space Telescope* imaging data cannot exclude strongly star-forming galaxies with moderate amounts of dust reddening. Thus, our results are consistent with either the 'evolutionary' or the 'orientation' scenarios. Future sub-mm observations of star formation in (FeLo)BAL host galaxies will hopefully settle this issue.

In principle, an investigation of morphological features related to recent major merger activity (i.e., tidal tails, multiple galaxy bulges, and other deviations from a Sersic luminosity profile) of FeLoBAL and non-BAL host galaxies would be a valuable complimentary test of the merger hypothesis. Unfortunately, our simulations show that detailed morphological studies are unreliable for these $0.8 < z < 2$ quasars, given the available data. Quasar host galaxies at these redshifts appear very faint in the rest-frame optical, and the images are dominated by the point spread function of the AGN emission component. For our observations, the inherent difficulties in separating the AGN and stellar components are compounded by the lack of dedicated stellar observations to determine the instrumental point spread function during the observations. I discuss these challenges in greater detail in Chapter 4.

1.1.7   The Narrow Line Region

Both Type 1 and Type 2 AGN display narrow emission lines with ionization potentials too high-energy to be excited by starlight. I do not study the narrow emission lines in this Thesis; for
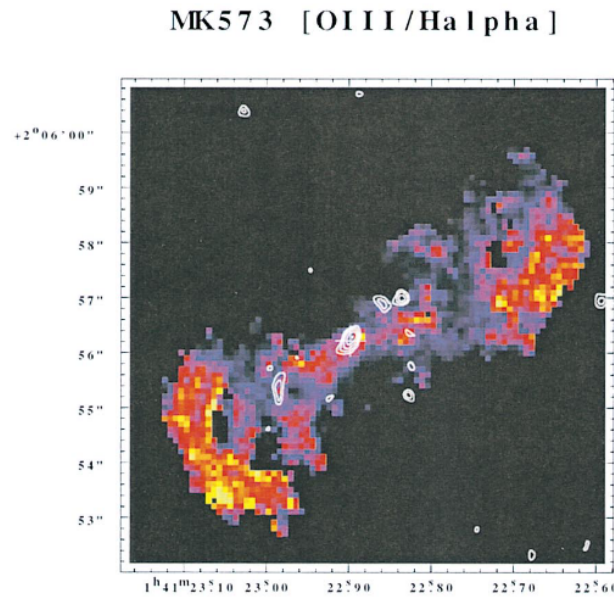
MK573 [OIII/Halpha]

Fig. 1.4 Ionization map showing the ratio of [OIII] to $H\alpha$ emission for the Type 2 AGN Mrk 573. The overlaid white contours indicate the radio emission. As the [OIII] emission line requires a hard AGN-like ionizing continuum to excite it, the 'butterfly' shape of this ionization map is interpreted as evidence that the continuum source is obscured by a torus-like dust structure. This figure is taken from Falcke et al. (1998).

completeness, I briefly mention some key results relevant to our current understanding of AGN structure here.

The narrow emission lines are ionized by the continuum source, but the physical conditions in the narrow line-emitting region are very different from the BLR. The lower velocity dispersions for the narrow lines indicate that they are produced further out from the central black hole. Narrow lines are produced both in forbidden transitions, such as [O III], and in permitted transitions such as the Balmer lines. The forbidden-line emission indicates that the gas is too diffuse for collisional de-excitation to occur (e.g., Netzer, 2013). Thus, the narrow line-emitting region is less dense than the BLR, and extends further into the host galaxy. For Type 2 AGN, resolved [O III] emission often extends to kpc scales (Figure 1.4), and occasionally displays a well-defined bi-conical geometry (e.g., Fischer et al., 2013; He et al., 2018; Pogge, 1988a,b; Schmitt et al., 2003). Also, the narrow-line emission is often extended along the radio axis in cases where extended radio emission is observed (Haniff et al., 1988; Nagar et al., 1999). These observations are consistent with the Type 1 and Type 2 unification scheme (§1.1.5), in that the ionizing continuum emission is absorbed by the dust torus along our line of sight, but is unabsorbed along the rotational axis of the central engine.

1.1.8   The Radio Jet

Sandage (1965) discovered that, for every 'quasi-stellar radio source', there were $\sim$10 sources with similar optical properties that were not detected in radio waves. Today, we use the labels *radio-loud quasars* and *radio-quiet quasars*, or more generally, radio-loud or -quiet AGN. In Chapters 5 and

6, I present optical–UV–X-ray spectral energy distributions for a statistical sample of radio-quiet and radio-loud quasars. Our sample is selected so as to approximately match the radio-loud and radio-quiet sources in terms of redshift and V-band luminosity, thus allowing a robust comparison of the spectral energy distributions for the two radio classes. I find that radio-loud and radio-quiet quasars have statistically indistinguishable UV-optical SEDs for this matched sample. I also confirm the previously discovered factor ~ 3 excess of unresolved X-ray emission for radio-loud quasars relative to radio-quiet sources at a given UV luminosity (e.g., Miller et al., 2011; Zamorani et al., 1981; Zhu et al., 2019). Most of this excess hard X-ray emission for radio-loud AGN is unresolved, and is thought to be due to processes in a small-scale radio jet near the black hole (e.g., Miller et al., 2011; Zamorani et al., 1981; Zhu et al., 2019).

Radio-loud AGN are typically defined as having $R > 10$, where R is the ratio of radio flux density to optical flux density. While obscured RLQs may be observed as powerful radio galaxies (Barthel, 1989), RQQs cannot be explained as unbeamed, intrinsically radio-loud sources, but represent a physically distinct class (e.g., Kellermann et al., 2016). Radio imaging reveals that RLQs launch spectacular kpc- or Mpc-scale jets (Figure 1.5). Very Long Baseline Interferometry techniques confirm that these jets extend down to $\sim$pc scales near the central black hole (e.g., Lister et al., 2016; Readhead et al., 1978). The reason that only $\sim 10\%$ of quasars launch a jet is not well understood. Electromagnetic interactions between a Kerr black hole and an accretion disk can power relativistic jets (Blandford and Payne, 1982; Blandford and Znajek, 1977; Narayan et al., 2014). This mechanism requires rapidly rotating black holes (Maraschi et al., 2012), and may additionally require that a strong magnetic field is formed in the accretion disk by external processes (Cao, 2016). The black hole spin affects the predicted disk spectrum for thin-disk models (§1.2), suggesting that the UV-optical SEDs for radio-loud AGN may deviate from those of radio-quiet AGN; however, I find no evidence for this in our V-band luminosity matched $z \sim 2$ sample. On the other hand, Schulze et al. (2017) find evidence for radio-loud quasars having stronger ionizing continua at a given mass accretion rate, which supports the suggestion that quasars with radio jets have more rapidly spinning black holes. Schultze et al. find this result based on accretion rate estimates using the optical continuum level, assuming an accretion disk SED with $F_\nu \propto \nu^{1/3}$; I discuss opportunities to investigate the black hole spin of RLQs and RQQs using an SED fitting method for our $z \sim 2$ sample in Chapter 5.

1.1.9   The Host Galaxy

Supermassive black holes reside at the very centers of virtually all massive galaxies (Magorrian et al., 1998; McConnell and Ma, 2013). The black hole masses correlate with various proxies for the host galaxy bulge mass, such as the bulge stellar luminosity (Magorrian et al., 1998) and infrared luminosity (Marconi and Hunt, 2003). The most well-studied of these relationships is the black hole mass – bulge stellar velocity dispersion, or M_{BH}–σ_*, relationship (e.g., Baldassare et al., 2020; Ferrarese and Merritt, 2000; Gebhardt et al., 2000; Gültekin et al., 2009; McConnell and Ma, 2013). More massive black holes reside in galaxies with a larger bulge stellar velocity dispersion, which implies an underlying relationship between black hole mass and bulge mass (e.g., Ferrarese

Fig. 1.5 Composite *Hubble Space Telescope V*- and *I*-band imaging, and Very Large Array radio imaging (purple) of the AGN 3C 348. For this radio-loud quasar, the kpc-scale radio jets extend far beyond the host galaxy stellar component. Image credit: NASA, ESA and the Hubble Heritage Team.

and Ford, 2005). This relationship is observed for both spiral and elliptical galaxies (Baldassare et al., 2020). As the luminosity from a thin accretion disk scales with black hole mass (§1.2), the $M_{BH}-\sigma_*$ relationship implies that bright quasars reside in bulge-dominated elliptical galaxies, while lower-luminosity AGN are found in disk-dominated galaxies. This prediction is borne out by AGN host galaxy studies at low redshifts (e.g., Dunlop et al., 2003; McLeod and McLeod, 2001; Seyfert, 1943; Silverman et al., 2009) and is at least consistent with the results of high-redshift studies, for which the host galaxy modeling results are more uncertain (e.g., McLeod and Bechtold, 2009; Targett et al., 2012). The physical mechanism that produces the observed correlations between host galaxy bulge and black hole mass are not well understood; various feedback mechanisms between black hole accretion, outflows, and star formation are suggested (e.g., Barai et al., 2014; Begelman and Nath, 2005; Ciotti and Ostriker, 2001; Ciotti et al., 2010; Hopkins et al., 2005).

In Chapter 4 I study the host galaxies of four Iron broad absorption line quasars (FeLoBALs; §1.1.6), testing a scenario suggested by Voit et al. (1993), where FeLoBAL absorption is a sign of a young, merger-triggered quasar during a 'blowout phase' (e.g., Hopkins et al., 2005; Sanders et al., 1988). The role of galaxy mergers in triggering AGN activity is, however, debated. Mergers are suggested as a way to force large reservoirs of gas towards the black hole (Barnes and Hernquist, 1991; Hopkins et al., 2005; Sanders et al., 1988). In this framework, quasar host galaxies may be expected to show signs of recent interactions and/or merger-triggered star formation, depending on the timescales involved. However, quasars at $z < 0.25$ have elliptical host galaxies with similar colors to quiescent ellipticals (Dunlop et al., 2003), and do not display excess signs of galaxy interactions relative to the quiescent population (Zhao et al., 2019). Treister et al. (2012) find evidence of a heightened merger rate (relative to the quiescent galaxy population) only for the most luminous AGN. Glikman et al. (2018) find that roughly 30% of quasars are highly reddened, and that these red quasars have high intrinsic luminosities. They suggest that the red quasars represent the 'blowout phase' during the early stages of quasar activity. It is not clear how FeLoBAL quasars fit into this scenario. Glikman et al. (2012) find an excess of FeLoBAL quasars in their red quasar sample; however, this may simply be due to FeLoBAL absorption and large-scale dust reddening producing

similar color distributions. Several studies find evidence for starburst activity in FeLoBAL host galaxies (e.g., Farrah et al., 2007, 2012; Pitchford et al., 2019), while Violino et al. (2016) find that FeLoBALs have sub-millimeter spectral energy distributions consistent with non-BAL quasars, suggesting similar star formation rates. (Villforth et al., 2019) find no morphological evidence for recent merger activity in FeLoBAL hosts.

My results for the FeLoBAL host galaxy UV and optical luminosities are consistent with them having moderate star formation rates, similar to non-BAL quasars in the same AGN luminosity range. However, our *Hubble Space Telescope* observations do not constrain the dust reddening in the host galaxy; it is possible that the FeLoBAL hosts have enhanced star formation rates that are obscured by UV dust absorption. I am only able to constrain the overall rest-frame UV and optical luminosities of the FeLoBAL hosts, while our observations are not sensitive to either the overall host galaxy morphology (as parameterized by the Sersic luminosity profile) or to detailed morphological features such as tidal tails. The main difficulty is in decomposing the bright point-source component due to the AGN emission and the faint extended component due to the host galaxy. I discuss these technical issues at length in Chapter 4.

1.2 Theoretical Accretion Disk Models

The UV–optical emission bump observed in observed AGN spectral energy distributions (§1.1.2) is generally attributed to direct emission from an accretion disk. The disk emission provides the ionizing continuum for the broad and narrow emission lines, and is also thought to provide seed photons for the X-ray emission regions. The physical processes in the accretion flow itself - and their dependencies on black hole mass, spin, and accretion rate - are therefore of key importance for our overall understanding of AGN activity. Here, I highlight those predictions of theoretical disk models that I work with in this Thesis. I compare the emission spectrum of theoretical accretion disk models with the observed spectral energy distributions of quasars in Chapter 6. I also test the theoretical disk sizes with those derived from continuum reverberation mapping (Chapters 2 and 3).

1.2.1 Geometrically Thin Accretion Disks

The most simple model for gas accretion onto a compact object is the spherically symmetrical case, so-called Bondi accretion (Bondi, 1952). However, for a SMBH, gas accreted from the host galaxy will have a non-zero angular momentum. The accretion flow is therefore expected to form some kind of rotating disk. The most analytically tractable solutions for a disk accretion flow are the *thin-disk* models, originally derived by Shakura and Sunyaev (1973) for Schwarzschild black holes, and by Novikov and Thorne (1973) for Kerr black holes. These models have a temperature-stratified, geometrically thin and optically thick disk which produces a bright, blue thermal continuum similar (at least to first order) to the observed AGN continuum. Due to their analytical simplicity (relative to other accretion disk models), and their rough correspondence to the observed continua, thin-disk models are commonly used to estimate AGN mass accretion rates and black-hole spin (e.g., Capellupo et al., 2016; Davis and Laor, 2011; Raimundo et al., 2012). The theoretical basis for the

thin-disk properties that I describe here are derived in detail in the textbooks by Choudhuri (1998) and Netzer (2013).

Viscosity Parameterization for Thin Disks: For the thin-disk models due to Shakura and Sunyaev (1973) and Novikov and Thorne (1973), angular momentum is removed from the gas in the disk via some form of local viscosity. The physical mechanisms that produce this viscosity are not fully understood. Inter-molecular forces in the gas do not produce sufficient viscosity to yield the observed accretion rates for bright AGN. Theoretical work (Balbus and Hawley, 1991) and simulations (e.g., Hawley and Balbus, 1991; Hogg and Reynolds, 2018) point towards turbulence due to a magneto-rotational instability as the dominant source of viscosity. In the thin disk models, the local viscosity ν is parameterized

$$\nu = \alpha h c_s. \tag{1.6}$$

Here, c_s is the local sound speed, h is the disk scale height, and the parameter α determines the efficiency of angular momentum transfer. This parameter also sets the so-called viscous timescale, i.e., the rate at which changes in the accretion rate can propagate through the disk. For accretion onto supermassive black holes, assuming a typical viscosity parameter $\alpha = 0.1$, the viscous timescale is approximately 4×10^5 years (Noda and Done, 2018). According to the thin-disk model, large changes in the accretion luminosity should occur only on timescales of thousands of years. This prediction is at odds with the observed short-timescale UV variability of AGN. In particular, it cannot explain the dramatic variability displayed by changing-look AGN (§1.5). In Chapter 3 I present observations of an AGN for which the accretion disk emission reappears over only a few years, with a factor ~ 3 increase from a very low level on a timescale of only a few weeks. Such extreme short-timescale variability presents a significant challenge to the thin-disk models (Dexter and Begelman, 2019; Lawrence, 2018; Noda and Done, 2018).

Energy Release in the Accretion Disk: Gas with negligible self-gravity moving in a circular Keplerian orbit of radius r around a central black hole of mass M_{BH} has an angular velocity Ω given by

$$\Omega = \left(\frac{GM_{\mathrm{BH}}}{r^3}\right)^{1/2}. \tag{1.7}$$

The dependence on r implies that the kinetic energy of the gas increases as it approaches the black hole. In the thin-disk model, the accreting gas is explicitly assumed to follow Keplerian orbits. Disks where radiation pressure is non-negligible in the radial direction might therefore deviate from the thin-disk predictions; I discuss models with radiation pressure support in §1.2.3.

The total available mechanical energy for infalling gas is the sum of its rotational kinetic energy and the gravitational potential energy. For a gas ring of thickness dm, the gravitational potential energy is equal to

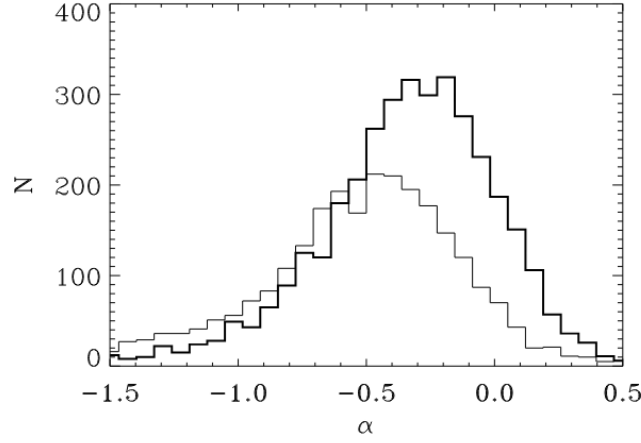$$E_{\mathrm{pot}} = -GM_{\mathrm{BH}}\frac{\mathrm{d}m}{r}. \tag{1.8}$$

Fig. 1.6 Histograms of the observed UV spectral index, α, for two quasar samples. The thin solid curve shows the distribution of α measured between 1450–2200 Å for quasars at redshifts $1.67 < z < 2.09$. The thick solid curve shows the distribution of α measured between 2200–4000 Å for quasars at $0.76 < z < 1.26$. The prediction of the thin-disk approximation is $\alpha \approx 0.3$; the observed spectra are much more shallow. This figure is taken from Davis et al. (2007).

The viscous interactions (parameterized by α as defined above) convert a fraction of the available mechanical energy in the accretion flow into heat, which ultimately is emitted as the thermal continuum radiation. For the thin-disk approximation, and assuming no torque on the disk from within the innermost stable circular orbit, the differential luminosity dL_r emitted per unit radius r due to the dissipation of mechanical energy is

$$\frac{dL_r}{dr} = \frac{3GM_{\mathrm{BH}}\dot{M}}{2r^2}\left(1 - \sqrt{\frac{r_{\mathrm{ICSO}}}{r}}\right). \tag{1.9}$$

Here, r_{ICSO} is the radius of the innermost circular stable orbit (ISCO), which depends on the black hole spin parameter, a_*. The luminosity at a given radius scales linearly with the accretion rate, $\dot{M}$. Integrating this expression over all disk radii to r_{ISCO} yields an expression for the total accretion luminosity of the thin disk:

$$L_{\mathrm{acc}} = \frac{G\dot{M}M_{\mathrm{BH}}}{2r_{\mathrm{ISCO}}}. \tag{1.10}$$

Thus, the accretion luminosity depends on the black hole mass, the accretion rate, and the radius of the ISCO. The accretion luminosity is exactly half of the total available power; the remainder of the gravitational potential energy as measured at infinity is converted into kinetic energy of the accreted material at the ISCO.

The Temperature Profile and Disk Size: In order to assess the disk sizes derived from continuum reverberation mapping (Chapters 2 and 3) in the context of the thin-disk model, I require a prediction of the accretion disk radii at which a given wavelength is emitted. The thin-disk models emit locally as blackbodies, with a radially stratified temperature structure. Thus, the far-UV emission is primarily due to the hottest regions of the disk, while the optical emission is primarily due to cooler regions.

Given the expression for the emission luminosity as a function of radius (Equation 1.9), and assuming that the disk emits equal amounts of energy from the top and bottom surfaces, the surface emissivity is given by

$$D(r) = \frac{3GM_{\mathrm{BH}}\dot{M}}{8\pi r^3}\left(1 - \sqrt{\frac{r_{\mathrm{ICSO}}}{r}}\right). \tag{1.11}$$

Assuming that the disk emits locally as a blackbody, the resulting temperature profile is:

$$T(r) = \left[\frac{3GM_{\mathrm{BH}}\dot{M}}{8\pi\sigma r^3}\left(1 - \sqrt{\frac{r_{\mathrm{ICSO}}}{r}}\right)\right]^{1/4}, \tag{1.12}$$

where σ denotes the Stefan-Boltzmann constant relating surface emissivity to temperature. Thus, the inner disk has the highest temperature, and the temperature decreases with radius as $T(r) \propto r^{-3/4}$. The overall scaling depends on the accretion rate as $\dot{M}^{1/4}$, i.e., the disk temperature increases gradually with accretion rate for a given black hole mass and spin. For supermassive black holes, the maximum disk temperature is $\sim 10^5$ K. The resulting spectral energy distribution for this disk is calculated by using the Planck law to determine the SED emitted by each radial annulus, and integrating from r_{ISCO} to the outer radius. The disk temperature profile then provides a connection between the disk size scales and emission wavelengths, which I use in the analysis of continuum reverberation mapping data (§1.4.3).

The temperature profile $T(r) \propto r^{-3/4}$ translates into a spectral index $F_\nu \propto \nu^{1/3}$ for the UV-optical continuum of thin accretion disks. However, the observed UV continua of AGN are generally more shallow than $F_\nu \propto \nu^{1/3}$ (Figure 1.6, Cheng et al., 2019; Davis et al., 2007). I discuss this discrepancy in §1.3. For the catalog of quasar SEDs presented in this Thesis, the continuum spectral indices are also more shallow than those predicted by the thin-disk model (Chapter 6).

Examples of Relativistic Thin-Disk Spectra: The above temperature and luminosity profiles are based on the Newtonian derivations for energy release in the disk, and become increasingly inaccurate in the inner regions. The dependence on r_{ISCO} in the Newtonian expressions already indicates that the black hole spin will affect the accretion luminosity, as a co-rotating black hole has a smaller ISCO. In practice, the full relativistic treatment is required for low-mass and/or rapidly spinning black holes. To illustrate the effect of black hole spin on the disk emission, I present Novikov-Thorne disk model SEDs in Figure 1.7. The disk SEDs are generated using the Novikov and Thorne (1973) disk model, including the hydrostatic equilibrium corrections presented by Riffert and Herold (1995), which modify the scale height of the disk. I generate the model SEDs using numerical code provided by Sandra Raimundo. The black hole spin is parameterized as a_*, i.e., the ratio of the angular momentum of the black hole to its mass; a maximally spinning black hole has $a_* \approx 0.998$ (Novikov and Thorne, 1973). Negative values of a_* correspond to retrograde black hole spin compared to the accretion disk rotation. The overall flux level is larger, and the SED turnover is located at higher energies, for rapidly co-rotating black holes. I compare these models to observed SEDs in Chapter 6.
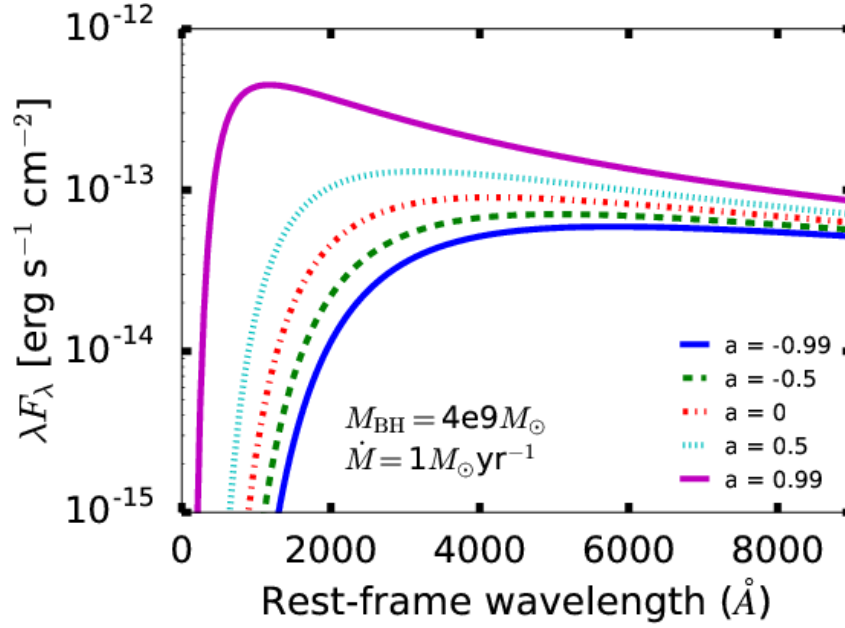
Fig. 1.7 The SED emitted by a Novikov-Thorne disk for a range of black hole spins, ranging from near-maximally spinning ($a = 0.99$, solid magenta curve) to near-maximally counter-rotating ($a = -0.99$, solid blue curve). The black hole mass is $4 \times 10^9 M_\odot$ in all cases, and the mass accretion rate is $\dot{M} = 1 M_\odot$ yr^{-1}. The disk inclination is $30°$.

The Radiative Efficiency: Conversion of gravitational energy into radiation via an accretion disk is a highly efficient source of energy, albeit somewhat impractical for humans to harness! The efficiency of the accretion process is parameterized as the radiative efficiency η, where

$$L_{\mathrm{acc}} = \eta \dot{M} c^2. \tag{1.13}$$

Here, L_{Edd} denotes the accretion luminosity, i.e., the bolometric luminosity released by the accretion flow, which for thin disks is given by Equation 1.10. Thus, $\eta = 1$ corresponds to the complete conversion of mass into energy. In the thin-disk approximation, the radiative efficiency depends on the accretion rate and black hole spin, with the highest efficiencies requiring a maximally spinning black hole, while the predicted efficiency is $\eta \sim 0.05$ in the Schwarzschild case. Accounting for various relativistic effects and physical effects in the inner disk, including the torque due to magnetic field lines connecting the event horizon to the disk, (Agol and Krolik, 2000) demonstrate that $\eta \lesssim 0.36$ for steady-state thin disks. While higher efficiencies may be possible in non-steady-state situations, they will result in the black hole losing angular momentum (Blandford and Znajek, 1977). The efficiencies for accretion onto a black hole greatly exceed that of nuclear hydrogen fusion in stars, which is of order 0.7%. The radiative efficiency is not directly observable, as it depends on an estimate of the accretion rate $\dot{M}$, which itself is model-dependent. One way to estimate the accretion luminosity for thin-disk sources is to measure the monochromatic luminosity at sufficiently low energies that the continuum emission follows the predicted $F_\nu \propto \nu^{1/3}$ low-energy slope (Davis and Laor, 2011; Raimundo et al., 2012). These estimates additionally require a determination of the

black hole mass. In Chapter 6 I demonstrate that the radiative efficiency is poorly constrained by the available data for our $z \sim 2$ quasar catalog.

1.2.2   The Eddington Limit, and its Relevance to AGN Activity

In the context of the stability of stars against radiation pressure, Eddington (1917) found a limit at which the radiation pressure on a gas equals the force of gravity, assuming spherically symmetric emission. This limit is also relevant to spherically symmetric accretion, as radiation pressure will halt any further accretion as the luminosity increases. For fully ionized hydrogen, the gravitational force on each proton-electron pair is approximately equal to

$$F_{\mathrm{g}} \approx \frac{M_{\mathrm{BH}} m_{\mathrm{p}} G}{R^2}, \tag{1.14}$$

where m_{p} is the proton mass and R is the distance from the center of mass. As photons primarily interact with the electrons, the force due to radiation pressure is

$$F_{\mathrm{rad}} \approx \frac{\sigma_{\mathrm{e}} L}{4 \pi c R^2}, \tag{1.15}$$

where σ_{e} is the Thomson cross-section for the electron. At the Eddington limit, these two forces are equal, and the Eddington luminosity L_{E} is given by

$$L_{\mathrm{E}} = \frac{4 \pi c M_{\mathrm{BH}} m_{\mathrm{p}} G}{\sigma_{\mathrm{e}}}. \tag{1.16}$$

While the above derivation is for Thomson scattering on pure ionized hydrogen, a similar expression can be found for different gas compositions, and considering alternative sources of opacity. The Eddington luminosity ratio λ_{Edd} is defined as

$$\lambda_{\mathrm{Edd}} = \frac{L_{\mathrm{acc}}}{L_{\mathrm{Edd}}}, \tag{1.17}$$

where the accretion luminosity for thin-disk models is given by Equation 1.10. Importantly, the thin-disk solutions are only valid at Eddington luminosities exceeding $\lambda_{\mathrm{Edd}} \sim 0.01$ (e.g., Narayan et al., 2014). In Chapter 3 I present observations of a flare-up event in the changing look AGN Mrk 590, for which the Eddington luminosity crossed this threshold, potentially transitioning to a thin-disk type accretion flow with a thermal UV continuum.

Determination of the Eddington ratio depends on the black hole mass, M_{BH}, and the bolometric equivalent isotropic-emission accretion luminosity. Given the thin geometry assumed for accretion disks, the observed luminosity depends on our viewing angle to the disk, which is often poorly constrained by the data (e.g., Raimundo et al., 2012). Black hole mass estimates are also generally only constrained to within a factor ~ 4–5 (Vestergaard and Peterson, 2006) for distant quasars. As both these quantities are difficult to measure observationally, measurements of λ_{Edd} for individual AGN are fraught with large uncertainties. However, studies of statistical samples of quasars generally find accretion luminosities corresponding to $\lambda_{\mathrm{Edd}} \leq 1$ (e.g., Kollmeier et al., 2006; McLure and Dunlop, 2004). Low Eddington ratios correspond to low luminosities, so flux-limited surveys are

biased against detecting sources with low Eddington ratios; Jones et al. (2016) estimate that the majority of AGN (including low-luminosity AGN) have $\lambda_{\rm Edd} \sim 0.01$ when the observed samples are corrected for this bias. Kelly et al. (2010) find that the Eddington ratio distribution peaks at ~ 0.05 for Type 1 quasars in the SDSS. I discuss the distribution of $\lambda_{\rm Edd}$, and its associated uncertainties, for our $z \sim 2$ quasar sample in Chapter 6.

The Eddington luminosity provides a limit on the mass accretion rate for spherical accretion,

$$\dot{M}_{\rm Edd} = \frac{L_{\rm Edd}}{\eta c^2}, \tag{1.18}$$

where η is the mass-to-luminosity conversion efficiency (Equation 1.13). However, accretion disks are not spherically symmetric. For a disk geometry, mass outflow and/or electromagnetic radiation may preferentially be directed along the rotation axis, whereas the mass infall happens in the disk plane. Also, while thin-disk solutions have $\dot{M}_{\rm Edd} \propto \dot{L}_{\rm Edd}$, advection-dominated accretion flows may have mass accretion rates larger than inferred from their accretion luminosities. For these reasons, the Eddington limit does not represent an absolute limit on AGN accretion rates. In the context of AGN studies, it is most usefully regarded as a measure of the accretion rate normalized by the black hole mass. For example, a low-mass AGN might be accreting at a slower absolute rate than a massive quasar, yet be accreting closer to the Eddington rate.

Nevertheless, $\lambda_{\rm Edd}$ does appear to have a physical significance for quasars. This can firstly be inferred from the rarity of super-Eddington AGN (e.g., Kollmeier et al., 2006; McLure and Dunlop, 2004). Also, the Narrow-line Seyfert 1 AGN, initially defined spectroscopically as sources with $H\beta$ broad emission line widths less than 2000 km s^{-1} (Osterbrock and Pogge, 1985), appear to be distinct in terms of their accretion properties, with low black hole masses and large Eddington ratios (e.g., Mathur, 2000; McLure and Dunlop, 2004). This may be due to them being young AGN in a rapid growth phase (e.g., Williams et al., 2018), although Viswanath et al. (2019) suggest that their black hole masses may instead be underestimated. Collin and Kawaguchi (2004) find that Narrow Line Seyfert 1 sources are accreting at $\dot{M}/\dot{M}_{\rm Edd} \gg 1$, whereas their luminosities saturate at a few times the Eddington ratio, consistent with slim-disk models (discussed below). In summary, while super-Eddington accretion is possible for AGN, the Eddington ratio (viewed as a normalized accretion rate) is still a useful diagnostic of AGN accretion.

1.2.3   Alternatives to thin-disk models

While commonly used and analytically tractable, the thin-disk models described above may not be applicable to all (or any) AGN, for several reasons. Firstly, the thin-disk approximations themselves break down at both low and high accretion rates. At accretion rates corresponding to $\lambda_{\rm Edd} < 0.01$, the accretion flow may become optically thin and geometrically thick. The *advection-dominated accretion flow* (ADAF) model (Narayan et al., 1998) is more appropriate in these cases. For ADAF disks, the density of the accreting gas is too low for it to cool radiatively, and thermal energy is instead advected onto the black hole, producing a much weaker optical-UV emission from the disk. The nearby low-luminosity AGN in M81 is a candidate ADAF source, as it displays a bright, compact X-ray source characteristic of AGN accretion, but shows no evidence for a thin, radiatively efficient

disk (Young et al., 2018, 2007). The changing look AGN that I study in Chapter 3 also displayed no AGN emission in the UV during its low state, while still emitting in the X-rays, consistent with an ADAF disk. On the other hand, for Eddington ratios exceeding $\lambda_{\rm Edd} \approx 0.3$, real accretion disks may also diverge from the thin-disk approximation. At these high accretion rates, the scale height of the disk ceases to be small relative to its radial extent. These 'slim disks' (Abramowicz et al., 1988, 1997) become radiatively inefficient as the thermal emission is trapped in the thick, advective inner disk. At high accretion rates, the slim-disk models produce outflows from the disk surface (Feng et al., 2019), which require 3D magneto-hydrodynamical simualtions to fully capture (e.g., Kitaki et al., 2018). Both the ADAF and the slim-disk models are under-luminous compared to the thin-disk prediction for a given accretion rate, and the relationship $\dot{M}_{\rm Edd} \propto \dot{L}_{\rm Edd}$ no longer holds, due to the advective nature of the accretion flow.

Secondly, even for AGN that are accreting in the intermediate regime for which the thin-disk approximation is applicable, a key prediction of the thin-disk model is not yet confirmed observationally. Namely, the thin-disk continuum SED has a spectral turnover at an energy determined by the ISCO radius, and thus by the black hole mass and spin. Observed AGN spectra, however, display a remarkably consistent SED turnover at wavelengths $\sim 1000\,{\rm \AA}$ (Shang et al., 2005; Stevans et al., 2014), irrespective of inferred black hole mass. Several authors suggest modifications to the 'naked' slim-disk model in order to explain the observed spectral turnovers. These suggestions include Comptonization in the disk atmosphere (Done et al., 2012; Hubeny and Hubeny, 1997), line-driven disk winds that moderate the temperature of the inner disk (Laor and Davis, 2014), and truncation of the inner thermal disk (Done et al., 2012). I discuss this issue further in §1.3.3.

Finally, as discussed above, the thin-disk models predict large variations in UV–optical luminosity only on the viscous timescale. Currently, the short-term UV–optical variability is best explained as being due to reprocessing of X-ray luminosity variations that are thermalized and heat the disk (§1.4.3). However, changing look AGN present a challenge to this explanation, as the disk emission is observed to fully disappear. In that case, the reprocessing scenario would require that the disk itself is only heated by X-rays and does not otherwise emit strongly in the UV, which is inconsistent with thin-disk models.

In summary, thin-disk models are likely only appropriate at intermediate accretion rates, and even in the appropriate accretion regime, they may not capture all the relevant physical processes at play in real AGN disks.

1.3   Observed Spectral Energy Distributions (SEDs)

In Chapters 5 and 6, I present broad-band UV–optical–X-ray spectral energy distributions for a statistical sample of radio-loud and radio-quiet quasars. I use these SEDs to ascertain whether this sample is representative of typical $z \sim 2$ quasars. I also investigate potential differences in the SED shapes of radio-loud and radio-quiet sources, as predicted if jetted quasars require higher black hole spins (§1.1.8). I use the SEDs to estimate the accretion luminosities for these quasars, and investigate whether our *Swift* observations constrain thin-disk model parameters (§1.2). Here, I discuss the use of broad-band SED studies as probes of AGN central engines, in order to contextualize my work on
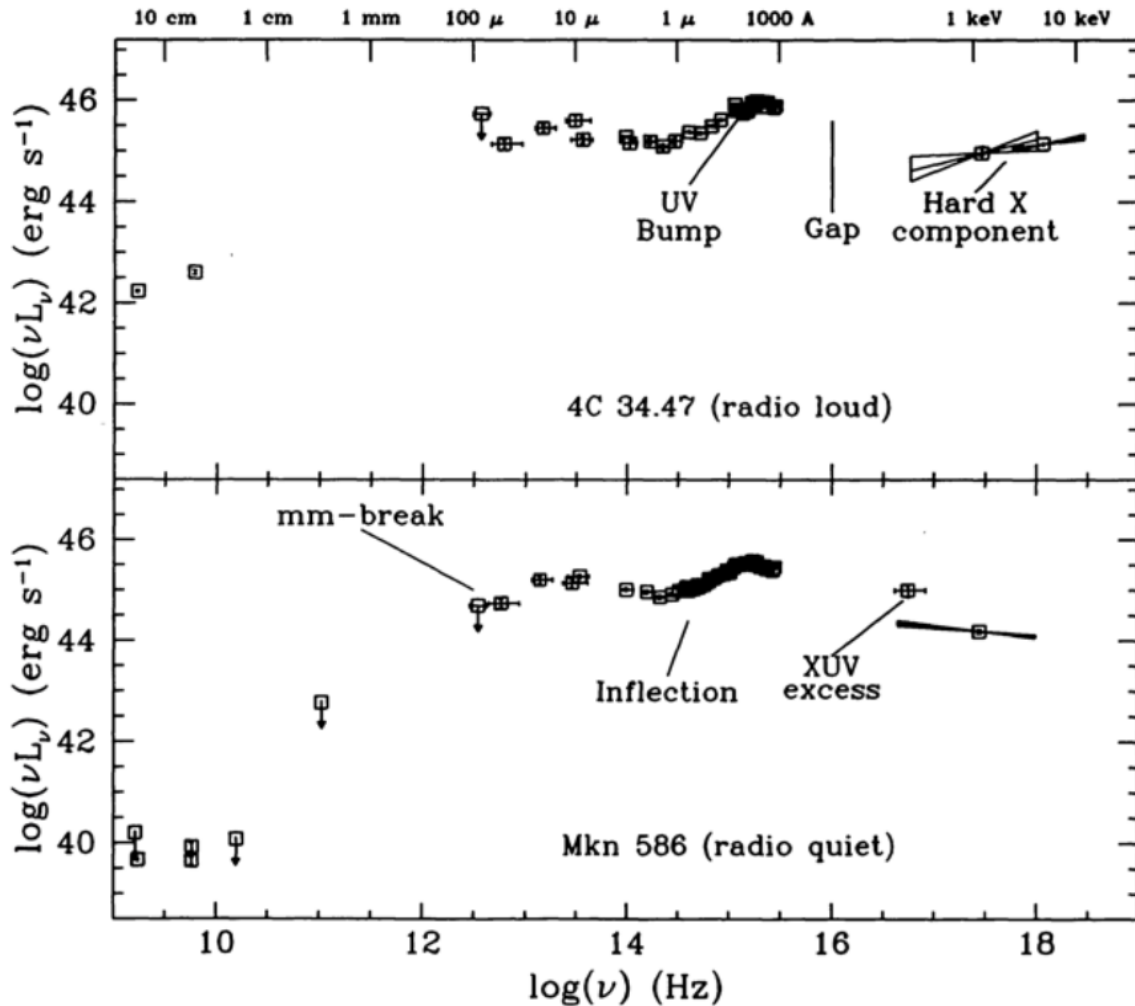
Fig. 1.8 Examples of radio-loud (top panel) and radio-quiet (bottom panel) quasar SEDs. The main differences for the two radio subtypes are the enhanced radio luminosity and X-ray luminosity for the radio-loud sources. The component marked 'XUV excess' in the upper panel is now commonly referred to as the soft X-ray excess (§1.1.3). While the radio-loud quasar shown here displays a harder X-ray continuum, I do not find a significantly different distribution of the continuum photon index for the two radio types (Chapter 6). Figure taken from Elvis et al. (1994). I note that the example quasars shown here are rather X-ray bright relative to the broader quasars population, due to the selection criteria employed by Elvis et al. (1994).

quasar SEDs. I focus on the observational challenges in obtaining UV–optical–X-ray SEDs due to quasar variability (§1.3.1), on the challenges in estimating the accretion luminosity (Equation 1.10; §1.3.2), and on comparisons of the UV–optical SED to thin-disk predictions (§1.3.3).

AGN emit over the entire electromagnetic spectrum, from radio waves to gamma rays. For bright AGN, much of this emission is non-stellar, although there is also a contribution from stars and gas in the host galaxy (§1.1.9). The broad-band SEDs for typical radiatively efficient AGN display a 'big blue bump' feature in the UV-optical, a broad emission feature in the infrared, and strong X-ray emission (Figure 1.8). Typical SEDs for radio-loud and radio-quiet quasars are included in Figure 1.8 as a visual guide . Radio-loud and radio-quiet sources differ in their relative flux levels in the radio and X-ray bands. I do not find any significant difference in their broad-band UV–optical SEDs for $z \sim 2$ quasars (Chapter 6). X-ray emission is detected in all AGN (given sufficiently deep observations), but is enhanced in radio-loud sources (§1.1.8), as I also find for our $z \sim 2$ quasar sample).

The big blue bump is thought to be the observational signature (e.g., Czerny and Elvis, 1987) of thermal emission from an optically thick accretion disk (§1.2). Far-UV observations reveal a flux turnover at rest-frame ~ 1000 Å (e.g. Stevans et al., 2014). AGN displaying broad emission lines (i.e., Type 1 AGN) display this continuum feature, whereas Type 2 AGN (lacking broad emission lines) have weak or negligible UV–optical continua. An additional 'small blue bump' at 2000–4000 Å is attributed to a blend of iron emission lines and Balmer continuum (e.g., Shang et al., 2005). The infrared bump redward of rest-frame 1 μm is attributed to dust emission Barvainis (1987); Hughes et al. (1993)), which I do not study in this Thesis.

1.3.1   SED Variability for Individual AGN

AGN display variable luminosities in every wavelength regime, from the radio (e.g., Kutkin et al., 2019) through the UV-optical (e.g., Sánchez-Sáez et al., 2019) to the X-rays (e.g., Zamorani et al., 1984) and γ-rays (e.g., Angioni et al., 2019). This variability is vital to reverberation mapping studies (§1.4) and can be used to select AGN candidates in wide-field surveys (e.g., Kutkin et al., 2019). However, it is a practical obstacle for SED studies. Due to scheduling constraints and instrumental limitations, it can be difficult to obtain simultaneous observations of the SED across all wavelength regimes of interest. If a given AGN varies in overall luminosity between the observations of, for example, the UV–optical and the X-ray component, the observed UV to X-ray SED shape will not represent the emission at any one observational epoch. Kilerci Eser and Vestergaard (2018) find that the integrated accretion luminosity of individual AGN can vary by a factor 2 or more between observations, introducing a substantial additional scatter to the observed SED shapes and bolometric luminosities for SED studies based on non-contemporaneous observations. In the SED catalogs presented in this thesis (Chapters 5 and 6), I harness the capability of the *Swift* satellite (Roming et al., 2005) to observe simultaneously in the UV–optical and X-ray regimes, in order to avoid this additional uncertainty.

1.3.2   Measuring the Accretion Luminosity

How accurately can we measure the accretion luminosity L_{acc} (§1.2), i.e, the luminosity ultimately due to conversion of gravitational potential energy into radiation? One might guess that the best approach is to integrate the luminosity across the entire electromagnetic spectrum. This integral is commonly referred to as the bolometric luminosity, L_{bol}. The bolometric luminosity can be estimated (with significant uncertainties, due to the unobservable extreme-UV gap and to the diversity of AGN SEDs) using broad-band SED observations (e.g., Elvis et al., 1994; Kilerci Eser and Vestergaard, 2018; Richards et al., 2006).

However, the bolometric luminosity is not expected to equal the accretion luminosity, for a few reasons. Secondly, the geometry and kinematics of the other components powered by the accretion disk lead to differences between the bolometric luminosity and that of the underlying accretion component. In particular, the infrared dust emission feature is due to reprocessed UV–optical continuum emission. For Type 1 AGN, for which we have a direct view of the continuum source, the dusty obscuring structure does not intersect our line of sight to the accretion disk. When measuring the bolometric luminosity, we receive an energy contribution from the continuum emission absorbed by the dust region, while still observing the *unabsorbed* continuum, leading to a 'double-counting' of continuum photons. For our $z \sim 2$ quasar sample, I approximate the UV–optical continuum using a power-law model; the continuum contribution is minimal in the infrared. I do not include the observed infrared emission in my accretion luminosity estimates. The UV–optical broad emission lines are also due to reprocessed continuum emission, in this case the unobservable extreme-UV continuum. To avoid a similar 'double-counting' of continuum luminosity, I use a broad emission line template to correct the observed UV–optical SEDs (in a statistical sense) for broad-line emission.

Secondly, the accretion disk itself is not spherically symmetric, and this introduces an inclination dependence into the observed disk continuum luminosity for individual objects, with face-on disks appearing brighter. A variety of approaches to this issue are applied in the literature. Some studies simply assume isotropic emission (e.g., Runnoe et al., 2012), or assume a disk inclination (e.g., Davis and Laor, 2011; Raimundo et al., 2012), which will introduce an additional scatter to the observed accretion luminosities (relative to any intrinsic scatter) if AGN are observed at a wide range of inclinations. Alternatively, thin-disk models can be fitted to the observed SEDs including the inclination as an additional free parameter (e.g., Capellupo et al., 2016); however, this approach depends on the validity of the thin-disk models, and requires high-quality photometric or spectroscopic data sampling a large range of rest-frame UV–optical wavelengths in order to capture the disk profile. In my accretion luminosities (Chapters 5 and 6), I make the simple assumption that the disk emission is isotropic, as I lack strong constraints on the inclination for individual sources in our $z \sim 2$ sample.

Thirdly, outflowing material with relativistic velocities projected along our line of sight will be beamed, and thus highly anisotropic. Beaming is particularly relevant for jet-dominated sources observed at small angles to the radio axis, e.g., blazars and BL Lac AGN (e.g., Urry and Padovani, 1995). As I do not study the SEDs of blazars or BL Lac sources in this Thesis, beaming effects should not strongly affect the work presented here. Finally, stars and gas in the AGN host galaxy will contribute to the observed SED; separating this host galaxy contribution from the AGN continuum

is non-trivial. I discuss this issue in Chapter 4, where I require a quantitative measure of the host galaxy emission for four FeLoBAL quasars. For the $z \sim 2$ quasar sample, I assume that the host galaxy contribution to the UV-optical emission is negligible, as these quasars are thought to be much brighter than their host galaxies. At least at $z \sim 0.3$, quasars tend to have elliptical host galaxies with low star formation Dunlop et al. (2003), in which case their contribution to the rest-frame UV should be very faint.

In the SED studies presented in this thesis (Chapters 5 and 6), we make a rough estimate of the accretion luminosity for individual sources in our $z \sim 2$ sample. Our approach is to isolate the accretion disk emission component in the observed SEDs, along with the X-ray component. While the physical mechanism transferring energy to the X-ray emitting component is not well understood, current models involve the X-ray corona extracting energy from the accretion disk (§1.1.3). Thus, it is appropriate to include the X-ray component in our $L_{\rm acc}$ estimate. Our sample quasars are unlikely to be strongly beamed, given that we select against blazar sources. We do not include the infrared dust emission, due to the 'double-counting' effect outlined above. While it is in principle appropriate to include the radio emission for RLQs, which is also powered by the accretion flow, this component is several orders of magnitude fainter than the UV–optical emission in terms of radiative energy (Figure 1.8), and its contribution to the total accretion luminosity is therefore negligible. We therefore estimate $L_{\rm acc}$ as the sum of the integrated UV-optical and X-ray luminosities. The main uncertainty in our estimate of the accretion luminosity is the unobservable extreme-ultraviolet regime, which for *Swift* UVOT and XRT observations spans the rest-frame ~ 1000 Å–1 keV range. Unfortunately, a significant fraction of the accretion luminosity is emitted at these unobservable energies, as predicted by thin-disk models (§1.2) and confirmed by statistical studies of the extreme-UV SED (e.g., Stevans et al., 2014). In order to include this contribution in our accretion luminosity estimates, we perform a simple power-law function interpolation between the observed *Swift* UVOT $UW2$ and XRT 0.3 keV luminosity densities, as discussed in Chapter 5. Kilerci Eser and Vestergaard (2018) find that this interpolation introduces a $\sim 25\%$ uncertainty to the measured accretion luminosity.

1.3.3   Testing Accretion Disk Models using SEDs

SED catalogs of radiatively efficient AGN provide an opportunity to test the predictions of thin-disk models described in §1.2. The UV-optical SED turnover (i.e., the emission peak of the big blue bump feature), and its dependence on black hole mass and spin, is an key prediction of the thin-disk model. Individual AGN suffer strong Lyman forest and Galactic Ly-α absorption in the extreme-UV. This makes it difficult to determine the SED turnover (and thus the implied ISCO radius) on a per-object basis, as it requires a statistical correction for the Lyman forest and Galactic absorption (e.g., Shang et al., 2005). This issue is alleviated if the SED turnover occurs at low energies, corresponding to wavelengths redward of $\sim$912 Å. As the thin-disk SED turnover energy decreases as a function of black hole mass, and increases at high black hole spin, we would expect to detect SED turnovers in the UV–optical regime only for massive black holes with near-zero spin. For quasars in our $z \sim 2$ sample (Chapter 6), we find evidence of an SED turnover in the UV–optical for only a few

objects. Most sources in this sample display power-law like continua extending into the unobserved extreme-UV. Given the estimated black hole masses of these quasars, this behavior is consistent with near-maximal black hole spin. However, our *Swift* UVOT and auxiliary observations do not strongly constrain the model parameters for individual quasars, as they do not sample the long-wavelength tail of the predicted thermal disk emission. This makes it difficult to detect the SED turnover for individual sources using the available broad-band photometry. In contrast, Capellupo et al. (2015) obtain satisfactory thin-disk model fits to VLT X-shooter spectroscopy of 37 $z \sim 1.55$ quasars, out of a sample of 39 observations. Importantly, their spectroscopic data allow for a determination of the intrinsic AGN continuum on a per-object basis, correcting for broad-line emission, and their spectra extend to longer rest-frame wavelengths, providing constraints on the low-energy power-law tail of the accretion disk component. They find non-zero black hole spins for all 37 quasars, with spin parameters ranging from $a_* = 0.6$ to maximal spin. The resulting spectral turnovers occur in the far-UV spectral regime; while our *Swift* UVOT observations do observe these energies for the $z \sim 2$ sample, it is likely that spectroscopic observations are required in order to reliably detect the curvature of the continuum component on a per-object basis.

I also investigate whether the distributions of UV–optical SED shapes, as parameterized by the UV spectral index, differ significantly for radio-loud and radio-quiet quasars. Any such difference might be due to radio-loud quasars having higher black hole spins, as discussed in §1.1.8, which would result in bluer UV continua relative to radio-quiet sources. I do not find any significant difference in the UV–optical SED properties for the two radio classes. While Capellupo et al. (2015) do not explicitly address the radio loudness of their sample, their findings indicate that the majority of $z \sim 1.5$ quasars have high black hole spins, which would explain their similar UV–optical SED characteristics. I also confirm that our radio-loud and radio-quiet subsamples are well-matched in terms of black hole mass distributions and UV–optical luminosities. These samples are therefore well-suited to future investigations of the properties of accretion disks for RLQs and RQQs.

1.4 Reverberation Mapping of the BLR and Accretion Disk

While great progress has recently been made on interferometry techniques to directly image the central regions of active galaxies (e.g., Event Horizon Telescope Collaboration, 2019; Gravity Collaboration et al., 2018), the BLRs and accretion disks of AGN are not generally resolved in direct imaging, as they have sub-parsec length scales and are located at extragalactic distances. *Reverberation mapping* (RM, Blandford and Payne, 1982) techniques are invaluable tools to study the compact central regions of AGN, and will likely remain so for the foreseeable future. In this Thesis, I work with reverberation mapping techniques to study the accretion disk and X-ray emitting region of the changing-look AGN Mrk 590 (Chapter 3), and to investigate the discrepancy between predicted and measured accretion disk sizes for NGC 5548 (Chapter 2). In my work on the spectral energy distributions of $z \sim 2$ quasars, I use a method for black hole mass estimation which is based on results from broad line region reverberation mapping observations. Here, I present the theoretical framework for 1-dimensional reverberation mapping (§1.4.1), outline the methods for estimating

black hole masses based on reverberation mapping (§1.4.2), and introduce continuum reverberation mapping of AGN accretion disks (§1.4.3).

1.4.1   Reverberation Mapping Methodology

Put simply, RM uses measurements of the light travel time between the ionizing source and reprocessing regions to glean information about the size and geometry of the central engine. The mathematical formalism for RM outlined below was developed by Blandford and Payne (1982). Broadly speaking, there are two approaches to reverberation mapping of emission lines: 'one-dimensional reverberation mapping', which uses the integrated emission line flux, and 'two-dimensional reverberation mapping' which uses the velocity information in the line profile, and therefore requires high-quality spectroscopic data in order to measure the reverberation signal as a function of wavelength. Most of the studies of BLR geometry discussed in §1.1.4 rely on the 2D methods in order to simultaneously constrain the distance from the continuum source and the velocity structure of the BLR. In this Thesis I work exclusively with one-dimensional reverberation mapping, and do not discuss the 2D methods further.

The one-dimensional approach to reverberation mapping is an analysis of the response of the velocity-integrated emission line flux to changes in the ionizing continuum. In practice, the ionizing continuum is largely unobservable, and the UV-optical continuum is used as a proxy, under the assumption that its flux variations follow those of the ionizing continuum. The 1D *transfer function* $\Psi(\tau)$ corresponds to the impulse response of the BLR to a delta-function continuum emission event, and thus encodes physical information about the BLR-emitting gas:

$$L(t) = \int_0^\infty C(t - \tau)\Psi(\tau)d\tau \tag{1.19}$$

Here, $L(t)$ is the broad-line flux at time t, $C(t)$ is the continuum flux, and τ is a time delay parameter. This prescription assumes that the BLR response is linear. While this is not true for large fluctuations in ionizing flux (as the photoionization conditions in the clouds depend non-linearly on the ionization parameter), it is common to linearize the continuum and broad-line flux levels around their average values for a given set of observations:

$$C(t) \simeq C_0 + \Delta C(t) \tag{1.20}$$

$$L(t) \simeq L_0 + \Delta L(t) \tag{1.21}$$

The *response function* Ψ' then encodes the response of the system to variations in luminosity, and is valid even for non-linear responses provided that the continuum fluctuations are sufficiently small:

$$\Delta L(t) = \int_0^\infty \Delta C(t - \tau)\Psi'(\tau)d\tau. \tag{1.22}$$
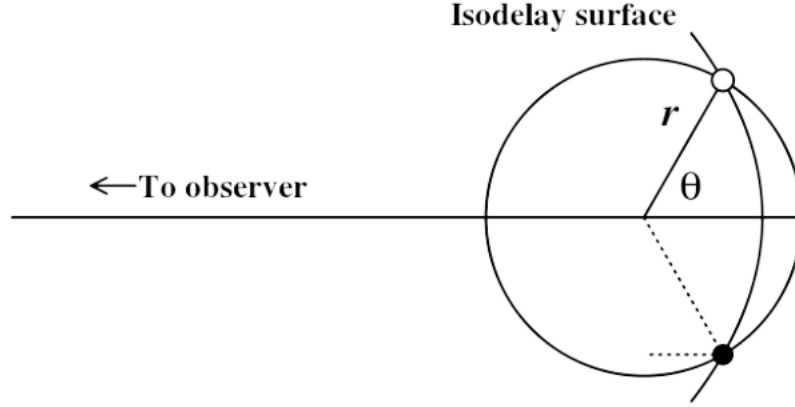
Fig. 1.9 The intersection of isodelay surfaces as measured by an observer with the line-of-sight plane correspond to parabola. In this diagram, the continuum source is located at the center of the circle; the circle illustrates a surface of constant radius from the black hole. The curve intersecting the circle represents an isodelay surface. Thus, a given observed delay does not uniquely correspond to any single radius. Figure taken from Peterson et al. (2004).

Interpreting the response function in terms of the BLR geometry is ambiguous: different geometries can produce identical response functions. E.g., axisymmetric inflows and outflows can produce identical measured response functions (Horne, 1994). This is due to the lack of a one-to-one correspondence between the delay time τ and the distance between BLR cloud and black hole, as illustrated in Figure 1.9.

In general, different emission lines respond differently to continuum variations, and a given emission line will respond differently depending the overall ionizing flux level, due to the local photoionization physics in the reprocessing regions. This effect must be taken into account when modeling the response of the BLR as a whole (e.g., the study I present in Chapter 2). The responsivity $\eta(r)$ of a given BLR cloud at radius r is defined as

$$\eta(r) = \frac{\Delta \log[L_c(r)]}{\Delta \log[\Phi_H(r)]} \tag{1.23}$$

where $L_c(r)$ is the line luminosity emitted by that cloud, and $\Phi_H(r)$ is the ionizing continuum flux. The responsivity can be small (i.e., the line does not respond strongly to continuum variations), or negative (i.e., the line becomes increasingly overionized and its emissivity falls as the continuum increases). As we do not spatially resolve the BLR, the observed responsivity for a given emission line depends on the emissivity-weighted responsivities integrated over the BLR.

Determining the full 1D response function based on sparsely and/or non-uniformly sampled lightcurves is challenging. A more easily attainable goal is to extract a mean delay between continuum variations and emission line responses. This provides an emissivity-weighted mean radius for the line-emitting gas. In my investigations of the BLR diffuse continuum contribution to the observed inter-band UV–optical continuum delays (Chapter 2), and my investigation of the UV response to X-ray flux variability for Mrk 590 (Chapter 3). I determine the mean delay time using
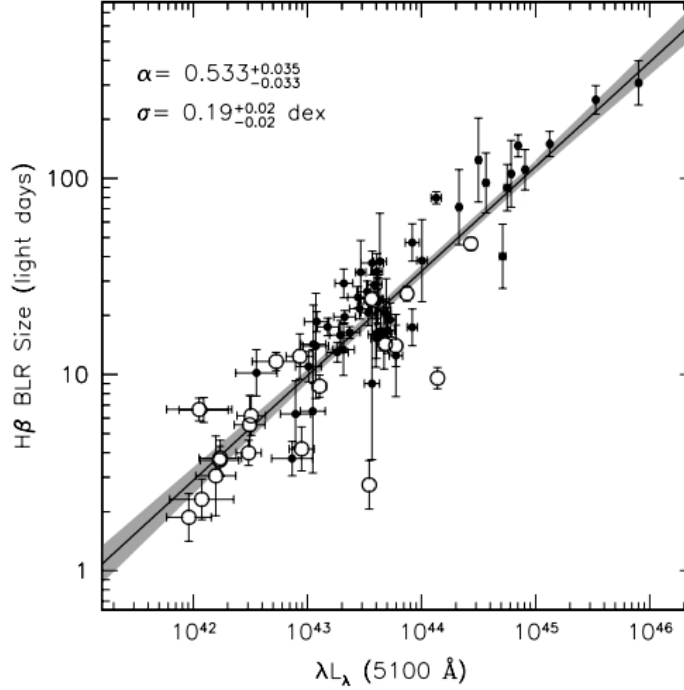
Fig. 1.10 BLR radius - 5100 Å continuum luminosity relationship for $z < 0.3$ Type 1 AGN. Figure taken from Bentz et al. (2013).

two different techniques. Namely, the interpolated cross-correlation function method developed by White and Peterson (1994), and the *Javelin* method developed by Zu et al. (2011). I describe these methods in detail, and compare the resulting time delays and uncertainties, in Chapter 3.

1.4.2   BLR Reverberation Mapping and Black Hole Mass Estimates

The BLR is the AGN emission component most studied in reverberation mapping. Importantly, reverberation mapping studies indicate that the velocity field of the BLR is dominated by virial motion in the gravitational potential of the central black hole; I highlight some of these results in §1.1.4. Another important finding is that the mean radius R_{BLR} of the broad line region for a given emission line,

$$\tau = cR_{BLR}, \tag{1.24}$$

scales with continuum luminosity (e.g., Koratkar and Gaskell, 1991; Peterson, 1993). When a careful treatment of the host galaxy contribution to the continuum luminosity is applied, the best-fit scaling is $R_{BLR} \propto L_{5100}^{0.53\pm0.03}$ (Figure 1.10, Bentz et al. (2013)). This is consistent with the expectation $R_{BLR} \propto L^{0.5}$ due to photoionization considerations in a Locally Optimally-emitting Cloud model (§1.1.4), assuming that the optical continuum luminosity is a proxy for variability in the unobserved ionizing continuum. Kaspi et al. (2007) and Hoormann et al. (2019) find similar relationships for luminous, high-redshift AGN using the C IV emission line. Different emission lines display different delay times (e.g., Bentz et al., 2010b), indicating a stratified BLR, which is again consistent with photoionization conditions in a LOC model.
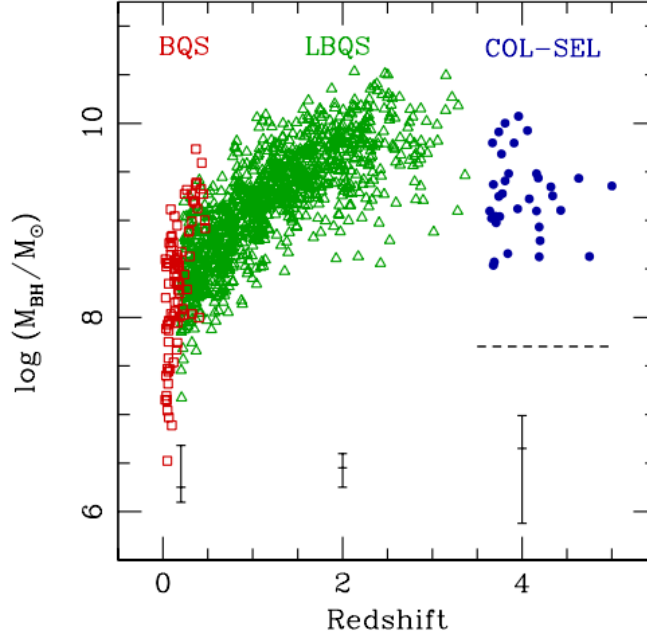
Fig. 1.11 Single-epoch M_{BH} estimates for quasars in the Bright Quasar Survey (red squares), Large Bright Quasar Survey (green triangles), and a subset of the *Sloan* Digital Sky Survey (blue dots), as a function of redshift. Representative M_{BH} error bars are shown for each sample. Figure taken from Vestergaard and Osmer (2009).

Given that the broad-line emitting gas undergoes virial motion in the gravitational potential of the central black hole, its line-of-sight velocity dispersion ΔV_{BLR} depends on the black hole mass, M_{BH}, and on R_{BLR}. Reverberation mapping thus provides an estimate of M_{BH}:

$$M_{\mathrm{BH}} = f \frac{R_{\mathrm{BLR}} \Delta V_{\mathrm{BLR}}^2}{G}. \tag{1.25}$$

The velocity dispersion for a given emission line, ΔV_{BLR}, can be measured directly from the linewidth of the variable component of the line profile, which is usually determined using the root-mean-square spectrum for the observing campaign. The factor f depends on the geometry of the BLR, which is currently not well constrained, and the potential deviations from virialized motion due to radiation pressure on the BLR. This factor is generally determined as a sample average, $\langle f \rangle$, by calibrating the AGN black hole mass scale (e.g., Onken et al., 2004) to the M_{BH}–σ_* relationship derived for quiescent galaxies (e.g., Ferrarese and Ford, 2005). Onken et al. (2004) find a sample average of $\langle f \rangle = 5.5 \pm 1.8$, with a typical uncertainty of a factor ~ 3 on M_{BH} (Onken et al., 2004).

In order to estimate the Eddington luminosity ratios of our $z \sim 2$ quasar sample, and to test thin-disk modeling of these sources (Chapter 6), I require estimates of M_{BH} for each source. Reverberation mapping-based mass estimates are not available for this sample. However, due to the R_{BLR} - continuum luminosity relationship described above, M_{BH} can be estimated using single-epoch spectra. These single-epoch spectroscopic mass estimates use the continuum luminosity as a proxy for R_{BLR}, and estimate the BLR velocity dispersion using the emission line profile (e.g., Vestergaard and Osmer, 2009; Vestergaard and Peterson, 2006; Wandel et al., 1999). ARM campaigns are observationally expensive, and require long monitoring programs, especially at higher redshifts

at which we typically observe luminous AGN and for which the cosmological time dilation is significant. For this reason, M_{BH} estimates for large AGN samples rely on the single-epoch method. It is therefore a vital tool for studying the M_{BH} distribution of quasars, and dependent properties such as the Eddington ratio (Shen et al., 2011; Vestergaard and Osmer, 2009). The most massive black holes in quasars have $M_{BH} \sim 10^{10}$ Solar masses (Figure 1.11).

1.4.3 Disk Reverberation Mapping

Short-term variability in the AGN optical-UV continuum is not explained by standard thin-disk models, which predict significant flux variability only on the viscous timescale (§1.2). However, we observe the X-ray emitting region to be highly variable on short timescales (§1.1.3). A common explanation for the observed UV-optical variability is that the X-ray corona illuminates the accretion disk (the so-called lamp-post model, Cackett et al., 2007). Assuming that the disk temperature profile adheres to the thin-disk prediction, Equation 1.12, yields a prediction for the disk reprocessing time delay τ as a function of wavelength, λ:

$$c\tau_{AD} \approx 0.09 \left(X \frac{\lambda}{1928} \right)^{4/3} M_8^{2/3} \left(\frac{\dot{m}_{Edd}}{\eta} \right)^{1/3}. \tag{1.26}$$

(e.g., Cackett et al., 2007). Here, M_8 is the black hole mass in units of $10^8 \, M_\odot$, $\dot{m}_{Edd}$ is the ratio of the accretion rate to the Eddington rate, and η is the radiative efficiency of the disk. The scaling factor $X = 2.49$ encapsulates the mapping from disk surface temperature to effective wavelength (Fausnaugh et al., 2016). Thus, if the lamp-post model is the correct interpretation of the observed UV-optical continuum variability, the measured disk reverberation signal provides a test of the thin-disk models.

Recently, high-cadence UV-optical and X-ray monitoring campaigns with the *Swift* observatory have measured an inter-band reverberation signal in the UV-optical continuum (e.g., Edelson et al., 2019; McHardy et al., 2014; Shappee et al., 2014) and in some cases a lag between the X-ray and UV lightcurves (e.g., Edelson et al., 2019). The results for the X-ray to UV lag are puzzling. Firstly, for several sources (e.g., NGC 4151, NGC 4593), the far-UV bands lag the X-ray source by $0.5 - 2$ rest-frame days. This is inconsistent with the lamp-post model, for which the X-ray emitting region is assumed to be very close to the central black hole, and the far-UV emission from the inner disk should also be located close to the innermost stable circular orbit. I find a similar ~ 2.5 day delay between the X-ray and UV variability for Mrk 590 (Chapter 3). In other sources, e.g., Mrk 509 (Edelson et al., 2019), the X-rays lag the far-UV bands, which is inconsistent with the disk responding to variable X-ray heating. In general, the observed correlations between the X-ray and UV bands are rather weak, while the lamp-post model predicts a strong correlation (Edelson et al., 2019; Gardner and Done, 2017). I find an unusually strong correlation between the X-ray and UV lightcurves for Mrk 590, as predicted by the lamp-post model. However, given the observed ~ 2.5 day time delay, the standard lamp-post model, where both the X-ray source and the UV disk are near the innermost stable orbit, is ruled out (Chapter 3).

The disk sizes implied by the inter-band UV-optical time delays are also somewhat larger than the thin-disk predictions for sources where UV–optical inter-band delays are detected (Cackett et al., 2007; Edelson et al., 2019, e.g.,). Assuming that these time delays are due to disk reverberation, the large disk sizes would require modifications to the thin-disk model in order to be consistent with it. A key assumption used to interpret continuum reverberation mapping results is that all the observed continuum emission variability is due to thermalization of X-ray photons in the disk itself. However, the BLR clouds must also emit Balmer continuum, given the photoionization conditions required to emit strong broad lines (Goad et al., 1993). In Chapter 2 I demonstrate that the diffuse Balmer continuum from the BLR contaminates the disk RM signal at all optical-UV wavelengths, given the ionizing continuum luminosity and broad-line spectrum of NGC 5548. The resulting overestimation of accretion disk sizes can explain, to first order, the inferred sizes for this source (Edelson et al., 2015; Fausnaugh et al., 2016; Starkey et al., 2017). In particular, our results explain the factor ~ 2 excess delay for the *Swift U* band, for which the diffuse BLR continuum contribution is strongest. Using spectroscopic reverberation mapping, Cackett et al. (2018) find 'smoking gun' evidence for excess UV lag consistent with Balmer continuum emission for NGC 4593. Korista and Goad (2019) perform diffuse continuum modeling similar to the work presented in Chapter 2, but using a Locally Optimally-emitting Cloud BLR model (Baldwin et al., 1995) instead of the pressure-law model used in my work. They also find substantial diffuse continuum emission across the entire UV–optical spectrum. It therefore appears that diffuse continuum emission contributes to the observed inter-band delays for a wide range of BLR models.

In summary, the modeling presented in Chapter 2 and the complimentary work of Korista and Goad (2019) demonstrate that it is essential to include the diffuse continuum contribution to the entire UV–optical spectrum in analyses of continuum inter-band delays. Although the diffuse continuum contribution can be ameliorated by excluding time delay measurements near the Balmer continuum feature from the disk modeling (e.g., Edelson et al., 2015), this procedure will still lead to overestimated accretion disk sizes, due to the diffuse continuum contribution at other wavelengths.

1.5 Changing-Look AGN

Recently, an increasing number of so-called *changing-look AGN* have been observed, both for lower-luminosity AGN (e.g., Denney et al., 2014; Parker et al., 2014; Ricci et al., 2020; Shappee et al., 2014). and in quasars (e.g., LaMassa et al., 2015; Runnoe et al., 2016). During changing-look events, the observational appearance of the AGN transitions between a Type 1 AGN with broad-line and continuum emission, and a Type 2 AGN state where only the narrow emission lines are observed in the UV–optical spectrum. This transition has been observed in either direction, i.e., from Type 1 to Type 2 or vice-versa. The changing look events occur on timescales of months to years. In Chapter 3 I study the possible re-ignition of the changing-look AGN Mrk 590, which began to dim in the late 1990s, and lost its broad-line emission at some point during 2006–2012 (Denney et al., 2014). Its soft X-ray excess component disappeared at some point between 2004-2011 (Rivers et al., 2012). It currently displays intermittent X-ray and UV flares, which have generally increased in brightness since 2016. I discovered a flare-up event in the UV and X-ray bands during August 2017.

Since that time, it has displayed a UV to X-ray spectral energy distribution consistent with those of bona fide AGN. Also, Raimundo et al. (2019) detect a reappearance of the broad emission lines shortly after the 2017 flare-up. Mrk 590 is thus one of the few AGN for which we have observed both a 'turn-off' changing look event, and a subsequent re-ignition.

The physical mechanism governing changing look behavior is poorly understood. As discussed in §1.1.5, the unification of Type 1 and Type 2 AGN via an obscuring dust structure cannot explain changing-look events, as this would require extreme variations in the X-ray absorbing column density, which are usually not observed (e.g., Denney et al., 2014). A natural explanation is an extreme variation in the continuum luminosity, coupled with an extended narrow-line region: as the continuum flux decreases rapidly, the narrow line emitting gas 'sees' the ionizing continuum emitted in an earlier high accretion state. LaMassa et al. (2015) favor this interpretation for the changing-look quasar J0159+0033, although they cannot rule out variable obscuration. However, the variability timescales are inconsistent with the predictions of the thin-disk model, for which large flux variations should only occur on viscous timescales (e.g., Noda and Done, 2018). Ross et al. (2018) suggest that a dramatic drop in the torque on the inner accretion disk will cause a cooling front to propagate through the disk, leading to luminosity variations on much shorter timescales than the viscous timescale. Alternatively, Jiang and Blaes (2020) demonstrate that density inversions in the accretion disk due to Iron opacity fronts can produce extreme AGN variability consistent with changing-look behavior. Intriguingly, their model prediction for the Eddington luminosity ratio as a function of time displays flaring behavior on timescales of ~ 1 year, which are qualitatively similar to the behavior I find for Mrk 590 (Chapter 3).

The disappearance of the thermal continuum component during the low-flux state for changing-look events may also be due to the inner accretion disk transitioning into a radiatively inefficient state (§1.2) at a sufficiently low accretion rate (Noda and Done, 2018; Ruan et al., 2019). In this scenario, a temporary lack of gas in the inner accretion flow results in the 'puffing up' of the inner disk, which is no longer radiatively efficient and ceases to produce sufficient ionizing photons for the broad emission lines. In Chapter 3 I estimate the Eddington luminosity ratio for Mrk 590 before and after the 2017 flare-up, and find that the accretion luminosity crosses the threshold Eddington ratio required for a standard thin-disk model between 2014 and 2017. Thus, Mrk 590 may have undergone a transition between the thin-disk and advection-dominated accretion flows. In that case, the transition was only temporary, as my *Swift* monitoring during 2017–2020 reveals that the UV to X-ray spectral energy distribution is now consistent with that of a Type 1 AGN.

Chapter 2

Quantifying the Effects of BLR Diffuse Continuum Emission on AGN Continuum Inter-band Delays

This chapter is comprised of the paper 'Quantifying the Diffuse Continuum Contribution of BLR Clouds to AGN Continuum Inter-band Delays' (Lawther et al., 2018a), accepted for publication in Monthly Notices of the Royal Astronomical Society. The authors are Daniel Lawther, Michael Goad, Kirk Korista, Otho Ulrich and Marianne Vestergaard.

The main scientific questions addressed by this paper are:

- For a simple pressure-law BLR model, what is the approximate contribution of diffuse continuum emission in the BLR to the *observed* continuum SED, for conditions thought relevant to typical Seyfert 1 sources?

- For these simple models, how much additional lag does the BLR diffuse continuum emission induce in the measured inter-band continuum delays?

- Are the additional delays induced by the diffuse continuum important in the context of the larger than expected accretion disk sizes inferred from inter-band continuum reverberation mapping? Might the observed delays be consistent with standard thin-disk models, accounting for the additional lags induced by the response of the diffuse continuum?

The main practical questions addressed by this paper are:

- What are the limitations of simple pressure-law BLR models? Can they roughly reproduce the observed broad emission line strengths? Pressure laws are unlikely to capture the detailed physics of real BLRs. So, are the physical conditions in these simple models at all relevant to the study of real AGN?

- Recent studies detect an elevated continuum delay signal near the Balmer continuum feature, relative to other wavelengths. This is interpreted as a signature of diffuse continuum emission.

Wavelengths immediately blue-wards of the Balmer break are therefore often excluded when modeling the delay structure of the UV–optical continuum (e.g., Edelson et al., 2015). What are the limitations of this approach? In particular, are there any UV–optical wavelength ranges that are not affected by additional delays induced by the diffuse continuum response?

2.1 Statement of Authorship

I (Daniel Lawther) performed the modeling and analysis described in this chapter. Otho Ulrich generated the *Cloudy* model grids for individual BLR clouds. I worked closely with Michael Goad on the programming and on interpretation of the results. I wrote the journal publication, which benefited from comments and suggestions from all authors over several drafts. I include a signed statement of authorship with this Thesis (Chapter 8).

2.2 Published Work

Quantifying the diffuse continuum contribution of BLR Clouds to AGN Continuum Inter-band Delays

D. Lawther [iD],[1]★ M. R. Goad,[2] K. T. Korista,[3] O. Ulrich[3] and M. Vestergaard[1,4]

[1]*Dark Cosmology Centre, Niels Bohr Institute, University of Copenhagen, Juliane Maries vej 30, DK-2100 Copenhagen Ø, Denmark*
[2]*Department of Physics and Astronomy, Leicester Institute of Space and Earth Observation, University of Leicester, Leicester, LE1 7RH, UK*
[3]*Department of Physics, Western Michigan University, 1120 Everett Tower, Kalamazoo, MI 49008-5252, USA*
[4]*Steward Observatory, University of Arizona, 933 N. Cherry Avenue, Tucson, AZ 85721, USA*

ABSTRACT

Disc reverberation mapping of a handful of nearby active galactic nuclei (AGNs) suggests accretion disc sizes that are a factor of a few too large for their luminosities, apparently at odds with the standard model. Here, we investigate the likely contribution to the measured delay signature of diffuse continuum emission arising from broad-line region gas. We start by constructing spherically symmetric pressure-law BLR models (i.e. $P(r) \propto r^{-s}$) that approximately reproduce the observed emission line fluxes of the strong UV–optical emission lines in the best-studied source, NGC 5548. We then determine the contribution of the diffuse continuum to the measured continuum flux and inter-band delays, accounting for the observed variability behaviour of the ionizing nuclear continuum. Those pressure-law models that approximately reproduce the observed emission-line luminosities unavoidably produce substantial diffuse continuum emission. This causes a significant contamination of the disc reverberation signature (i.e. wavelength-dependent continuum delays). Qualitatively, the diffuse continuum delay signatures produced by our models resemble that observed for NGC 5548, including the deviation of the lag spectrum above that of a simple power law in wavelength, short-ward of the Balmer and Paschen jumps. Furthermore, for reasonable estimates of the BLR covering fraction, the delay induced by diffuse continuum emission causes elevated inter-band delays over the entire UV–optical regime; for these pressure-law models, there are no 'disc-dominated' wavelength intervals. Thus, the diffuse continuum contribution must be taken into account in order to correctly infer AGN accretion disc sizes based on inter-band continuum delays.

Key words: accretion, accretion discs – methods: numerical – galaxies: active – galaxies: Seyfert.

1 INTRODUCTION

The immense energy outputs of active galactic nuclei (AGNs) are ultimately fueled by gas accretion onto supermassive black holes (e.g. Lynden-Bell & Rees 1971), which reside at the centres of most – perhaps all – massive galaxies (e.g. Kormendy & Gebhardt 2001). Thus, supermassive black holes in the local Universe probably achieved their current masses through bouts of AGN activity. The details of these accretion episodes are not well-understood. The in-falling gas is thought to form an accretion disc that heats up and emits much of the observed continuum radiation; Shakura & Sunyaev (1973) develop the standard α-disc model of steady-state disc accretion, originally in the context of X-ray binaries. The nuclear

continuum in turn excites fast-moving gas (clouds) near the central engine, which emit the observed broad emission lines (BELs); these clouds reside in the so-called broad line region (BLR). On larger scales, the nuclear continuum also excites the dusty obscuring structure (e.g. Antonucci 1993) to produce the infrared dust emission feature (e.g. Barvainis 1987), and excites gas in the host galaxy bulge to produce the narrow emission lines, the kinematics of which are dominated by the host galaxy potential (e.g. Nelson & Whittle 1996).

The large distances to AGN, coupled with the small sizes of their central regions means that the central regions of AGN remain unresolved, even for the nearest objects, defying scrutiny using conventional techniques (e.g. direct imaging). Indirect methods must therefore be used to probe their internal structure. Reverberation mapping (hereafter, RM) (Blandford & McKee 1982) is one such method, and has proven a particularly powerful probe of the central

★ E-mail: unclellama@gmail.com

regions of AGN. In its traditional form, RM utilizes correlations between continuum and emission-line variations to map the spatial distribution and (with high quality velocity-resolved data) the kinematics of the broad emission-line gas (e.g. Bentz et al. 2010b; Denney et al. 2010; Skielboe et al. 2015). This has revealed a compact, yet spatially extended BLR, sitting deep within the gravitational potential of the central supermassive black hole. RM studies of multiple emission lines, spanning a broad range in ionization state in a handful of individual sources, suggest that the BLR is radially stratified, with strong gradients in gas density and/or ionization. Importantly, the gas appears to be largely virialized (Peterson & Wandel 1999), a property that when coupled to measured BLR sizes (Peterson et al. 2004) has been usefully exploited to measure the mass of the central supermassive black hole in ≈60, mostly nearby, AGN (Bentz & Katz 2015). Ongoing multi-object spectroscopic surveys (e.g. King et al. 2015; Shen et al. 2015) should vastly increase the number of reverberation mapped AGN, albeit at reduced fidelity, and importantly, extend the number of objects for which black hole mass estimates are available to higher luminosity and redshift.

1.1 Disc reverberation mapping

More recently, correlated multiwavelength inter-band continuum variations have been used to test the standard model for accretion (Collier et al. 2001; Collier & Peterson 2001; Sergeev et al. 2005; Cackett, Horne & Winkler 2007; Troyer et al. 2016; Edelson et al. 2017, see also Section 1.2), with some surprising results. With a few assumptions (a standard α-disc irradiated from above by a compact variable X-ray emitting source), the wavelength-dependent variations reveal the disc radial temperature profile $T(R)$ and, if the black hole mass is known, the mass accretion rate through the disc. Formally, in the standard model the inter-band continuum delays $\tau(\lambda)$ increase with increasing wavelength λ according to

$$\tau(\lambda) \propto (M\dot{M})^{1/3}\lambda^{4/3} \qquad (1)$$

(e.g. Fausnaugh et al. 2016), where M is the black hole mass, and $\dot{M}$ the mass accretion rate through the disc. However, results from the most intensive multiwavelength monitoring campaigns (most notably NGC 5548; see Section 1.2) reveal continuum inter-band delays which are too large (by a factor of a few) for an α-disc emitting at the observed luminosity (Edelson et al. 2015; Fausnaugh et al. 2016; Edelson et al. 2017; Starkey et al. 2017; Cackett et al. 2018; Fausnaugh et al. 2018). That is, the standard model for accretion developed for accreting binaries may be incorrect when applied to AGN. Similarly, quasar microlensing studies also point to larger than expected disc sizes (Poindexter, Morgan & Kochanek 2008; Morgan et al. 2010; Mosquera et al. 2013).

So, are AGN accretion discs non-standard? In order to address this question, it is crucial that all known variable contributions to the measured continuum bands are properly accounted for. Since the nuclear regions are unresolved, there will be additional contributions to the measured disc continuum emission, some of which may vary. Known contaminants include the non-variable contributions to the observed continuum emission from stars in the host galaxy, and the variable broad emission lines. The latter are particularly problematic for broad band photometric data. Their contributions to the observed delays may be estimated given an estimate of the BEL delays, together with the relative flux contribution to the filter bandpass, as determined from single epoch spectra (e.g. Fausnaugh et al. 2016). However, a factor often neglected from these studies is the possibly substantial contribution to the con-

tinuum bands by variable continuum emission arising from the same gas responsible for emitting the broad emission-lines, the so-called diffuse continuum component (hereafter, DC)[1] (e.g. Korista & Goad 2001). As noted by Korista & Goad (2001), the DC component, if significant, introduces a delay signature that broadly mimics the disc continuum interband delays, with delays generally increasing with increasing wavelength. Importantly, these authors show that the DC emission introduces a delay signature over and above that arising from simple disc reprocessing, particularly in the Balmer and Paschen continua. This contaminant may be partially responsible for the larger than expected disc sizes. Thus, interpreting the measured continuum interband delays (and thus disc sizes) *solely* in terms of a simple disc reprocessing scenario is formally incorrect.

1.2 AGN STORM monitoring of NGC 5548: a test-bed for AGN accretion disc physics

NGC 5548 is a low-redshift ($z = 0.01718$) Seyfert 1.5 galaxy that has been a target of multiple RM campaigns, including the 13-y *AGN Watch* campaign (Clavel et al. 1991; Krolik et al. 1991; Korista et al. 1995; Peterson et al. 2002). In 2014, the *AGN Space Telescope and Optical Reverberation Mapping* (AGN STORM; Peterson, PI) campaign observed NGC 5548 using the *Hubble* Space Telescope, obtaining 171 usable epochs with ≈ daily cadence (De Rosa et al. 2015). The target was observed concurrently in the UV-optical to X-ray regime using *Swift* (Edelson et al. 2015) and in the optical from ground-based observatories spanning a range in longitude (Fausnaugh et al. 2016; Pei et al. 2017). In terms of cadence and spectral coverage, the AGN STORM program is arguably the most intensive RM campaign to date. Key findings of the AGN STORM campaign on NGC 5548 include:

(i) The response of the BELs appears to 'decouple' from the continuum variations during a substantial portion of the 2014 campaign, showing very little response to the UV continuum variations (De Rosa et al. 2015; Goad et al. 2016).

(ii) The lags obtained during the 'coupled' portion of the campaign suggest BLR size scales substantially smaller than those expected given the global BLR radius–luminosity relation (Pei et al. 2017), or indeed, the single-object radius–luminosity relation for NGC 5548 (Kilerci Eser et al. 2015).

(iii) High-cadence *Swift* UVOT monitoring reveals inter-band continuum delays (Edelson et al. 2015; Fausnaugh et al. 2016). These delays generally increase with increasing wavelength and are broadly consistent with a $\tau(\lambda) \propto \lambda^{4/3}$ dependency (equation 1). However, they are larger (by a factor of a few) than those predicted given the estimated M and $\dot{M}$ for NGC 5548 (Fausnaugh et al. 2016; Starkey et al. 2017). Thus, if the measured delays are solely due to disc reprocessing, the disc in NGC 5548 is larger than predicted by the standard α-disc model.

(iv) The continuum lag for the *Swift U* band, which samples the continuum in the vicinity of the Balmer jump, is elevated relative to the best-fitting $\tau(\lambda) \propto \lambda^{4/3}$ delay model (Edelson et al. 2015; Fausnaugh et al. 2016).

---

[1] The narrow line region will also emit a diffuse continuum component, though the size scales for the NLR would imply that their contribution, as for the narrow emission-lines, is non-variable on the time-scales relevant to RM campaigns.

1.3 Outline of this work

Here, we determine the likely contribution of the diffuse continuum emission from BLR gas to the measured continuum inter-band delays for AGN. We use the well-studied source NGC 5548 (Section 1.2) as a test case. Of particular relevance to this work is the larger than expected UV–optical inter-band continuum delays measured during the AGN STORM 2014 campaign. These delays may be affected by DC emission, as evidenced by the elevated lag signal near the Balmer jump. Our intention is not to model the AGN STORM 2014 data in detail. Rather, by constructing a straw-man model which approximately reproduces the observed emission-line luminosities of the strongest UV and optical emission lines in NGC 5548, we aim to quantify the DC contribution arising from its BLR, in terms of both flux and variability behaviour, and thereby assess its influence on the measured inter-band continuum delays. This prepares the necessary groundwork for more detailed models of NGC 5548 and other AGN at comparable luminosities.

While studies of inter-band continuum delays exist even for quasar-luminosity objects (Mudd et al. 2018), the highest-cadence RM data available are for lower-luminosity AGN in the local Universe. Thus, we expect our modeling results to be broadly relevant to current and future studies of disc inter-band delays. We proceed as follows: in Section 2 we construct a model BLR for which the run of gas physics with radius is completely specified by a simple radial pressure-law, $P \propto r^{-s}$ (Rees, Netzer & Ferland 1989; Netzer, Laor & Gondhalekar 1992; Goad, O'Brien & Gondhalekar 1993; Kaspi & Netzer 1999). We then use photoionization calculations to determine the emergent emission-line fluxes $\varepsilon(r)$ as a function of radial distance r, integrating over the cloud distribution to determine the total emission-line luminosities (Section 3). We investigate both constant ionization and constant density models, and assess their ability to match the gross properties (i.e. BEL luminosities, their ratios, and their variability time-scales) of the strongest UV–optical broad emission lines (Section 4.1). From these same models, we then compute the wavelength-dependent flux and delay distribution of the DC emission (Section 4.3), and its dependence on the density and ionization state of the BLR gas (Section 4.4). Finally, we perform Monte Carlo calculations, driving our model BLR with simulated continuum light curves, in order to estimate the measured delays of both the BEL and the diffuse continuum bands, and their dependence on the characteristics (amplitude and variability time-scale) of the driving continuum light curve (Section 5). We make a rough estimate of the total continuum lag spectrum (including that due to reprocessing in an α-disc), and compare with the measured delays for NGC 5548, in Section 6. In what follows we adopt a luminosity distance $D_L = 72.5$ Mpc to NGC 5548 (Bentz & Katz 2015), assuming a Λ CDM cosmology with $\Omega_\Lambda = 0.7$ and $\Omega_M = 0.3$.

2 PRESSURE-LAW BROAD-LINE REGION MODELS

We refer to models for which the pressure P depends on the radial distance r from the central continuum source,

$$P(r) \propto r^{-s} , \tag{2}$$

as pressure-law models. In this work, we examine two limiting cases, $s = 0$ and $s = 2$, representing constant density and constant ionization parameter models, respectively. We here adopt a spherically symmetric BLR geometry spanning more than two decades in radial extent. This model is chosen for (i) its simplicity, and because

(ii) we can compare our radial pressure-law models with the Local Optimally emitting Cloud model for this source presented by Korista & Goad (2001), which also adopts spherical symmetry. Here, we summarize the radial dependencies of various physical quantities for spherically symmetric pressure-law models; the derivations in this section follow Rees et al. (1989) and Goad et al. (1993). We make the simplifying assumption that the cloud temperature does not vary with radius; for solar composition, photoionization equilibrium is achieved at temperatures $T \sim 10^4$ K across a wide range of ionization parameter (equation 5), and the gas temperature will therefore vary weakly with radius (e.g. Netzer 1990; Ilić, Kovačević & Popović 2009). For constant cloud temperatures, the cloud hydrogen gas density n_H is proportional to the pressure, P, and so

$$n_H(r) \propto r^{-s} . \tag{3}$$

Thus, $s = 0$ corresponds to a constant n_H throughout the BLR. The ionization parameter U is defined as

$$U(r) = \frac{Q_H}{n_H(r) 4\pi r^2 c} , \tag{4}$$

where Q_H is the number of hydrogen-ionizing photons emitted by the central continuum source per second. Thus, $s = 2$ corresponds to a constant ionization parameter model, since:

$$U(r) \propto r^{s-2} . \tag{5}$$

The surface area per cloud, A_c, is proportional to R_c^2, where R_c denotes the radius of a cloud. In general, R_c depends on the pressure P, and is therefore constant for $s = 0$. If we demand that the mass of each cloud is conserved as the clouds move radially outwards (i.e. clouds do not break up or coalesce within our region of interest), mass conservation implies that $R_c^3 n_H = $ constant. Thus, we obtain the relation

$$A_c(r) \propto R_c^2(r) \propto r^{2s/3} . \tag{6}$$

The column density of each cloud, N_{col}, depends on the gas density and cloud radius:

$$N_{col}(r) \propto R_c n_H \propto r^{-2s/3} . \tag{7}$$

The above relations determine the local physical conditions, as parametrized by N_{col}, n_H and incident ionizing photon flux Φ_H, at any radius in a spherically symmetric pressure-law BLR model. These conditions determine the local surface emissivity $\varepsilon(r)$ of a BLR cloud at radius r (as determined via CLOUDY modeling; Section 3.1). The total luminosity for an emission line is then found by integrating over the distribution in cloud properties such that

$$L_{line} = 4\pi \int_{r_{in}}^{r_{out}} \epsilon(r) A_c(r) n_c(r) r^2 dr , \tag{8}$$

where r_{in} and r_{out} are the inner and outer BLR radii, respectively, A_c is the surface area of a single cloud, and n_c is the local number density of clouds. As dust grains strongly absorb UV photons, r_{out} is chosen to approximately coincide with the distance at which dust grains can form and survive (≈ 140 light-days for NGC 5548).

Finally we determine the local cloud surface area, $d(A_c n_c)$. Given our assumption that clouds do not break up or coalesce, mass conservation implies that the term $n_c v r^2$ is constant, for cloud velocity v. We make the additional simplifying assumption that the clouds are in virial motion ($v(r) \propto r^{-1/2}$). In that case, a cloud number density distribution $n_c(r) \propto r^{-3/2}$ fulfills the requirement of mass conservation, and the differential covering factor of the BLR obeys the

relation

$$dC(r) \propto A_c(r)n_c(r)dr \propto r^{2s/3-3/2}dr \,. \tag{9}$$

This allows us to determine a normalization $K(s, r_{\rm in}, r_{\rm out})$ for the total line-emitting surface of the clouds, for a given BLR covering fraction. The luminosity integral becomes:

$$L = 4\pi K \int_{r_{\rm in}}^{r_{\rm out}} \epsilon(r) r^{2s/3+1/2} dr \,, \tag{10}$$

while the normalization, for $\Omega = 4\pi$ steradians at $r_{\rm out}$, is given by

$$K = \left[\frac{2}{\sqrt{r_{\rm in}}} - \frac{2}{\sqrt{r_{\rm out}}} \right]^{-1} \quad (s=0)$$

$$\text{or } K = \frac{5}{6} \left[r_{\rm out}^{5/6} - r_{\rm in}^{5/6} \right]^{-1} \quad (s=2) \,. \tag{11}$$

3 METHOD: FROM PHOTOIONIZATION GRIDS TO BLR MODELS

3.1 Photoionization models for individual clouds

To obtain the local surface emissivity $\varepsilon(r)$ for a cloud located at radius r, we generate a grid of photoionization models using CLOUDY version C13.05 (Ferland et al. 2013). CLOUDY performs photoionization modeling of individual spherical clouds of gas with radius R_c, situated at a radial distance r from the central ionizing continuum source. We generate the photoionization models assuming that the covering fraction for the BLR is small, so that only a single reprocessing occurs,[2] and with r sufficiently large that the clouds are effectively plane parallel slabs. In that case, the emission from both the inwards-facing (i.e. directly illuminated by the continuum) and outwards-facing surfaces eventually escapes to infinity. The ratio of inwards-facing to total emission does, however, affect the form of the emission-line response functions (Section 3.4.2).

For the incident ionizing continuum, we utilize the continuum SED for NGC 5548 as presented by Mehdipour et al. (2015) (Fig. 1) based on multiwavelength (X-ray–UV–optical–IR) observations performed 2013 June – 2014 February. This SED is composed of an accretion disc emission feature, a power-law hard X-ray continuum component, and a reflection feature producing the Fe K emission complex. The hard X-ray component has a photon index $\Gamma \approx 1.8$, a high-energy cut-off set to $T_e = 400$ keV and a low-energy cut-off at ~ 1 keV. The accretion disc component includes Compton upscattering of seed photons at temperature $T_{\rm seed} \approx 0.8$ eV in a corona with $T_c \approx 150$ keV; this up-scattering produces the observed soft X-ray excess. Much of the intrinsic continuum emission responsible for powering the broad emission lines is produced in the unobservable extreme-UV spectral region (photon energies ≥ 1 Ryd), which for this model is dominated by the Compton up-scattered accretion disc component.

Our model grids span two decades in hydrogen gas column density, $22 \leq \log[N_{\rm col} /{\rm cm}^{-2}] \leq 24$, seven decades in hydrogen gas density, $7 \leq \log[n_{\rm H} /{\rm cm}^{-3}] \leq 14$, and seven decades in incident ionizing photon flux, $17 \leq \log[\Phi_{\rm H} /{\rm cm}^{-2}{\rm s}^{-1}] \leq 24$, with a resolution of 0.25 in the logarithm of each of these quantities. For each grid point, we use CLOUDY to obtain the local surface emissivities not only for an extensive list of atomic transitions, but also for reprocessed continuum emission (the diffuse continuum, DC) at UV-optical and infra-red wavelengths emitted from the same

[2]Such geometries are referred to as 'open' in the CLOUDY modeling parlance.
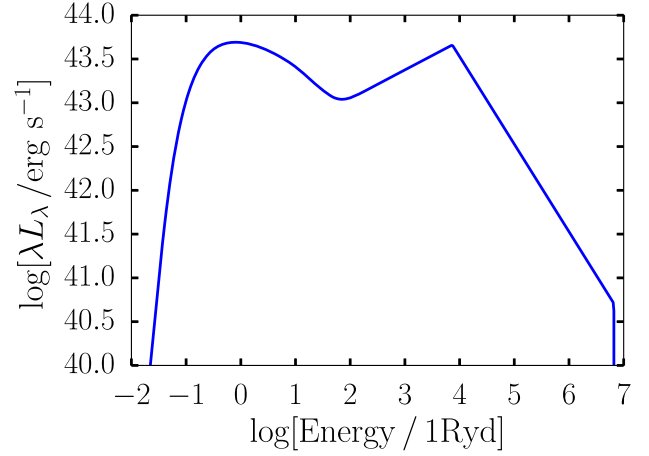
Figure 1. The NGC 5548 continuum SED presented by Mehdipour et al. (2015), which we use to generate the CLOUDY photoionization grids. The SED is scaled to the source-frame luminosity based on the observed mean continuum flux for the 2014 AGN STORM campaign, $F_\lambda(1367$ Å$) = 42.64 \pm 8.6 \times 10^{-15}$ erg s^{-1} cm^{-2} Å^{-1}, applying the reddening curve presented by Cardelli, Clayton & Mathis (1989) with $E(B-V) = 0.03$ and $R(v) = 3.1$ (as discussed in Section 4.1), and assuming a luminosity distance of $D_{\rm L} = 72.5$ Mpc (Bentz & Katz 2015).

gas. For the $s = 2$ models, given the steady-state luminosity and BLR size for NGC 5548, we subsequently found that a substantial emission line flux is produced by gas with $\log[N_{\rm col} /{\rm cm}^{-2}] \sim 21.5$. For the particular $s = 2$ BLR we study in-depth (Model 2, Section 4.1), we therefore generate additional CLOUDY models with $\log[N_{\rm col} /{\rm cm}^{-2}] \geq 21$, so as to obtain accurate emissivity and responsivity functions in the outer BLR.

In Fig. 2 we present representative CLOUDY emission line equivalent widths (hereafter, EW), measured relative to the incident continuum at $\lambda 1215$ Å for two of the strongest observed emission lines, Lyα and C IV, for a fixed hydrogen gas column density $\log[N_{\rm col} /{\rm cm}^{-2}] = 23$ cm^{-2}. The Lyα emission line emits most efficiently at low-ionizing photon fluxes; indeed, its efficiency increases towards $\log[\Phi_{\rm H} /{\rm cm}^{-2}{\rm s}^{-1}] < 17$, the lower limit of the parameter space probed by our photoionization grids. This implies that the hydrogen lines could in principle be produced very efficiently at low ionizing fluxes. However, such conditions are unlikely to be relevant here: the outer edge of the BLR is most likely determined by the dust sublimation radius (at which $\log[\Phi_{\rm H} /{\rm cm}^{-2}{\rm s}^{-1}] > 17$), as the ionizing continuum is efficiently absorbed by dust grains. In contrast, high-ionization lines such as C IV tend to be produced efficiently along a diagonal 'ridge' in $(\Phi_{\rm H}, n_{\rm H})$ space, corresponding to a particular ionization parameter, U; for C IV the optimal ionization parameter, i.e. one that passes through the peak EW, is $\log(U) \sim -1.5$. We present photoionization grids for two representative DC bands in Fig. 3. These may be compared to the more extensive model grids of DC bands presented in Korista & Goad (2001) spanning the entire UV–optical continuum. While their results differ from ours in detail, mainly due to the use of different ionizing continua, the gross shapes of their contour plots are similar to those used here.

In general, the gas becomes overionized at high ionization parameters, thus the DC does not emit efficiently at high $\Phi_{\rm H}$ and low $n_{\rm H}$ (upper left regions of the photoionization grids), while the DC is not strongly sensitive to $\Phi_{\rm H}$ and $n_{\rm H}$ (hence the widely spaced contour lines) once the ionization parameter becomes sufficiently low.
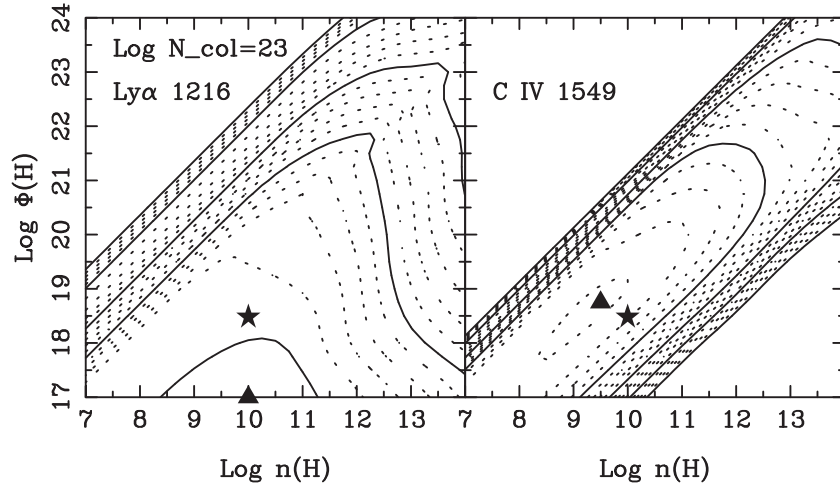
Figure 2. Example CLOUDY photoionization grids for Lyα (left-hand panel) and C IV (right-hand panel), for $\log[N_{col}/\mathrm{cm}^{-2}] = 23$. The contours display the total line equivalent width, i.e. the sum of the emission from the directly illuminated and the outward-facing cloud faces, normalized to the incident continuum flux at λ1215 Å. The solid curves represent increments of 1 dex in equivalent width, while the dashed curves show 0.25 dex increments; the lowest contour represents an equivalent width of 1. Black triangles show the maximum value of the line fluxes; black stars indicate the location in (n_H, Φ_H) space of a representative BLR cloud that approximately reproduces the emission-line strengths of Lyα and C IV in a typical AGN (Davidson & Netzer 1979). Vertical 'slices' through these grids represent constant-density ($s = 0$) pressure law models, while diagonal slices (at a 45° angle to the horizontal) represent constant ionization parameter ($s = 2$) models; we note that the latter require an interpolation across multiple CLOUDY grids, as N_{col} is constant only for $s = 0$ pressure laws. The C IV emission line emits most efficiently along a 'ridge' centred on an ionization parameter $\log(U) \sim -1.5$, while the Lyα emission line emits efficiently at low incident ionizing photon fluxes.
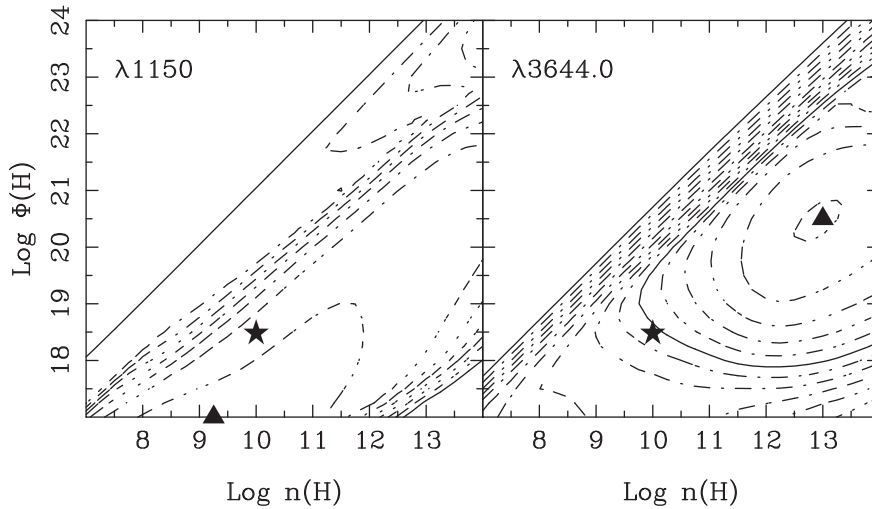

Figure 3. Example CLOUDY photoionization grids for the diffuse continuum at various UV-optical wavelengths, for $\log[N_{col}/\mathrm{cm}^{-2}] = 23$. The contours display the sum of the emission F_λ from the directly illuminated and the outward-facing cloud faces, normalized to the incident continuum flux at λ1215 Å. The solid curves represent increments of 1 dex in equivalent width, while the dashed curves show 0.1 dex increments; the lowest contour represents $\log[\lambda F_\lambda / \lambda F_\lambda(1250\ \text{Å})] = -1$. Symbols as Fig. 2. At short wavelengths ($\lambda \lesssim 2000$ Å) the brightest DC component is electron scattering, mostly free-free, which is most effective at low densities and low ionizing fluxes. Immediately bluewards of the Balmer break ($\lambda = 3646$ Å), the DC is dominated by Balmer continuum emission, which emits most effectively at high densities and fairly high ionizing fluxes.

3.2 Extent and geometry of the model BLR

In the absence of a clear consensus on the broad line region geometry, we limit this investigation to spherical BLR geometries only. Pêrez, Robinson & de La Fuente (1992b) showed that, in the absence of additional constraints, a well-determined 1-d transfer function cannot *uniquely* determine the geometry of the BLR, while even 2-d transfer functions reveal some ambiguity. For NGC 5548, the highest fidelity reverberation maps for the strong UV and optical emission lines from the AGN STORM campaign suggest

that the variable BLR may occupy a more flattened configuration (Horne, private communication). Our objective in this paper, however, is simply to illustrate the dependencies of the flux and lag spectra of the DC on a range of BLR cloud physical conditions and radial distributions, as a prelude to more detailed models for which constraints on the geometry are also included. In this context, a spherical BLR geometry allows a more intuitive interpretation of the model flux and delay spectra in terms of the cloud distribution and local photoionization physics. Alternative BLR geometries would introduce additional assumptions for which we currently
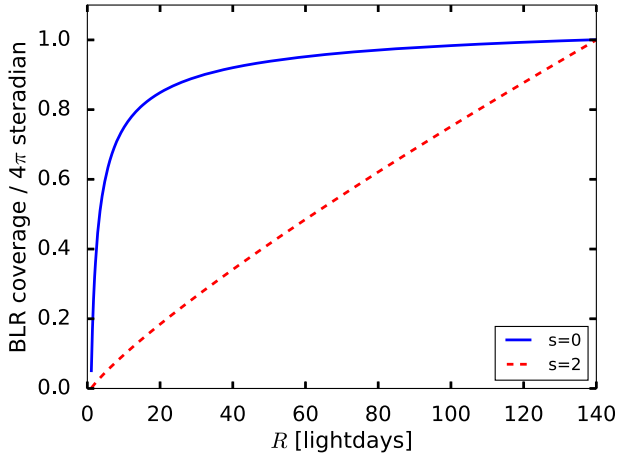
Figure 4. Cumulative sky coverage (as seen from the continuum source), as a function of radial distance r, for BLR models with a total cumulative covering fraction of $\Omega = 4\pi$ steradians at the outer radius. For a given Ω, the constant-density ($s = 0$) models distribute the clouds at smaller radii relative to the $s = 2$ models.

lack strong independent constraints, e.g. the BLR viewing angle and opening angles. Adoption of a spherical BLR geometry also aids comparison with the spherically symmetric locally optimally emitting cloud model for NGC 5548 presented by Korista & Goad (2001). We note that deviations from spherical symmetry may prove necessary in any future work aimed at reproducing the observed flux and delay spectra in detail (Section 6).

For a spherical BLR, the integrated emission-line luminosities produced by our models depend on our choice of inner and outer BLR radii (r_{in} and r_{out}), the total covering fraction at the outer radius (equation 10), and our chosen normalization, i.e. for a given s, the value of Φ_H, n_H and N_{col} at some fixed radial distance r. The constant pressure models ($s = 0$) distribute a large fraction of the BLR clouds close to the inner radius (Fig. 4). This causes the emission line luminosities to depend strongly on r_{in} for $s = 0$ models: much of the BLR becomes overionized as r_{in} decreases, and the emission line luminosity decreases sharply. The $s = 2$ models are less sensitive to this effect, as they are constant in ionization parameter, U. In this work, we adopt $r_{in} = 1$ light-day, and $r_{out} = 140$ light-days (the approximate dust sublimation radius, given the luminosity of NGC 5548). We note that due to the central concentration of BLR clouds for $s = 0$, r_{in} cannot be much smaller than 1 light-day if our constant-density models are to produce the required emission line luminosities for reasonable values of the total covering fraction. In their phenomenological BLR model for NGC 5548, Pancoast et al. (2014) find $r_{in} = 1.39^{+0.80}_{-1.01}$ light-days, consistent with our adopted value.

3.3 Radial distribution of clouds

Our CLOUDY modeling assumes that the BLR clouds do not self-shadow, and that there is no intrinsic reddening of the nuclear continuum as seen at the inward-facing cloud surface. In that case, the ionizing continuum at the inward-facing surface of a given cloud scales as r^{-2}. We parametrize the radial dependence of $\log[\Phi_H / cm^{-2}s^{-1}]$ as

$$\log(r) = -0.5(\log[\Phi_H / cm^{-2}s^{-1}] - 20) + 15.413 + r_{20} . \quad (12)$$

Here r_{20} is the radius (in light-days) at which $\log[\Phi_H / cm^{-2}s^{-1}] = 20$. The value of r_{20} depends on the continuum SED and its luminos-

ity. For NGC 5548, $r_{20} \approx 14.8$ light-days, as determined using the observed continuum flux, $F_\lambda(1367 \text{ Å}) = 42.6(\pm 8.6) \times 10^{-15}$ erg cm^{-2} s^{-1} Å^{-1} (De Rosa et al. 2015), corrected for Galactic extinction adopting $E(B - V) = 0.03$ (Korista & Goad 2000; we discuss this choice in Section 4.1), and assuming a luminosity distance to NGC 5548 of $D_L = 72.5$ Mpc (Bentz & Katz 2015).

In combination with the pressure-law relations (Section 2), r_{20} allows us to convert the emergent surface emissivities $\varepsilon(\Phi_H, n_H, N_{col})$ extracted from our photoionization grids into radial emissivity functions $\varepsilon(r)$. For $s = 0$ models, both N_{col} and n_H are constant throughout the BLR (Section 2). Therefore, the relevant emissivities for such models comprise a vertical 'slice' through a single n_H, Φ_H grid. We perform a linear interpolation in log-space over Φ_H to obtain $\varepsilon(r)$. For $s = 2$, the ionization parameter U is constant, $n_H \propto r^{-2}$, and $N_{col} \propto r^{-4/3}$. Such models correspond to diagonal lines in (n_H, Φ_H) space, with N_{col} decreasing radially as per equation (7). To obtain $\varepsilon(r)$ for these models, we perform a linear interpolation in log-space over Φ_H, n_H, and N_{col}.

With the emissivity distribution $\varepsilon(r)$ in hand, we numerically integrate equation (8) from r_{in} to r_{out} to obtain the total luminosity for a given BEL (or diffuse continuum band), assuming full coverage ($\Omega = 4\pi$ steradian) as seen from the continuum source, at the BLR outer radius. A reduced covering fraction (i.e. $<4\pi$ steradian) then corresponds to a downwards linear scaling of the emission-line luminosity.

3.4 Determining the response functions

The observed BLR emission signal is due to the integrated emission of individual BLR clouds located at radii $r_{in} < r < r_{out}$. Thus, the BLR responds to continuum variations over a distribution of time delays $0 \leq \tau \leq 2r_{out}/c$; the detailed shape of the emission line response function will depend on BLR geometry and on viewing angle (e.g. O'Brien, Goad & Gondhalekar 1994), as well as on the detailed gas physics. (e.g. Goad et al. 1993). In addition, the *measured* emission-line response will depend on the variability behavior (i.e. amplitude and characteristic time-scale) of the ionizing continuum source (see also Section 5.1; Goad & Korista 2014).

For a given BEL, the luminosity-weighted effective radius of the BLR is given by the centroid of the differential luminosity as a function of radius:

$$r_\epsilon = \frac{\int_{r_{in}}^{r_{out}} r L_{line}(r) dr}{\int_{r_{in}}^{r_{out}} L_{line}(r) dr} . \quad (13)$$

A similar relation can be defined for the diffuse continuum bands, replacing L_{line} with λF_λ, the monochromatic diffuse continuum emission at r.

3.4.1 Why responsivity matters

If the emission of each BLR cloud varies linearly (though not necessarily 1:1) with respect to the nuclear continuum variations, and the clouds emit isotropically, r_ε would also represent the observed effective reverberation radius. However, the responsivity and isotropy of realistic BLR clouds depend on the local photoionization physics of the individual clouds. We define the local responsivity $\eta(r)$ for the contribution $L_{line}(r)$ to a given emission line from radius r as

$$\eta(r) = \frac{\Delta \log[L_{line}(r)]}{\Delta \log[\Phi_H(r)]} . \quad (14)$$

If $0 < \eta < 1$ for all r, the line equivalent width decreases when the continuum luminosity increases (i.e. an intrinsic Baldwin effect;

Goad, Korista & Knigge 2004), while $\eta < 0$ produces an inverse correlation between line flux and continuum luminosity.

For $s = 0$ models, given our assumption that there is no internal extinction or cloud–cloud shadowing in the BLR, a change in ionizing flux corresponds to an instantaneous 'shift' of the clouds along the radial axis, allowing us to measure $\eta(r)$ directly for each CLOUDY (n_H, Φ_H) grid as

$$\eta(r) = -\frac{\delta \log(\epsilon)}{2\delta \log(r)}; \ (s = 0), \tag{15}$$

where the factor 2 is due to the radial dependence of the ionizing flux. For a constant steady-state ionization parameter U (i.e. $s = 2$ models), as both n_H and Φ_H follow inverse-square laws in radius, a small increase in flux corresponds to a constant increase in U at all radii:

$$\eta(r) = \frac{\delta \log(\epsilon)}{\delta \log(U)}; \ (s = 2). \tag{16}$$

RM measures the effective radius of those BLR regions that respond to luminosity variations. In the specific case of $\eta(r) = 1$ for all r, the line equivalent widths remain constant as the continuum luminosity varies, and the effective variability radius of the BLR is equal to r_ε. Otherwise, the measured time delays will approximately correspond to the responsivity-weighted BLR radius,

$$r_\eta = \frac{\int_{r_{in}}^{r_{out}} r \eta(r) L_{line}(r) dr}{\int_{r_{in}}^{r_{out}} \eta(r) L_{line}(r) dr}. \tag{17}$$

In general, $\eta(r)$ is luminosity-dependent. In the linear regime (i.e. small fluctuations about some mean level), the responsivity is simply the logarithmic slope of the Φ_H versus ε relationship at a given r. This linear approximation will break down for large changes in continuum luminosity. Formally, under these circumstances, the responsivity corresponding to a particular continuum level is best-determined directly from a grid of photoionization model calculations.

3.4.2 Accounting for anisotropic emission

If the BLR clouds emit anisotropically, the expected values of both r_ε and r_η will be modified accordingly (e.g. Ferland et al. 1992; O'Brien et al. 1994). For example, consider a BLR cloud located along the line of sight to the observer. If this cloud emits isotropically, it will contribute to the response function at a time delay $\tau = 0$ relative to the ionizing continuum. However, if this cloud emits only from its inwards-facing surface, it is not observed, and does not contribute to the response at $\tau = 0$. On the other hand, an identical cloud located on the opposite side of the broad-line region will contribute to the response function at a time delay $\tau = 2r/c$. Thus, while the steady-state line luminosity is not affected by anisotropy (assuming spherical symmetry), the line response is shifted towards larger delays if the BLR clouds preferentially emit from their illuminated face.

Following O'Brien et al. (1994), we define an anisotropy factor, $F(r) = \varepsilon_{inwd}(r)/\varepsilon_{tot}(r)$, where ε_{inwd} and ε_{tot} are the inwards-facing emissivity and effective total emissivity for the cloud, respectively. Isotropic emission corresponds to $F = 0.5$. The value of F depends upon the local photoionization physics for individual clouds, and thus are determined directly from our CLOUDY modeling. The 'observed emissivity' of a given cloud then depends on the fraction of the inwards-facing and outwards-facing surfaces we observe. Since the cloud geometry is unknown, we choose an emission line

radiation pattern that approximates the phases of the moon:

$$\epsilon_{obs}(r, \theta) = \epsilon_{tot}(r) \left[1 - (2F(r) - 1) \cos(\theta)\right]. \tag{18}$$

Here, θ denotes the angle between the line of sight and the cloud radial vector. Given that there is a linear mapping between $\cos(\theta)$ and the time delay τ at a given radius, we numerically integrate out the angular dependence, and reformulate equations (13) and (17) in terms of τ to obtain an emissivity-weighted effective delay, τ_ε, and a responsivity-weighted effective delay, τ_η. These quantities correspond to r_ε/c and r_η/c, respectively, for isotropically emitting clouds. The total luminosity can then be recovered by integrating $dL(\tau)$ over $0 < \tau < 2r_{out}/c$, where $dL(\tau)$ is the 1-d response function. We note that, as the responsivity of a given emission line may be negative at some or all radii, the response function may not have a well-defined responsivity-weighted centroid τ_η; in practice, we find that $s = 2$ models tend to display negative responsivity at large radii.

4 STEADY-STATE MODELS

As the available parameter space for our pressure-law BLR models spans several orders of magnitude in Φ_H, n_H, and N_{col}, we first determine which steady-state models are roughly consistent with the observed luminosities of the strongest UV and optical BEL in NGC 5548. This allows us to exclude models for which the BEL emission is too weak to be relevant for this test case. We then select two representative models, one each for $s = 0$ and $s = 2$ (Section 4.1). For these models we investigate the BEL responses (Section 4.2) and, of particular relevance here, the relative contribution and wavelength-dependent behavior of the diffuse continuum (Section 4.3). Lastly, we examine the dependence of the diffuse continuum luminosity, response functions, and measured lags, on the parameters n_H, Φ_H, and U, for the broader class of $s = 0$ and $s = 2$ pressure laws (Section 4.4).

4.1 BEL luminosities

Here, we determine the range of pressure law models able to roughly reproduce the observed BEL luminosities. Ideally we require our model integrated BEL luminosities (as calculated for a covering factor of 4π steradian) to exceed their corresponding measured values. This is because our model does not account for BLR self-shadowing, making it unreliable at high covering factors. Reducing the covering factor corresponds to a linear scaling of the BEL luminosities, e.g. for a covering fraction of $4\pi/3$ steradian, the model luminosities given by equation (10) should exceed observations by a factor of 3.

4.1.1 Observed line luminosities

We compare our models to the observed UV BEL (De Rosa et al. 2015) and optical BEL (Pei et al. 2017) luminosities for NGC 5548 during the 2014 AGN STORM campaign. While Schlafly & Finkbeiner (2011) find a Galactic reddening of $E(B - V) = 0.02$ towards NGC 5548, Kraemer et al. (1998) find that the narrow-line region in NGC 5548 has an additional intrinsic reddening of $E(B - V) \approx 0.04$. For consistency with previous photoionization studies of this AGN (e.g. Korista & Goad 2000), and given the uncertainty on the total (Galactic plus intrinsic) reddening of the BLR, we adopt $E(B - V) = 0.03$. We de-redden the observed luminosities using the reddening curve presented by Cardelli et al. (1989), with

Table 1. Observed L_{line} and line lags for NGC 5548

Line	log $[L_{line}]$	Lag [days]	Reference
(1)	(2)	(3)	(4)
Lyα	42.4	$6.2^{+0.3}_{-0.3}$	de Rosa+
C IV	42.6	$5.3^{+0.4}_{-0.5}$	de Rosa+
Hβ	41.7	$6.14^{+0.74}_{-0.98}$	Pei+
He II 1640 Å	41.7	$2.5^{+0.3}_{-0.3}$	de Rosa+
He II 4686 Å	40.7	$2.46^{+0.49}_{-0.25}$	Pei+

*Note*s. (1) Broad emission line name. (2) Log of the line luminosity in units of erg s^{-1}, corrected for Galactic reddening and with narrow-line components subtracted; we use the decompositions presented by Korista & Goad (2000) for the UV lines, and those of Peterson et al. (1991) for the Balmer lines. (3) Observed CCF centroid for the 2014 RM campaign, as measured using the ICCF method. (4) References: De Rosa et al. (2015) and Pei et al. (2017).

$R(V) = 3.1$. For C IV and Hβ, we subtract a narrow emission-line component from the observed BEL luminosities, as determined by Peterson et al. (1991) and Korista & Goad (2000), respectively; while the narrow emission line strengths for NGC 5548 have shown some variation on multiyear time-scales (Peterson et al. 2013), we only require a first-order correction for the purposes of this study. The inferred emission-line luminosities, corrected for reddening and for narrow-line emission, are listed in Table 1.

4.1.2 Model 1, constant density (s = 0)

We calculate the BEL luminosities produced by constant-density ($s = 0$) models spanning the full range of hydrogen gas densities $7 \leq \log[n_H /cm^{-3}] \leq 14$ and gas column densities $22 \leq \log[N_{col} /cm^{-2}] \leq 24$. A density of $\log[n_H /cm^{-3}] > 10$ is required to produce sufficient C IV luminosity to match the 2014 observations (Fig. 5), and to produce stratification in the emission-line delays (Fig. 7). For a column density of $\log[N_{col} /cm^{-2}] = 22.5$, our model emission-line luminosities cannot simultaneously exceed the measured Lyα, Hβ, C IV, and He II 4686 Å BEL luminosities (Fig. 5, upper left). In terms of observed line ratios, the model Hβ line is underproduced relative to Lyα except at very high gas densities ($\log[N_{col} /cm^{-2}] \gtrsim 13$). While we do find one model that marginally exceeds the observed luminosities of all four lines (namely, that with $\log [n_H/cm^{-3}] = 9$ and $\log[N_{col} /cm^{-2}] = 24$), this extreme case would imply a Compton-thick yet low-density BEL at all r. The diameters of individual BLR clouds are ∼0.5 light-day for this extreme case; the smoothness of observed BEL velocity profiles excludes such large sizes (e.g. Laor 2004). Thus, if the underlying photoionization modeling is correct, a single $s = 0$ pressure-law component cannot account for the measured BEL strengths in NGC 5548. At least one additional high-density ($\log[n_H /cm^{-3}] \gtrsim 12.5$) component would be required to produce sufficient luminosity in all BELs. However, the underproduction of Hβ in our models may instead be an issue with the treatment of radiative transfer in our photoionization modeling. The CLOUDY algorithm uses the local escape probability formalism, which becomes unreliable at the very high hydrogen optical depths typical of BLR clouds (Netzer 1990; Kaspi & Netzer 1999). In the absence of an exact treatment of radiative transfer, it is difficult to determine whether the low Hβ line emission for single-component models actually implies the existence of additional BLR emission regions with higher densities. All else equal, the simplicity of a single-component model is attractive in the context of studying the diffuse continuum component (Section 4.3).

We therefore define our **Model 1** as an $s = 0$ pressure-law BLR with $\log[n_H /cm^{-3}] = 10.75$ and $\log[N_{col} /cm^{-2}] = 22.5$; this model fulfills our luminosity criterion for all of the strongest UV and optical BEL apart from Hβ. Our choice of N_{col} here is somewhat arbitrary; the emission-line luminosities and response function centroids are only strongly sensitive to N_{col} for low column densities, $\log[N_{col} /cm^{-2}] < 22.5$. Specifically, the observed C IV, Lyα and He II 4686 Å luminosities are exceeded for $10.25 < \log[n_H /cm^{-3}] < 11.25$ for $22.5 \leq N_{col} \leq 24$.

4.1.3 Model 2, constant ionization parameter (s = 2)

The family of constant ionization parameter ($s = 2$) models described here display an increasing column density and increasing density towards the centre (equations 3 and 7). The $s = 2$ models generally produce more BEL luminosity than do the $s = 0$ models because they distribute a larger fraction of the BLR clouds at large r (Fig. 4), i.e. at lower incident ionizing photon flux, at which the optical recombination lines (Hα and Hβ) and Mg II tend to have higher surface emissivities. In contrast to our chosen $s = 0$ model, constant U models are capable of exceeding the measured emission line luminosities of all of the strong UV–optical emission lines (including Hβ) for $\log (U) \lesssim -1.1$ (Fig. 6). We do not explore models with $\log U < -2.1$, as for these models n_H lies outside the bounds of our model grids for radii $\leq r_{in}$. We define **Model 2** as an $s = 2$ pressure law BLR with constant ionization parameter $\log (U) = -1.23$. This is the $s = 2$ model for which the Hβ and C IV BEL luminosities are maximized (Fig. 6). By construction, Model 2 has locally identical steady-state physical conditions (i.e. n_H, N_{col}, and U) to Model 1 at r_{20}, where $r_{20} \approx 14.8$ light-days for NGC 5548. For $r_{in} = 1$ light-day and $r_{out} = 140$ light-days, Model 2 spans $21 \lesssim \log[N_{col} /cm^{-2}] \lesssim 24$, and $8.8 < \log[n_H /cm^{-3}] < 13.1$.

4.2 BEL response functions

We summarize the measured broad emission line delays for the strong UV and optical emission lines for the AGN STORM 2014 monitoring campaign in Table 1, and present the response function centroids generated by our models in Table 2. For Model 1, the lines tend to be most responsive at lower ionizing photon flux, i.e. in the outer BLR. Thus, we see $\tau_\eta > \tau_\varepsilon$ for Model 1. Model 2 tends to produce larger emissivity-weighted response function centroids than Model 1; this is a direct consequence of the $s = 2$ pressure law distributing more coverage (and, therefore, more line-emitting gas) at larger radii relative to the $s = 0$ models (Fig. 4). However, Model 2 has small (and often slightly negative) line responsivities at large radii. Thus, the lines respond most strongly in the inner BLR, and we have $\tau_\eta < \tau_\varepsilon$ for Model 2. For Lyα, C IV, and Hα, the response functions are positive in the inner regions but strongly negative at large r for Model 2. They therefore lack a well-defined centroid; however, the effective radius that would be measured using RM observations can still be estimated by calculating the BEL response to continuum variations, as we explore via Monte Carlo modeling (Section 5).

For lines with a well-determined response function centroid τ_η, both models produce values of τ_η that are somewhat larger than the measured lags reported for the strong UV and optical broad emission lines in NGC 5548 prior to the AGN STORM campaign (Clavel et al. 1991; Korista et al. 1995; Peterson et al. 2002; Bentz et al. 2010a; Denney et al. 2010; Cackett et al. 2015). For example, for Model 1, we find a Hβ response function centroid of $\tau_\eta \approx 62$ d, which is significantly larger than the Hβ lag predicted by either
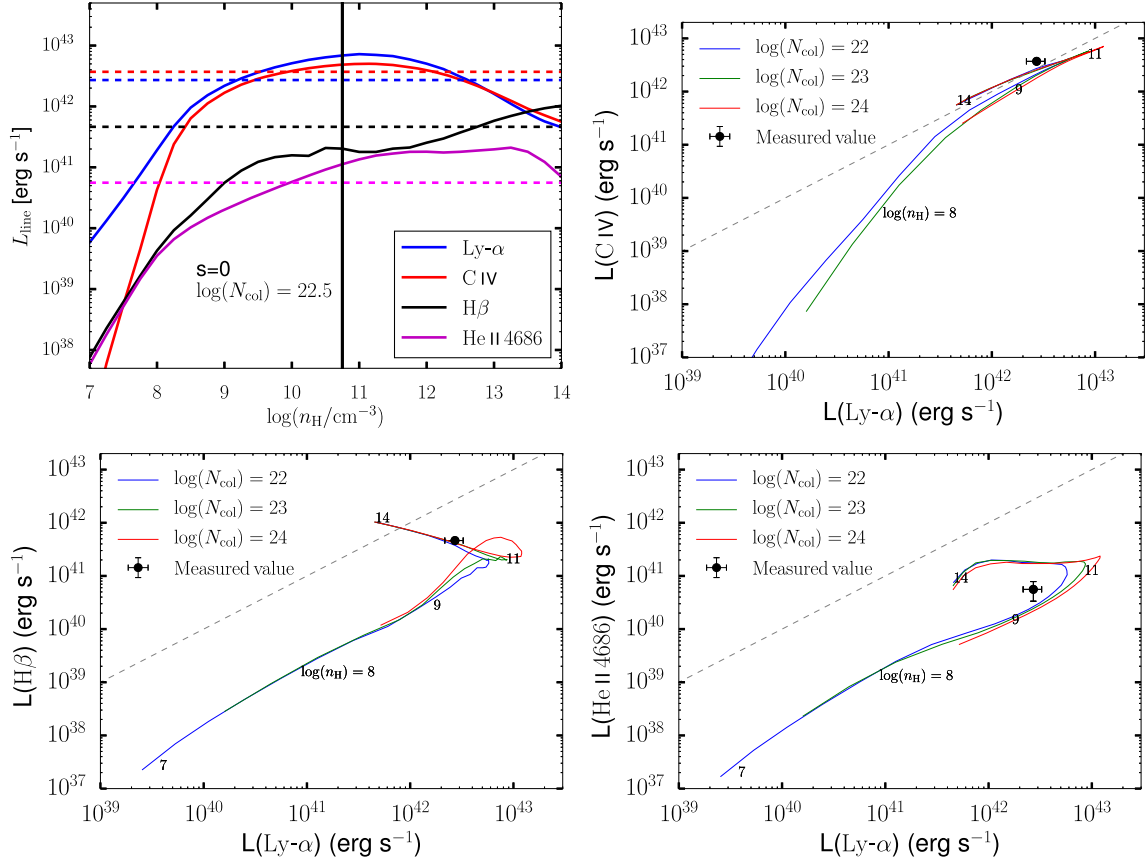
Figure 5. *Top left:* Model BEL luminosities as a function of n_H (solid curves). Here we assume that the BLR covers 4π steradian of the continuum source (see discussion in Section 4.1). The measured broad emission-line luminosities for NGC 5548 (De Rosa et al. 2015; Pei et al. 2017) are shown as dashed lines. For the observed C IV and H β luminosities, we subtract a narrow emission-line component (see Section 4.1 for details). The black vertical line shows $\log[n_H/cm^{-3}] = 10.75$, corresponding to our Model 1. The main conclusion to be drawn here is that the measured emission-line luminosities for Lyα, C IV, and He II 4686 Å are exceeded for $9.75 \lesssim \log[n_H/cm^{-3}] \lesssim 12.25$, while higher densities are required to reproduce the H β luminosity (Section 4.1). *Other panels:* Predicted BEL luminosities for C IV *(top right)*, H β *(bottom left)*, and He II 4686 Å *(bottom right)*, relative to Lyα, for a grid of our $s = 0$ BLR models. Each of the three 'tracks' represents a single value of $\log[N_{col}/cm^{-2}]$; the density n_H ranges over $7 \leq \log[n_H/cm^{-3}] \leq 14$, and increases in a counterclockwise direction. We indicate the location of selected values of n_H for the $\log[N_{col}/cm^{-2}] = 22$ track; the tracks with larger column densities have higher line luminosities at low n_H but are similar at high gas densities. As a visual aid, the dashed black lines indicate 1:1 line ratios. Black circles represent the observed line luminosities for NGC 5548, after correcting for reddening and narrow-line contamination. In general, we note that gas densities of $\log[n_H/cm^{-3}] \sim 11$ tend to maximize the line intensities, and that the relative intensities of the BELs investigated here are not strongly sensitive to N_{col} (as the 'tracks' are not widely separated) for the range of column densities explored here.

the empirically determined global radius–luminosity relationship (Bentz et al. 2013), or by the single-object $L(1350)$ Å-H β RL relationship for NGC 5548 as determined by Kilerci Eser et al. (2015). Much of the discrepancy with the pre-2014 RM results can be attributed to the variability behavior of the continuum source, as discussed in Section 5.

The AGN STORM campaign detected anomalously short (given the source luminosity) BEL lags, of less than 10 d, for NGC 5548 in 2014. None of our $s = 0$ models produce H β response function centroids of less than ~ 50 d (Fig. 7), nor do the $s = 2$ models with $-2 \leq \log(U) \lesssim -0.5$. While $s = 2$ models with $\log(U) > -0.5$ do produce centroids at shorter delays ($\tau_\eta \approx 10$ d for H β), such models do not produce sufficient luminosity in C IV to match observations (Fig. 6).

4.3 The diffuse continuum for Models 1 and 2

Using CLOUDY, we generate radial surface emissivity distributions $\varepsilon(r, \lambda)$ for the DC emission at more than 60 discrete wavelengths,

sampling the UV to near-infrared regime from $\lambda\lambda$ 910–41137Å. This range encompasses the Lyman limit to just beyond the K band, the longest wavelength band sampled from the ground in disc and dust reverberation mapping studies (e.g. Kishimoto et al. 2007; Mandal et al. 2018).

Each continuum wavelength is processed separately as per the methodology described in Section 3. We first determine the DC luminosity $\nu L_\nu(\text{diff.})$ at each wavelength, by integrating equation (8) from r_{in} to r_{out} (Fig. 8, top panels), replacing the emission line surface emissivity $\varepsilon(r)$ with the monochromatic DC emissivity $\varepsilon(r, \lambda)$. For both $s = 0$ and $s = 2$ models, the diffuse continuum represents a significant fraction of the total continuum (incident+diffuse), contributing up to ~ 40 per cent of the measured continuum luminosity blue-wards of the Balmer jump, assuming that the nuclear source is fully covered by the BLR (more realistic covering fractions are explored in Section 6). Furthermore, both models display strong Balmer and Paschen continua, rising towards longer wavelengths, with a significant drop in emission redwards of the Balmer (λ3648 Å) and Paschen (λ8204 Å) jumps.
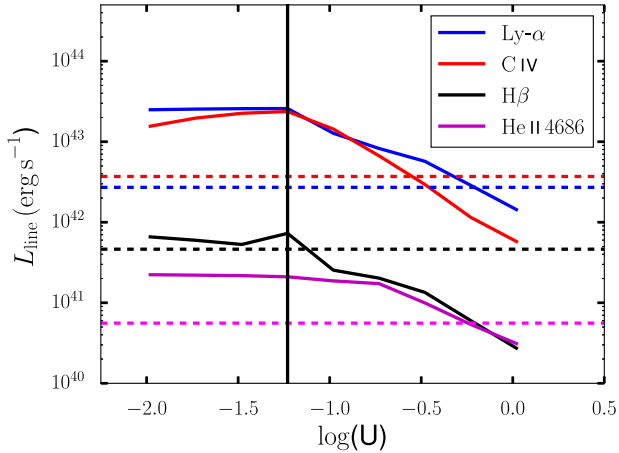
Figure 6. Model BEL luminosities for Lyα, C IV, Hβ, and He II 4686 Å, for the $s = 2$ (constant ionization parameter) steady-state model. These values of L_{line} assume that the BLR covers 4π steradian of the continuum source (see discussion in Section 4.1). The measured emission-line luminosities (dashed lines) are exceeded for ionization parameters $\log(U) \lesssim -1.1$. The solid vertical line indicates $\log(U) = -1.23$, corresponding to our Model 2; for our chosen normalization of N_{col}, this value approximately maximizes the line intensities.

Next we determine the wavelength-dependent response functions for each of the DC bands. We include the effects of responsivity (Section 3.4) and anisotropy (Section 3.4.2) in the same fashion as for the BELs. The inclusion of anisotropic emission does not strongly affect the measured centroids for either model; this demonstrates that the DC emits fairly isotropically. The Model 1 ($s = 0$) DC has a higher responsivity at large radii, so $\tau_\varepsilon < \tau_\eta$ (Fig. 8, bottom left). For Model 2 ($s = 2$), the DC is more responsive in the inner regions, thus $\tau_\varepsilon > \tau_\eta$ for that model (Fig. 8, bottom right). We also highlight that the DC delays at wavelengths near $H\beta$ are *significantly smaller* (by a factor of ~ 2) than the delays predicted for the Hβ BEL itself.

While the wavelength dependence of the DC luminosities for the two models are broadly similar, their temporal behavior is markedly different. For Model 1, the lags are larger blue-wards of the Balmer and Paschen jumps, while Model 2 displays the opposite behaviour, with elevated lags red-wards of the jumps. Whether such differences in temporal behaviour are ever realized in practice will depend on the fractional contribution of the DC emission to the total continuum emission F_{diff} (see Section 5.4 for details).

4.4 Comparison of diffuse continuum properties for pressure-law BLRs

As noted above, our single-component pressure-law models do not reproduce the measured emission-line luminosities or their ratios for NGC 5548 in detail; multiple components (spanning a broad range in density and/or ionization) would be required. For this reason, we now extend the analysis of Section 4.3 to encompass models spanning a broader range of n_H and U.

4.4.1 Density dependence

We investigate the DC emitted by a range of $s = 0$ models spanning $8 \leq \log[n_H/\text{cm}^{-3}] \leq 14$, with other parameters identical to Model 1. The behaviour of the DC depends strongly on n_H. At

low densities, the gas is highly ionized, and the reprocessed continuum is dominated by electron scattering, mostly free–free. For $\log[n_H/\text{cm}^{-3}] = 8$, the DC luminosity is almost two orders of magnitude smaller than that of the incident continuum, and is produced at radii of ~ 20 light-days (Fig. 9, top panels). As n_H increases, the DC emission becomes more prominent, its SED becomes dominated by the Balmer and Paschen continuum features (mostly free–bound recombination continuum), and it is produced at larger radii, $20 \lesssim \tau_\eta \lesssim 80$ light-days (Fig. 9, middle panels). The delay centroid τ_η shows a strong wavelength dependence, with longer lags blue-wards of the Balmer and Paschen jumps. At the highest n_H ($\log[n_H/\text{cm}^{-3}] > 10^{12}$ cm^{-3}), the BLR reprocesses so much of the ionizing continuum that, for full source coverage, the DC actually exceeds the brightness of the incident nuclear continuum over much of the UV–optical regime. At these high densities, unlike Hβ, the DC is dominated by gas at small BLR radii (high incident ionizing photon flux), and therefore responds on comparatively shorter time-scales, $\tau_\eta < 20$ d (see also Korista and Goad 2001, their Figs 1a and b).

4.4.2 Ionization parameter dependence

We investigate a range of $s = 2$ models spanning $-1.98 \leq \log(U) \leq 0.52$, altering the density normalization at r_{20}, and keeping the N_{col} normalization the same as before, i.e. a high U model corresponds to a lower density normalization at r_{20} (the highest U model shown here has a density at r_{20} of $\log n_h = 9.0$ cm^{-3}). For $s = 2$ models, the response function centroids $\tau_\eta(\lambda)$ show the opposite trend in wavelength to $s = 0$ models, that is, $\tau_\eta(\lambda)$ is slightly smaller blue-wards of the Balmer and Paschen jumps (Fig. 10). The DC contribution is not strongly sensitive to the ionization state of the gas over a broad range in U, as the gas is cooled primarily by line emission in this regime; the flux contours for the DC bands on the n_H–Φ_H plane are widely separated (e.g. Fig. 3). At high values of U the reprocessed continuum is dominated by weak free–free continuum and electron scattering and thus resembles a power law. This continuum is weak relative to the incident UV–optical continuum (<1 per cent of the total), while the total line emission from such gas is insufficient to match the measured broad emission-line luminosities.

5 MONTE CARLO MODELING OF BLR LIGHT CURVES

The values of $\tau(\lambda)$ presented thus far, for both the broad emission lines and reprocessed continuum, represent the 'steady-state' values. In practice, such values are seldom (if ever) realized because measured values depend not only on where the lines and continuum form, but also on the nature of the driving continuum (i.e. amplitude and characteristic variability time-scale), and on the precise details of the monitoring program (e.g. campaign duration and sampling rate). See Goad & Korista (2014) for details. A possible exception would be for a short sharp continuum event (i.e. a delta-function pulse in the continuum). Here, we simulate an ensemble of driving continuum light curves that have similar statistical properties to those observed for NGC 5548, and combine these with the response functions of our BLR models to obtain simulated light curves for the broad emission lines and diffuse continuum bands. We then measure the lags directly from the cross-correlation of our model light curves with the driving continuum light curve, mimicking a real observing situation. In general, this process results in measured delays that are significantly shorter than the 'steady-state' values (as indicated by the centroid of the response function).
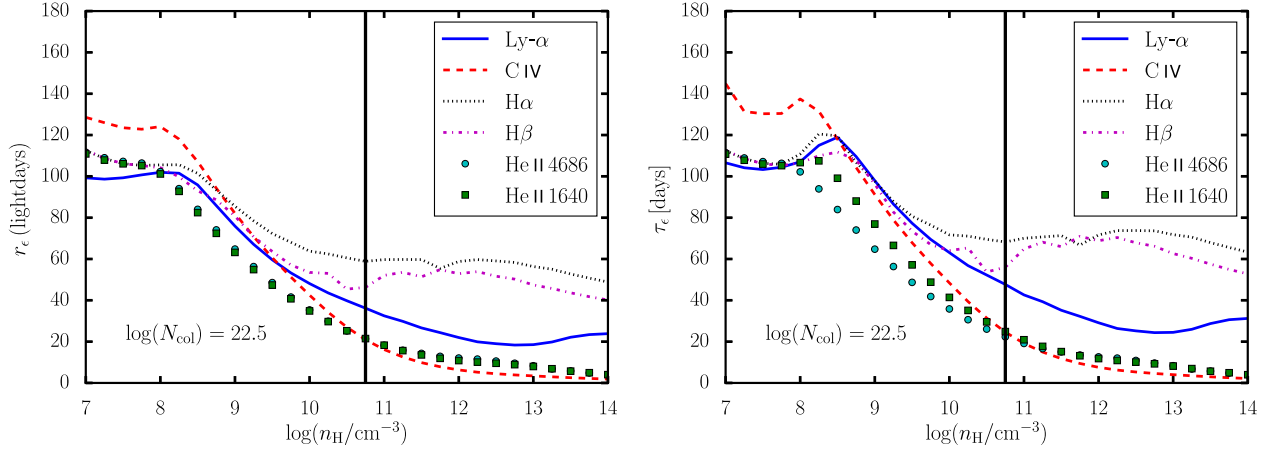
Figure 7. The emissivity-weighted effective radii, r_ε (left-hand panel), and emissivity-weighted delay τ_ε (right-hand panel), as a function of n_H, for $s = 0$ models with $\log[N_{col}/cm^{-2}] = 22.5$. The delays shown in the right-hand panel accounts for anisotropic emission from the BLR clouds, which acts to increase the time delays relative to the isotropic case. In general, lower values of n_H result in a BLR that emits most efficiently at larger radii, increasing the emissivity-weighted delay. The black solid lines show the location of $\log[n_H/cm^{-3}] = 10.75$, corresponding to our Model 1.

Table 2. Steady-state models

Line	$\log[L_{line}]$	r_ε [light-days]	r_η [light-days]	τ_ε [days]	τ_η [days]	$\tau_{CCF, peak}$ [days]	$\tau_{CCF, cent}$ [days]
(1)	(2)	(3)	(4)	(5)	(6)	(7)	(8)
— **Model 1:** $s = 0$, $\log[n_H/cm^{-3}] = 10.75$, $\log[N_{col}/cm^{-2}] = 22.5$							
Lyα	42.8	36.2	46.5	47.7	61.6	35.7 ± 6.6	39.4 ± 8.6
C IV	42.7	20.9	35.0	24.6	40.9	29.7 ± 3.5	33.6 ± 4.8
Hα	41.9	58.9	70.2	68.3	81.4	41.2 ± 25.6	44.9 ± 24.4
Hβ	41.3	46.3	52.8	56.0	63.6	34.1 ± 4.7	33.3 ± 7.2
He II 4686 Å	41.1	21.4	30.1	22.3	31.2	17.6 ± 1.2	20.5 ± 2.7
Mg II	42.0	74.4	101.3	92.7	126.8	76.8 ± 65.7	77.4 ± 65.1
— **Model 2:** $s = 2$, $\log(U) = -1.23$, $\log[N_{col}/cm^{-2}](r_{20})$=22.5, $\log[n_H/cm^{-3}](r_{20})$=10.75							
Lyα	43.1	50.5	Cx	50.5	Cx	28.6 ± 3.6	29.8 ± 3.8
C IV	43.1	51.0	Cx	55.5	Cx	32.9 ± 10.7	36.1 ± 10.6
Hα	42.0	53.7	Cx	59.0	Cx	21.7 ± 10.2	22.4 ± 10.6
Hβ	41.4	53.7	32.4	57.9	34.3	23.3 ± 10.1	27.6 ± 12.8
He II 1640 Å	42.2	56.7	39.4	63.9	47.8	36.0 ± 19.8	40.4 ± 19.1
He II 4686 Å	41.3	54.3	37.3	54.6	37.8	26.0 ± 8.1	30.6 ± 9.7
Mg II	41.2	22.2	35.9	24.0	37.3	− 25.2 ± 89.8	− 25.2 ± 89.6

Notes. The responsivity of the Mg II BEL in our models is very low; thus, the CCF lags measured for that line are highly uncertain and would not be accurately measurable in a real observing situation. (1) Broad emission line name. (2) Log of the line luminosity in units of erg s^{-1}, for a BLR covering 4π steradian of the continuum source. (3) Emissivity-weighted BLR radius, in units of light-days. (4) Responsivity-weighted BLR radius, in units of light-days. 'Cx' denotes lines that have negative repsonsivity for a non-negligible fraction of the radial extent of the BLR; the integrated line luminosities may respond positively or negatively to continuum changes, and their response functions do not have a well-defined responsivity-weighted centroid. (5) Emissivity-weighted transfer function centroid, in days, allowing for anisotropic emission. (6) Responsivity-weighted transfer function centroid, allowing for anisotropic emission. 'Cx' denotes lines that have negative repsonsivity for a non-negligible fraction of the radial extent of the BLR. (7) Mean CCF peak delay time for the continuum versus line response, using response functions that include the effects of local anisotropy and responsivity. The BELs are driven using a Damped Random Walk continuum with a 500-day baseline (Section 5.1). The measurement is repeated for 10 000 realizations of the DRW continuum; for each realization, the CCF is obtained using the methodology of White & Peterson (1994) (Section 5.2). The uncertainty shown is the standard deviation of the peak values. (7) Mean CCF centroid, and its standard deviation, for 10 000 realizations of the DRW continuum.

For comparison with recovered response functions, we here adopt a 'locally linear' response approximation, estimating the marginal response of the emission lines (and diffuse continuum bands) to continuum variations about their steady-state (average) values. This approach is suitable (and computationally less expensive) for small continuum variations about the mean, but becomes progressively poorer as the amplitude of the continuum variations increases. Key assumptions underpinning this method include:

(i) The driving ionizing continuum source as seen from the BLR is point-like.

(ii) There is a linear relationship (though not necessarily 1:1) between the driving continuum variations and the emission-line (or DC) response.

(iii) The emission-lines (or DC) respond effectively instantaneously to local variations in the incident ionizing continuum flux.

(iv) No new material is added or destroyed.

(v) The dominant time-scale is the light crossing time.

(vi) As the driving continuum varies, only its amplitude changes, not its overall shape.
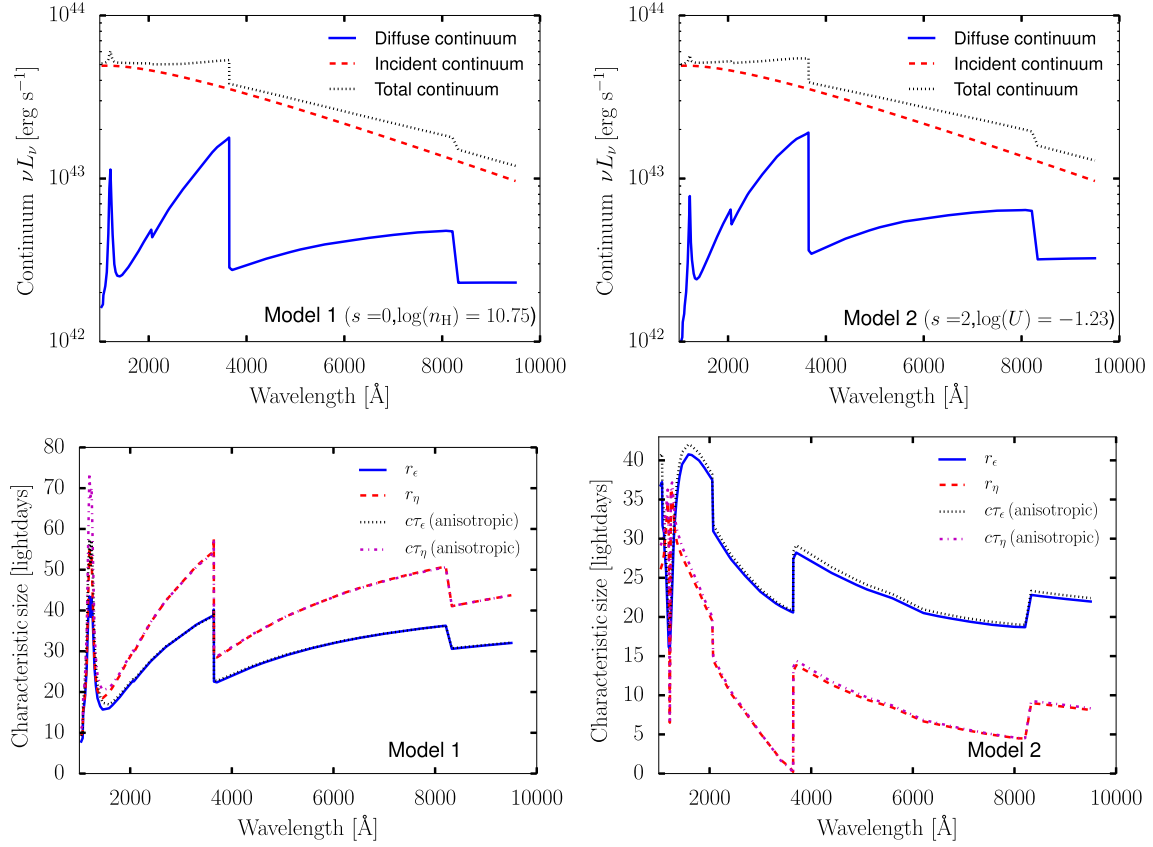
Figure 8. *Top:* The specific luminosities λL_λ for the diffuse BLR continuum components, as a function of rest-frame wavelength, for Model 1 ($s = 0$, left-hand panel) and Model 2 ($s = 2$, right-hand panel). We also show the luminosities of the nuclear continuum as presented by Mehdipour et al. (2015), and the total continuum that would be observed for these models, i.e. the sum of the nuclear and diffuse components. *Bottom:* The effective emissivity-weighted (r_ε) and responsivity-weighted (r_η) radii in units of light-days, and centroids of the emissivity–weighted (τ_ε) and responsivity-weighted (τ_η) response functions in units of days, for the diffuse continuum response functions, as a function of wavelength. As the response functions describe the response of the BLR to a delta-function pulse in the continuum luminosity, their centroids do not take the variability properties of an AGN-like driving continuum into account; see Fig. 12 for the corresponding driven lags. We note that for both models r_ε and τ_ε almost overlap, as do r_η and τ_η – this implies that the diffuse continuum emits fairly isotropically at all radii.

These assumptions are adopted only for expediency. For all but the highest ionization lines, the assumption of a point-like continuum source remains a valid approximation. SED variations can and do occur, but are generally secondary to changes in the ionizing continuum flux. A locally linear response can be justified provided that the amplitude of the continuum variations remain small. Under these conditions, the emission line (or DC) light curve at time t, $L(t)$ can be represented by the convolution of the emission-line (or DC) transfer function $\Psi(\tau)$ with the driving ionizing continuum light curve at previous times $C(t - \tau)$:

$$L(t) = \int_{-\infty}^{\infty} \Psi(\tau) C(t - \tau) \mathrm{d}\tau \,. \tag{19}$$

Typically, this equation is solved in its linearized form,

$$\Delta L(t) = \int_{-\infty}^{\infty} \Psi'(\tau) \Delta C(t - \tau) \mathrm{d}\tau \,, \tag{20}$$

with non-variable emission-line (DC) components consigned to a background term.

5.1 Driving the BLR with a model continuum

On time-scales of approximately weeks to months, the continua of AGN vary approximately as a damped random walk (DRW) in the logarithm of the flux (e.g. Kelly, Bechtold & Siemiginowska 2009; Kozłowski et al. 2010; Zu et al. 2013; Edelson et al. 2014). A DRW process is characterized by a variability amplitude σ_{DRW}, along with a damping (or characteristic) time-scale T_{char} upon which it tends to return to the mean. For model BLRs driven by DRW continua, Goad & Korista (2014) perform an in-depth investigation of the influence of both the observational constraints (campaign length, observational cadence) and the DRW parameters, on the measured lags. The lag for emission line light curves produced by their model BLR, as measured using the interpolated cross-correlation function (ICCF) method (White & Peterson 1994), is strongly dependent on T_{char} of the input continuum, in the sense that short characteristic time-scales lead to underestimated lags (relative to the centroid of the response function). The measured lags approach the expected (i.e. steady-state) values for $T_{\mathrm{char}} > r_{\mathrm{out}}/c$.

The continuum variability displayed by NGC 5548 over the period 1989–1993 can be described as a DRW with characteristic time-scale $T_{\mathrm{char}} \approx 40$ d and signal variance $\sigma_{\mathrm{DRW}} = 0.04$ (Collier et al. 2001). This damping time-scale is considerably shorter than the maximum light travel times for our model BLR (i.e. $2r_{\mathrm{out}}/c =$
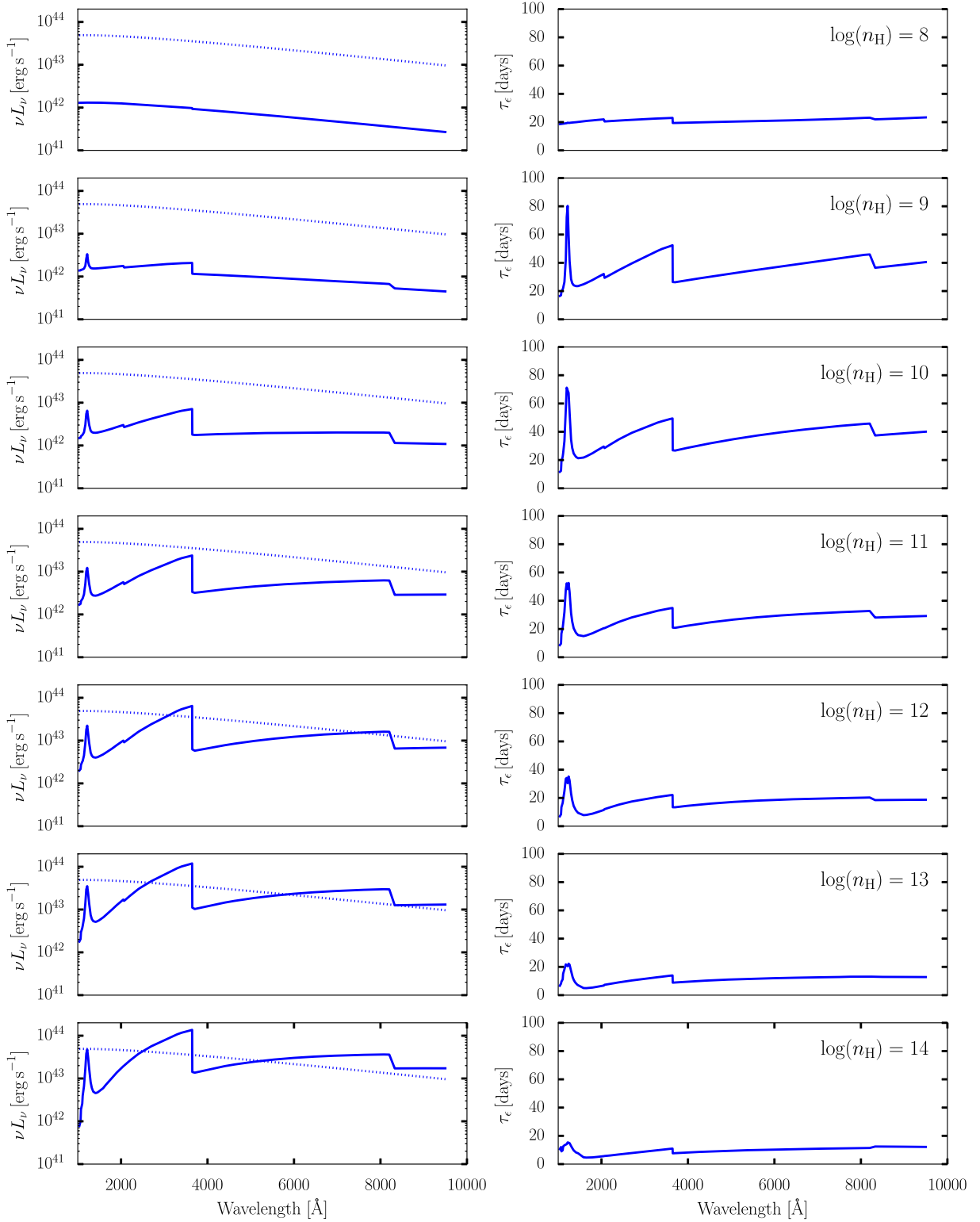
Figure 9. *Left-hand panels:* Specific luminosity of the diffuse (solid line) and incident (dashed line) continuum components, for $s = 0$ models spanning a range of n_H, $8 \leq \log[n_H / cm^{-3}] \leq 14$. The DC contribution is stronger, and the Balmer and Paschen features are more pronounced, at higher n_H. *Right-hand panels:* The corresponding wavelength-dependent response function centroids $\tau_\eta(\lambda)$ for the diffuse continuum, including the effects of anisotropy. For higher n_H, the DC is efficiently emitted closer to the black hole, producing shorter delays. As these quantities are measured from the response functions, they do not take the properties of the driving continuum into account; see Fig. 13 for the corresponding driven lags.
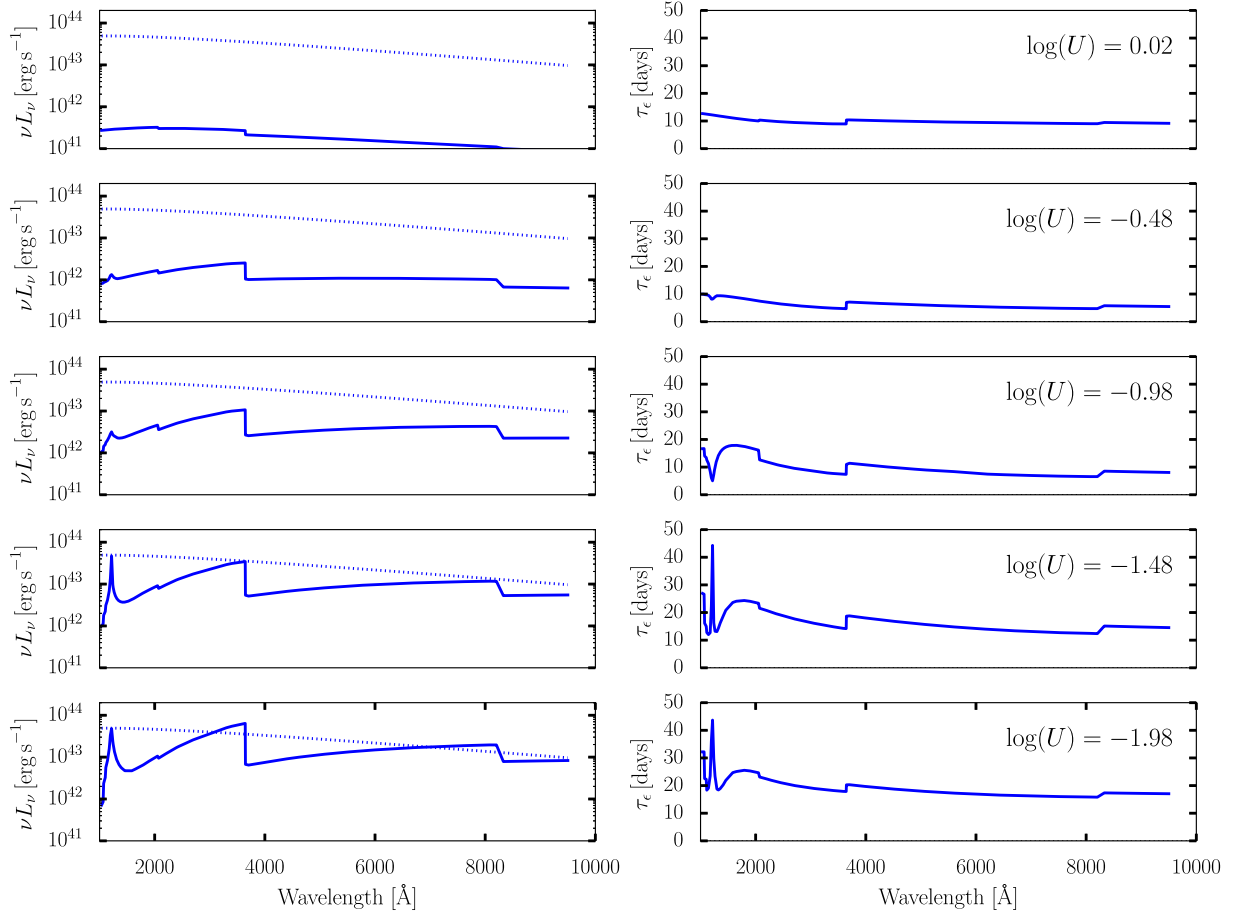
Figure 10. *Left-hand panels:* Specific luminosity of the diffuse (solid line) and incident (dashed line) continuum components, for $s = 2$ models spanning a range of ionization parameter, $0.52 \geq \log[n_H/cm^{-3}] \geq -1.98$. The DC emits more brightly for models with lower U. *Right-hand panels:* the corresponding wavelength-dependent responsivity-weighted centroid $\tau_\eta(\lambda)$ of the response function for the diffuse continuum, including the effects of anisotropy. The temporal behavior near the Balmer and Paschen breaks for the $s = 2$ models is qualitatively different from the $s = 0$ case (Fig. 9). As these quantities are measured from the response functions, they do not take the properties of the driving continuum into account; see Fig. 14 for the corresponding driven lags.

280 d). It is therefore important to take the continuum variability behavior into account when comparing our model lags to measured values. To this end, we generate DRW continuum light curves with which to drive the BLR. For uniform sampling, the DRW is equivalent to a discrete, autoregressive AR(1) process (Kelly et al. 2009, as detailed in their Appendix); we generate light curves with a cadence of 1 rest-frame day, using the AR(1) algorithm to obtain the logarithm of the flux in each subsequent time-step. Unless otherwise indicated, the DRW continuum light curves used in this work are generated using $T_{DRW} = 40$ d and $\sigma_{DRW} = 0.04$, with a campaign duration of 500 rest-frame days.

The BEL and DC light curves, as driven by this ionizing continuum, are then generated by convolving the DRW light curve with the relevant BLR response function (Section 3.4) representative of a particular emission line or diffuse continuum band. We show an example DRW continuum light curve, along with the driven BEL light curves for four emission line species (Lyα, C IV, Hβ, and Mg II), in Fig. 11. These indicate a broad range in amplitude and delay, i.e. a stratified and spatially extended BLR, as is commonly observed.

5.2 Lag determination via cross-correlation

Given the continuum and the BEL (or DC) light curves described in Section 5.1, we measure the *as-observed* lag, following the ICCF method (White & Peterson 1994), commonly used to determine lags for real RM campaigns (e.g. Kilerci Eser et al. 2015; Lu et al. 2016; Pei et al. 2017). We measure both the peak value of the cross-correlation function ($\tau_{CCF, peak}$) and the centroid ($\tau_{CCF, cent}$), determining the centroid over the range in which the CCF coefficient exceeds 80 per cent of its peak value. We primarily work with $\tau_{CCF, cent}$ in our analysis, as this measure is less susceptible to bias towards shorter lags (Pêrez, Robinson & de La Fuente 1992a). The detailed shape of the CCF depends strongly on the specific realization of the DRW continuum (i.e. the continuum autocorrelation function), which is stochastic in nature. We therefore generate 10 000 realizations of the DRW continuum for each of our model BLRs, and determine the CCF peak and CCF centroid for each realization. This allows us to determine the mean and standard deviation of $\tau_{CCF,cent}$ for each BEL and each diffuse continuum waveband, holding the DRW parameters T_{char} and σ_{DRW} constant. Quoted lags (Table 2,
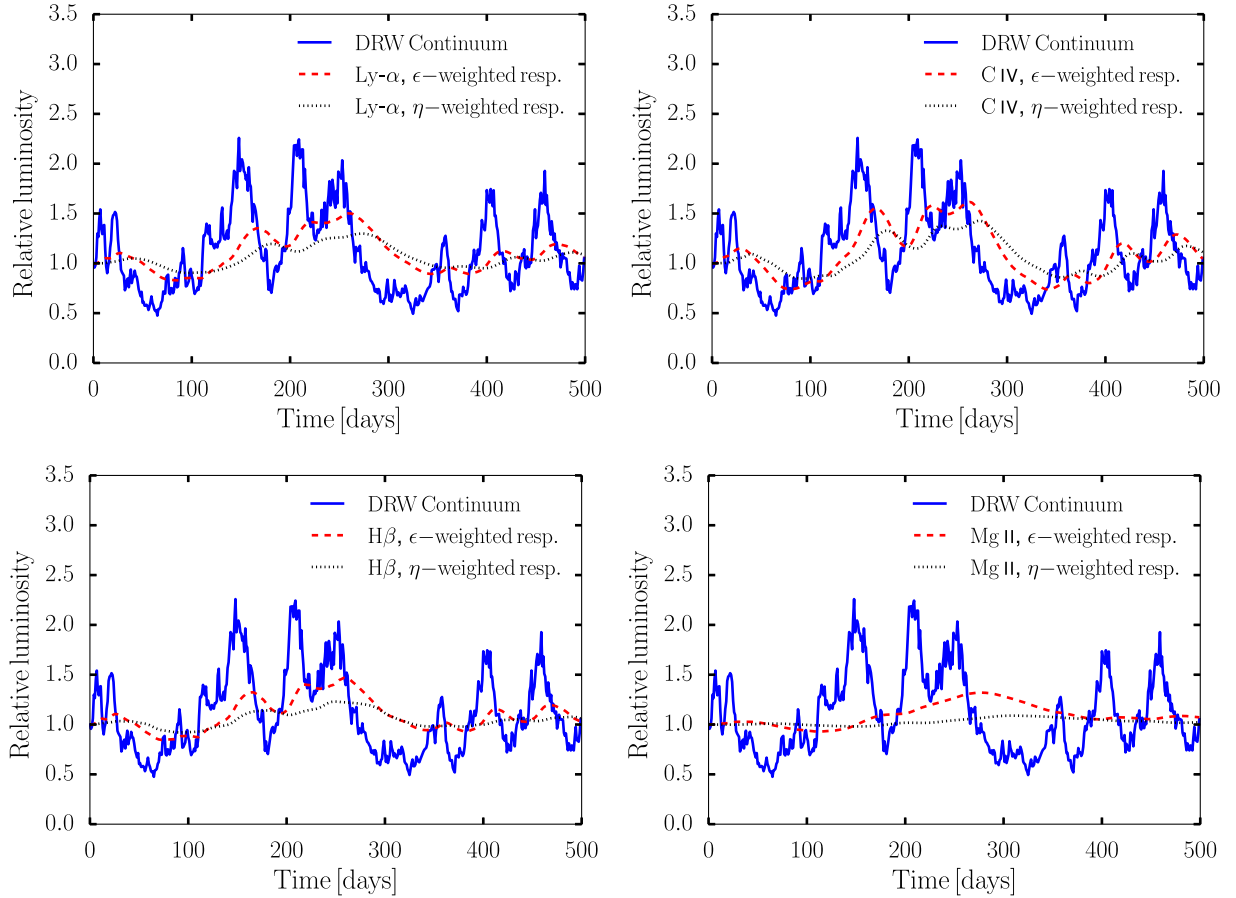
Figure 11. Driving the BELs for model 1 using a DRW continuum with $T_{char} = 40$ d and $\sigma_{char} = 0.4$ (Section 5.1). Here, we show one example realization of the DRW continuum; in order to determine the average delays and their statistical uncertainties, we generate 10 000 realizations of this continuum light curve. Including the effects of anisotropic emission generally increases the observed lag and decreases the response amplitude. As an extreme example, the Mg II BEL responds very weakly in our model when anisotropic emission is taken into account (i.e. the η-weighted light curve).

columns 7 and 8) represent the mean and standard deviation of the lag distributions (peak and centroid), given 10 000 DRW continuum realizations. We assume measurement errors of 1 per cent for the driving continuum light curve, and of 5 per cent for the BEL (or DC) light curve.

5.3 CCF lags for the emission lines

We show light curves for four Model 1 BEL, as driven by a single realization of the DRW continuum, in Fig. 11. For each BEL we show two light curves, one of which is generated for a response function that includes the effects of line responsivity (Section 3.4.1); these effects tend to delay and weaken the line response. Of the lines tested, the C IV BEL shows the strongest response, while the response of Mg II is negligible once the line responsivity is taken into account. A weak response for Mg II appears to be a general property of photoionization model calculations (e.g. Goad et al. 1993). Observationally, Cackett et al. (2015) find for NGC 5548 that the Mg II broad-line luminosity does not correlate with continuum variations. For a sample of 68 quasars with multiple Sloan Digital Sky Survey observations, Blanton et al. (2017); Zhu, Sun & Wang (2017) find that Mg II responds only weakly to continuum variations ($\eta \sim 0.46$). These findings may preclude the use of this line for reverberation mapping studies, though we note that a handful of significant lag measurements have been reported for this line (e.g. Metzroth, Onken & Peterson 2006; Shen et al. 2016). Further, while

Mg II line widths have been used as proxies for the BLR velocity field in single-epoch M_{BH} estimates (e.g. Vestergaard & Osmer 2009; Shen et al. 2011), for a fraction of objects, the Mg II line width is not representative of the Hβ line width, as is often assumed (Vestergaard et al. 2011).

We present the BEL CCF centroids for Models 1 and 2 in Table 2. Much of the discrepancy between the response function centroids (Section 4.2) and the pre-2014 observed lags can be attributed to the variability behaviour of the continuum source: for Hβ we retrieve a lag of $\tau_{CCF,cent} = 33.3 \pm 7.2$ d (Model 1), or $\tau_{CCF,cent} = 27.6 \pm 12.8$ (Model 2). Both are formally consistent with the longest Hβ delays measured historically for NGC 5548 ($26.9^{+1.5}_{-2.2}$ d; Zu, Kochanek & Peterson 2011), which are observed at continuum luminosities similar to those of the 2014 campaign.

The lags obtained using the CCF method are, however, still significantly larger than the values obtained by Pei et al. (2017) for the 2014 campaign. The damping time-scale is considerably shorter during the 2014 campaign (≈ 12 d, as measured from the Structure function by MG). We therefore test the sensitivity of the measured Hβ lags to the damping time-scale of our model continuum. While larger values of T_{DRW} do yield larger lags, approaching τ_η (as also found by Goad & Korista 2014), we find CCF centroids of $\tau_{CCF,cent} \sim 30$ d (albeit with a larger standard deviation of the lag distribution) even for small $T_{DRW} \sim 5$ d. Thus, our pressure law models

cannot reproduce the very short lags observed in 2014, even allowing for an abnormally short characteristic time-scale for the driving continuum.

5.4 CCF lags for the diffuse continuum

For Models 1 and 2, the recovered CCF centroids for the DC ($\tau_{\mathrm{CCF,cent}}$, Fig. 12, top panels) are a factor of ~ 2 smaller than the corresponding response function centroids as derived in Section 4.3. This is the lag signal we would measure for the DC emission if it could be isolated from the total continuum light curve (incident + diffuse + constant components). To first order, and assuming that the nuclear continuum has zero lag at the wavelength of interest, we can determine a rough estimate for the *measured* continuum lag as the product of the diffuse continuum lag and the diffuse continuum fraction, $\tau_{\mathrm{CCF,cent}} \times F_{\mathrm{diff}}$, where $F_{\mathrm{diff}} = L_\nu(\mathrm{diff.})/(L_\nu(\mathrm{diff.}) + L_\nu(\mathrm{nuc.}))$. For example, if the DC component dominates the measured continuum flux, we expect to measure a delay for the measured continuum bands similar to that found for the DC. Conversely, for a weak DC component, the continuum flux is dominated by the (in this case lag-less) disc component, yielding zero delay. For intermediate DC contributions, the measured continuum delay will lie somewhere between these two extremes, depending on the exact details of the driving continuum variations.

Given values of F_{diff} in the range 0.1–0.3 (Fig. 12, bottom panels), the continuum for Models 1 and 2 will thus lag the incident continuum by several days at wavelengths short-ward of the Balmer and Paschen jumps. These estimates of the lag assume full coverage of the continuum source by the BLR. The ratio F_{diff}, and thus the observed lag will, according to this prescription, scale linearly with source covering fraction. The measured continuum lag may therefore be smaller than that shown in Fig. 12 by a factor of approximately few. Note that here we neglect any intrinsic inter-band continuum lag due to the accretion disc geometry. We address both these issues in Section 6.

5.4.1 Dependence of CCF lags on n_H for s = 0

At $\log[n_{\mathrm{H}}\,/\mathrm{cm}^{-3}] < 10$, F_{diff} is low, and thus the DC contributes little to the delay signal (Fig. 13, top panels). As n_{H} increases, the luminosity of the DC approaches and eventually exceeds that of the nuclear continuum, i.e. F_{diff} increases with n_{H} (Fig. 13, right panels). We note that, for $\log[n_{\mathrm{H}}\,/\mathrm{cm}^{-3}] \geq 10$, a substantial lag will be introduced into the observed continuum, as the product $\tau_{\mathrm{CCF,cent}} \times F_{\mathrm{diff}}$ becomes non-negligible. While the higher-density models produce DC emission primarily at smaller radii, this effect is balanced to some degree by the increase in F_{diff}. In particular, for $\log[n_{\mathrm{H}}\,/\mathrm{cm}^{-3}] > 10$, the product $\tau_{\mathrm{CCF,cent}} \times F_{\mathrm{diff}}$ yields lags of between 4 and 12d immediately blue-wards of the Balmer and Paschen jumps (assuming full source coverage).

5.4.2 Dependence of CCF lags on $\log(U)$ for s = 2

As noted in Section 4.4, the wavelength dependence of the response function centroids for $s = 2$ models is in a sense 'reversed' compared to that of the $s = 0$ models, and tends to decrease with increasing wavelength. While the strength of the DC component is marginally larger for Model 2, the wavelength dependence of the DC delays is a relatively weak function of wavelength (Fig. 14, left-hand panels), while F_{diff} depends strongly on wavelength. The scaled lags therefore will tend to show behaviour resembling that of Model 1,

with delays generally increasing with increasing wavelength, but with less significant reductions in delay longward of the Balmer and Paschen jumps.

The DC responds on very short time-scales for high ionization parameters $\log(U) \sim 0$; however, very little diffuse continuum is produced at these ionization levels. On the density-flux plane (n_{H}, Φ_{H}), the diffuse continuum contours are widely spaced for $\log[U] \lesssim 0$ (roughly the bottom-right regions for the continuum bands shown in Fig. 3) and thus the DC contribution is largely insensitive to U over a broad range in ionization parameter, $-1 \gtrsim \log(U) \gtrsim -2$. For ionization parameters small enough to produce sufficient BEL luminosity to match observations (i.e. $\log(U) \lesssim -0.5$, Fig. 6), the product $\tau_{\mathrm{CCF,cent}} \times F_{\mathrm{diff}}$ is $\sim 2 - 8$ d blue-wards of the Balmer and Paschen jumps, assuming full BLR coverage.

### 5.4.3 Dependence of the diffuse continuum lags on T_{DRW}

To test the effect of the driving continuum behavior on the measured DC lags, we repeat our measurements of $\tau_{\mathrm{CCF,cent}}$ for Model 1, applying a range of characteristic DRW time-scales, 5 d $\leq T_{\mathrm{DRW}} \leq 160$ d. We keep the variability amplitude constant at $\sigma_{\mathrm{DRW}} = 0.04$. For small values of T_{DRW}, the DC lags we recover are between 50 per cent and 100per cent smaller immediately shortward of the Balmer jump, relative to the $T_{\mathrm{DRW}} = 40$-d realizations (Fig. 15). Even so, we find $T_{\mathrm{CCF,cent}} \sim 20$ d for this wavelength region even for $T_{\mathrm{DRW}} \sim 5$ d. Thus, after scaling by the appropriate F_{diff} and source covering fraction, we do expect to observe some contamination of the observed lag spectrum due to DC, even assuming very short variability time-scales for the driving nuclear continuum.

6 DISCUSSION

Our main finding is that for pressure-law models that roughly reproduce the observed BEL luminosities, a substantial DC component is also present. Contamination of the observed UV–optical continuum by this DC component introduces a delay signature distinct from that arising in the reverberating disc. This additional delay is of order approximately few days, as estimated by the product of $F_{\mathrm{diff}} \times \tau_{\mathrm{CCF}}$ at the Balmer continuum peak (Figs 13 and 14). The only pressure law models that do not introduce a substantial additional lag signal are those with low gas densities (for $s = 0$ models) or high ionization parameters (for $s = 2$ models); such models also fail to produce sufficient BEL flux to match the observed emission-line luminosities.

6.1 The BLR covering fraction

The lags determined in Sections 5.3–5.4 assume that the BLR covers the entire continuum source, which is unphysical for AGN where we observe the continuum directly; realistic BLRs must have lower source coverage. The ratios of the model emission-line luminosities to the observed luminosities provide a rough lower limit on the BLR covering fraction allowed by the data for pressure-law density distributions. For Model 1, the Hβ BEL is in any case underluminous, possibly due to limitations of the photoionization modeling (Section 4.1). However, the observed C IV luminosity constrains the covering fraction (as seen from the continuum source) to be larger than ~ 60 per cent for Model 1. For Model 2, the covering fraction must exceed ~ 32 per cent in order to produce sufficient luminosity in all the BELs. Typical global BLR covering fractions for AGNs are ~ 0.4, as inferred from the statistics of intervening UV absorption lines (Dunn et al. 2007). Thus, the required covering fractions are not unreasonable, given our simple density distributions.
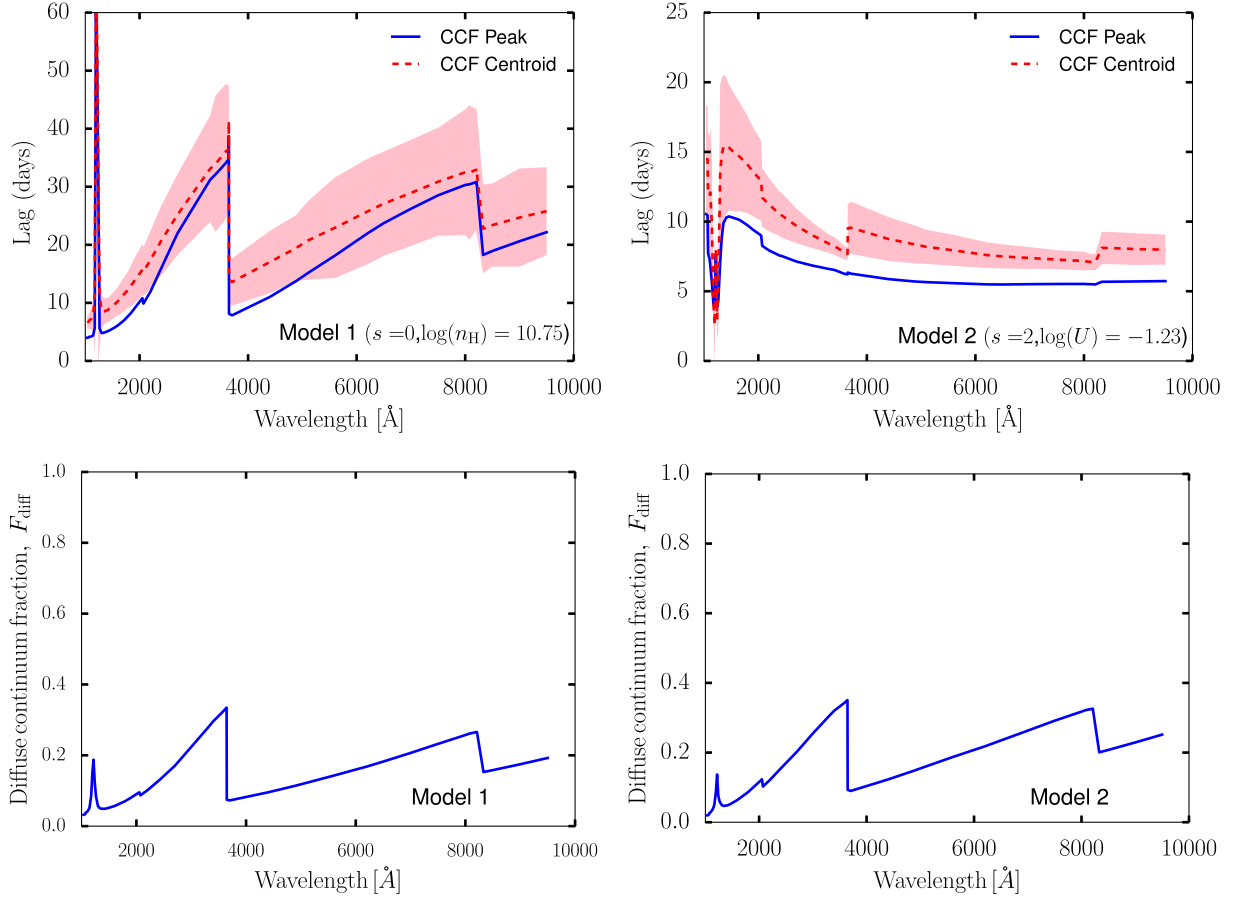
Figure 12. *Top:* CCF peak lags and centroids for the BLR diffuse continuum component, in units of days, for Model 1 ($s = 0$, left-hand panel) and Model 2 ($s = 2$, right-hand panel). To obtain the lags, we drive the steady-state BLR models using a nuclear continuum light curve with the logarithm of the flux following a DRW with $T_{DRW} = 40$ d and $\sigma_{DRW} = 0.04$, similar to the continuum variation properties observed for NGC 5548 during 1989–1993. We repeat this simulation 10 000 times; the lags presented are the mean values of the lag distribution at a given wavelength. The pink shaded region displays the 1σ standard deviation of the CCF centroid distribution at each wavelength. *Bottom:* F_{diff}, the ratios of diffuse continuum λL_λ (DC), to total continuum λL_λ(incident+DC), as a function of wavelength.

6.2 Combined DC and disc lag spectrum

The DC lag spectra (scaled by F_{diff}) are shown in Fig. 16 (red dashed curves), assuming covering fractions of 60 per cent and 33 per cent for Models 1 and 2, respectively. A DC lag of this magnitude can be differentiated from the standard X-ray disc reprocessing models due to the prominent Balmer and Paschen features in the lag spectrum. Fausnaugh et al. (2016) find an additional lag of $\sim 0.6 - 1.2$ d in their *Swift u*-band data for NGC 5548, in comparison to the $\tau \propto \lambda^{4/3}$ model. In a qualitative sense, this resembles the signature of DC contamination predicted by our models. To facilitate a quantitative comparison with the observed lags, we now make a rough estimate of the lag spectra that are expected for our Models 1 and 2, including the effects of illumination of a temperature-stratified accretion disc by an X-ray corona. For the disc reprocessing lags, we employ the wavelength–disc size scaling relation presented by Edelson et al. (2017) (their equation 3):

$$r = ct_{AD} \approx 0.09 \left(X \frac{\lambda}{1928\,\text{Å}} \right)^{4/3} M_8^{2/3} \left(\frac{\dot{m}_{Edd}}{\eta} \right)^{1/3}, \quad (21)$$

where λ denotes the wavelength observed, M_8 is the black hole mass in units of $10^8\ M_\odot$, $\dot{m}_{Edd}$ is the ratio of the accretion rate to the Eddington rate, and η is the radiative efficiency. The accretion disc delay t_{AD} is in units of days. For NGC 5548, $M_8 = 0.52$ (Bentz &

Katz 2015); we assume $\eta = 0.1$. The scaling factor X encapsulates the mapping from disc surface temperature to effective wavelength at a given accretion disc radius r; we assume a flux-weighted radius based on the temperature stratification of the Shakura & Sunyaev (1973) α-disc model, in which case $X = 2.49$ (Fausnaugh et al. 2016). For each wavelength bin, we calculate the weighted sum of t_{AD} and the DC lags,

$$\text{Total lag} = (\text{CF} \times F_{diff})\tau_{CCF,cent} + (1 - \text{CF} \times F_{diff})t_{AD}, \quad (22)$$

where CF denotes the total covering fraction. We note that this is merely a first-order approximation of the lag that would result from a combined accretion disc and DC lag signal; in particular, the assumption that the observed lag scales linearly with the relative luminosities may not be valid in practice. Nevertheless, this expression reduces to t_{AD} for small F_{diff}, and to $\tau_{CCF,cent}$ for large F_{diff} and covering fraction, as expected.

We display the total lag spectra for Models 1 and 2, assuming the minimum covering fractions allowed by the observations, in Fig. 16 (black dotted curve). Comparison with the observed delays (Fausnaugh et al. 2016) is complicated by the fact that most of these are derived from broadband photometry. Thus, each filter samples a range of delays. To illustrate this effect, we estimate the observed delay expected in the UVOT *U* bandpass, given our Mod-
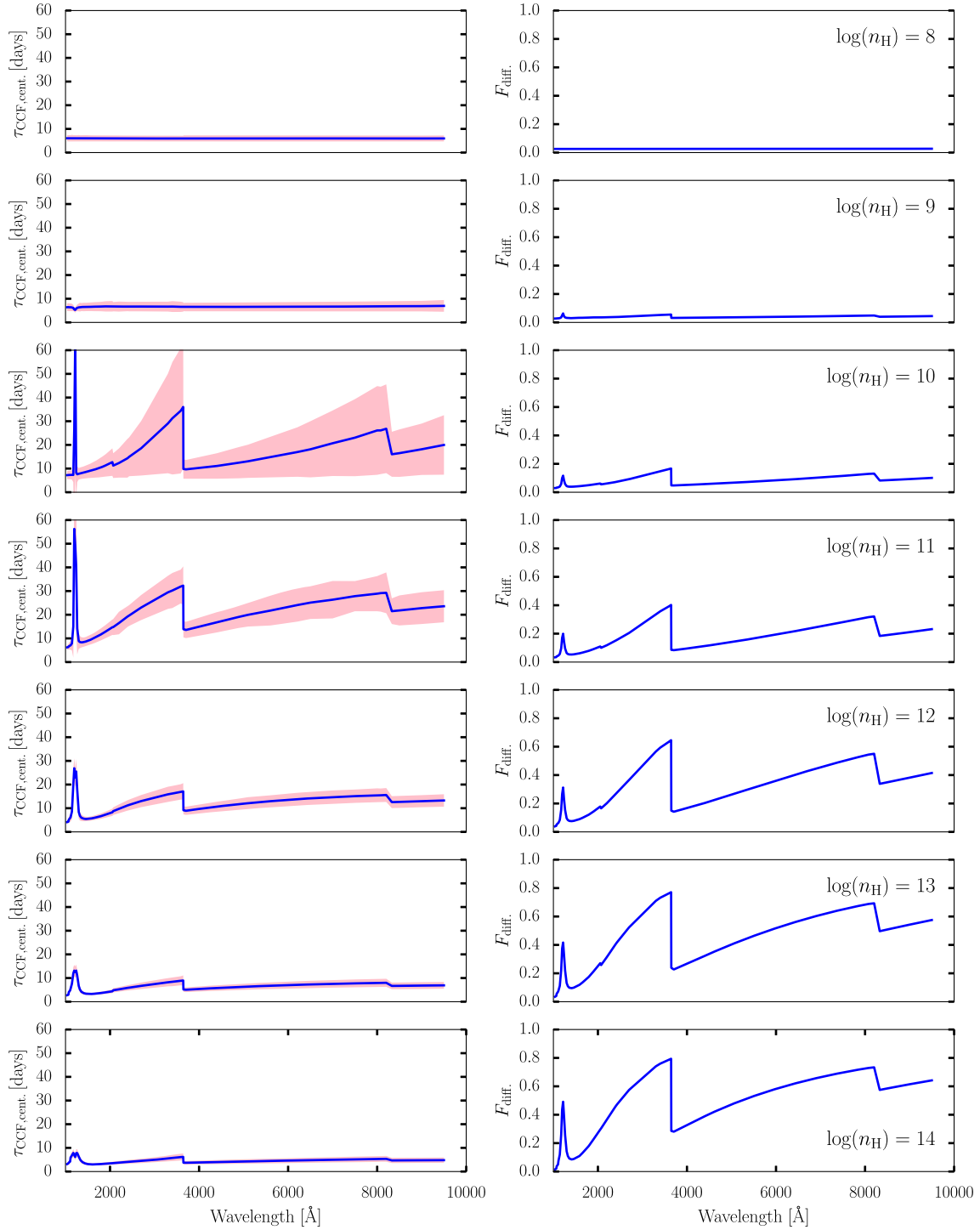
Figure 13. *Left-hand panels:* CCF centroids, in days, for the diffuse continuum component, for $s = 0$ models spanning a range of n_H, $8 \leq \log[n_H / cm^{-3}] \leq 14$. The CCF is determined using the interpolated-CCF method (Section 5.2), for 10 000 realizations of a DRW driving continuum (Section 5.1). The pink-shaded region displays the 1σ standard deviation of the CCF centroid distribution at each wavelength. *Right-hand panels:* The diffuse continuum fraction, $F_{diff} = L_\nu(diff.)/(L_\nu(diff.) + L_\nu(nuc.))$, for each model.

els 1 and 2 with covering fractions of 60 per cent and 33 per cent, respectively (Fig. 16, magenta stars). We calculate these delays by making a weighted sum of the DC response functions at each discrete wavelength probed by our photoionization modeling, using weights corresponding to the normalized *Swift* UVOT *U* filter throughput function. This yields an approximate response function

for the *U* bandpass, for which we generate simulated *U* band light curves using a DRW driving continuum, as per Section 5.4. We then estimate F_{diff} for the *U* band as the weighted average F_{diff} for the individual continuum bands, again using weights corresponding to the normalized filter throughput function. We calculate the observed *U* band delay using equation (22), including the weighted
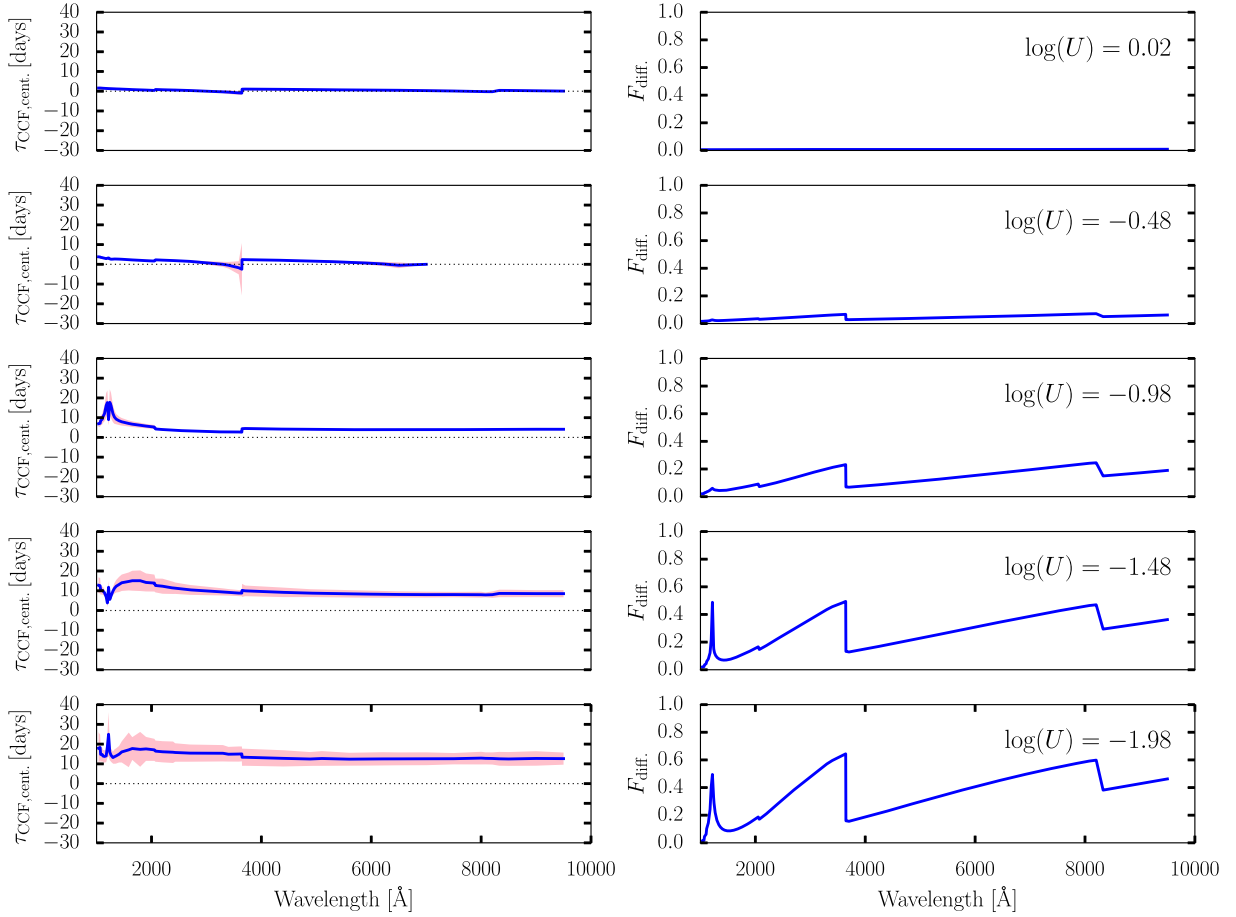
Figure 14. *Left-hand panels:* CCF centroids, in days, for the diffuse continuum component, for $s = 2$ models spanning a range in ionization parameter, $0.52 \geq \log U \geq -1.98$. The CCF is determined using the interpolated–CCF method (Section 5.2), for 10 000 realizations of a DRW driving continuum (Section 5.1). The pink-shaded region displays the 1σ standard deviation of the CCF centroid distribution at each wavelength. For the $\log(U) = -0.48$ model, the DC responds extremely weakly at wavelengths between 6500 and 8000Å, and the ICCF method fails to find a centroid for almost all DRW continuum realizations. We therefore do not include the $\tau_{\rm CCF}$ at wavelengths beyond than 6000 Å for this model. *Right-hand panels:* The diffuse continuum fraction, $F_{\rm diff} = L_\nu({\rm diff.})/(L_\nu({\rm diff.}) + L_\nu({\rm nuc.}))$, for each model.

average $t_{\rm AD}$ across the bandpass. For both models, our estimated U band delay is somewhat shorter than the monochromatic delay just bluewards of the Balmer break, as expected given that the U band also samples the region redwards of the Balmer break, for which the delay induced by the DC is short. We do not include the effects of BLR kinematics in this calculation. Rotational broadening will tend to smooth out any sharp features seen in the delay spectrum (e.g. at the Balmer and Paschen jumps), but we expect this effect to be negligible for the U band, for which the continuum longward of the Balmer jump contributes only a small fraction of the total light.

The accretion rate dependency of the underlying disc delay spectrum introduces an additional uncertainty when comparing to the observed lags. We assume $\dot{M}_{\rm Edd} = 0.1$ for the disc spectrum displayed in Fig. 16; higher Eddington ratios (or lower accretion efficiencies) produce steeper accretion disc lag spectra. Fausnaugh et al. (2016) argue that $\dot{M}_{\rm Edd}$ is unlikely to be much higher than 0.1 for NGC 5548 in 2014, unless the disc is seen very close to edge-on. Given these uncertainties, the simplicity of our pressure-law models, and choice of BLR geometry, we do not expect an exact correspondence between the predicted and observed delay spectra. In particular, Model 1 predicts total (disc plus DC) de-

lays that roughly match the observed delays in the far-UV and the optical regimes, while the model lags near the Balmer continuum feature exceed the measured values. Model 2 matches the observed delays only in the far-UV. However, a significant delay contribution from DC emission, with a similar gross wavelength dependence, is likely ubiquitous for pressure law models capable of emitting strong broad-line flux (Section 5.4). These results strongly suggest that DC contamination is responsible for a substantial fraction of the observed delays *across the entire UV-optical spectral region*, and not just at the Balmer continuum feature. Thus, DC contamination must be taken into account when interpreting the larger than expected accretion disc sizes inferred from continuum reverberation mapping (Section 1.1). Indeed, for the nearby Seyfert 1 galaxy NGC 4593, Cackett et al. (2018) find strong evidence for the DC Balmer continuum feature in their inter-band spectroscopic (*HST*) and *Swift* delay spectrum. Given the strength of this feature, they suggest that there may be a significant DC contamination of the delay spectrum at all UV-optical-NIR wavelengths. That is not to say that DC contamination is the *only* significant cause of the observed long delays. In particular, scattering effects in the accretion disc atmosphere may influence the observed delays and their wavelength dependence, producing increased inter-band delays for the standard
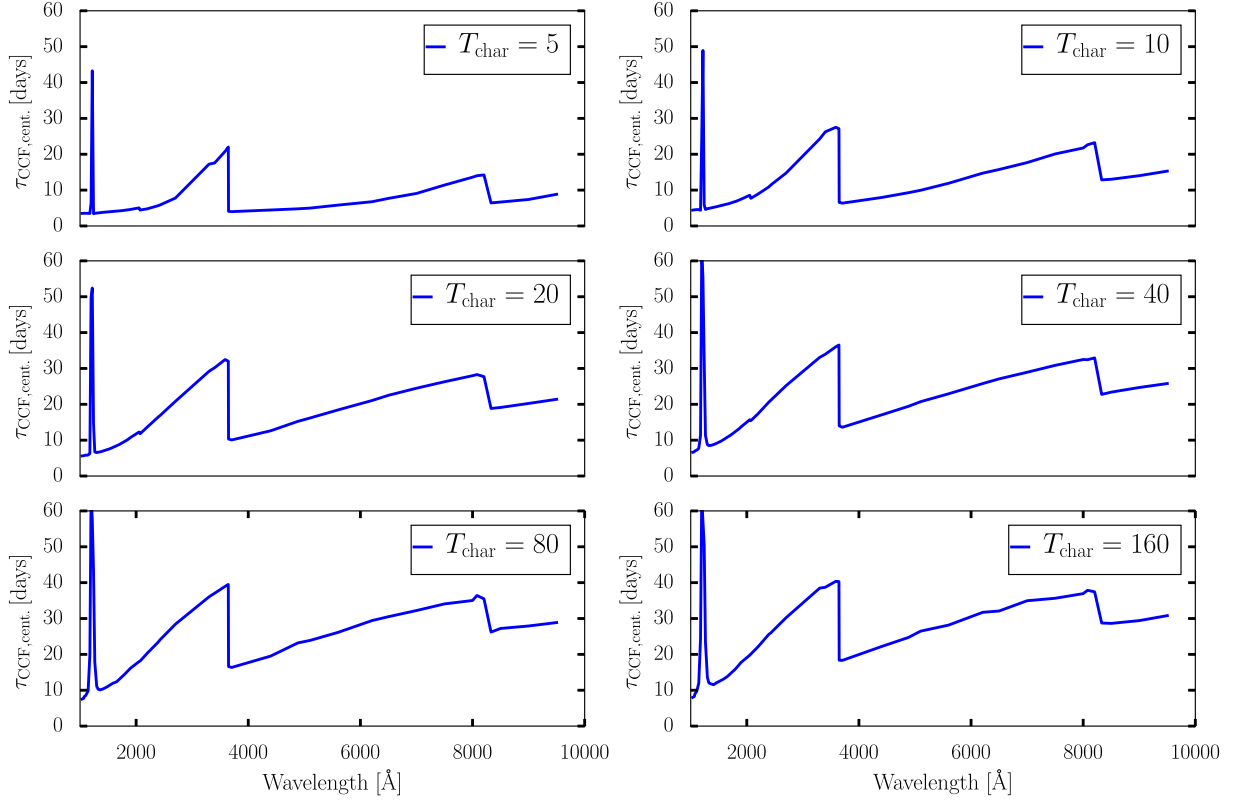
Figure 15. Diffuse continuum CCF centroids, in days, for Model 1, but with driving continua spanning a range of damping time-scales T_{DRW}. The CCF is determined using the interpolated-CCF method (Section 5.2), for 10 000 realizations of each DRW driving continuum (Section 5.1).
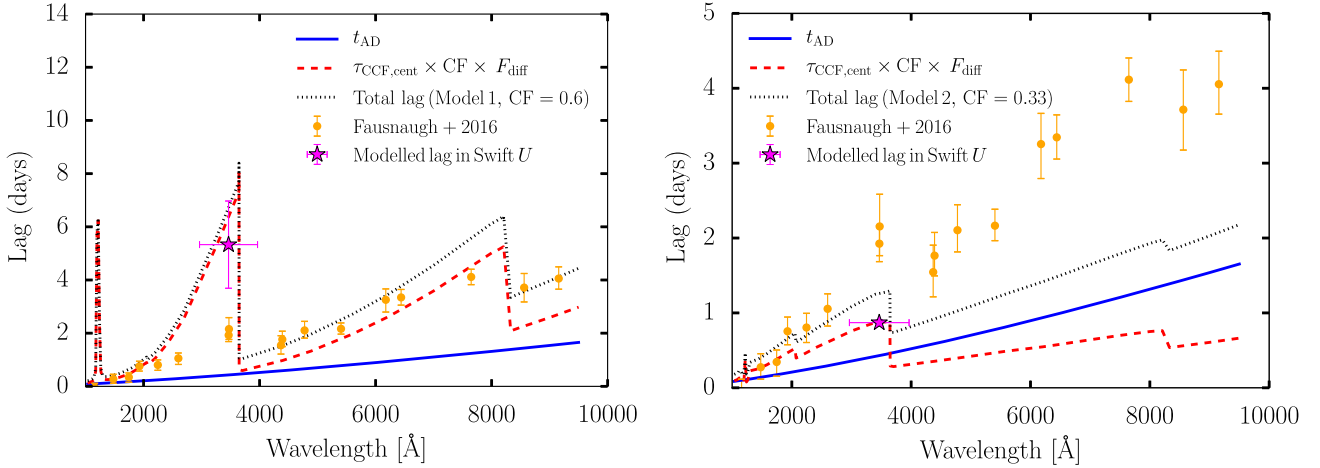
Figure 16. An estimate of the total lag spectrum (black-dotted curves) comprising the accretion disc lag τ_{AD} (blue solid curves) and the DC lag (red dashed curves), for the minimum source covering fraction allowed by the line luminosities, i.e. 60 per cent for Model 1 (*left-hand panel*), and 33 per cent for Model 2 (*right-hand panel*). The accretion disc lag is calculated using equation (21), assuming an Eddington ratio of 0.1. The total lag is the weighted sum of the two components (equation (22)). Yellow circles indicate the measured total continuum lags for the 2014 AGN STORM (Peterson, PI) RM campaign of NGC 5548 (Fausnaugh et al. 2016). Clearly, for spherically symmetric pressure law models that generate sufficient BEL luminosity to match observations, the delay induced by DC contamination represents a significant contribution to the total observed delay at a given UV-optical wavelength. To illustrate the effect of measuring inter-band delays using broadband photometry, we estimate the observed lag in the *Swift* UVOT *U* bandpass for our Models 1 and 2 (magenta stars). The uncertainty on the *U* band delay represents the standard deviation of the distribution of ICCF delay centroids obtained for 10 000 realizations of the DRW continuum, while the horizontal 'error-bar' represents the filter FWHM.

disc geometry (Hall, Sarrouh & Horne 2018). Non-standard accretion discs are also a distinct possibility. For example, Starkey et al. (2017) suggest that the observed delays for NGC 5548 may be due to a tilted inner-disc geometry (Nealon, Price & Nixon 2015).

We emphasize that these single component pressure-law models are intended to grossly match the observed emission-line luminosities and not their detailed temporal behavior. Kaspi & Netzer (1999) study the temporal behavior of $s = 2$ pressure law BLR mod-

els. Their models reproduce the observed steady-state luminosities and typical delays for the strongest UV BEL (excluding H β), but do not reproduce the observed BEL light curves for NGC 5548 in detail. Thus, while pressure laws capture the gross properties of real BLRs, additional model complexity and/or deviations from spherical symmetry are required to reproduce all salient features. For this reason we do not attempt to 'fit' our models (e.g. varying the normalizations of n_H and N_{col} along with the covering factor) to the observed inter-band continuum delays.

6.3 Atypically small BEL lags for NGC 5548

The BEL lags measured during the 2014 campaign are unusually small, given the continuum luminosity at the time (Pei et al. 2017). Our models cannot simultaneously produce sufficient BEL luminosity to match observations, and produce H β lags of order $\sim$5 d. One possible explanation for the short observed BEL lags is that the nuclear continuum lacks variational power on sufficiently long time-scales during this campaign; this may decrease the measured BEL lags (e.g. Goad & Korista 2014). However, we do not find that adopting small values of T_{DRW} reduces the H β lags produced by our model sufficiently to explain the lags observed in 2014.

In early 2000 NGC 5548 went into an historic low-state during which the strong broad UV emission-lines, most notably C IV, disappeared. We speculate that during this time the nuclear region became enshrouded with gas and dust. Large dust grains are robust to destruction by UV photons. Thus when climbing out of this low luminosity state, the destruction of UV photons on grains will reduce the strength of the emission lines relative to what one would normally expect for the same continuum luminosity. The reduction in the strength of the C IV emission-line core relative to the emission-line wings in NGC 5548 during 2014 cf. 1993, when the continuum luminosity was of similar strength, is consistent with this expectation.

Our models suggest that the diffuse continuum contamination induces some additional delay in the observed far-UV continuum. We note that Pei et al. (2017) determine the H β lags relative to the continuum light curves at 1150 Å and at 1367 Å. At these wavelengths the additional lag induced by the diffuse continuum is less than 0.5 d for Model 2. For Model 1, the H I Rayleigh scattering feature in the DC produces significant additional lag in a narrow peak near these continuum bands (Fig. 16). While we do not include kinematics in our models, this feature would be rotationally broadened in a real BLR. Even making the extreme assumption that the Rayleigh feature causes an $\sim$2-d shift in the adopted 'zero lag' bandpass relative to the true ionizing continuum light curve, it is still insufficient to explain the measured $\sim$5-d lags in relation to the expected values at this continuum luminosity.

7 CONCLUSION

Our conclusions are as follows.

(1) For conditions thought relevant to the BLR of Seyfert 1 galaxies, simple radial pressure-law models with spherical geometry can broadly match the observed emission-line luminosities and variability behaviour of the majority of the strongest broad UV and optical emission lines. These models span 1–140 light-days in BLR radius, and require large (30–60 per cent) covering fractions.

(2) Pressure-law models able to reproduce (or exceed) the observed emission-line luminosities also produce a significant amount of diffuse continuum emission over the entire UV–optical wave-

length regime. Thus, the behaviour of the diffuse continuum must be taken into account when interpreting observed continuum inter-band delays in terms of accretion disc sizes. In our models, the diffuse continuum is produced over a broad range in radii, and shows a strong wavelength dependence. The bulk of the diffuse continuum originates in high-density, moderately ionized gas, i.e. at radii *smaller* than the typical formation radius of H β.

(3) After accounting for the fractional contribution of the wavelength-dependent diffuse continuum to the total continuum emission, we find additional lags of approximately a few days relative to the disc reprocessing model. The wavelength dependence of the delays produced by our models qualitatively resembles the measured inter-band continuum delays in NGC 5548. In particular, our models produce excess delays above the underlying disc power law in the vicinity of the Balmer continuum, and a sharp drop in the delay signature long-ward of the Balmer jump, in agreement with the inferred delay spectra (Edelson et al. 2015; Fausnaugh et al. 2016). While we do not attempt to match the observed inter-band delays in detail, the elevated delays due to the diffuse continuum can roughly account for much of the discrepancy between observations and the predictions of reprocessing models. Better constraints on the covering fraction for the BLR, and on its radial density distribution and geometry, would help constrain the expected diffuse continuum lag spectrum.

REFERENCES

Antonucci R., 1993, ARA&A, 31, 473
Barvainis R., 1987, ApJ, 320, 537
Bentz M. C., Katz S., 2015, PASP, 127, 67
Bentz M. C. et al., 2010a, ApJ, 716, 993
Bentz M. C. et al., 2010b, ApJ, 720, L46
Bentz M. C. et al., 2013, ApJ, 767, 149
Blandford R. D., McKee C. F., 1982, ApJ, 255, 419
Blanton M. R. et al. 2017, AJ, 154, 28
Cackett E. M., Horne K., Winkler H., 2007, MNRAS, 380, 669
Cackett E. M., Gültekin K., Bentz M. C., Fausnaugh M. M., Peterson B. M.,
   Troyer J., Vestergaard M., 2015, ApJ, 810, 86
Cackett E. M., Chiang C.-Y., McHardy I., Edelson R., Goad M. R., Horne
   K., Korista K. T., 2018, ApJ, 857, 53
Cardelli J. A., Clayton G. C., Mathis J. S., 1989, ApJ, 345, 245
Clavel J. et al., 1991, ApJ, 366, 64
Collier S., Peterson B. M., 2001, ApJ, 555, 775
Collier S. et al., 2001, ApJ, 561, 146
Davidson K., Netzer H., 1979, Rev. Mod. Phys., 51, 715
De Rosa G. et al., 2015, ApJ, 806, 128
Denney K. D. et al., 2010, ApJ, 721, 715
Dunn J. P., Crenshaw D. M., Kraemer S. B., Gabel J. R., 2007, AJ, 134,
   1061
Edelson R., Vaughan S., Malkan M., Kelly B. C., Smith K. L., Boyd P. T.,
   Mushotzky R., 2014, ApJ, 795, 2
Edelson R. et al., 2015, ApJ, 806, 129
Edelson R. et al., 2017, ApJ, 840, 41
Fausnaugh M. M. et al., 2016, ApJ, 821, 56
Fausnaugh M. M. et al., 2018, ApJ, 854, 107
Ferland G. J., Peterson B. M., Horne K., Welsh W. F., Nahar S. N., 1992,
   ApJ, 387, 95

Ferland G. J. et al., 2013, RMxAA, 49, 137
Goad M. R., Korista K. T., 2014, MNRAS, 444, 43
Goad M. R., O'Brien P. T., Gondhalekar P. M., 1993, MNRAS, 263, 149
Goad M. R., Korista K. T., Knigge C., 2004, MNRAS, 352, 277
Goad M. R. et al., 2016, ApJ, 824, 11
Hall P. B., Sarrouh G. T., Horne K., 2018, ApJ, 854
Ilić D., Kovačević J., Popović L. Č., 2009, New A Rev., 53, 149
Kaspi S., Netzer H., 1999, ApJ, 524, 71
Kelly B. C., Bechtold J., Siemiginowska A., 2009, ApJ, 698, 895
Kilerci Eser E., Vestergaard M., Peterson B. M., Denney K. D., Bentz M. C., 2015, ApJ, 801, 8
King A. L. et al., 2015, MNRAS, 453, 1701
Kishimoto M., Hönig S. F., Beckert T., Weigelt G., 2007, A&A, 476, 713
Korista K. T., Goad M. R., 2000, ApJ, 536, 284
Korista K. T., Goad M. R., 2001, ApJ, 553, 695
Korista K. T. et al., 1995, ApJS, 97, 285
Kormendy J., Gebhardt K., 2001, in Wheeler J. C., Martel H., eds, AIP Conf. Ser. Vol. 586, 20th Texas Symp. on Relativistic Astrophysics. Am. Inst. Phys., New York, p. 363
Kozłowski S. et al., 2010, ApJ, 708, 927
Kraemer S. B., Crenshaw D. M., Filippenko A. V., Peterson B. M., 1998, ApJ, 499, 719
Krolik J. H., Horne K., Kallman T. R., Malkan M. A., Edelson R. A., Kriss G. A., 1991, ApJ, 371, 541
Laor A., 2004, in Richards Gordon T., Hall Patrick B., eds, ASP Conf. Ser., Vol. 311, AGN Physics with the Sloan Digital Sky Survey. Astron. Soc. Pac., San Francisco, p. 169
Lu K.-X. et al., 2016, ApJ, 827, 118
Lynden-Bell D., Rees M. J., 1971, MNRAS, 152, 461
Mandal A. K. et al., 2018, MNRAS, 475, 5330
Mehdipour M. et al., 2015, A&A, 575, A22
Metzroth K. G., Onken C. A., Peterson B. M., 2006, ApJ, 647, 901
Morgan C. W., Kochanek C. S., Morgan N. D., Falco E. E., 2010, ApJ, 712, 1129
Mosquera A. M., Kochanek C. S., Chen B., Dai X., Blackburne J. A., Chartas G., 2013, ApJ, 769, 53
Mudd D. et al., 2018, ApJ, 862, 123
Nealon R., Price D. J., Nixon C. J., 2015, MNRAS, 448, 1526
Nelson C. H., Whittle M., 1996, ApJ, 465, 96

Netzer H., 1990, in Blandford R. D., Netzer H., Woltjer L., Courvoisier T. J.-L., Mayor M., eds, Active Galactic Nuclei. Springer-Verlag, Berlin, Heidelberg, p. 57
Netzer H., Laor A., Gondhalekar P. M., 1992, MNRAS, 254, 15
O'Brien P. T., Goad M. R., Gondhalekar P. M., 1994, MNRAS, 268, 845
Pancoast A., Brewer B. J., Treu T., Park D., Barth A. J., Bentz M. C., Woo J.-H., 2014, MNRAS, 445, 3073
Pei L. et al., 2017, ApJ, 837, 131
Pêrez E., Robinson A., de La Fuente L., 1992a, MNRAS, 255, 502
Pêrez E., Robinson A., de La Fuente L., 1992b, MNRAS, 256, 103
Peterson B. M., Wandel A., 1999, ApJ, 521, L95
Peterson B. M. et al., 1991, ApJ, 368, 119
Peterson B. M. et al., 2002, ApJ, 581, 197
Peterson B. M. et al., 2004, ApJ, 613, 682
Peterson B. M. et al., 2013, ApJ, 779, 109
Poindexter S., Morgan N., Kochanek C. S., 2008, ApJ, 673, 34
Rees M. J., Netzer H., Ferland G. J., 1989, ApJ, 347, 640
Schlafly E. F., Finkbeiner D. P., 2011, ApJ, 737, 103
Sergeev S. G., Doroshenko V. T., Golubinskiy Y. V., Merkulova N. I., Sergeeva E. A., 2005, ApJ, 622, 129
Shakura N. I., Sunyaev R. A., 1973, A&A, 24, 337
Shen Y. et al., 2011, ApJS, 194, 45
Shen Y. et al., 2015, ApJS, 216, 4
Shen Y. et al., 2016, ApJ, 818, 30
Skielboe A., Pancoast A., Treu T., Park D., Barth A. J., Bentz M. C., 2015, MNRAS, 454, 144
Starkey D. et al., 2017, ApJ, 835
Troyer J., Starkey D., Cackett E. M., Bentz M. C., Goad M. R., Horne K., Seals J. E., 2016, MNRAS, 456, 4040
Vestergaard M., Osmer P. S., 2009, ApJ, 699, 800
Vestergaard M., Denney K., Fan X., Jensen J. J., Kelly B. C., Osmer P. S., Peterson B. M., Tremonti C. A., 2011, Proc. Sci., Black Hole Mass Estimations: Limitations and Uncertainties. SISSA, Treiste, PoS(NLS1)038
White R. J., Peterson B. M., 1994, PASP, 106, 879
Zhu D., Sun M., Wang T., 2017, ApJ, 843, 30
Zu Y., Kochanek C. S., Peterson B. M., 2011, ApJ, 735, 80
Zu Y., Kochanek C. S., Kozłowski S., Udalski A., 2013, ApJ, 765, 106

This paper has been typeset from a TEX/LATEX file prepared by the author.

Chapter 3

The Re-ignition of the Changing-Look AGN Mrk 590

I monitored the changing look AGN Mrk 590 using *Swift* UVOT and XRT as part of my PhD studies. Initially, our monitoring was intermittent, with observations a few times per year during 2016 and the first half of 2017. The intent was to 'keep an eye' on the flux level of this AGN, which was in a low-flux state since around 2012. Mrk 590 lost its AGN UV–optical continuum and broad emission lines at some point during 2008–2012 (Denney et al., 2014), along with its soft X-ray excess emission (Rivers et al., 2012), during this changing look event. However, it continued to emit faintly in hard X-rays in the low state, indicating that some small amount of gas might still be accreting. While Koay et al. (2016) do not detect any molecular gas in the nucleus, their upper limit allows for $\sim 10^5 M_\odot$ of molecular gas, sufficient to fuel the AGN for ∼tens of thousands of years. It therefore seemed plausible that the AGN might re-ignite at some point. Indeed, in August 2017 I observed a sharp rise in the X-ray and UV emission; Mrk 590 has flared repeatedly since this initial flare-up, and has not fully returned to its 2013–14 low-flux state.

This chapter is comprised of a paper to be submitted (§3.2), along with the full tabulated *Swift* XRT and UVOT lightcurves during December 2013 – February 2020 (§3.3), and a continuum reverberation mapping analysis based on these lightcurves (§3.4). The authors of the draft journal paper are Daniel Lawther, Marianne Vestergaard and Sandra Raimundo. In the paper, I document the luminosity evolution of Mrk 590 since 2013, and study the overall shape of the optical to X-ray SED, based on our *Swift* UVOT photometry and XRT spectroscopy. I also test for a reappearance of the soft X-ray component, last observed in a high-flux state in 2011 (Rivers et al., 2012). Based on the evolution of the Eddington luminosity ratio and on the reappearance of the AGN UV emission component, I argue that Mrk 590 may have undergone an accretion state transition, from an advection-dominated state (§1.2.3) to a standard thermal accretion disk. In §3.4 I then use the *Swift* UV–optical and X-ray lightcurves to perform an X-ray to UV–optical timing analysis. The results of the timing analysis are discussed in the context of the 'lamp-post' model (e.g., Cackett et al., 2007), in which the X-ray variations cause reprocessing in an accretion disk. I find a ~ 2.5 day time delay between the X-ray and UV flux variability, with a high correlation strength between the X-ray and UVOT UV (but not the optical) lightcurves. An X-ray to UV delay of this duration is a common result of

high-cadence AGN monitoring campaigns with *Swift*, but is much longer than the delay predicted by the X-ray reprocessing model.

The scientific questions addressed in this chapter are:

- Does the recent UV and X-ray flaring activity in the changing-look AGN Mrk 590 represent a return to bona fide AGN activity, i.e., with a typical UV to X-ray SED?

- Has the Eddington luminosity ratio increased appreciably since the very low luminosity state observed in 2013, at which point the UV emission was consistent with only a host galaxy component?

- The soft X-ray excess emission for Mrk 590 disappeared at some point between 2006 and 2011. Given that the X-ray emission now has a similar level as that observed in 2006, which constraints can we place on the reappearance of soft excess?

- We have observed simultaneous X-ray and UV flares in Mrk 590 since August 2017. How well do the X-ray and UV flux variations correlate? Is the variability consistent with the 'lamp-post' model (e.g., Cackett et al., 2007), for which the UV-optical continuum varaitions are due to reprocessing of the variable X-ray emission in a thin accretion disk?

The main practical questions addressed in this chapter are:

- How well can we constrain soft X-ray excess using *Swift* XRT and *NuSTAR* spectra?

- Do the *Javelin* and ICCF methods produce comparable results for the X-ray to UV reverberation lag in Mrk 590?

3.1   Statement of Authorship

All data processing and analysis in this Chapter is performed by Daniel Lawther. The manuscript is written by Daniel Lawther, who also produced the figures; I note that the Python code used to produce the ICCF figures in the reverberation mapping analysis (i.e., Figures 3.2 to 3.7 of §3.4) is originally written by Catherine Grier. All co-authors provided feedback during the writing process. My work on Mrk 590 has benefited greatly from discussions with Marianne Vestergaard, Sandra Raimundo, Kevin Koay and Dirk Grupe. I thank Kristin Madsen for reprocessing and checking the December 2016 *NuSTAR* data, due to intercalibration issues with regards to the *Swift* XRT flux (§3.2). I include a signed statement of authorship with this Thesis (Chapter 8).

3.2   Paper to be Submitted

This journal article is at an advanced draft stage. However, our collaborators (led by Giovanni Miniutti) recently obtained *XMM-Newton* observations of Mrk 590. These June 2020 observations display soft X-ray excess emission (G. Miniutti, private communication), which we do not detect

in our joint *Swift* XRT and *NuSTAR* analysis (January 2020) at a similar X-ray flux level. We do, however, see unexpected spectral complexity near ~ 2 keV in our stacked XRT spectra. We currently lack a physical explanation for these features; their presence may impair our ability to detect faint soft excess emission. When the *XMM-Newton* data become available, we hope to gain additional insight into any additional X-ray emission components that may affect our XRT modeling. For this reason, parts of the work presented here may require major revision before they are submitted. In particular, the continuum window model described in §4.2 of the current draft may fail if the spectrum at ~ 2 keV is not dominated by the power-law continuum. Our preliminary conclusions on the soft excess strength (§5.2) depend on this method, and may therefore require an alternative approach, which we will develop based on our future analysis of the *XMM-Newton* data. Of course, it is also possible that the soft excess component appeared between January 2020 and July 2020. To account for this possibility, we will perform a detailed comparison of the *XMM-Newton* spectrum with stacked XRT spectra observed in Summer 2020.

X-ray and UV Flares in the Changing Look AGN Mrk 590. I: X-ray and UV–optical Observations Since 2014

Lawther, D.,[1] Vestergaard, M.,[1,2] Raimundo, S.,[1]

[1] *Dark Cosmology Centre, Niels Bohr Institute, University of Copenhagen.*
[2] *Steward Observatory, University of Arizona, 933 N. Cherry Avenue, 85721 Tucson, AZ, USA*

August 17, 2020

ABSTRACT
Mrk 590 is a changing-look AGN which transitioned into a dormant state at some time between 2006 and 2012. We have monitored Mrk 590 in the X-ray and UV–optical since 2013 in order to document any changes in its spectral energy distribution if it should re-ignite, in an effort to constrain the evolution of the accretion flow during re-ignition. Here, we present *Swift* XRT and UVOT lightcurves of Mrk 590, observed during 2013–2020, and *NuSTAR* (0.3-79 keV) observations obtained during 2016–2020. The X-ray and UV luminosities increase sharply in August 2017. Since this initial flare-up, Mrk 590 displays a broad-band UV to X-ray SED consistent with those of bona fide broad-line AGN, although it is still highly variable on timescales of ∼weeks to months. The Eddington luminosity ratio, L/L_{Edd}, has increased from ∼ 0.3% in 2013 to around 4.5% during 2018. We use simultaneous *Swift* XRT and *NuSTAR* observations to constrain the behavior of the soft X-ray excess and X-ray reflection components in the low-flux and high-flux states. The soft excess component is not detected in any of our observations, and (if present) is much fainter than it was in the previous high-flux state (2004). The hard X-ray continuum luminosity has increased since 2016, but its spectral index and reflection properties are consistent with that observed during the low-flux state. In summary, Mrk 590 appears to have resumed its broad-line AGN activity, although it is currently less luminous than in its historic high state. This places it in the rare category of AGN for which we observe both 'turn-off' and 'turn-on' changing look events.

Key words: galaxies: active – methods: numerical – galaxies : Seyfert

1 INTRODUCTION

Active Galactic Nuclei (AGN) emit brightly across the entire electromagnetic spectrum, from radio waves to X-rays and Gamma radiation (e.g., Elvis et al. 1994; Richards et al. 2006). To first order, the UV–optical 'big blue bump' emission feature (e.g., Siemiginowska et al. 1995; Scott & Stewart 2014; Grupe et al. 1998) is consistent with thermal emission from a geometrically thin, optically thick accretion disk (e.g., Shakura & Sunyaev 1973) accreting onto a supermassive black hole. However, AGN display additional emission features that are not predicted by the simple thin-disk models. In particular, thin-disk models do not produce strong X-ray emission for accretion onto supermassive black holes. The observed X-ray spectral energy distributions therefore require non-standard accretion disks and/or additional reprocessing mechanisms. The hard X-ray power-law continuum (e.g., Turner & Pounds 1989; Elvis et al. 1994) is likely due to Comptonization of disk photons in a hot, optically thin medium (e.g., Haardt & Maraschi 1993; Petrucci et al.

2000; Lusso & Risaliti 2016). The soft X-ray excess feature commonly detected at energies < 2 keV (e.g., Turner & Pounds 1989; Porquet et al. 2004; Piconcelli et al. 2005) is too energetic to be attributed to thin-disk thermal emission. Suggested explanations for this soft excess component include Comptonization of disk photons in a warm, optically thick medium (e.g., Petrucci et al. 2018), relativistically smeared absorption (e.g., Gierliński & Done 2004), and relativistically broadened X-ray reflection (e.g., Crummy et al. 2006).

The observed variability of AGN is also difficult to reconcile with standard thin-disk models. Large variations in the accretion flow are predicted to occur on timescales corresponding to the viscous timescale of the disk, which for AGN is of order hundreds of years (Noda & Done 2018). However, the UV emission famously displays strong variability on timescales of ∼days to months (e.g., Collier & Peterson 2001; Kelly et al. 2009; Cackett et al. 2015; McHardy et al. 2018). The rapid UV variability observed in the majority of AGN may be due to reprocessing of X-ray variability

in the disk (the 'lamp-post' model, Cackett et al. 2007) or disk instabilities not captured by the standard model (e.g., Collier & Peterson 2001; Hameury et al. 2009; Noda & Done 2018; Jiang & Blaes 2020).

In recent years, a number of extreme AGN variability events have been observed (Penston & Perez 1984; Denney et al. 2014; Runnoe et al. 2016; LaMassa et al. 2017; MacLeod et al. 2019; Rumbaugh et al. 2018). These so-called changing look AGN (CLAGN) involve the appearance or disappearance of the UV–optical continuum and broad emission line components, on timescales of months to years. This corresponds to a transition between broad-line (Seyfert 1-type) and narrow-line (Seyfert 2-type) spectra. A few CLAGN are consistent with variable absorption along our line of sight to the continuum source (e.g., Goodrich 1989, 1995), while the remainder are likely due to changes in the luminosity of the ionizing continuum (e.g., Penston & Perez 1984; Runnoe et al. 2016; Noda & Done 2018; Kynoch et al. 2019). Changing-look events represent a challenge to the standard disk model, as they occur on timescales much shorter than the viscous timescale (Noda & Done 2018; Lawrence 2018; Dexter & Begelman 2019). Instead, disk density inversions due to Hydrogen or Iron opacity fronts may produce the observed extreme variability on timescales of ∼years (Jiang & Blaes 2020).

Mrk 590 is a nearby AGN with a black hole mass $M_{\rm BH} = 4.75(\pm 0.74) \times 10^7$ M$_\odot$, as determined via reverberation mapping (Peterson et al. 2004). During the 1980s and 1990s, this source displayed a typical Seyfert 1 UV-optical spectrum, including the AGN continuum component and broad Hβ, C IV and Lyα emission. Denney et al. (2014) report a gradual decline in the continuum and broad emission line fluxes between 1989 and 2013. In particular, their 2014 optical (3500 Å–7200 Å) spectrum is consistent with host galaxy emission plus AGN narrow-line emission, displaying no evidence of AGN continuum or broad Hβ emission. Similarly, the UV continuum at 1450 Å is decreased by a factor ∼ 100 between 1991 and 2013, while the broad components of the C IV and Lyα lines disappear (or are severely diminished) over the same period. Based on analysis of their 2013 *Chandra* 0.5-10 keV X-ray observation, Denney et al. (2014) do not find evidence for an increase in intrinsic absorbing column density in the low-flux state. Instead, they suggest that the AGN 'turned off' in terms of its UV–optical continuum emission. They find that the narrow emission line flux is fainter in 2013–2014 than in earlier observations. This supports the 'turn-off' scenario: the narrow-line emitting region is extended, and responds gradually and on longer time scales to the diminishing flux of ionizing continuum photons. The changing-look event in Mrk 590 is particularly notable, as its soft X-ray excess component also disappeared a few years before the disappearance of the UV continuum (Rivers et al. 2012). Extreme variability of soft excess emission during changing-look events is also observed for Mrk 1018 (Noda & Done 2018) and NGC 7589 (Liu et al. 2020). It may be due to a change in the accretion disk physics, e.g., a transition to an advection-dominated accretion flow at low accretion rates (Narayan & Yi 1994; Noda & Done 2018).

Our study: Given the rarity of changing-look events, and our lack of understanding of the physical mechanisms driving the extreme variability, it is important to investigate the aftermath of a 'turn-off' event such as that observed for Mrk 590. We initiated intermittent X-ray and UV-optical monitoring observations of Mrk 590 with *Swift* XRT and UVOT starting December 2013. During 2017 we observe a factor ∼ 5 increase in the X-ray flux, over a timescale of a few months; since this event, we have monitored Mrk 590 on a roughly bi-weekly basis. Here, we report the results of our monitoring during 2013–2020. We also present an analysis of hard X-ray spectra (3-79 keV; *NuSTAR*) obtained during the 2016 low-flux state and the post-2017 high-flux state. Based on our *Swift* monitoring, we study the reappearing AGN UV–optical emission during these flares, and the evolution of the Eddington luminosity ratio. We also place constraints on the reappearance of the soft X-ray excess emission, which we do not detect in our *Swift* XRT spectra. We describe our *Swift* and *NuSTAR* observations in §2, and our data processing in §3. In §4 we describe our X-ray spectral analysis methods for the *Swift* XRT and *NuSTAR* spectra. We present the results of our X-ray analyses, including the detection of a weak reflection component and the non-detection of soft excess, in §5. In §6 we present the UV–optical lightcurves and study the evolution of the UV–optical–X-ray spectral energy distribution. We discuss our results in §7, and conclude in §8.

2 OBSERVATIONS

2.1 *Swift* XRT and UVOT monitoring

We observed Mrk 590 with the Niel Gehrels *Swift* (Burrows et al. 2005) Ultraviolet/Optical Telescope (UVOT) and X-ray Telescope (XRT) intermittently since 2013 (*Swift* Cycles 14 and 15 - PI: Vestergaard; joint *NuSTAR* Cycle 5 - PI: Vestergaard), performing a total of 160 individual observations up to 25th February 2020. Following a sharp rise in the X-ray flux in August 2017, we obtained ∼bi-weekly observations, with an additional period of high-cadence (1-2 days) monitoring during September 2017 – February 2018. Listed in order of the first observation, the *Swift* target IDs for the data presented here are 37590, 80903, 88014, 94095, 10949, 11481, 11542, and 13172. The individual observation IDs and XRT exposure times are listed in Table 1. Mrk 590 is unobservable with *Swift* from ∼ 1st March through early June due to a Sun constraint.

Swift observes simultaneously with the UVOT and XRT instruments, with a single UVOT imaging filter in operation at any one time. For the majority of our UVOT observations, we utilize all six imaging filters (*UW2*, *UM2*, *UW1*, *U*, *B* and *V*). Most of our UVOT observations use a blue-weighted exposure time distribution with hex code '0x30ed'[1], in order to securely detect any AGN UV emission. We observe with the XRT in photon counting (PC) mode. We verify that the observations are not affected by photon pile-up during any observations (§3.2). While our typical monitoring observations have exposure times of ∼2 ks, we also secured longer-duration XRT observations upon observing flare-up

---

[1] The various UVOT exposure time weighting schemes are listed at URL: https://www.swift.psu.edu/operations/mode_lookup.php?modes=all .

events, in order to support our joint *Swift* XRT and *NuS-TAR* spectral analysis.

2.2 *NuSTAR* observations

The *NuSTAR* observatory (Harrison et al. 2013) consists of two identical Wolter X-ray telescopes. The two focal-plane detectors, FPMA and FPMB, are sensitive to energies 3-79 keV. *NuSTAR* has observed Mrk 590 on five separate occasions. The first observation (PI: Harrison, Harrison et al. (2016)) took place in February 2016, while the source was in a low-flux state. Thereafter, we obtained a DDT observation in December 2016 (PI: Lawther) along with one joint *Swift/NuSTAR* observation (Program ID: 1417159, PI: Vestergaard) and two *NuSTAR* Cycle 5 observations (Program ID: 05252, PI: Vestergaard). These observations were triggered based on our XRT monitoring. The individual observation IDs and exposure times are listed in Table 2.

3 DATA PROCESSING

3.1 *Swift* UVOT data processing

We process the UVOT data using the standard pipeline tools provided as part of the *HEASoft* package[2]. The UVOT detector suffers from small-scale sensitivity issues, as identified by Edelson et al. (2015) and subsequently documented in the CALDB release note SWIFT-UVOT-CALDB-17-01[3]. The affected detector regions depend on the applied imaging filter. Using the provided small-scale sensitivity maps, we identify observations for which the source region is affected, and discard these observations from our analysis. Of the 160 observations in each imaging filter, we discard 6 observations using *UVW1*, five *UVM2* observations, and four *UVW2* observations. The *U*, *B* and *V* bands are not affected by the small-scale sensitivity issue in our observations.

We combine the individual UVOT snapshots for each observation using the standard UVOT pipeline processing for imaging mode (HEASoft version 6.26.1 or above, UVOTA CALDB version 20170922). We extract source and background fluxes from the resulting images using the *'uvotsource'* task, using a circular source extraction aperture with a radius of 3" as recommended by the *'uvotsource'* documentation[4], and positioning the background region on blank sky in the same detector quadrant as the source. The *'uvotsource'* task converts the observed count-rates to flux densities at the filter central wavelength, assuming a mean GRB spectrum (Poole et al. 2008). We list the flux densities for each observation in Table 3.

Given the small angular size of Mrk 590, our source extraction region covers much of the host galaxy bulge in addition to the AGN point-source emission. We address our treatment of the host galaxy emission in §6.2.

---

[2] URL: `https://heasarc.gsfc.nasa.gov/lheasoft/`
[3] URL: `SWIFT-UVOT-CALDB-17-01`
[4] URL: `https://heasarc.gsfc.nasa.gov/ftools/caldb/help/uvotsource.html`

3.2 *Swift* XRT data processing

We process the XRT PC mode event files using the standard pipeline software (HEASOFT version 6.26.1 or above), using the *'xselect'* task to prepare source and background '.pha' files for analysis. We set the *'xselect'* grading threshold to 0–12, also discarding events with energies outside the 0.3-10 keV XRT sensitivity range, and events taking place outside the 'good time intervals' (e.g., while the spacecraft is slewing). We use a circular source extraction region with a radius of 47", and a larger circular background region, positioned to avoid an additional faint X-ray source at RA: 2:14:35.3, Dec: -0:42:44.6. We also generate Auxiliary Response Files (ARFs) for each observation using the task *'xrtmkarf'*. These files include information on the effective area, quantum efficiency, and PSF profile for a given observation, and are used in the spectral analysis. While the majority of our observations consist of a single telescope pointing, we use XSELECT to combine observations in cases where the exposure time is split over two or more pointings.

For observations with 0.3-10 keV count-rates exceeding 0.5 cts s^{-1}, we test for the effects of photon pile-up by modelling the observed azimuthally averaged point spread function as a King profile, excluding the inner 10". In all cases, an extrapolation of this model to the central region confirms that the point spread function core is consistent with the King profile. Thus, our XRT observations are not affected by pile-up.

For the purposes of our joint *Swift* XRT, *NuSTAR* spectral analysis (§4.2), we require integrated XRT observations of duration $\sim$ 10 ks, preferably observed contemporaneously with the *NuSTAR* spectra. This requirement is fulfilled for the August 2019 and January 2020 observations. For the remaining *NuSTAR* observations, we supplement the contemporaneous XRT data with additional data observed as close in time as possible to the *NuSTAR* observation. For the stacked data, we first process the raw data for each observation individually using the pipeline software. We then use the *'xselect'* task to construct stacked spectra for the joint analysis, and use *'xrtmkarf'* to generate an effective ARF for the stack. The *Swift* XRT observation IDs and total exposure times for each stacked XRT observation are listed in Table 2.

3.3 *NuSTAR* FPMA and FPMB data processing

We process the *NuSTAR* observations using the standard pipeline processing (HEASOFT v. 6.27.2, NuSTARDAS v. 1.9.5). This version of NuSTARDAS includes a time-dependent correction to the FPMA detector's effective area due to a tear in the thermal blanket (Madsen et al. 2020). We extract the source and background spectra for each *NuSTAR* detector (FPMA and FPMB) using the *'nuproducts'* task, which also generates appropriate Auxiliary Response Files for the observations. We use a circular source extraction region of radius 30" and a background extraction region of radius 67". The additional X-ray source detected in our *Swift* XRT imaging is not significantly detected with *NuSTAR*; we ensure that neither the source nor background extraction regions sample its sky coordinates.

The August 2019 observation is impacted by passage through the South Atlantic Anomaly and displays the addi-

tional 'tentacle' pattern, as described in the NuSTAR Data Analysis Software Guide[5]. We compare the various SAA filtering algorithms provided by the 'nucalcsaa' task. Algorithm 2 using an 'optimized' SAA cut, including the parameter *tentacle=yes*, filters out the anomalously high countrates near the SAA passage and the 'tentacle' feature, while preserving $> 95\%$ of the exposure time. While the remaining observations are less severely affected by the SAA passage, we apply Algorithm 2 consistently to all our *NuSTAR* data.

The August 2019 and January 2020 *NuSTAR* observations are performed at similar X-ray flux levels. As part of our analysis to place tighter constraints on X-ray reflection features, we combine these two observations using the HEA-SOFT tool *'addspec'*, which also generates combined ARF and instrumental response files for use in the analysis. We combine data for the FPMA and FPMB detectors individually. The combined on-source exposure time for the stacked observations is 118 ks.

4 X-RAY SPECTRAL ANALYSIS METHODS

Here, we describe the methods used to analyze *1)* the individual *Swift* XRT monitoring observations, *2)* the joint *Swift* XRT and *NuSTAR* data used to constrain soft X-ray excess, and *3)* the X-ray reflection spectrum. In all cases, we use the XSPEC software package to model the spectra. We determine the best-fit model by minimizing the Cash statistic (Cash 1979) for the unbinned data. This is particularly appropriate for modeling of spectra with few photon counts; we choose to use it throughout for the sake of consistency. To ascertain the goodness of fit, we rebin the spectra to a minimum of 25 counts per bin in order to ensure the validity of χ^2 statistics. We calculate the reduced-χ^2 statistic for these binned data, relative to the best-fit model for the unbinned spectra.

4.1 *Swift* XRT single-observation analysis

We model each individual XRT spectrum as a power-law continuum plus Galactic absorption, using the Galactic absorption column density towards Mrk 590, $N_{\mathrm{H,Gal}} = 2.77 \times 10^{20}$ cm^{-2} (HI4PI Collaboration et al. 2016). The free parameters of this model are the photon index Γ_{XRT}, and the flux normalization at 1 keV. The majority of our individual XRT observations have short exposure times (~ 2 ks) and correspondingly low numbers of counts. These data are only used to determine the integrated 0.3-10 keV flux, and do not warrant additional model components. As a crude measure of the X-ray spectral shape, we also measure the X-ray hardness ratio for each individual observation. We define the hardness ratio as HR= $(H - S)/(H + S)$ (e.g., Grupe et al. 2008), where H denotes the number of photons detected in the 1.5-10 keV band after background subtraction, and S is the background-subtracted counts in the 0.3-1.5 keV band. We use the *'Bayesian estimation of hardness ratios'* software (Park et al. 2006) to determine the uncertainties on the hardness ratio for each individual XRT observation.

4.2 Joint *Swift* XRT and *NuSTAR* Analysis

For each of the five *NuSTAR* observations, our objectives are to constrain the presence of a soft X-ray excess below ~ 2 keV, and to perform a preliminary test for the presence of hard X-ray reflection features features (Compton hump and Fe K complex), before and after the transition to a higher-luminosity state in 2017. *NuSTAR* (3-79 keV) is not sensitive to the soft excess component, but provides improved constraints on the hard X-ray photon index relative to those provided by *Swift* XRT alone. We therefore perform a joint analysis for each *NuSTAR* observation, where we include the ~ 10 ks stacked *Swift* XRT observations as described in 3.2. For each *NuSTAR* observation epoch, we fit three baseline models to the joint data, as follows.

0.3-79 keV power-law: We model the entire 0.3-10 keV spectrum as a power law continuum ('*zpowerlaw*') with a Galactic absorption component ('*phabs*'). The model is given by:

$$A(E) = C_i K (E(1 + z))^{-\Gamma} \exp\left(N_{\mathrm{H,Gal}} \sigma(E)\right).$$

$A(E)$ denotes the count-rate as a function of energy E, in units of photons keV^{-1} cm^{-2} s^{-1}. The photo-electric cross-section $\sigma(E)$ is set assuming Solar relative abundances. The Galactic absorption column density is held constant at $N_{\mathrm{H,Gal}} = 2.77 \times 10^{20}$ cm^{-2} (HI4PI Collaboration et al. 2016). We include the arbitrary scaling parameters C_i to allow for flux calibration inconsistencies for the FPMB and XRT detectors, relative to FPMA. In particular, the flux offsets between the *Swift* XRT and the FPMA detectors can be rather large, as the stacked ~ 10 ks XRT data are not fully contemporaneous with the *NuSTAR* observations.

Continuum window power-law: In the presence of either soft X-ray excess or hard X-ray reflection, the power-law fit to 0.3-79 keV will overestimate the continuum level, and may impair our determination of the continuum photon index. We therefore repeat power-law modeling, now minimizing the Cash statistic only in spectral windows that we assume to be dominated by the X-ray continuum emission. We define windows that avoid the soft X-ray component below ~ 2 keV, the iron K complex at ~ 6.4 keV, and the broad Compton reflection feature at ~ 20 keV. The spectral windows are as follows: 2–5.5 keV, 7.5–12.5 keV, and 35–79 keV. We perform a series of simulations in order to determine our sensitivity to the soft excess component using this method. The simulations are described in Appendix A. To summarize, we require an XRT exposure time of at least 10 ks in order to detect and accurately measure soft X-ray excess at 50% of the soft excess level reported by Mathur et al. (2018) and with no false-positive detections.

Model fit with intrinsic absorber: Our analysis of the August 2019 and January 2020 observations using the continuum window method reveals a flux deficit at low energies < 0.7 keV (§5). This flux deficit may indicate the presence of intrinsic absorption, which was not reported for X-ray observations in the low-flux state (Denney et al. 2014; Mathur et al. 2018). In order to test this hypothesis and place constraints on the column density of the putative intrinsic absorber, we perform an additional model fit to each joint *NuSTAR*, XRT observation including a photoelectric absorption component ('*zphabs*'). The resulting model is:

$$A(E) = C_i K (E(1+z))^{-\Gamma} \exp\left(N_{\mathrm{H,Gal}} \sigma(E)\right) \exp\left(N_{\mathrm{H,int}} \sigma(E)\right).$$

---

[5] URL: https://heasarc.gsfc.nasa.gov/docs/nustar/analysis/nustar_swguide.pdf .

The intrinsic absorber column density, $N_{\rm H,int}$, is modeled as a free parameter, with the photo-electric cross section $\sigma(E)$ set assuming Solar relative abundances. We fit this model to the spectral windows 0.3–5.5 keV, 7.5–12.5 keV, and 35–79 keV.

4.3 Hard X-ray reflection modeling

In order to place constraints on the strength of X-ray reflection features, we model the 3-79 keV spectrum for each *NuSTAR* observation using the XSPEC *'pexmon'* model (Nandra et al. 2007). This model combines the *'pexrav'* model for reflection in a neutral medium (Magdziarz & Zdziarski 1995), which generates the broad 'Compton hump' at ~ 20 keV (Lightman & White 1988), with an energetically self-consistent treatment of the Fe K complex emission lines and the Fe K Compton shoulder (e.g., Ross & Fabian 2005). We include a constant flux scaling factor between FPMA and FPMB, and a Galactic absorption component with $N_{\rm H,gal} = 2.77 \times 10^{20}$ cm^{-2}. We do not include intrinsic absorber components in this analysis, as the moderate intrinsic column densities measured in §4.2 do not influence the observed X-ray spectrum at energies above 3 keV.

The *'pexmon'* model generates a power-law incident continuum with photon index $\Gamma_{\rm pex}$ and a high-energy cutoff at energy $E_{\rm c}$. The incident spectrum is reflected in a slab of neutral gas with heavy element abundance Z and iron abundance $Z_{\rm Fe}$. The reflection scaling factor $R_{\rm pex}$ is defined such that $R_{\rm pex} = 1$ corresponds to a slab covering a solid angle of 2π as seen from the X-ray source. The viewing angle i is defined relative to a normal vector to the slab.

As an additional test of the validity of our *'pexmon'* modeling, we use the XSPEC command 'goodness' to assess the quality of the best-fit model. This command performs a comparison of the observed data with multiple Monte Carlo realizations of the model, including photon noise, and drawing the Monte Carlo model parameters from distributions based on the uncertainties on the best-fit model parameters.

5 RESULTS OF X-RAY ANALYSES

5.1 The *Swift* XRT lightcurve

We present the integrated fluxes and 0.3-10 keV photon indices for our individual *Swift* XRT observations in Table 1. The 0.3-10 keV lightcurve reveals a gradual increase in the 0.3-10 keV flux since the 2013 low state, with an abrupt rise in late August 2017 (Figure 1). After this initial flare-up, the X-ray emission is highly variable on timescales of days to weeks. We observe three prominent flare-up events beginning in August 2017, October 2018, and October 2019. Each of these major flare-up events displays multiple X-ray flux peaks. The overall spectral shape of the 0.3-10 keV emission, as represented by the hardness ratio of each XRT spectrum, does not change appreciably during 2014-2020, even as the 0.3-10 keV flux increases by an order of magnitude (Figure 2). We do not see any correlation between $F(0.3-10)$ keV and the photon index; the latter is poorly constrained in our individual XRT observations prior to the 2017 flare, so we

prefer to use the hardness ratio as a measure of the overall spectral shape evolution.

5.2 The 0.3-79 keV spectrum

Here, we describe our phenomenological, power-law models for the 0.3-79 keV spectrum for each of the five *NuSTAR* observations of Mrk 590. We follow the strategy described in §4.2, modeling each observation using *1)* a power-law fit to the 0.3-79 keV spectrum, *2)* a power-law fit to continuum-dominated windows, and *3)* a power-law fit including intrinsic absorption. For each observation, we present the best-fit model parameters in Table 4.

The 2016 low-flux state: We have two *NuSTAR* observations prior to the 2017 flare. The 0.3-79 keV spectrum in February 2016 is well-described by a power-law continuum, with $\Gamma = 1.69 \pm 0.05$, plus Galactic absorption (reduced χ^2=0.98). The continuum window model for this observation over-predicts the soft X-ray flux, and yields a poor fit (reduced χ^2=2.35) when extrapolated below 2 keV (Figure 3, left panel). Given the poor statistics for this ~ 21 ks *NuSTAR* observation in the low-flux state, we are uncertain whether the implied spectral curvature is physically meaningful. Inclusion of an intrinsic absorber component provides a better data/model ratio at < 2 keV (Figure 3, right panel), but this additional component over-fits the data (reduced χ^2=0.88).

The December 2016 observations are at similar overall flux levels to, and the photon index ($\Gamma = 1.67 \pm 0.03$) is consistent with, the February 2016 result. For this ~ 51 ks *NuSTAR* observation, a power-law model to the 0.3-79 keV spectrum does not provide an acceptable model (reduced χ^2=1.69). The data/model ratio for the continuum window model indicates emission at ~ 6.4 keV, along with deviations from a power-law in the soft X-ray spectrum. In particular, we see spectral curvature near 2 keV (4) which suggests the presence of additional absorption or emission features not included in our model. Inclusion of an intrinsic absorption component improves the model fit relative to the 0.3-79 keV power-law, yielding a reduced χ^2 of 1.21. However, neither model adequately captures the spectral features at ~ 2 keV.

The 2018-2020 high-flux state: For the three *NuSTAR* observations obtained after the 2017 flare-up, the overall 0.3-10 keV flux increases by a factor ~ 3. The best-fit 0.3-79 keV photon indices for these observations are remarkably consistent with those measured in 2016. For the 21 ks *NuSTAR* observation in October 2018, the 0.3-79 keV spectrum is adequately described by a power-law ($\Gamma = 1.67 \pm 0.03$) with Galactic absorption, yielding a reduced χ^2 of 1.01. Inclusion of an intrinsic absorption component does not improve the model fit (Figure 5). We see hints of similar spectral features near 2 keV as for the December 2016 observation, although the deviations from the power-law model are less significant.

For the August 2019 and January 2020 observations, the continuum window model over-predicts the soft X-ray spectrum (Figures 6 and 7), yielding reduced χ^2 values of 1.27 and 1.12, respectively. For both of these observations, inclusion of an intrinsic absorber component produces a modest improvement in the fit quality relative to the pure
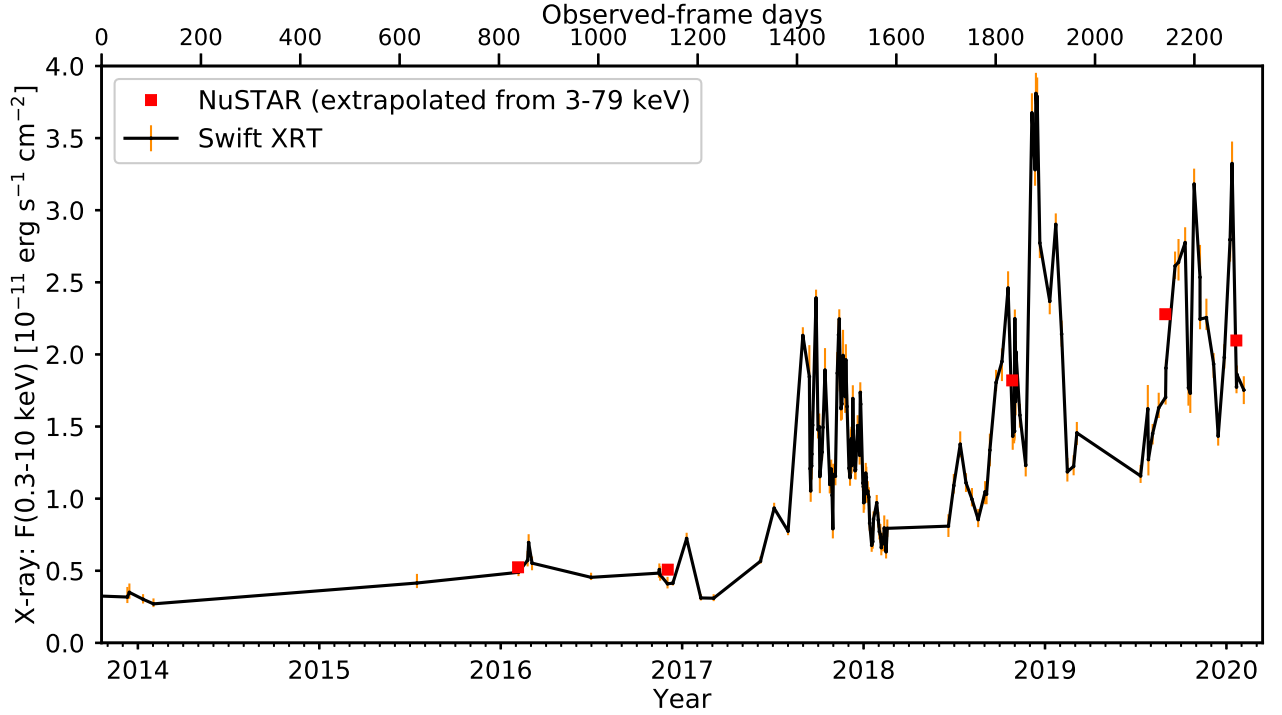
Figure 1. *Swift* XRT lightcurve for the period December 2013 – February 2020. The XRT lightcurve (black curve; orange error bars) provides the absorption-corrected integrated flux between 0.3 - 10.0 keV, based on a power-law continuum model and corrected for Galactic absorption. Gray error bars represent the 90% confidence interval on the model flux. The five *NuSTAR* data points represent the 0.3-10 keV model flux, as extrapolated from a power-law fit to the 3-79 keV spectrum and corrected for Galactic absorption. Mrk 590 is unobservable with *Swift* between ~1st March – early June each year, due to a Sun constraint.
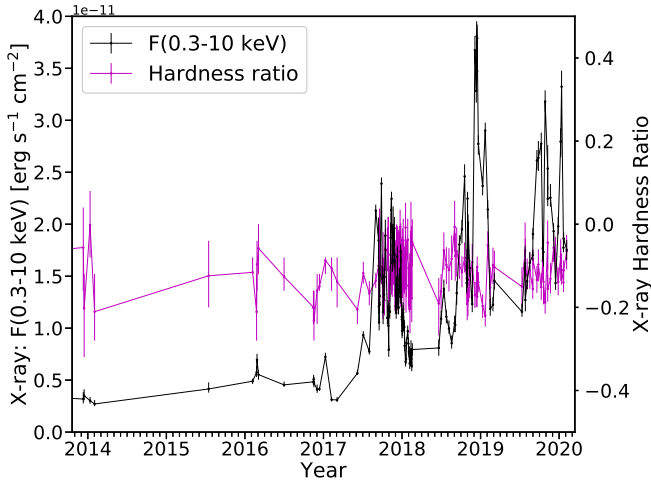

Figure 2. For our individual monitoring observations, the X-ray hardness ratio (magenta curve) does not appear to vary systematically, even as the 0.3-10 keV X-ray flux (black curve) increases by a factor ~ 10 between 2014 and the 2018 flare.

power-law model, with $\Delta\chi^2_\nu = 0.06$ in both cases (Table 4). The inferred intrinsic column densities are $N_{\rm H,int} = 2.65(^{+1.11}_{-1.10})\times10^{20}$ cm^{-2} and $N_{\rm H,int} = 1.83(^{+1.06}_{-1.03})\times10^{20}$ cm^{-2} for August 2019 and January 2020, respectively.

Implications of the observed soft X-ray deficit: None of our joint *NuSTAR* and *Swift* XRT spectra display evidence of a strong soft X-ray excess component. In fact, for three of these observations, the goodness of fit is significantly improved by including an intrinsic absorption component. This is due to a deficit of soft X-ray emission at < 2 keV relative to the extrapolated continuum window models.

According to the simulations described in Appendix A, our continuum window method (§4.2) can reliably detect soft excess at 50% of the relative emission strength detected by Mathur et al. (2018) in 2014, measured relative to the 1 keV continuum flux density. However, our simulations do not account for the observed additional spectral complexity near 2 keV (e.g., Figure 4). The continuum window method depends on the assumption that the *Swift* XRT spectrum is continuum-dominated between 2 keV and 5.5 keV. If that is not the case, our modeling may yield an incorrect flux calibration factor between the XRT and *NuSTAR* spectra. Emission features above 2 keV might also produce spurious evidence for intrinsic absorption, due to overestimation of the continuum level. While our observations do not suggest a soft excess component, we caution that our difficulties in modeling the XRT spectra at ~ 2 keV likely influence our sensitivity to weak soft excess emission. We note that an *XMM-Newton* observation of Mrk 590 on 4th July 2020 does display evidence of soft X-ray excess (G. Miniutti, private communication). When these data are made available, we will perform a re-analysis of the existing *Swift* XRT spectra,
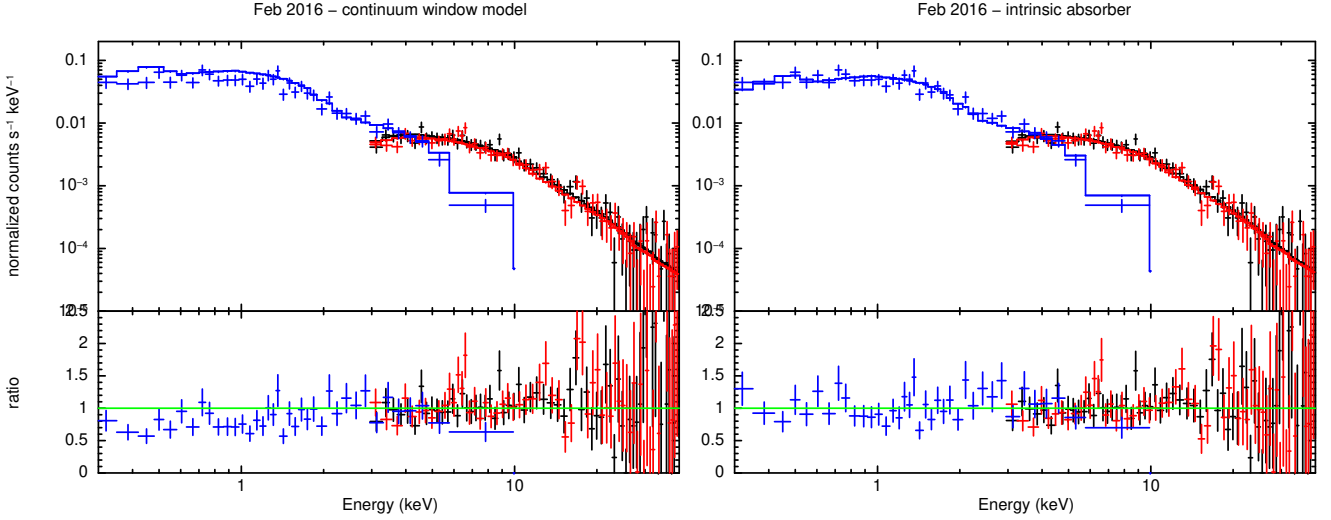
Figure 3. Observed count rates and data/model ratio for the February 2016 observation. Black and red crosses: *NuSTAR* FPMA and FPMB spectra, blue crosses: *Swift* XRT spectrum. *Left:* Power-law model, including Galactic absorption, fitted to continuum-dominated spectral regions (§4.2). *Right:* Power-law model, including Galactic and intrinsic absorption components. We see hints of an emission line at 6.4 keV in the FPMB spectrum, but not for FPMA. While the inclusion of an intrinsic absorber improves the fit at soft X-ray energies relative to the continuum window model, the data are equally well-described by a power-law fit to the entire 0.3-10 keV spectrum.
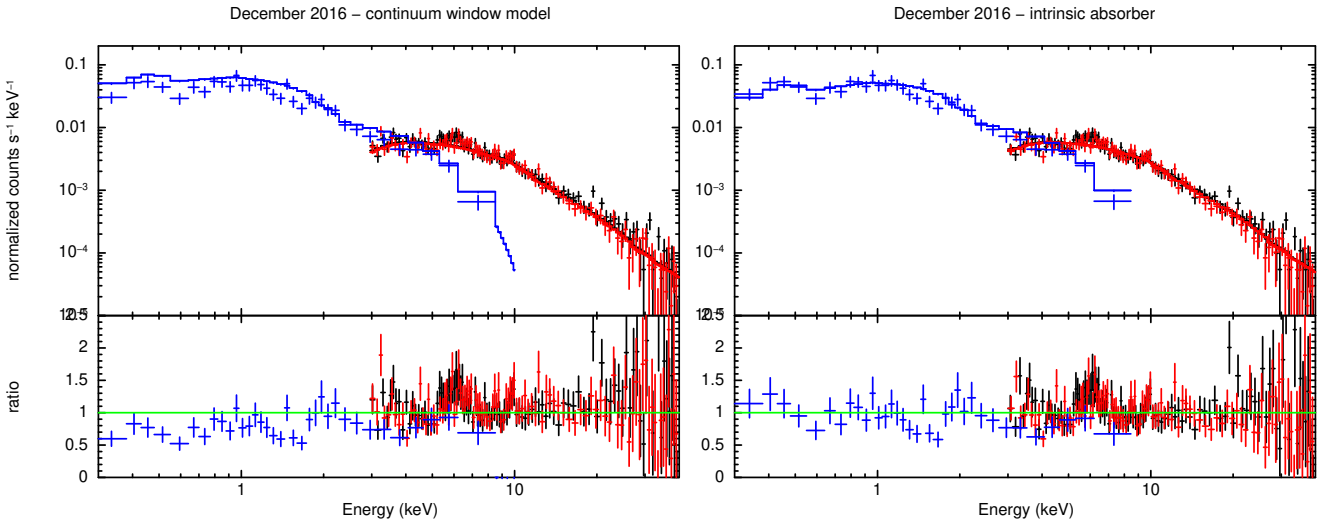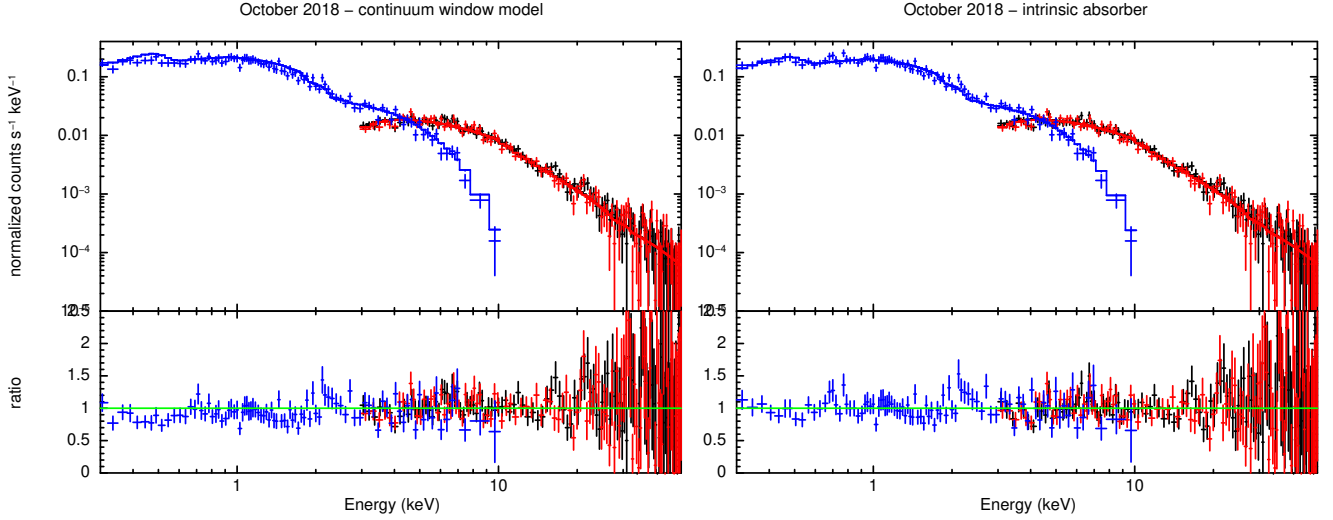

Figure 4. As Figure 3, but for the December 2016 observations. The continuum window method reveals a flux deficit below 2 keV. Inclusion of an intrinsic absorber component improves the goodness of fit relative to the power-law fit to 0.3-79 keV. However, we see additional spectral features at ~ 2 keV that are not consistent with either model. We also note the prominent emission line at ~ 6.4 keV for this observation.

including any additional emission and absorption features present in the higher-quality *XMM-Newton* spectra.

The Fe K emission complex: Iron emission features at ~ 6.4 keV are ubiquitous in AGN spectra. Our *NuSTAR* spectra display deviations from the power-law continuum models near 6.4 keV; this feature is most visually apparent in the data/model ratio for the December 2016 observation (Figure 4). This behavior is consistent with the reflected component being brighter relative to the direct emission in the low-flux state, as indicated by our *'pexmon'* modeling (§5.3). We also see hints of Fe K emission in the high-flux state (Figures 5, 6 and 7). In Figure 8 we display the 3–10 keV *NuSTAR* spectrum for December 2016. Using a power-

law model, we find excess flux at ~ 6.4 keV (left panels). We model this emission as a redshifted Gaussian component, with a best-fit line energy of $6.34^{+0.19}_{-0.18}$ keV and a linewidth of $0.38^{+0.20}_{-0.18}$ keV. We find an equivalent width of 358 ± 4 eV for this component. This equivalent width is larger than typically observed for the Fe K emission lines of bona fide AGN at redshifts $z < 0.04$, which have equivalent widths of ~ 100 eV (Nandra et al. 2007). We suspect that the unusually strong Fe K emission during the low-flux state may be due to reprocessing in a distant medium with a corresponding time delay, as discussed in §7.3.

In order to constrain the more faint Fe K complex emission in the high-flux state, we turn to the stacked August 2019 + January 2020 *NuSTAR* data. We model the spec-

Figure 5. As Figure 3, but for the October 2018 observations. The spectrum is modeled adequately by a power-law fit to 0.3-79 keV, and inclusion of an intrinsic absorber does not improve the χ^2 statistic. While not highly significant, we do note the apparent deviations from the power-law model in the soft X-rays, which appear qualitatively similar to those observed in December 2016.
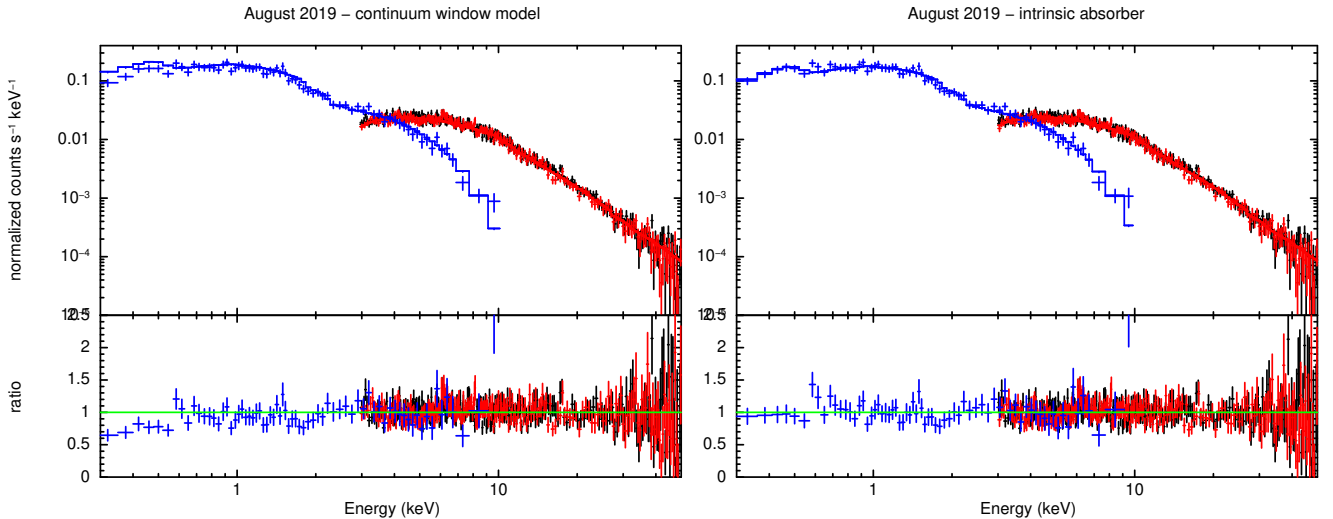
Figure 6. As Figure 3, but for the August 2019 observations. The continuum window model reveals a deficit of soft X-ray flux relative to the extrapolated hard X-ray continuum. Inclusion of an intrinsic absorber component improves the goodness of fit statistic (χ^2=1.00) slightly, relative to the 0.3-79 keV power-law model (χ^2=1.05).

trum as a power-law with Galactic absorption, plus a red-shifted Gaussian emission line (Figure 9). We find a line energy of $6.37^{+0.08}_{-0.06}$ keV, a line width of 0.20±0.10 keV, and an equivalent width of 107±1 eV. Thus, the Fe K emission in the high-flux state is consistent with the typical values for $z < 0.04$ AGN presented by Nandra et al. (2007).

5.3   Hard X-ray reflection features

Here, we describe the results of our *'pexmon'* modeling (§4.3) of the *NuSTAR* 3-79 keV spectra. For the February 2016 *NuSTAR* observation, the X-ray spectrum is poorly constrained at energies > 15 keV due to a lack of photon counts, and the *'pexmon'* model does not converge at a reasonable model fit. For the remaining observations, the *NuSTAR* data do not constrain all *'pexmon'* model parameters independently. This is due to the inclination parameter i and reflection strength R being somewhat degenerate, and to the reflection features being rather faint in the high-flux state. We choose to hold $E_c = 1000$ keV, $Z = 1$ (i.e., Solar metallicity), $Z_{Fe} = 1$ (Solar iron abundance), and $i = 60°$ constant when modeling the individual observations. The choice of $E_c = 1000$ keV corresponds in practice to an unbroken power-law continuum in the 3-79 keV range. The inclination parameter $i = 60°$ is chosen somewhat arbitrarily, due to our ignorance of the true inclination. However, sources with inclinations $i \sim 90°$ are expected to be obscured by a dust torus according to unification models (e.g., Antonucci 1993), while small inclinations are less likely given a random intrinsic distribution of AGN orientations. We test the sensitivity of the measured reflection strength R to the unknown inclination parameter below. The metallicities and
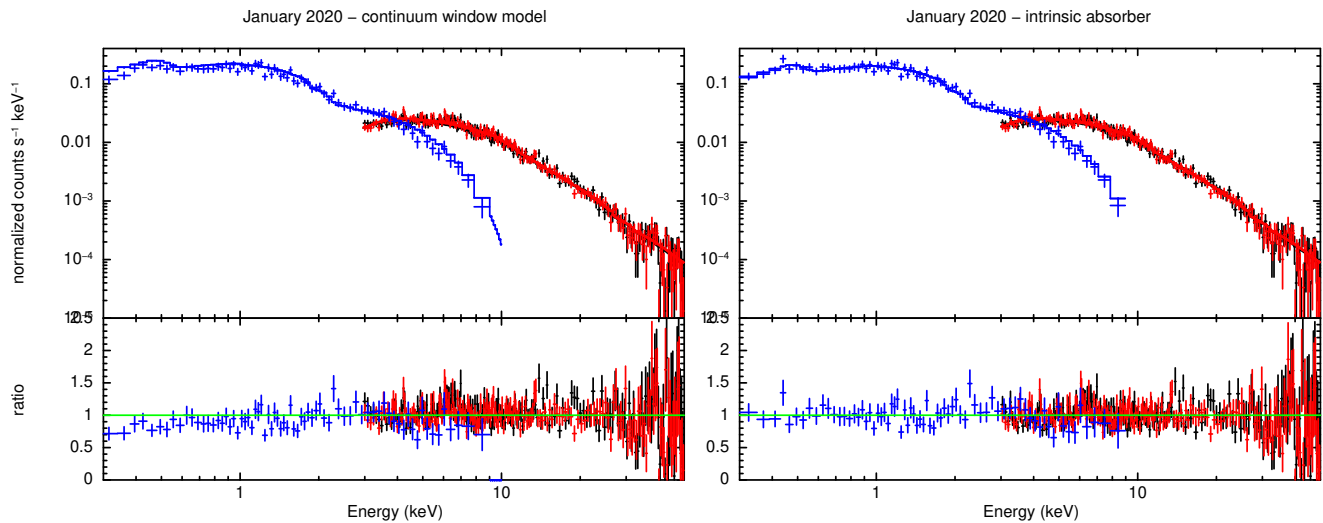
Figure 7. As Figure 3, but for the January 2020 observations. Inclusion of an intrinsic absorber component improves the goodness of fit statistic (χ^2=1.00) slightly, relative to the 0.3–79 keV power-law model (χ^2=1.06).
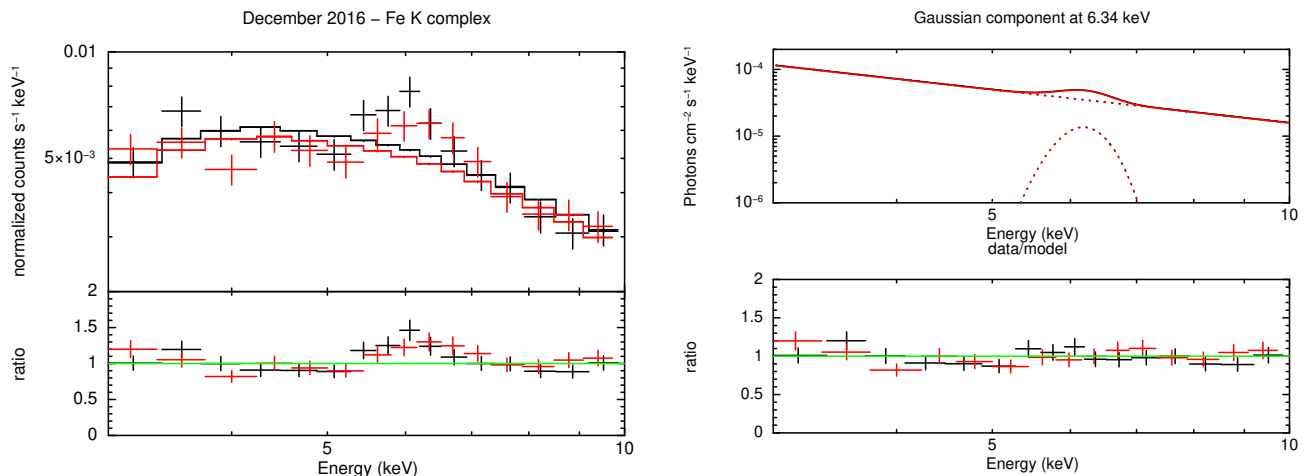
Figure 8. *NuSTAR* spectrum for our December 2016 observation, during the low-flux state. Here, we show the 3–10 keV spectrum in order to highlight the Fe K complex emission. *Left panels:* Observed count rates and data/model ratio for a power-law continuum fit, revealing excess flux near 6.4 keV. *Right panels:* Inclusion of a redshifted Gaussian line profile (XSPEC model *zgauss*) provides an improved model fit near 6.4 keV. The line energy is $6.34^{+0.19}_{-0.18}$ keV, with a linewidth of $0.38^{+0.20}_{-0.18}$ keV. The corresponding equivalent width is 358±4 eV.

iron abundances for AGN X-ray reflecting regions are not well understood (e.g., García et al. 2018), so our choices of Z and $Z_{\rm Fe}$ are somewhat arbitrary. Again, we discuss the sensitivity of R to the metallicity parameters below.

We display the spectra and data/model ratios for *'pexmon'* model fits to the remaining four *NuSTAR* observations in Figure 10, and list the best-fit model parameters R and $\Gamma_{\rm pex}$ in Table 5. The *'pexmon'* models are acceptable fits to all four spectra, with reduced $\chi^2 \sim 1$ and XSPEC *'goodness'* values (as defined in §4.3) below 50%. For the December 2016 observation, the reflection scaling factor is poorly constrained, with $R = 1.15^{+0.77}_{-0.58}$ (90% confidence intervals). The integrated 3–79 keV flux of the direct continuum emission component is $6.48^{+1.11}_{-1.35} \times 10^{-12}$ erg s^{-1}, while the integrated flux of the reflection spectrum is $3.63^{+1.05}_{-0.94} \times 10^{-12}$ erg s^{-1} (90% confidence intervals). For such a high reflection factor,

the reflection component is thus securely detected relative to the continuum flux, even at the low flux level in 2016.

We obtain somewhat better constraints on R for the remaining three observations, during which the 3–79 keV X-ray luminosity is a factor ~ 3 higher than in 2016. The average reflection factor for the three post-2017 observations is $R = 0.36$. A reflection factor of $R = 1$ corresponds to a semi-infinite reflecting slab as seen from the X-ray source. Thus, our results are consistent with a patchy reflecting surface in the high-flux state. Based on our 90% confidence intervals, the reflection features in December 2016 are significantly stronger than those observed in August 2019. This discrepancy is consistent with, and likely driven by, the unusually large Fe K equivalent width in the December 2016 observation (§5.2). We discuss the enhanced reflection strength in the low-flux state in §7.3.
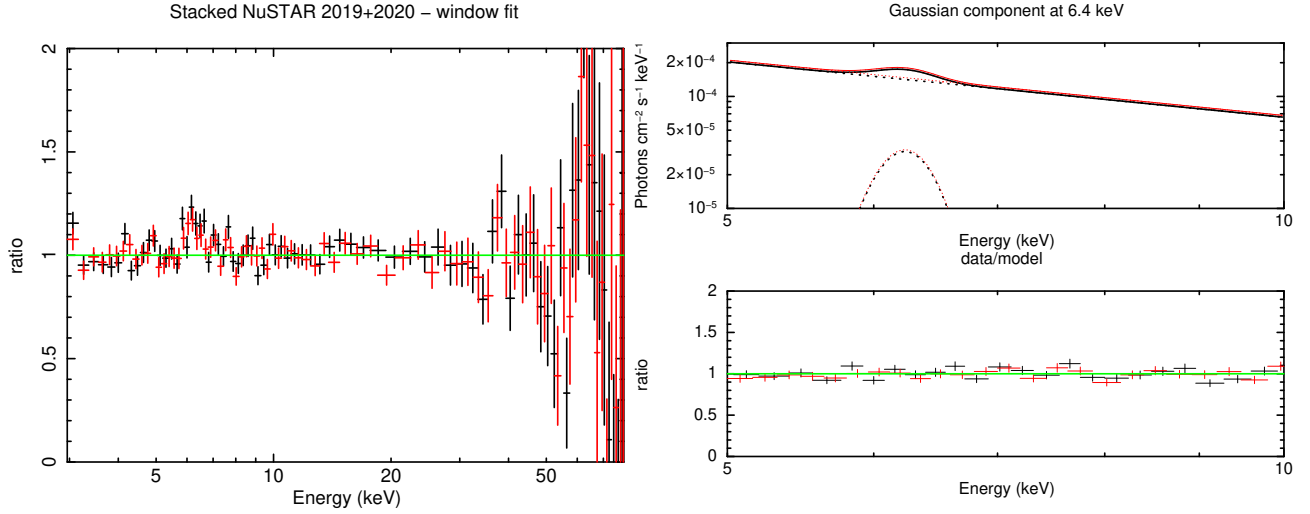
Figure 9. *Left:* Data/model ratio for the stacked August 2019, January 2020 *NuSTAR* FPMA (black crosses) and FPMB (red crosses) spectra. We see an emission feature at ∼ 6.4 keV, and deviations from a power-law continuum at energies > 20 keV. *Upper right:* Model photon flux for the stacked spectrum, including a Gaussian emission line (XSPEC model *'zgauss'*) to represent the Fe K complex. *Lower right:* Data/model ratio when including the Gaussian component.
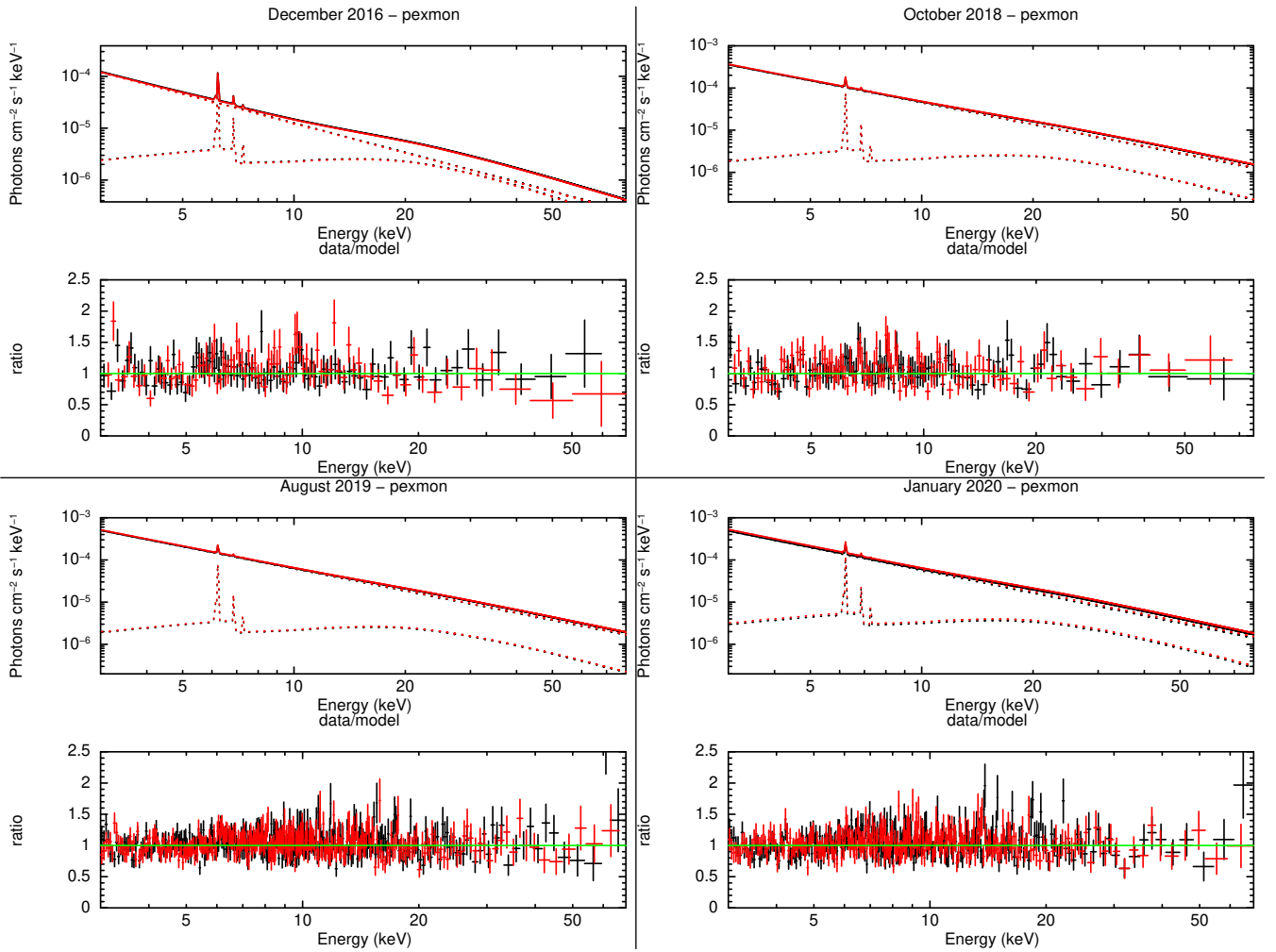
Figure 10. Reflection component (*'pexmon'*) models (upper panels) and data/model ratios (lower panels), for the four observations for which the X-ray reflection modeling converges. *NuSTAR* FPMA and FPMB data are colored black and red, respectively. The cutoff power-law and reflection model components are shown individually (dashed curves) along with the sum of these components (solid curves). The best-fit Compton reflection hump at energies > 15 keV is very weak for the 2018 and 2019 observations.
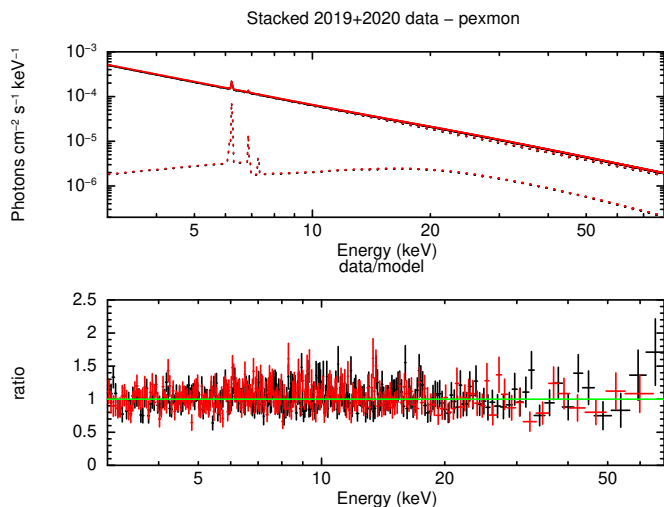
Figure 11. Reflection component (*'pexmon'*) models (upper panels) and data/model ratios (lower panels), for the stacked August 2019 and January 2020 *NuSTAR* observations. The FPMA and FPMB data are colored black and red, respectively. The cutoff power-law and reflection model components are shown individually (dashed curves) along with the sum of these components (solid curves). The Compton reflection hump is faint, and the model fit of the reflection scaling factor is likely driven by the Fe K complex at ~ 6.4 keV.

Model fits to stacked *NuSTAR* data: We also model the stacked *NuSTAR* 2019 and 2020 observations using the *'pexmon'* model. This stacked observation has an on-source exposure time of 118 ks, allowing us to constrain additional *'pexmon'* model parameters. For an inclination $i = 60°$ and metallicities $Z = 1$ and $Z_{\rm Fe} = 1$, we find a best-fit reflection factor of $R = 0.24^{+0.11}_{-0.10}$ for the stacked spectrum (Figure 11). This is consistent with our results for the individual post-2017 observations. Modeling the inclination angle as an additional free parameter, we obtain a best-fit inclination of $i = 79°~^{+6}_{-23}$, i.e., almost edge-on relative to the reflecting slab. In that case, the reflected emission along our line-of-sight is weakened relative to the direct X-ray emission, assuming that the direct emission is isotropic. The *'pexmon'* parameters i and R are thus somewhat degenerate; we find $R = 0.57^{+0.77}_{-0.34}$ for the $i = 79°$ model.

Modeling the iron abundance $Z_{\rm Fe}$ as a free parameter leads to a 'runaway fit', where XSPEC maximizes $Z_{\rm Fe}$ in order to minimize the Cash statistic. García et al. (2018) point out that AGN reflection spectrum modeling often yields very high iron abundances, $Z_{\rm Fe} \sim 5$ (i.e., five times Solar), which are likely unphysical. In order to determine the sensitivity of our reflection modeling to the iron abundance, we perform a model fit with the extreme value $Z_{\rm Fe} = 10$. In that case, we find $R = 0.20 \pm 0.05$, consistent with our result for $Z_{\rm Fe} = 1$.

We also attempt to include the cutoff energy for the underlying power-law as a free parameter in our *'pexmon'* modeling. However, our stacked *NuSTAR* data do not constrain this parameter.

In summary, our analysis of the stacked 2019 and 2020 observations confirms that Mrk 590 displays a weak X-ray reflection component during its recent activity. However, we cannot distinguish between a small covering fraction for the

reflecting material and an edge-on viewing angle for the reflecting slab.

6 THE UV–OPTICAL–XRAY SED AND EDDINGTON RATIO

Here, we first present the observed *Swift* UVOT lightcurves, which display qualitatively similar flaring behavior as does the X-ray lightcurve. We then isolate the AGN UV–optical emission component. This allows us to study the SED shape evolution and the integrated X-ray–UV–optical luminosity, and to determine the evolution of the Eddington luminosity ratio. We quantify the UV–optical and X-ray variability, and demonstrate that the UV bands indeed respond to the X-ray variability, in Chapter 3.4 of this Thesis.

6.1 *Swift* UVOT lightcurves

We present the full UV–optical lightcurves since 2014 in Figure 12, and the individual *Swift* UVOT flux densities for each observation in Table 3. The far–UV and U bands display flares concurrently with the X-ray emission. The brightest UV–optical flare occurred during 2018, roughly concurrently with the brightest X-ray emission. The $UW2$ flux varies by a factor $\sim$12.8 between the 2014 low-flux state and its 2018 peak flux. The B band flux also increases during the X-ray flares, although its fractional variability between the lowest and highest flux is only a factor ~ 1.4. The V band responds weakly, if at all. The coherent flares in the X-rays and UV–optical indicate that the excess UV–optical emission is related to the accretion process, and not due to other processes in the host galaxy. We note that, while a supernova explosion occurred[6] in Mrk 590 during 2018, its light does not contribute to the measured UVOT fluxes of the nuclear region.

6.2 Isolating the AGN UV–optical Component

In order to study the AGN UV–optical emission as a function of time, we now address the host galaxy emission in our *Swift* UVOT source extraction aperture. Denney et al. (2014) find that the UV-optical SED in 2013 is fully attributable to host galaxy emission, i.e., with no AGN component. Based thereon, we use the lowest-flux UVOT observation from 2013 as a simple, first-order host galaxy emission template. We subtract the template flux densities in each *UVOT* bandpass for all subsequent measurements, and attribute any remaining emission to the AGN. For all observations obtained later than 2014, we detect emission in the far-UV bands ($UVW1$, $UVM2$ and $UVW2$) at a significance > 3σ relative to the uncertainties on the flux density. In Figure 13 we present two examples of this template subtraction. For the observation dated February 1st 2014 (top panel), we do not detect significant emission above the host galaxy template. On 6th October 2018, we detect additional

---

[6] The supernova triggered the All Sky Automated Survey for SuperNovae (url: http://www.astronomy.ohio-state.edu/asassn/index.shtml) and is documented by ATel 11848 (http://www.astronomerstelegram.org/?read=11848).
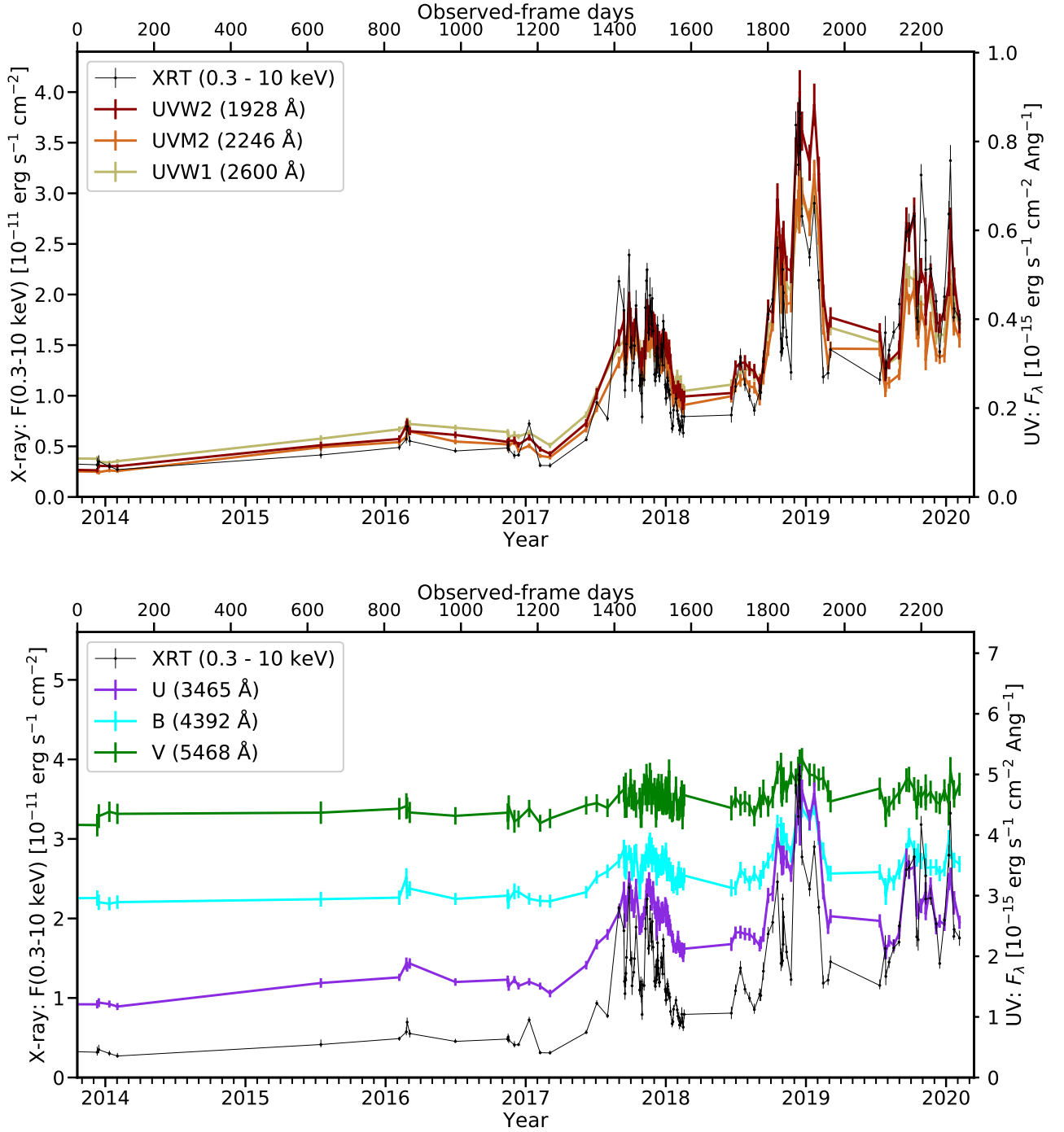
Figure 12. *Swift* UVOT lightcurves for the period December 2013 – February 2020. The flux densities are corrected for Galactic reddening, but are not corrected for host galaxy emission. We overlay the XRT lightcurve (black) to illustrate the correspondence between flares in the X-ray and UV–optical bandpasses. *Top:* Far-UV lightcurves. Each UVOT lightcurve provides the flux density at the central wavelength of each filter, assuming a power-law SED. Mrk 590 is unobservable with *Swift* between ∼1st March – early June each year, due to a Sun constraint. *Bottom:* Near-UV and visual lightcurves.

emission in all UVOT filter bandpasses, with the dominant contribution to the far-UV bandpasses being the AGN component.

6.3 The UV to X-ray SED shape

Over a wide range of redshifts and source luminosities, AGN display a non-linear relationship between their UV and X-ray luminosities (Zamorani et al. 1981; Vignali et al. 2003;
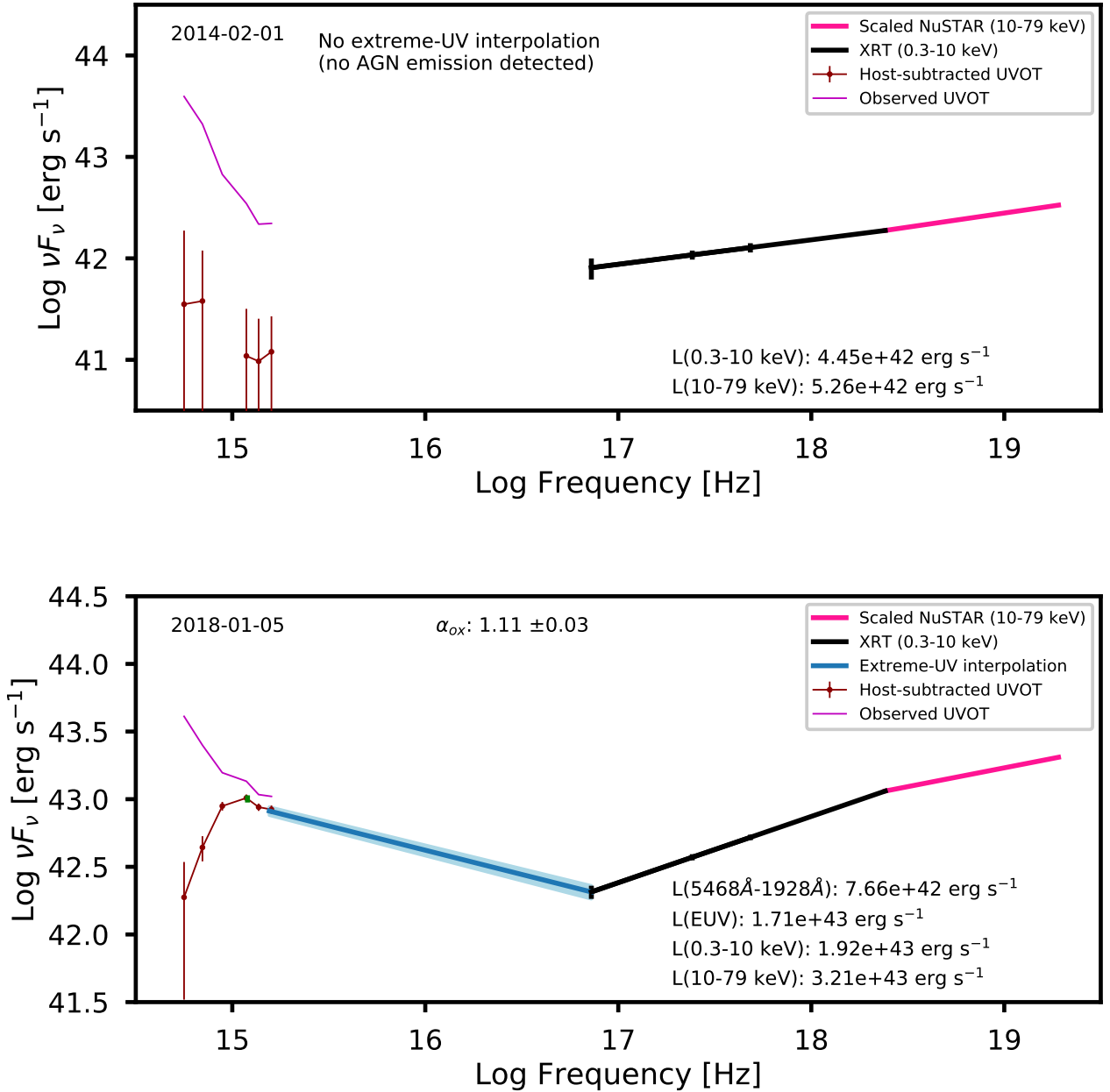
Figure 13. *Top:* UV-optical (*Swift* UVOT, violet curve) and 0.3–10 keV (*Swift* XRT, black line) luminosities for Mrk 590 in the low-flux state. The host galaxy subtracted UVOT luminosities are shown as red curves, including the 1σ error bars on the *observed* luminosities prior to template subtraction. Here, we do not detect additional emission at the $> 3\sigma$ level relative to the host galaxy, and do not perform an extrapolation over the extreme-UV region. The estimated 10-79 keV emission (pink line) is a power-law in frequency, scaled to the observed 10 keV luminosity, and using the average photon index $\Gamma = 1.722$ for our five *NuSTAR* observations. *Bottom:* UV-optical and X-ray luminosities for Mrk 590 in a high-flux state. The UV emission is significantly enhanced relative to our host galaxy template. The power-law extrapolation (blue curve) and its uncertainty (blue shaded region) yield a rough estimate of the extreme-UV emission, which represents a significant contribution to of the AGN bolometric luminosity (e.g., Kilerci Eser & Vestergaard 2018)

Steffen et al. 2006; Just et al. 2007). This relationship is quantified either as a linear relationship between the log-luminosity at rest-frame 2500 Åand at 2 keV (Lusso & Risaliti 2016), or using the UV to X-ray spectral index, $\alpha_{\rm ox}$ (Tananbaum et al. 1979). For non-homogeneous AGN sam-

ples, the observed scatter of $L_{\rm 2keV}$ at fixed L_{2500} is of order 0.4 dex. However, Lusso & Risaliti (2016) demonstrate that the intrinsic scatter is of order 0.21 dex. The tight relationship between the UV and X-ray luminosities implies a physical link between the disk and coronal emission, which
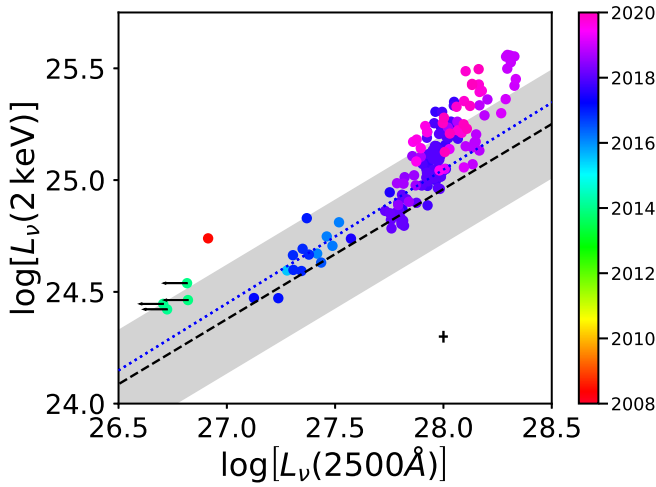
Figure 14. The distribution of $L_\nu(2500$ Å$)$ versus L_ν (2 keV) for our monitoring observations of Mrk 590. We subtract the host galaxy template before determining the 2500 Å luminosity. The colorbar illustrates the observation date (2008–2020). The black cross illustrates the median observational uncertainties on the UV and X-ray luminosities. The four green data points represent lower limits on $L_\nu(2500$ Å$)$ during the 2013–2014 low-flux state, as no AGN UV–optical emission is detected for these observations. The majority of our measurements are consistent with the UV–X-ray luminosity relationships for statistical samples of AGN presented by Lusso et al. (2010) (dotted blue line) and Lusso & Risaliti (2016) (dashed black line); the gray shaded region represents the 0.24 dex scatter found by Lusso & Risaliti (2016). We note a tendency for Mrk 590 to become more X-ray luminous at high UV luminosities than predicted by the Lusso et al. relationships.

is likely governed by the effects of black hole mass and accretion rate (Lusso & Risaliti 2017).

We present measurements of $\log(L_{2\mathrm{keV}})$ as a function of $\log(L_{2500})$ for Mrk 590 in Figure 14. As the UV luminosity of Mrk 590 ranges between $26.6 < \log(L_{2500}) < 28.3$ during 2014–2020, the most appropriate comparison sample of bona fide AGN is that presented by Lusso et al. (2010), containing AGN with $\log(L_{2500})$ as faint as 26.5. Our measurements are consistent with their best-fit linear relationship between $\log(L_{2500})$ and $\log(L_{2\mathrm{keV}})$ (Figure 14, blue dotted line), given that their sample displays a ~ 0.4 dex scatter. The majority of our measurements are also consistent with the relationship presented by Lusso & Risaliti (2016), derived for sources with $\log(L_{2500}) > 29$ (Figure 14, black dashed line), given the ~ 0.24 dex statistical scatter for their 'cleaned' sample.

While our measurements are consistent with the existing relationships given their *statistical* scatter for large samples of AGN, we do find that Mrk 590 becomes relatively X-ray brighter at observational epochs where its UV emission is either particularly bright ($\log(L_{2500}) > 28$) or faint ($\log(L_{2500}) < 27$). The $\sim 5\%$ observational uncertainties for individual measurements of $L_{2\mathrm{keV}}$ and L_{2500} do not account for this trend. We conclude that Mrk 590 displays a UV to X-ray SED shape consistent with that of bona fide AGN during 2017–2020, but becomes systematically X-ray brighter in high-flux states.

6.4 Integrated optical–UV–X-ray luminosities

Here, we make a rough estimate of the integrated optical–UV–X-ray luminosity of Mrk 590 as a function of time, in order to determine the evolution of its Eddington luminosity ratio (§6.5) during the reappearance of its UV emission. Detailed modeling of the AGN component SED will require an improved treatment of the host galaxy and AGN broad-line emission. In particular, while our host galaxy subtractions are conservative in the sense that they place lower limits on the total AGN emission strength, they do not fully isolate the AGN continuum emission. This is due to the potential presence of reprocessed far-UV continuum emission in the form of broad UV–optical emission lines. In fact, Raimundo et al. (2019) do find broad Hα and Hβ emission in their 2017 spectroscopic observations of Mrk 590. For a sample of seven AGN at redshifts $z < 0.07$, Kilerci Eser & Vestergaard (2018) find that the typical contribution of broad UV–optical emission lines to the integrated optical to X-ray luminosity is only $\approx 5\%$. Thus, to first order, we expect our integrated luminosities based on the host galaxy subtracted *Swift* UVOT broad-band photometry to be roughly correct. We defer detailed modeling of the AGN continuum emission to future work, pending analysis of *Hubble Space Telescope* spectroscopy (PI: Vestergaard). These observations will both directly constrain the UV continuum profile, and provide indirect constraints on the ionizing EUV continuum, derived from the broad emission line luminosities (e.g., Korista et al. 1997).

During the X-ray flares, the energy output of the AGN component is brightest in the UV (Figure 13). While we see hints of a spectral turnover at ~ 2600 Å, the host galaxy subtracted SED is rather flat between the $UW1$ (~ 2600 Å) and $UW2$ band (~ 1900 Å). We therefore expect that the UV emission component extends into the unobservable extreme-UV (EUV). Several physically motivated models that describe the EUV emission are available. Done et al. (2012) present a Novikov-Thorne thermal accretion disk model modified by a color correction due to radiative transfer in the disk atmosphere. The resulting disk SED extends into the EUV, with a spectral turnover occuring at higher energies for higher Eddington ratios, as illustrated by their Figure 1. Korista et al. (1997) demonstrate that the EUV SED should peak at ~ 54 eV, based on photoionization considerations, and present a broken power-law model for the AGN continuum emission. For Seyfert 1 AGN, Kilerci Eser & Vestergaard (2018) find that a simple power-law interpolation between the far-UV and soft X-ray luminosities yields an integrated EUV luminosity that is roughly halfway between that produced by the Done et al. (2012) and Korista et al. (1997) models. The uncertainty on the integrated extreme-UV luminosity due to model selection is of order $\sim 25\%$, with the Korista et al. (1997) model being systematically more EUV-luminous than the power-law interpolation, and the Done et al. (2012) model being less luminous. As our current aim is to make a rough estimate of the EUV luminosity, we opt for the simple power-law interpolation. For each *Swift* observational epoch, we perform a power-law interpolation between the UVOT $UW2$ and XRT 0.3 keV luminosities (Figure 13, bottom panel). The observational uncertainties for this model are calculated by interpolating between the 1σ limits on the *Swift* UVOT $UW2$ and XRT
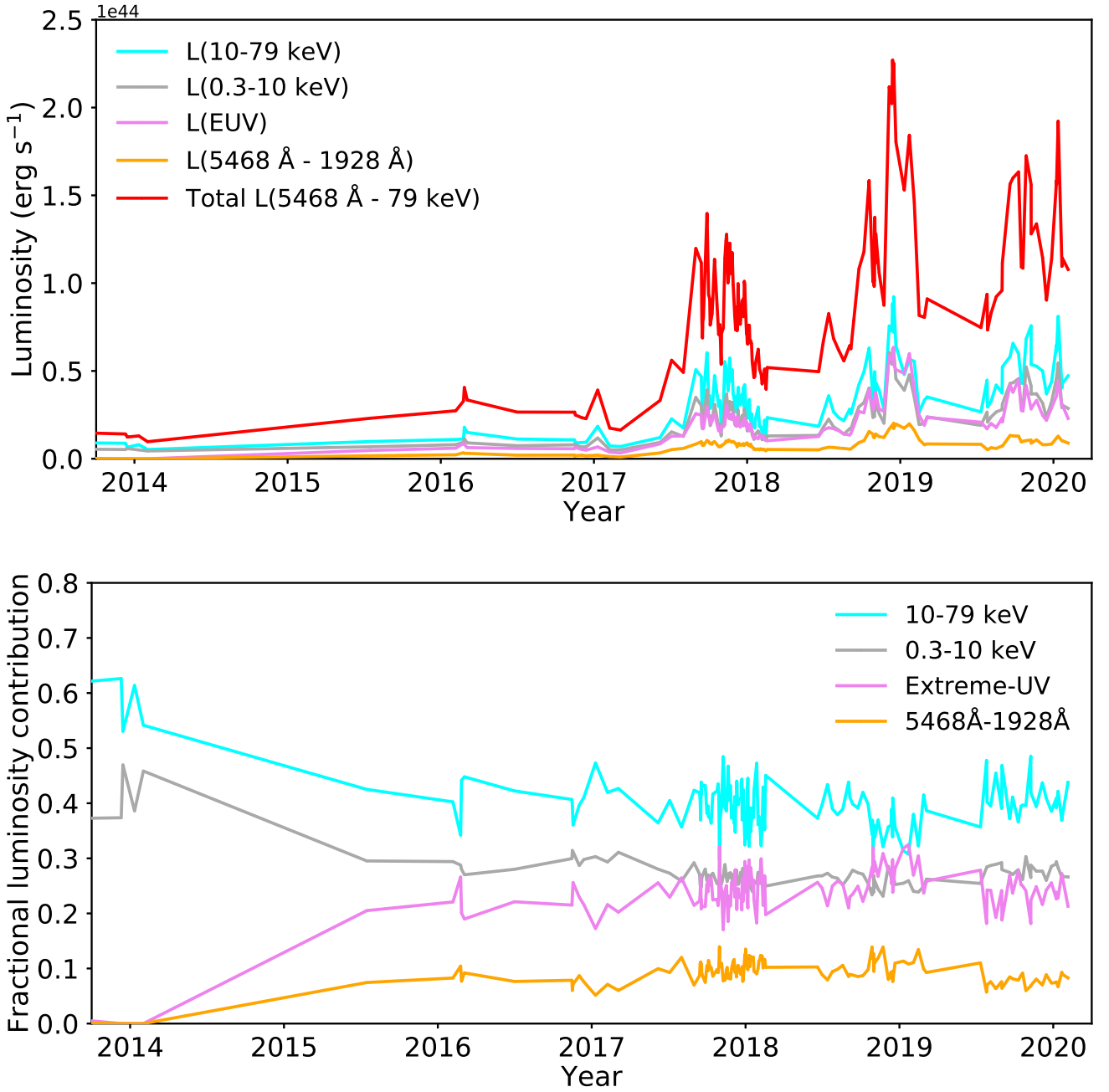
Figure 15. *Top panel:* The estimated 10–79 keV luminosity (cyan curve), observed *Swift* XRT 0.3-10 keV luminosity (gray curve), estimated extreme-UV luminosity (violet curve), and host galaxy subtracted UV–optical luminosity (orange curve). We note that the very low extreme-UV luminosity during 2013–2014 is an artefact of our modeling procedure (§6.4). *Bottom panel:* Fractional contribution of each luminosity component to the total AGN luminosity. Even during the brightest UV–optical flares, more than half the luminous energy output is in the X-ray regime.

0.3 keV luminosity densities. We note that the uncertainty due to EUV model selection, of order $\sim 25\%$, is much larger than the observational uncertainties calculated in this way.

To estimate the integrated UV–optical AGN luminosity, L_{UV}, we perform a piecewise linear interpolation of the host galaxy subtracted luminosity densities for each *Swift* UVOT bandpass. To obtain a conservative error estimate for L_{UV}, we repeat our interpolation, now using the 1σ lim-

iting UVOT flux densities. We do not extend the model to wavelengths longer than the UVOT V band (~ 5468 Å), as the AGN emission is faint compared to the host galaxy in the V band. Raimundo et al. (2019) find that the AGN continuum in the optical regime is negligible in 2017. Inclusion of the long-wavelength tail of the AGN continuum component is therefore not necessary for these first-order estimates of the integrated luminosities.
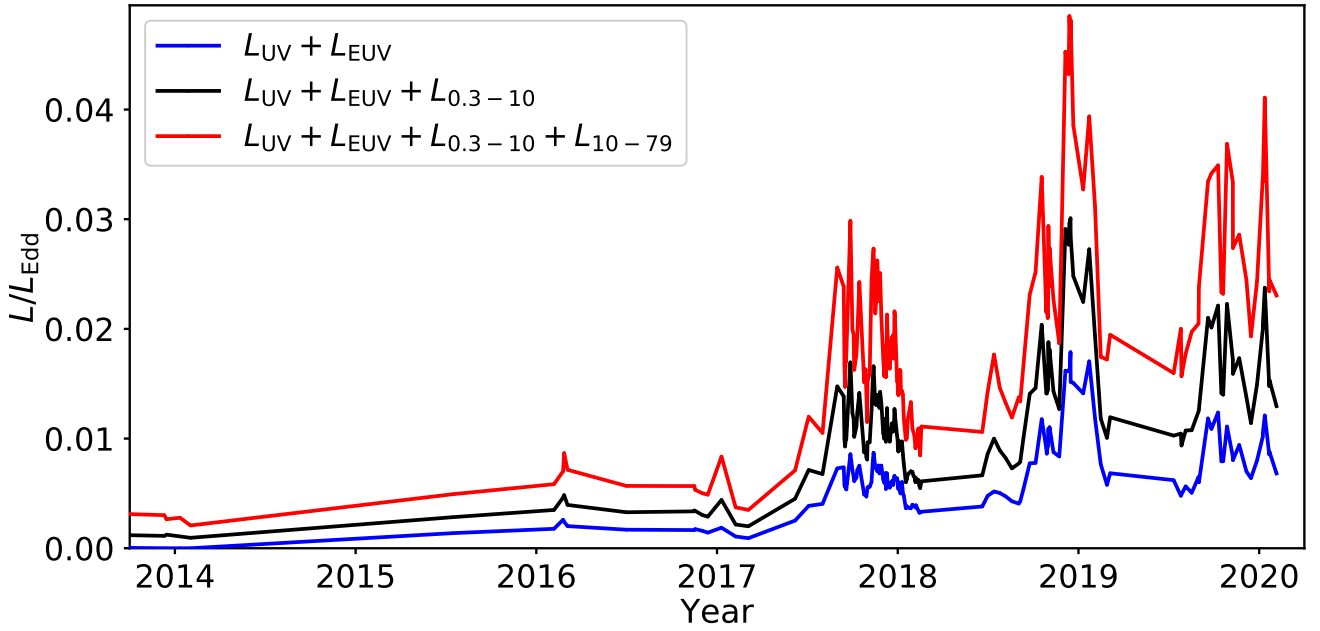
Figure 16. The Eddington luminosity ratio, $L/L_{\rm Edd}$, as a function of time. The X-ray emission represents a substantial contribution to the total observed luminosity for Mrk 590. The Eddington ratios calculated using only $L_{\rm UV} + L_{\rm EUV}$ (blue curve) are a factor ~ 2 smaller than those including the 0.3-10 keV X-ray spectrum (black curve), and a factor ~ 3 smaller than those that also include the 10-79 keV contribution (red curve).

We estimate the EUV luminosity, $L_{\rm EUV}$, as the integrated 1900 Å–0.3 keV luminosity of our power-law EUV interpolation. We derive the integrated 0.3-10 keV luminosity, $L_{0.3-10}$, and its uncertainties using our power-law X-ray continuum model after correcting for Galactic absorption (§3.2). While we lack *NuSTAR* hard X-ray observations for most *Swift* observing epochs, the observed 10-79 keV emission during our five *NuSTAR* observations does contribute significantly to the total observed luminosity. To estimate the 10-79 keV luminosity L_{10-79} as a function of time, we use a power-law model with spectral index $\Gamma = 1.722$, i.e., the average hard X-ray spectral index measured for the five *NuSTAR* observations using the continuum window method (§4.2). We scale this model to match the luminosity density at 10 keV, as determined using our power-law model fits to the individual *Swift* XRT observations. We tabulate the integrated UV–optical, EUV, 0.3-10 keV, and 10-79 keV luminosities in Table 3.

The host galaxy subtracted UV–optical luminosity rises gradually throughout mid-2017, and does not return to its previous very low state during 2018–2020. This component is brightest during the late 2018 flare (Figure 15, top panel). The UV–optical luminosity does not exceed $\sim$10% of the total AGN luminosity at any observational epoch (Figure 15, bottom panel). In terms of its fractional contribution to the total luminosity, the most dramatic change in the UV–optical component occurs between 2014 and 2016. According to our power-law EUV interpolation, the EUV emission accounts for roughly 25% of the total AGN luminosity since 2016. Even after the reappearance of the UV–optical emission component, over half the energy output is in the X-ray regime. We note that, while our estimated 10-79 keV luminosity contributes the majority of the total luminosity in the 2013–2014 minimum-flux state, our first *NuSTAR* observations of Mrk 590 took place in 2016. The relative contributions of the 0.3-10 keV and 10-79 keV X-ray bands in 2013–2014 are therefore unknown.

6.5 Evolution of the Eddington luminosity ratio

The Eddington luminosity ratio is a useful diagnostic of AGN accretion flows, as it provides a black hole mass-independent comparison of the luminous accretion between sources. In the context of highly variable AGN, the Eddington luminosity ratio may also be relevant to the physics of the accretion flow, as Shakura & Sunyaev (1973)-type thin accretion disks may transition into advection-dominated thick disks at Eddington ratios of approximately 1% (Narayan & Yi 1994; Noda & Done 2018; Liu et al. 2020, e.g.,). Here, we study the evolution of the Eddington ratio for Mrk 590 as its UV emission component reappears.

The Eddington luminosity is defined as that luminosity for which the force of gravity balances radiation pressure, for spherically symmetric accretion. For accretion of ionized hydrogen, it is given by

$$L_{\rm Edd} = 4\pi c G m_{\rm p} M_{\rm BH} \sigma_{\rm T}^{-1}.$$

Here, G is the gravitational constant, c is the speed of light, $m_{\rm p}$ is the proton mass, $M_{\rm BH}$ is the black hole mass, and $\sigma_{\rm T}$ is the Thomson cross-section. In practice, AGN accretion is not spherically symmetric, so $L_{\rm Edd}$ does not represent an absolute limit on the luminosity. Instead, the Eddington luminosity ratio, $L_{\rm bol}/L_{\rm Edd}$, provides a measure of the accretion luminosity normalized by $M_{\rm BH}$.

The Eddington ratio as defined above requires the bolometric luminosity, $L_{\rm bol}$. However, the infrared luminosity is dominated by dust reprocessing (e.g., Barvainis 1987). It is therefore not appropriate to include the infrared luminosity contribution in the calculation of $L_{\rm bol}/L_{\rm Edd}$. Given the available data, our best approximation of the bolometric luminosity due to the accretion flow is

$$L_{\rm bol} \approx L_{\rm UV} + L_{\rm EUV} + L_{0.3-10} + L_{10-79}.$$

By this approximation, the Eddington ratio for Mrk 590 varies between ~ 0.003 in the 2014 low-flux state, and ~ 0.045 during the 2018 flare (Figure 16, red curve). Much of this energy is released in the hard X-ray corona: the quantity $(L_{\rm UV} + L_{\rm EUV})/L_{\rm Edd}$, which might be attributed to direct emission from an accretion disk, does not exceed ~ 0.02 (Figure 16, blue curve). We discuss the increase in $L_{\rm bol}/L_{\rm Edd}$ during the 2017 flare-up in §7.1.

7   DISCUSSION

Our primary goal with this work is to document the flaring behavior exhibited by Mrk 590 in UV and X-ray emission since 2017. Our main results are as follows:

• Based on the Eddington ratios, $L/L_{\rm Edd} \sim 0.05$, and UV to X-ray SED shapes observed during the flares, the observational appearance of Mrk 590 is now that of a bona fide (albeit highly variable) broad-line AGN.
• There is no evidence of soft X-ray excess in our *Swift* XRT observations either prior to or after the 2017 flare-up.
• We detect Fe K complex emission in both the low-flux state (2016) and during the subsequent flares. The equivalent width of this feature is larger in the low-flux state than in the high-flux state.
• Our *NuSTAR* data are consistent with the presence of X-ray reflection features in both the low-flux state and during the flares. The reflection factor is $R \approx 0.3$ in the high-flux state, consistent with patchy reflection. In the low-flux state, the reflection factor is $R = 1.15^{+0.77}_{-0.58}$, (90% confidence intervals).

We discuss each of these results in turn below.

7.1   Re-ignition of the UV-optical emission

The UV–optical emission of Mrk 590 in 2013–2014 is consistent with only host galaxy emission (Denney et al. 2014). The X-ray emission is also rather faint at that time, with $L(0.3\text{-}10 \text{ keV}) \approx 5 \times 10^{43}$ erg s^{-1} in the low-flux state. Denney et al. (2014) do not detect broad optical emission lines in their 2012 and 2013 spectroscopic observations; they detect only a faint broad component for the Ly-α and CIV UV emission lines. While Mathur et al. (2018) do detect broad Mg II in November 2014, this emission line displays low responsivity to continuum variations (Cackett et al. 2007), and is therefore an unreliable indicator of the instantaneous ionizing continuum level. The ionizing continuum was thus likely very faint in 2013–2014; we find an Eddington ratio of only $L/L_{\rm Edd} \approx 0.003$ at this time (§6.5, Figure 16).

The simultaneous increase in the X-ray and UV emission during 2017 reveal that the central engine has now re-ignited from its previous UV-faint state. The Eddington ratio exceeds $L/L_{\rm Edd} \approx 0.01$ for all observational epochs since August 2017 (Figure 16), and reaches $L/L_{\rm Edd} \approx 0.045$ during the brightest observed flare. During the post-2017 re-ignition, the UV to X-ray SED shapes are consistent with those observed for bona fide AGN (§6.3), suggesting the reappearance of a typical UV continuum source. The detection of broad $H\alpha$ and $H\beta$ emission lines in the nuclear region in late 2017 (Raimundo et al. 2019) provides independent evidence that the 2017 flare produced substantial EUV emission, as required in order to photo-ionize the broad-line gas (e.g., Korista et al. 1997).

The increase in Eddington ratio above $L/L_{\rm Edd} = 0.01$, with a corresponding sharp increase in UV luminosity and reappearance of the broad emission lines, is suggestive of a transition in accretion modes. At Eddington ratios below ~ 0.01, Narayan & Yi (1994) find a stable advection-dominated solution for the accretion flow, a so-called ADAF disk. These accretion disks are not thermalized, and do not emit a bright UV continuum component. Liu et al. (2020) find evidence of such an accretion state transition for the low-luminosity AGN NGC 7589, for which the Eddington ratio increased from $L/L_{\rm Edd} \approx 0.001$ to $L/L_{\rm Edd} \approx 0.13$. They base their claim of an accretion mode transition upon the reappearance of the soft X-ray excess component, which we do *not* detect for Mrk 590 in our joint *NuSTAR* and *Swift* XRT analysis (§5.2). Instead, we can infer the reappearance of a typical EUV-bright AGN emission bump from the increase in UV luminosity and the reappearance of broad emission lines. However, we cannot exclude the presence of a faint soft excess component given the currently available data, as further discussed in §7.2.

Noda & Done (2018) also discuss the transition between ADAF disks and thermal accretion disks in the context of CLAGN. They find that the UV–X-ray SED changes for the CLAGN Mrk 1018 are consistent with an accretion mode transition. However, they point out that the state change for black hole binaries are observed to occur on the viscous timescale. As this timescale scales with the black hole mass, it is too long to explain the observed changing-look events for AGN. It is therefore necessary to explain how such transitions can occur in AGN disks on timescales of ∼months to years. Sniegowska et al. (2020) suggest that, for a truncated disk where only the inner region becomes advection-dominated, an accretion mode transitions may occur in the UV-luminous inner disk on timescales much shorter than the viscous timescale. Alternatively, in radiation-pressure dominated disks, the state change may occur more quickly. For example, the Hydrogen ionization dynamic instability mechanism (e.g., Hameury et al. 2009) may provide rapid transitions in accretion state. In the context of extreme-variability AGN, Jiang & Blaes (2020) perform magneto-hydrodynamical modeling of a related mechanism, i.e., density inversion fronts due to Iron opacity. They find that these density inversions cause the accretion disk to become convectively unstable, causing large variations in the disk luminosity on timescales of ∼years. Intriguingly, the evolution of Eddington luminosity ratio for their magneto-hydrodynamic simulation model (Figure 14 of Jiang & Blaes 2020) displays flare-like peaks on timescales of ∼years, similar to our results

for Mrk 590 (Figure 16). In future work we will perform UV and X-ray accretion disk modeling in the low-flux and high-flux states, which we hope will provide further constraints on the accretion physics during the 2017 flare-up.

7.2   Evolution of the soft X-ray spectrum

Mrk 590 was first observed at soft X-ray energies by Turner & Pounds (1989), during its historical high-flux state. They model the spectrum as a power-law with Galactic absorption, and find no evidence of either soft excess or intrinsic absorption. Gallo et al. (2006) observe Mrk 590 in 2002, at which point it had already dimmed substantially, with an X-ray flux of $F(0.3 - 10\mathrm{keV}) = 8.43 \times 10^{-12}$ erg cm^{-2} s^{-1}. They find evidence for fairly bright soft excess emission, which they model as a blackbody component with $kT = 161$ eV and an integrated flux of 8% relative to the 0.3-10 keV continuum. Longinotti et al. (2007) confirm the presence of a soft excess component with $kT = 156$ eV in their 2004 *XMM-Newton* and *Chandra* observations, at an X-ray flux $F(2 - 8\mathrm{keV}) = 6.72 \times 10^{-12}$ erg cm^{-2} s^{-1}. They report that the soft excess luminosity is similar in 2004 to that found in 2002, although they do not quantify this. Rivers et al. (2012) then report the disappearance of the soft excess at some point between 2004 and their 2011 *Suzaku* (0.7-12 keV) observations. The broadband X-ray flux in 2011 is similar to the 2002-2004 levels; the soft excess component is not detected, and must be at least a factor ~ 30 fainter than in 2004 according to their analysis.

Denney et al. (2014) do not detect soft excess in their 2013 *Chandra* observations. However, the soft excess returned at a low level shortly afterwards. Mathur et al. (2018) find evidence for a weak soft X-ray excess in their November 2014 *Chandra* observation of Mrk 590, ~ 10 months after our 2013-2014 *Swift* observations in the low-flux state. They re-analyze the 2013 *Chandra* observations, and demonstrate that the soft excess found in 2014 is not present in 2013. They interpret this result as an early sign of the re-ignition of Mrk 590.

Mrk 590 has now returned to somewhat higher X-ray flux levels than those observed in 2002 and 2004. For example, we measure $F(2 - 8\mathrm{keV}) = 8.54 \times 10^{-12}$ erg cm^{-2} s^{-1}, and $F(0.3 - 10\mathrm{keV}) = 1.57 \times 10^{-11}$ erg cm^{-2} s^{-1}, during the August 2019 joint *NuSTAR* and *Swift* observations. We do not detect soft X-ray excess emission in either the low-flux state (2016) or during the post-2017 flaring activity (§5). We emphasize that our X-ray analysis is not sensitive to soft excess emission at the *absolute* flux level detected by Mathur et al. (2018) in 2014. It is thus plausible that Mrk 590 still produces a soft X-ray excess at a similar low level. However, given the appearance of the XRT spectra presented in 5.2, it seems unlikely that the soft excess emission has returned to its 2002 level, i.e., 8% of the integrated 0.3-10 keV continuum luminosity. Our simulations (Appendix A) indicate that, *in the absence of additional X-ray spectral complexity,* we are sensitive to soft X-ray excess emission much fainter than the 2002 level. Overall, our post-2017 X-ray spectra are qualitatively similar to the 2011 result presented by Rivers et al. (2012). They find a hard X-ray continuum with $\Gamma \approx 1.7$, and an Fe K emission line consistent with a $R \sim 0.30$ reflection spectrum. Thus, it appears that the X-ray spectrum has returned to its 2011 state, i.e., dominated by a power-

law continuum, with weak or absent soft excess. In fact, an *XMM-Newton* observation of Mrk 590 on 4th July 2020 does display a faint soft X-ray excess (G. Miniutti, private communication). While it is possible that the soft excess emission has reappeared between January 2020 and July 2020, it is also possible that the compponent is too faint to be detected in our *Swift* XRT spectra, especially if there are other features in the soft X-rays that we did not include in our simulation work. We will analyze the *XMM-Newton* observations when they become available, and hope to harness their superior spectral resolution in order to better understand our *Swift* XRT non-detections.

The physical cause of soft X-ray excess in AGN is not fully understood. The leading candidates are Comptonization in a warm, optically thick corona (e.g., Petrucci et al. 2018), and relativistic reflection in the accretion disk (e.g., Crummy et al. 2006). Both these scenarios depend on the presence of an accretion flow in the vicinity of the black hole, and thus predict a disappearing soft excess at a sufficiently low accretion rate. It is possible that the accretion rate in Mrk 590 is not currently high enough to generate substantial soft X-ray excess emission. Alternatively, the factor ≈ 30 dimming of the soft excess component between 2004-2011 might be a delayed response to the gradual drop in source luminosity between the late 1990s and early 2000s, as documented by Denney et al. (2014). We now observe a brightening of the hard X-ray emission to above the 2004 level, with no reappearance of the soft excess at the level observed in 2004; this non-detection is also consistent with a scenario in which strong variability in the soft excess lags the variations in the (extreme-)UV ionizing continuum by a few years. In that case, continued X-ray monitoring of Mrk 590 may reveal the reappearance of the soft excess component in the near future.

7.3   The X-ray reflecting geometry

While we detect Fe K emission indicative of X-ray reflection in both December 2016 and in our stacked 2019–2020 *NuSTAR* observations, the hard X-ray Compton reflection hump appears rather faint after 2017. We find an average reflection scaling factor $R = 0.36$ for the three post-2017 *NuSTAR* observations, where $R = 1$ corresponds to reflection in a semi-infinite plane. While Lightman & White (1988) demonstrate that an X-ray reflection spectrum is *predicted* if a thermal emission disk is present, it is not a sufficient condition for the presence of a thermal disk. Other possible X-ray reflection regions include a distant neutral medium, such as the obscuring torus posited by AGN unification models (e.g., Antonucci 1993). The observed faint reflection spectrum is thus consistent with either a distant reflector, or patchy reflection in an accretion disk. Detection of relativistically broadened Fe K emission would represent 'smoking-gun' evidence of reflection in the inner accretion disk. Unfortunately, the weak observed Fe K emission lines in our *NuSTAR* data do not allow for dynamic modeling, as we cannot resolve the individual emission lines of the Fe K complex.

Nandra et al. (2007) analyze the *XMM-Newton* spectrum of Mrk 590 in July 2004. Using the *'pexmon'* model, they find $R = 0.38^{+0.12}_{-0.35}$, consistent with our post-2017 modeling. Thus, it appears that the reflection geometry is unchanged before and after the $\sim$2010 changing-look event.

This is consistent with the X-ray reflecting material being distant from the central source, although it may instead indicate the reappearance of an accretion disk with similar 'patchy' reflection properties as in 2004. Nandra et al. (2007) also find a narrow Fe Kα line with an equivalent width of 64 eV in their 2004 observations. They do not find evidence for a broad component of the Fe Kα emission line. Longinotti et al. (2007) do find a broad component in their 2004 *Chandra* observation of Mrk 590, but their Fe Kα linewidth of ~ 4000 km s^{-1} suggests reflection in the BLR or torus rather than the inner accretion disk.

Our best-fit reflection spectrum model for December 2016 has a reflection factor of $R = 1.15^{+0.77}_{-0.58}$ (90% confidence intervals). While the uncertainties on R are rather large for this observation, the December 2016 reflection component does appear stronger relative to either our August 2019 modeling ($R = 0.29^{+0.17}_{-0.15}$) or the 2004 observation presented by (Nandra et al. 2007) ($R = 0.38^{+0.12}_{-0.35}$). One possible interpretation is that the X-ray reflecting medium is distant to the central source, so that we observe 'echoes' of the pre-2010 continuum emission in the 2016 reflection spectrum. There is evidence for a similar scenario in the CLAGN Mrk 1018. This source lost its broad emission lines at some point between 2009 and 2015 (McElroy et al. 2016), with a simultaneous factor ~ 7.5 drop in X-ray flux. LaMassa et al. (2017) find evidence for an anomalously strong X-ray reflection component ($R > 3$) in the 2016 low-flux state. They suggest that the strong reflection is due to a reflector located at distances of at least ~ 1 light-year from the central source.

Our collaborators have recently obtained X-ray observations of Mrk 590 using the *XMM-Newton* satellite (G. Miniutti - private communication). Future analysis of these observations will place better constraints on the Fe K emission profile, and thus provide a test of reflection from the inner accretion disk during the current flaring activity.

8 CONCLUSION

The changing-look AGN Mrk 590 lost its UV continuum and broad-line emission components at some point between 2006 and 2013 (Denney et al. 2014). Its soft X-ray excess component also dimmed significantly during 2004–2011 (Rivers et al. 2012), before reappearing at a low level in 2014 (Mathur et al. 2018). We find that Mrk 590 has now re-ignited, displaying a standard UV to X–ray SED and an Eddington luminosity ratio of $L/L_{\rm Edd} \sim 0.04$. It is currently highly variable, displaying simultaneous flare-up events in UV and X-ray emission since 2017. The increase in Eddington luminosity ratio, from ~ 0.003 in 2014 to $L/L_{\rm Edd} > 0.01$ after August 2017, may indicate a transition in the physics of the accretion flow; the lack of UV emission from the AGN in the low-flux state is consistent with an advection-dominated accretion disk in 2013–2014. However, we do not detect strong soft X-ray excess emission in either the low-flux state (2016) or during the recent flaring behavior. This contrasts with the results of Liu et al. (2020), who find a reappearance of the soft excess in NGC 7589 as the Eddington ratio increases from $L/L_{\rm Edd} \approx 0.001$ to $L/L_{\rm Edd} \approx 0.13$. As Mrk 590 has not yet exceeded $L/L_{\rm Edd} \approx 0.05$, it is possible that strong soft excess emission will reappear if the

Eddington luminosity ratio continues to increase. Alternatively, we speculate that there may be a time delay between variations in the ionizing continuum luminosity and in the soft X-ray excess.

References

Antonucci R., 1993, ARA&A, 31, 473
Barvainis R., 1987, ApJ, 320, 537
Burrows D. N., et al., 2005, Space Sci. Rev., 120, 165
Cackett E. M., Horne K., Winkler H., 2007, MNRAS, 380, 669
Cackett E. M., Gültekin K., Bentz M. C., Fausnaugh M. M., Peterson B. M., Troyer J., Vestergaard M., 2015, ApJ, 810, 86
Cash W., 1979, ApJ, 228, 939
Collier S., Peterson B. M., 2001, ApJ, 555, 775
Crummy J., Fabian A. C., Gallo L., Ross R. R., 2006, MNRAS, 365, 1067
Denney K. D., et al., 2014, ApJ, 796, 134
Dexter J., Begelman M. C., 2019, MNRAS, 483, L17
Done C., Davis S. W., Jin C., Blaes O., Ward M., 2012, MNRAS, 420, 1848
Edelson R., et al., 2015, ApJ, 806, 129
Elvis M., et al., 1994, ApJS, 95, 1
Gallo L. C., Lehmann I., Pietsch W., Boller T., Brinkmann W., Friedrich P., Grupe D., 2006, MNRAS, 365, 688
García J. A., Kallman T. R., Bautista M., Mendoza C., Deprince J., Palmeri P., Quinet P., 2018, in Workshop on Astrophysical Opacities. p. 282 (arXiv:1805.00581)
Gierliński M., Done C., 2004, MNRAS, 349, L7
Goodrich R. W., 1989, ApJ, 340, 190
Goodrich R. W., 1995, ApJ, 440, 141
Grupe D., Beuermann K., Thomas H. C., Mannheim K., Fink H. H., 1998, A&A, 330, 25
Grupe D., Leighly K. M., Komossa S., 2008, AJ, 136, 2343
HI4PI Collaboration et al., 2016, A&A, 594, A116
Haardt F., Maraschi L., 1993, ApJ, 413, 507
Hameury J. M., Viallet M., Lasota J. P., 2009, A&A, 496, 413
Harrison F. A., et al., 2013, ApJ, 770, 103
Harrison F. A., et al., 2016, ApJ, 831, 185
Jiang Y.-F., Blaes O., 2020, arXiv e-prints, p. arXiv:2006.08657
Just D. W., Brandt W. N., Shemmer O., Steffen A. T., Schneider D. P., Chartas G., Garmire G. P., 2007, ApJ, 665, 1004
Kelly B. C., Bechtold J., Siemiginowska A., 2009, ApJ, 698, 895
Kilerci Eser E., Vestergaard M., 2018, MNRAS, 474, 1590
Korista K., Ferland G., Baldwin J., 1997, ApJ, 487, 555
Kynoch D., Ward M. J., Lawrence A., Bruce A. G., Landt H., MacLeod C. L., 2019, MNRAS, 485, 2573
LaMassa S. M., Yaqoob T., Kilgard R., 2017, ApJ, 840, 11
Lawrence A., 2018, Nature Astronomy, 2, 102
Lightman A. P., White T. R., 1988, ApJ, 335, 57
Liu Z., Liu H.-Y., Cheng H., Qiao E., Yuan W., 2020, MNRAS, 492, 2335
Longinotti A. L., Bianchi S., Santos-Lleo M., Rodríguez-Pascual P., Guainazzi M., Cardaci M., Pollock A. M. T., 2007, A&A, 470, 73
Lusso E., Risaliti G., 2016, ApJ, 819, 154
Lusso E., Risaliti G., 2017, A&A, 602, A79
Lusso E., et al., 2010, A&A, 512, A34

MacLeod C. L., et al., 2019, ApJ, 874, 8

Madsen K. K., Grefenstette B. W., Pike S., Miyasaka H., Brightman M., Forster K., Harrison F. A., 2020, arXiv e-prints, p. arXiv:2005.00569

Magdziarz P., Zdziarski A. A., 1995, MNRAS, 273, 837

Mathur S., et al., 2018, ApJ, 866, 123

McElroy R. E., et al., 2016, A&A, 593, L8

McHardy I. M., et al., 2018, MNRAS, 480, 2881

Nandra K., O'Neill P. M., George I. M., Reeves J. N., 2007, MNRAS, 382, 194

Narayan R., Yi I., 1994, ApJ, 428, L13

Noda H., Done C., 2018, MNRAS, 480, 3898

Park T., Kashyap V. L., Siemiginowska A., van Dyk D. A., Zezas A., Heinke C., Wargelin B. J., 2006, ApJ, 652, 610

Penston M. V., Perez E., 1984, MNRAS, 211, 33P

Peterson B. M., et al., 2004, ApJ, 613, 682

Petrucci P. O., et al., 2000, ApJ, 540, 131

Petrucci P. O., Ursini F., De Rosa A., Bianchi S., Cappi M., Matt G., Dadina M., Malzac J., 2018, A&A, 611, A59

Piconcelli E., Jimenez-Bailón E., Guainazzi M., Schartel N., Rodríguez-Pascual P. M., Santos-Lleó M., 2005, A&A, 432, 15

Poole T. S., et al., 2008, MNRAS, 383, 627

Porquet D., Reeves J. N., O'Brien P., Brinkmann W., 2004, A&A, 422, 85

Raimundo S. I., Vestergaard M., Koay J. Y., Lawther D., Casasola V., Peterson B. M., 2019, MNRAS, 486, 123

Richards G. T., et al., 2006, ApJS, 166, 470

Rivers E., Markowitz A., Duro R., Rothschild R., 2012, ApJ, 759, 63

Ross R. R., Fabian A. C., 2005, MNRAS, 358, 211

Rumbaugh N., et al., 2018, ApJ, 854, 160

Runnoe J. C., et al., 2016, MNRAS, 455, 1691

Scott A. E., Stewart G. C., 2014, MNRAS, 438, 2253

Shakura N. I., Sunyaev R. A., 1973, A&A, 24, 337

Siemiginowska A., Kuhn O., Elvis M., Fiore F., McDowell J., Wilkes B. J., 1995, ApJ, 454, 77

Sniegowska M., Czerny B., Bon E., Bon N., 2020, arXiv e-prints, p. arXiv:2007.06441

Steffen A. T., Strateva I., Brandt W. N., Alexander D. M., Koekemoer A. M., Lehmer B. D., Schneider D. P., Vignali C., 2006, AJ, 131, 2826

Tananbaum H., et al., 1979, ApJ, 234, L9

Turner T. J., Pounds K. A., 1989, MNRAS, 240, 833

Vignali C., Brandt W. N., Schneider D. P., 2003, AJ, 125, 433

Zamorani G., et al., 1981, ApJ, 245, 357

Table 1.   Individual *Swift* XRT observations

MJD	Observation ID	Exposure time [s]	0.3-10 keV counts	$F_{0.3-10}$	$F_{0.3-2}$	F_{2-10}	$\Gamma_{0.3-10}$
(1)	(2)	(3)	(4)	(5)	(6)	(7)	(8)
54627	00037590001	4465	514.4	$5.75^{+0.30}_{-0.39}$	$2.21^{+0.12}_{-0.09}$	$3.53^{+0.30}_{-0.30}$	$1.64^{+0.06}_{-0.06}$
56636	00037590002	1068	70.3	$3.18^{+0.70}_{-0.42}$	$1.05^{+0.11}_{-0.14}$	$2.13^{+0.48}_{-0.34}$	$1.50^{+0.17}_{-0.17}$
56640	00037590003	963	82.2	$3.50^{+0.62}_{-0.44}$	$1.56^{+0.16}_{-0.15}$	$1.94^{+0.43}_{-0.37}$	$1.78^{+0.16}_{-0.16}$
56668	00037590004	2010	130.6	$3.02^{+0.35}_{-0.29}$	$1.03^{+0.10}_{-0.09}$	$1.99^{+0.31}_{-0.33}$	$1.53^{+0.12}_{-0.12}$

Note. — The full version of this table is available in Chapter 3.3 of this Thesis. All uncertainties represent 90% confidence intervals.

Columns: (1) Modified Julian Date (MJD), i.e., the number of days since November 17th, 1858.

(2) *Swift* Observation ID.

(3) XRT on-source exposure time.

(4) Background-subtracted XRT counts in the energy range 0.3-10 keV.

(5) Integrated 0.3-10 keV flux, in units of 10^{-12} erg cm^{-2} s^{-1}.

(6) Integrated 0.3-2 keV flux, in units of 10^{-12} erg cm^{-2} s^{-1}.

(7) Integrated 2-10 keV flux, in units of 10^{-12} erg cm^{-2} s^{-1}.

(8) Photon index for 0.3-10 keV model fit.

Table 2.   *NuSTAR* Observation Log

Date	*NuSTAR* Obs.ID	*NuSTAR* time [s]	*Swift* Obs.ID	*Swift* XRT time [s]
(1)	(2)	(3)	(4)	(5)
2016-02-05	60160095002	21206	00080903001, 00037590009, 00037590010	9922
2016-12-02	90201043002	51003	00088014001, 00037590015	10224
2018-10-27	80402610002	21069	00010949001, 00010949002, 00010949003, 00010949005, 00010949006, 00094095014, 00010949004	12978
2019-08-31	80502630002	68123	00011542001, 00011542002	9965
2020-01-21	80502630004	50168	00013172002, 00013172003	9333

Note. — Columns: (1) *NuSTAR* observation date. (2) *NuSTAR* observation ID. (3) *NuSTAR* on-source observation time, in seconds. (4) *Swift* observation IDs for the observations used in the joint analysis. For the 2019 and 2020 analyses, the *Swift* XRT data are contemporaneous with the *NuSTAR* observations. For our 2016 and 2018 analyses, we collect *Swift* observations spanning a few weeks around the *NuSTAR* observation date, in order to obtain stacked XRT exposure times of ~ 10 ks. (5) Total stacked *Swift* XRT on-source observation time.

Table 3.   Individual *Swift* UVOT observations and integrated luminosities

MJD (1)	F_V (2)	F_B (3)	F_U (4)	F_{UW1} (5)	F_{UM2} (6)	F_{UW2} (7)	L_{UV} (8)	L_{EUV} (9)	$L_{0.3-10}$ (10)	L_{10-79} (11)
54627	4.32±0.15	2.92±0.10	1.23±0.05	0.88±0.05	0.74±0.04	4.32±0.05	$0.57^{+0.49}_{-0.49}$	$3.78^{+0.60}_{-0.61}$	$9.43^{+0.67}_{-0.47}$	13.20
56636	4.16±0.19	2.96±0.13	1.21±0.07	0.60±0.05	0.57±0.05	4.16±0.05	—	—	$5.27^{+1.01}_{-0.78}$	8.84
56640	4.31±0.20	2.89±0.13	1.24±0.07	0.70±0.06	0.56±0.06	4.31±0.06	—	—	$5.81^{+0.77}_{-0.59}$	6.56
56668	4.38±0.17	2.87±0.11	1.21±0.06	0.69±0.05	0.60±0.04	4.38±0.05	—	—	$5.03^{+0.65}_{-0.65}$	7.99
56689	4.35±0.17	2.89±0.11	1.17±0.06	0.69±0.05	0.58±0.04	4.35±0.05	—	—	$4.45^{+0.46}_{-0.31}$	5.26
57219	4.37±0.19	2.94±0.12	1.56±0.08	1.16±0.08	1.12±0.08	4.37±0.08	$1.72^{+0.66}_{-0.66}$	$4.73^{+0.88}_{-0.89}$	$6.81^{+0.88}_{-0.54}$	9.80

Note. — The full version of this table is available in Chapter 3.3 of this Thesis. Observations for which we do not detect AGN UV–optical emission are marked with "—" in Columns (8) and (9).
Columns: (1) Modified Julian Date.
(2) to (7): *Swift* UVOT flux density in the filters V to $UW2$, assuming a power-law SED within the filter bandpass. Units of 10^{-15} erg cm-2 Å^{-1} s^{-1}. Integrated 2-10 keV flux, units of 10^{-12} erg cm^{-2} s^{-1}.
(8) Integrated UV–optical luminosity, as calculated using a piecewise linear interpolation over the host galaxy subtracted UVOT flux densities. Units of 10^{42} erg s^{-1}.
(9) Integrated extreme-UV luminosity, estimated using a power-law interpolation between the UVOT $UW2$ band luminosity and the 0.3 keV luminosity. Units of 10^{42} erg s^{-1}.
(10) Integrated 0.3-10 keV luminosity, derived from the Galactic absorption corrected XSPEC model fit to the XRT spectrum. Units of 10^{42} erg s^{-1}.
(11) Estimated 10-79 keV integrated luminosity, assuming $\Gamma = 1.72$ (i.e., the average photon index for our five *NuSTAR* observations), and scaled to the 10 keV luminosity density of the 0.3-10 keV power-law model. Units of 10^{42} erg s^{-1}.

Table 4.   Joint *NuSTAR*, stacked *Swift* XRT power-law spectral modeling

Date (1)	C_{FPMB} (2)	C_{XRT} (3)	$\Gamma_{0.3-79}$ (4)	$A_{0.3-79}$ (5)	$\chi^2_{0.3-79}$ (6)	Γ_{win} (7)	A_{win} (8)	χ^2_{win} (9)	$N_{H,int}$ (10)	χ^2_{int} (10)
2016-02-05	1.00 ± 0.05	0.94 ± 0.08	1.69 ± 0.05	$8.6^{+1.1}_{-1.0}$	0.98	1.82 ± 0.07	$9.43^{+1.60}_{-1.30}$	2.35	$2.40^{+2.10}_{-2.00}$	0.88
2016-12-02	0.99 ± 0.05	$0.74^{+0.11}_{-0.10}$	1.67 ± 0.03	$8.05^{+0.86}_{-0.78}$	1.69	1.77 ± 0.04	9.15 ± 0.70	2.42	$0.13^{+1.70}_{-0.13}$	1.21
2018-10-27	1.04 ± 0.04	$1.09^{+0.08}_{-0.07}$	1.67 ± 0.03	$23.7^{+1.9}_{-1.7}$	1.01	1.70 ± 0.06	$24.7^{+3.1}_{-2.7}$	1.19	$0.01^{+1.76}_{-0.01}$	1.00
2019-08-31	1.03 ± 0.01	0.73 ± 0.03	1.66 ± 0.02	32.1 ± 1.7	1.05	1.67 ± 0.03	$32.4^{+1.8}_{-1.7}$	1.27	$2.65^{+1.11}_{-1.10}$	1.00
2020-01-21	1.08 ± 0.02	0.81 ± 0.04	1.67 ± 0.02	$31.4^{+1.3}_{-1.4}$	1.06	1.69 ± 0.03	$31.2^{+2.0}_{-1.9}$	1.12	$1.83^{+1.06}_{-1.03}$	0.99

Note. — Parameter uncertainties correspond to 90% confidence intervals, and are determined using the XSPEC 'error' command. Columns: (1) *NuSTAR* observation date. (2) Flux scaling factor for the *NuSTAR* FPMB detector, relative to FPMA. (3) Flux scaling factor for the *Swift* XRT detector, relative to FPMA. (4) Photon index for the joint *NuSTAR* and *Swift* XRT modeling of the entire 0.3-79 keV spectrum. (5) Amplitude of power-law model at 1 keV, as fitted to the entire 0.3-79 keV spectrum, in units of 10^{-4} photons keV^{-1} cm^{-2} s^{-1}. (6) Reduced χ^2 for the power-law model to the entire 0.3-79 keV spectrum. (7) Photon index for the joint *NuSTAR* and *Swift* modeling, using the continuum window method. (8) Amplitude of the power-law continuum at 1 keV, using the continuum window method, in units of 10^{-4} photons keV^{-1} cm^{-2} s^{-1}. (9) Reduced χ^2 for the continuum window model, without intrinsic absorption. (10) Intrinsic absorber component column density, in units of 10^{20} cm^{-2}. (11) Reduced χ^2 for the model including an intrinsic absorber.

Table 5.   *NuSTAR pexmon* spectral modeling

Date (1)	C_{FPMB} (2)	Γ_{pex} (3)	A_{pex} (4)	R_{pex} (5)	Reduced χ^2 (6)	XSPEC 'goodness' (7)
2016-12-02	0.97 ± 0.05	$1.88^{+0.11}_{-0.07}$	$10.6^{+1.7}_{-1.6}$	$1.15^{+0.77}_{-0.58}$	0.97	0.31
2018-10-27	$1.04^{+0.05}_{-0.04}$	$1.77^{+0.09}_{-0.09}$	$26.5^{+3.7}_{-3.2}$	$0.38^{+0.41}_{-0.31}$	0.91	0.08
2019-08-31	1.03 ± 0.02	1.74 ± 0.04	$34.6^{+2.2}_{-2.1}$	$0.29^{+0.17}_{-0.15}$	0.97	0.18
2020-01-21	1.08 ± 0.03	1.78 ± 0.05	$35.4^{+2.5}_{-2.6}$	$0.42^{+0.22}_{-0.19}$	1.01	0.38
Stacked	1.04 ± 0.02	1.72 ± 0.03	$32.5^{+1.5}_{-1.4}$	$0.24^{+0.11}_{-0.10}$	1.00	0.34
Best-fit $i = 79°$ $^{+6}_{-23}$	$1.04^{+0.01}_{-0.02}$	$1.74^{+0.03}_{-0.04}$	$33.4^{+1.6}_{-1.7}$	$0.57^{+0.78}_{-0.34}$	0.97	0.27
$Z_{Fe} = 10$	1.04 ± 0.02	1.67 ± 0.01	30.4 ± 0.9	0.20 ± 0.05	0.97	0.20

Note. — Parameter uncertainties correspond to 90% confidence intervals, and are determined using the XSPEC *'error'* command. We tabulate them as $'\pm'$ if the positive and negative uncertainties are numerically equal to within the given precision. Columns: (1) *NuSTAR* observation date. The entries *'Stacked'*, *'Best-fit $i = 79°$ $^{+6}_{-23}$'*, and *'$Z_{Fe} = 10$'* denote our three models for the August 2019 + January 2020 stacked data. The *'Stacked'* model holds both the inclination angle $i = 60°$ and iron abundance $Z_{Fe} = 1$ constant. The *'Best-fit $i = 79°$ $^{+6}_{-23}$'* model allows the inclination to vary. The *'$Z_{Fe} = 10$'* model sets the iron abundance to ten times Solar. (2) Flux scaling factor for the *NuSTAR* FPMB detector, relative to FPMA. (3) Photon index for the power-law continuum of the *'pexmon'* model. (4) Amplitude of the power-law continuum at 1 keV, units of 10^{-4} photons keV^{-1} cm^{-2} s^{-1}. (5) Reflection scaling factor for the *'pexmon'* model. (6) Reduced χ^2 for the best-fit model, after rebinning the spectra to a minimum of 25 counts per bin. (7) The fraction of simulated model spectra that have a lower test statistic than the best-fit model, calculated using the XSPEC *'goodness'* command. An acceptable model has *'goodness'* $\leqslant 0.5$.

XRT exposure time (1)	Soft excess level (2)	Detection rate (3)	False positives (4)
2 ks	100%	84%	46%
2 ks	50%	70%	
2 ks	25%	62%	
4 ks	100%	92%	40%
4 ks	50%	70%	
4 ks	25%	52%	
6 ks	100%	96%	10%
6 ks	50%	86%	
6 ks	25%	60%	
8 ks	100%	96%	14%
8 ks	50%	86%	
8 ks	25%	70%	
10 ks	100%	> 99%	< 1%
10 ks	50%	96%	
10 ks	25%	65%	

Table A1. Results for simulated *Swift* XRT and *NuSTAR* spectra, modeled using the continuum window method (§4.2). For each combination of XRT exposure time and soft excess strength, we simulate 50 spectra. We also simulate 100 spectra without a soft excess component for each exposure time, in order to determine the false positive rate. Columns: (1) the XRT exposure time for the simulated spectra; all *NuSTAR* simulations have a 20 ks exposure time. (2) The scaling of the soft excess component, listed as a percentage of the relative soft excess strength above the 1 keV continuum emission detected by Mathur et al. (2018). (3) The percentage of simulated spectra for which we detect the soft excess component using the continuum window method. (4) The false positive rate, i.e., the percentage of simulated spectra with no soft excess component for which we detect soft excess using the continuum window method.

APPENDIX A: SIMULATIONS TO DETERMINE X-RAY ANALYSIS SENSITIVITY

Here, we describe the simulations performed in order to determine the sensitivity of our continuum window method (4.2) to soft X-ray excess in our joint *Swift* XRT and *NuSTAR* analyses.

Simulation procedure: We use the XSPEC tool *'fakeit'* to generate simulated XRT spectra composed of a power-law continuum with $\Gamma = 1.71$, Fe K emission lines (represented by Gaussian features), and a black-body soft excess component with $kT = 0.11$ keV. We adjust the normalizations of these components to match the emission strengths observed by Mathur et al. (2018), relative to the 1 keV normalization of the power-law continuum component in their 2013 observation. We scale the absolute flux levels of these components to match our Swift XRT observations of Mrk 590 in March 2019. We also generate spectra with soft excess normalizations corresponding to 50% and 25% of the relative normalizations presented by Mathur et al. For each soft excess scaling, we generate 50 XRT spectra and 50 *NuSTAR* spectra, including appropriate photon counting noise for a 10 ks XRT observation and a 20 ks *NuSTAR* observation. We repeat this process for XRT observation times of 2 ks, 4 ks, 6 ks and 8 ks, not varying the *NuSTAR* observation time.

Detection of soft excess: In order to test the continuum window method described in §4.2, we first model the NuSTAR spectrum with a power-law component, using fitting windows at energies of $3.0 - 5.5$ keV, $8.5 - 15$ keV, and $40 - 79$ keV. For the model fit, the start values of Γ and normalization A are drawn from a uniform distribution; the *NuSTAR* modeling reliably converges on the correct input values. We use the best-fit power law index from the NuSTAR spectrum to determine the power-law index for the Swift XRT spectrum. To determine the overall scaling of the Swift XRT continuum model, we fit a power-law continuum to the simulated Swift XRT data the 2.0-5.5 keV and 8.5-10.0 keV fitting windows, so as to avoid the soft X-ray excess and Fe K lines. Finally, we inspect the data/model ratio at energies below 2 keV, and claim a detection of soft excess if the observed data exceed the power-law continuum model at the $> 2\sigma$ level in this region, binning the XRT spectra to 25 counts per bin.

We present the detection and false-positive rates in Table A1. For simulated observations with XRT exposure times of 10 ks, we always detect the soft excess component, for the relative soft excess level observed in 2014. We find no false-positive soft excess detections for the 10 ks exposures. For 10 ks exposures, our detection rate falls to 70% for a soft excess scaling of 25%. For shorter XRT exposure times, our detection rate falls, and we find some false-positive detections. For this reason, we require 10 ks of *Swift* XRT exposure time in order to securely detect soft excess emission at the 2014 level. Based thereon, we requested (and were granted) 10 ks of contemporaneous XRT observations for our 2019 and 2020 *NuSTAR* ToO triggers. For our earlier *NuSTAR* observations, we instead prepare stacked XRT spectra with exposure times exceeding 10 ks, as described in §3.2, in order to avoid false-positive detections. In general, we cannot securely detect soft excess emission at the 25% level relative to the Mathur et al. (2018) detection, even for 10 ks XRT observations.

Soft excess parameter retrieval: Given 6 ks *Swift* XRT observations, we are able to retrieve the blackbody component flux with an average error of 7% relative to the input value, and a maximum error of 28%, using a soft excess component at the same relative flux level as in 2014. At 50% of the 2014 soft excess level, we retrieve the flux with an average error of 12% and a maximum error of 29%. At 25% of the relative soft excess level observed in 2014, we have an average error of 22% and a maximum error of 62%. The measured blackbody temperature is within the range 0.02 keV$< kT < 0.13$ keV, and often very close to the input value, $kT = 0.11$ keV. If the XRT exposure time is instead 2 ks, we find errors in excess of 100% relative to the input flux scaling, and in many cases the fit does not converge on a reasonable blackbody temperature. Thus, we require at least 6 ks XRT exposure time in order to reliably measure the emission strength and temperature for a blackbody-like soft X-ray excess.

3.3 Full *Swift* UVOT and XRT monitoring data for Mrk 590

Here, I present full versions of Tables 2 and 3 from our draft paper *X-ray and UV Flares in the Changing Look AGN Mrk 590. I: X-ray and UV–optical Observations Since 2014* (Section §3.2 of this Thesis). These long Tables are not included in full in the paper itself.

Table 3.1 presents our *Swift* XRT monitoring data. The fluxes and the photon index $\Gamma_{0.3-10}$ are measured using a power-law model including Galactic absorption, as described in the paper. Table 3.2 presents our *Swift* UVOT flux measurements, along with the integrated luminosities, estimated as described in §6.4 of the paper.

Table 3.1 Individual *Swift* XRT observations. All uncertainties represent 90% confidence intervals. Columns: (1) Modified Julian Date. (2) *Swift* Observation ID. (3) XRT on-source exposure time. (4) Background-subtracted XRT counts in the energy range 0.3-10 keV. (5) Integrated 0.3-10 keV flux, units of 10^{-12} erg cm^{-2} s^{-1}. (6) Integrated 0.3-2 keV flux, units of 10^{-12} erg cm^{-2} s^{-1}. (7) Integrated 2-10 keV flux, units of 10^{-12} erg cm^{-2} s^{-1}. (8) Photon index for 0.3-10 keV model fit.

MJD	Observation ID	Exposure time [s]	0.3-10 keV counts	$F_{0.3-10}$	$F_{0.3-2}$	F_{2-10}	$\Gamma_{0.3-10}$
(1)	(2)	(3)	(4)	(5)	(6)	(7)	(8)
54627.6	00037590001	4465	514.4	$5.75^{+0.3}_{-0.39}$	$2.21^{+0.12}_{-0.09}$	$3.53^{+0.3}_{-0.3}$	$1.64^{+0.06}_{-0.06}$
56636.9	00037590002	1068	70.3	$3.18^{+0.7}_{-0.42}$	$1.05^{+0.11}_{-0.14}$	$2.13^{+0.48}_{-0.34}$	$1.5^{+0.17}_{-0.17}$
56640.9	00037590003	963	82.2	$3.5^{+0.62}_{-0.44}$	$1.56^{+0.16}_{-0.15}$	$1.94^{+0.43}_{-0.37}$	$1.78^{+0.16}_{-0.16}$
56668.5	00037590004	2010	130.6	$3.02^{+0.35}_{-0.29}$	$1.03^{+0.1}_{-0.09}$	$1.99^{+0.31}_{-0.33}$	$1.53^{+0.12}_{-0.12}$
56689.4	00037590005	1997	123.3	$2.7^{+0.38}_{-0.23}$	$1.17^{+0.11}_{-0.1}$	$1.53^{+0.27}_{-0.29}$	$1.75^{+0.13}_{-0.13}$
57219.4	00037590007	1388	129.0	$4.15^{+0.63}_{-0.35}$	$1.56^{+0.19}_{-0.12}$	$2.58^{+0.51}_{-0.41}$	$1.62^{+0.12}_{-0.12}$
57423.8	00080903001	6815	701.0	$4.89^{+0.25}_{-0.27}$	$1.92^{+0.07}_{-0.08}$	$2.97^{+0.22}_{-0.2}$	$1.65^{+0.05}_{-0.05}$
57442.3	00037590009	933	126.2	$5.73^{+0.64}_{-0.43}$	$2.48^{+0.22}_{-0.18}$	$3.25^{+0.39}_{-0.49}$	$1.75^{+0.13}_{-0.13}$
57444.3	00037590010	2172	206.5	$6.95^{+0.58}_{-0.45}$	$2.44^{+0.15}_{-0.15}$	$4.51^{+0.67}_{-0.55}$	$1.55^{+0.1}_{-0.1}$
57451.2	00037590011	1972	223.9	$5.53^{+0.46}_{-0.49}$	$1.85^{+0.11}_{-0.13}$	$3.67^{+0.45}_{-0.36}$	$1.51^{+0.09}_{-0.09}$
57570.3	00080903002	6270	584.2	$4.54^{+0.32}_{-0.19}$	$1.65^{+0.07}_{-0.08}$	$2.89^{+0.27}_{-0.17}$	$1.58^{+0.06}_{-0.06}$
57707.1	00037590012	3376	364.4	$4.84^{+0.22}_{-0.32}$	$1.91^{+0.09}_{-0.08}$	$2.93^{+0.35}_{-0.23}$	$1.66^{+0.07}_{-0.07}$
57708.0	00037590013	2292	270.6	$5.08^{+0.43}_{-0.34}$	$2.12^{+0.1}_{-0.13}$	$2.96^{+0.49}_{-0.31}$	$1.71^{+0.09}_{-0.09}$
57709.6	00037590014	1410	161.0	$4.72^{+0.59}_{-0.4}$	$2.08^{+0.15}_{-0.1}$	$2.64^{+0.49}_{-0.4}$	$1.77^{+0.11}_{-0.11}$
57724.5	00088014001	1972	174.2	$4.1^{+0.48}_{-0.32}$	$1.59^{+0.1}_{-0.12}$	$2.5^{+0.48}_{-0.29}$	$1.65^{+0.11}_{-0.11}$
57735.2	00037590015	8251	767.8	$4.14^{+0.2}_{-0.16}$	$1.61^{+0.04}_{-0.06}$	$2.52^{+0.2}_{-0.16}$	$1.65^{+0.05}_{-0.05}$
57763.0	00037590016	7804	953.8	$7.23^{+0.4}_{-0.27}$	$2.56^{+0.07}_{-0.1}$	$4.68^{+0.28}_{-0.24}$	$1.56^{+0.04}_{-0.04}$
57791.6	00037590017	7282	490.0	$3.11^{+0.26}_{-0.18}$	$1.18^{+0.05}_{-0.04}$	$1.93^{+0.18}_{-0.16}$	$1.62^{+0.06}_{-0.06}$
57817.4	00037590018	3004	205.1	$3.1^{+0.28}_{-0.2}$	$1.21^{+0.08}_{-0.09}$	$1.88^{+0.33}_{-0.24}$	$1.65^{+0.1}_{-0.1}$
57911.6	00037590019	6393	740.3	$5.66^{+0.33}_{-0.17}$	$2.3^{+0.07}_{-0.1}$	$3.36^{+0.23}_{-0.24}$	$1.69^{+0.05}_{-0.05}$
57939.1	00037590020	7596	1400.8	$9.34^{+0.38}_{-0.25}$	$3.44^{+0.09}_{-0.06}$	$5.9^{+0.19}_{-0.3}$	$1.59^{+0.04}_{-0.04}$
57967.1	00037590021	6570	1125.5	$7.75^{+0.31}_{-0.28}$	$3.02^{+0.08}_{-0.08}$	$4.73^{+0.31}_{-0.28}$	$1.65^{+0.04}_{-0.04}$
57996.8	00037590022	6932	2956.7	$21.31^{+0.57}_{-0.39}$	$7.99^{+0.15}_{-0.16}$	$13.32^{+0.55}_{-0.46}$	$1.61^{+0.03}_{-0.03}$
58009.9	00037590023	861	146.4	$18.45^{+2.19}_{-1.82}$	$6.57^{+0.63}_{-0.49}$	$11.88^{+1.65}_{-1.63}$	$1.56^{+0.11}_{-0.11}$
58011.3	00037590024	2097	496.7	$12.08^{+0.7}_{-0.72}$	$4.15^{+0.16}_{-0.24}$	$7.93^{+0.81}_{-0.69}$	$1.53^{+0.06}_{-0.06}$
58012.6	00037590025	1865	422.5	$10.54^{+0.5}_{-0.76}$	$3.91^{+0.24}_{-0.13}$	$6.63^{+0.73}_{-0.75}$	$1.6^{+0.07}_{-0.07}$

Table 3.1 Continued.

MJD	Observation ID	Exposure time [s]	0.3-10 keV counts	$F_{0.3-10}$	$F_{0.3-2}$	F_{2-10}	$\Gamma_{0.3-10}$
(1)	(2)	(3)	(4)	(5)	(6)	(7)	(8)
58013.8	00037590026	1910	362.4	$12.44^{+0.68}_{-0.73}$	$3.93^{+0.2}_{-0.24}$	$8.5^{+1.08}_{-0.84}$	$1.46^{+0.07}_{-0.07}$
58014.6	00037590027	1193	299.1	$12.26^{+1.09}_{-0.94}$	$4.12^{+0.26}_{-0.16}$	$8.14^{+1.08}_{-0.77}$	$1.51^{+0.08}_{-0.08}$
58015.0	00037590028	1698	330.7	$13.09^{+0.88}_{-0.93}$	$4.44^{+0.24}_{-0.27}$	$8.65^{+0.63}_{-0.88}$	$1.52^{+0.08}_{-0.08}$
58016.5	00037590029	2045	512.3	$15.1^{+0.96}_{-0.7}$	$5.19^{+0.24}_{-0.26}$	$9.91^{+0.58}_{-0.74}$	$1.53^{+0.06}_{-0.06}$
58023.4	00037590032	3960	1944.5	$23.91^{+0.58}_{-0.77}$	$8.54^{+0.19}_{-0.17}$	$15.37^{+0.73}_{-0.68}$	$1.57^{+0.03}_{-0.03}$
58027.4	00037590033	2682	753.0	$14.78^{+0.75}_{-0.61}$	$5.48^{+0.21}_{-0.16}$	$9.3^{+0.69}_{-0.6}$	$1.6^{+0.05}_{-0.05}$
58029.9	00037590034	986	308.1	$14.98^{+0.93}_{-1.06}$	$5.58^{+0.31}_{-0.29}$	$9.4^{+1.04}_{-1.01}$	$1.6^{+0.08}_{-0.08}$
58031.0	00037590035	1086	267.4	$11.53^{+1.14}_{-1.15}$	$4.18^{+0.23}_{-0.24}$	$7.35^{+1.34}_{-0.76}$	$1.58^{+0.09}_{-0.08}$
58035.5	00037590036	2057	566.8	$13.23^{+0.84}_{-0.57}$	$5.07^{+0.21}_{-0.26}$	$8.16^{+0.77}_{-0.53}$	$1.63^{+0.06}_{-0.06}$
58037.3	00037590037	1947	669.7	$14.94^{+0.7}_{-0.91}$	$5.92^{+0.25}_{-0.25}$	$9.02^{+0.78}_{-0.69}$	$1.66^{+0.05}_{-0.05}$
58041.4	00037590038	973	383.0	$18.91^{+1.53}_{-1.45}$	$6.8^{+0.34}_{-0.33}$	$12.1^{+1.36}_{-1.18}$	$1.57^{+0.07}_{-0.07}$
58051.2	00037590040	1508	346.9	$11.0^{+0.78}_{-0.63}$	$3.68^{+0.16}_{-0.18}$	$7.32^{+0.74}_{-0.68}$	$1.51^{+0.07}_{-0.07}$
58051.2	00037590040	1508	346.9	$11.0^{+0.81}_{-0.62}$	$3.68^{+0.21}_{-0.17}$	$7.32^{+0.66}_{-0.65}$	$1.51^{+0.07}_{-0.07}$
58053.9	00037590041	1920	455.5	$12.05^{+0.66}_{-0.48}$	$3.98^{+0.19}_{-0.2}$	$8.07^{+0.71}_{-0.66}$	$1.5^{+0.06}_{-0.06}$
58055.6	00037590042	601	109.6	$10.23^{+1.62}_{-0.85}$	$3.45^{+0.35}_{-0.33}$	$6.78^{+1.99}_{-0.89}$	$1.52^{+0.13}_{-0.13}$
58057.2	00037590043	1830	345.9	$7.92^{+0.41}_{-0.68}$	$3.35^{+0.15}_{-0.2}$	$4.57^{+0.45}_{-0.45}$	$1.73^{+0.08}_{-0.08}$
58058.0	00037590044	1605	408.7	$11.67^{+0.75}_{-0.6}$	$4.59^{+0.22}_{-0.24}$	$7.08^{+0.8}_{-0.5}$	$1.66^{+0.07}_{-0.07}$
58062.3	00037590045	2125	513.8	$11.56^{+0.57}_{-0.64}$	$4.1^{+0.19}_{-0.19}$	$7.46^{+0.77}_{-0.67}$	$1.56^{+0.06}_{-0.06}$
58066.0	00037590047	709	257.2	$18.7^{+1.46}_{-1.27}$	$5.78^{+0.31}_{-0.38}$	$12.92^{+1.61}_{-1.3}$	$1.44^{+0.09}_{-0.09}$
58068.6	00037590048	1805	798.8	$21.36^{+1.05}_{-0.92}$	$7.9^{+0.27}_{-0.24}$	$13.46^{+0.83}_{-0.76}$	$1.6^{+0.05}_{-0.05}$
58070.1	00037590049	1900	803.4	$22.45^{+0.68}_{-0.9}$	$8.84^{+0.22}_{-0.35}$	$13.61^{+0.89}_{-0.84}$	$1.66^{+0.05}_{-0.05}$
58073.5	00037590050	1615	561.8	$16.25^{+0.92}_{-0.83}$	$6.09^{+0.19}_{-0.29}$	$10.15^{+0.89}_{-0.79}$	$1.61^{+0.06}_{-0.06}$
58075.4	00037590051	814	283.5	$16.57^{+1.41}_{-1.09}$	$5.65^{+0.29}_{-0.42}$	$10.92^{+1.48}_{-1.29}$	$1.53^{+0.08}_{-0.08}$
58077.6	00037590052	809	331.2	$19.92^{+1.78}_{-1.77}$	$6.31^{+0.45}_{-0.32}$	$13.61^{+1.62}_{-1.15}$	$1.46^{+0.08}_{-0.08}$
58080.1	00037590053	1141	415.2	$18.3^{+1.21}_{-1.2}$	$6.73^{+0.32}_{-0.38}$	$11.57^{+1.12}_{-1.12}$	$1.59^{+0.07}_{-0.07}$
58081.9	00037590054	1885	684.1	$17.08^{+0.82}_{-1.13}$	$5.82^{+0.24}_{-0.21}$	$11.26^{+1.02}_{-0.74}$	$1.52^{+0.05}_{-0.05}$
58083.4	00037590055	1937	696.3	$19.62^{+1.09}_{-0.89}$	$6.87^{+0.27}_{-0.3}$	$12.74^{+0.85}_{-0.86}$	$1.55^{+0.05}_{-0.05}$
58085.8	00037590056	1955	730.2	$16.39^{+0.85}_{-0.65}$	$6.4^{+0.25}_{-0.2}$	$9.99^{+0.92}_{-0.52}$	$1.65^{+0.05}_{-0.05}$
58089.6	00037590057	1950	501.7	$12.11^{+0.6}_{-0.65}$	$4.16^{+0.19}_{-0.17}$	$7.96^{+0.58}_{-0.72}$	$1.53^{+0.06}_{-0.06}$
58091.7	00037590058	2000	462.8	$11.46^{+0.82}_{-0.57}$	$4.37^{+0.23}_{-0.16}$	$7.09^{+0.57}_{-0.43}$	$1.63^{+0.07}_{-0.07}$
58093.5	00037590059	1595	472.7	$13.9^{+0.9}_{-0.76}$	$4.9^{+0.29}_{-0.21}$	$9.0^{+0.84}_{-0.78}$	$1.55^{+0.06}_{-0.06}$
58094.5	00037590060	2017	619.3	$14.14^{+0.84}_{-0.49}$	$5.86^{+0.32}_{-0.23}$	$8.29^{+0.63}_{-0.73}$	$1.71^{+0.06}_{-0.06}$
58095.1	00037590061	1505	421.7	$12.3^{+0.81}_{-0.55}$	$4.84^{+0.2}_{-0.25}$	$7.46^{+0.68}_{-0.57}$	$1.66^{+0.07}_{-0.07}$
58096.4	00037590062	1967	555.1	$13.28^{+0.73}_{-0.68}$	$4.64^{+0.18}_{-0.24}$	$8.65^{+0.64}_{-0.59}$	$1.55^{+0.06}_{-0.06}$
58097.4	00037590063	1286	478.0	$16.93^{+0.93}_{-0.96}$	$6.4^{+0.32}_{-0.25}$	$10.54^{+0.92}_{-0.87}$	$1.62^{+0.06}_{-0.06}$
58098.3	00037590064	1660	488.0	$14.7^{+0.8}_{-0.85}$	$4.84^{+0.17}_{-0.23}$	$9.86^{+0.82}_{-0.74}$	$1.49^{+0.06}_{-0.06}$
58099.5	00037590065	1768	517.3	$13.74^{+0.9}_{-0.89}$	$4.9^{+0.21}_{-0.19}$	$8.84^{+0.82}_{-0.84}$	$1.56^{+0.06}_{-0.06}$
58100.0	00037590066	1263	347.3	$13.0^{+0.78}_{-0.82}$	$4.61^{+0.24}_{-0.23}$	$8.39^{+1.07}_{-0.64}$	$1.56^{+0.07}_{-0.07}$
58101.9	00037590067	2067	527.3	$11.94^{+0.72}_{-0.58}$	$4.19^{+0.2}_{-0.17}$	$7.75^{+0.59}_{-0.59}$	$1.55^{+0.06}_{-0.06}$

Table 3.1 Continued.

MJD	Observation ID	Exposure time [s]	0.3-10 keV counts	$F_{0.3-10}$	$F_{0.3-2}$	F_{2-10}	$\Gamma_{0.3-10}$
(1)	(2)	(3)	(4)	(5)	(6)	(7)	(8)
58102.8	00037590068	1940	470.3	$12.0^{+0.78}_{-0.68}$	$4.19^{+0.25}_{-0.24}$	$7.81^{+0.74}_{-0.62}$	$1.55^{+0.06}_{-0.06}$
58107.1	00037590069	2147	667.0	$15.06^{+0.73}_{-0.72}$	$5.53^{+0.15}_{-0.2}$	$9.53^{+0.83}_{-0.83}$	$1.59^{+0.05}_{-0.05}$
58108.0	00037590070	2022	573.0	$14.51^{+0.85}_{-0.69}$	$5.19^{+0.23}_{-0.25}$	$9.32^{+0.7}_{-0.62}$	$1.57^{+0.06}_{-0.06}$
58109.7	00037590071	1743	533.2	$13.87^{+0.58}_{-0.57}$	$5.05^{+0.23}_{-0.25}$	$8.82^{+0.75}_{-0.62}$	$1.58^{+0.06}_{-0.06}$
58110.1	00037590072	1937	572.8	$14.26^{+0.8}_{-0.71}$	$4.59^{+0.22}_{-0.19}$	$9.67^{+0.6}_{-0.73}$	$1.47^{+0.06}_{-0.06}$
58111.1	00037590073	2007	588.0	$13.02^{+0.8}_{-0.66}$	$5.02^{+0.25}_{-0.21}$	$8.0^{+0.53}_{-0.61}$	$1.64^{+0.06}_{-0.06}$
58112.4	00037590074	2122	825.2	$17.36^{+0.71}_{-0.71}$	$6.47^{+0.28}_{-0.19}$	$10.89^{+0.58}_{-0.9}$	$1.61^{+0.05}_{-0.05}$
58113.2	00037590075	1648	581.0	$16.55^{+0.94}_{-0.85}$	$5.87^{+0.28}_{-0.21}$	$10.68^{+0.84}_{-0.85}$	$1.56^{+0.06}_{-0.06}$
58117.6	00037590076	1638	430.0	$11.08^{+0.56}_{-0.53}$	$4.59^{+0.12}_{-0.28}$	$6.49^{+0.59}_{-0.68}$	$1.71^{+0.07}_{-0.07}$
58118.8	00037590077	1570	358.7	$10.83^{+0.61}_{-0.57}$	$4.23^{+0.28}_{-0.19}$	$6.6^{+0.77}_{-0.53}$	$1.65^{+0.07}_{-0.07}$
58118.8	00037590077	1570	358.7	$10.83^{+0.54}_{-0.75}$	$4.23^{+0.19}_{-0.26}$	$6.6^{+0.63}_{-0.58}$	$1.65^{+0.07}_{-0.07}$
58119.2	00037590078	1688	325.1	$9.72^{+0.51}_{-0.71}$	$3.51^{+0.19}_{-0.19}$	$6.22^{+0.83}_{-0.77}$	$1.58^{+0.08}_{-0.08}$
58120.2	00037590079	1643	351.0	$9.77^{+0.64}_{-0.53}$	$3.56^{+0.24}_{-0.19}$	$6.21^{+0.76}_{-0.54}$	$1.59^{+0.07}_{-0.07}$
58121.2	00037590080	3238	786.6	$10.78^{+0.41}_{-0.42}$	$4.36^{+0.11}_{-0.17}$	$6.42^{+0.49}_{-0.38}$	$1.68^{+0.05}_{-0.05}$
58122.4	00037590081	1975	472.8	$11.09^{+0.7}_{-0.54}$	$4.08^{+0.18}_{-0.17}$	$7.01^{+0.77}_{-0.6}$	$1.59^{+0.06}_{-0.06}$
58123.4	00037590082	2142	512.8	$11.76^{+0.72}_{-0.82}$	$3.92^{+0.16}_{-0.15}$	$7.84^{+0.65}_{-0.62}$	$1.51^{+0.06}_{-0.06}$
58124.5	00037590083	1640	370.8	$11.47^{+0.74}_{-0.9}$	$3.56^{+0.18}_{-0.19}$	$7.91^{+0.51}_{-0.93}$	$1.44^{+0.07}_{-0.07}$
58125.5	00037590084	1520	351.7	$10.36^{+0.9}_{-0.65}$	$3.96^{+0.16}_{-0.24}$	$6.4^{+0.65}_{-0.55}$	$1.63^{+0.07}_{-0.07}$
58127.5	00037590085	1700	412.4	$10.52^{+0.69}_{-0.68}$	$4.4^{+0.22}_{-0.2}$	$6.12^{+0.65}_{-0.49}$	$1.72^{+0.07}_{-0.07}$
58129.5	00037590086	1870	392.8	$10.11^{+0.68}_{-0.6}$	$3.59^{+0.15}_{-0.19}$	$6.52^{+0.62}_{-0.66}$	$1.56^{+0.07}_{-0.07}$
58131.2	00037590087	1992	367.4	$8.3^{+0.59}_{-0.53}$	$3.17^{+0.22}_{-0.13}$	$5.13^{+0.46}_{-0.45}$	$1.63^{+0.07}_{-0.07}$
58135.3	00037590089	1967	277.5	$6.77^{+0.56}_{-0.46}$	$2.3^{+0.14}_{-0.11}$	$4.47^{+0.52}_{-0.45}$	$1.52^{+0.08}_{-0.08}$
58137.4	00037590090	2025	270.0	$7.02^{+0.56}_{-0.49}$	$2.53^{+0.15}_{-0.13}$	$4.49^{+0.31}_{-0.52}$	$1.57^{+0.08}_{-0.08}$
58139.0	00037590091	1243	202.3	$8.58^{+0.54}_{-0.79}$	$2.91^{+0.19}_{-0.25}$	$5.67^{+0.83}_{-0.51}$	$1.52^{+0.1}_{-0.1}$
58145.5	00037590092	2130	390.5	$9.71^{+0.54}_{-0.75}$	$2.92^{+0.18}_{-0.16}$	$6.79^{+0.6}_{-0.53}$	$1.42^{+0.07}_{-0.07}$
58148.7	00037590093	1970	385.6	$8.51^{+0.57}_{-0.52}$	$3.43^{+0.14}_{-0.15}$	$5.08^{+0.62}_{-0.42}$	$1.68^{+0.07}_{-0.07}$
58150.8	00037590094	1768	286.3	$7.71^{+0.55}_{-0.54}$	$2.86^{+0.18}_{-0.14}$	$4.85^{+0.8}_{-0.55}$	$1.6^{+0.08}_{-0.08}$
58152.8	00037590095	1718	277.2	$7.51^{+0.73}_{-0.57}$	$2.88^{+0.18}_{-0.13}$	$4.63^{+0.65}_{-0.39}$	$1.63^{+0.08}_{-0.08}$
58154.7	00037590096	2082	246.6	$6.6^{+0.58}_{-0.53}$	$2.65^{+0.16}_{-0.13}$	$3.96^{+0.54}_{-0.41}$	$1.67^{+0.09}_{-0.09}$
58156.0	00037590097	1972	311.4	$7.02^{+0.62}_{-0.3}$	$2.96^{+0.16}_{-0.17}$	$4.06^{+0.52}_{-0.43}$	$1.72^{+0.08}_{-0.08}$
58158.3	00037590098	2007	301.7	$6.88^{+0.45}_{-0.53}$	$2.66^{+0.17}_{-0.15}$	$4.22^{+0.55}_{-0.51}$	$1.64^{+0.08}_{-0.08}$
58160.6	00037590099	1992	202.4	$7.96^{+0.88}_{-0.64}$	$2.63^{+0.19}_{-0.17}$	$5.33^{+0.82}_{-0.62}$	$1.5^{+0.1}_{-0.1}$
58162.5	00037590100	1877	224.9	$7.05^{+0.64}_{-0.51}$	$2.57^{+0.12}_{-0.21}$	$4.48^{+0.48}_{-0.52}$	$1.59^{+0.09}_{-0.09}$
58164.3	00037590101	2082	272.6	$6.32^{+0.54}_{-0.47}$	$2.51^{+0.14}_{-0.11}$	$3.81^{+0.39}_{-0.52}$	$1.67^{+0.08}_{-0.08}$
58166.7	00037590102	2117	299.2	$7.94^{+0.62}_{-0.59}$	$2.46^{+0.12}_{-0.19}$	$5.48^{+0.62}_{-0.77}$	$1.44^{+0.08}_{-0.08}$
58289.7	00094095002	1106	194.0	$8.09^{+0.82}_{-0.75}$	$3.13^{+0.13}_{-0.2}$	$4.96^{+0.55}_{-0.72}$	$1.64^{+0.1}_{-0.1}$
58300.5	00094095003	2195	521.5	$10.9^{+0.81}_{-0.55}$	$4.03^{+0.15}_{-0.16}$	$6.88^{+0.61}_{-0.62}$	$1.6^{+0.06}_{-0.06}$
58313.4	00094095004	1605	473.8	$13.77^{+0.89}_{-0.91}$	$4.79^{+0.28}_{-0.17}$	$8.98^{+1.06}_{-0.82}$	$1.54^{+0.06}_{-0.06}$
58325.1	00094095005	1982	484.0	$11.1^{+0.67}_{-0.63}$	$4.13^{+0.17}_{-0.17}$	$6.97^{+0.66}_{-0.52}$	$1.6^{+0.06}_{-0.06}$

Table 3.1 Continued.

MJD	Observation ID	Exposure time [s]	0.3-10 keV counts	$F_{0.3-10}$	$F_{0.3-2}$	F_{2-10}	$\Gamma_{0.3-10}$
(1)	(2)	(3)	(4)	(5)	(6)	(7)	(8)
58337.0	00094095006	1800	354.6	$9.96^{+0.77}_{-0.5}$	$3.76^{+0.2}_{-0.16}$	$6.2^{+0.59}_{-0.54}$	$1.62^{+0.07}_{-0.07}$
58349.6	00094095007	1808	334.8	$8.55^{+0.73}_{-0.53}$	$3.04^{+0.19}_{-0.17}$	$5.51^{+0.49}_{-0.66}$	$1.56^{+0.08}_{-0.08}$
58363.4	00094095008	1635	265.5	$10.47^{+0.74}_{-0.85}$	$3.53^{+0.21}_{-0.23}$	$6.94^{+0.74}_{-0.61}$	$1.52^{+0.08}_{-0.08}$
58366.4	00094095009	1413	293.9	$10.31^{+0.79}_{-0.7}$	$3.72^{+0.17}_{-0.2}$	$6.59^{+0.74}_{-0.69}$	$1.58^{+0.08}_{-0.08}$
58373.1	00094095010	971	281.3	$13.36^{+1.14}_{-1.12}$	$5.07^{+0.28}_{-0.28}$	$8.3^{+0.88}_{-1.12}$	$1.62^{+0.08}_{-0.08}$
58385.6	00094095011	1985	767.5	$18.05^{+0.88}_{-0.6}$	$6.85^{+0.25}_{-0.37}$	$11.21^{+0.78}_{-0.84}$	$1.62^{+0.05}_{-0.05}$
58397.4	00094095012	1695	687.7	$19.51^{+0.91}_{-1.36}$	$6.94^{+0.24}_{-0.27}$	$12.57^{+1.08}_{-0.99}$	$1.56^{+0.05}_{-0.05}$
58409.7	00094095013	1588	745.6	$24.6^{+1.16}_{-0.96}$	$8.67^{+0.27}_{-0.37}$	$15.93^{+1.03}_{-0.78}$	$1.55^{+0.05}_{-0.05}$
58419.0	00010949001	1987	605.2	$14.34^{+0.63}_{-0.95}$	$5.31^{+0.28}_{-0.2}$	$9.03^{+0.79}_{-0.75}$	$1.6^{+0.06}_{-0.06}$
58420.0	00010949002	1987	677.8	$15.65^{+0.61}_{-0.8}$	$5.7^{+0.24}_{-0.19}$	$9.95^{+0.87}_{-0.81}$	$1.58^{+0.05}_{-0.05}$
58421.8	00094095014	2067	642.2	$14.64^{+0.64}_{-0.81}$	$6.02^{+0.3}_{-0.22}$	$8.62^{+0.83}_{-0.61}$	$1.7^{+0.06}_{-0.06}$
58422.5	00010949003	2015	613.5	$14.68^{+0.84}_{-0.66}$	$5.68^{+0.24}_{-0.24}$	$9.01^{+0.73}_{-0.8}$	$1.64^{+0.06}_{-0.06}$
58422.5	00010949003	2015	613.5	$14.68^{+0.84}_{-0.51}$	$5.68^{+0.18}_{-0.29}$	$9.01^{+0.62}_{-0.69}$	$1.64^{+0.06}_{-0.06}$
58423.3	00010949004	1987	1024.6	$22.47^{+0.65}_{-0.9}$	$8.93^{+0.24}_{-0.28}$	$13.53^{+1.09}_{-0.63}$	$1.67^{+0.04}_{-0.04}$
58424.7	00010949005	1316	494.6	$16.74^{+0.73}_{-0.96}$	$6.49^{+0.21}_{-0.35}$	$10.24^{+0.78}_{-0.65}$	$1.64^{+0.06}_{-0.06}$
58425.5	00010949006	1615	751.8	$20.17^{+0.75}_{-0.97}$	$8.18^{+0.26}_{-0.32}$	$11.99^{+0.78}_{-0.86}$	$1.69^{+0.05}_{-0.05}$
58433.5	00094095015	1840	523.6	$15.79^{+0.79}_{-0.86}$	$5.72^{+0.36}_{-0.23}$	$10.07^{+0.77}_{-0.84}$	$1.58^{+0.06}_{-0.06}$
58445.2	00094095016	1800	436.8	$12.31^{+0.8}_{-0.77}$	$4.77^{+0.29}_{-0.23}$	$7.54^{+0.69}_{-0.66}$	$1.64^{+0.07}_{-0.07}$
58457.7	00094095017	1098	944.8	$36.74^{+1.36}_{-1.22}$	$15.36^{+0.52}_{-0.54}$	$21.38^{+1.3}_{-1.01}$	$1.72^{+0.05}_{-0.05}$
58464.0	00010949008	1720	1203.5	$32.81^{+1.34}_{-1.12}$	$13.0^{+0.41}_{-0.47}$	$19.82^{+1.31}_{-0.81}$	$1.66^{+0.04}_{-0.04}$
58465.7	00010949009	1443	997.7	$38.09^{+1.43}_{-1.65}$	$14.58^{+0.42}_{-0.38}$	$23.51^{+1.6}_{-1.22}$	$1.63^{+0.04}_{-0.04}$
58466.9	00010949010	1865	1563.0	$37.41^{+1.41}_{-1.07}$	$15.12^{+0.37}_{-0.41}$	$22.29^{+0.94}_{-1.18}$	$1.68^{+0.04}_{-0.04}$
58467.9	00010949011	1818	1477.1	$34.71^{+0.93}_{-1.01}$	$14.4^{+0.31}_{-0.32}$	$20.31^{+0.97}_{-1.19}$	$1.71^{+0.04}_{-0.04}$
58468.2	00010949012	2070	1711.6	$37.88^{+1.33}_{-1.03}$	$13.94^{+0.33}_{-0.35}$	$23.94^{+0.99}_{-0.98}$	$1.59^{+0.03}_{-0.03}$
58473.6	00094095019	2639	1607.2	$27.73^{+0.83}_{-1.05}$	$10.6^{+0.28}_{-0.22}$	$17.13^{+0.92}_{-0.92}$	$1.63^{+0.03}_{-0.03}$
58493.5	00094095020	2050	1144.3	$23.68^{+0.89}_{-0.9}$	$10.01^{+0.28}_{-0.31}$	$13.68^{+0.76}_{-0.67}$	$1.73^{+0.04}_{-0.04}$
58505.7	00094095021	1995	1308.1	$29.01^{+0.77}_{-1.05}$	$12.57^{+0.43}_{-0.33}$	$16.45^{+0.93}_{-0.51}$	$1.75^{+0.04}_{-0.04}$
58517.4	00094095022	1940	852.3	$21.41^{+0.94}_{-0.87}$	$7.47^{+0.25}_{-0.27}$	$13.94^{+0.85}_{-0.86}$	$1.55^{+0.05}_{-0.05}$
58529.0	00094095023	1635	359.2	$11.86^{+0.96}_{-0.68}$	$4.7^{+0.22}_{-0.28}$	$7.17^{+0.74}_{-0.73}$	$1.66^{+0.07}_{-0.07}$
58541.6	00094095024	2075	488.9	$12.24^{+0.76}_{-0.63}$	$4.08^{+0.17}_{-0.17}$	$8.16^{+0.38}_{-0.69}$	$1.51^{+0.06}_{-0.06}$
58548.1	00094095025	2025	648.6	$14.56^{+0.76}_{-0.84}$	$5.39^{+0.28}_{-0.21}$	$9.17^{+0.58}_{-0.61}$	$1.6^{+0.05}_{-0.05}$
58676.3	00011481002	2080	403.2	$11.57^{+0.76}_{-0.49}$	$4.45^{+0.26}_{-0.21}$	$7.12^{+0.76}_{-0.54}$	$1.64^{+0.07}_{-0.07}$
58690.8	00011481003	1173	221.0	$16.22^{+1.66}_{-1.33}$	$5.36^{+0.42}_{-0.39}$	$10.87^{+1.32}_{-1.46}$	$1.5^{+0.09}_{-0.09}$
58692.0	00011481004	691	199.6	$12.71^{+0.89}_{-1.1}$	$4.86^{+0.34}_{-0.34}$	$7.85^{+1.12}_{-1.1}$	$1.63^{+0.1}_{-0.1}$
58700.5	00011481005	2127	683.9	$14.5^{+0.67}_{-0.75}$	$5.66^{+0.25}_{-0.24}$	$8.84^{+0.72}_{-0.64}$	$1.65^{+0.05}_{-0.05}$
58712.7	00011481006	1600	507.0	$16.29^{+1.05}_{-0.7}$	$5.72^{+0.26}_{-0.2}$	$10.57^{+0.88}_{-0.77}$	$1.55^{+0.06}_{-0.06}$
58726.6	00011542001	4964	1627.0	$17.03^{+0.44}_{-0.5}$	$6.79^{+0.11}_{-0.21}$	$10.24^{+0.55}_{-0.32}$	$1.67^{+0.03}_{-0.03}$
58727.3	00011542002	4959	1697.1	$19.05^{+0.58}_{-0.51}$	$6.32^{+0.18}_{-0.15}$	$12.73^{+0.53}_{-0.62}$	$1.5^{+0.03}_{-0.03}$
58745.7	00011481009	1598	907.7	$26.13^{+1.0}_{-0.9}$	$10.32^{+0.41}_{-0.35}$	$15.81^{+1.01}_{-1.03}$	$1.66^{+0.05}_{-0.05}$

Table 3.1 Continued.

MJD	Observation ID	Exposure time [s]	0.3-10 keV counts	$F_{0.3-10}$	$F_{0.3-2}$	F_{2-10}	$\Gamma_{0.3-10}$
(1)	(2)	(3)	(4)	(5)	(6)	(7)	(8)
58752.6	00011481010	1111	644.9	$26.39^{+1.61}_{-1.27}$	$9.53^{+0.4}_{-0.35}$	$16.86^{+1.55}_{-1.12}$	$1.58^{+0.05}_{-0.05}$
58765.9	00011481012	1410	903.6	$27.75^{+1.07}_{-1.07}$	$11.22^{+0.36}_{-0.38}$	$16.53^{+1.27}_{-1.11}$	$1.68^{+0.05}_{-0.05}$
58772.6	00011481013	1083	402.9	$17.69^{+1.18}_{-1.24}$	$6.51^{+0.35}_{-0.35}$	$11.18^{+1.17}_{-1.06}$	$1.59^{+0.07}_{-0.07}$
58776.3	00011481014	928	338.6	$17.32^{+1.22}_{-1.38}$	$6.27^{+0.38}_{-0.39}$	$11.05^{+1.17}_{-1.09}$	$1.58^{+0.08}_{-0.08}$
58784.0	00011481015	1668	1232.6	$31.81^{+1.08}_{-1.0}$	$12.9^{+0.38}_{-0.48}$	$18.9^{+1.36}_{-0.95}$	$1.69^{+0.04}_{-0.04}$
58795.8	00011481016	554	278.4	$25.35^{+2.24}_{-2.1}$	$7.75^{+0.51}_{-0.35}$	$17.6^{+2.0}_{-1.45}$	$1.43^{+0.08}_{-0.08}$
58796.0	00011481017	1967	896.2	$22.45^{+1.23}_{-0.7}$	$8.39^{+0.2}_{-0.27}$	$14.06^{+0.91}_{-0.72}$	$1.61^{+0.05}_{-0.05}$
58808.7	00011481018	1508	715.9	$22.55^{+1.32}_{-0.85}$	$8.58^{+0.3}_{-0.34}$	$13.97^{+1.16}_{-0.86}$	$1.62^{+0.05}_{-0.05}$
58823.2	00011481020	1962	797.0	$19.33^{+0.76}_{-0.96}$	$6.76^{+0.27}_{-0.28}$	$12.57^{+0.79}_{-0.89}$	$1.55^{+0.05}_{-0.05}$
58832.4	00011481021	2055	632.0	$14.34^{+0.63}_{-0.66}$	$5.03^{+0.25}_{-0.21}$	$9.31^{+0.69}_{-0.67}$	$1.55^{+0.06}_{-0.06}$
58844.7	00011481022	1902	855.4	$19.79^{+0.92}_{-0.77}$	$7.84^{+0.26}_{-0.28}$	$11.95^{+0.89}_{-0.65}$	$1.66^{+0.05}_{-0.05}$
58856.4	00011481023	923	585.0	$27.96^{+1.28}_{-1.52}$	$10.71^{+0.54}_{-0.42}$	$17.25^{+0.93}_{-1.3}$	$1.63^{+0.06}_{-0.06}$
58856.4	00011481023	923	598.0	$27.95^{+1.25}_{-1.25}$	$11.24^{+0.45}_{-0.44}$	$16.71^{+1.28}_{-1.23}$	$1.67^{+0.07}_{-0.05}$
58860.3	00011481024	1176	681.8	$33.23^{+1.53}_{-1.66}$	$12.21^{+0.32}_{-0.52}$	$21.02^{+1.49}_{-1.28}$	$1.59^{+0.05}_{-0.05}$
58869.3	00013172002	5276	1827.2	$17.74^{+0.57}_{-0.43}$	$6.89^{+0.19}_{-0.2}$	$10.86^{+0.37}_{-0.41}$	$1.64^{+0.03}_{-0.03}$
58870.0	00013172003	4018	1683.7	$18.62^{+0.61}_{-0.53}$	$7.17^{+0.2}_{-0.19}$	$11.45^{+0.51}_{-0.54}$	$1.64^{+0.03}_{-0.03}$
58884.0	00011481027	1775	565.5	$17.54^{+0.95}_{-0.98}$	$5.92^{+0.31}_{-0.25}$	$11.62^{+0.66}_{-0.88}$	$1.52^{+0.06}_{-0.06}$

Table 3.2 Individual *Swift* UVOT observations and integrated luminosities. Columns: (1) Modified Julian Date. (2) to (7): *Swift* UVOT flux density in the filters V to $UW2$, assuming a power-law SED within the filter bandpass. Units of 10^{-15} erg cm-2 Å^{-1} s^{-1}. Integrated 2-10 keV flux, units of 10^{-12} erg cm^{-2} s^{-1}. (8) Integrated UV–optical luminosity, as calculated using a piecewise linear interpolation over the host galaxy subtracted UVOT flux densities. Units of 10^{43} erg s^{-1}. Observations for which we do not detect AGN UV–optical emission are marked with "——". (9) Integrated extreme-UV luminosity, estimated using a power-law interpolation between the UVOT $UW2$ band luminosity and the 0.3 keV luminosity. Units of 10^{43} erg s^{-1}. Observations for which we do not detect AGN UV–optical emission are marked with "——". (10) Integrated 0.3-10 keV luminosity, derived from the Galactic absorption corrected XSPEC model fit to the XRT spectrum. (11) Estimated 10-79 keV integrated luminosity, assuming $\Gamma = 1.72$ (i.e., the average photon index for our five *NuSTAR* observations), and scaled to the 10 keV luminosity density of the 0.3-10 keV power-law model.

Table 3.2 Continued.

MJD	F_V	F_B	F_U	F_{UW1}	F_{UM2}	F_{UW2}	L_{UV}	L_{EUV}	$L_{0.3-10}$	L_{10-79}
(1)	(2)	(3)	(4)	(5)	(6)	(7)	(8)	(9)	(10)	(11)
54627.6	4.32±0.15	2.92±0.1	1.23±0.05	0.88±0.05	0.74±0.04	4.32±0.05	$0.57^{+0.49}_{-0.49}$	$3.78^{+0.6}_{-0.61}$	$9.43^{+0.67}_{-0.47}$	13.2
56636.9	4.16±0.19	2.96±0.13	1.21±0.07	0.6±0.05	0.57±0.05	4.16±0.05	$0.0^{+0.0}_{-0.0}$	$0.0^{+0.0}_{-0.0}$	$5.27^{+1.01}_{-0.78}$	8.84
56640.9	4.31±0.2	2.89±0.13	1.24±0.07	0.7±0.06	0.56±0.06	4.31±0.06	$0.0^{+0.0}_{-0.0}$	$0.0^{+0.0}_{-0.0}$	$5.81^{+0.77}_{-0.59}$	6.56
56668.5	4.38±0.17	2.87±0.11	1.21±0.06	0.69±0.05	0.6±0.04	4.38±0.05	$0.0^{+0.0}_{-0.0}$	$0.0^{+0.0}_{-0.0}$	$5.03^{+0.65}_{-0.65}$	7.99
56689.4	4.35±0.17	2.89±0.11	1.17±0.06	0.69±0.05	0.58±0.04	4.35±0.05	$0.0^{+0.0}_{-0.0}$	$0.0^{+0.0}_{-0.0}$	$4.45^{+0.46}_{-0.31}$	5.26
57219.4	4.37±0.19	2.94±0.12	1.56±0.08	1.16±0.08	1.12±0.08	4.37±0.08	$1.72^{+0.66}_{-0.66}$	$4.73^{+0.88}_{-0.89}$	$6.81^{+0.88}_{-0.54}$	9.8
57423.8	4.43±0.18	2.97±0.12	1.65±0.06	1.3±0.08	1.23±0.08	4.43±0.08	$2.26^{+0.61}_{-0.61}$	$6.03^{+0.67}_{-0.67}$	$8.04^{+0.34}_{-0.34}$	11.0
57442.3	4.48±0.21	3.3±0.15	1.88±0.1	1.6±0.11	1.35±0.09	4.48±0.11	$3.43^{+0.82}_{-0.82}$	$8.74^{+1.41}_{-1.43}$	$9.45^{+1.21}_{-0.83}$	11.23
57444.3	4.45±0.17	3.06±0.12	1.83±0.08	1.66±0.1	1.53±0.08	4.45±0.1	$3.13^{+0.66}_{-0.66}$	$8.16^{+1.08}_{-1.08}$	$11.39^{+0.84}_{-0.94}$	17.94

MJD	F_V	F_B	F_U	F_{UW1}	F_{UM2}	F_{UW2}	L_{UV}	L_{EUV}	$L_{0.3-10}$	L_{10-79}
(1)	(2)	(3)	(4)	(5)	(6)	(7)	(8)	(9)	(10)	(11)
57451.2	4.37±0.17	3.12±0.12	1.88±0.09	1.48±0.09	1.47±0.08	4.37±0.09	$3.08^{+0.68}_{-0.68}$	$6.35^{+0.86}_{-0.86}$	$9.04^{+0.8}_{-0.9}$	15.0
57570.3	4.32±0.14	2.95±0.1	1.58±0.06	1.4±0.08	1.25±0.06	4.32±0.08	$2.03^{+0.54}_{-0.54}$	$5.88^{+0.61}_{-0.61}$	$7.45^{+0.37}_{-0.4}$	11.23
57707.1	4.37±0.15	3.0±0.11	1.61±0.07	1.24±0.07	1.18±0.06	4.37±0.07	$2.09^{+0.57}_{-0.57}$	$5.71^{+0.71}_{-0.71}$	$7.94^{+0.44}_{-0.53}$	10.79
57708.0	4.25±0.16	2.89±0.11	1.56±0.07	1.24±0.07	1.1±0.07	4.25±0.07	$1.6^{+0.58}_{-0.58}$	$6.15^{+0.85}_{-0.85}$	$8.35^{+0.47}_{-0.63}$	10.48
57709.6	4.47±0.19	2.92±0.12	1.51±0.08	1.26±0.08	1.14±0.08	4.47±0.08	$1.78^{+0.66}_{-0.66}$	$6.38^{+1.07}_{-1.07}$	$7.77^{+0.93}_{-0.77}$	8.99
57724.5	4.23±0.19	3.07±0.13	1.61±0.06	1.27±0.09	1.25±0.09	4.23±0.09	$2.04^{+0.67}_{-0.67}$	$5.38^{+0.88}_{-0.88}$	$6.73^{+0.7}_{-0.34}$	9.3
57735.2	4.27±0.14	3.06±0.1	1.51±0.06	1.17±0.06	1.05±0.05	4.27±0.06	$1.73^{+0.51}_{-0.51}$	$4.93^{+0.53}_{-0.53}$	$6.8^{+0.39}_{-0.24}$	9.36
57763.0	4.44±0.14	2.95±0.1	1.58±0.06	1.34±0.07	1.15±0.05	4.44±0.07	$2.01^{+0.52}_{-0.52}$	$6.74^{+0.64}_{-0.64}$	$11.85^{+0.34}_{-0.5}$	18.5
57791.6	4.19±0.14	2.91±0.1	1.51±0.06	1.08±0.06	0.92±0.05	4.19±0.06	$1.24^{+0.5}_{-0.5}$	$3.76^{+0.48}_{-0.48}$	$5.11^{+0.36}_{-0.28}$	7.31
57817.4	4.27±0.16	2.91±0.11	1.39±0.06	0.97±0.06	0.89±0.05	4.27±0.06	$0.98^{+0.55}_{-0.55}$	$3.31^{+0.59}_{-0.59}$	$5.09^{+0.5}_{-0.28}$	6.98
57911.6	4.49±0.15	3.06±0.1	1.85±0.07	1.66±0.09	1.52±0.07	4.49±0.09	$3.31^{+0.58}_{-0.58}$	$8.49^{+0.76}_{-0.76}$	$9.31^{+0.35}_{-0.44}$	12.1
57939.1	4.53±0.15	3.31±0.11	2.2±0.08	2.32±0.12	2.0±0.09	4.53±0.12	$5.21^{+0.64}_{-0.64}$	$12.87^{+0.92}_{-0.92}$	$15.31^{+0.43}_{-0.42}$	22.73
57967.1	4.45±0.15	3.4±0.11	2.36±0.09	2.44±0.13	2.25±0.11	4.45±0.13	$5.91^{+0.68}_{-0.68}$	$13.01^{+0.96}_{-0.96}$	$12.72^{+0.47}_{-0.45}$	17.54
57996.8	4.67±0.15	3.57±0.12	2.73±0.1	3.58±0.19	3.03±0.13	4.67±0.19	$8.37^{+0.77}_{-0.77}$	$25.71^{+1.45}_{-1.45}$	$34.97^{+0.8}_{-0.83}$	50.72
58009.9	4.75±0.21	3.77±0.16	3.09±0.14	3.97±0.23	3.31±0.23	4.75±0.23	$9.73^{+1.07}_{-1.07}$	$24.81^{+3.01}_{-3.07}$	$30.24^{+3.63}_{-3.09}$	46.75
58011.3	4.73±0.18	3.46±0.13	2.88±0.12	3.45±0.19	3.17±0.16	4.73±0.19	$8.58^{+0.87}_{-0.87}$	$18.37^{+1.57}_{-1.58}$	$19.78^{+0.87}_{-0.9}$	31.87
58012.6	4.46±0.17	3.43±0.13	2.58±0.11	3.43±0.19	3.15±0.16	4.46±0.19	$7.7^{+0.86}_{-0.86}$	$18.39^{+1.62}_{-1.63}$	$17.29^{+0.98}_{-0.72}$	25.41
58013.8	4.66±0.18	3.61±0.13	2.89±0.12	3.35±0.19	2.95±0.15	4.66±0.19	$8.63^{+0.88}_{-0.88}$	$17.06^{+1.61}_{-1.62}$	$20.32^{+1.76}_{-1.19}$	35.9
58014.6	4.83±0.2	3.68±0.15	2.77±0.13	3.37±0.2	2.9±0.17	4.83±0.2	$8.57^{+0.95}_{-0.95}$	$17.83^{+1.77}_{-1.78}$	$20.06^{+1.6}_{-1.52}$	33.18
58015.0	4.51±0.17	3.39±0.13	2.74±0.11	3.14±0.18	2.98±0.24	4.51±0.18	$7.62^{+0.89}_{-0.89}$	$17.45^{+1.76}_{-1.77}$	$21.43^{+1.69}_{-1.67}$	35.07
58016.5	4.45±0.17	3.57±0.13	2.68±0.11	3.33±0.19	3.01±0.15	4.45±0.19	$8.05^{+0.85}_{-0.85}$	$19.56^{+1.71}_{-1.71}$	$24.72^{+1.41}_{-1.63}$	39.83
58023.4	4.63±0.16	3.71±0.13	3.28±0.13	4.38±0.24	3.68±0.17	4.63±0.24	$10.46^{+0.88}_{-0.88}$	$29.68^{+1.79}_{-1.8}$	$39.17^{+1.27}_{-1.03}$	60.37
58027.4	4.91±0.18	3.66±0.13	3.06±0.12	4.04±0.22	3.46±0.16	4.91±0.22	$9.82^{+0.89}_{-0.89}$	$23.71^{+1.77}_{-1.77}$	$24.24^{+0.87}_{-1.26}$	35.65
58029.9	4.63±0.21	3.56±0.15	2.88±0.14	3.54±0.21	3.34±0.19	4.63±0.21	$8.7^{+1.01}_{-1.01}$	$21.79^{+2.22}_{-2.24}$	$24.57^{+1.81}_{-1.39}$	35.94
58031.0	4.63±0.21	3.39±0.14	2.96±0.14	3.72±0.22	3.28±0.18	4.63±0.22	$8.72^{+1.0}_{-1.0}$	$19.9^{+2.16}_{-2.19}$	$18.91^{+1.48}_{-1.13}$	28.58
58035.5	4.57±0.17	3.43±0.13	2.75±0.12	3.7±0.21	3.24±0.16	4.57±0.21	$8.29^{+0.86}_{-0.86}$	$21.84^{+1.8}_{-1.8}$	$21.72^{+1.26}_{-1.24}$	30.66
58037.3	4.73±0.18	3.7±0.14	2.83±0.12	3.8±0.21	3.34±0.17	4.73±0.21	$9.28^{+0.91}_{-0.91}$	$24.1^{+1.9}_{-1.9}$	$24.55^{+0.87}_{-1.23}$	33.13
58041.4	4.5±0.21	3.7±0.16	3.13±0.15	4.02±0.24	3.47±0.19	4.5±0.24	$9.77^{+1.07}_{-1.07}$	$25.49^{+2.45}_{-2.46}$	$30.99^{+1.94}_{-1.77}$	47.31
58051.2	4.6±0.18	3.06±0.12	2.46±0.11	3.1±0.18	3.05±0.16	4.6±0.18	$6.92^{+0.83}_{-0.83}$	$15.97^{+1.51}_{-1.52}$	$17.99^{+0.78}_{-1.41}$	29.9
58051.2	4.6±0.18	3.06±0.12	2.46±0.11	3.1±0.18	3.05±0.16	4.6±0.18	$6.92^{+0.83}_{-0.83}$	$15.97^{+1.51}_{-1.52}$	$17.99^{+1.39}_{-1.19}$	29.9
58053.9	4.29±0.17	3.39±0.13	2.56±0.11	3.09±0.18	2.97±0.15	4.29±0.18	$7.06^{+0.83}_{-0.83}$	$16.37^{+1.48}_{-1.48}$	$19.71^{+1.31}_{-1.06}$	33.23
58055.6	4.36±0.24	3.37±0.17	2.53±0.14	2.98±0.2	2.66±0.18	4.36±0.2	$6.87^{+1.09}_{-1.09}$	$15.15^{+2.19}_{-2.25}$	$16.75^{+2.83}_{-1.98}$	27.57
58057.2	4.53±0.18	3.55±0.13	2.58±0.11	3.18±0.18	2.67±0.14	4.53±0.18	$7.51^{+0.85}_{-0.85}$	$17.28^{+1.63}_{-1.64}$	$13.04^{+0.92}_{-0.63}$	16.01
58058.0	4.67±0.19	3.36±0.13	2.6±0.11	3.11±0.18	2.78±0.15	4.67±0.18	$7.36^{+0.86}_{-0.86}$	$18.67^{+1.76}_{-1.77}$	$19.17^{+1.11}_{-0.99}$	26.15
58062.3	4.83±0.18	3.55±0.13	2.72±0.11	3.34±0.19	2.78±0.14	4.83±0.19	$8.15^{+0.85}_{-0.85}$	$18.06^{+1.54}_{-1.54}$	$18.94^{+1.07}_{-0.94}$	29.43
58066.0	4.72±0.23	3.56±0.16	2.81±0.14	3.3±0.21	3.36±0.22	4.72±0.21	$8.84^{+1.1}_{-1.1}$	$19.45^{+2.07}_{-2.09}$	$30.54^{+2.3}_{-2.66}$	55.3
58068.6	4.98±0.19	3.72±0.14	3.07±0.13	3.95±0.22	3.58±0.18	4.98±0.22	$10.04^{+0.94}_{-0.94}$	$27.14^{+2.07}_{-2.07}$	$35.03^{+1.45}_{-1.36}$	51.73
58070.1	4.56±0.18	3.66±0.14	3.15±0.13	4.22±0.23	3.69±0.19	4.56±0.23	$10.06^{+0.94}_{-0.94}$	$30.7^{+2.27}_{-2.27}$	$36.89^{+1.82}_{-1.84}$	50.16
58073.5	4.72±0.19	3.6±0.14	3.11±0.13	4.09±0.23	3.43±0.18	4.72±0.23	$9.75^{+0.95}_{-0.95}$	$25.1^{+2.06}_{-2.06}$	$26.66^{+1.46}_{-1.41}$	38.67
58075.4	4.72±0.22	3.81±0.17	3.23±0.16	4.05±0.24	3.67±0.21	4.72±0.24	$10.71^{+1.14}_{-1.14}$	$23.26^{+2.36}_{-2.38}$	$27.12^{+1.93}_{-1.25}$	44.08
58077.6	4.96±0.23	3.87±0.17	3.12±0.15	3.85±0.23	3.51±0.21	4.96±0.23	$10.08^{+1.11}_{-1.11}$	$22.76^{+2.35}_{-2.37}$	$32.55^{+3.27}_{-2.54}$	57.38
58080.1	4.87±0.21	3.68±0.15	3.02±0.14	3.97±0.23	3.57±0.2	4.87±0.23	$9.9^{+1.02}_{-1.02}$	$25.43^{+2.37}_{-2.39}$	$30.01^{+1.87}_{-1.9}$	44.58
58081.9	4.52±0.18	3.82±0.14	2.87±0.12	3.8±0.21	3.51±0.17	4.52±0.21	$9.44^{+0.92}_{-0.92}$	$22.47^{+1.78}_{-1.78}$	$27.96^{+1.16}_{-1.61}$	45.53
58083.4	4.68±0.18	3.52±0.13	2.99±0.13	3.97±0.22	3.58±0.17	4.68±0.22	$9.51^{+0.92}_{-0.92}$	$25.13^{+1.99}_{-1.99}$	$32.13^{+1.32}_{-1.32}$	50.63
58085.8	4.68±0.18	3.7±0.14	3.11±0.13	3.95±0.22	3.6±0.2	4.68±0.22	$9.87^{+0.93}_{-0.93}$	$25.42^{+1.95}_{-1.95}$	$26.91^{+1.7}_{-1.23}$	37.01
58089.6	4.76±0.18	3.65±0.14	2.8±0.12	3.9±0.22	3.19±0.16	4.76±0.22	$9.18^{+0.9}_{-0.9}$	$20.13^{+1.69}_{-1.69}$	$19.83^{+1.48}_{-0.94}$	32.02
58091.7	4.63±0.18	3.52±0.13	2.73±0.12	3.41±0.19	3.31±0.17	4.63±0.19	$8.53^{+0.88}_{-0.88}$	$19.33^{+1.68}_{-1.69}$	$18.81^{+1.01}_{-1.36}$	26.72
58093.5	4.3±0.18	3.65±0.14	2.73±0.12	3.47±0.2	3.21±0.17	4.3±0.2	$8.19^{+0.9}_{-0.9}$	$19.88^{+1.77}_{-1.78}$	$22.77^{+0.96}_{-1.48}$	35.62
58094.5	4.42±0.17	3.58±0.13	2.79±0.12	3.63±0.2	3.22±0.16	4.42±0.2	$8.39^{+0.87}_{-0.87}$	$23.69^{+1.88}_{-1.88}$	$23.27^{+1.1}_{-0.89}$	29.5
58095.1	4.55±0.18	3.29±0.13	2.36±0.1	2.97±0.17	3.07±0.16	4.55±0.17	$6.76^{+0.83}_{-0.83}$	$18.48^{+1.66}_{-1.66}$	$20.21^{+1.48}_{-1.09}$	27.5
58096.4	4.69±0.18	3.45±0.13	2.72±0.11	3.56±0.2	3.18±0.16	4.69±0.2	$8.36^{+0.87}_{-0.87}$	$19.76^{+1.66}_{-1.67}$	$21.75^{+1.51}_{-1.06}$	34.43
58097.4	4.69±0.24	3.46±0.13	2.73±0.12	3.61±0.21	3.29±0.22	4.69±0.21	$8.44^{+0.98}_{-0.98}$	$23.52^{+2.08}_{-2.08}$	$27.79^{+1.75}_{-1.6}$	39.93
58098.3	4.7±0.21	3.55±0.13	2.87±0.12	3.44±0.19	3.12±0.18	4.7±0.19	$8.53^{+0.92}_{-0.92}$	$19.13^{+1.68}_{-1.69}$	$24.04^{+1.39}_{-1.06}$	40.65
58099.5	4.57±0.18	3.42±0.13	2.71±0.11	3.39±0.19	3.12±0.17	4.57±0.19	$8.11^{+0.87}_{-0.87}$	$19.64^{+1.74}_{-1.75}$	$22.51^{+0.84}_{-1.22}$	34.76
58100.0	4.8±0.21	3.54±0.15	2.81±0.13	3.45±0.2	3.11±0.18	4.8±0.2	$8.67^{+0.96}_{-0.96}$	$19.39^{+1.86}_{-1.87}$	$21.3^{+2.06}_{-1.0}$	33.07
58101.9	4.71±0.18	3.48±0.13	2.68±0.11	3.54±0.2	3.03±0.15	4.71±0.2	$8.14^{+0.85}_{-0.85}$	$18.93^{+1.56}_{-1.56}$	$19.56^{+0.77}_{-0.99}$	30.76
58102.8	4.57±0.18	3.46±0.13	2.52±0.11	3.33±0.19	2.89±0.15	4.57±0.19	$7.73^{+0.85}_{-0.85}$	$18.07^{+1.58}_{-1.59}$	$19.66^{+1.09}_{-0.98}$	31.11
58107.1	4.6±0.17	3.57±0.13	2.66±0.11	3.29±0.18	2.98±0.15	4.6±0.18	$8.07^{+0.85}_{-0.85}$	$20.49^{+1.65}_{-1.66}$	$24.69^{+1.23}_{-1.3}$	36.75
58108.0	4.83±0.18	3.46±0.13	2.77±0.12	3.47±0.19	2.92±0.15	4.83±0.19	$8.28^{+0.86}_{-0.86}$	$20.5^{+1.7}_{-1.71}$	$23.78^{+1.53}_{-1.23}$	36.53
58109.7	4.51±0.17	3.51±0.13	2.65±0.11	3.2±0.18	3.13±0.2	4.51±0.18	$7.76^{+0.87}_{-0.87}$	$19.26^{+1.67}_{-1.67}$	$22.74^{+1.46}_{-1.27}$	34.18
58110.1	4.68±0.18	3.69±0.14	2.79±0.12	3.5±0.2	2.99±0.16	4.68±0.2	$8.59^{+0.88}_{-0.88}$	$18.79^{+1.57}_{-1.58}$	$23.3^{+1.82}_{-1.24}$	40.42

MJD	F_V	F_B	F_U	F_{UW1}	F_{UM2}	F_{UW2}	L_{UV}	L_{EUV}	$L_{0.3-10}$	L_{10-79}
(1)	(2)	(3)	(4)	(5)	(6)	(7)	(8)	(9)	(10)	(11)
58111.1	4.6±0.17	3.63±0.13	2.69±0.11	3.57±0.2	3.19±0.16	4.6±0.2	$8.35^{+0.87}_{-0.87}$	$21.28^{+1.75}_{-1.76}$	$21.38^{+0.88}_{-1.33}$	29.91
58112.4	4.5±0.17	3.48±0.13	2.7±0.11	3.54±0.2	2.97±0.14	4.5±0.2	$7.75^{+0.84}_{-0.84}$	$23.17^{+1.76}_{-1.76}$	$28.48^{+1.26}_{-1.4}$	41.65
58113.2	4.52±0.18	3.55±0.14	2.67±0.12	3.59±0.21	3.15±0.16	4.52±0.21	$7.92^{+0.89}_{-0.89}$	$22.02^{+1.85}_{-1.85}$	$27.12^{+1.52}_{-1.32}$	42.15
58117.6	4.73±0.19	3.65±0.14	2.85±0.12	3.52±0.2	3.13±0.16	4.73±0.2	$8.93^{+0.91}_{-0.91}$	$20.95^{+1.84}_{-1.85}$	$18.23^{+1.14}_{-1.2}$	23.09
58118.8	4.56±0.18	3.59±0.14	2.79±0.12	3.5±0.2	3.21±0.17	4.56±0.2	$8.61^{+0.91}_{-0.91}$	$19.67^{+1.78}_{-1.78}$	$17.79^{+0.95}_{-1.08}$	24.46
58118.8	4.56±0.18	3.59±0.14	2.79±0.12	3.5±0.2	3.21±0.17	4.56±0.2	$8.61^{+0.91}_{-0.91}$	$19.67^{+1.78}_{-1.78}$	$17.79^{+0.99}_{-1.01}$	24.46
58119.2	4.78±0.19	3.73±0.14	2.82±0.12	3.45±0.2	3.04±0.16	4.78±0.2	$9.02^{+0.91}_{-0.91}$	$17.53^{+1.66}_{-1.68}$	$15.94^{+1.15}_{-0.84}$	24.27
58120.2	4.51±0.18	3.54±0.14	2.6±0.11	3.34±0.19	3.05±0.16	4.51±0.19	$7.96^{+0.88}_{-0.88}$	$17.28^{+1.65}_{-1.66}$	$16.02^{+1.15}_{-0.84}$	24.05
58121.2	4.78±0.17	3.49±0.12	2.77±0.11	3.37±0.18	3.05±0.14	4.78±0.18	$8.39^{+0.82}_{-0.82}$	$19.68^{+1.49}_{-1.49}$	$17.73^{+0.85}_{-0.76}$	23.22
58122.4	4.54±0.17	3.36±0.13	2.72±0.11	3.3±0.19	2.81±0.14	4.54±0.19	$7.72^{+0.85}_{-0.85}$	$18.11^{+1.59}_{-1.59}$	$18.19^{+1.34}_{-1.24}$	27.04
58123.4	4.52±0.17	3.45±0.13	2.73±0.11	3.28±0.18	2.9±0.15	4.52±0.18	$7.66^{+0.83}_{-0.83}$	$17.09^{+1.47}_{-1.47}$	$19.25^{+1.04}_{-1.04}$	32.09
58124.5	4.59±0.18	3.42±0.13	2.58±0.11	3.26±0.19	2.88±0.15	4.59±0.19	$7.42^{+0.86}_{-0.86}$	$15.93^{+1.48}_{-1.49}$	$18.73^{+1.02}_{-1.21}$	33.77
58125.5	4.63±0.19	3.49±0.14	2.45±0.11	3.17±0.18	2.72±0.15	4.63±0.18	$7.34^{+0.87}_{-0.87}$	$17.65^{+1.69}_{-1.7}$	$17.0^{+1.01}_{-1.17}$	24.04
58127.5	5.05±0.2	3.5±0.13	2.57±0.11	3.35±0.19	2.93±0.15	5.05±0.19	$8.31^{+0.89}_{-0.89}$	$19.95^{+1.78}_{-1.78}$	$17.31^{+1.17}_{-0.72}$	21.62
58129.5	4.44±0.17	3.36±0.13	2.51±0.11	3.19±0.18	2.59±0.14	4.44±0.18	$6.78^{+0.82}_{-0.82}$	$16.55^{+1.54}_{-1.55}$	$16.57^{+0.94}_{-0.96}$	25.67
58131.2	4.52±0.17	3.43±0.13	2.43±0.1	3.05±0.17	2.69±0.14	4.52±0.17	$6.77^{+0.81}_{-0.81}$	$15.68^{+1.46}_{-1.47}$	$13.63^{+0.89}_{-0.8}$	19.3
58135.3	4.38±0.17	3.2±0.12	2.32±0.1	2.59±0.15	2.13±0.11	4.38±0.15	$5.43^{+0.76}_{-0.76}$	$11.62^{+1.21}_{-1.22}$	$11.08^{+0.92}_{-0.63}$	18.1
58137.4	4.4±0.17	3.38±0.13	2.28±0.1	2.58±0.15	2.14±0.11	4.4±0.15	$5.67^{+0.76}_{-0.76}$	$12.27^{+1.29}_{-1.3}$	$11.51^{+1.02}_{-0.73}$	17.56
58139.0	4.51±0.19	3.17±0.13	2.16±0.1	2.47±0.15	2.2±0.13	4.51±0.15	$5.17^{+0.82}_{-0.82}$	$12.2^{+1.46}_{-1.48}$	$14.04^{+1.15}_{-1.33}$	22.98
58145.5	4.78±0.18	3.2±0.12	2.13±0.09	2.39±0.14	2.37±0.12	4.78±0.14	$5.63^{+0.76}_{-0.76}$	$11.39^{+1.11}_{-1.12}$	$15.85^{+1.04}_{-1.01}$	29.47
58148.7	4.41±0.17	3.13±0.12	2.19±0.1	2.35±0.14	2.04±0.11	4.41±0.14	$5.09^{+0.75}_{-0.75}$	$13.5^{+1.35}_{-1.35}$	$14.0^{+1.1}_{-0.66}$	18.42
58150.8	4.42±0.18	3.35±0.13	2.32±0.1	2.48±0.14	2.21±0.12	4.42±0.14	$5.64^{+0.79}_{-0.79}$	$12.6^{+1.34}_{-1.35}$	$12.65^{+0.98}_{-0.89}$	18.62
58152.8	4.41±0.18	3.43±0.13	2.15±0.1	2.41±0.14	2.35±0.13	4.41±0.14	$5.52^{+0.78}_{-0.78}$	$12.56^{+1.32}_{-1.33}$	$12.33^{+0.88}_{-0.56}$	17.35
58154.7	4.43±0.17	3.25±0.12	2.17±0.09	2.35±0.14	2.23±0.12	4.43±0.14	$5.27^{+0.75}_{-0.75}$	$12.1^{+1.29}_{-1.3}$	$10.86^{+0.79}_{-0.81}$	14.42
58156.0	4.46±0.17	3.27±0.13	2.07±0.09	2.41±0.14	2.11±0.11	4.46±0.14	$5.14^{+0.75}_{-0.75}$	$13.22^{+1.39}_{-1.4}$	$11.56^{+0.86}_{-0.6}$	14.28
58158.3	4.62±0.18	3.34±0.13	2.09±0.09	2.28±0.13	2.05±0.11	4.62±0.13	$5.41^{+0.76}_{-0.76}$	$11.64^{+1.26}_{-1.27}$	$11.3^{+1.0}_{-0.48}$	15.75
58160.6	4.72±0.18	3.25±0.12	2.13±0.09	2.3±0.13	2.01±0.11	4.72±0.13	$5.16^{+0.75}_{-0.75}$	$10.97^{+1.28}_{-1.3}$	$13.02^{+0.88}_{-0.99}$	21.93
58162.5	4.26±0.17	3.26±0.13	2.05±0.09	2.11±0.12	2.11±0.11	4.26±0.12	$4.63^{+0.74}_{-0.74}$	$10.49^{+1.18}_{-1.19}$	$11.55^{+0.79}_{-0.8}$	17.36
58164.3	4.47±0.17	3.21±0.12	1.99±0.09	2.07±0.12	1.96±0.11	4.47±0.12	$4.61^{+0.72}_{-0.72}$	$10.62^{+1.18}_{-1.19}$	$10.39^{+0.76}_{-0.53}$	13.94
58166.7	4.66±0.18	3.33±0.13	2.12±0.09	2.26±0.13	2.07±0.11	4.66±0.13	$5.3^{+0.75}_{-0.75}$	$10.27^{+1.12}_{-1.13}$	$12.97^{+0.78}_{-1.12}$	23.41
58289.7	4.45±0.21	3.13±0.14	2.2±0.11	2.34±0.15	2.27±0.14	4.45±0.15	$5.1^{+0.87}_{-0.87}$	$12.71^{+1.58}_{-1.59}$	$13.29^{+1.11}_{-1.13}$	18.49
58300.5	4.62±0.17	3.12±0.12	2.39±0.1	2.91±0.16	2.48±0.13	4.62±0.16	$5.93^{+0.77}_{-0.77}$	$16.4^{+1.44}_{-1.44}$	$17.88^{+0.75}_{-1.01}$	26.45
58313.4	4.5±0.18	3.42±0.13	2.4±0.11	3.02±0.17	2.62±0.14	4.5±0.17	$6.56^{+0.83}_{-0.83}$	$17.67^{+1.62}_{-1.62}$	$22.56^{+1.05}_{-1.06}$	35.87
58325.1	4.55±0.18	3.32±0.13	2.37±0.1	3.02±0.17	2.68±0.14	4.55±0.17	$6.47^{+0.8}_{-0.8}$	$17.1^{+1.56}_{-1.57}$	$18.2^{+1.17}_{-0.96}$	26.69
58337.0	4.49±0.18	3.2±0.12	2.36±0.1	2.89±0.17	2.49±0.14	4.49±0.17	$6.1^{+0.81}_{-0.81}$	$16.01^{+1.55}_{-1.56}$	$16.35^{+0.81}_{-0.85}$	23.49
58349.6	4.32±0.17	3.37±0.13	2.29±0.1	2.83±0.16	2.46±0.13	4.32±0.16	$5.9^{+0.79}_{-0.79}$	$14.15^{+1.42}_{-1.43}$	$14.01^{+0.97}_{-0.9}$	21.69
58363.4	4.61±0.18	3.23±0.13	2.18±0.1	2.55±0.15	2.18±0.12	4.61±0.15	$5.51^{+0.79}_{-0.79}$	$13.52^{+1.49}_{-1.5}$	$17.13^{+1.35}_{-1.11}$	28.23
58366.4	4.48±0.19	3.29±0.13	2.22±0.1	2.59±0.16	2.51±0.15	4.48±0.16	$5.59^{+0.82}_{-0.82}$	$14.39^{+1.56}_{-1.57}$	$16.9^{+1.53}_{-1.09}$	25.73
58373.1	4.7±0.21	3.43±0.15	2.35±0.12	2.96±0.18	2.71±0.18	4.7±0.18	$6.93^{+0.95}_{-0.95}$	$18.49^{+2.04}_{-2.06}$	$21.93^{+1.98}_{-1.34}$	31.37
58385.6	4.48±0.17	3.58±0.13	3.0±0.13	4.21±0.23	3.34±0.17	4.48±0.23	$9.25^{+0.91}_{-0.91}$	$26.99^{+2.03}_{-2.04}$	$29.63^{+1.16}_{-0.93}$	42.35
58397.4	4.63±0.18	3.71±0.14	3.04±0.13	4.14±0.23	3.92±0.2	4.63±0.23	$10.25^{+0.97}_{-0.97}$	$26.14^{+2.1}_{-2.1}$	$31.96^{+1.73}_{-1.66}$	49.45
58409.7	5.03±0.19	4.18±0.15	3.96±0.16	6.7±0.37	5.66±0.32	5.03±0.37	$15.52^{+1.19}_{-1.19}$	$39.54^{+2.87}_{-2.88}$	$40.3^{+1.93}_{-1.3}$	63.05
58419.0	5.17±0.19	4.15±0.15	3.68±0.15	5.33±0.29	4.57±0.24	5.17±0.29	$14.0^{+1.08}_{-1.08}$	$28.54^{+2.17}_{-2.18}$	$23.52^{+1.37}_{-1.05}$	34.63
58420.0	4.7±0.17	3.72±0.13	3.66±0.15	5.03±0.27	4.44±0.32	4.7±0.27	$12.4^{+1.06}_{-1.06}$	$27.93^{+2.09}_{-2.1}$	$25.65^{+1.23}_{-1.47}$	38.61
58421.8	4.64±0.18	3.75±0.14	3.47±0.14	5.36±0.29	4.66±0.22	4.64±0.29	$11.93^{+1.01}_{-1.01}$	$31.33^{+2.37}_{-2.37}$	$24.08^{+1.37}_{-0.86}$	30.83
58422.5	4.82±0.18	3.87±0.14	3.49±0.14	5.61±0.31	5.09±0.24	4.82±0.31	$12.87^{+1.05}_{-1.05}$	$30.81^{+2.31}_{-2.32}$	$24.11^{+1.32}_{-1.04}$	33.62
58422.5	4.82±0.18	3.87±0.14	3.49±0.14	5.61±0.31	5.09±0.24	4.82±0.31	$12.87^{+1.05}_{-1.05}$	$30.81^{+2.31}_{-2.32}$	$24.11^{+1.22}_{-1.13}$	33.62
58423.3	4.76±0.18	3.84±0.14	3.58±0.15	5.75±0.31	4.69±0.22	4.76±0.31	$13.04^{+1.06}_{-1.06}$	$37.95^{+2.57}_{-2.58}$	$36.92^{+1.51}_{-1.5}$	49.56
58424.7	4.9±0.2	3.88±0.15	3.51±0.15	5.68±0.32	4.73±0.24	4.9±0.32	$12.99^{+1.12}_{-1.12}$	$32.81^{+2.65}_{-2.66}$	$27.49^{+1.41}_{-1.2}$	38.14
58425.5	4.93±0.19	4.05±0.15	3.67±0.15	5.89±0.33	5.05±0.25	4.93±0.33	$14.14^{+1.13}_{-1.13}$	$37.52^{+2.72}_{-2.73}$	$33.17^{+1.37}_{-1.27}$	43.32
58433.5	4.72±0.18	3.89±0.15	3.6±0.15	5.14±0.28	4.34±0.21	4.72±0.28	$12.63^{+1.05}_{-1.05}$	$28.35^{+2.29}_{-2.3}$	$25.88^{+1.13}_{-1.58}$	39.2
58445.2	5.03±0.19	3.68±0.14	3.37±0.14	5.09±0.28	4.37±0.22	5.03±0.28	$12.15^{+1.03}_{-1.03}$	$26.98^{+2.24}_{-2.26}$	$20.22^{+0.85}_{-1.09}$	28.07
58457.7	4.89±0.21	4.18±0.17	4.04±0.18	7.67±0.43	6.38±0.33	4.89±0.43	$16.99^{+1.32}_{-1.32}$	$58.73^{+4.02}_{-4.02}$	$60.47^{+3.1}_{-1.85}$	75.63
58464.0	5.1±0.19	4.4±0.16	4.62±0.19	8.43±0.46	6.61±0.3	5.1±0.46	$18.87^{+1.29}_{-1.29}$	$56.7^{+3.58}_{-3.58}$	$53.92^{+1.81}_{-1.8}$	72.76
58465.7	4.83±0.25	4.42±0.16	4.47±0.18	8.21±0.45	7.0±0.38	4.83±0.45	$18.54^{+1.37}_{-1.37}$	$57.64^{+3.9}_{-3.91}$	$62.53^{+2.82}_{-2.83}$	88.34
58466.9	4.89±0.19	4.21±0.16	4.47±0.18	8.15±0.44	6.22±0.29	4.89±0.44	$18.0^{+1.27}_{-1.27}$	$59.65^{+3.57}_{-3.57}$	$61.51^{+2.01}_{-2.24}$	80.73
58467.9	5.21±0.2	4.41±0.16	4.97±0.2	9.11±0.49	7.33±0.33	5.21±0.49	$20.27^{+1.36}_{-1.36}$	$63.4^{+3.8}_{-3.8}$	$57.11^{+2.11}_{-2.24}$	72.22
58468.2	4.64±0.18	4.15±0.15	3.99±0.16	7.77±0.42	6.62±0.3	4.64±0.42	$17.21^{+1.22}_{-1.22}$	$53.7^{+3.19}_{-3.19}$	$62.12^{+2.03}_{-1.84}$	92.25
58473.6	5.25±0.19	4.44±0.16	4.73±0.18	8.23±0.44	6.88±0.31	5.25±0.44	$19.79^{+1.28}_{-1.28}$	$50.71^{+3.02}_{-3.02}$	$45.53^{+1.33}_{-1.18}$	64.39
58493.5	5.0±0.19	4.22±0.15	4.25±0.17	7.52±0.41	6.15±0.29	5.0±0.41	$17.36^{+1.22}_{-1.22}$	$48.69^{+3.11}_{-3.11}$	$38.99^{+1.36}_{-1.18}$	47.99
58505.7	4.99±0.19	4.49±0.16	4.68±0.19	8.83±0.48	7.26±0.33	4.99±0.48	$19.9^{+1.33}_{-1.33}$	$59.86^{+3.67}_{-3.67}$	$47.8^{+1.41}_{-1.53}$	56.68

MJD	F_V	F_B	F_U	F_{UW1}	F_{UM2}	F_{UW2}	L_{UV}	L_{EUV}	$L_{0.3-10}$	L_{10-79}
(1)	(2)	(3)	(4)	(5)	(6)	(7)	(8)	(9)	(10)	(11)
58517.4	4.91±0.18	3.98±0.15	4.06±0.16	7.26±0.39	5.96±0.29	4.91±0.39	$16.18^{+1.18}_{-1.18}$	$39.36^{+2.71}_{-2.71}$	$35.06^{+1.82}_{-1.31}$	55.51
58529.0	4.94±0.19	3.74±0.14	3.07±0.13	4.53±0.25	3.85±0.19	4.94±0.25	$10.97^{+1.0}_{-1.0}$	$24.85^{+2.23}_{-2.25}$	$19.49^{+1.51}_{-1.13}$	26.33
58541.6	4.72±0.18	3.37±0.13	2.47±0.11	3.72±0.21	2.99±0.15	4.72±0.21	$7.97^{+0.86}_{-0.86}$	$19.07^{+1.61}_{-1.62}$	$20.03^{+1.08}_{-1.14}$	33.42
58548.1	4.56±0.18	3.36±0.13	2.66±0.12	4.04±0.23	3.34±0.16	4.56±0.23	$8.45^{+0.9}_{-0.9}$	$23.55^{+1.86}_{-1.86}$	$23.88^{+1.38}_{-1.19}$	35.19
58676.3	4.77±0.18	3.39±0.13	2.58±0.11	3.7±0.21	3.33±0.17	4.77±0.21	$8.23^{+0.87}_{-0.87}$	$20.81^{+1.87}_{-1.88}$	$19.01^{+1.02}_{-1.33}$	26.66
58690.8	4.44±0.19	3.16±0.13	2.05±0.1	2.78±0.17	2.39±0.14	4.44±0.17	$5.35^{+0.85}_{-0.85}$	$17.03^{+2.05}_{-2.07}$	$26.53^{+2.31}_{-1.87}$	44.75
58692.0	4.36±0.22	2.99±0.15	2.07±0.12	2.86±0.19	2.54±0.18	4.36±0.19	$5.17^{+0.98}_{-0.98}$	$17.78^{+2.14}_{-2.16}$	$20.87^{+1.43}_{-1.87}$	29.51
58700.5	4.47±0.17	3.33±0.12	2.25±0.1	3.05±0.17	2.57±0.13	4.47±0.17	$6.31^{+0.79}_{-0.79}$	$20.09^{+1.63}_{-1.63}$	$23.82^{+0.96}_{-1.25}$	32.79
58712.7	4.59±0.18	3.21±0.13	2.18±0.1	2.74±0.16	2.34±0.13	4.59±0.16	$5.86^{+0.81}_{-0.81}$	$17.8^{+1.62}_{-1.63}$	$26.69^{+1.62}_{-1.38}$	41.96
58726.6	4.7±0.17	3.47±0.12	2.38±0.1	3.28±0.18	2.75±0.12	4.7±0.18	$7.28^{+0.78}_{-0.78}$	$23.12^{+1.51}_{-1.51}$	$27.99^{+0.71}_{-0.81}$	37.42
58727.3	4.68±0.17	3.39±0.12	2.42±0.1	3.34±0.18	2.77±0.12	4.68±0.18	$7.16^{+0.78}_{-0.78}$	$20.97^{+1.37}_{-1.37}$	$31.16^{+0.98}_{-0.94}$	52.28
58745.7	4.91±0.19	3.73±0.14	3.63±0.15	6.18±0.34	4.69±0.23	4.91±0.34	$13.27^{+1.1}_{-1.1}$	$42.12^{+2.96}_{-2.96}$	$42.94^{+1.68}_{-1.36}$	58.19
58752.6	4.92±0.21	3.96±0.16	3.43±0.15	5.85±0.33	4.34±0.23	4.92±0.33	$13.02^{+1.16}_{-1.16}$	$37.86^{+2.98}_{-2.99}$	$43.26^{+2.31}_{-2.31}$	65.76
58765.9	4.76±0.2	3.76±0.15	3.48±0.15	6.38±0.36	4.69±0.24	4.76±0.36	$12.86^{+1.11}_{-1.11}$	$45.05^{+3.16}_{-3.16}$	$45.63^{+1.84}_{-1.51}$	59.82
58772.6	4.45±0.2	3.63±0.15	2.79±0.13	4.55±0.27	3.75±0.21	4.45±0.27	$9.56^{+1.04}_{-1.04}$	$27.52^{+2.53}_{-2.54}$	$29.01^{+2.33}_{-1.41}$	43.1
58776.3	4.7±0.21	3.7±0.16	2.74±0.13	4.6±0.27	3.58±0.21	4.7±0.27	$9.95^{+1.09}_{-1.09}$	$27.14^{+2.59}_{-2.6}$	$28.39^{+1.96}_{-1.71}$	43.04
58784.0	4.63±0.18	3.57±0.14	2.83±0.12	5.1±0.28	4.21±0.21	4.63±0.28	$10.34^{+0.97}_{-0.97}$	$41.6^{+2.73}_{-2.73}$	$52.3^{+2.73}_{-1.69}$	68.28
58795.8	4.74±0.26	3.68±0.18	3.05±0.17	4.77±0.31	3.76±0.24	4.74±0.31	$10.65^{+1.29}_{-1.29}$	$28.35^{+2.99}_{-3.02}$	$41.38^{+4.61}_{-3.25}$	75.74
58796.0	4.62±0.21	3.46±0.12	2.7±0.11	4.09±0.23	3.09±0.23	4.62±0.23	$8.87^{+0.95}_{-0.95}$	$28.7^{+2.1}_{-2.1}$	$36.83^{+1.88}_{-1.45}$	53.66
58808.7	4.71±0.19	3.47±0.14	3.17±0.14	4.98±0.28	3.96±0.21	4.71±0.28	$10.79^{+1.02}_{-1.02}$	$33.27^{+2.56}_{-2.56}$	$37.02^{+2.14}_{-2.18}$	52.71
58823.2	4.55±0.18	3.47±0.13	2.47±0.11	3.93±0.22	3.2±0.16	4.55±0.22	$8.02^{+0.87}_{-0.87}$	$24.73^{+1.9}_{-1.9}$	$31.67^{+1.19}_{-1.47}$	50.02
58832.4	4.52±0.17	3.36±0.13	2.58±0.11	3.91±0.22	3.15±0.16	4.52±0.22	$8.02^{+0.86}_{-0.86}$	$21.87^{+1.76}_{-1.76}$	$23.48^{+1.18}_{-1.05}$	36.96
58844.7	4.74±0.18	3.45±0.13	2.53±0.11	4.2±0.24	3.19±0.16	4.74±0.24	$8.38^{+0.89}_{-0.89}$	$29.08^{+2.14}_{-2.15}$	$32.52^{+1.4}_{-1.56}$	43.89
58856.4	4.5±0.34	3.93±0.15	3.23±0.14	4.79±0.27		4.5±0.27	$11.82^{+1.39}_{-1.39}$	$35.82^{+2.92}_{-2.92}$	$45.9^{+1.64}_{-2.43}$	64.78
58856.4	4.5±0.34	3.93±0.15	3.23±0.14	4.79±0.27		4.5±0.27	$11.82^{+1.39}_{-1.39}$	$37.26^{+3.0}_{-3.0}$	$45.9^{+2.29}_{-1.49}$	61.22
58860.3	5.07±0.21	3.76±0.15	3.32±0.15	6.16±0.35	4.67±0.24	5.07±0.35	$12.88^{+1.15}_{-1.15}$	$43.78^{+3.34}_{-3.34}$	$54.5^{+3.02}_{-1.88}$	81.08
58869.3	4.75±0.16	3.58±0.12	2.79±0.11	4.78±0.26	3.8±0.17	4.75±0.26	$10.2^{+0.86}_{-0.86}$	$29.82^{+1.79}_{-1.79}$	$29.14^{+0.99}_{-0.55}$	40.41
58870.0	4.61±0.16	3.59±0.12	2.96±0.12	4.9±0.26	3.89±0.18	4.61±0.26	$10.28^{+0.88}_{-0.88}$	$30.74^{+1.9}_{-1.9}$	$30.57^{+0.94}_{-1.1}$	42.83
58884.0	4.84±0.19	3.52±0.13	2.56±0.11	3.9±0.22	3.55±0.19	4.84±0.22	$8.95^{+0.92}_{-0.92}$	$22.98^{+1.95}_{-1.96}$	$28.7^{+1.44}_{-1.86}$	47.21

3.4 Continuum reverberation mapping of the 2017 high-cadence monitoring data

Here, I present a continuum reverberation mapping analysis using the *Swift* UVOT and XRT lightcurves for Mrk 590 presented in our draft paper, *"X-ray and UV Flares in the Changing Look AGN Mrk 590. I: X-ray and UV–optical Observations Since 2014"* (Section §3.2 of this Thesis).

3.4.1 Motivation

The rapid UV-optical continuum variability displayed by AGN is not explained by the geometrically thin, optically thick accretion disk models (1.2). In these models, large-amplitude variability should only occur on the viscous timescale, which for accretion disks around SMBHs is of order hundreds of years (e.g., Noda and Done, 2018). As discussed in §3.2, both the UV-optical variability displayed by typical AGN, and the extreme variability of changing-look AGN, pose challenges to the standard thin-disk approximations. Currently, the most common explanation for AGN UV–optical variability is reprocessing of X-ray flux variations in the accretion disk. In this 'lamp-post' scenario, the compact hard X-ray source is situated above (and below) the accretion disk. The compact X-ray corona is the source of the variability, which then illuminates the disk, causing the observed UV–optical lightcurves. A correlation between the X-ray and UV–optical continuum fluxes, with an associated time delay corresponding to the geometry of the X-ray source and the accretion disk, is a key prediction of this model. Given the temperature profile predicted by thin-disk models (§1.2, Equation 1.12), the longer-wavelength continuum is produced in the outer disk and should display a longer lag relative to the X-ray source. These predictions for the time delay as a function of continuum wavelength can then be tested using reverberation mapping techniques (§1.4.1). Currently, the observational evidence for the lamp-post model is not conclusive for AGN in general. In particular, the X-ray lightcurves are often poorly correlated with the UV–optical variability, and the X-ray to far-UV delay is much larger than predicted (e.g., Edelson et al., 2019; Gardner and Done, 2017). The inter-band continuum delays are also longer than those predicted by the thin-disk model, although some of this discrepancy is likely due to the influence of diffuse BLR continuum emission, as I demonstrate in Chapter 2.

As a changing-look source that has recently increased its Eddington luminosity from $L/L_{\mathrm{Edd}} \approx$ 0.003 to $L/L_{\mathrm{Edd}} > 0.01$ (§3.2), the nature of the accretion flow in Mrk 590 is not well understood. The UV–optical emission from the AGN reappeared during the 2017 flare, and we see flares in the UV and X-rays roughly simultaneously, supporting (to first order) the disk reprocessing interpretation. However, the simultaneous increase in the X-ray and reappearance of the UV emission components for Mrk 590 is qualitatively different from the variability observed for non changing-look AGN, where the UV emission displays fluctuations around a non-zero average level. This poses the question of whether such a dramatic increase can be attributed to reprocessing of the X-ray emission in the thermal disk. Here, I address this issue from an observational standpoint by quantifying the correlations between the X-ray and UV–optical lightcurves during 2017–2018. I investigate *1)* whether the extreme variability observed for Mrk 590 is consistent with the variability behavior

found in disk reverberation mapping campaigns for other AGN, and *2)* whether this behavior is consistent with the 'lamp-post' model.

3.4.2   Method

Due to its sensitivity, scheduling flexibility, and ability to observe simultaneously in the X-rays and UV-optical regimes, the *Swift* satellite is a valuable instrument for detailed reverberation mapping studies of low-redshift AGN (e.g., Cackett et al., 2015; McHardy et al., 2014, 2017; Shappee et al., 2014), including the study of inter-band continuum delays (e.g., Edelson et al., 2015). Constraining the continuum inter-band delays in AGN provides an important test of accretion disk sizes (versus the predictions of, e.g., standard α-disk models). Similarly, determining the correlation strength and lag behavior of the X-rays relative to the UV emission may constrain the relative physical locations of X-ray emitting and UV-emitting components, and provide clues as to the physical source of AGN flux variations.

While our primary motivation in our *Swift* monitoring campaign of Mrk 590 was to monitor the overall flux level and SED shape during the flare-up event, the extended period of short-cadence ($\sim$1–3 day) monitoring in 2017–2018 also allows a determination of the X-ray to UV delays for Mrk 590. Indeed, visual inspection of the *Swift* XRT and UVOT UV lightcurves during 2017–2018 indicates that the variations in UV flux are correlated with the XRT $F(0.3–10\ \mathrm{keV})$ flux level (Figure 3.1). The X-ray flux itself varies by a factor ~ 4 during the flare event, and displays significant variations on timescales of ~ 1–2 days. While our observing cadence is too long to accurately measure the predicted inter-band delays in the UV continuum, I demonstrate in the following that the UVOT UV bands are highly correlated with the XRT variations, and lag them by ~ 2 days.

I include the short-cadence monitoring observations between August 31st 2017 – 29th February 2018 in this analysis. As X-ray to UV and inter-band continuum lags are expected at timescales of $\sim$hours to days, the longer-cadence observations prior to August 31st are not useful here. For this preliminary analysis, due to time constraints, I have not attempted to remove long-term trends from the lightcurve data. Such a treatment may improve the accuracy of determination of short delays (e.g., Edelson et al., 2015), and I will investigate whether it makes a difference for our data in future work. I use two different methods to determine the delay times, as follows.

Interpolated Cross-Correlation method: I firstly apply the interpolated cross-correlation function (ICCF) method described by White and Peterson (1994). The cross-correlation function is a measure of the similarity of two signals (e.g., time series) as a function of the displacement of one relative to the other. As an extreme example, if a driving continuum signal is reprocessed in a single cloud located at a distance of five light-days from the continuum source, the CCF of the continuum and reprocessed lightcurves would show a sharp peak at a delay of five days. Given that real observing situations seldom have uniform sampling, it is necessary to interpolate one of the lightcurves in order to obtain an estimate of the CCF. For the algorithm applied here, the resulting CCF is the average of that obtained when interpolating over the continuum lightcurve, and that obtained when interpolating over the 'driven' lightcurve (in this case, the *Swift* UVOT lightcurves).
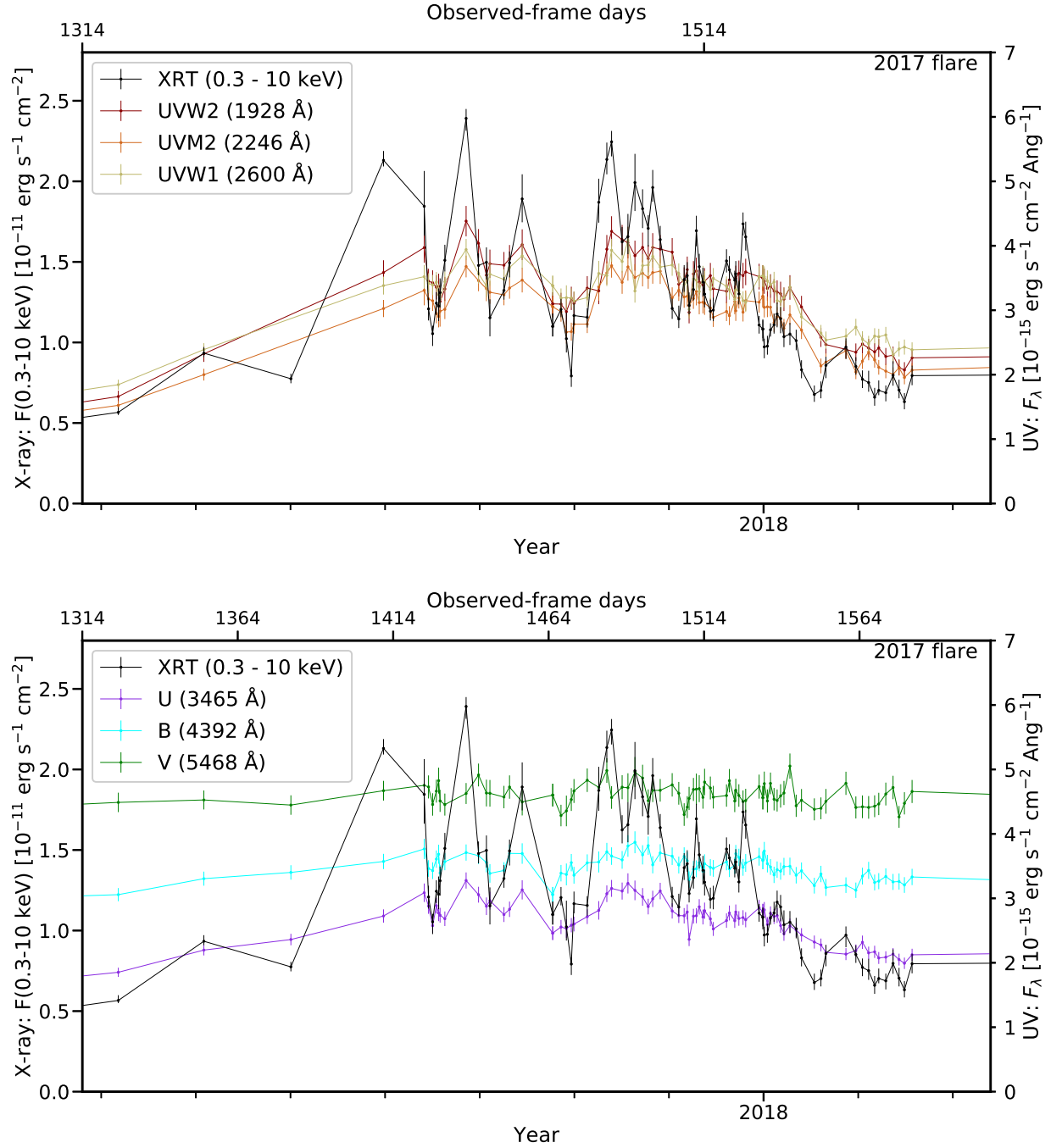
Fig. 3.1 *Swift* UVOT and XRT lightcurves for Mrk 590 during June 2017 – February 2018. The flux densities are corrected for Galactic reddening, but are not host galaxy subtracted. *Top panel: Swift* UVOT UW2 (dark red), UM2 (orange) and UW1 (yellow) bandpasses, along with the *Swift* XRT 0.3-10 keV lightcurve. *Bottom panel:* UVOT U, B and V lightcurves. Need to update x axis for this figure.

For this analysis, I use a Python implementation of the ICCF method, which includes Monte Carlo flux randomization and random subset selection (Peterson et al., 1998). The Python implementation is written by Catherine Grier[1].

In this analysis, I assume that the XRT variability drives the UV variability. This assumption is supported by visual inspection of Figure 3.1: the UV variability appears to lag the X-ray variability. For each UVOT bandpass, I therefore determine its cross-correlation function with the XRT lightcurve. I measure the peak correlation strength R_{ICCF} for each UVOT filter. A peak correlation strength of unity implies that the lightcurves are identical when shifted by the peak delay time, whereas a peak correlation strength $R_{ICCF} \sim 0$ implies that the lightcurves are not correlated. I determine the time delays via a Gaussian profile fit to the cross-correlation function. To minimize the influence of noise in the correlation signal, the centroid is determined using all points on the CCF for which the correlation exceeds 80% of the peak correlation strength. Use of the centroid time delay instead of the cross-correlation fucntion peak is preferred, as the peak delays are biased towards short radii, at least for realistic extended broad-line regions (Pêrez et al., 1992); I am not aware of similar comparison studies for reverberation in an accretion disk. To account for the effects of discrete sampling and of flux uncertainties, I generate 1000 realizations of each lightcurve, following Peterson et al. (1998). For each lightcurve, I discard a subset of the data points (on average 37%), and replace the fluxes with a random value drawn from a Gaussian distribution with its width determined by the flux uncertainty. The ICCF analysis is repated on each of these simualted lightcurves, providing a distribution of ICCF centrods that is used to determine the time delay uncertainty.

Damped random walk continuum modeling using Javelin: As an alternative estimate of the delay times, I apply the lightcurve analysis software Javelin (Zu et al., 2011). This software models the driving lightcurve (here, the XRT lightcurve) as a damped random walk (DRW) process in the logarithm of the flux. I discuss the DRW model as applied to AGN in more detail in Chapter 2. Here, I note that the applicability of the DRW model to short-timescale variations is debated (Zu et al., 2013), as is our ability to determine the correct DRW timescale based on typical RM campaign lengths of ∼hundreds of days (Kozłowski, 2017). However, Yu et al. (2020) demonstrate that the derived time delays are not strongly sensitive to the correct determination of the DRW relaxation timescale, τ_{DRW}. An important advantage of the Javelin method is that it uses all available lightcurves simultaneously to constrain the continuum behavior, and takes the flux uncertainites into account. In contrast, the ICCF method treats each correlation function as independent, and determines the correlation between the data points without directly accounting for their uncertainties. While the use of multiple realizations of the lightcurves with flux randomization and sampling randomization does provide uncertainty estimates on the time delay centroids, these estimates are (by design) conservative (Peterson et al., 1998). Yu et al. (2020) find that the ICCF method systematically overestimates the uncertainties on the time delays, while Javelin provides better estimates of the true uncertainties.

---

[1]URL: http://ascl.net/code/v/1868

Table 3.3 JAVELIN and ICCF reverberation mapping results for Mrk 590.

Bandpass	JAVELIN analysis		ICCF analysis	
	τ_J	σ_J	R_{ICCF}	τ_{ICCF}
	(days)	(days)		(days)
(1)	(2)	(3)	(4)	(5)
UW2	2.9	0.5	0.86	$2.5^{+1.2}_{-1.4}$
UM2	3.2	0.6	0.86	$2.5^{1.4}_{-1.3}$
UW1	3.5	0.7	0.80	$2.9^{+1.7}_{-2.1}$
U	3.2	0.5	0.86	$2.0^{+1.4}_{-1.5}$
B	2.7	1.2	0.71	1.8 ± 2.7
V	1.5	5.7	0.40	-1.3 ± 5.4

Columns: (1) *Swift* UVOT filter name.

(2) Median of *Javelin* posterior distribution for the lag between the XRT lightcurve and this UVOT band, in units of observed-frame days.

(3) 1σ width of the lag distribution, in units of observed-frame days.

(4) Maximum correlation strength of the interpolated cross-correlation function, for this UVOT bandpass relative to the XRT lightcurve.

(5) Maximum of the ICCF centroid distribution, for 1000 realizations of the lightcurves, including flux randomization and random flux resampling. The quoted uncertainties correspond to the 1σ width of the centroid distribution.

3.4.3 Results of Timing Analysis

ICCF Correlation Strengths and Delay Centroids: According to my ICCF analysis, the UVOT *UVW2*, *UVM2*, *UVW1* and *U* lightcurves are highly correlated with the XRT lightcurve, with correlation strength $R_{ICCF} > 0.8$ (Table 3.3). The *B* lightcurve displays a somewhat weaker correlation ($R_{ICCF} = 0.71$), while the *V* band variability is not strongly corelated with the X-rays ($R_{ICCF} = 0.40$). I present the cross-correlation functions for each UVOT filter in Figures 3.2 to 3.7, along with histograms of the cross-correlation centroid distributions and peak distributions. For the far-UV and *U* bands, I find centroid time delays of between 2.0 and 2.9 days, in the positive sense - i.e., the UV variability lags that of the X-rays (Table 3.3). However, the 1σ uncertainties derived from the centroid distributions are large, and none of the delays are significantly different from zero lag at the 3σ level. Unsurprisingly given these large uncertainties, inter-band UV–optical delays are not detected.

JAVELIN Time Delays and Uncertainties: The posterior median DRW relaxation parameter derived from my JAVELIN analysis has a relaxation timescale of $\tau_{DRW} = 13.9$ days, and a fractional variability amplitude of 5.8 (Figure 3.8). Thus, the X-ray continuum displays large-amplitude flares with durations of around 14 days during the 2017 flare-up event. I present the time delay distributions for each UVOT lightcurve according to the the JAVELIN analysis in Figure 3.9, all measured relative to the X-ray lightcurve. The posterior median delays as determined by JAVELIN range between 2.9 and 3.5 days for the far-UV and *U* bands (Table 3.3). Based on the Full Widths at Half-Maximum of the posterior distributions of lags, the 1σ uncertainties on the JAVELIN lag
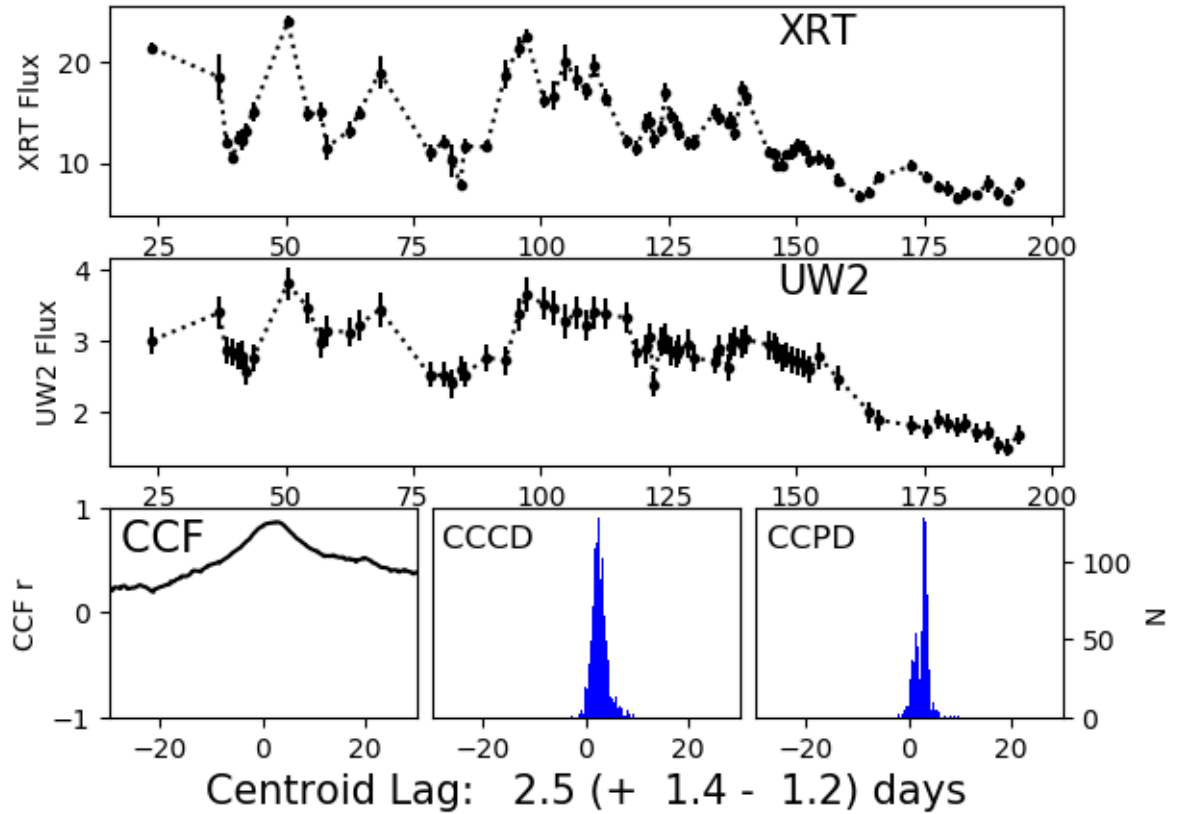
Fig. 3.2 Interpolated cross-correlation function analysis for the *Swift* UVOT *UW*2 filter, treating the *Swift* XRT lightcurve as the driving continuum, during 1st July 2017 – 29th February 2018. *Upper and middle panels: Swift* XRT and UVOT lightcurves (arbitrary flux scaling). The linear interpolations between consecutive data points are shown as dotted lines. The *x* axes have units of days after 1st July 2017. *Bottom left:* Cross-correlation function for the two lightcurves. The *x* axis shows the time delay in days, and the *y* axis dispalys the correlation strength. *Bottom center:* Cross-correlation function centroid distribution, for 1000 realizations of the lightcurves, including flux randomization and random subset selection. *Bottom left:* Cross-correlation function peak distribution for 1000 realizations of the lightcurves.

Fig. 3.3 Interpolated cross-correlation function analysis for the *Swift* UVOT *UM*2 filter, treating the *Swift* XRT lightcurve as the driving continuum, during 1st July 2017 – 29th February 2018. *Upper and middle panels: Swift* XRT and UVOT lightcurves (arbitrary flux scaling). The linear interpolations between consecutive data points are shown as dotted lines. The *x* axes have units of days after 1st July 2017. *Bottom left:* Cross-correlation function for the two lightcurves. The *x* axis shows the time delay in days, and the *y* axis dispalys the correlation strength. *Bottom center:* Cross-correlation function centroid distribution, for 1000 realizations of the lightcurves, including flux randomization and random subset selection. *Bottom left:* Cross-correlation function peak distribution for 1000 realizations of the lightcurves.
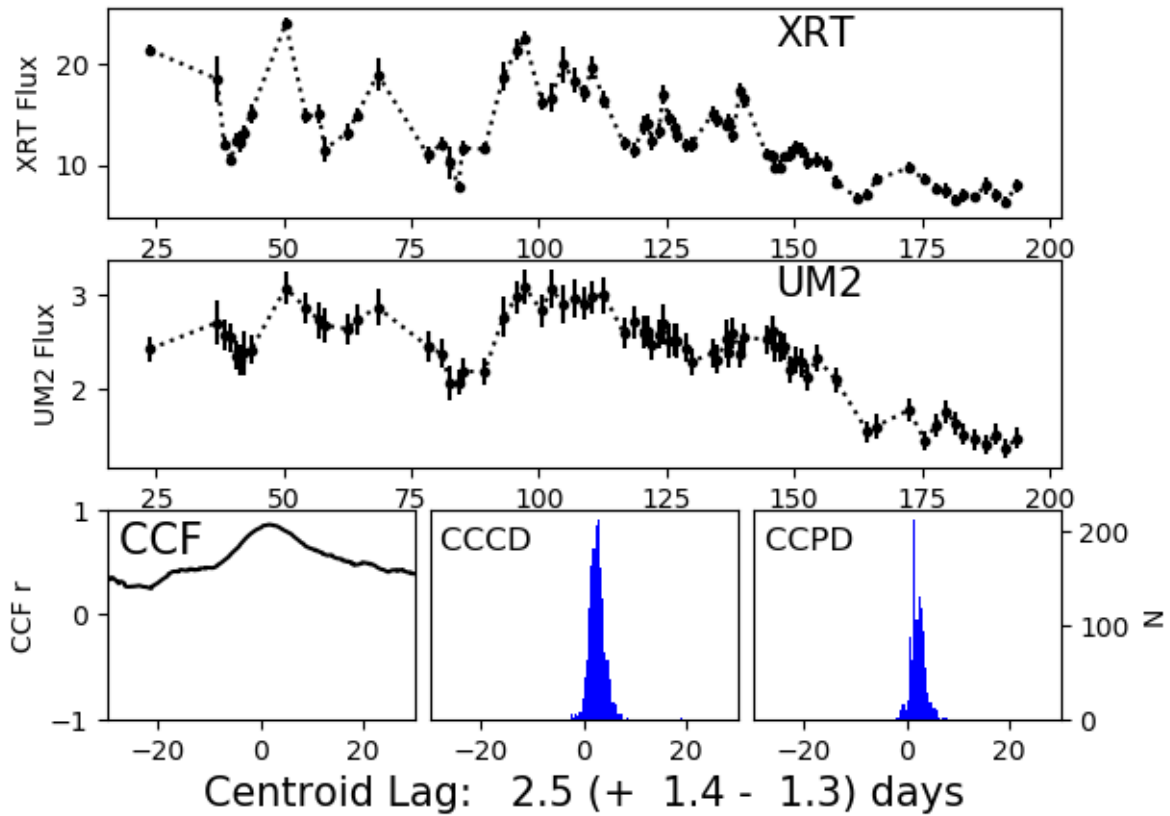
Fig. 3.4 Interpolated cross-correlation function analysis for the *Swift* UVOT *UW*1 filter, treating the *Swift* XRT lightcurve as the driving continuum, during 1st July 2017 – 29th February 2018. *Upper and middle panels: Swift* XRT and UVOT lightcurves (arbitrary flux scaling). The linear interpolations between consecutive data points are shown as dotted lines. The *x* axes have units of days after 1st July 2017. *Bottom left:* Cross-correlation function for the two lightcurves. The *x* axis shows the time delay in days, and the *y* axis dispalys the correlation strength. *Bottom center:* Cross-correlation function centroid distribution, for 1000 realizations of the lightcurves, including flux randomization and random subset selection. *Bottom left:* Cross-correlation function peak distribution for 1000 realizations of the lightcurves.
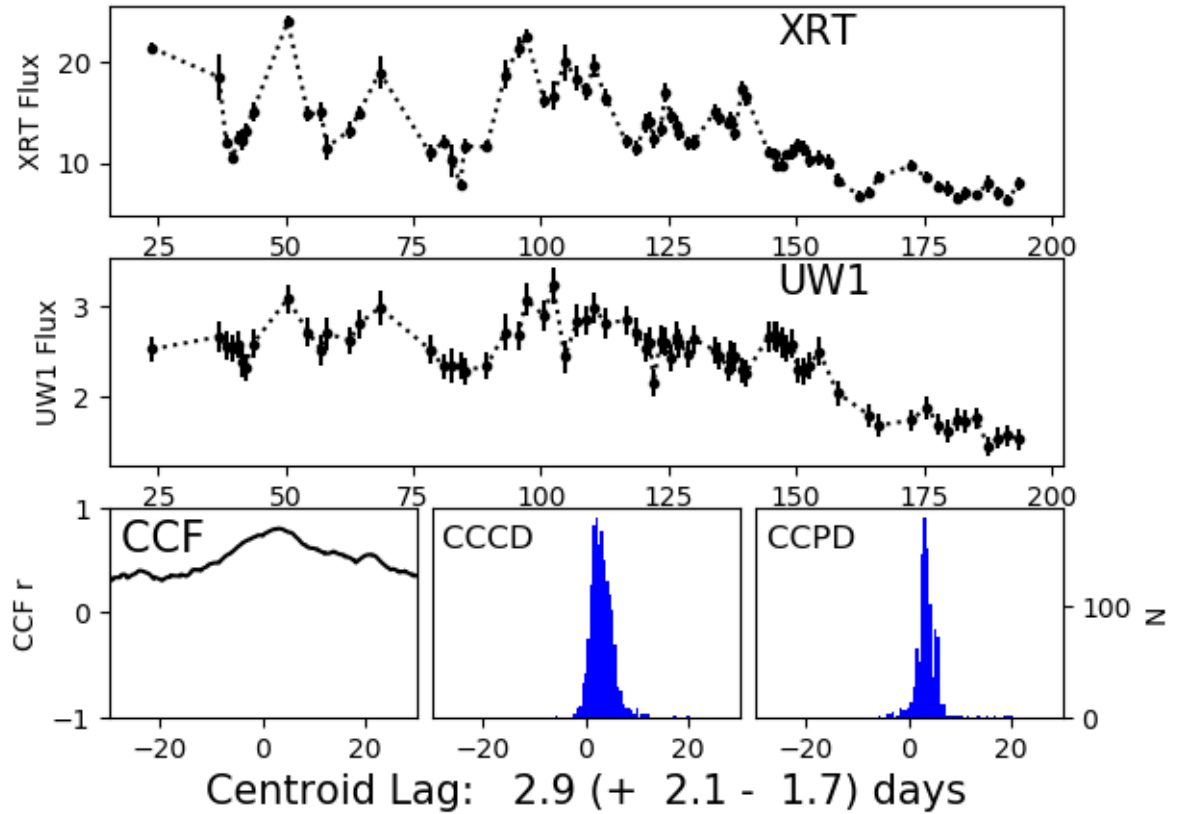
Fig. 3.5 Interpolated cross-correlation function analysis for the *Swift* UVOT *U* filter, treating the *Swift* XRT lightcurve as the driving continuum, during 1st July 2017 – 29th February 2018. *Upper and middle panels: Swift* XRT and UVOT lightcurves (arbitrary flux scaling). The linear interpolations between consecutive data points are shown as dotted lines. The *x* axes have units of days after 1st July 2017. *Bottom left:* Cross-correlation function for the two lightcurves. The *x* axis shows the time delay in days, and the *y* axis dispalys the correlation strength. *Bottom center:* Cross-correlation function centroid distribution, for 1000 realizations of the lightcurves, including flux randomization and random subset selection. *Bottom left:* Cross-correlation function peak distribution for 1000 realizations of the lightcurves.
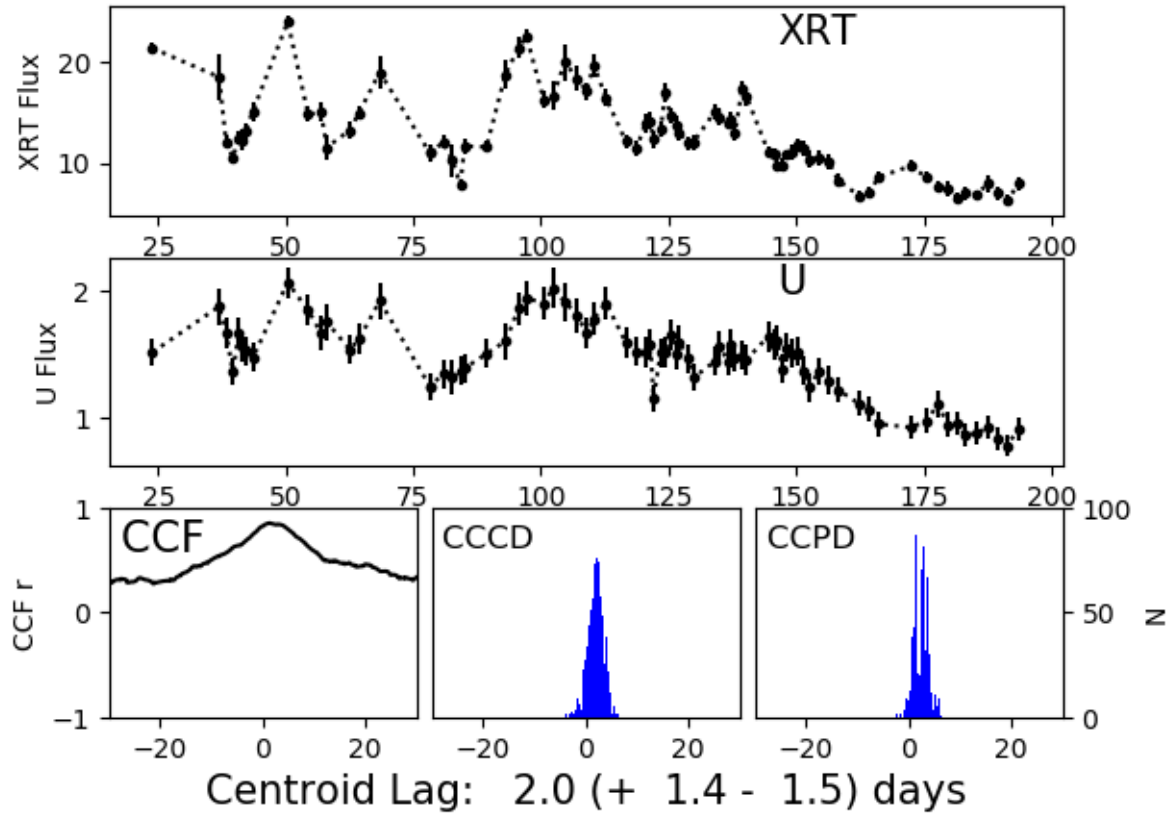
Fig. 3.6 Interpolated cross-correlation function analysis for the *Swift* UVOT *B* filter, treating the *Swift* XRT lightcurve as the driving continuum, during 1st July 2017 – 29th February 2018. *Upper and middle panels: Swift* XRT and UVOT lightcurves (arbitrary flux scaling). The linear interpolations between consecutive data points are shown as dotted lines. The *x* axes have units of days after 1st July 2017. *Bottom left:* Cross-correlation function for the two lightcurves. The *x* axis shows the time delay in days, and the *y* axis dispalys the correlation strength. *Bottom center:* Cross-correlation function centroid distribution, for 1000 realizations of the lightcurves, including flux randomization and random subset selection. *Bottom left:* Cross-correlation function peak distribution for 1000 realizations of the lightcurves.
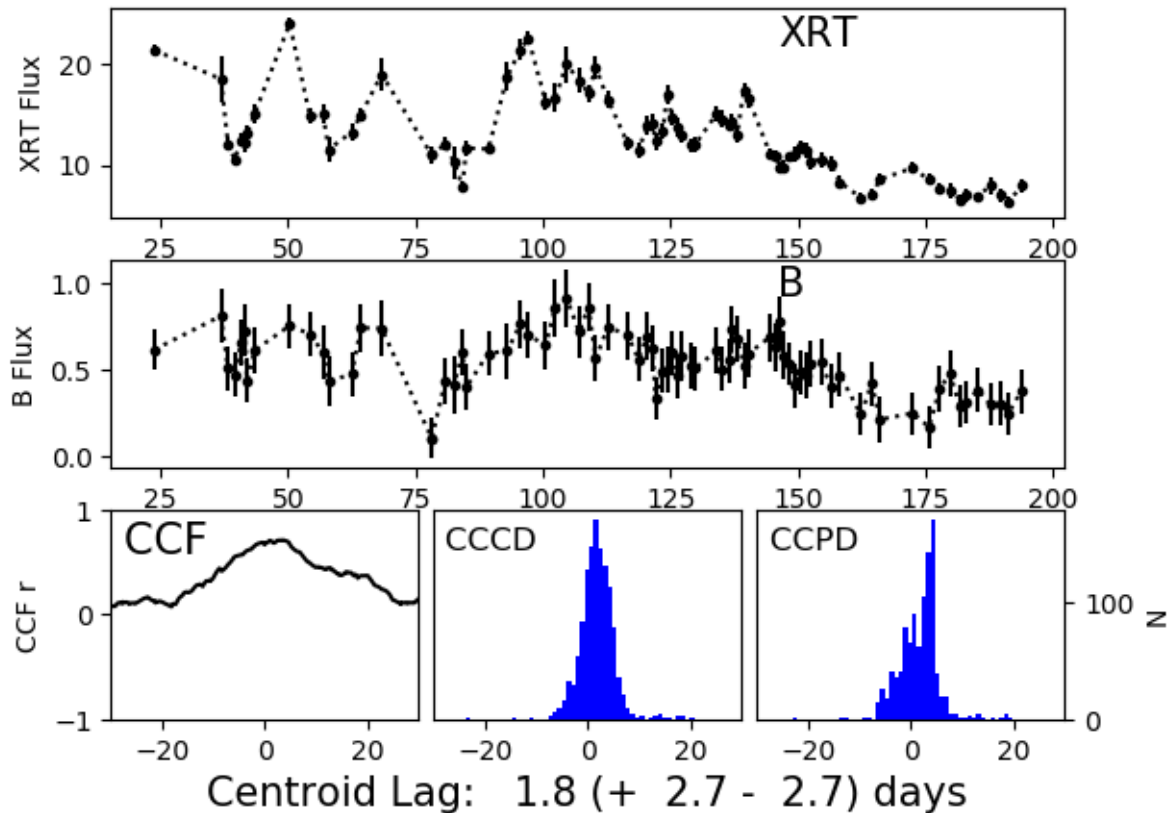
Fig. 3.7 Interpolated cross-correlation function analysis for the *Swift* UVOT *V* filter, treating the *Swift* XRT lightcurve as the driving continuum, during 1st July 2017 – 29th February 2018. *Upper and middle panels:* *Swift* XRT and UVOT lightcurves (arbitrary flux scaling). The linear interpolations between consecutive data points are shown as dotted lines. The *x* axes have units of days after 1st July 2017. *Bottom left:* Cross-correlation function for the two lightcurves. The *x* axis shows the time delay in days, and the *y* axis dispalys the correlation strength. *Bottom center:* Cross-correlation function centroid distribution, for 1000 realizations of the lightcurves, including flux randomization and random subset selection. *Bottom left:* Cross-correlation function peak distribution for 1000 realizations of the lightcurves.
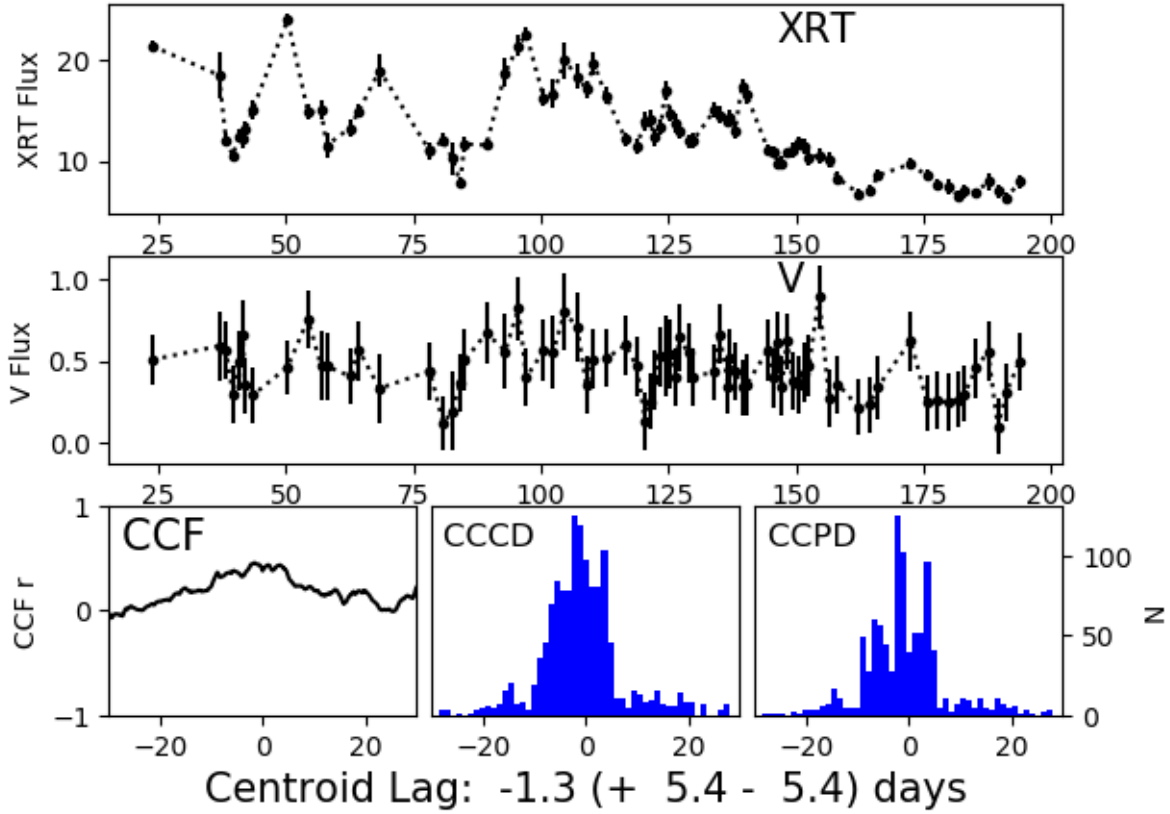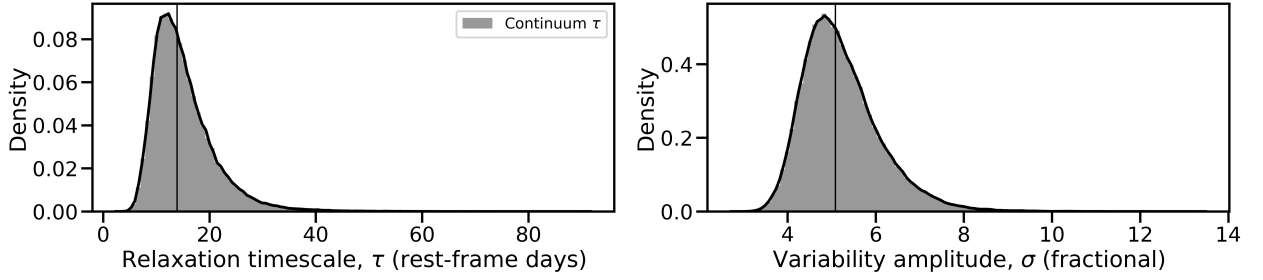
Fig. 3.8 Histograms of *Javelin* Monte Carlo Markov Chain posterior lag distributions for the DRW continuum model. The XRT lightcurve represents the continuum in our modeling. *Upper panel:* The relaxation time τ, i.e., the timescale upon which the lightcurve becomes uncorrelated with its previous behavior. *Lower panel:* The short-scale variability amplitude, σ. The black vertical lines denote the median values, $\langle \tau \rangle = 13.9$ days and $\langle \sigma \rangle = 5.8$.

determinations are of order 0.6 days for the UV bands; thus, the modeling is inconsistent with zero lag at the 3σ level for these bands. The modeling is consistent with zero lag at the 3σ level for the *B* and *V* lightcurves, in agreement with the smaller peak correlation values found in the ICCF modeling for these bandpasses. No significant UV–optical inter-band delays are detected. The JAVELIN posterior median time delays are consistent with the ICCF centroids for all bands. Thus, the main difference between the time delays derived using JAVELIN and using the ICCF method is the factor ~ 2 smaller uncertainties derived using JAVELIN. I emphasize that the JAVELIN method is found to produce more accurate delay uncertainites (Yu et al., 2020). Given the results of the Yu et al. study, and the consistency of the delays found using the JAVELIN and ICCF methods, I conclude that the UV lightcurves indeed lag the X-rays by roughly 2–3 days during the 2017 flare-up event. I discuss the implications of this result for the X-ray reprocessing model for AGN continuum variations below.

3.4.4 Discussion

The strong correlation between the X-ray and UV lightcurves

According to my ICCF analysis, the *UVOT* UV lightcurves are strongly correlated with the X-ray lightcurve (Table 3.3), while the *V* band flux variations are largely uncorrelated with the X-rays. The strong X-ray to UV correlation, with $R_{\text{ICCF}} \geq 0.8$ for the UV lightcurves, is rather unusual. Edelson et al. (2019) present *Swift* high-cadence X-ray and UV monitoring data for the low-redshift AGN Mrk 509, NGC 5548, NGC 4151, and NGC 4593. Their average X-ray to far-UV correlation strength using the ICCF method is $R_{\text{ICCF}} \sim 0.6$. For the highly accreting AGN Mrk 142, Cackett et al. (2020) find an X-ray to far-UV correlation strength of $R_{\text{ICCF}} = 0.54$. Fausnaugh et al. (2018) find only a weak X-ray to UV correlation for the changing-look AGN NGC 2617; Morales et al. (2019) find no significant correlation between the X-ray and far-UV emission for the Seyfert 1.5 AGN Mrk 817. To the best of my knowledge, the 2017 flare-up in Mrk 590 represents the strongest short-timescale correlation between the X-ray and far-UV lightcurves yet detected using the ICCF method for AGN.
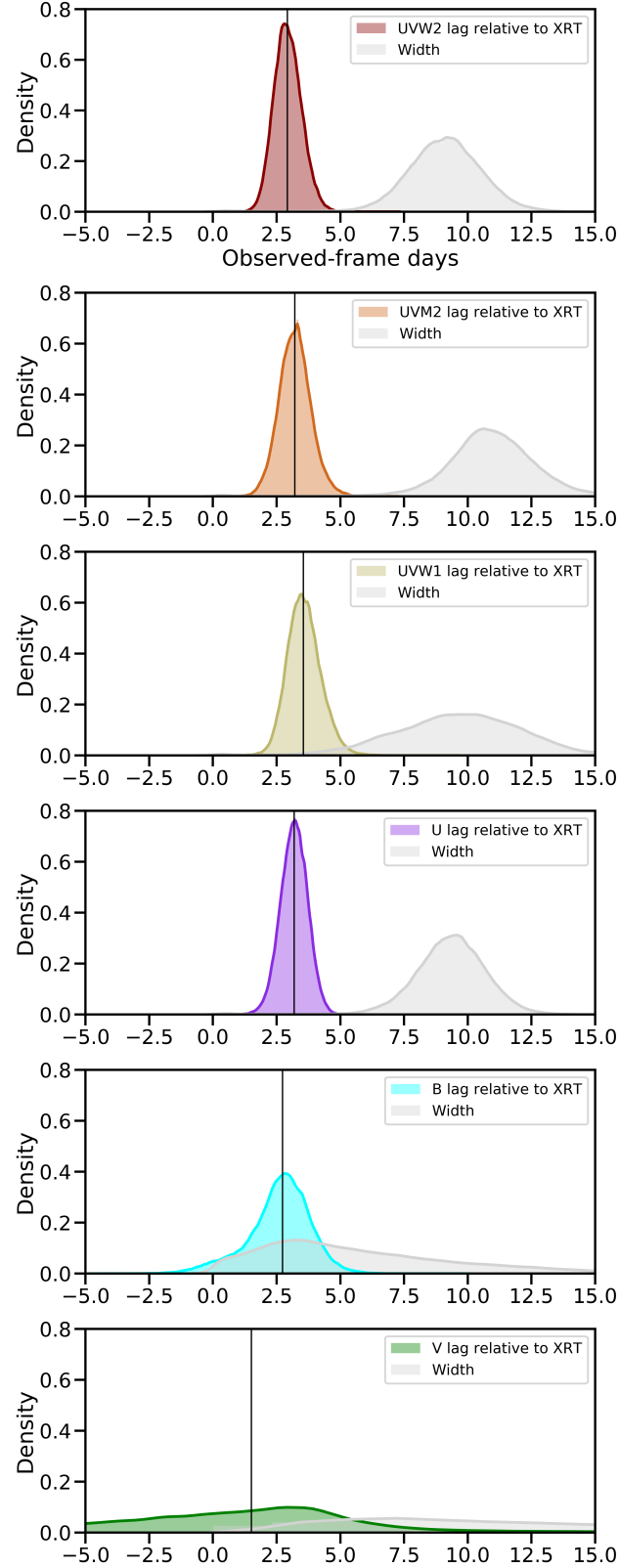
Fig. 3.9 Histograms of *Javelin* MCMC posterior lag distributions for each UVOT filter, relative to the XRT 0.3 - 10 keV lightcurve, during 1st July 2017 – 29th February 2018. The colored histograms represent the lag distributions, while the gray histograms represent the top-hat transfer function width distribution. The black vertical lines display the median lag for each band relative to the XRT lightcurve.
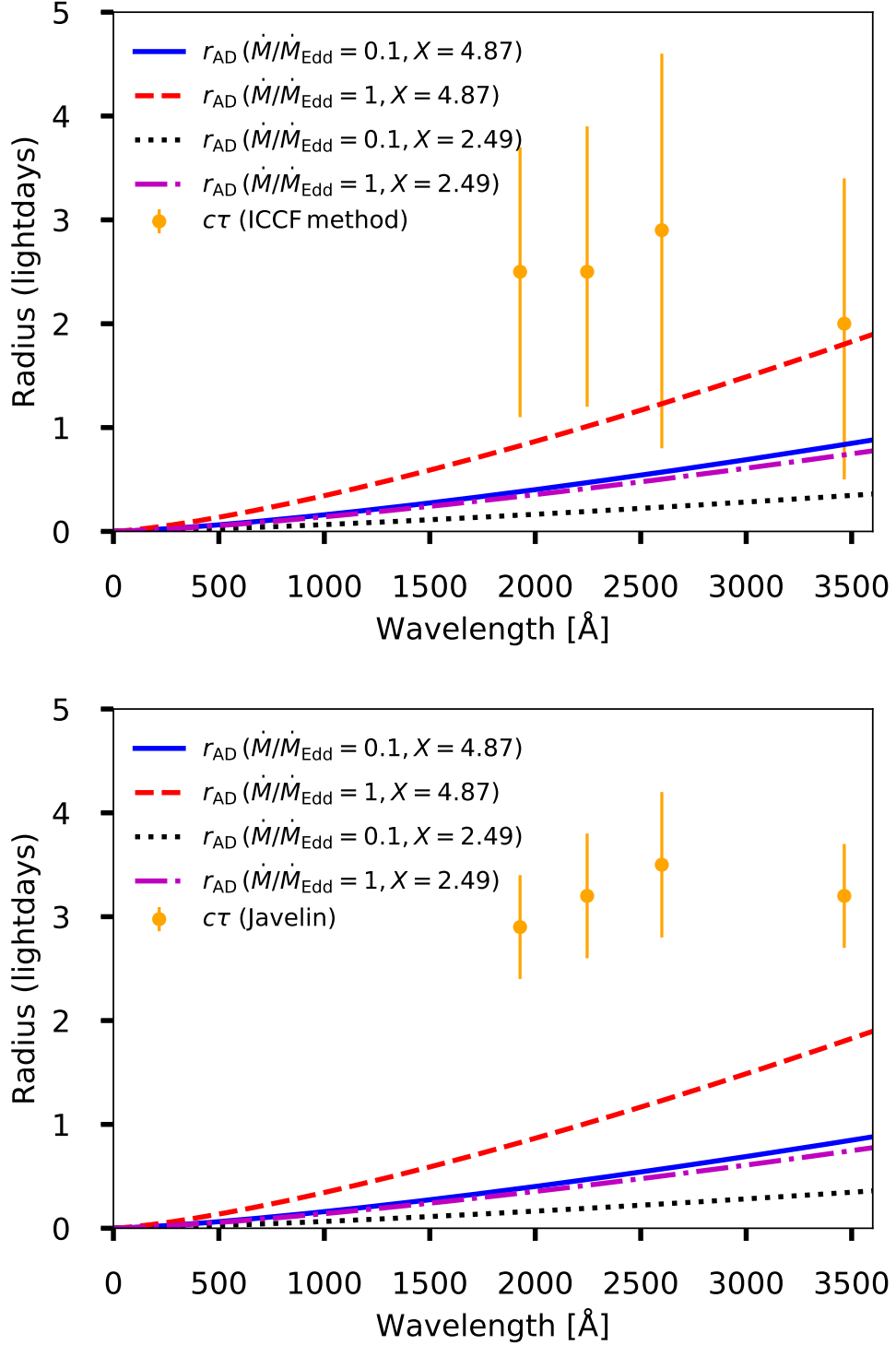
Fig. 3.10 Predicted radii of the accretion disk as a function of wavelength, for various combinations of Eddington ratios $\dot{M}/\dot{M}_{\mathrm{Edd}}$ and temperature scaling factors X, for the M_{BH} measured for Mrk 590 in reverberation mapping studies, and assuming a radiative efficiency $\eta = 0.1$. The data points show the measured UVOT lags *relative to the XRT lightcurve*, using the ICCF method (*top panel*) and the *Javelin* analysis (*bottom panel*). This corresponds to assuming that the X-ray emitting region is very close to the central black hole, in which case the measured XRT-UVOT lags will correspond roughly to the radii at which the UV emission is produced. In principle, our data are also consistent with a variable X-ray emitting region located $\sim$2 lightdays above and/or below the disk, as we do not detect a significant delay between the UVOT filters that would rule out this possibility.

The disk reprocessing model for UV variability predicts a strong correlation between the X-ray and UV lightcurves. Gardner and Done (2017) perform a simulation of variable hard X-ray continuum that is reprocessed in an accretion disk, for which they generate lightcurves and determine the cross-correlation functions for the X-ray to UV variability. They find that the correlation strength for this scenario is $R_{\mathrm{ICCF}} \sim 0.9$, i.e., an even higher correlation than I find for Mrk 590. To explain this discrepancy between their simulations and observational results, they suggest that the UV emission region may not be directly illuminated by the hard X-ray continuum. Instead, in their model a warm Comptonization region is responsible for the extreme-UV and soft X-ray excess emission. This region is 'puffed up' to a scale height much larger than that of the thermal disk, and obscures the hard X-ray corona as seen from the disk. In the context of this model, it is interesting to note that we do not detect a soft X-ray excess in our *Swift* XRT spectra for Mrk 590 (§3.2). If the soft X-ray excess indeed is emitted by a structure with large scale height that can obscure the outer disk, the lack of such a structure in Mrk 590 may explain the strong X-ray to UV correlation that we observe.

An alternative possibility is that the stronger correlation that I find for Mrk 590 is due to the difference in observational cadence for our *Swift* monitoring, relative to previous studies. The candence of our monitoring observations during this period is variable, with short periods of daily monitoring and longer periods of $\sim$ 2-day monitoring. Edelson et al. (2019) obtain an observational cadence of ~ 0.5 days with *Swift*. If the high-frequency UV variability is less strongly correlated with the X-rays relative to the lower-frequency component, our discrete sampling would overestimate the true correlation strength. Higher-cadence monitoring of Mrk 590 would be required to further investigate the anomalously strong X-ray to UV correlation.

The X-ray to UV time delay

My X-ray to UV timing analysis indicates a delay of roughly 2–3 days between the X-ray emitting and the UV-emitting regions. This delay is inconsistent with zero, based on the uncertainties derived from the JAVELIN analysis. If we interpret these delays purely in terms of light travel time, it implies that the UV-emitting region is located at a distance of $\sim$2 light-days with respect to the X-ray emitting region. The *sign* of the delay (i.e., that the UV lags the X-rays) implies that either the X-rays are directly responsible for the UV variations via reflection/reprocessing, or that the source of the driving emission component is located closer to the X-ray region than to the UV emitter. I also note that the $UW2$ to U band delays are identical to within their 1σ uncertainties, suggesting that their emitting regions are located at similar distances from the driving continuum.

I now examine these results in the context of the lamp-post disk reprocessing model (e.g., Cackett et al., 2007), using a standard Shakura and Sunyaev (1973) thin disk as the reprocessing medium. In this model, the X-ray continuum is emitted from a region very close to the central black hole. The disk temperature decreases as a function of radius, i.e., the longer-wavelength continuum is emitted from larger radii. The relationship between radius r_{AD}, continuum time delay τ_{AD} and continuum wavelength λ is presented by Edelson et al. (2017) and given by:

$$r_{\mathrm{AD}} = c\tau_{\mathrm{AD}} \approx 0.09 \left(X \frac{\lambda}{1928} \right)^{4/3} M_8^{2/3} \left(\frac{\dot{m}_{\mathrm{Edd}}}{\eta} \right)^{1/3}. \tag{3.1}$$

Here, M_8 is the black hole mass in units of $10^8 \, M_\odot$, $\dot{m}_{\mathrm{Edd}}$ is the ratio of the accretion rate to the Eddington rate, and η is the radiative efficiency. The accretion disk delay t_{AD} is in units of days. For Mrk 590, $M_8 = 0.37^{+0.06}_{-0.06}$ (Peterson et al., 2004). The radiative efficiency is unknown for Mrk 590; I assume $\eta = 0.1$, appropriate for accretion onto a black hole that is not rapidly rotating. The scaling factor X encapsulates the mapping from disk surface temperature to effective wavelength at a given accretion disk radius r. I investigate two values of X: firstly, $X = 4.87$ which is appropriate if the observed wavelength at a given r corresponds to the temperature given by Wien's Law, and secondly a more realistic assumption using a flux-weighted radius ($X = 2.49$) (Fausnaugh et al., 2016), which produces smaller r at a given wavelength.

The standard X-ray lamp-post model makes the following assumptions::

- The X-ray emitting region is very close to the black hole, i.e., at $r_{\mathrm{AD}} << 1$ lightday, corresponding to the highest observational cadence for our 2017–2018 monitoring.

- The observed X-ray to UV delay is due to light travel time between the X-ray emitting region and the accretion disk; there is no secondary reprocessing of X-ray emission.

- The wavelength-radius relationship derived from the α-disk model (Equation 3.1) is correct.

In that case, the measured X-ray to UV delays should correspond to r_{AD} for a given UV bandpass. Figure 3.10 illustrates that one or more of the above assumptions is incorrect for Mrk 590 during the 2017 accretion event. In this figure, the X-ray emission is assumed to be the driving continuum, and placed at $r_{\mathrm{AD}} = 0$. The X-ray to UV delays are then identified with r_{AD} at the central wavelength of each UVOT filter. Even at Eddington-limited accretion, and assuming $X = 4.87$, which yields the largest predicted disk size, the JAVELIN time delays for *UVW2* and *UVW1* are inconsistent with the model predictions. For $L_{\mathrm{bol}}/L_{\mathrm{Edd}} \approx 0.1$, the JAVELIN delays disagree strongly with the model radii, irrespective of the choice of flux-weighted radial scaling factor X.

Similar long X-ray to UV lags are found in some short-cadence AGN monitoring campaigns. In particular, the UV lags the X-ray by ~ 3 days for NGC 4151 (Edelson et al., 2017), strongly inconsistent with the lamp-post reprocessing model, while Cackett et al. (2018) find a ~ 0.4-day X-ray to 1150 Å lag for NGC 4593, which is only mildly inconsistent with the lamp-post model. For NGC 5548, McHardy et al. (2014) find a lag of ~ 0.7 days between XRT and *UVW2* lightcurves, while the X-ray to UV lag was not securely determined during the AGN STORM campaign (Fausnaugh et al., 2016). As discussed above, the X-ray to UV correlations reported in the literature are usually fairly weak, whereas I find a strong correlation for Mrk 590.

For the changing-look AGN NGC 2617, Shappee et al. (2014) find a ~ 2.2-day delay between the *Swift* XRT and *UVW2* lightcurves in 2013, as it entered its high state. Fausnaugh et al. (2018) find a ~ 2.6-day delay between the X-rays and UV for the same AGN one year later (2014), at which time its luminosity had fallen by a factor 1.8 compared to the 2013 outburst. Thus, a longer than expected X-ray to UV delay (relative to the lamp-post reprocessing model) is found for at least one other changing-look AGN. In the following, I discuss possible explanations for these long delays.

Non-standard accretion disk sizes?:   Recent results regarding the observed UV-optical continuum inter-band delays, and the X-ray to UV delays, challenge the disk size predictions of the thin-disk model. See the Introduction of the work presented in Chapter 2 for a full discussion thereon. For changing-look AGN that flare up from a very low accretion rate, there is an additional complication due to the unknown nature of the accretion disk during the changing-look event. For Eddington ratios less than ~ 0.01, the accretion disk is predicted to be in a geometrically thick, optically thin state (an ADAF state, e.g., Narayan and Yi, 1994). I estimate that the Eddington ratio increases from ~ 0.003 to ~ 0.02 during the 2017 flare (Figure 15 in the paper presented in §3.2). Thus, the onset of the flare might represent a change of accretion state. Non-standard accretion disks might be particularly relevant to changing-look AGN that have recently transitioned from, e.g., an advection-dominated state. However, the unexpectedly long X-ray to UV delays are observed in several non changing-look AGN, as noted above. I also note that the overall SED characteristics of Mrk 590 are consistent with those of bona fide AGN from the onset of the flare: the accretion disk is not unusually faint relative to non changing look AGN (§3.2). I therefore see no obvious reason to assume a link between the changing-look phenomenon and the X-ray to UV time delays.

Edelson et al. (2019) find that the inter-band UV delays (although not the X-ray to UV delays) are roughly consistent with the predictions of the disk model. Our *Swift* monitoring during 2017–2018 does not have sufficiently high observational cadence to detect inter-band delays, so a direct test of the expected behavior (i.e., longer-wavelengh bandpasses displaying larger time delays) is not possible. Given the uncertainties derived from my JAVELIN modeling, I cannot exclude the disk model for the UV bandpasses alone. I demonstrate this in Figure **??**, where I have subtracted 2.5 days from all delays, in order to (very roughly) account for the X-ray to UV lag. *Ignoring the anomalously long X-ray to UV delay*, our results are thus consistent with reprocessing in a standard thin disk, in that the inter-band delays are predicted to be too short for us to detect.

A distant X-ray emitting region?:   As the X-ray emitting region in AGN is known to vary coherently on timescales of $\sim$hours, it must be compact. The compact nature of the corona is confirmed by microlensing measurements (e.g., Reis and Miller, 2013, and references therein). However, the analysis presented here does not in itself constrain the location of the X-ray emitting region relative to the UV reprocessor. In principle, our measured delays are consistent with an X-ray 'lamp-post' located ~ 2 lightdays distant from the inner accretion disk. This would then explain the similar X-ray to UV lags detected for the four UVOT bands that display a correlation. It is also consistent with the non-detection of UV inter-band delays for our data, as the light travel time from a distant X-ray emitting region would be roughly equal for the inner and outer regions of the disk. However, Shappee et al. (2014) perform detailed modeling of the 'lamp-post' scenario for NGC 2617 (for which inter-band UV delays are detected, allowing this analysis). They find that an X-ray emitting region high above the accretion disk fails to generate the observed inter-band delays. They therefore argue against a purely geometrical interpretation of the long X-ray to UV delay.

Additional UV delay due to diffuse continuum contamination?:   In Chapter 2, we demonstrate that the *observed* continuum lags with respect to the ionizing continuum contain a significant
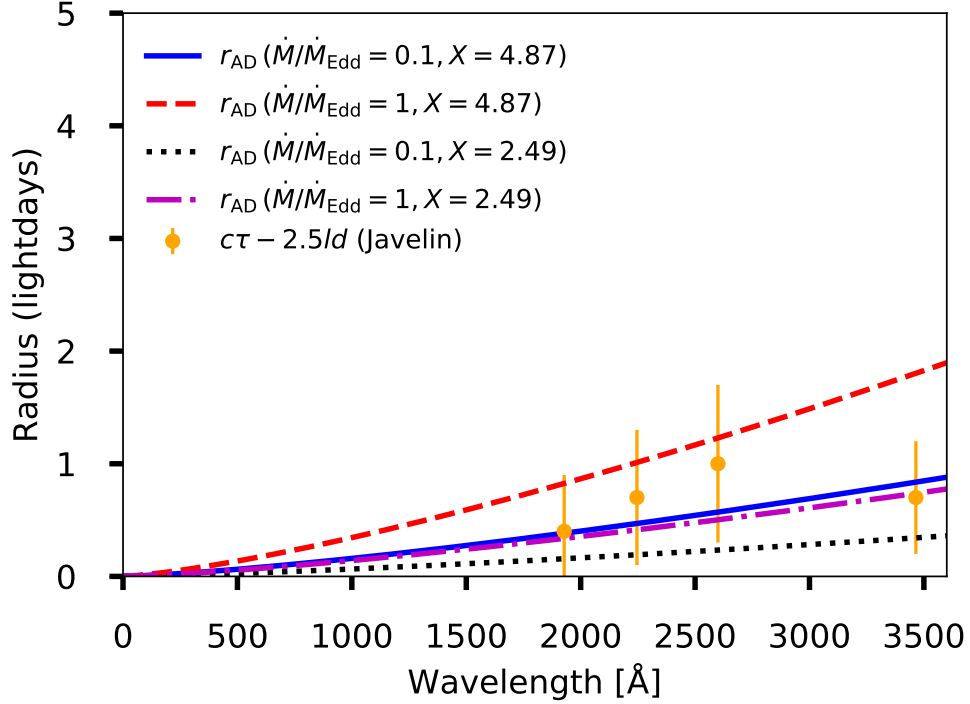
Fig. 3.11 As Figure 3.10, but here I subtract 2.5 days from all JAVELIN-derived X-ray to UV delays. This demonstrates that the difference in delays between the individual UV bands do not constrain the disk reverberation signature, as the uncertainties are too large.

additional lag component due to diffuse BLR continuum. Modeling of the diffuse continuum component for Mrk 590 is beyond the scope of this work (and in any case requires spectroscopic observations that constrain the BLR emission strength and its distance from the continuum source). I note, however, that the diffuse continuum contamination may induce an additional delay of order ~ 1 day at ~ 2000 Å for a Seyfert 1 AGN of comparable black hole mass (see Figure 16 in the work presented in Chapter 2).

An additional reprocessing between the X-ray source and the disk?:   For NGC 4151, Edelson et al. (2017) detect inter-band UV continuum delays that are consistent with the disk sizes predicted by the standard thin-disk model. However, they also detect long X-ray to UV delays. This latter finding is inconsistent with the lamp-post X-ray reprocessing model. They find that the elevated X-ray to UV delays are best explained by the Gardner and Done (2017) model. This model invokes an additional component that emits in the EUV and is identified with the soft X-ray excess component. The X-rays emitted from an X-ray corona near the central black hole illuminate this EUV component. The observed X-ray to UV lag is then consistent with evolution of the EUV component on the dynamical timescale of the EUV-emitting region (i.e., 1–3 days, for black hole masses $\sim 10^7 M_\odot$). Physically, the EUV-emitting region might need to 'puff up' to a certain minimum scale height in order to illuminate the outer thin-disk region. This scale height evolution would occur on the local dynamical timescale.

If such a second reprocessing region is present in Mrk 590 and causes the long X-ray to UV delay in 2017, the purported 'puffed-up' inner disk EUV component presumably reappeared at some point during 2015–2017, as the UV emission was very faint in 2014. However, the only evidence currently supporting the existence of a second reprocessing region for Mrk 590 is the X-ray to UV lag. As discussed above, the Gardner and Done (2017) model does *not* predict the strong X-ray to UV correlation displayed by Mrk 590 during 2017–2018. We also find no evidence of soft X-ray excess in our joint analysis of *Swift* and *NuSTAR* spectra (**?**), although our collaborators do find evidence of a faint soft excess in their July 2020 *XMM-Newton* observations (G. Miniutti, private communication). Future analysis of these *XMM-Newton* observations will place better constraints on the presence of a soft excess component.

3.4.5   Summary of timing analysis

I have presented an X-ray and UV timing analysis of our short-cadence *Swift* XRT and UVOT monitoring of Mrk 590 during the 2017–2018 flare-up. This analysis reveals a ~ 2.5–day X-ray to UV delay, in agreement with previous *Swift* monitoring results for a handful of AGN, including the changing-look AGN NGC 2617. This delay is significant at the $> 3\sigma$ level based on the uncertainities derived using JAVELIN. This long X-ray to UV delay is inconsistent with the 'lamp-post' disk reprocessing model for AGN continuum variability, if we assume that the X-rays are the driving continuum. One possible explanation is that the X-rays do not directly illuminate the disk, but instead illuminate a secondary reprocessing structure that then illuminates the disk Gardner and Done (2017). However, the X-ray lightcurve is strongly correlated with the UV variability, with correlation strength $R_{\mathrm{ICCF}} > 0.8$ for all UVOT bands, according to the ICCF analysis. This strong correlation is not expected for the Gardner and Done (2017) scenario. I conclude that Mrk 590 displays a long UV to X-ray lag that is a common result of *Swift* monitoring campaigns for other AGN, but that its X-ray to UV correlation strength is anonamously high. The physical mechanisms that produce this behavior are not yet fully understood.

Chapter 4

A *Hubble Space Telescope* Imaging Study of Four FeLoBAL Quasar Host Galaxies

The work presented in this chapter is originally published by MNRAS, with the title 'A *Hubble Space Telescope* Imaging Study of Four FeLoBAL Quasar Host Galaxies' (MNRAS 475, 3213–3239). The authors are Daniel Lawther, Marianne Vestergaard and Xiaohui Fan.

The main scientific question addressed by this paper is:

- Do FeLoBAL quasars represent those sources that we happen to observe at a particular evolutionary stage, e.g., young quasars? Or are they intrinsically 'ordinary' quasars observed at a particular narrow range of inclinations relative to the accretion disk, and/or relative to outflowing material? In particular, do the properties of FeLoBAL host galaxies suggest that they are an intrinsically separate population? Is there evidence that FeLoBAL host galaxies have experienced recent (or ongoing) mergers?

The practical questions addressed by this paper are:

- How well can we measure quasar host galaxy properties in observed-frame NIR imaging, for sources at redshifts $z > 0.8$, given the available data and PSF models?

- How sensitive are our *HST* NICMOS observations to signs of recent galaxy interactions for these $z > 0.8$ quasars?

- Which additional observations are required in order to exclude that the FeLoBAL host galaxies are recent mergers and/or harbor ongoing starburst activity?

4.1   Differences to M.Sc. Thesis Work

My M.Sc. thesis (Lawther 2013, University of Copenhagen) describes a pilot project to determine the host galaxy properties in the same four FeLoBAL quasars addressed in this Chapter, using the same *Hubble* Space Telescope observations. As discussed in §6.5 of Lawther 2013, the results of

this pilot study were fraught with large uncertainties, primarily due to the lack of bright Point Spread Function (PSF) star observations with which to model the point-source emission due to the active nuclei. Significant background structure in the imaging data also limited our ability to determine the host galaxy brightnesses at that time (Lawther 2013, Appendix C). As part of my PhD project, I have expanded on the original pilot study in several ways in order to address these issues.

The work described in §3.1 and §4.2 of the attached journal publication (Lawther et al., 2018b) is originally presented by Lawther 2013; the quantitative results in these sections are unchanged. All other work included in the published article was performed as part of my Ph.D study. My conclusions with regards to the quasar host galaxies are qualitatively different, and more robust to modeling uncertainties, compared to the preliminary investigation presented by Lawther 2013. However, several analysis approaches applied in this thesis are originally presented by Lawther 2013. To avoid any ambiguities with regards to the extent of my PhD work on FeLoBAL quasars, I include a detailed statement delineating the two projects, as follows.

HST ACS (rest-frame ultraviolet) imaging data: Data processing and analysis for the ACS observations are originally presented by Lawther 2013, and included as-is by Lawther et al. (2018b). This includes the ACS image combination using the MULTIDRIZZLE software, and the Point Spread Function (PSF) modeling analysis of ACS imaging using the GALFIT software. Thus, the work presented in §3.1 of Lawther et al. (2018b) should *not* be considered part of my PhD study for purposes of assessment.

ACS simulation study: Given that we do not detect host galaxies in the ACS observations, the initial proof-of-concept simulation design presented by Lawther 2013 proved adequate to determine upper limits on host galaxy brightness. Thus, the work presented in §4.2 of Lawther et al. (2018b) should *not* be considered part of my PhD study for purposes of assessment.

HST NICMOS (rest-frame optical) imaging data: The NICMOS data processing as presented by Lawther 2013 is not used by Lawther et al. (2018b). This is due to difficulties in obtaining a precise determination of the sky background for the NICMOS imaging during the initial pilot study. I subsequently developed the more robust method used in the final analysis (Lawther et al., 2018b, §3.2). For technical reasons, *all* NICMOS data processing steps, including the initial pipeline processing using the PYRAF task *'calnica'* and image combination using MULTIDRIZZLE, are redone in order to incorporate the new treatment of the sky background.

NICMOS host galaxy analysis: The 'two-step' PSF and host galaxy modeling described by Lawther 2013 was motivated by two difficulties regarding the NICMOS data. Firstly, I lacked detailed knowledge of the behavior of available PSF models as used in the GALFIT modeling. Secondly, the sky background in the imaging data displayed significant residual structure. My PhD work addresses the first issue via a series of simulations using various combinations of the available PSF models. The second issue is alleviated by the improved NICMOS image processing described above. This allows me to simultaneously constrain the host galaxy and PSF brightness in my final

GALFIT analysis. Thus, the NICMOS image analysis methodology in the final analysis differs significantly from that presented by Lawther 2013, as do the quantitative results.

NICMOS simulation study: For the initial proof-of-concept NICMOS simulation study (Lawther 2013), I used analytical galaxy surface brightness functions to represent quasar host galaxies; such models proved sufficient to constrain host galaxy brightnesses for the non-detections in ACS observations. However, we do detect faint extended emission in the NICMOS imaging for three FeLoBALs. For my GALFIT analysis of the rest-frame optical imaging to be robust, it is vital that the uncertainties due to modeling distant, faint quasar hosts are quantified. In this context, use of analytical profiles is likely to underestimate the uncertainty on the host galaxy brightness, as real galaxies deviate from analytical profiles. The low signal-to-noise of available PSF models for the NICMOS imaging generates an additional systematic uncertainty in the host galaxy modeling. To address these concerns, I designed a comprehensive suite of simulated quasar observations using the FERENGI software. Thus, all NICMOS simulation work presented by Lawther et al. (2018b) is performed as part of my PhD study.

Template scaling to constrain star formation in the FeLoBAL hosts: Lawther 2013 applied spectral template scaling in an attempt to determine whether the host galaxies of the FeLoBAL quasars are starbursting, based on the preliminary GALFIT modeling results. While I apply the same basic template-scaling approach in my PhD work, the data are entirely re-analyzed. This resulted in quantitatively different results, due to the new, more robust constraints on the host galaxy rest-frame optical brightnesses developed during my PhD project.

Analysis of FeLoBAL quasar environments: In order to fully address the nature of FeLoBAL host galaxies, Lawther et al. (2018b) present a study of the environments of the four FeloBAL quasars. The entirety of this analysis is performed during my PhD project.

I include a signed statement of authorship with this Thesis (Chapter 8).

4.2 Published Work

A *Hubble Space Telescope* imaging study of four FeLoBAL quasar host galaxies

D. Lawther,[1][*] M. Vestergaard[1,2] and X. Fan[2]

[1]*Dark Cosmology Centre, Niels Bohr Institute, University of Copenhagen, Juliane Maries vej 30, DK-2100 Copenhagen ϕ, Denmark*
[2]*Steward Observatory, University of Arizona, 933 N. Cherry Avenue, Tucson, AZ 85721, USA*

ABSTRACT

We study the host galaxies of four Iron Low-Ionization Broad Absorption-line Quasars (FeLoBALs), using *Hubble Space Telescope* imaging data, investigating the possibility that they represent a transition between an obscured active galactic nucleus (AGN) and an ordinary optical quasar. In this scenario, the FeLoBALs represent the early stage of merger-triggered accretion, in which case their host galaxies are expected to show signs of an ongoing or recent merger. Using PSF subtraction techniques, we decompose the images into host galaxy and AGN components at rest-frame ultraviolet and optical wavelengths. The ultraviolet is sensitive to young stars, while the optical probes stellar mass. In the ultraviolet we image at the BAL absorption trough wavelengths so as to decrease the contrast between the quasar and host galaxy emission. We securely detect an extended source for two of the four FeLoBALs in the rest-frame optical; a third host galaxy is marginally detected. In the rest-frame UV we detect no host emission; this constrains the level of unobscured star formation. Thus, the host galaxies have observed properties that are consistent with those of non-BAL quasars with the same nuclear luminosity, i.e. quiescent or moderately star-forming elliptical galaxies. However, we cannot exclude starbursting hosts that have the stellar UV emission obscured by modest amounts of dust reddening. Thus, our findings also allow the merger-induced young quasar scenario. For three objects, we identify possible close companion galaxies that may be gravitationally interacting with the quasar hosts.

Key words: quasars: general – galaxies: star formation.

1 INTRODUCTION

Considering the central gravitational potentials required to power quasar activity, galaxies that have harbored quasars should host inactive 'relic' black holes with masses of order $10^8 \, M_\odot$ today (Soltan 1982). Indeed, studies of stellar dynamics in galaxy bulges reveal that most or all massive galaxies at low redshift contain a central supermassive black hole (SMBH) with masses of approximately 10^6–$10^9 \, M_\odot$ (e.g. Kormendy & Gebhardt 2001). Unless there are alternative ways of growing black holes to such high masses, the ubiquity of inactive SMBHs suggests that most galaxies underwent an active phase at some point in their lifetimes. Given the large energy output involved, the onset of quasar activity may affect the evolution of the ambient gas (and therefore, the future star formation). The observed correlations between black hole mass and host galaxy bulge luminosities and stellar velocity dispersions (e.g. Magorrian et al. 1998; Ferrarese & Merritt 2000; Tremaine

et al. 2002; Marconi & Hunt 2003; Gültekin et al. 2009) support this picture. Therefore, to understand the evolution of massive galaxies, we need to understand the quasar phase.

However, the triggering mechanisms for quasar activity are as yet poorly understood. Several authors have proposed that galaxy mergers may trigger quasar activity by forcing large amounts of gas to sink towards the SMBH at the centre of the galaxy, and that the subsequent quasar activity may subsequently expel some of this gas through radiation pressure (e.g. Sanders et al. 1988; Fabian 1999). This scenario has been explored in numerical simulations of galaxy mergers including supermassive black hole components capable of accreting gas and exerting feedback on their surroundings (e.g. Barnes & Hernquist 1991; Di Matteo, Springel & Hernquist 2005; Hopkins et al. 2005); the feedback prescriptions applied may represent direct radiation pressure due to the central source or kinetic feedback from outflowing gas launched at small radii. According to the simulations performed by Hopkins et al. (2005), merger-triggered quasars are intrinsically brightest around the time at which the two galaxies coalesce. However, this phase also displays the highest gas column densities ($N_\mathrm{H} \gtrsim 10^{24} \, \mathrm{cm}^{-2}$)

along the line of sight to the black hole. Thus, the intrinsically most luminous quasar phase is heavily obscured to a distant observer. As the quasar exerts radiative feedback on the obscuring gas and dust at the centre of the host galaxy, it becomes detectable as a reddened quasar, before entering an unobscured phase, and eventually becomes quiescent as the lack of gas in the nucleus starves the SMBH of fuel.

How would this young evolutionary phase reveal itself to observations? Glikman et al. (2012) find that the reddest quasars at a given redshift tend to be intrinsically the most luminous, as expected for the scenario described above. Urrutia, Lacy & Becker (2008) and Glikman et al. (2015) show that the reddest quasars (at $z < 1$ and $z \approx 2$, respectively) tend to show disturbed morphologies, indicative of recent or ongoing merger activity. However, Mechtley et al. (2016) demonstrate that inactive galaxies at $z \approx 2$ show evidence of merger activity at a similar rate to quasar hosts. This raises the possibility that the 'red quasars' found by Glikman et al. (2015) tend to be merger-hosted simply due to their selecting[1] heavily reddened quasars, where the excess reddening is due to merger-fueled starburst activity, with no causal relationship between the active galactic nucleus (AGN) activity and the merger. As noted by Cisternas et al. (2011), the interpretation of the observed merger fractions depends critically on our knowledge of the time-scales involved for the (observable) merger and quasar activity.

An alternative approach is to search for observational evidence of the purported 'blowout' phase. Broad Absorption Line (BAL) quasars, which display outflow velocities ranging from $\sim 2000\,\mathrm{km\,s^{-1}}$ up to $\sim 0.1c$, have been considered as candidate transition objects (e.g. Weymann et al. 1991). They are classified as high-ionization BAL quasars (HiBALs), which display broad absorption only in high-ionization lines such as C IV $\lambda 1549$, or as low-ionization BAL quasars (LoBALs), which additionally display broad absorption in low-ionization transitions such as Mg II λ 2798. FeLoBALs are a subclass of LoBAL quasars that display absorption in excited states of Fe II and Fe III in addition to the LoBAL absorption lines (e.g. Becker et al. 1997; Hall et al. 2002).

In the context of AGN unification scenarios, some authors have proposed that BAL outflows may be present in all quasars, but are observed only in absorption at certain orientation angles (e.g. Elvis 2000). This orientation-based model is supported by the work of Gallagher et al. (2007), who find the mid-infrared emission in HiBAL and non-BAL quasars to be statistically indistinguishable; Schulze et al. (2017) also find this for LoBAL quasars in the redshift range $0.6 < z < 2.5$. This argues against a large covering fraction for the BAL-absorbing material. Conversely, based on the lower levels of [O III] observed for LoBALs, Voit, Weymann & Korista (1993) suggest that the BAL absorbing material has a high covering fraction, and speculate that LoBALs may be young quasars in the process of expelling an optically thick cocoon of gas and dust; we note, however, that Schulze et al. (2017) do not find significantly reduced [O III] emission in stacked $z \sim 1.5$ LoBAL spectra. Canalizo & Stockton (2001) find a connection between LoBALs and merger-triggered Ultraluminous Infrared Galaxies at low redshift: three out of six of their objects for which the BAL status could be unambiguously tested are indeed LoBALs. Indeed, FeLoBALs are overrepresented amongst the reddest quasars (Urrutia et al. 2009; Glikman

et al. 2012), suggesting that FeLoBAL activity may play a role in the proposed transition scenario. Interestingly, Farrah et al. (2012) report an anticorrelation between absorption strength and star formation activity for a sample of 31 FeLoBALs observed with the *Spitzer Space Telescope*. This finding adds observational support to suggestions (e.g. Granato et al. 2004) that the kinetic feedback due to LoBAL outflows may represent the sought-after quenching mechanism for star formation in massive galaxies. Such quenching is otherwise often modelled using a semi-empirical AGN feedback prescription (e.g. Bower et al. 2006; Croton et al. 2006). On the other hand, recent detections of FeLoBAL variability are best explained by a low covering fraction for BAL absorption, with the BAL-absorbing gas situated at $\sim$pc radii from the central black hole (Vivek et al. 2012; McGraw et al. 2015). Such findings are difficult to reconcile with a scenario where BAL outflows provide galaxy-wide quenching of star formation.

One way to test the evolutionary scenario for FeLoBAL quasars is to compare their host galaxy properties to those of non-BAL quasars. If the FeLoBAL absorption is intrinsically present in all quasars but with a small covering factor, e.g. in the disc-wind scenario of Elvis (2000), their host galaxies are expected to be massive elliptical galaxies with little recent star formation, as seen for non-BAL quasar hosts at $z \lesssim 0.2$ (e.g. Nolan et al. 2001; Dunlop et al. 2003), or perhaps massive ellipticals that are still actively star-forming at rates of $\sim 100\,\mathrm{M_\odot\,yr^{-1}}$ (Floyd et al. 2012).[2] On the other hand, if FeLoBALs are young quasars triggered by mergers, they may display merger-triggered starburst activity, and/or display interacting companion galaxies or highly disturbed morphologies due to recent interactions. Here we present *Hubble Space Telescope* (*HST*) imaging data for four overlapping-trough FeLoBAL quasars, as defined by Hall et al. (2002). These objects are so strongly absorbed by Fe II and Fe III that their ultraviolet (UV) spectra are barely recognizable as quasar spectra (Fig. 1). The quasar continuum emission is reduced by a factor ~ 10 for these objects. Assuming that the BAL obscuration is centrally concentrated and does not absorb the host galaxy emission, this will reduce the nucleus-to-host brightness contrast when using a filter that covers the deepest BAL absorption. Thus, the heavy attenuation of the UV nuclear emission aids our study of the host galaxy stellar populations.

This paper is structured as follows. In Section 2 we outline our sample selection criteria and describe the *HST* observations. We describe the image processing in Section 3. In Section 4 we describe our image decomposition strategy and present the host galaxy modelling results. We discuss our findings with regard to the nature of the FeLoBAL host galaxies in Section 5. We use a cosmology with *Hubble* constant $H_0 = 67.8 \pm 0.9\,\mathrm{km\,s^{-1}\,Mpc^{-1}}$ and matter density parameter $\Omega_\mathrm{m} = 0.308 \pm 0.012$ throughout.

2 SAMPLE SELECTION AND *HST* IMAGING OBSERVATIONS

2.1 FeLoBAL quasar sample selection

One important objective of this study is to measure the rest-frame UV and optical brightnesses of FeLoBAL host galaxies, in an effort to characterize the stellar population. We expect the quasar continuum emission to outshine the host galaxy in the rest-frame UV,

---

[1] The FIRST-2MASS sample is detected in 20 cm and in 2 micron surveys, while being optically faint; details of their selection criteria are presented by Glikman et al. (2012).

[2] For $2 < z < 3$ AGN, star formation rates appear to increase with the luminosity of the central source, reaching $\sim 600\,\mathrm{M_\odot\,yr^{-1}}$ for the brightest quasars (Harris et al. 2016).
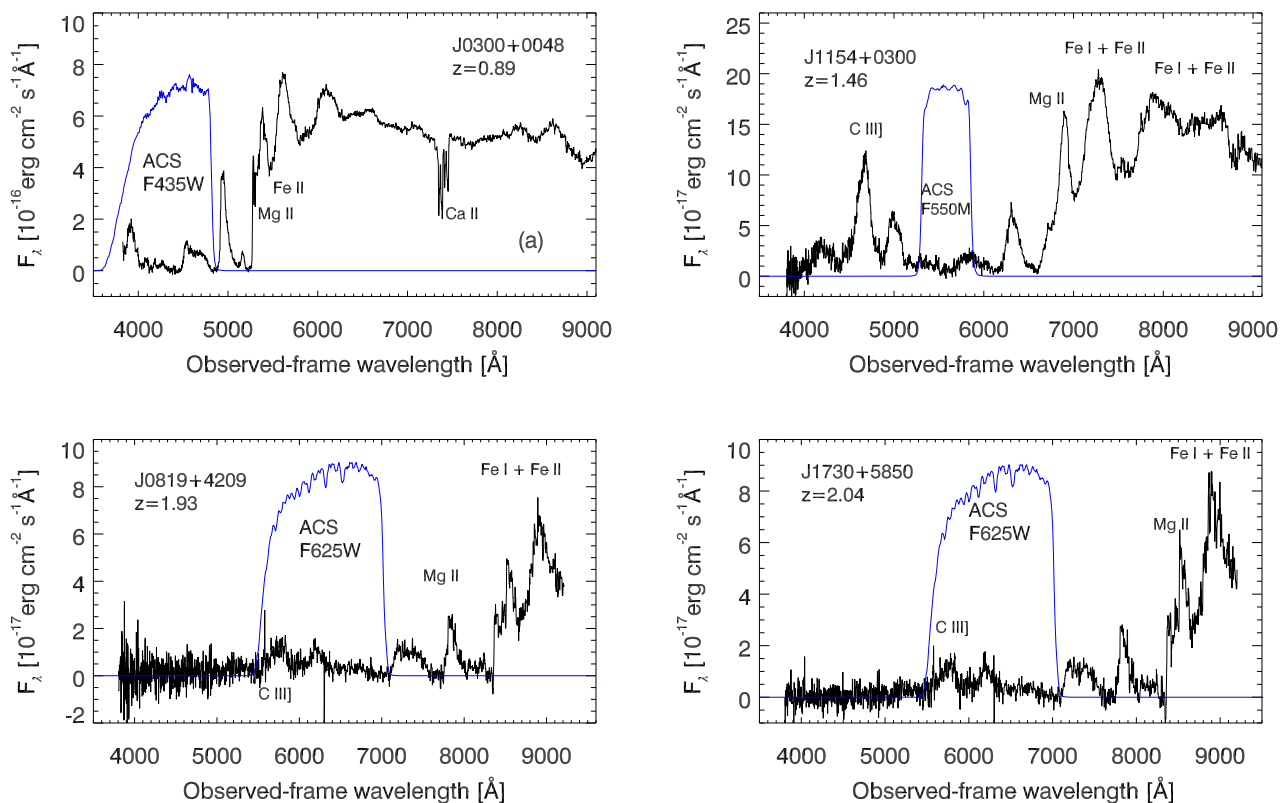
Figure 1. SDSS Data Release 8 spectra of the four FeLoBAL quasars in our sample, demonstrating our utilization of the 'natural coronagraph' offered by the BAL absorption (Section 2.1). The flux densities are median-smoothed using a 5-pixel smoothing window. The (arbitrarily scaled) throughput curve of the ACS/WFC broad-band filter chosen for each quasar is shown as a blue curve. While we show selected emission line identifications here, we direct the reader to Hall et al. (2002) for detailed redshift determinations.

especially if the stellar population is quiescent and therefore faint in the UV (e.g. Kinney et al. 1996; Bruzual & Charlot 2003). Host galaxy detection is therefore challenging for these high-redshift quasars. The very broad absorption troughs of FeLoBAL quasars may provide a 'natural coronagraph' effect aiding host galaxy detection. If the absorbing material is concentrated near the nucleus, as generally expected due to the high velocities of the BAL-absorbing gas being attributed to the central engine (although cf. Faucher-Giguère, Quataert & Murray 2012), the nuclear emission will be absorbed more heavily than that of the host galaxy. In this study, we therefore select rest-frame UV filter bandpasses that coincide with the BAL absorption, with the aim of reducing the nuclear-to-host brightness contrast.

Due to their red colours, heavily-absorbed FeLoBAL quasars are often selected as serendipitous targets (as opposed to quasar candidates) by the Sloane Digital Sky Survey (SDSS; York et al. 2000) photometric selection pipeline (Stoughton et al. 2002). To identify unusual BAL quasars, Hall et al. (2002) perform a visual inspection of all spectra which could not be identified in an automated fashion by the SDSS Early Data Release (EDR) spectroscopic pipeline, along with a re-inspection of all objects identified as quasars. These authors find 18 unusual BAL quasars in the EDR, along with two unidentified objects that may or may not be BALs. We select our FeLoBALs from this sample of unusual objects. The authors note that this sample is not statistically complete, as the EDR selection criteria varied during the spectroscopic observing campaign. The total number of quasar spectra in the EDR is ∼8000. However, the observed rarity of these 'unusual BALs' relative to ordinary quasars is likely to be extremely sensitive to selection effects.

Our main selection criterion is that the BAL trough should be sufficiently broad and deep that we can utilize the 'natural coronagraph' effect for our UV broad-band imaging observations. The 'overlapping-trough' class of FeLoBAL quasars, five of which are presented by Hall et al. (2002), fulfill this requirement: J0300+0048, J1154+0300, J0819+4209, J1730+5850, and J0437-0045. One of these objects, J0437-0045 located at $z = 2.82$, was not selected as it would require more than 4 orbits to be detected with NICMOS. The remaining four FeLoBAL objects, residing at $0.89 \leq z \leq 2.04$, were observed under the *HST* GO-10237 program (PI: X. Fan). Fig. 1 shows the rest-frame optical-UV spectra of the four FeLoBAL quasars, extracted from the SDSS Data Release 8. The imaging filters selected for the ACS/WFC observations are overlaid.

We use the redshifts provided by Hall et al. (2002), who present detailed discussion of this issue. The redshift determination is secure (if perhaps imprecise) for J0300+0048, as it is based on intrinsic Ca II absorption, and confirmed by broad Hydrogen emission lines. For J1154+0300, the redshift is based on various optical iron emission lines redwards of Mg II. For the remaining objects, the redshift is less secure, as it is based on various emission and absorption features in the BAL-absorbed part of the spectrum, where the continuum level is unknown.

2.2 *HST* observations

Each FeLoBAL quasar was observed in Cycle 13 in two *HST* imaging bands, covering the rest-frame optical (with NICMOS) and UV (with ACS) wavelengths. The rest-frame optical regime is sensitive to the stellar mass, while the rest-frame UV is sensitive

Table 1. Observation log.

Object (1)	Observation date (2)	Redshift (3)	Filter (4)	Number of orbits (5)	Number of exposures[a] (6)	Total exp. time (s) (7)	10σ detection limit (mag)[b] (8)
			ACS/WFC				
J0300+0048	2004-12-10	0.89	F435W	1	4	2185	27.0
J1154+0300	2005-05-16	1.46	F550M	2	4	5141	26.9
J0819+4209	2004-11-21	1.93	F625W	3	6	8150	27.9
J1730+5850	2006-12-09	2.04	F625W	4	5	6517	27.7
			NICMOS/NIC2				
J0300+0048	2004-12-30	0.89	F110W	1	5	2688	25.2
J1154+0300	2007-02-11	1.46	F110W	2	10	5887	25.9
J0819+4209	2005-02-19	1.93	F160W	3	12	8695	25.6
J1730+5850	2006-12-09	2.04	F160W	4	4	8191	25.9

Notes. [a]The total number of exposures across all dither points. All observations were performed using a 4-point dither pattern, albeit distributed over several orbits. Due to an instrumental failure, the ACS observations of J1730+5850 lack the final exposures granted, and the dither pattern is unevenly sampled. [b]The 10σ detection limit for a point source in the combined image for this observation, calculated based on the standard deviation of the background level as measured in the combined images.

to ongoing star formation. For both instruments, the observations were performed using a 4-point dither pattern utilizing non-integer pixel shifts. This allows us to identify cosmic ray hits and hot/cold pixels during image combination, and provides an improved spatial resolution in the combined images. The dither patterns 'ACS-WFC-DITHER-BOX' and 'NIC-SPIRAL-DITH' were used for the ACS/WFC and NICMOS observations, respectively.[3] Table 1 summarizes the observations, including the imaging filters and exposure times adopted for each source .

ACS/WFC. Imaging of the rest-frame UV regime was obtained using the Advanced Camera for Surveys (ACS) Wide Field Camera (WFC). The ACS/WFC has a pixel scale of $0.05\,\mathrm{arcsec}^2$ and a 202×202-arcsec field of view. When selecting a filter to utilize the 'natural coronagraph' effect, we considered both the absorption strength and the observing efficiency. Although the use of narrowband filters would maximize the integrated absorption strength in the bandpass, we elect to use broad- or medium-band filters, so as to avoid unreasonably long exposure times. We estimate that the quasar continuum emission is reduced by a factor of 7–15 in the selected ACS/WFC filters for objects J0300+0048 (Fig. 1). The intrinsic continuum levels in the relevant bandpasses are difficult to determine for the other quasars, as the SDSS spectra lack regions of unabsorbed continuum emission.

NICMOS. The *HST* Near Infrared Camera and Multi-Object Spectrometer (NICMOS) was used to observe rest-frame optical wavelengths. The NICMOS 2 detector (hereafter NIC2) has a pixel size of 0.076 arcsec × 0.075 arcsec, and a 19.2 arcsec × 19.2 arcsec field of view. The PSF core FWHM is around 0.14 arcsec for wavelengths below ∼1.6 μm, i.e. the images are somewhat undersampled for the bluer NIC2 filters.[4] Due to lack of spectral coverage in the rest-frame optical, we do not have the opportunity to utilize a 'natural

coronagraph' effect here. On the other hand, we expect a smaller intrinsic (i.e. unabsorbed) nucleus-to-host contrast in our NICMOS imaging, as we expect the host galaxies to be brighter, and the quasar power-law continuum fainter, in the rest-frame optical relative to the UV. While the host galaxy is brightest relative to the active nucleus at near-infrared wavelengths ∼1 μm, we chose somewhat bluer bandpasses so as to allow a robust comparison with quasar host samples available at the time of our *HST* proposal (Section 5.1). We select broad-band filters, as a high signal-to-noise ratio is required for our image decomposition analysis. These bandpasses also cover the [O III] narrow emission line. As the narrow line-emitting region can extend to kpc scales for some AGNs (e.g. Pogge 1989), there is a risk of contamination of the host galaxy signal. However, LoBAL quasars generally display weak [O III] emission (Weymann et al. 1991), mitigating this issue.

Limiting apparent magnitudes. The limiting apparent magnitudes reached for a 10σ detection of a point source for each observation is listed in Table 1. Our observations have a depth equal to or greater than that of the NICMOS imaging of the quasar samples of Kukula et al. (2001) and Hutchings et al. (2002) at similar redshifts. This allows a robust comparison to these studies, which were state of the art at the time of our *HST* proposal; we also reach a similar depth to later studies that are better matched to our sample in terms of AGN luminosity (Section 5).

2.3 Point spread function star observations

No separate point spread function (PSF) star observations were performed for this *HST* observing program; our original intention was to use analytical PSF templates for this purpose. However, the current consensus on such models is that they do not reproduce the PSF core accurately, and therefore perform poorly in PSF-host decomposition studies of bright quasars (e.g. Kim et al. 2008; Mechtley et al. 2012). We confirm these findings in a series of preliminary tests (Appendix A). We therefore use stellar observations as PSF models in this study. For the ACS imaging we construct a stacked PSF template using stars observed in the ACS field during the science observations. For the NICMOS imaging we stack archival stellar observations performed within 3 months of the science observation. We discuss our PSF modelling strategies and considerations,

---

[3] To allow observations to be distributed over multiple orbits, the dither pattern was in some cases implemented using the POS-TARG mode. However, the resulting pixel offsets and exposure time distributions are the same as for the specified standard dither patterns.

[4] For two quasars we are able to achieve Nyquist sampling in our MULTIDRIZ-ZLE -combined images, see Section 3.3.

including the selection criteria for PSF star observations in each bandpass, in Appendix A.

3 PROCESSING AND CALIBRATION OF THE DATA

We calibrate the individual exposures using tools from the PYRAF/STSDAS[5] package *hst_calib*; we outline this calibration for ACS/WFC and NICMOS/NIC2 in Sections 3.1 and 3.2, respectively. After calibrating the individual images, we combine the individual exposures for a given quasar using the MULTIDRIZZLE package (Section 3.3), thereby obtaining a single, combined ACS/WFC image and a single, combined NICMOS/NIC2 image for each quasar.

3.1 ACS individual exposure image calibration

We calibrate the ACS/WFC imaging data following the method of the ACS pipeline calibration, as outlined in the ACS Data Handbook (Gonzaga 2011). We process the raw imaging data using the *calacs* script, version 2012.2; this version includes a correction for charge transfer efficiency degradation. Cosmic ray hits and hot/cold pixels are identified in an automated fashion during a preliminary processing using the MULTIDRIZZLE algorithm (Section 3.3). Upon visual inspection of the single-exposure images, we identified and flagged a few additional bad pixels not identified as such by the MULTIDRIZZLE processing. These included several 'hot pixels' that were not included in the static bad pixel mask for the detector, and that are not bright enough to be flagged by MULTIDRIZZLE .

3.2 NICMOS individual exposure image calibration

The NICMOS images display signatures of detector anomalies that require treatment in addition to the pipeline processing. These anomalies are common in NICMOS data, and are described in detail in the NICMOS Data Handbook (Thatte et al. 2009). We process the raw images using the PYRAF/STSDAS script *calnica*. Here we briefly describe the additional processing steps applied.

Pedestal offset and amplifier glow. The single-exposure images display a residual flat-field pattern due to the so-called pedestal offset. As advised by Thatte et al. (2009), we apply the *biaseq* script partway through the *calnica* processing, and apply the task *pedsub* after *calnica* processing. The *biaseq* task is designed to remove the non-linear component of the NICMOS DC bias offset; *pedsub* addresses the linear component. However, we find that the application of these two tasks does not remove the anomalous background structure completely. We measure a residual amplifier glow at a count rate of between 0.03 counts s^{-1} and 0.07 counts s^{-1} above the median background level. As it is vital for our host galaxy analysis that we can determine the sky background level precisely, we perform an additional correction to the large-scale background structure, based on a method presented by Hsiao et al. (2010). These authors find that the residual background in NIC2 F110W and F160W imaging, after flatfielding and *pedsub* processing, can be modelled by two components. The first component scales with exposure time and is dominated by the amplifier glow contribution, while the second component scales with the background level. Scaling these components as prescribed by Hsiao et al. (their equation 4) overestimates

the amplifier glow signal in our data. We instead scale and subtract the two components using least-squares minimization, using the MP-FIT software,[6] and masking bright sources for the fitting procedure. Compared to the pipeline-processed images, the standard deviation of the mean pixel intensity, measured in background-dominated regions, is reduced by $\approx$47 per cent for three of our quasars. The improvement is more modest ($\approx$13 per cent) for J1730+5850, as this observation was not impacted by SAA persistence (see below). While the subtraction of an empirical template increases the photon shot noise in the resulting images, this increase is in all cases less than 2 per cent.

Photon persistence. The NICMOS detector suffers from photon persistence, i.e. pixels amassing a large amount of charge during an exposure generate a spurious signal in subsequent exposures. Photon persistence gives rise to two issues identified in our data. First, the passage of the *HST* through the South Atlantic Anomaly (SAA) between exposures results in an increased flux of cosmic rays. As the persistence behaviour varies across the detector, this bombardment causes a persistent signal in a characteristic pattern. We see this pattern for all observations apart from that of J1730+5850. We use the *SAAclean* algorithm (Barker, Laidler & Koekemoer 2007) to remove the SAA persistence signal; we find that this algorithm removes the SAA signal more effectively when combined with the Hsiao et al. treatment described above. Secondly, the quasar itself leaves a point-like persistent signal at its previous dither position; we mask these regions before image combination.

Non-linearity correction. The final calibration step for our single-exposure images addresses the count rate-dependent non-linearity identified by Bohlin, Riess & de Jong (2006). We process each image with the PYRAF/STSDAS script *rnlincor*, which models the non-linearity as a power law with an empirically determined wavelength-dependent exponent, and corrects the measured count rate in each pixel using this model.

3.3 Combination of dithered images

We combine the dithered single-exposure images using the PYRAF/STSDAS package 'MULTIDRIZZLE '.[7] This results in a single combined NICMOS image and a single combined ACS image for each quasar. 'MULTIDRIZZLE ' identifies cosmic rays and other bad pixels in the single-exposure images by comparison with a median image shifted into a common reference frame. We use the resulting bad pixel maps as the sole method of cosmic ray identification for the ACS images, and as a supplementary method for the NICMOS data. For the ACS data, we weight the input pixels using the inverse of the error image generated by the *calacs* pipeline. For the NICMOS data, several observations suffer cosmic ray hits near the PSF core, and the affected pixels are not suitable for inclusion in the combined image. As the inverse-error weighting scheme biases output images towards low fluxes when combining a small amount of input frames (Cracraft & Sparks 2007), we instead use exposure-time weighting for the NICMOS data.

Table 2 lists the 'MULTIDRIZZLE' settings that we select for the final image combination for each quasar. For each image we select the

---

[5] STSDAS and PYRAF are products of the Space Telescope Science Institute, which is operated by AURA for NASA.

[6] The IDL package MPFIT is written by Craig Markwardt and is available from http://cow.physics.wisc.edu/~craigm/idl/fitting.html.

[7] The 'MULTIDRIZZLE' routine is based on the drizzle algorithm developed by Fruchter & Hook (2002).

Table 2. MULTIDRIZZLE parameter settings.

Object	Kernel[a]	Pixfrac[b]	Scale[c] [pix (arcsec)]	PSF FWHM[d] [pix (arcsec)]
(1)	(2)	(3)	(4)	(5)
NICMOS/NIC2				
J0300+0048	Square	0.65	0.8 (0.0604)	1.89 (0.107)
J1154+0300	Gaussian	0.65	0.6 (0.0453)	2.16 (0.098)
J0819+4209	Square	0.6	0.9 (0.06795)	2.06 (0.140)
J1730+5850	Gaussian	0.7	0.8 (0.0604)	2.57 (0.155)
ACS/WFC				
J0300+0048	Gaussian	0.7	0.8 (0.0392)	2.04 (0.0800)
J1154+0300	Square	0.7	0.8 (0.0392)	2.06 (0.081)
J0819+4209	Gaussian	0.7	0.8 (0.0392)	2.21 (0.0866)
J1730+5850	Gaussian	0.85	0.85 (0.04165)	2.40 (0.100)

Notes. – MULTIDRIZZLE parameters adopted for the final combined image for each quasar. The PSF parameters are measured via a simple Gaussian fit.
[a]The convolution kernel used to distribute the flux of each input pixel in the output grid.
[b]The factor by which each input pixel is resized before being transferred to the common WCS.
[c]The size of the output pixels, listed as a fraction of the input pixel size and in arcseconds (in parentheses).
[d]The FWHM of the FeLoBAL quasar PSF, expressed in pixels and (in parentheses) in arcseconds.

settings that yield the narrowest PSF FWHM in terms of angular size, while avoiding image combination artefacts. We test for such artefacts via visual inspection, and by measuring the standard deviation of the combined weight image (Fruchter & Hook 2002). Full Nyquist sampling is not achievable for J0300+0048(NIC2) and J0819+4209(NIC2) without introducing image artefacts. To test the sensitivity of our image decomposition to this issue, we repeat the modelling of Section 4.3 for these two observations after broadening the data and PSF images to Nyquist sampling via convolution with a Gaussian smoothing kernel, as suggested by Kim et al. (2008). This treatment makes no qualitative difference to our PSF-only and PSF-plus-Sérsic modelling (Section 4.3) for these quasars.

4 IMAGING ANALYSIS

Here, we describe our 2D image decomposition strategy and define detection criteria (Section 4.1), and present our modelling results for the ACS (Section 4.2) and NICMOS (Section 4.3) imaging of the FeLoBAL quasars.

4.1 Modeling strategy for the imaging data

We use GALFIT (version 3.0.5; Peng et al. 2011) to model the emission in the 2-D MULTIDRIZZLE -combined images of the FeLoBAL quasars. This software models astronomical images using analytical surface brightness profiles that are convolved with the instrumental PSF. The best-fitting model is determined via least-squares minimization, and the modelling therefore requires error maps for each astronomical image. For the ACS data we generate these using the inverse-error maps produced by MULTIDRIZZLE , which include an estimate of the cumulative error due to photon noise, readout noise and all image calibration operations. For the NICMOS images, which are combined using exposure-time weighting (Section 3.3), we calculate the per-pixel uncertainties as the standard deviation of the background level in the combined images, added

in quadrature to the per-pixel photon-counting error. As the image combination causes the uncertainties of adjacent pixels to be correlated, these NICMOS error maps represent upper limits on the true uncertainty.

PSF-only models. To determine whether there is any significant extended emission present, we first model each combined image as a point source along with a sky-background component with linear gradients in the x and y directions (hereafter, *PSF-only models*). The PSF and background components are fitted simultaneously. Any other bright stars or galaxies in the image are modelled using PSF or Sérsic components, respectively. To minimize the influence of detector-edge anomalies, most of the PSF fits are performed using 201 × 201-pixel (around 66 kpc for $z = 1$) cutouts of the data and of the PSF template, centred on the quasar PSF. We ensure that the best-fitting PSF and sky background scalings are not significantly altered if larger image regions are adopted. For the J0300+0048(NIC2/F110W) observation we model the entire image, so as to determine the sky level more accurately; this is necessary because the field is somewhat crowded. The best-fitting PSF scalings are insensitive to the input parameter guesses, and the modelling converges within 10–20 iterations of the fitting routine. Our NICMOS PSF templates tend to model the quasar PSF diffraction spikes poorly. We therefore perform all NICMOS modelling with the diffraction spikes masked, so that FALFIT does not include them in its least-squares minimization. We do not include these regions in the radially averaged brightness profiles for NICMOS (i.e. Figs A2 and 5).

PSF-plus-Sérsic models. To quantify the total brightness and flux distribution of any extended emission, we model each image a second time, now including a Sérsic component to represent the extended emission (hereafter, *PSF-plus-Sérsic models*). The Sérsic profile is given by:

$$\Sigma(r) = \Sigma_e \exp[-\kappa((r/R_e)^{1/n} - 1)], \qquad (1)$$

where $\Sigma(r)$ is the surface brightness at a given radius, R_e is the half-light radius of the profile, and n is the Sérsic index; κ is not a free parameter, being fully determined, for a given n, by the definition of R_e. Again, we perform the analysis using 201 × 201-pixel cutouts of the quasar image and of the PSF template, and fit all components simultaneously. For J0300+0048(NIC2/F110W) we again find it necessary to model the entire image. We experiment with including an elliptical deformation of this profile as a free parameter in our FeLoBAL modelling, but find that the resulting host galaxy magnitudes are insensitive to this parameter, while the χ^2 statistic of the fit only weakly depends on the ellipticity. We therefore impose radial symmetry for all Sérsic profiles. We also find it necessary to impose constraints on the allowed values of n and R_e. This is due to PSF mismatch, i.e. differences between the 'true' instrumental PSF at the time of the quasar observations and the PSF template used to model the point source, as described in detail in Appendix A. Given the significant PSF mismatch that our modelling suffers, and the faintness of the host galaxies relative to the PSF, the largest improvement in the χ^2 statistic is achieved by minimizing R_e and/or maximizing n so as to create a narrow, unresolved feature that alleviates the mismatch in the central region. We therefore restrict R_e to be larger than the FWHM of the quasar PSF in a given observation. Given our low sensitivity to the Sérsic index, we fit models with constant values of n and average over their host magnitudes, as described in detail below.

Table 3. PSF-only GALFIT Modelling.

Object	Filter	Quasar FWHM[a] [arcsec (pix)]	PSF FWHM[b] [arcsec (pix)]	m_{PSF}[c] (mag)
(1)	(2)	(3)	(4)	(5)
ACS:				
J0300+0048	F435W	0.08 (2.03)	0.09 (2.29)	20.51
J1154+0300	F550M	0.08 (2.07)	0.09 (2.39)	21.40
J0819+4209	F625W	0.09 (2.21)	0.08 (2.07)	22.62
J1730+5850	F625W	0.09 (2.41)	0.09 (2.28)	21.70
NICMOS:				
J0300+0048	F110W	0.11 (1.81)	0.13 (2.10)	16.05
J1154+0300	F110W	0.12 (2.55)	0.12 (2.62)	17.29
J0819+4209	F160W	0.15 (2.15)	0.14 (2.09)	18.96
J1730+5850	F160W	0.16 (2.67)	0.15 (2.44)	16.98

Notes. [a]Full width at half maximum of the quasar emission, as measured using the IRAF task *'imexamine'*.
[b]Full width at half maximum of the stacked stellar PSF template used to model the point source emission.
[c]The apparent AB magnitude of the quasar in the listed bandpass, as determined by our PSF-only modelling.

Host galaxy detection criteria. The sensitivity of a quasar host galaxy study depends strongly on the quality of the available PSF templates. For this work, we lack dedicated PSF star observations (Section 2), and instead construct stacked stellar PSF templates using stacked observations of field stars (for ACS imaging) and of calibration stars (for NICMOS), as described in Appendix A. To quantify the fidelity of these PSF templates, we perform an extensive series of star–star PSF subtraction tests (Appendix A) and host galaxy decomposition simulations (Appendix B). Based thereon (as discussed in Appendix C), we apply the following detection criteria:

(1) At least three contiguous 1-pixel bins in our azimuthally averaged intensity plots show a positive residual at a significance $>3\sigma$ after PSF-only modelling. This must occur outside the inner 0.2 arcsec of the radial profile for NICMOS and ACS/F425W, outside the inner 0.3 arcsec for ACS/F550M, or outside the inner 0.4 arcsec for ACS/F625W.

(2) The PSF wings are not significantly ($>3\sigma$) oversubtracted in any azimuthally averaged bin exterior to the radial constraint given in (1).

4.2 ACS (rest-frame UV) modelling results

PSF-only modelling, ACS. The quasar and template PSFs have FWHM of between 0.08 and 0.09 arcsec (Table 3). All residual images appear consistent with point sources (Fig. 2). The quasars are relatively faint in ACS imaging, with best-fitting AB magnitudes $m_{PSF} > 20.5$ mag for all objects; the ACS observations are, on average, 4.2 mag fainter than the NICMOS observations, corresponding to a factor of ~ 47 in flux. This confirms that our ACS observations sample the heavily absorbed BAL trough (Fig. 1). We present upper limits on m_{host} in the rest-frame UV for each quasar in Table 4.

PSF-plus-Sérsic modelling, ACS. For J0300+0048, the Sérsic component magnitude converges at $m_{host} \sim 24$ mag, and is unresolved, with $R_e \approx 1$ kpc. Our simulation work indicates that this extended component may be a spurious result due to PSF mismatch, as it is fainter than our detection limit (Table 4). For the three remaining quasars, the Sérsic components diverge towards infinite faintness. In

Table 4. Upper limits on FeLoBAL host galaxy flux in ACS observations.

Object	Filter	m_{nuc}[a] (mag)	Limiting m_{host}[b] (mag)
(1)	(2)	(3)	(4)
J0300+0048	F435W	20.51	22.76
J1154+0300	F550M	21.40	23.15
J0819+4209	F625W	22.62	24.37
J1730+5850	F625W	21.70	23.70

Notes. [a]The nuclear (PSF) AB magnitude of the source, as determined by PSF-only modelling.
[b]The limiting AB magnitude of the host galaxy, calculated using the limiting nuclear-to-host contrast level determined in our simulations (Appendix B). While we are ignorant of the scale size of non-detected host galaxies, the detection limits are in fact strongly sensitive to this parameter; the upper limits listed here assume 0.5 kpc $\leq R_e \leq 10$ kpc, for which range we quote the most conservative (i.e. brightest) upper limit.

summary, we see no evidence of extended emission in the rest-frame UV for any of the FeLoBAL quasars. As established by our simulation work (Appendix B), the UV non-detections may be due to very centrally concentrated UV emission with scale size $R_e < 1$ kpc (e.g. a nuclear starburst). A very extended UV source ($R_e \gtrsim 10$ kpc) would also yield a non-detection, assuming $m_{nuc} - m_{host} > 2$ mag. Alternatively, the host galaxies may simply have quiescent or dust-obscured stellar populations, as discussed in Section 5.2.

4.3 NICMOS (rest-frame optical) modelling results

For J0300+0048, J1154+0300, and J0819+4209, the NICMOS imaging reveals neighbour galaxies at sufficiently small angular separations to potentially affect our image decompositions (Fig. 4). We model these galaxies using a single Sérsic component; the fluxes attributed to them are not included in our analyses. We discuss these neighbouring galaxies further in Section 5.4.

PSF-only modelling, NICMOS. All the residual images show over-subtracted central pixels and residual PSF diffraction spikes due to mismatch between the PSF template and the quasar PSF (Fig. 4). As the PSF template for J0300+0048 has a low signal-to-noise ratio (S/N) relative to the quasar observation, the entire PSF-subtracted image is noisy, and the residual features have a lower significance than would be expected if using an ideal PSF. Nonetheless, J0300+0048 shows an extended residual that is detected at a significance of $\sim 3\sigma$–5σ between radii of 0.7 arcsec and 1.1 arcsec, extending to around 1.6 arcsec at a lower significance (Fig. 5). J1154+0300 displays a bright, compact residual core at radii less than ~ 0.6 arcsec (corresponding to a physical transverse distance of around 4 kpc). Both these objects fulfill our detection criteria for extended emission. The very compact residual for J0819+4209 just barely fulfills our detection criteria, while the residuals for J1730+5850 are consistent with zero extended emission.

PSF-plus-Sérsic modelling, NICMOS. Our PSF-plus-Sérsic modelling converges at a finite brightness for the Sérsic component for all four quasars. In Table 5 we present the best-fitting models for each quasar. For three quasars, the best-fitting solution has $n = 0.75$, i.e. at the imposed lower limit for n. However, in terms of the χ^2 statistic, the modelling does not strongly favour any particular values of the Sérsic index, n. We therefore fit three different models
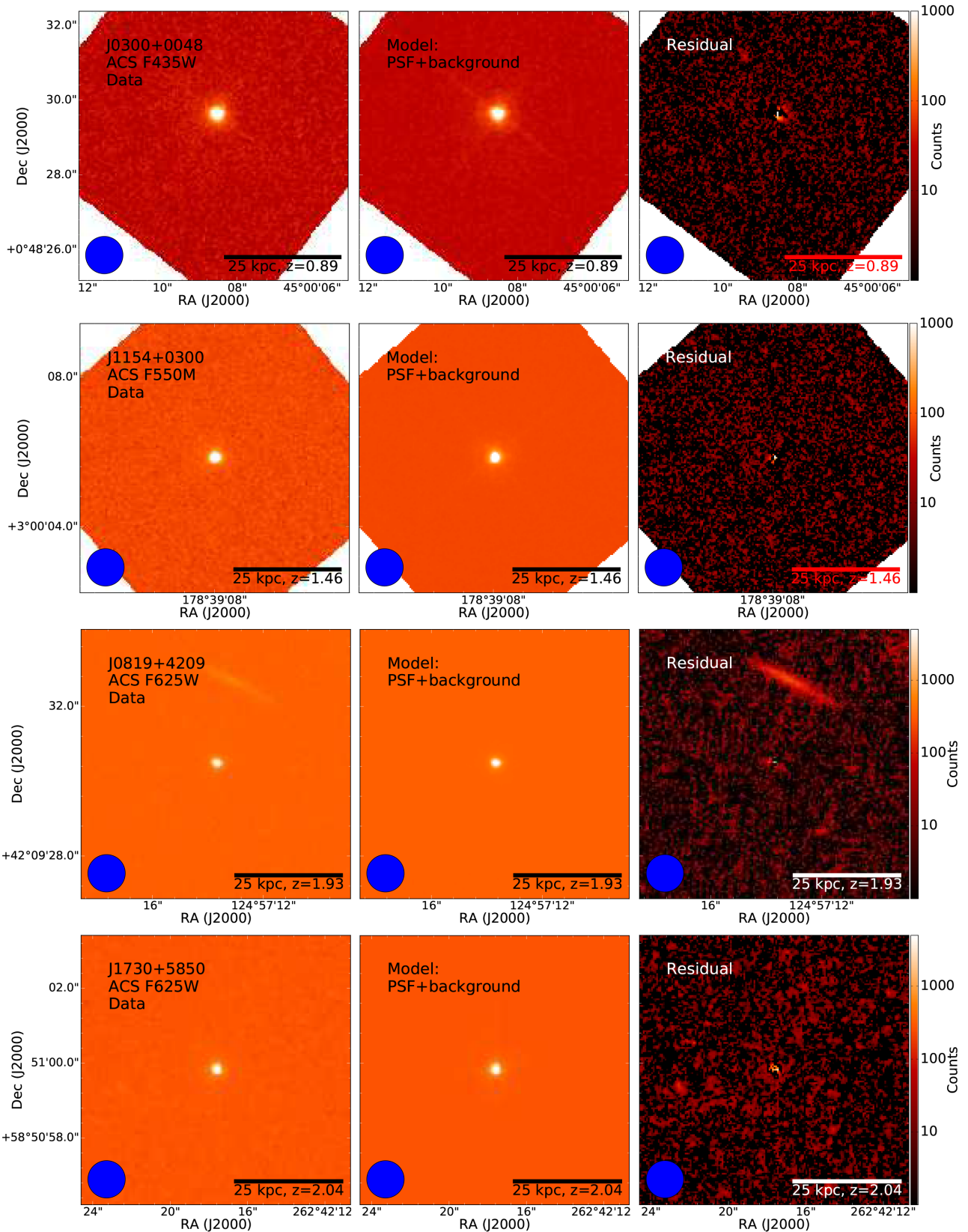
Figure 2. PSF-only modelling of the ACS imaging of the FeLoBAL quasars. The intensity is shown in units of total counts. The blue circle shows a diameter of 1 arcsec; the image size is 7.2 × 7.2 arcsec. The scale bars illustrate an angular size corresponding to 25 kpc at the quasar redshift. *Left:* Original image. *Centre:* Best-fitting PSF model and background component. *Right:* Residual after model subtraction. For J0819+4209, a close companion galaxy is visible in the residual image; however, we model and subtract this galaxy prior to our analysis of radial flux profiles (Fig. 3), to avoid attributing its flux to the quasar host galaxy.

with constant Sérsic indices ($n = 1$, $n = 2.5$, and $n = 4$) to each image, so as to explore a range of central concentrations. While non-BAL quasars in the local Universe tend to have giant elliptical hosts (Dunlop et al. 2003), suggesting $n \approx 4$, we prefer not to assume an a priori value of n for these high-redshift host galaxies. For a morphologically diverse sample of template galaxies, our simulation work (Appendix B1) suggests that the accuracy of the m_{host} measurements are improved by averaging over the values obtained for $n = 1$ and $n = 4$ models, as opposed to adopting m_{host} from the best-fitting model. Note that the magnitudes themselves are averaged, i.e. the averaging is done in log-flux space. We present the average properties $\langle m_{\text{host}} \rangle$ and $\langle R_e \rangle$ for a grid of model fits to each quasar (Table 6). The best-fitting scale sizes R_e are highly sensitive to the choice of n, and should therefore be regarded as order-of-magnitude estimates of the true R_e. For quasars J0300+0048 and J1154+0300, we find values of $m_{\text{nuc}} - m_{\text{host}}$ and R_e that are consistent with those found for detected, resolved sources in our simulations. We therefore consider these objects to have detected host galaxies. For J0819+4209, the Sérsic profile converges at the imposed lower limit $R_e = \text{FWHM}_{\text{PSF}}$, i.e. the extended flux is only marginally resolved. While we consider the detection of extended emission to be real, given the faintness of false-positive detections to *bona fide* point sources in NICMOS data (Appendix A), we consider our PSF-plus-Sérsic modelling results to be highly uncertain for this object, as discussed below.

Uncertainties on m_{host}, *NICMOS.* For each quasar, we estimate ranges of uncertainty for m_{host} by performing PSF-plus-Sérsic modelling of real galaxies artificially redshifted to the quasar redshift, including a superimposed point source, and with appropriate noise properties for the NICMOS observations. Full details are presented in Appendix B. These uncertainties are rather conservative, as they represent the largest error in m_{host} found for any of our simulations for a given observation, covering a range of possible host galaxy morphologies. They are in rough agreement with the typical uncertainties found by Simmons & Urry (2008) for GALFIT image decomposition of simulated AGN with $m_{\text{nuc}} - m_{\text{host}} \sim 3$. We adopt the following uncertainties (in AB magnitudes) for the remainder of this work: $m_{\text{host}} = 19.6 (\pm 0.5)$ mag for J0300+0048, $m_{\text{host}} = 20.8 (\pm 0.5)$ mag for J1154+0300, and $m_{\text{host}} = 21.2^{+1.3}_{-0.5}$ mag for J0819+4209. The latter object has a relatively large uncertainty on m_{host} due to the compactness of the detected host component. For J1730+5850, we see no evidence of extended emission. We therefore use our simulations to establish the limiting value of $m_{\text{nuc}} - m_{\text{host}}$ for which the host galaxy is no longer detected. This is done for a range of host morphologies, and we adopt the most conservative (i.e. brightest), upper limit m_{host}. For J1730+5850 this yields $m_{\text{host}} \geq 20.0$.

Consistent m_{host} *when using alternative PSF templates.* We lack dedicated PSF star observations for this study. For our NICMOS analysis, we instead use stacked observations of the calibration star P330-E as a PSF template (Appendix A). The stacking process unavoidably broadens the PSF slightly due to centring uncertainties. Also, the three-month time window that we allow for the PSF star observations relative to the quasar observation date may lead to additional mismatch due to long-term PSF variability (Kim et al. 2008). There is therefore a concern that the extended flux that we attribute to host galaxy emission may instead be caused by severe PSF mismatch. For J1154+0300, we perform additional tests using high-S/N PSF templates (Appendix A5). These were observed at time separations of years from the quasar observation, and are therefore expected to display significant PSF mismatch due to

time evolution. We detect extended flux for J1154+0300 using any of these alternative PSF templates. While R_e becomes unresolved for certain high-SN PSF templates, m_{host} is in all cases consistent with our our original modelling to within the quoted uncertainties. We elect to use the results obtained using P330-E, as presented in Table 6, in the remainder of our analysis.

5 DISCUSSION

5.1 Similar nucleus-to-host luminosity ratios for FeLoBALs and non-BAL quasars

In Fig. 6 we compare the nuclear and host galaxy V band absolute magnitudes for our FeLoBAL quasars with those of non-BAL quasars with host galaxy detections at similar redshifts. As the NIC2 filter bandpasses were chosen to sample the rest-frame V band, and the spectral term in the K-correction therefore should be minimal, we only apply the bandwidth-narrowing $(1 + z)$ term to derive the absolute magnitudes. Given the ~ 2 mag scatter in $m_{\text{nuc}} - m_{\text{host}}$ displayed by the non-BAL quasars, and the uncertainties on m_{host} for our measurements, the four FeLoBALs are consistent with the existing $m_{\text{nuc}} - m_{\text{host}}$ relationship for non-BAL quasar host galaxies. Quasar J1730+5850 is highly luminous in the V band; the upper limit host galaxy V magnitude appears consistent with the existing relationship.

5.2 No direct evidence for ongoing star formation

In the local Universe, LoBAL quasars are often found in ULIRG galaxies, which also display merger-induced star formation (e.g. Canalizo & Stockton 2001). Here, we use our measurements of m_{host} in the rest-frame optical, along with the limiting values of m_{host} in the UV, to investigate the presence of strong, unobscured star formation activity of the type seen in some local-Universe starburst galaxies.

In Fig. 7, we show template spectra of a 1 Gyr single-age stellar population model (Bruzual & Charlot 2003), and of an unobscured starbursting galaxy (Calzetti, Kinney & Storchi-Bergmann 1994), scaled to the F110W flux densities of the host galaxies of J0300+0048 and J1154+0300. The blue shaded region shows the error margins of the template scaling due to the uncertainties on m_{host}. We also show the upper limits on the rest-frame UV host galaxy magnitude. For these two quasars, the UV non-detections exclude unobscured starbursting hosts, while being fully consistent with single-age stellar populations of age 1 Gyr or older, as expected for quiescent elliptical galaxies at $z \sim 1$. For J0819+4208 (not shown), m_{host} is highly uncertain, and we cannot rule out an unobscured starburst. We apply the Calzetti et al. (2000) dust reddening law to the templates, and find that the template fluxes become marginally consistent with the UV non-detections for $E(B - V) \approx 0.5$ (J0300+0048) or $E(B - V) \approx 0.4$ (J1154+0300). Thus, our *HST* observations cannot be used to discriminate a quiescent host from a vigorously star-forming, dust-obscured galaxy. We note that Glikman et al. (2012) find an overabundance of FeLoBALs in their sample of the reddest quasars. Many objects in their sample show a reddening of $E(B - V) \geq 0.5$, which would yield UV non-detections for our observations, even for starbursting host galaxies.

5.3 Comparison with optical to mid-infrared SED modelling

Two of the quasars in our sample are well-studied in the infrared by Farrah and coworkers. For J1154+0300, Farrah et al. (2010)
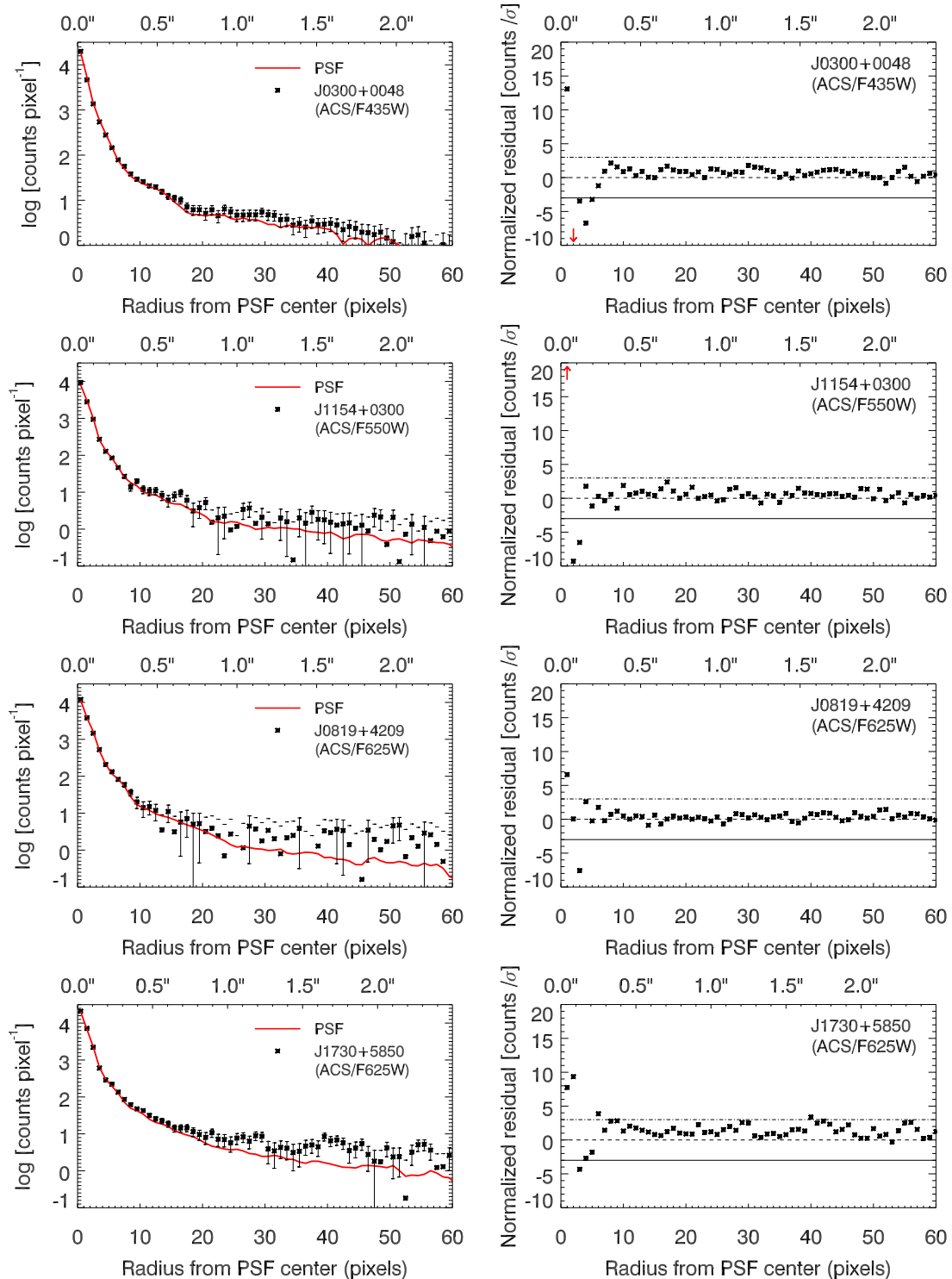
Figure 3. PSF-only modelling results for our ACS (rest-frame UV) imaging. *Left:* radially averaged intensity plot showing a scaled version of the stacked stellar PSF (red solid lines) and the sky-subtracted quasar emission profiles (black points). Emission attributed to companion galaxies is not included in these profiles. The error bars on the data points include a contribution due to photon noise in the PSF template. *Right:* Offset of the sky-subtracted quasar profiles from the PSF templates, expressed in terms of the 1σ error bars on the data. The horizontal dashed, dash-dot, and dot-dot-dot–dashed lines represent a zero offset, a 3σ positive residual, and a 3σ negative residual, respectively. Red arrows indicate annuli for which the offset exceeds the *y*-axis limits.

estimate the star formation rate (SFR) in the host galaxy based on the luminosity of polycyclic aromatic hydrocarbon emission lines (PAH), finding SFR=$900\pm1100\,M_\odot\,yr^{-1}$; they only detect one (of three) PAH lines at a significance $>1\sigma$, yielding an SFR

consistent with zero. For J0300+0048 and J1154+0300, Farrah et al. (2012) estimate the starburst contribution to the total luminosities via modelling of the broad-band photometric SEDs using pure-AGN and starburst components. For J1154+0300, at 1.1 μm,
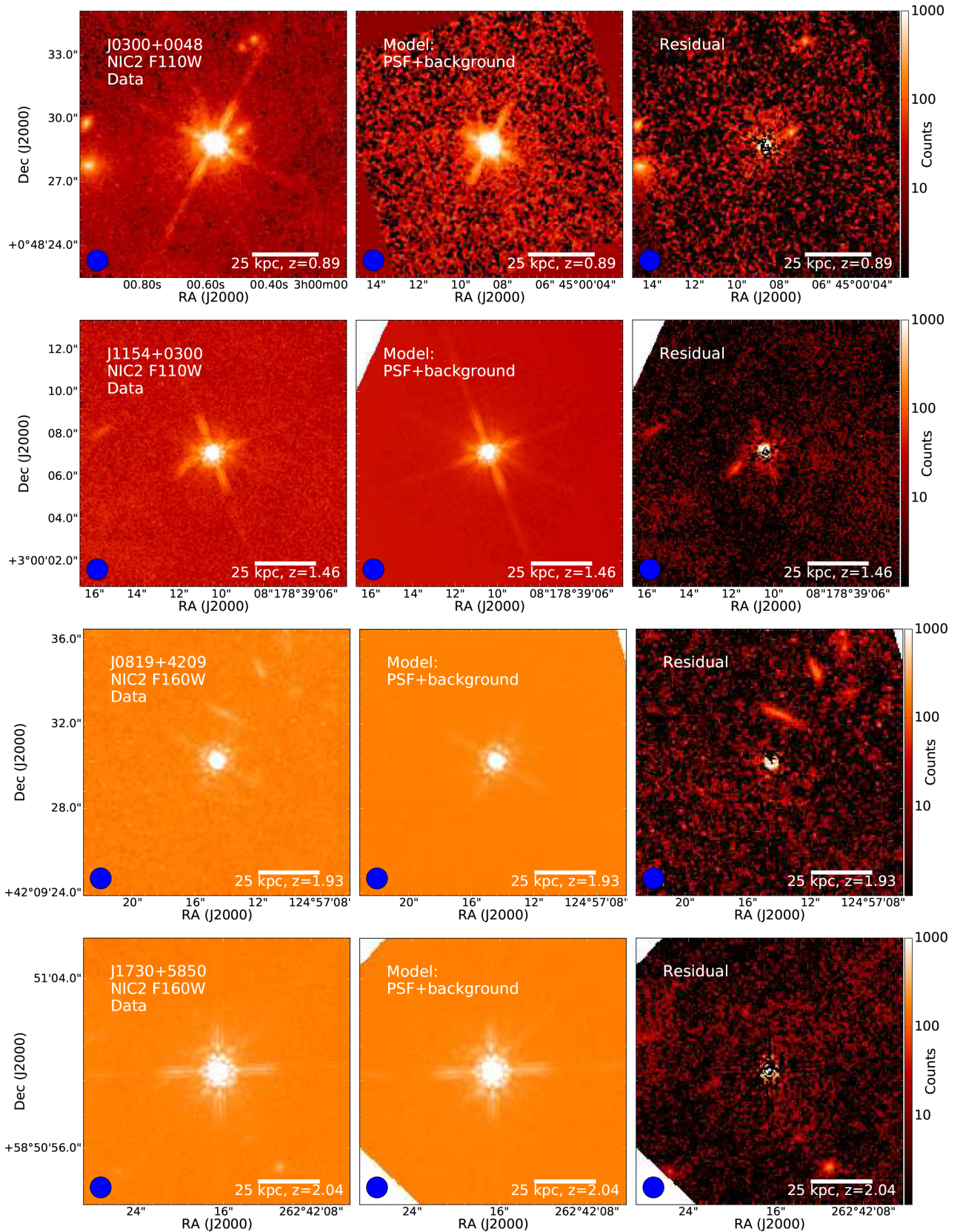
Figure 4. PSF-only modelling of NICMOS imaging of the FeLoBAL quasars. The intensity is shown in units of total counts. The blue circle shows a diameter of 1 arcsec; the image size is 12.6 × 12.6 arcsec. The scale bars illustrate an angular size corresponding to 25 kpc at the quasar redshift. *Left:* Original image. *Centre:* Best-fitting PSF model and background component. *Right:* Residual after model subtraction. The PSF templates for J0300+0048 has a low S/N (Appendix A), resulting in a noisy residual image (top right). The distinct neighbouring galaxies visible for J0300+0048, J1154+0300, and J0819+4209 are modelled individually and subtracted before generating radial flux profiles (Fig. 5); their flux is thus not attributed to the quasar host galaxy.
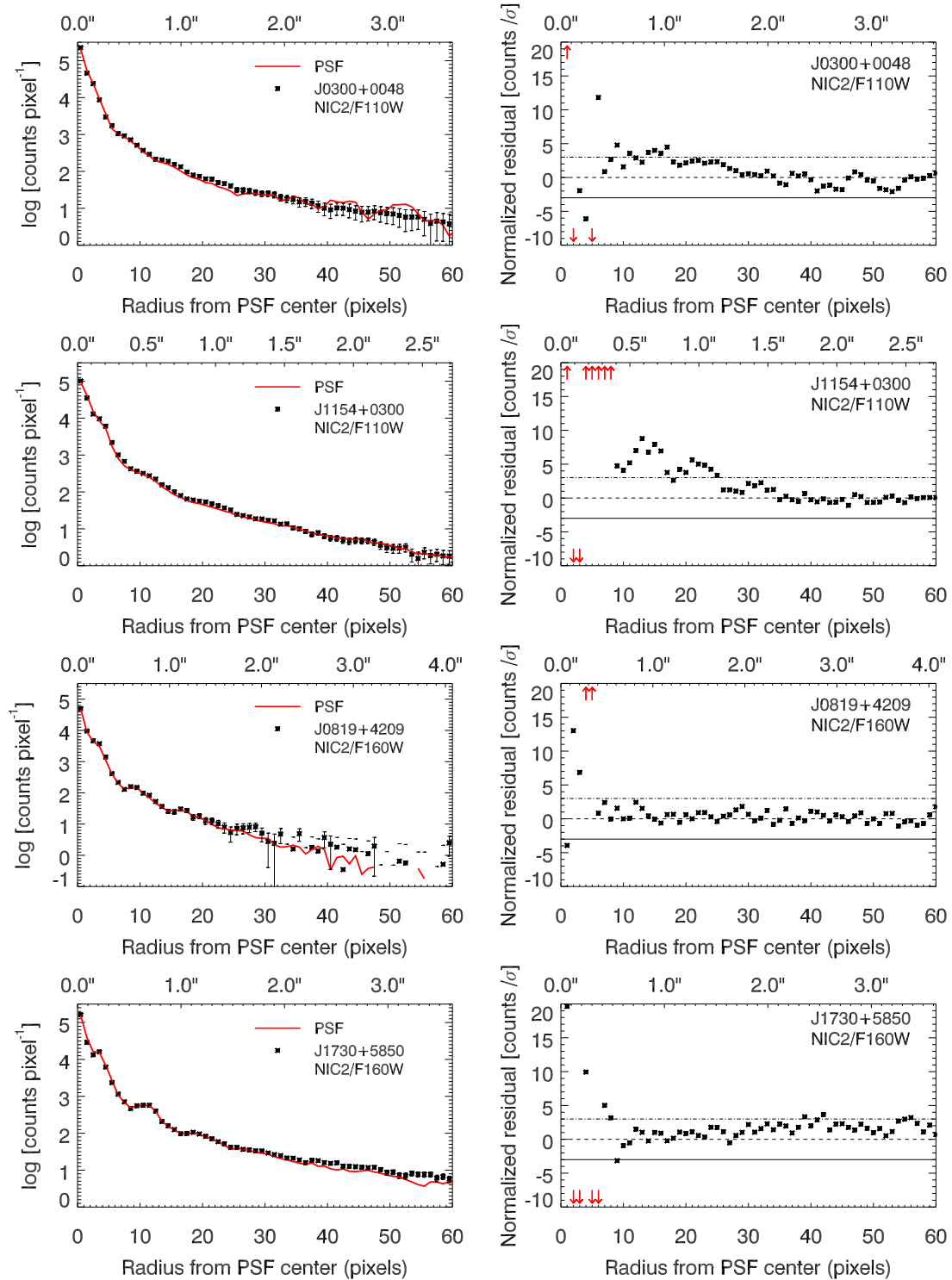
Figure 5. PSF-only modelling results for our NICMOS imaging. See the caption of Fig. 3 for details.

they attribute a flux of around 0.07 mJy to the starburst-component (their Fig. 4 panel 19), consistent with our estimate of the host galaxy flux (Fig. 8, right panel). We note, however, that their results are consistent at the 3σ level with no starburst-component emission at 1.1 µm for this quasar. For J0300+0048, their best-fitting starburst component (Farrah et al. 2012, Fig. 1, panel 3) is fainter than

our host galaxy model (Fig. 8, left-hand panel). This discrepancy may be due to the lack of a quiescent stellar population component in their modelling.

While these results suggest a lack of vigorous starburst activity in the FeLoBAL hosts, we note that the starburst component in the Farrah et al. (2012) modelling is primarily constrained by the MIPS

**Table 5.** Best-fitting PSF-plus-Sérsic GALFIT models of FeLoBAL quasars, NICMOS.

Object	Filter	m_{nuc} (mag)	m_{host} (mag)	$m_{nuc} - m_{host}$ (mag)	R_e (kpc)	n
(1)	(2)	(3)	(4)	(5)	(6)	(7)
J0300+0048	F110W	16.06 ± 0.01	19.64 ± 0.32	3.58	10.4 ± 6.0	3.05 ± 1.79
J1154+0300	F110W	17.34 ± 0.00	21.09 ± 0.03	3.75	2.9 ± 0.1	[0.75]
J0819+4209	F160W	19.01 ± 0.00	21.48 ± 0.03	2.47	[1.2]	[0.75]
J1730+5850	F160W	17.12 ± 0.00	20.26 ± 0.15	3.14	[1.6]	[0.75]

Note. – Best-fitting parameters for PSF-plus-Sérsic modelling of the FeLoBALs in NICMOS imaging. Square brackets denote parameters that converge at the imposed limiting values ($0.75 \leq n \leq 5$, $R_e > FWHM_{PSF}$). The uncertainties listed are statistical errors as calculated by the GALFIT software. As the χ^2 minimization scheme does not explicitly account for PSF mismatch, or for mismatch between the surface flux distributions of the Sérsic profile and the real galaxy, the listed uncertainties are likely to underestimate the true parameter uncertainties. Our simulations indicate that the average values of m_{host} as determined using a range of Sérsic indies (Table 6) are more accurate than the best-fitting values presented here.

**Table 6.** Parameter ranges for PSF-plus-Sérsic GALFIT modelling, NICMOS

Object	$\langle m_{host} \rangle$ (mag)	Max. m_{host} (mag)	Min. m_{host} (mag)	$\langle m_{nuc} \rangle - \langle m_{host} \rangle$ (mag)	$\langle R_e \rangle$ (kpc)	Max. R_e (kpc)	Min. R_e (kpc)
(1)	(2)	(3)	(4)	(5)	(6)	(7)	(8)
J0300+0048	19.62	19.76	19.44	3.54	2.0	3.5	1.4
J1154+0300	20.75	21.38	20.09	3.45	5.2	9.3	3.1
J0819+4209	21.22	21.39	21.06	2.17	<1.3	–	–
J1730+5850	20.12	20.26	19.98	2.99	<1.6	–	–

Notes. – Our data do not strongly constrain the Sérsic index, n. The average values of m_{host}, and R_e presented here are calculated based on three model fits per quasar, with $n = 1$, $n = 2.5$, and $n = 4$, respectively; our simulations (Appendix B) suggest that this averaging minimizes the uncertainty due to our ignorance of n. We also show the minimum and maximum values found for m_{host} and R_e, given this range of n.
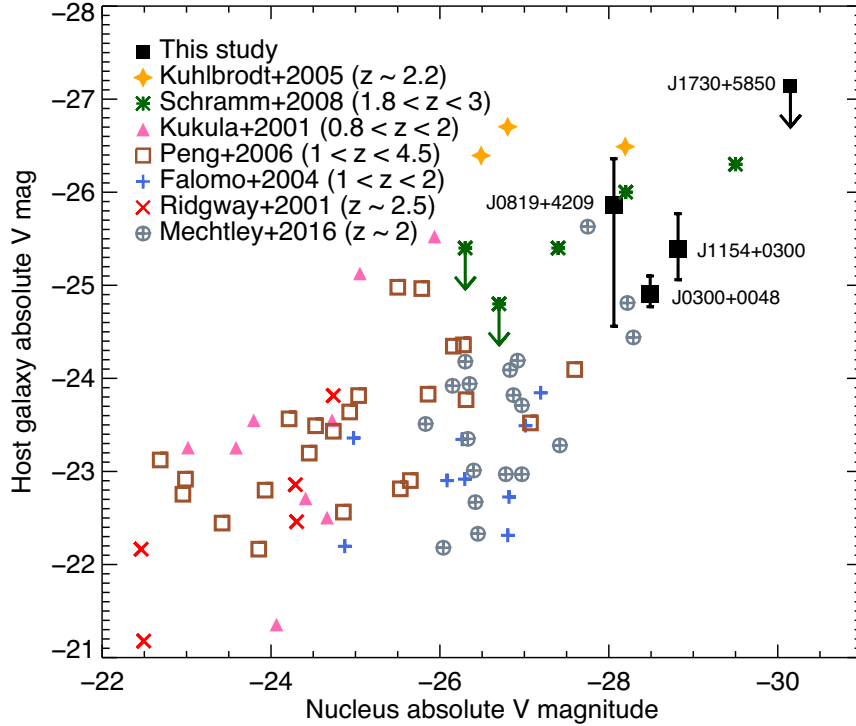
Figure 6. Comparison of the rest-frame V-band nuclear and host galaxy magnitudes of the FeLoBALs with those of non-BAL quasars in taken from the literature (Kukula et al. 2001; Ridgway et al. 2001; Falomo et al. 2004; Kuhlbrodt et al. 2005; Peng et al. 2006; Schramm et al. 2008; Mechtley et al. 2016). The black diamonds represent the four quasars studied in this work; the error bars are not statistical errors, but represent the most severe errors on m_{host} found in our simulations at a given redshift and $m_{nuc} - m_{host}$ level. Downward-pointing arrows denote upper limits on the host galaxy magnitude (e.g. for J1730+5850). The pre-2008 results are compiled (and converted to a $\Omega_\lambda = 0.7$ cosmology where necessary) by Schramm, Wisotzki & Jahnke (2008).
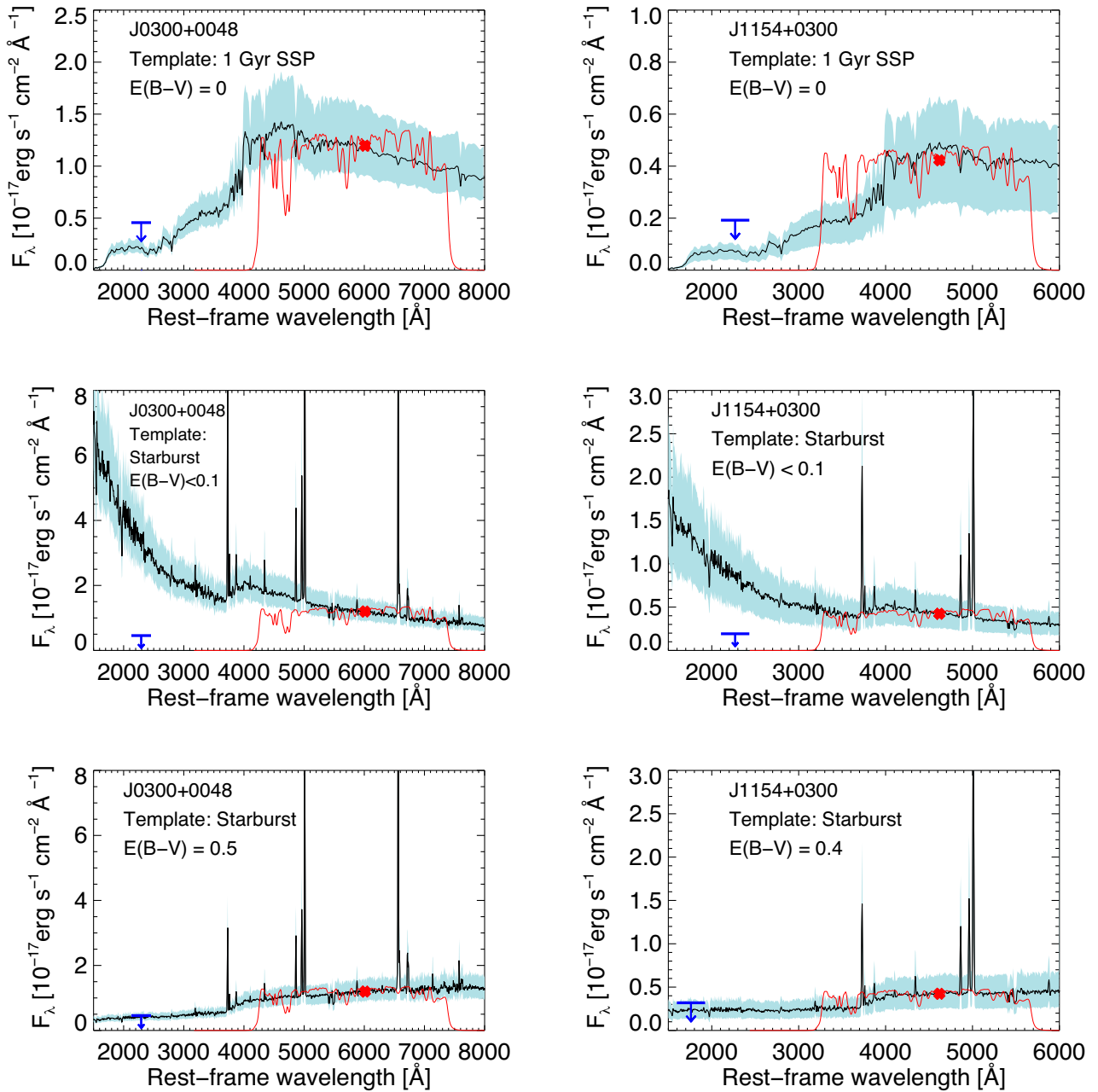
Figure 7. UV-optical spectral galaxy templates (black curves), scaled to have observed fluxes, integrated over the NIC2 filter bandpass (thin red curves), corresponding to the $\langle m_{\mathrm{host}}\rangle$ that we find for J0300+0048 and J1154+0300 (Section 4). The shaded area corresponds to the uncertainty on the template spectrum scaling, as derived from the simulations described in Appendix B. The red cross shows the estimated host galaxy flux density at the bandpass pivot wavelength. The blue arrow shows the upper limit rest-frame UV host galaxy magnitude, as determined by the non-detection of extended flux in ACS imaging. The starburst template spectrum is provided by Calzetti et al. (1994), while the 1 Gyr single stellar population template is based on the stellar synthesis model presented by Bruzual & Charlot (2003). We apply the dust reddening law presented by Calzetti et al. (2000).

160 μm data point, for which neither quasar is detected at the 3σ level. For J1154+0300, especially, the starburst component scaling is not strongly constrained by the available upper limits.

5.4 Neighbor galaxies of the FeLoBALs

In NICMOS imaging, three of the four FeLoBALS in our sample have companion galaxies within an angular separation corresponding to 25 kpc at the quasar redshift; one of these companion galaxies

(for J0819+4209) is also detected in ACS imaging. If these galaxies are physical neighbours to the FeLoBAL quasars, they may be involved in gravitational interactions with the quasar hosts, supporting the merger-triggering scenario for FeLoBAL quasars. However, we lack redshifts of all three of these galaxies, and therefore cannot currently confirm that they are physically close neighbours. Obtaining spectroscopic redshifts for these galaxies would require prohibitively long exposure times (∼10 h to achieve S/N∼4 in the rest-frame optical for the brightest neighbour galaxy, assuming a 2-m-class telescope).
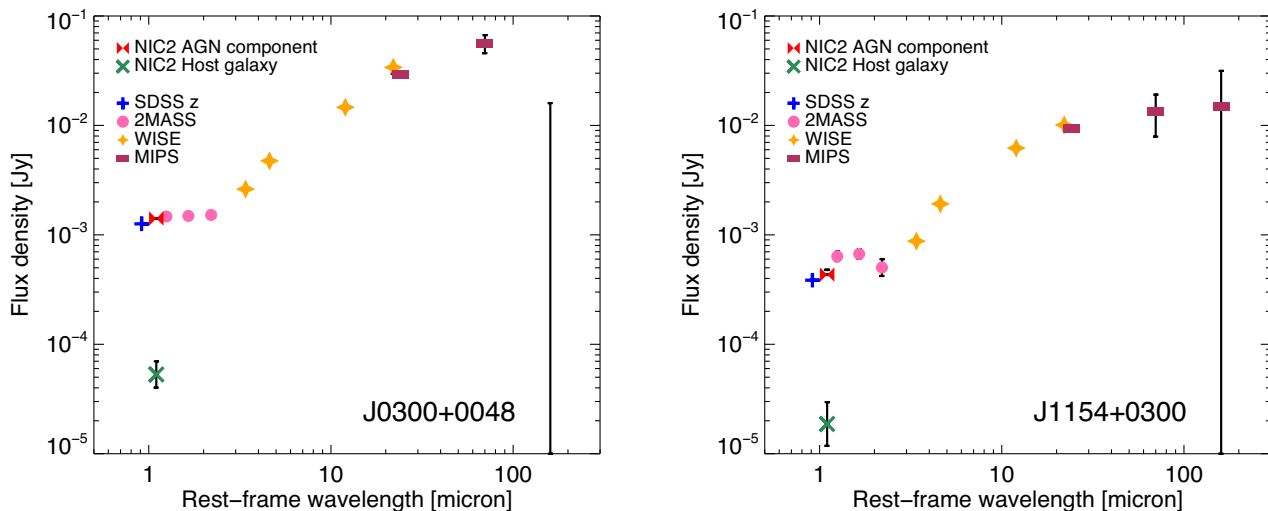
Figure 8. Infrared photometry of the FeLoBAL quasars J0300+0048 and J1154+0300, taken from the SDSS, 2MASS (Skrutskie et al. 2006), WISE (Wright et al. 2010), and MIPS (Rieke et al. 2004) surveys, and originally compiled by Farrah et al. (2012). We include the estimated host galaxy and AGN contribution (green and red diamonds, respectively) based on our image decomposition (Section 4).

The companion galaxy of J0819+4209 appears to have an edge-on disc morphology, and can be modelled satisfactorily with GALFIT using a single Sérsic component with $n = 1$, yielding AB magnitudes of 23.0 mag in NICMOS and 23.7 mag in the ACS imaging. We are unable to strongly constrain the redshift of this galaxy, using our two-band photometry; the data are consistent with a starburst SED at $z \lesssim 2$ or a spiral (Sc) galaxy SED at $z \lesssim 1.1$. If situated at the quasar redshift, this disc galaxy would have a scale size of 4.9 kpc, and an absolute magnitude of -22.9 (in roughly the rest-frame V band), comparable to the characteristic galaxy magnitude $M^\star_{AB} = -22.67$ at $z \approx 2$ (Marchesini et al. 2007). Thus, this object could plausibly be a massive spiral galaxy at $z \sim 2$.

Likewise, we cannot place strong constraints on the redshifts of the companion galaxies of J0300+0048 and J1154+0300. These galaxies are modelled satisfactorily using a single Sérsic profile with $n = 4$, yielding AB magnitudes of 21.2 and 22.9 mag, respectively; these magnitudes are somewhat sensitive to the quasar PSF scaling, as they are partially hidden by the PSF wings (Fig. 4). The UV non-detections suggest quiescent or dust-obscured galaxies. Again, these galaxies would approximately correspond to the characteristic magnitude $M^\star_R = -22.4$ at $z \sim 1$ (Dahlen et al. 2005), and thus represent massive galaxies if they are local to the quasars.

Probability of chance associations. As discussed above, we cannot determine the redshifts of the closest neighbour galaxies, and therefore cannot definitively establish whether these galaxies are physically close to the quasars; we note that the measured host galaxy properties are plausible for massive galaxies located at the quasar redshifts. We instead consider the probability that a field galaxy not associated with the quasar would be observed due to chance alignment.

The probability P of a chance association in a small region of angular area A is given by

$$P = 1 - \exp(-A \times n(m < m_{gal})) \qquad (2)$$

(Bloom, Kulkarni & Djorgovski 2002; Perley et al. 2012). Here, $n(m < m_{gal})$ denotes the number density (per arcsec^2) of galaxies brighter than m_{gal}, the apparent magnitude of the candidate associated galaxy. We use the J-band number densities presented by

Cristóbal-Hornillos et al. (2009), supplemented with galaxy number counts from deep-field *Subaru* observations (Maihara et al. 2001), to obtain $n(m < m_{gal})$ in the F110W filter. For F160W, we use the number densities provided by Yan et al. (1998).

As the relative position uncertainty of our observations is negligible compared to the angular separation between the quasar and galaxy, we use for A the area of a circle with a radius equal to this separation. This yields an estimate of the probability of a chance alignment of a galaxy at least as bright as observed, located at an angular separation at least as close to the quasar as observed. The probabilities of chance association within a circle defined by the quasar-galaxy separation are 2 per cent (J0300+0048), 9 per cent (J1154+0300), and 10 per cent (J0819+4209). The probability that all host galaxies are chance associations is less than 0.2 per cent. The probability that none of the host galaxies are chance alignments is given by

$$P(\text{no chance alignments}) = \prod_{k=1}^{3}(1 - P_k) \qquad (3)$$

(e.g. Bloom et al. 2002), where P_k denotes the probabilities of each individual galaxy being a chance association. Thus, the probability that all three galaxies are physically related to the FeLoBAL quasars is 80 per cent.

We note that there is no uniquely appropriate choice of A, given that we did not define criteria for candidate neighbour galaxies before examining the data. More conservatively, we can calculate the probability of a chance alignment in a set area around the quasar (e.g. a radius corresponding to a 25 kpc radius at the quasar redshift). The probabilities of one or more chance associations within a 25 kpc radius are 7 per cent, 20 per cent, and 17 per cent for J0300+0048, J1154+0300, and J0819+4209, respectively; in that case, the probability of all three galaxies is physically associated with the quasars is 62 per cent.

Mass ratios of merger candidates. Assuming that the neighbour galaxy is at the quasar redshift, and assuming a constant stellar mass-to-light ratio between the quasar host and the neighbour galaxy, we estimate their mass ratio. We find mass ratios of approximately 4:1 (J0300+0048), 7:1 (J1154+0300), and 5:1 (J0819+4209). All three

Table 7. Potential neighbour galaxy counts.

Object (1)	$N(R < 25\,\mathrm{kpc})$ (2)	$N(R < 40\,\mathrm{kpc})$ (3)	$N(R < 80\,\mathrm{kpc})$ (4)	$N(R < 200\,\mathrm{kpc})$ (5)
NICMOS/NIC2				
J0300+0048	1	2	4(+1F)	–
J1154+0300	1	1	5	–
J0819+4209	1	1	3	–
J1730+5850	0	1	3	–
ACS/WFC				
J0300+0048	0	0	(1F)	8(+1F,+1A)
J1154+0300	0	0	0	9
J0819+4209	1	1	5	25
J1730+5850	0	1	3	15

Notes. – Number N of galaxies located at an angular separation corresponding to a transverse radius R at the quasar redshift. We lack redshifts for these potential companion galaxies. Massive, unobscured starbursting galaxies situated at the quasar redshift are expected to be detectable in both bandpasses, whereas quiescent neighbour galaxies are not expected to be detected in the ACS/WFC images. For J0300+0048 we also see one foreground galaxy (denoted *1F*), and one additional AGN (denoted *1A*). The AGN is physically close to the FeloBAL, at $z = 0.89$ (Hall et al. 2003).

putative mergers would be classified as minor mergers according to the standard cut-off ratio (3:1). Given the uncertainties on the quasar host galaxy magnitudes, we cannot exclude major mergers for J0300+0048 and J0819+4209.

The merger fraction for FeLoBALs. Based upon the above discussion, we detect physically associated galaxies (i.e. members of the same galaxy group) for at least one, and at most three, FeLoBALs. We cannot determine whether the FeLoBALs are actually undergoing mergers given the available data: faint indicators of merger activity, such as tidal tails, bridges, or shells, cannot be detected in NICMOS imaging at $z \gtrsim 1$ (Appendix B). Should all three quasars be involved in gravitational interactions, the implied merger rate of 75 per cent for our FeLoBAL sample is consistent with the findings of Glikman et al. (2015) for luminous, dust-reddened quasars at $z \approx 2$. While the measured luminosity ratios suggest minor mergers, we cannot exclude a major merger fraction of ~50 per cent, given the uncertainties on m_{host}.

The minor merger fraction observed for inactive galaxies over the relevant redshift range is ~5–15 per cent, while the major merger fraction is ~5–20 per cent (Man, Zirm & Toft 2016); a combined merger fraction of 75 per cent for quiescent galaxies is strongly excluded. We note that Man et al. base their merger classification exclusively on physical proximity, i.e. they would classify all three of our quasar-galaxy pairs as mergers if they fulfill their redshift-separation criterion. Treister et al. (2012) compile major merger fractions (based on visual merger classification) for AGN spanning a wide range of redshifts and luminosities, and find merger fractions exceeding ~25 per cent for quasars with bolometric luminosities $L_{\mathrm{bol}} > 10^{45}\,\mathrm{erg\,s^{-1}}$, with the merger fraction approaching 100 per cent for the most luminous quasars. Due to the extreme UV absorption, it is difficult to determine the intrinsic bolometric luminosities of our FeLoBAL sample. However, three of the FeLoBALs are detected in WISE W2 and W3 (Wright et al. 2010), allowing us to estimate the flux density at $10^{14}\,\mathrm{Hz}$ (3 μm) in the rest-frame, and calculate a guideline estimate of their luminosities using the bolometric correction $\mathrm{BC}_{10^{14}\mathrm{Hz}} = 9.12 \pm 2.62$ presented by Richards et al. (2006). According to this approximation, these FeLoBALs are indeed intrinsically luminous quasars, with L_{bol} ranging from $1.5 \times 10^{47}\,\mathrm{erg\,s^{-1}}$ (J0300+0048) to $5.0 \times 10^{47}\,\mathrm{erg\,s^{-1}}$ (J1730+5850). We note that young stars in the host galaxy would

contribute to the WISE photometry (especially in W3), so these luminosities will overestimate the brightness of the central source if the FeLoBALs indeed harbor obscured starbursts.

In conclusion, given the non-negligible probability of chance alignments and the small sample size, we cannot exclude that the FeLoBAL quasars have merger fractions comparable to quiescent galaxies at $z \gtrsim 1$. On the other hand, the merger fraction may be as high as 75 per cent. Given that the FeLoBAL quasars are likely intrinsically highly luminous, this high merger rate would be consistent with the merger fraction observed for non-BAL quasars of similar luminosity.

Environments of the FeLoBAL quasars. Via visual inspection of the ACS imaging, we identify between 9 and 25 galaxies per quasar at an angular separation corresponding to 200 kpc or less at the quasar redshift (Table 7). We exclude one face-on spiral galaxy that we classify as a foreground source due to its large angular size. The faintest of these candidate companion galaxies has an AB apparent magnitude of $m_V \sim 23.8$ as modelled by GALFIT. Using the *HST* Exposure Time Calculator,[8] we estimate that we are sensitive to extended sources as faint as $\mu_V \approx 23.5\,\mathrm{mag\,arcsec^{-2}}$ at the 3σ level in our ACS imaging. Assuming that all companion galaxies are located at the quasar redshift yields an average upper-limit galaxy number density of $1.1 \times 10^{-4}\,\mathrm{kpc^{-2}}$, within a radius of 200 kpc, for the four FeLoBAL environments. This density is consistent with that found for (predominantly non-BAL) quasar environments at $z \sim 1.5$ within a redshift interval of $\Delta z = 0.15$ (Karouzos, Jarvis & Bonfield 2014). For our NICMOS imaging, we find an average upper limit galaxy number density of $1.9 \times 10^{-4}\,\mathrm{kpc^{-2}}$ within an 80 kpc radius. This result is consistent at the 2σ level with the number density found for ACS imaging, given the sampling uncertainty on the galaxy counts in the four NICMOS fields. In summary, we do not find evidence for the FeLoBAL quasars residing in overdense environments compared to other quasars; relative to quiescent galaxies, quasars have been reported to reside in overdense regions at ~100 kpc scales (e.g. Serber et al. 2006), although this finding may be an artefact due to control sample selection (Karhunen et al. 2014).

---

[8] http://etc.stsci.edu/

6 CONCLUSION

We present host galaxy detections in the rest-frame optical for three FeLoBAL quasars, of a sample of four objects. The host galaxy luminosities of the FeLoBAL quasars are consistent with those found for non-BAL quasars with similar nuclear luminosities. None of the host galaxies are detected in the rest-frame UV. These results are consistent with the FeLoBAL hosts being either quiescent elliptical galaxies or dust-obscured starbursts. Three of the quasars have a companion galaxy at an angular separation corresponding to less than 25 kpc at the quasar redshift. Given the probability of chance alignments, at least one of these neighbour galaxies is very likely to be physically associated with the FeLoBAL; there is an 80 per cent chance that all three companion galaxies are physically associated. These companion galaxies may represent early-stage mergers, with intermediate stellar mass ratios of ∼5:1. While the FeLoBAL hosts do not appear to be late-stage major mergers, our NICMOS observations, while relatively deep, do not have the sensitivity required to exclude fainter indicators of merger activity such as morphological distortions and tidal tails.

REFERENCES

Barden M., Jahnke K., Haussler B., 2008, ApJ, 175, 105
Barker E. A., Laidler V. G., Koekemoer A. M., 2007, Technical Report, Removing Post-SAA Persistence in NICMOS Data. Space Telescope Science Institute (STScI), Baltimore, MD, USA
Barnes J. E., Hernquist L. E., 1991, ApJ, 370, L65
Becker R. H., Gregg M. D., Hook I. M., McMahon R. G., White R. L., Helfand D. J., 1997, ApJ, 479, L93
Blanton M. R., Roweis S., 2007, AJ, 133, 734
Bloom J. S., Kulkarni S. R., Djorgovski S. G., 2002, AJ, 123, 1111
Bohlin R. C., Riess A., de Jong R., 2006, Technical Report, NICMOS Count Rate Dependent Non-Linearity in G096 and G141. Space Telescope Science Institute (STScI), Baltimore, MD, USA
Bower R. G., Benson A. J., Malbon R., Helly J. C., Frenk C. S., Baugh C. M., Cole S., Lacey C. G., 2006, MNRAS, 370, 645
Bruzual G., Charlot S., 2003, MNRAS, 344, 1000
Calzetti D., Kinney A. L., Storchi-Bergmann T., 1994, ApJ, 429, 582
Calzetti D., Armus L., Bohlin R. C., Kinney A. L., Koornneef J., Storchi-Bergmann T., 2000, ApJ, 533, 682
Canalizo G., Stockton A., 2001, ApJ, 555, 719
Cisternas M. et al., 2011, ApJ, 726, 57
Cracraft M., Sparks W. B., 2007, Technical Report, ACS Polarization Calibration – Data, Throughput, and Multidrizzle Weighting Schemes. Space Telescope Science Institute (STScI), Baltimore, MD, USA
Cristóbal-Hornillos D. et al., 2009, ApJ, 696, 1554
Croton D. J. et al., 2006, MNRAS, 365, 11
Dahlen T., Mobasher B., Somerville R. S., Moustakas L. A., Dickinson M., Ferguson H. C., Giavalisco M., 2005, ApJ, 631, 126
Di Matteo T., Springel V., Hernquist L., 2005, Nature, 433, 604
Dunlop J. S., McLure R. J., Kukula M. J., Baum S. A., O'Dea C. P., Hughes D. H., 2003, MNRAS, 340, 1095
Elvis M., 2000, ApJ, 545, 63
Fabian A. C., 1999, MNRAS, 308, L39
Falomo R., Kotilainen J. K., Pagani C., Scarpa R., Treves A., 2004, ApJ, 604, 495
Farrah D. et al., 2010, ApJ, 717, 868
Farrah D. et al., 2012, ApJ, 745, 178
Faucher-Giguère C.-A., Quataert E., Murray N., 2012, MNRAS, 420, 1347
Ferrarese L., Merritt D., 2000, ApJ, 539, L9
Floyd D. J. E., Dunlop J. S., Kukula M. J., Brown M. J. I., McLure R. J., Baum S. A., O'Dea C. P., 2012, MNRAS, 429, 2
Fruchter A. S., Hook R. N., 2002, PASP, 114, 144
Gallagher S. C., Hines D. C., Blaylock M., Priddey R. S., Brandt W. N., Egami E. E., 2007, ApJ, 665, 157
Glikman E. et al., 2012, ApJ, 757, 51
Glikman E., Simmons B., Mailly M., Schawinski K., Urry C. M., Lacy M., 2015, ApJ, 806, 218
Gonzaga S. et al., 2011, ACS Data Handbook. Space Telescope Science Institute (STScI), Baltimore, MD, USA
Granato G. L., De Zotti G., Silva L., Bressan A., Danese L., 2004, ApJ, 600, 580
Gültekin K. et al., 2009, ApJ, 698, 198
Hall P. B. et al., 2002, ApJS, 141, 267
Hall P. B., Hutsemékers D., Anderson S. F., Brinkmann J., Fan X., Schneider D. P., York D. G., 2003, ApJ, 593, 189
Harris K. et al., 2016, MNRAS, 457, 4179
Hopkins P. F., Hernquist L., Cox T. J., Di Matteo T., Martini P., Robertson B., Springel V., 2005, ApJ, 630, 705
Hsiao E. Y. et al., 2010, in Hubble after SM4. Preparing JWST. Space Telescope Science Institute (STScI), Baltimore, MD, USA
Hutchings J. B., Frenette D., Hanisch R., Mo J., Dumont P. J., Redding D. C., Neff S. G., 2002, AJ, 123, 2936
Karhunen K., Kotilainen J. K., Falomo R., Bettoni D., 2014, MNRAS, 441, 1802
Karouzos M., Jarvis M. J., Bonfield D., 2014, MNRAS, 439, 861
Kim M., Ho L. C., Peng C. Y., Barth A. J., Im M., 2008, ApJS, 179, 283
Kinney A. L., Calzetti D., Bohlin R. C., McQuade K., Storchi-Bergmann T., Schmitt H. R., 1996, ApJ, 467, 38

Kormendy J., Gebhardt K., 2001, AIPC, 586, 363

Krist J., 1995, in Shaw R. A., Payne H. E., Hayes J. J. E., eds, AIP Conf. Ser. Vol. 77, Astronomical Data Analysis Software and Systems IV. Astron. Soc. Pac., San Francisco, p. 349

Kuhlbrodt B., Örndahl E., Wisotzki L., Jahnke K., 2005, A&A, 439, 497

Kukula M. J., Dunlop J. S., McLure R. J., Miller L., Percival W. J., Baum S. A., O'Dea C. P., 2001, MNRAS, 326, 1533

Magorrian J. et al., 1998, AJ, 115, 2285

Maihara T. et al., 2001, PASJ, 53, 25

Man A. W. S., Zirm A. W., Toft S., 2016, ApJ, 830, 89

Marchesini D. et al., 2007, ApJ, 656, 42

Marconi A., Hunt L. K., 2003, ApJ, 589, L21

McGraw S. M., Shields J. C., Hamann F. W., Capellupo D. M., Gallagher S. C., Brandt W. N., 2015, MNRAS, 453, 1379

Mechtley M. et al., 2012, ApJ, 756, L38

Mechtley M. et al., 2016, ApJ, 830, 156

Nolan L. A., Dunlop J. S., Kukula M. J., Hughes D. H., Boroson T., Jimenez R., 2001, MNRAS, 323, 308

O'Dwyer I. J., Chu Y.-H., Gruendl R. A., Guerrero M. A., Webbink R. F., 2003, AJ, 125, 2239

Peng C. Y., Impey C. D., Rix H.-W., Falco E. E., Keeton C. R., Kochanek C. S., Lehár J., McLeod B. A., 2006, New Astron. Rev., 50, 689

Peng C. Y., Ho L. C., Impey C. D., Rix H.-W., 2011, GALFIT: Detailed Structural Decomposition of Galaxy Images. Astrophysics Source Code Library, record ascl:1104.010

Perley D. A., Modjaz M., Morgan A. N., Cenko S. B., Bloom J. S., Butler N. R., Filippenko A. V., Miller A. A., 2012, ApJ, 758, 122

Pogge R. W., 1989, ApJ, 345, 730

Ramos B. H. F. et al., 2011, AJ, 142, 41

Richards G. T. et al., 2006, ApJS, 166, 470

Ridgway S. E., Heckman T. M., Calzetti D., Lehnert M., 2001, ApJ, 550, 122

Rieke G. H. et al., 2004, ApJS, 154, 25

Sanders D. B., Soifer B. T., Elias J. H., Madore B. F., Matthews K., Neugebauer G., Scoville N. Z., 1988, ApJ, 325, 74

Schramm M., Wisotzki L., Jahnke K., 2008, A&A, 478, 311

Schulze A. et al., 2017, ApJ, 848, 104

Serber W., Bahcall N., Ménard B., Richards G., 2006, ApJ, 643, 68

Simmons B. D., Urry C. M., 2008, ApJ, 683, 644

Skrutskie M. F. et al., 2006, AJ, 131, 1163

Soltan A., 1982, MNRAS, 200, 115

Stoughton C. et al., 2002, AJ, 123, 485

Thatte D., Dahlen T., Barker E., de Jong R., Koekemoer A., Pirzkal N., Viana A., Wiklind T., 2009, in Casertano S., Jedrzejewski R., Keyes T., Stevens M., eds, The NICMOS Data Handbook. Space Telescope Science Institute (STScI), Baltimore, MD, USA, p. 255

Treister E., Schawinski K., Urry C. M., Simmons B. D., 2012, ApJ, 758, L39

Tremaine S. et al., 2002, ApJ, 574, 740

Urrutia T., Lacy M., Becker R. H., 2008, ApJ, 674, 80

Urrutia T., Becker R. H., White R. L., Glikman E., Lacy M., Hodge J., Gregg M. D., 2009, ApJ, 698, 1095

Vivek M., Srianand R., Petitjean P., Noterdaeme P., Mohan V., Mahabal A., Kuriakose V. C., 2012, MNRAS, 423, 2879

Voit G. M., Weymann R. J., Korista K. T., 1993, ApJ, 413, 95

Weymann R. J., Morris S. L., Foltz C. B., Hewett P. C., 1991, ApJ, 373, 23

Wright E. L. et al., 2010, AJ, 140, 1868

Yan L., McCarthy P. J., Storrie-Lombardi L. J., Weymann R. J., 1998, ApJ, 503, L19

York D. G. et al., 2000, AJ, 120, 1579

APPENDIX A: ASSEMBLY AND TESTING OF PSF TEMPLATES

Here, we describe the assembly of our empirical PSF templates, and the tests performed to determine the sensitivity of our study to false-positive host galaxy detections.

A1 Construction of PSF templates

Dedicated PSF star observations were not obtained for this observing program. In agreement with Mechtley et al. (2012), we find that the currently available analytical PSF models for NICMOS and ACS/WFC (TinyTim; Krist 1995) lack the accuracy required for the study of high-redshift quasar host galaxies: the TINY TIM PSF, assembled from multiple TINY TIM models using the same dither pattern and processed using the same MULTIDRIZZLE settings as our data, is generally too narrow. Instead, we use available *HST* data to construct empirical PSF templates. The *HST* PSF displays both temporal and position-dependent PSF variations (Kim et al. 2008). For the *HST* WFC3 detector, Kim et al. (2008) find that PSF mismatch is minimized by observing the PSF star within around a month of the science observation, and within 100 pixels of the detector position of the object to be modelled. It is also advantageous to use a PSF template with high signal-to-noise (S/N) in the PSF wings, to minimize the additional noise introduced into the modelling. The ideal empirical PSF template is therefore a bright but unsaturated star, observed quasi-contemporaneously to the science observation, at the same detector position.

PSF stars for ACS/WFC observations: Each ACS/WFC combined quasar image contains 7–10 stars suitable for use as PSF templates. Use of these stars removes the risk of PSF mismatch due to time evolution of the PSF. However, each of these stars suffers from some degree of mismatch with respect to the quasar PSF, due to position-dependent aberrations. To maximize the S/N in the PSF template, we construct stacked stellar PSF templates for the ACS imaging using these field stars; the stacking should also mitigate the field dependence of the PSF shape to some extent. We shift each sky-subtracted star to a common centroid using a linear sub-pixel interpolation kernel, and co-add the stars using uniform weights.

PSF stars for NICMOS observations: Due to the small field of view of the NIC2 detector, bright stars are seldom observed serendipitously; our data contain no suitable stars. We therefore turn to calibration star observations. For each quasar observation we construct a stacked PSF using all *HST* MAST[9] archival observations of the G2-V star P330-E within a 3-month window,[10] during which 2–3 data sets exist with the same instrumental set-up as the quasar observations. While NICMOS did observe a few calibration stars other than P330-E within this time window, the observations were too short to adequately sample the PSF wings, and their inclusion did not improve the overall signal-to-noise of the PSF template. We use the same stacking method as used for the ACS/WFC. The S/N of each stacked PSF template exceeds that of the quasar, with the exception of J0300+0048(NIC2/F110W), for which the PSF has a significantly lower S/N (Section 4.3).

A2 Testing method for PSF templates

To establish detection limits for our analysis, we perform PSF-only and PSF-plus-Sérsic modelling of archival stellar observations, hereafter referred to as *test stars*. The PSF-only modelling quantifies the amount and distribution of residual flux we can expect due to PSF mismatch, while the PSF-plus-Sérsic modelling quantifies the

---

[9] The Mikulski Archive for Space Telescopes, online resource: https://archive.stsci.edu/hst/.

[10] Adhering to a 1-month window, as recommended by Kim et al. (2008), yields too few stars to provide a high-S/N stacked PSF.

maximum flux of a spurious 'host galaxy' component fitted to a true point source, for each instrument and filter combination. For the ACS/WFC data, we use the bright, uncrowded stars used to construct the stacked PSF template as test stars; we remove the test star from the stacked PSF prior to performing the fitting. For the NICMOS data, we use archival images of stars other than P330-E as test stars. We first turn to a sample of NICMOS test stars observed at a separation of no more than 3 months from the quasar observation; three are available for filter F110W, four for F160W. Unfortunately, these are all short-exposure images, with low S/N in the PSF wings. The quasar observations themselves are deep images with high S/N. To test the modelling of high-S/N point sources, we turn to an additional sample of NICMOS test stars, observed outside the 3-month window (hereafter, the *high-S/N sample*).

For the purposes of these tests, we define a *significant deviation* from the radial profiles of the test stars as a deviation with a significance of greater than 3σ over a contiguous interval of three pixels or greater.

A3 Accuracy of PSF templates, ACS/WFC

PSF-only modelling: Most of our PSF-only fits display significant deviations from the template radial profile in the PSF core. We therefore define an 'inner radius' for each filter, inside of which we expect deviations from the PSF template even for a bona-fide point source. We find the following inner radii: 0.2, 0.3 and 0.4 arcsec for filters ACS/F425W, ACS/F550M, and ACS/F625W, respectively. We use these inner radii to establish the detection criteria for PSF-only modelling (Appendix C). We present radial profiles of four representative test stars in Fig. A1.

PSF-plus-Sérsic modelling: For the PSF-plus-Sérsic fits, the best-fitting extended components are negligibly faint in most cases, as expected if the PSF template is accurate. However, for one of our test stars (of a sample of 34) our method finds a spurious extended component only 3.4 mag fainter than the PSF component, i.e. consistent with the contrast regime expected for bright quasars. This demonstrates that the PSF+Sérsic fit method is in rare cases susceptible to false-positive detections. This motivates us to use the PSF-only modelling results as the primary test for extended emission in Section 4.

A4 Accuracy of PSF templates, NICMOS, low S/N sample

These test stars are observed within a time interval of 3 months with regard to the science observation. However, the observations are short, and therefore have low S/N in the PSF wings.

PSF-only modelling: PSF subtraction of the test stars leaves a characteristic 'criss-cross' pattern in the 2D residuals (Fig. A2). The NICMOS PSF templates tend to oversubtract the test stars, leaving negative residuals, and are thus a conservative test for extended emission. However, one of our seven NICMOS test stars is problematic: WD 1657+343 shows residual flux in the PSF wings (Fig. A2, bottom row), suggesting the presence of an extended component. We suspect this white dwarf to be a member of an X-ray binary system given its *Swift* XRT detection in hard X-rays (O'Dwyer et al. 2003), in which case the light from a faint, undetected companion, or any outflowing material due to their interaction, may explain the broadening of the surface brightness profile. The χ^2_ν fit statistic does not favour the inclusion of higher-order background curvature for this short exposure.

PSF-plus-Sérsic modelling: In multicomponent modelling we find that the PSF templates are robust against false-positive detections: we measure nucleus-to-host contrasts of $m_{\rm nuc} - m_{\rm host} \lesssim 7$ mag for test stars (including for the 'problematic' star WD 1657+343 mentioned above).

A5 Results of PSF template tests for NICMOS, high-S/N test star sample

We retrieved an additional sample of 10 test stars that have high S/N in the PSF wings, but were observed at large time separations (of order 1–2 yr) from the science observation.[11] These stars were generally only observed in two dither positions, forcing us to set the MULTIDRIZZLE output pixel size to be identical to the input pixel size. All other steps in the data processing and modelling procedure are carried out identically to that of our quasar images.

PSF-only modelling: We find that empirical PSF templates constructed from the high-S/N sample subtract the PSF wings more cleanly than for our low-S/N sample. The mismatch within the inner 1 acsec of the PSF centroid is more statistically significant here than for PSF-only fits to our low-S/N sample; this is unsurprising, as we expect PSF shape mismatch to scale linearly with total flux, unlike shot noise.

PSF-plus-Sérsic modelling: We perform multicomponent modelling of each star in our high-S/N sample, using one of the other high-S/N stars as a PSF template. Some of these fits yield a spurious 'host galaxy' at brightness contrasts of $m_{\rm nuc} - m_{\rm host} \approx 2$ mag. However, for each of these false-positive detections, the modelling converges on an 'unresolved' host galaxy component, with the scale size at its lower limit $R_e = {\rm FWHM}_{\rm PSF}$. This motivates us to be suspicious of 'unresolved' host galaxy components when modelling the quasar emission.

Alternative FeLoBAL analysis using high-S/N PSF: To test the robustness of our host galaxy detection for J1154+0300 to our choice of NICMOS PSF template, we repeat the modelling of Section 4.3, using stars from the high-S/N test star sample as PSF templates. In all cases, we find significant residual flux for J1154+0300. In most cases we find more residual extended flux using these PSF stars, compared to the original analysis using the stacked P330-E PSF (Section 4.3). This behaviour is consistent with our expectation that the stacked PSF may be broadened somewhat due to centring issues. However, the difference in residual strength may also be due to long-time-scale variation of the PSF shape: all stars in our high-S/N sample are observed at time separations of order 1–2 yr before the observation of J1154+0300. Due to the risk of long-term PSF variation, we rely on the P330-E PSF template, with time separations of no more than 3 months, in our final analysis. We also repeat the PSF-plus-Sérsic modelling using the high-S/N PSF templates, and find that while the host galaxy brightness is consistent with that found using P330-E to within the uncertainties presented in Section 4.3, the scale size R_e converges at its lower limit for some of the

---

[11] All these stars were observed later than the HST Servicing Mission 3B, during which the NICMOS detector was repaired, likely altering the PSF characteristics.
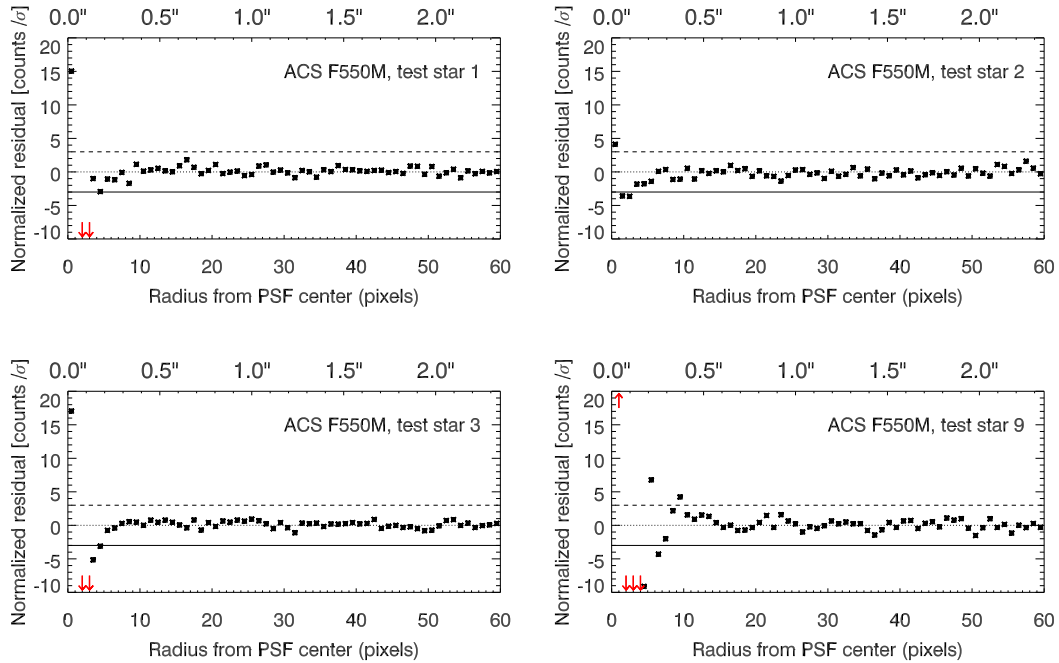
Figure A1. Radial intensity plots for PSF template fits to test stars 1–3 and 9 in the ACS J1154+0300 field. In total, we have 10 test stars for J1154+0300. Of these 10 stars, test star 9 shows the most significant deviation from the scaled PSF template. Black points: azimuthally averaged offset of the best-fitting stacked stellar PSF from the test star PSF, expressed in units of the 1σ error on the data, as a function of radius. Dotted, dashed, and dash-dot lines show the zero-point and positive, negative 3σ levels, respectively.

high S/N PSF stars. This confirms that R_e is not well-determined by our data and is sensitive to PSF mismatch.

APPENDIX B: SIMULATED QUASAR OBSERVATIONS

Here we describe simulated quasar observations used to quantify the uncertainties inherent to our image analysis (Section 4). We aim to simulate as accurately as possible the appearance (in *HST* observations) of quasars residing at the redshifts of our target FeLoBALs. We use these simulations to estimate upper limits on the host galaxy flux for non-detections, and to quantify our measurement uncertainties for detected host galaxies.

One approach to the generation of simulated observations is to use suitably degraded images of real galaxies, with a superimposed point source corresponding to an AGN nucleus. We use this approach for our NICMOS data (Appendix B1). Another option is to use analytical galaxy models representing the quasar host, with a superimposed point source representing the nucleus. The use of analytical profiles runs the risk of underestimating parameter uncertainty, as real galaxies deviate from simple models. However, we do not expect the detailed morphology to be important when observing at the limit of marginal detection. We therefore use analytical profiles to simulate host galaxies in ACS data (Appendix B2), as none of our ACS observations yield host galaxy detections. In general, for either instrument, we find that the primary source of uncertainty is the addition of a bright point source.

B1 Simulated NICMOS observations using FERENGI

Sample of low-redshift galaxy templates: We use artificially red-shifted images of low-redshift non-AGN galaxies to represent

quasar host galaxies for the NICMOS simulations. We require wide-field, multiband imaging of template galaxies as input for the artificial redshifting procedure. We select six low-redshift galaxies, spanning a range of morphologies, imaged by the Sloan Digital Sky Survey (SDSS). We choose a morphologically diverse sample of large, luminous galaxies that we expect to be visible and resolved at $z \sim 1$ in NICMOS imaging, and that have accurate distance measurements in the literature, allowing the determination of their absolute magnitude and physical size. The selected objects are as follows: (1) NGC 474, a face-on S0 galaxy which displays shells or tidal tails in the SDSS imaging; (2) PCG 6110, a massive E3 galaxy; (3) Arp 220, the lowest-redshift archetypical Ultraluminous Infrared Galaxy (ULIRG), displaying an irregular morphology with two distinct cores in the SDSS imaging; (4) NGC 5746, an edge-on SB(r)bc with a star formation rate of $1.2\,\mathrm{M_\odot\,yr^{-1}}$; (5) NGC 151, a face-on starbursting SB(r)bc galaxy; and (6) NGC 6166, a cD galaxy.

Artificial redshifting, cosmological dimming, and rebinning of template galaxies: We use the FERENGI software (Barden, Jahnke & Haussler 2008) to generate images of the SDSS template galaxies as they would appear at high redshift as observed using the NIC2 instrument. First, the images are scaled to account for the change in angular size at the target output redshift. Next, a cosmological dimming corresponding to the output redshift is applied, and the image is rebinned to the pixel scale of the NIC2 instrument. SED template fitting is then applied on a per-pixel basis using the IDL routine *kcorrect* (Blanton & Roweis 2007), so as to determine the K-corrected flux in the relevant NICMOS bandpass. The galaxy image is then scaled to the target exposure time and superimposed on a background image containing background signal and simulated readout noise at the level measured in our *HST* observations. We generate an artificially redshifted image for each galaxy template at each of the target redshifts $z = 0.89$, $z = 1.46$, and $z = 1.93$; all
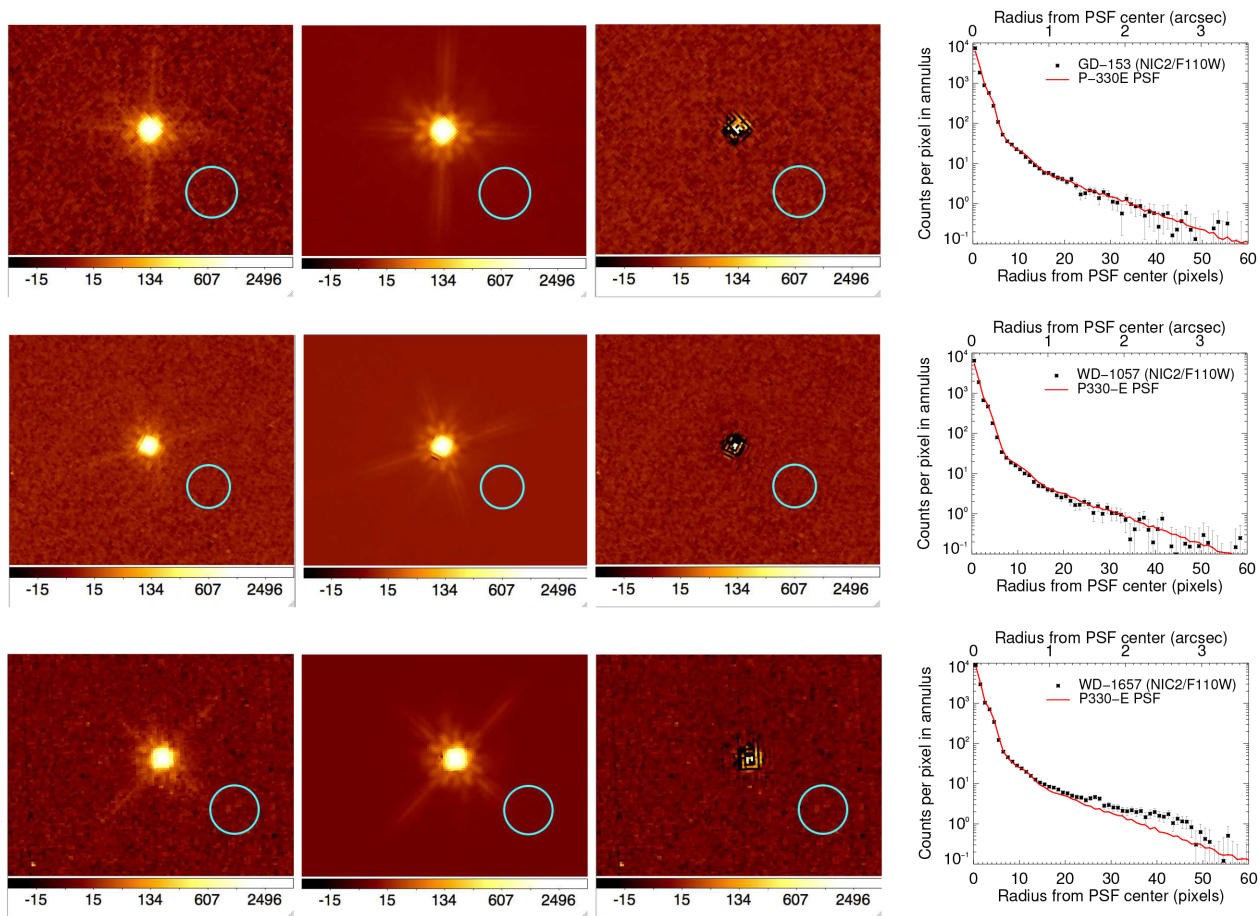
Figure A2. Stacked P330-E stellar PSF fits to representative test stars observed with the NIC2/F110W filter. From top to bottom: GD-153, WD 1057, WD 1657. North is up and east is to the left. The cyan circle depicts a 1 arcsec diameter. *Left:* Original image. *Center left:* Model image consisting of a point source fitted to the star and a sky component. *Center right:* residuals after subtracting the model. *Right:* azimuthally averaged intensity profile of test star (black points) and stacked stellar PSF template (red line) as a function of distance from the point-source centroid. WD-1657 (top right), which displays a significantly broadened PSF compared to the P330-E stacked PSF, is likely an X-ray binary (Section A4).

FERENGI output parameters (e.g. exposure time) are set to mimic the FeLoBAL observations.[12] Lastly, we add Poisson noise due to the host galaxy and the background component; the noise in the galaxy template itself is negligible due to the much smaller amount of pixels in the output images. We show the FERENGI output images, with no superimposed point source, in Figs B1 and B2. To quantify the uncertainty due to our redshift range and instrumental set-up, we first perform single-component modelling of these output images, prior to introducing a central point source. The measured absolute magnitudes are consistent with those of the input SDSS imaging to within 0.3 mag. The physical scale sizes of the single-component fits are too small by up to a factor of 2. The Sérsic index was recovered to within a value of ± 1 at all redshifts. It is difficult to determine the galaxy type via visual inspection, especially at $z = 1.46$ and $z = 1.93$ (Figs B1 and B2). Faint features such as the tidal tails/shells, visible for NGC 474 in the SDSS imaging, are not detected at cosmological distances.

Accounting for luminosity evolution: Galaxies are expected to dim with time throughout their post-starburst lifetime, due to the quiescent aging of the stellar populations (e.g. Bruzual & Charlot 2003). We find it necessary to include luminosity evolution for the simulated galaxies, as they otherwise become too faint at the source redshifts, especially compared to the host galaxy component we detect for J1154+0300. To explore the possibility of brightness evolution, we generate two sets of simulated NICMOS observations: one without brightness evolution, and another where the host galaxies become 1 mag brighter per unit redshift. We set this parameter so as to generate apparent brightnesses comparable to that which we measure for the host of J1154+0300 – it is, however, in broad agreement with Ramos et al. (2011), who find that the Schechter characteristic galaxy luminosity decreases by 0.7 mag between $z = 1.8$ and $z = 0.3$. Without luminosity evolution, the redshifted galaxy templates have apparent brightnesses as faint as 24th magnitude at $z = 1.46$ (Table B1); as we detect FeLoBAL hosts with apparent magnitudes of $\lesssim 22$ mag, it is appropriate to include luminosity evolution in our simulations.

---

[12] The redshift of and observing conditions for the last member of our FeLoBAL sample, J1730+5850(NIC2/F160W), were similar to that of J0819+4209. Tests performed on simulated images for the J0819+4209 observation therefore apply to both objects.

Tests of PSF-host decomposition: To quantify the uncertainties of our PSF-host decomposition method, we add a point-source component to the centroids of the galaxy templates in the FERENGI output
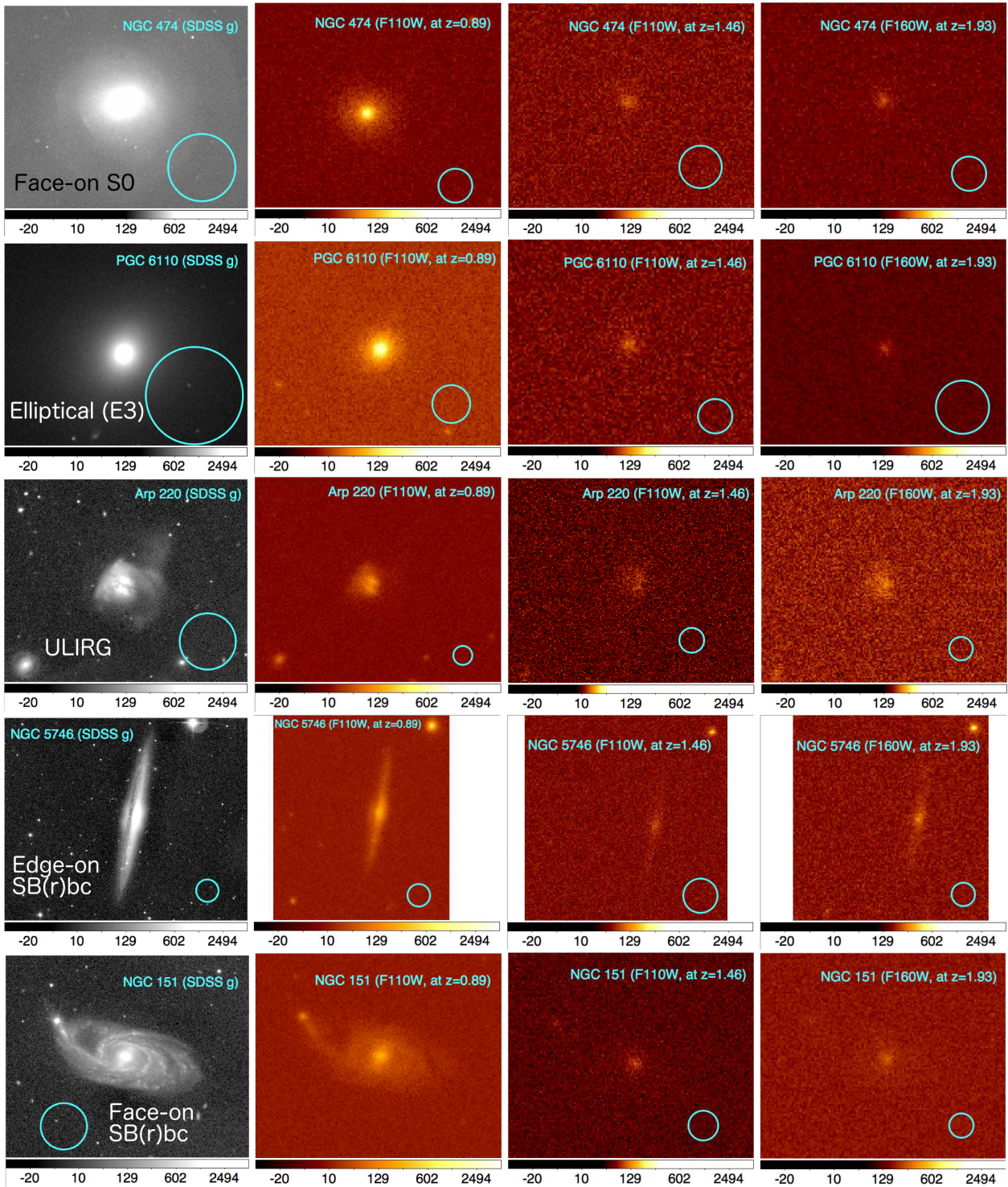
Figure B1. What would local galaxies look like if they were as distant as the FeLoBAL quasars in the present sample? FERENGI images of five low-redshift galaxies as they would appear in NIC2 images at z=0.89, z=1.46, and z=1.93, given exposure times of 2688, 5141, and 8695 s, respectively. No luminosity evolution (Appendix B1) is applied here. The leftmost column shows the input SDSS g-band images. Cyan circles represent a diameter of 1 arcmin in the SDSS image, 1 arcsec in the FERENGI output images. The remaining template galaxy (NGC 6166) is shown in Fig. B2.

images. We utilize one or two stacked observations of the NICMOS calibration star P330-E (Appendix A) to provide the point source; the remaining P330-E observations in the appropriate filter are then used as a PSF template for the GALFIT analysis. This provides an ap-

proximation of the temporal PSF variation relevant to our study. For each galaxy template, at each output redshift, we generate a range of images at host-to-nucleus brightness contrasts $0 \leq m_{nuc} - m_{host} \leq 4$ mag, in increments of 0.25 mag. These images are analysed
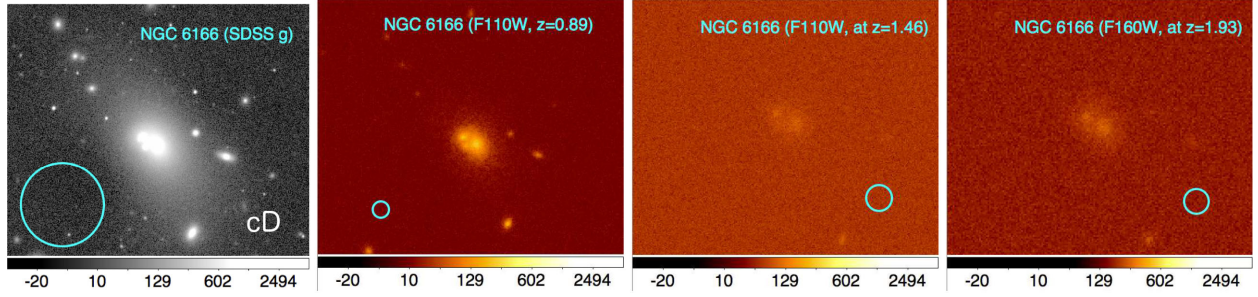
Figure B2. FERENGI output images for the final galaxy in our template sample. Panels are arranged as in Fig. B1.

Table B1. Host galaxy detection limits for NICMOS imaging.

Host galaxy template[a] (1)	m_{F110W}[b] z=0.89 (2)	Lim. contrast[c] z=0.89 (3)	m_{F110W}[b] z=1.46 (4)	Lim. contrast[c] z=1.46 (5)	m_{F160W}[b] z=1.93 (6)	Lim. contrast[c] z=1.93 (7)
No luminosity evolution:						
Ell./S0	21.35	3 mag	23.62	1.5 mag	23.54	0.5 mag
Elliptical	21.20	3 mag	24.15	0.5 mag	24.07	0.75 mag
Edge-on spiral	20.75	2.75 mag	24.15	2 mag	22.87	2.25 mag
Face-on spiral	20.03	3.5 mag	23.37	3 mag	22.31	3.5 mag
Irr., ULIRG	21.13	3.5 mag	23.37	4 mag	23.34	3 mag
cD	19.62	> 4.75 mag	23.10	> 4.75 mag	21.85	4.25 mag
dL/dz = 1						
Ell./S0	20.50	3.5 mag	22.16	4 mag	21.54	3.25 mag
Elliptical	20.88	3 mag	22.60	3.5 mag	22.03	3 mag
Edge-on spiral	19.88	3 mag	21.69	4.5 mag	20.97	3.25 mag
Face-on spiral	19.33	> 4.75 mag	20.80	> 4.75 mag	20.37	3.75 mag
Irr./ULIRG	20.25	> 4.75 mag	21.93	> 4.75 mag	21.38	4 mag
cD	18.71	> 4.75 mag	20.58	> 4.75 mag	19.88	4.25 mag

Notes. The first part of the table shows results for host components redshifted to the target redshift, applying cosmological dimming and assuming no luminosity evolution for the galaxies; these galaxies are rather faint as observed in NICMOS imaging. The second part of the table shows results for the same galaxies, assuming 1 mag of luminosity evolution per unit redshift. We use the latter results in our analysis (Section 4), as the values of m_{host} obtained assuming 1 mag of luminosity evolution more closely resemble those measured in our NICMOS images.
[a]The galaxy type of the host galaxy template. See Appendix B for details of the specific galaxies used.
[b]The apparent brightness of the galaxy after artificially redshifting it to the target redshift, as imaged in the specified filter. This brightness was measured using a single Sérsic component fit to the galaxy, without any superimposed point source component.
[c]The nucleus-to-host brightness contrast ($m_{nuc} - m_{host}$) at which the host galaxy is only marginally detected upon fitting and subtracting a PSF component and examining the residuals.

identically to the real NICMOS observations, i.e. we first perform PSF-only modelling to determine whether a host galaxy is detected, and secondly perform PSF-plus-Sérsic modelling to determine the host galaxy brightness and scale size.

For the PSF-only fits, Table B1 presents the limiting nucleus-to-host brightness contrasts beyond which we can no longer detect extended emission. The limiting brightness contrast depends on both the host galaxy type and whether any luminosity evolution is applied; without luminosity evolution, the limiting contrast values are small (reaching 0.5 mag for the elliptical/S0 template at $z = 1.93$). We note that the host galaxy detections presented in Section 4 are brighter than the no-evolution templates at $z > 1$. Thus, while the no-evolution simulations indicate that we would not detect *typical local-Universe galaxies* at $z > 1$ (where they have $m_{host} \gtrsim 23$ mag), the with-evolution simulations confirm that we indeed are able to detect an ∼22nd magnitude host at $z = 1.46$. Further supporting the FeLoBAL host detections, we note that any false-positive de-

tections in NICMOS imaging are much fainter than $m_{host} \sim 22$ mag, according to our PSF tests (Appendix A4).

For the PSF-plus-Sérsic fits, Figs B3 and B4 show the error on the measured host galaxy brightness as a function of the measured $m_{host} - m_{nuc}$; points located along the horizontal line 'input $m_{host}-$ output $m_{host} = 0$' represent ideal decompositions. The main source of uncertainty for m_{host} is our ignorance of the Sérsic index. This parameter is not well-constrained (in terms of the χ_ν^2 fit statistic) in our FeLoBAL analysis; this is in general also true of the 'simulated quasars' discussed here. Assuming no prior knowledge of the Sérsic index, 'randomly' choosing a model with a constant Sérsic index ($n = 1$ or $n = 4$) can lead to an error on m_{host} of ∼1 mag. On the other hand, models for which n is fitted as a free parameter can diverge drastically from the correct m_{host}. Taking the average (in log-flux space) of the brightnesses of the $n = 1$ and $n = 4$ models provides a more reliable measurement of m_{host} compared to either a freely fitted Sérsic index, or assuming a single value of n. We therefore use
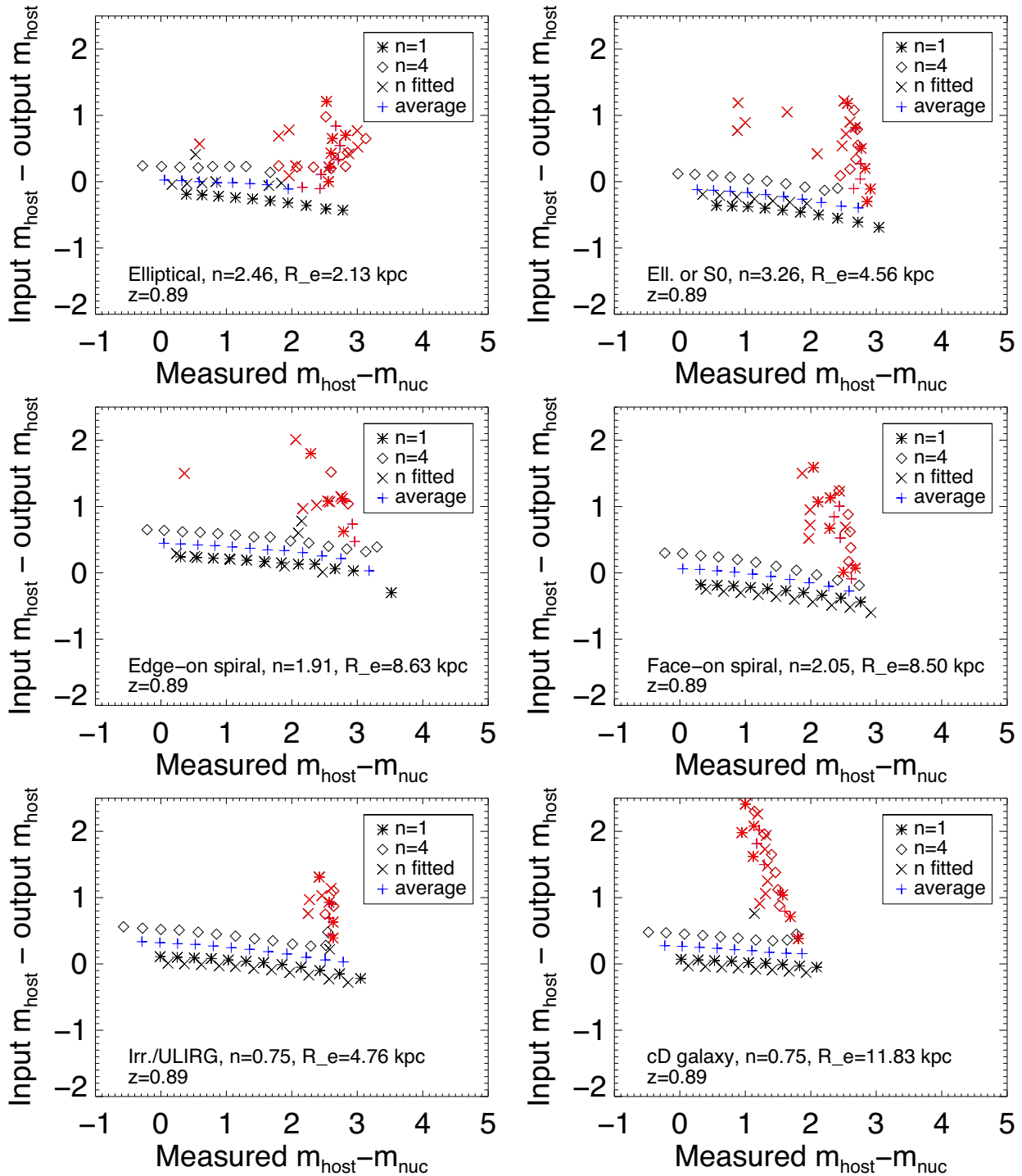
Figure B3. Uncertainty in measured host galaxy magnitudes for simulated quasar images at $z = 0.89$ as observed using NIC2, with $0 \leq m_{nuc} - m_{host} \leq$ 4 mag, in increments of 0.25 mag. The horizontal axis shows $m_{nuc} - m_{host}$ as measured using GALFIT. The vertical axis shows the difference between input and measured m_{host}, i.e. positive values on the y-axis correspond to underestimated m_{host} (thus, overestimated host brightness). Input m_{host} is measured using a single Sérsic component, prior to adding a superimposed point source to the image. Black crosses show models for which the Sérsic index is fitted as a free parameter, while diamonds and asterisks denote constant Sérsic indices; we note that the free-n fits are often further away from the input value than either of the constant-n models. Blue plus-symbols show the average (in log-space) m_{host} and average m_{nuc} between the $n = 4$ and $n = 1$ models. Models which converge with R_e equal to the PSF FWHM have red symbols; these fits are typically unreliable, and tend to overestimate m_{host}.

these averaged values in our FeLoBAL analysis, instead of relying on any one model.

Unresolved host galaxy components (for which the best-fitting R_e converges on the lower bound, $R_e = \text{FWHM}_{PSF}$) tend to under-

estimate m_{host} (i.e. overestimate the host flux) by up to 2 mag; we show these unresolved fits using red symbols in Figs B3 and B4. Simmons & Urry (2008) report similar findings in their simulated ACS imaging of AGN host galaxies at $z \lesssim 1$: when the host
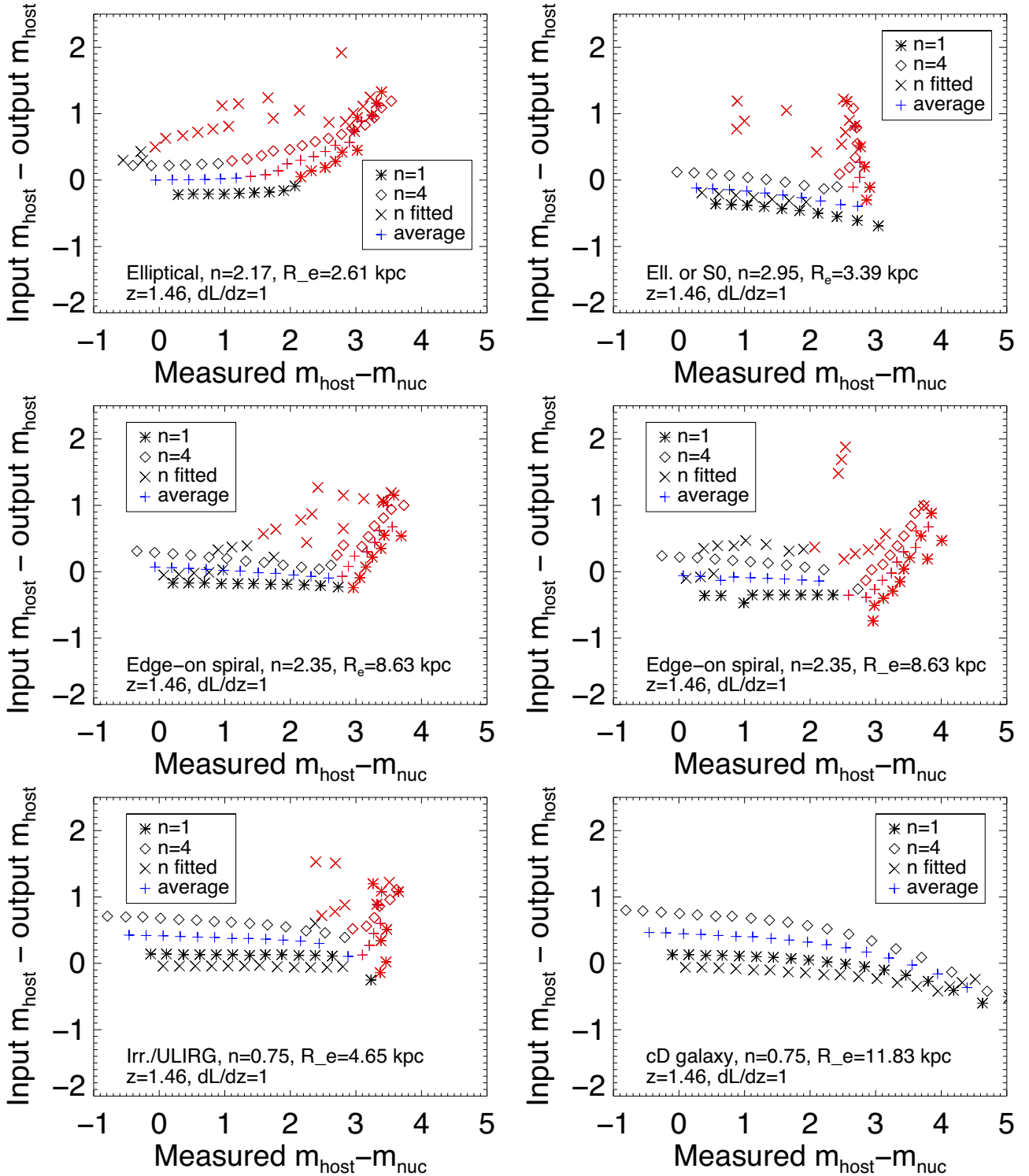
Figure B4. Error in measured host galaxy magnitudes for simulated quasar images at $z = 1.46$ as observed using NIC2, assuming 1 mag of luminosity evolution per unit redshift, such that the host galaxies in the simulated observations are artificially brightened compared to the local-Universe template galaxies, as described in Section B1. Symbols coded as for Fig. B3.

component R_e becomes small, the measured m_{host} tends to be inaccurate by up to 1.3 mag. Thus, $R_e > \mathrm{FWHM_{PSF}}$ is an important diagnostic for our modelling methodology. In particular, the recovered host component for J0819+4209 is unresolved, suggesting that our decomposition may severely overestimate the host flux. We

therefore assume an uncertainty of 1.3 mag towards fainter m_{host} for this quasar. For the quasars with resolved host galaxy components (J0300+0048 and J1154+0300), our simulations indicate that the uncertainty on m_{host} is of order 0.5 mag.
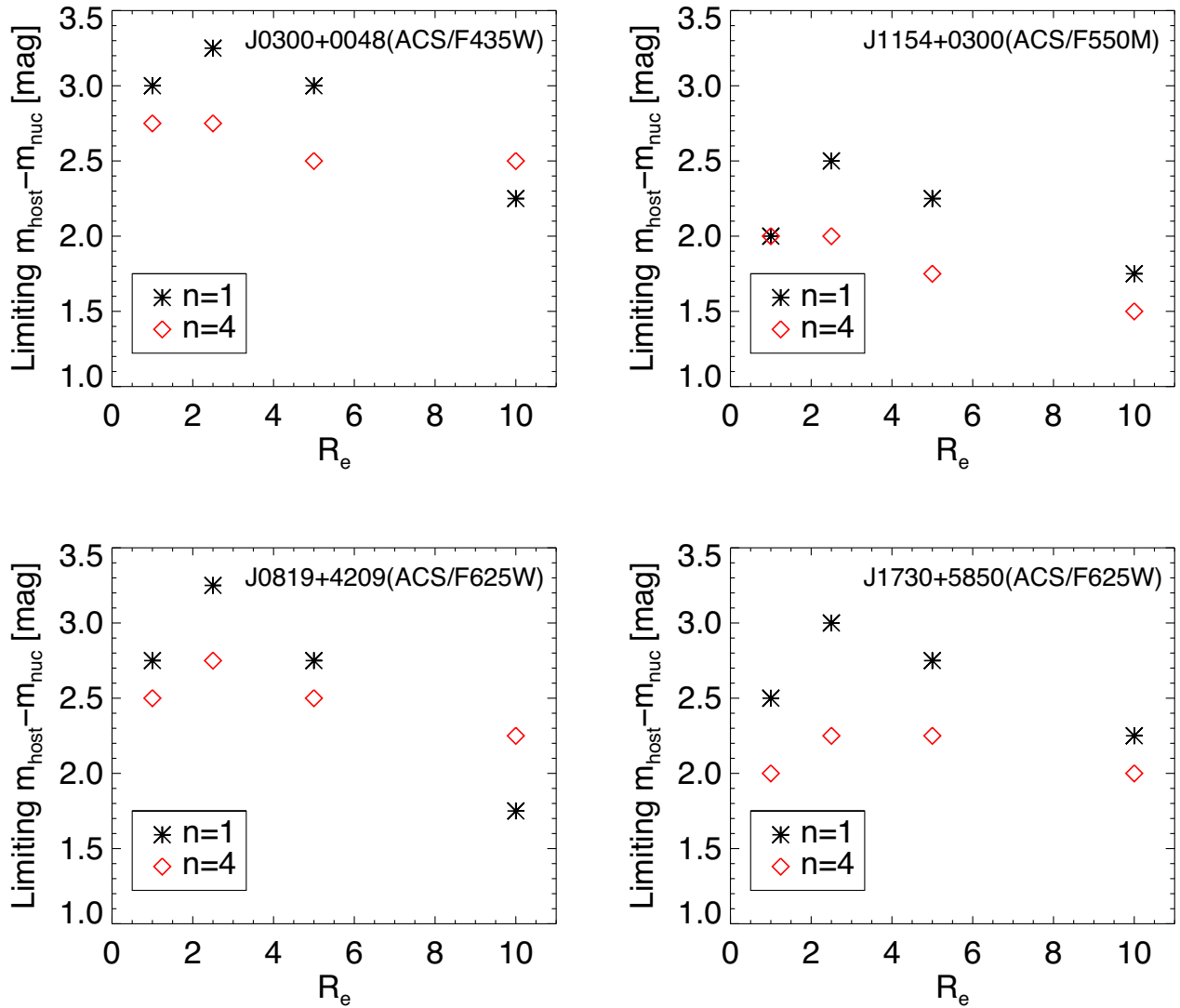
Figure B5. Detection limits for extended components in ACS observations of FeLoBAL quasars, expressed in terms of the nucleus-to-host brightness contrast. These measurements allow us to place upper limits on the rest-frame UV host galaxy components (Section 4). The upper limits depend both on the host galaxy properties (being weaker for very compact and very extended hosts) and on the observational situation (filter bandpass, exposure time, etc.). As we are ignorant of the host galaxy properties for a non-detection, it is appropriate to use the smallest limiting value of $m_{nuc} - m_{host}$ for the parameter range explored. For example, for J0300+0048, the limiting contrast is $m_{nuc} - m_{host}=2.25$ mag, as a $n = 1$ galaxy with $R_e = 10$ kpc becomes undetectable at this level.

Summary of NICMOS simulations: Due to our ignorance of the host galaxy Sérsic index, quoting an average measured m_{host} between $n = 1$ and $n = 4$ models reduces the uncertainty on the host galaxy brightness compared to using m_{host} measured for either model directly. Applying this averaging approach, our PSF-plus-Sérsic modelling of the FeLoBAL quasars measures the host galaxy magnitude with an accuracy of ±0.5 mag or less for quasars for which the best-fitting models are resolved. For unresolved host galaxies (i.e. those for which the fit converges at the limiting R_e), the uncertainty on the host galaxy brightness is much larger, up to 1.3 mag.

B2 Simulated ACS observations

Using FERENGI to artificially redshift SDSS galaxies to $z \approx 1$ as observed with ACS/WFC would involve an uncertain extrapolation of the SDSS imaging into the UV, an approach that Barden et al.

(2008) advise against. Instead, we use analytical profiles to generate simulated observations for ACS. While these analytical-profile simulations do not account for the detailed morphological structure of real galaxies, we do not find this level of detail necessary for this study, as we do not detect any of the FeLoBAL hosts in ACS imaging. Thus, we simply need to determine the values of $m_{nuc} - m_{host}$ at which the host galaxies are no longer detectable, so as to provide upper limits on the host galaxy magnitudes. We therefore produce a set of simulated images spanning nucleus-to-host contrasts $0 \leq m_{nuc} - m_{host} \leq 4$ mag, scale sizes 0.5 kpc $\leq R_e \leq 10$ kpc, and with Sérsic indices of either $n = 1$ or $n = 4$. We prepare the simulated images as follows: we use the GALFIT software to generate a Sérsic profile representing a quasar host galaxy, and add Poisson noise due to this host component. We then add a point source and a sky background component. A cutout image of a PSF star from the relevant ACS observation provides both the point-source and background components. We use the PSF star most similar in

brightness to the FeLoBAL quasar PSF. This procedure provides an image with a similar point-source brightness to the FeLoBAL quasar, and with the same observing conditions (e.g. exposure time, background level, and readout noise) as the real observation. We perform a PSF-only fit to each of the simulated observations, and classify them as detections or non-detections. Fig. B5 shows the limiting nucleus-to-host brightness contrasts at which a host component of a given scale size and Sérsic index is still detected, given the observing conditions of each ACS FeLoBAL observation. As we are ignorant of the host galaxy properties for a non-detection, it is appropriate to use the smallest limiting value of $m_{\rm nuc} - m_{\rm host}$ for the parameter range explored. This yields the most conservative, i.e. brightest, upper limit on $m_{\rm host}$. We use these limiting values of $m_{\rm nuc} - m_{\rm host}$ to calculate the upper limits in Table 4. In general, the more centrally concentrated ($n = 4$) hosts disappear at smaller limiting contrasts, as do the very extended ($R_e = 10$) hosts. The observations J1154+0300(ACS/F550M) and J1730+5850(ACS/F625W) require relatively bright host galaxies ($m_{\rm nuc} - m_{\rm host} < 1.5$ mag and < 2.0 mag, respectively) if they are to provide a detection. This is due to these observations being less deep than the other ACS observations: in the case of J1154+0300(ACS/550M) this is due to the use of the narrower F550M filter, while J1730+5850(ACS/F625W) has a shorter total exposure time than originally granted, due to a technical failure during the observation.

APPENDIX C: ESTABLISHING HOST GALAXY DETECTION CRITERIA AND UPPER LIMITS

Here, we discuss the host galaxy detection criteria applied in our analysis of the FeLoBAL imaging (Section 4). First, we must consider the modelling of *bona fide* point sources presented in Appendix A. Due to PSF mismatch, the residual images of star-star subtractions display a characteristic 'criss-cross' residual pattern (Fig. A2). When we add an extended component (Appendix B), the PSF-only fit tends to oversubtract the centre of the object, and leaves a broad 'fuzzy ring' of positive residuals. As the contrast between the nuclear and host galaxy apparent magnitudes, $m_{\rm nuc} - m_{\rm host}$ increases, the residual ring becomes fainter relative to the original flux. At a limiting value of $m_{\rm nuc} - m_{\rm host}$, the residuals become dominated by PSF mismatch and PSF shot noise, and are thus indistinguishable from the residuals shown in Fig. A2. Based on these tests and simulations, we establish the following detection criteria for extended emission:

(1) At least three contiguous 1-pixel bins in our azimuthally averaged intensity plots show a positive residual at a significance $> 3\sigma$ after PSF-only modelling. This must occur outside the inner 0.2

arcsec of the radial profile for NICMOS and ACS/F425W, outside the inner 0.3 arcsec for ACS/F550M, or outside the inner 0.4 arcsec for ACS/F625W. These radial constraints are due to the severe mismatch in the PSF core, and a general tendency to oversubtract the inner regions when performing PSF-only fits in the presence of extended flux.

(2) The PSF wings are not significantly (3σ) oversubtracted in any azimuthally averaged bin exterior to the radial constraints given in (1). This requirement selects against spurious detections due to mismatch in the PSF curvature: true extended emission should be broader than a point source at all radii.

Only one star in our test sample (Appendix A) yields a spurious detection according to these criteria. Namely, WD 1657+343, as imaged in NICMOS F110W. We suspect that this test star is an X-ray binary, which may therefore display real extended emission. As our simulations reveal a small risk (~3 per cent) of a false-positive host galaxy detection (at $m_{\rm nuc} - m_{\rm host} \sim 3$ mag) in PSF-plus-Sérsic modelling (Appendix B), we base these criteria exclusively on PSF-only modelling.

Upper limits for non-detections: For the observations where we do not detect extended flux, we estimate an upper limit on the brightness of an extended host galaxy, based on the limiting values of $m_{\rm nuc} - m_{\rm host}$ found in our simulations (Appendix B). As we are ignorant of the morphology of the FeLoBAL host galaxies, we establish detection limits for a range of galaxy types, and quote the most conservative (i.e. brightest) upper limit for a given observation. Our limiting $m_{\rm nuc} - m_{\rm host}$ values are generally smaller for our ACS analysis compared to those obtained for NICMOS. There are two reasons for this. First, we consider smaller values of R_e (down to $R_e = 0.5$ kpc) for the Sérsic component in our rest-frame UV simulations, as the star formation may be concentrated towards the nucleus. Secondly, the quasars themselves are fainter in the ACS imaging, causing host galaxies at a given contrast level to be fainter in terms of flux. The asymmetry of the galaxy templates used in our NICMOS simulations may also aid detection; for the ACS analysis we used analytical, radially symmetric host galaxy profiles. We note that adopting larger (i.e. less conservative) limiting values of $m_{\rm nuc} - m_{\rm host}$ for the ACS analysis would only strengthen the conclusions drawn in Section 5.2 with regard to the host galaxy spectral energy distribution.

This paper has been typeset from a TeX/LaTeX file prepared by the author.

Chapter 5

Swift $z \sim 2$ Quasar Catalog. I: First Results

This chapter is published in MNRAS as 'A catalog of optical to X-ray spectral energy distributions of $z \approx 2$ quasars observed with *Swift*. I: First results'. The authors are Daniel Lawther, Marianne Vestergaard, Sandra Raimundo and Dirk Grupe. All SED Figures and measurements presented in the Tables are superseded by those presented in our second publication for this sample (Chapter 6). In particular, the UV–optical modeling in that work includes a correction for emission-line and Balmer continuum contribution, which improves the accuracy of the best-fit continuum model.

5.1   Statement of Authorship

All data processing and analysis was performed by Daniel Lawther. The initial experimental design is due to Marianne Vestergaard and Dirk Grupe. The V-band apparent magnitudes, radio fluxes, radio spectral indices, and radio classifications (Table 1) are provided by Marianne Vestergaard, who also defined the quasar sample. The manuscript and figures are produced by Daniel Lawther; all co-authors provided feedback during the writing process. I include a signed statement of authorship with this Thesis (Chapter 8).

5.2   Published Work

A catalogue of optical to X-ray spectral energy distributions of $z \approx 2$ quasars observed with *Swift* – I. First results

D. Lawther,[1][*] M. Vestergaard,[1,2] S. Raimundo[1] and D. Grupe[3]

[1]*Dark Cosmology Centre, Niels Bohr Institute, University of Copenhagen, DK-2300 Copenhagen, Denmark*
[2]*Steward Observatory, University of Arizona, 933 N. Cherry Avenue, Tucson, AZ 85721, USA*
[3]*Department of Earth and Space Sciences, Morehead State University, 235 Martindale Dr., Morehead, KY 40351, USA*

ABSTRACT

We present the *Swift* optical to X-ray spectral energy distributions (SEDs) of 44 quasars at redshifts $z \approx 2$ observed by *Swift*, part of a larger program to establish and characterize the optical through X-ray SEDs of moderate-redshift quasars. Here, we outline our analysis approach and present preliminary analysis and results for the first third of the full quasar sample. Not all quasars in the sample are detected in X-rays; all of the X-ray-detected objects so far are radio loud. As expected for radio-loud objects, they are X-ray bright relative to radio-quiet quasars of comparable optical luminosities, with an average $\alpha_{ox} = 1.39 \pm 0.03$ (where α_{ox} is the power-law slope connecting the monochromatic flux at 2500 Å and at 2 keV), and display hard X-ray spectra. We find integrated 3000 Å–25 keV accretion luminosities of between 0.7×10^{46} erg s^{-1} and 5.2×10^{47} erg s^{-1}. Based on single-epoch spectroscopic virial black hole mass estimates, we find that these quasars are accreting at substantial Eddington fractions, $0.1 \lesssim L/L_{Edd} \lesssim 1$.

Key words: catalogues – quasars: general.

1 INTRODUCTION

The extreme energy output of quasars is almost certainly due to accretion of gas on to a central black hole (e.g. Lynden-Bell & Rees 1971; Lynden-Bell 1978). According to the unification paradigm (e.g. Urry & Padovani 1995), unobscured quasars are an intrinsically luminous subset of active galactic nuclei (AGN) for which we have a direct view of the continuum source and of the broad emission-line region. However, we still lack a detailed explanation of how the accretion physics of the central engine, together with reprocessing of the continuum emission on small scales and in the host galaxy, produces the observed spectral energy distributions (SEDs) of quasars.

Standard models for the UV–optical continuum source posit a geometrically thin, optically thick accretion disc around a black hole (so-called α-disk models, Shakura & Sunyaev 1973). The 'big blue bump' feature observed in the UV–optical energy range is consistent with partially reprocessed thermal emission from such a disc (e.g. Siemiginowska et al. 1995; Kishimoto et al. 2008). For α-disc models, the main intrinsic parameters that determine the disc emission are the mass (M_{BH}), spin and mass accretion rate ($\dot{M}_{BH}$) of the black hole. For $M_{BH} \approx 10^9 \, M_{\odot}$ quasars, the peak emission temperature for an α-disc model corresponds to UV or extreme-UV (hereafter EUV) energies (e.g. Krolik & Kallman 1988; Davis & Laor 2011). This peak is difficult to determine observationally

for individual quasars, due to strong EUV absorption by Galactic gas. Studies of composite spectra find evidence of a spectral turnover at roughly 1000 Å in the rest frame (e.g. Shang et al. 2005; Barger & Cowie 2010; Shull, Stevans & Danforth 2012, but see also Capellupo et al. 2016 for a recent study identifying some quasars with a lower energy turnover).

The α-disc model predicts very little hard X-ray emission for accretion on to supermassive black holes. Additional components are therefore necessary to explain the observed X-ray spectra, as follows. To first order, the hard X-ray SEDs follow power-law functions (e.g. Nandra & Pounds 1994). Recent studies using the *NuSTAR* X-ray telescope (XRT) have greatly improved our knowledge of the high-energy cutoff of this continuum emission, measuring cutoff energies of $\sim$50–250 keV (e.g. Brenneman et al. 2014; Fabian et al. 2015).[1] Radio-loud quasars (hereafter, RLQs) differ from radio-quiet quasars (RQQs) in that they are more X-ray luminous (Zamorani et al. 1981), have harder X-ray spectra (e.g.

---

[1] Interestingly, an unusually high cutoff energy $\sim$720 keV is found for the X-ray continuum of NGC 5506 (Matt et al. 2015). This X-ray continuum may be due to inverse-Compton upscattering of accretion disc photons by hot ($kT_e \sim 100$ keV) electrons in an optically thin corona or inner disc region (Zdziarski, Johnson & Magdziarz 1996; Ghosh, Dewangan & Raychaudhuri 2016). Analyses of X-ray variation time-scales, and of X-ray reverberation lags due to reflection in the accretion flow, suggest that the coronas have sizes of the order of 3–10 times the gravitational radius of the black hole (e.g. Emmanoulopoulos et al. 2014; Uttley et al. 2014; Fabian et al. 2015).

[*] E-mail: unclellama@gmail.com

Elvis et al. 1994), and display a correlation between X-ray and radio-core flux (Tananbaum et al. 1983). These results suggest the presence of an additional X-ray emitting component for RLQs. Indeed, extended X-ray emission from the radio jet is observed for some RLQs (e.g. Worrall 2009). In addition to the hard X-ray continuum, many AGN display a 'soft excess' component[2] below rest-frame 1 keV (Porquet et al. 2004; Piconcelli et al. 2005), possibly due to upscattering of UV photons in the warm ($kT_e \approx 1$ keV) atmosphere of the accretion disc (e.g. Czerny & Elvis 1987; Haardt & Maraschi 1991).

In summary, UV–optical and X-ray observations support a scenario where a fraction of the available accretion energy is reprocessed by Compton upscattering in one or more regions of hot, diffuse electron gas. The remainder of the accretion energy not consumed by the black hole is either emitted as thermal radiation, or (for RLQs) channelled into the radio jet. The relative emission strengths of these components can be estimated using observations of optical to X-ray SED. For 47 quasars spanning $0.01 < z < 3.3$, the pioneering work of Elvis et al. (1994) reveals flux deviations of up to 1 dex from the mean SED for individual objects, when normalized in the near-infrared. Richards et al. (2006) compile a larger SED catalogue while expanding the spectral coverage to the mid-IR, while Elvis et al. (2012) present an X-ray-selected SED catalogue (in contrast to Elvis et al. 1994, who select quasars primarily based on UV excess). While these authors attribute some of the dispersion in quasar SED properties to reddening and host galaxy contamination, other shape variations may be due to changes in the accretion physics of the central engine. In particular, variations in the ratio of UV to X-ray luminosity (as parametrized by α_{ox}, Tananbaum et al. 1979) may be due to the physical relationship between the accretion disc and the X-ray corona (Lusso & Risaliti 2016). At $z < 0.4$, SED studies that include UV–optical spectroscopy find several correlations between broad emission-line widths and spectral shape parameters (Jin, Ward & Done 2012). These correlations suggest that the black hole mass, accretion rate and Eddington ratio largely determine the SED shape, with the X-ray spectrum steepening and the SED becoming more disc dominated at higher Eddington ratios; the latter is also found by Grupe et al. (2010).

Quasars are variable in luminosity over rest-frame time-scales of days (in the X-ray, e.g. Gibson & Brandt 2012) to years (e.g. Kaspi et al. 1996, 2007; Vanden Berk et al. 2004). This can introduce uncertainty to SED measurements if there are time delays between the observations of the different spectral regions. In fact, Jin et al. (2012) find that the bolometric correction for a given AGN correlates with the Eddington ratio of that object, while Kilerci-Eser & Vestergaard (in preparation) find that the bolometric corrections display temporal variation of the order of 10 per cent (up to 100 per cent in extreme cases) for individual AGN. These findings emphasize the importance of simultaneous multiband observations for accurate measurement of the bolometric luminosity and study of the Eddington ratio. X-ray observatories such as *XMM–Newton* (Jansen et al. 2001) and *Swift* (Roming et al. 2005) include UV–optical detectors, allowing contemporaneous observation of the optical to X-ray SED. The *Swift* Gamma-ray Burst Explorer telescope has been used to study low-redshift AGN (Grupe et al. 2010), and to study a large, serendipitously observed sample of AGN at $z < 5.5$ (Wu et al. 2012). We are currently observing a sample of 133 quasars using *Swift*, carefully selected to probe a diverse set of quasar prop-

erties at $z \approx 2$ (Section 2). Here, we present and characterize the SEDs of 44 quasars with Swift detections or bona fide upper limits. We describe the data processing procedure for our *Swift* XRT and UV/Optical Telescope (UVOT) data in Section 3. We include data from the Sloan Digital Sky Survey (SDSS) to support our analysis (Section 4). We present the SEDs (Section 4) and provide a preliminary statistical analysis of this sample subset (Section 6), including a characterization of the UV to X-ray SED shapes of these quasars as parametrized by the UV–optical to X-ray spectral index α_{ox} (Tananbaum et al. 1979). In the same section, we present a preliminary study of their mass accretion rates and Eddington ratios. We use a cosmology with $H_0 = 67.48 \pm 0.98$ and $\Omega_m = 0.313 \pm 0.013$ throughout (Planck Collaboration XIII 2016).

2 SAMPLE SELECTION AND OBSERVATIONS

2.1 Sample selection

Our $z \approx 2$ quasar sample is selected to span a wide range in luminosity, radio strength and (when possible) radio spectral index, thereby allowing us to test for dependences of the SED shape on these properties. We use the quasar sample presented by Vestergaard, Wilkes & Barthel (2000), containing roughly equal numbers of RLQs and RQQs, the majority of which are pair-matched in redshift and in absolute *V*-band magnitude. The sample quasars fulfil the following criteria:

(a) redshift $z \geq 1.5$, to ensure that the Lyman α emission line is observable in ground-based spectroscopy;
(b) *V*-band absolute magnitudes that satisfy $-29.5\,\mathrm{mag} < M_V < -26.5\,\mathrm{mag}$.
(c) *V*-band apparent magnitudes $m_V < 20$, so as to ensure that high-signal-to-noise spectroscopy can be obtained within reasonable exposure times;
(d) strongly variable objects (e.g. blazars) are excluded;
(e) objects identified as broad absorption line (BAL) quasars as per 1998 are also excluded by Vestergaard et al. (2000). Note that two sample objects (Q1227+120 and Q2350−007) were subsequently found to be BAL or mini-BAL quasars.

The Vestergaard et al. (2000) sample does not include the most luminous quasars at a given redshift, as the original intention was to study objects with a range of 'population-typical' luminosities. For the RLQs, measurements of the radio fluxes, the radio spectral index and the radio-core fraction at 5 GHz are compiled by Vestergaard et al. (2000). The sample spans the full range of radio spectral indices, α_{5000}^{1400}, typically observed for bright quasars. Assuming that α_{5000}^{1400} can be interpreted as a measure of our viewing angle relative to the radio jet (e.g. Jarvis & McLure 2006), the RLQ sample thus spans the full range of viewing angles, i, for unobscured (type 1) quasars ($5° \lesssim i \lesssim 45°$, Barthel 1989). To increase the statistical power of our study, we also include 16 quasars from the SDSS Data Release 7 (SDSS DR7) that fulfil $z > 1.6$ and $m_V < 18$ mag. These 16 quasars have been observed in X-rays prior to our observing campaign, and are selected to be sufficiently X-ray bright as to be detectable with *Swift* for modest exposure times. We refer to objects from the Vestergaard et al. (2000) sample using the name convention Q*xxxx* ± *xxx*, while J*xxxx* ± *xxx* denote the additional SDSS DR7 quasars.

At present, our full sample comprises 133 quasars in the redshift interval $1.5 < z < 3.6$, with a roughly equal number of RLQs and RQQs. This paper presents an analysis of 44 quasars from our sample, for which the initially requested *Swift* observations are

---

[2] The soft excess component can only be unambiguously identified at $z \lesssim 0.4$ using current XRTs.

Table 1. Quasars in our current sample.

| Object name	RA (deg)	Dec. (deg)	Redshift	m_V (mag)	Radio class	$F_{408\mathrm{MHz}}$ (mJy)	$F_{1.4\mathrm{GHz}}$ (mJy)	$F_{5\mathrm{GHz}}$ (mJy)	α^{1400}_{5000}	SDSS phot.?
(1)	(2)	(3)	(4)	(5)	(6)	(7)	(8)	(9)	(10)	(11)
J014725.50−101439.11	26.8562	−10.2442	2.147 77	17.41	RQQ	–	–	–	–	✓
J082328.62+061146.07	125.869	6.196 13	2.815 24	18.0	RLQ	–	(67.1)	–	–	✓
J094853.60+085514.40	147.223	8.920 67	1.981 79	17.3	RLQ	–	(33.1)	–	–	✓
J104915.44−011038.18	162.312	−1.1772	2.129 43	17.9	RQQ	–	–	–	–	✓
J110607.48−173113.60	166.531	−17.5204	2.549 25	17.8	RQQ	–	–	–	–	✓
J111159.70+023719.76	167.999	2.622 15	1.882 47	17.8	RQQ	–	–	–	–	✓
J112542.30+000101.33	171.426	0.017 037	1.692 30	17.6	RLQ	–	(29.9)	–	–	✓
J114449.32+032751.96	176.206	3.464 43	2.100 35	17.7	RQQ	–	–	–	–	✓
J131810.74+011140.86	199.545	1.194 68	1.648 97	17.9	RQQ	–	–	–	–	✓
J142923.92+024023.14	217.35	2.673 09	1.672 83	17.4	RQQ	–	–	–	–	✓
J145717.86+024747.36	224.324	2.79649	1.975 51	16.98	RQQ	–	–	–	–	✓
J234830.41+003918.57	357.127	0.655 158	2.000 07	17.78	RIQ	–	(3.3)	–	–	✓
Q0002−008	1.25178	−0.563 437	2.173 29	18.91	RQQ	–	–	–	–	✓
Q0015+026	4.5474	2.9441	2.470	18.7	RQQ	–	–	–	–	✓
Q0020+022	5.8535	2.566	1.80	18.6	RQQ	–	–	–	–	✓
Q0038−019	10.3584	−1.721 02	1.674	18.5	SSS	3191	1424	417	−0.96	✓
Q0040−017	10.7304	−1.4267	2.396	18.0	RQQ	–	–	–	–	✓
Q0106+013	17.1615	1.583 42	2.099	18.4	FSS	–	2890	1950	−0.31	✓
Q0115−011	19.6166	−0.877 753	2.186 06	18.37	RQQ	–	–	–	–	✓
Q0123+257	21.6783	25.9837	2.358	17.5	FSS	–	857	1130	0.22	
Q0226−038	37.2217	−3.626 98	2.066	17.0	FSS	2230	650	650	−0.25	✓
Q0238+100	40.3428	10.3132	1.816	18.0	SSS	980	303	76	−1.09	
Q0244+017	41.7401	1.986 53	1.945	19.26	RQQ	–	–	–	–	✓
Q0249−184	42.9496	−18.2414	3.209	18.6	RQQ	–	–	–	–	
Q0252+016	43.8134	1.807 98	2.470	18.23	RQQ	–	–	–	–	✓
Q0445+097	72.0906	9.847 59	2.110	19.5	SSS	2609	1007	543	−0.49	
Q0458−020	75.3034	−1.987 29	2.286	19.5	FSS	2600	950	480	0.48	
Q0504+030	76.9021	3.131 11	2.453	19.0	SSS	2600	950	480	−0.54	
Q0808+289	122.904	28.751	1.890 17	18.37	SSS	260	125	50	−0.72	✓
Q1311−270	198.447	−27.2803	2.186	17.4	SSS	1717	125	212	−1.10	
Q1402−012	211.191	−1.506 07	2.499 24	18.2	FSS	–	620	340	−0.12	✓
Q1442+101	221.319	9.976 69	3.529 52	17.3	FSS	2200	2415	1200	−0.55	✓
Q1542+042	236.248	4.129 57	2.182 94	18.0	FSS	1610	766	490	−0.35	✓
Q1614+051	244.156	4.992 42	3.197	19.5	GPS	–	306	875	0.83	✓
Q1626+115	247.939	11.9342	1.782 88	18.5	CSS	–	1628	974	−0.40	✓
Q1656+477	254.512	47.6303	1.622	18.0	FSS	–	783	1420	–	✓
Q1726+344	261.958	34.3778	2.429	18.5	SSS	280	75	25	−0.86	✓
Q2212−299	333.817	−29.7398	2.706	17.3	FSS	–	410	410	−0.30	
Q2223+210	336.409	21.3018	1.959	17.8	SSS	–	1995	1206	−0.40	
Q2251+244	343.539	24.7565	2.328	18.2	SSS	3331	2064	915	−0.64	✓
Q2334+019	354.233	2.2033	2.193	19.0	RQQ	–	–	–	–	✓
Q2341+010	356.097	1.3347	1.960	19.5	RQQ	–	–	–	–	✓
Q2350−007	358.223	−0.480 693	1.623 61	18.48	RQQ	–	–	–	–	✓
Q2359+002	0.550 084	0.548 188	2.670	19.8	RQQ	–	–	–	–	✓

Notes. (1) Object name. (2,3) Coordinates are given in degrees for the standard epoch J2000. (4) Spectroscopic redshifts as retrieved from the NASA Extragalactic Database (https://ned.ipac.caltech.edu/). The NASA/IPAC Extragalactic Database (NED) is operated by the Jet Propulsion Laboratory, California Institute of Technology, under contract with the National Aeronautics and Space Administration. (5) *V*-band apparent magnitudes, compiled by Hewitt & Burbidge (1993). (6) Radio classification. SSS: steep-spectrum source. FSS: flat-spectrum source. GPS: GHz-peaked source. CSS: compact steep-spectrum source. RQQ: radio quiet quasar. RLQ: radio-loud quasar with unknown radio spectral index. RIQ: radio-intermediate quasar with unknown radio spectral index. (7,8,9) The radio flux densities at 408 MHz, 1.4 GHz and 5 GHz. References: Barthel et al. (1988, steep-spectrum sources). Barthel, Tytler & Thomson (1990), 3C, 4C (e.g. Murphy, Browne & Perley 1993, flat-spectrum sources). Parentheses denote data from the FIRST survey (Becker et al. 1995). (10) The radio spectral index between the flux at 1400 MHz and 5 GHz, as compiled by Vestergaard (2000). (11) A checkmark indicates that SDSS broad-band photometry is available (Section 4).

complete as per 2015 September: we either have a secure X-ray detection, or find that the X-ray count rate is so low that additional X-ray observations would not yield a detection (as defined in Section 3.1.2). Basic information for the 44 quasars in the current subsample is listed in Table 1; their redshift distribution is shown in Fig. 1. An expanded analysis of the full sample will be presented in future work.

2.2 *Swift* observations

The *Swift* Gamma-ray Burst Explorer satellite (Gehrels et al. 2004) is equipped with two Narrow Field Instruments: the XRT (Burrows et al. 2005) and the UVOT (Roming et al. 2005). In this study, we utilize simultaneously observed XRT (0.3–10 keV) and UVOT data. *Swift* observed the current sample between 2010 June and 2015 August; most of the observations were performed during
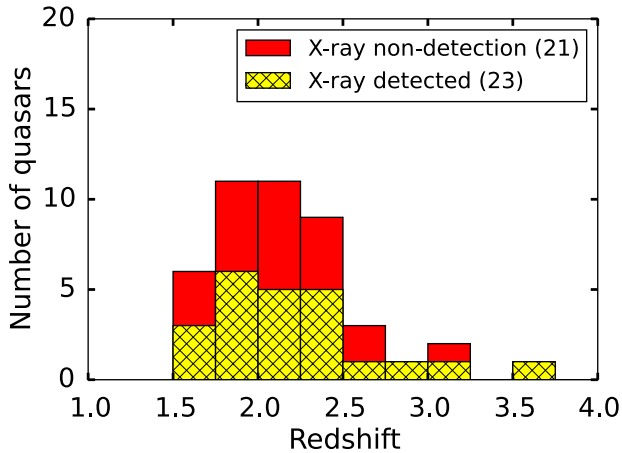
Figure 1. The redshift distribution of quasars in the current sample. Stacked histogram: the bar height shows the total number of quasars at a given redshift, while the areas of the hash-marked yellow and plain red regions show the distribution of X-ray detections and non-detections, respectively.

2013–2015. As our targets have not been observed in the X-ray regime prior to this study, the necessary XRT exposure times are estimated based on the *V*-band fluxes, assuming an optical to X-ray flux ratio α_{ox} =1.35, typical for unobscured quasars (e.g. Laor et al. 1997; Jin et al. 2012). For objects where these initial observations did not yield a secure X-ray detection, we are currently obtaining additional observations, unless the object appeared to be strongly absorbed (i.e. have $\alpha_{ox} \gtrsim 2$), in which case additional observations would not provide a secure detection. The total UVOT exposure time per object is approximately equal to the total XRT exposure time. However, as we require multiband photometry in order to determine the UV/optical SED, the total UVOT exposure time is distributed across several UVOT imaging filters. All XRT observations were performed in photon-counting (PC) mode (Hill et al. 2004).

The quasars were observed by *Swift* as 'fill-in' observations (i.e. observed while the telescope was not responding to a Gamma-ray Burst trigger or performing other time-critical observations) as part of the Danish *Swift* programme. Most of the quasars were observed multiple times so as to fulfil the requested exposure time. For bright quasars, the typical intrinsic source variability is expected to be of the order of 10 per cent and to take place on time-scales of months to years in the rest frame (e.g. Kaspi et al. 2007). The observations for individual objects were performed over rest-frame time intervals not exceeding two months. As a result, we do not expect strong source variability to occur between individual *Swift* observations. Indeed, we see no significant variability in the data (Section 3.2).

3 PROCESSING OF *SWIFT* XRT AND UVOT DATA

3.1 XRT data

The basic processing steps are as follows. We first select X-ray events from the XRT event files in a source and a background region, respectively (Section 3.1.1). We then establish whether an X-ray source was detected at the 3σ level (Section 3.1.2), and finally fit a model to the X-ray data, and measure X-ray fluxes and photon indices of the best-fitting model (Section 3.1.3). For non-detections, in the last step, we only measure an upper-limit flux (Section 3.1.4) and a hardness ratio (HR) (Section 6.2). These basic measurements are presented in Table 2.

3.1.1 Event selection

We use the High Energy Astrophysics Science Archive Research Center (HEASARC) tool *'xrtpipeline'* to perform basic pipeline processing on the raw XRT data for each individual observation. We select events using the default grading threshold (0–12) for the XRT PC mode. For each observation, we generate separate event files for the source and background regions using the *'xselect'* tool. We define a default source region of radius 20 pixels centred on the quasar coordinates, and an annulus of width 60 pixels for background extraction. We resize these default regions (or change the shape of the background region) if visual inspection of the XRT image reveals a contaminating source. We discard events with energies outside the 0.3–10.0 keV window within which the XRT is sensitive, along with events that took place outside the 'good time intervals' for each observation, e.g. events that took place while the spacecraft was slewing. As none of our objects have an X-ray flux larger than 0.1 counts s^{-1}, photon pile-up is not an issue.[3]

We use the task *'xrtmkarf'* to generate auxiliary response files (ARFs) for each observation. The information in these files is used by XSPEC to account for the effective area, quantum efficiency, and point spread function shape of the instrument. For the extraction of the X-ray spectra, we use the Redistribution Matrix File, located in the HEASARC calibration data base,[4] to account for the finite energy resolution of the detector. As a final preparation for the X-ray analysis, we use the task *'grppha'* to group the events in bins with at least one event per bin; this is necessary for model fitting using the Cash statistic (Cash 1979) to be robust (Section 3.1.3).

3.1.2 Establishing source detections

To establish whether a source is detected in our XRT observations, we generate 99.73 per cent (3σ) confidence intervals for the source count rate given the observed number of counts using the Bayesian formalism of Kraft, Burrows & Nousek (1991), which assumes that the observed source count rate is Poisson distributed. This method produces confidence intervals that are valid for PC experiments even if the background-subtracted source counts are negative; this can happen if the background signal in the source aperture fluctuates downwards (relative to the background extraction region). We use a flat non-negative prior probability on the mean count rate. Following Kraft et al. (1991), we define a source as non-detected if the 3σ lower bound on the source count rate (as given by the lower confidence interval) equals zero. For non-detections, we propagate the upper 3σ confidence interval on the source count rate to an upper limit on the source flux, as described in Section 3.1.4. We list the number of background-subtracted XRT counts N_{sub} and the XRT detection status for each quasar in Table 2. We also provide the detection significance, σ, calculated based on the total number of counts detected in the background and source apertures.

3.1.3 Spectral modelling for XRT-detected quasars

We use the XSPEC software (Arnaud 1996) to model the X-ray spectra of each quasar. Although long-exposure observations of AGNs often

---

[3] For the XRT detector in PC mode, a correction for pile-up is advised at count rates of 0.5 counts s^{-1} or higher (http://www.swift.ac.uk/analysis/xrt/pileup.php). The three highest flux objects in our sample, with count rates of between 0.02 and 0.07 counts s^{-1}, show no evidence of pile-up.

[4] As all observations took place later than 2007, we use the latest XRT Response Matrix File (RMF) file *(swxpc0to12s6_20070901v011.rmf)*.

Table 2. *Swift* XRT observation log and X-ray modelling.

Object name (1)	$N_{obs}{}^a$ (2)	XRT exp. time (s) (3)	XRT detect? (4)	σ_{det} (5)	$F_{0.3-10}$ (6)	F_ν(2 keV) (7)	Γ $(10^{22}\,cm^{-2})$ (8)	N_H (9)	N_{sub} (10)	HR (11)	N_{soft} (12)	N_{soft} (background) (13)
J014725.50−101439.11	1	6650	(P)	−0.2	≤0.63	≤0.03	–	0.0268	−0.4	–	0	1.2
J082328.62+061146.07	3	11 490	✓	8.7	$2.94^{+0.30}_{-0.36}$	5.40 ± 0.98	$1.85^{+0.18}_{-0.17}$	0.0229	84.4	$-0.18^{+0.11}_{-0.12}$	55	5.1
J094853.60+085514.40	5	5139	✓	6.3	$4.05^{+0.54}_{-1.16}$	4.27 ± 1.03	$1.56^{+0.22}_{-0.22}$	0.0252	42.4	$-0.18^{+0.15}_{-0.16}$	27	1.3
J104915.44−011038.18	2	11 001		1.5	≤0.54	≤0.91	–	0.0363	5.1	$-0.11^{+0.24}_{-0.56}$	6	3.1
J110607.48−173113.60	1	5769		1.8	≤1.16	≤2.21	–	0.0439	5.4	$-0.25^{+0.23}_{-0.53}$	5	1.6
J111159.70+023719.76	2	5711		1.0	≤1.26	≤1.97	–	0.0367	2.3	$0.30^{+0.70}_{-0.20}$	2	1.7
J112542.30+000101.33	1	5364	✓	7.5	$5.25^{+0.69}_{-1.06}$	6.42 ± 1.18	$1.73^{+0.19}_{-0.19}$	0.0297	59.4	$-0.22^{+0.12}_{-0.13}$	38	1.7
J114449.32+032751.96	2	5507		0.9	≤0.97	≤1.62	–	0.0199	2.2	$0.04^{+0.96}_{-0.06}$	3	2.0
J131810.74+011140.86	1	5676		0.8	≤0.88	≤1.27	–	0.0206	2.0	$0.29^{+0.71}_{-0.21}$	3	2.4
J142923.92+024023.14	1	5020		1.0	≤0.97	≤1.41	–	0.0244	2.7	$-0.42^{+0.13}_{-0.58}$	5	2.2
J145717.86+024747.36	2	4885	(P)	−0.7	≤0.91	≤0.05	–	0.0402	−1.2	–	2	2.7
J234830.41+003918.57	3	11 585	✓	10.6	$5.67^{+0.71}_{-0.99}$	5.29 ± 0.90	$1.47^{+0.13}_{-0.13}$	0.0337	117.8	$0.08^{+0.09}_{-0.09}$	57	2.6
Q0002−008	6	3936	(P)	0.0	≤1.22	≤0.07	–	0.0303	−0.1	–	3	2.4
Q0015+026	3	3481		0.4	≤1.54	≤2.83	–	0.0308	0.8	$-0.44^{+0.05}_{-0.56}$	4	2.4
Q0020+022	3	3494		1.3	≤0.32	≤0.48	–	0.0324	3.2	$-0.25^{+0.21}_{-0.75}$	4	1.7
Q0038−019	4	8109	✓	10.7	$7.54^{+0.78}_{-1.05}$	8.28 ± 1.13	$1.64^{+0.13}_{-0.13}$	0.0256	120.2	$-0.06^{+0.09}_{-0.09}$	66	2.4
Q0040−017	5	3609		1.8	≤1.57	≤2.84	–	0.025	4.8	$0.26^{+0.53}_{-0.23}$	3	1.3
Q0106+013	3	5090	✓	11.9	$15.40^{+0.89}_{-2.46}$	12.72 ± 1.61	$1.39^{+0.12}_{-0.12}$	0.0242	148.3	$-0.00^{+0.08}_{-0.08}$	79	4.6
Q0115−011	4	5946		1.4	≤1.13	≤1.94	–	0.0389	4.6	$0.31^{+0.69}_{-0.23}$	6	4.7
Q0123+257	4	2814	✓	9.1	$17.19^{+1.32}_{-3.58}$	16.18 ± 3.17	$1.45^{+0.16}_{-0.16}$	0.0687	86.2	$0.04^{+0.11}_{-0.11}$	43	1.6
Q0226−038	3	5859	✓	9.7	$8.87^{+1.26}_{-1.87}$	8.32 ± 1.40	$1.47^{+0.14}_{-0.14}$	0.0221	98.6	$-0.01^{+0.10}_{-0.10}$	52	1.6
Q0238+100	12	14 190	✓	10.0	$4.11^{+0.39}_{-0.66}$	5.37 ± 0.82	$1.77^{+0.15}_{-0.15}$	0.0935	107.0	$-0.13^{+0.10}_{-0.10}$	64	3.5
Q0244+017	7	3963		0.9	≤2.11	≤3.37	–	0.0432	1.9	$0.64^{+0.36}_{-0.06}$	1	2.2
Q0249−184	4	2889		1.7	≤1.47	≤3.22	–	0.03	4.1	$-0.50^{+0.15}_{-0.50}$	4	0.6
Q0252+016	3	2987		1.2	≤1.35	≤2.49	–	0.0743	2.4	$-0.46^{+0.14}_{-0.54}$	3	0.7
Q0445+097	7	3758	✓	5.8	$7.35^{+0.59}_{-1.38}$	6.85 ± 1.75	$1.46^{+0.27}_{-0.27}$	0.131	47.1	$0.37^{+0.17}_{-0.16}$	24	8.7
Q0458−020	5	4235	✓	12.9	$21.17^{+1.50}_{-2.40}$	24.53 ± 3.33	$1.59^{+0.11}_{-0.11}$	0.0602	170.2	$-0.01^{+0.08}_{-0.08}$	87	1.1
Q0504+030	5	4258	✓	6.0	$6.40^{+0.86}_{-2.77}$	3.82 ± 1.39	$1.18^{+0.24}_{-0.25}$	0.0894	39.3	$0.28^{+0.17}_{-0.15}$	16	1.9
Q0808+289	5	2897	✓	5.0	$4.67^{+0.72}_{-1.69}$	5.43 ± 1.58	$1.65^{+0.28}_{-0.28}$	0.0295	27.1	$-0.13^{+0.19}_{-0.20}$	16	0.8
Q1311−270	6	10 966	✓	9.1	$3.50^{+0.39}_{-0.51}$	6.10 ± 1.04	$1.93^{+0.17}_{-0.16}$	0.0589	89.1	$-0.28^{+0.10}_{-0.11}$	61	4.0
Q1402−012	7	7852	✓	5.6	$2.87^{+0.39}_{-1.05}$	1.51 ± 0.42	$1.11^{+0.28}_{-0.29}$	0.0423	36.2	$0.41^{+0.18}_{-0.16}$	14	3.4
Q1442+101	3	6980	✓	11.9	$13.76^{+1.07}_{-2.49}$	10.19 ± 2.03	$1.26^{+0.12}_{-0.12}$	0.018	147.7	$0.12^{+0.08}_{-0.08}$	70	4.9
Q1542+042	8	7102	✓	12.3	$10.32^{+0.64}_{-1.24}$	15.90 ± 2.04	$1.82^{+0.12}_{-0.12}$	0.0455	158.2	$-0.17^{+0.08}_{-0.08}$	97	4.6
Q1614+051	1	4415	✓	6.9	$6.88^{+0.14}_{-3.75}$	5.22 ± 1.74	$1.28^{+0.21}_{-0.21}$	0.049	52.6	$0.19^{+0.15}_{-0.14}$	25	3.6
Q1626+115	6	6500	✓	9.3	$7.77^{+1.08}_{-1.03}$	6.89 ± 1.09	$1.46^{+0.28}_{-0.27}$	0.0474	93.9	$0.10^{+0.17}_{-0.16}$	54	5.0
Q1656+477	3	4220	✓	9.8	$10.42^{+1.16}_{-1.45}$	10.97 ± 1.55	$1.62^{+0.14}_{-0.14}$	0.0172	98.8	$-0.22^{+0.09}_{-0.10}$	62	1.0
Q1726+344	3	3339		1.7	≤2.10	≤3.83	–	0.028	4.5	$0.20^{+0.59}_{-0.24}$	3	1.3
Q2212−299	5	6765	✓	6.8	$4.25^{+0.36}_{-1.32}$	3.06 ± 0.88	$1.27^{+0.21}_{-0.21}$	0.0105	53.4	$0.00^{+0.14}_{-0.15}$	31	4.3
Q2223+210	2	4248	✓	16.7	$39.90^{+1.48}_{-3.97}$	29.52 ± 3.09	$1.33^{+0.08}_{-0.08}$	0.0388	282.7	$0.05^{+0.06}_{-0.06}$	136	1.9
Q2251+244	2	2919	✓	11.4	$32.19^{+2.16}_{-5.44}$	16.01 ± 3.01	$1.08^{+0.12}_{-0.12}$	0.0488	132.8	$0.23^{+0.09}_{-0.08}$	53	1.3
Q2334+019	7	3923		0.5	≤3.39	≤5.79	–	0.0498	1.0	$-0.52^{+0.04}_{-0.48}$	4	1.9
Q2341+010	3	3369		0.6	≤0.11	≤0.18	–	0.0373	1.1	$-0.32^{+0.13}_{-0.68}$	3	1.5
Q2350−007	5	4375	(P)	−0.2	≤1.02	≤0.56	–	0.0323	−0.3	–	2	1.6
Q2359+002	3	3649		1.6	≤0.22	≤1.52	–	0.0289	4.4	$-0.45^{+0.14}_{-0.55}$	6	2.3

Notes. (1) Object name. (2) Number of individual *Swift* observations that were combined. (3) XRT exposure time (s). (4) A checkmark indicates an XRT detection, otherwise we do not detect this quasar with XRT. (P): a non-detection for which we use PIMMS to estimate the 3σ upper limit on the flux (3.1.4). (5) Detection significance, calculated using the counts in the source and background extraction apertures. (6) *Swift* XRT integrated flux, observed-frame energy interval 0.3–10.0 keV, units of 10^{-13} erg s^{-1} cm^{-1}. The 3σ limiting flux is given for non-detections (Section 3.1.4). (7) Flux density F_ν at rest-frame energy of 2 keV, units of 10^{-31} erg s^{-1} cm^{-1} Hz^{-1}. (8) The X-ray photon index, measured for the observed-frame energy interval 0.3–10 keV. For non-detections, we assume $\Gamma = 1.91$ (not tabulated). (9) The Galactic column density of neutral hydrogen towards the quasar, adopted from the work of Kalberla et al. (2005). (10) The background-subtracted number of X-ray counts collected in the source aperture over all observations for this quasar. (11) The X-ray HR (Section 6.2), calculated using the BEHR software (Park et al. 2006) using the 'quadrature' algorithm. Uncertainties shown are based on 1σ posterior intervals. (12) The number of soft-band (0.3–1.5 keV) photons detected in the source aperture, before background subtraction. (13) The expected number of soft-band background counts in the source aperture.
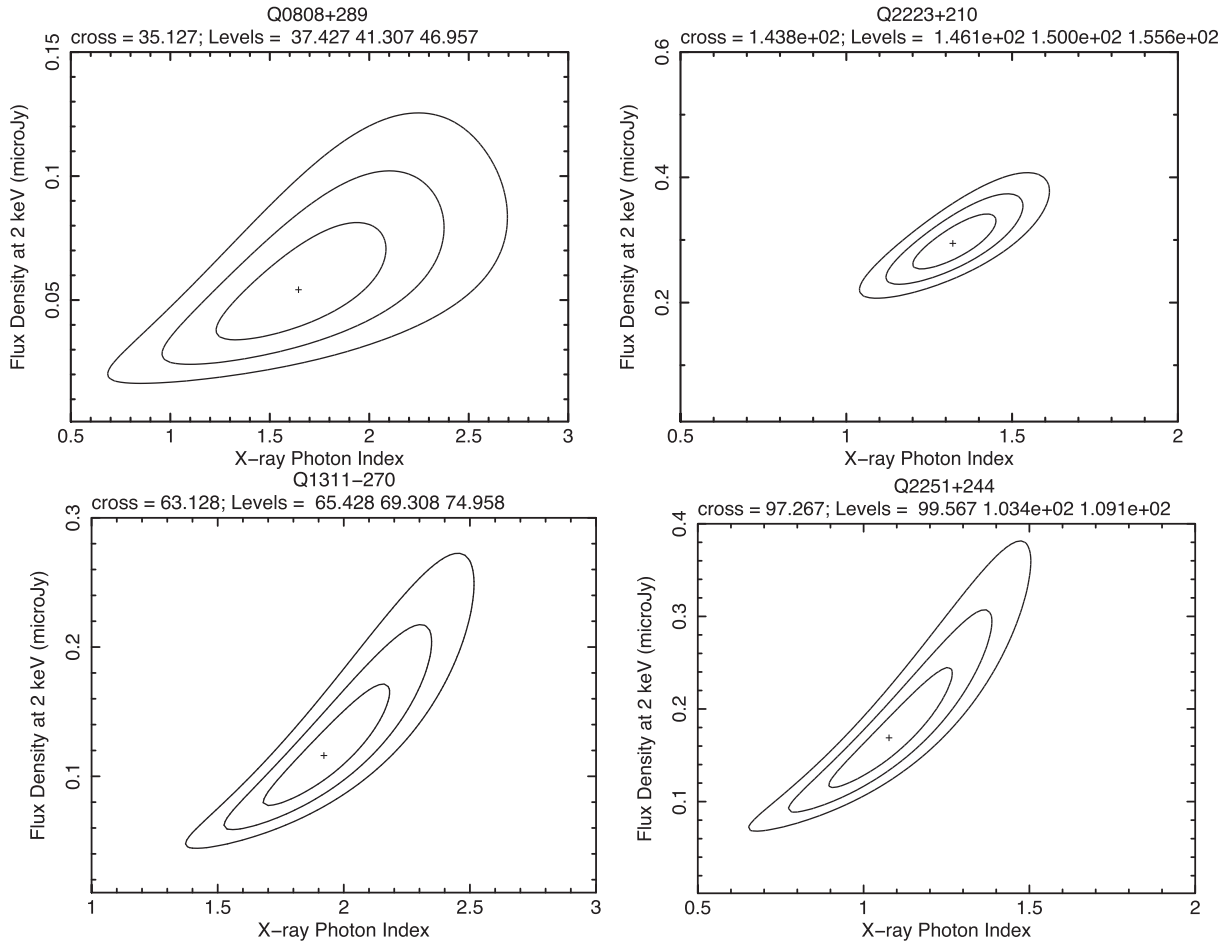
Figure 2. Confidence region contours for the photon index and normalization, for XRT modelling of four quasars. The best-fitting solution for Γ and $F_\nu(2\,\mathrm{keV})$ is marked with a cross symbol, while the curves show confidence regions corresponding to the 1σ, 2σ and 3σ levels. 'Cross' and 'Levels' denote the Cash statistic for the best-fitting solution and for the three contour levels. Q0808+289 has the smallest number of background-subtracted counts for all X-ray-detected quasars in the present sample, $N_{\mathrm{sub}} \approx 27$, while Q2223+210 has $N_{\mathrm{sub}} \approx 283$. Q1311−270 and Q2251+244 have the largest and smallest best-fitting values of Γ (softest and hardest spectra), respectively.

reveal multiple emission components, to first order the X-ray spectra of quasars resemble a power law (e.g. Nandra & Pounds 1994). The observations in this study have too few background-subtracted XRT counts for us to perform a detailed study of the X-ray spectral shape. We therefore model the X-ray emission of each quasar as an absorbed power-law function,[5]

$$A(E) = K\,[E(1+z)]^{-\Gamma}\,\mathrm{e}^{-N_{\mathrm{H}}\sigma(E)}, \qquad (1)$$

where $A(E)$ is the count rate in units of photons keV^{-1} cm^{-2} s^{-1} at energy E, and Γ is the photon index.[6] The exponential term represents Galactic absorption. We adopt the Galactic column density towards the quasar from the work of Kalberla et al. (2005), as retrieved from the HEASOFT N_{H} task, and use the photoelectric absorption cross-sections $\sigma(E)$ calculated by Morrison & McCammon (1983). Our observations contain too few detected X-ray photons for Gaussian statistics to be applicable. Instead, we find the best-fitting model by minimizing the Cash statistic (Cash 1979),

which is the appropriate maximum-likelihood statistic for Poisson-distributed data. The Cash statistic performs optimally when the data are binned such that each bin has at least one count – we ensured this using the task *'grppha'* (Section 3.1.1).

Our modelling yields the best-fitting value of the normalization K and of the photon index Γ. We use the XSPEC *'error'* task to estimate the 1σ confidence intervals on these parameters. We use the best-fitting model directly to calculate the integrated X-ray flux between 0.3 and 10 keV in the observed frame, $F(0.3–10\,\mathrm{keV})$, and the flux density at 2 keV in the quasar rest frame, $F_\nu(2\,\mathrm{keV})$. These flux measurements are presented in Table 2. All listed fluxes are unabsorbed values (i.e. we fit the model including the Galactic absorption component, but calculate the fluxes we would receive for the unabsorbed power-law component alone). To investigate the parameter space, we use the XSPEC task *'steppar'* to generate two-dimensional confidence regions [Γ versus $F_\nu(2\,\mathrm{keV})$] for each X-ray-detected quasar. In general, the spectral index and normalization are not fully independent: a smaller value of Γ (i.e. a harder spectrum) allows a higher F_ν (Fig. 2). We therefore advise caution in using our measurements to investigate any putative relationship between Γ and X-ray luminosity.

We are in the process of obtaining follow-up *Swift* observations for objects in the full quasar sample which are marginally detected

---

[5] This model is expressed in XSPEC modelling syntax as wabs(*nH*) · zpowerlw(*z, K, Γ*).

[6] In the X-ray literature, the spectral index α is occasionally used, where $f_\nu \propto (\nu/\nu_0)^{-\alpha}$. This implies that $\Gamma = \alpha + 1$.

(with source counts $N_{sub} \approx 15$) during the initial set of observations (Section 2). The quasars scheduled for follow-up observations are not included in the current analysis. We do, however, include very faint objects for which a follow-up observation of reasonable duration would not yield a secure XRT detection (Section 2). This results in a bimodal distribution of N_{sub}: all detected objects have $N_{sub} > 25$, while all non-detections have $N_{sub} < 6$.

3.1.4 Limiting fluxes for non-detected quasars

For non-detections, as defined in Section 3.1.2, we follow the approach of Wu et al. (2012) to establish upper limits on $F(0.3-10\,\mathrm{keV})$ and $F_\nu(2\,\mathrm{keV})$. Again, we use XSPEC to model the X-ray spectrum as an absorbed power law (equation 1). This allows us to include the per-pixel exposure map and the calibration information, as contained in the ARF file generated for the observation. For non-detections, we hold the value of the photon index constant at $\Gamma = 1.91$, a typical value for AGN X-ray spectra (e.g. Young et al. 2009; Jin et al. 2012). This yields values of $F(0.3-10\,\mathrm{keV})$ and $F_\nu(2\,\mathrm{keV})$ corresponding to the background-subtracted count rate, which in these cases are below our detection limit. To obtain 3σ upper limits on $F_\nu(2\,\mathrm{keV})$, we scale the best-fitting Galactic absorption-corrected $F_\nu(2\,\mathrm{keV})$ value as

$$F_{lim} = F_\lambda(2\,\mathrm{keV})\frac{N_{sub}}{N_{lim}}, \tag{2}$$

where N_{sub} is the observed number of background-subtracted source counts, and N_{lim} is the number of counts corresponding to the 3σ upper limit on the mean source count rate (as determined in Section 3.1.2).

For objects with very small (or negative) background-subtracted total counts, XSPEC is unable to model the data. For these objects, we calculate the ratio of photon flux to detected XRT counts, and use this to correct the upper-limit source counts, so as to account for the same calibration information used in our XSPEC processing. Following Wu et al. (2012), in practice we obtain this correction by processing the event file with the same tool (*xrtmkarf*) that we use to generate ARF files for the XSPEC analysis, as it produces the flux-to-counts ratio as part of its output. We convert the corrected limiting count rate to a limiting $F_\nu(2\,\mathrm{keV})$ using the HEASOFT task PIMMS,[7] assuming a power-law spectrum with $\Gamma = 1.91$.

3.1.5 Sensitivity to intrinsic absorption

Our observations are not deep enough, and do not cover enough of the soft X-ray regime for $z \sim 2$, to accurately measure the intrinsic absorption column density; we establish this using the following test. For observations with $N_{sub} > 50$, we fit an alternative model:[8]

$$A(E) = K\,[E(1+z)]^{-\Gamma_{abs}}\,e^{-N_H\sigma(E)}e^{-N_{H,int}\sigma(E(1+z))}. \tag{3}$$

The intrinsic column density $N_{H, int}$ is an additional free parameter in this model compared to equation (1). The best-fitting values of $N_{H, int}$ have large uncertainties and are consistent with zero for most objects, i.e. the intrinsic column density is not well constrained by our data (Fig. 3). For this reason, we adopt the simpler model of equation (1) (i.e. no intrinsic absorption) for all quasars in the remainder of this work.

[8] This model is expressed in XSPEC modelling syntax as wabs(*nH*) · zwabs(*nH*int) · zpowerlw(z, K, Γ).
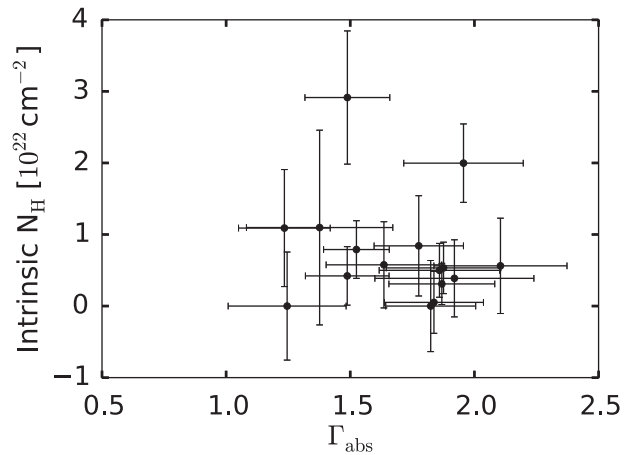
Figure 3. The best-fitting value of the H I column density $N_{H, int}$ is shown as a function of the X-ray photon index, Γ_{abs}, as measured for models including an intrinsic absorber component, for quasars with $N_{sub} > 50$. Note the large uncertainties on $N_{H, int}$: for many objects, the intrinsic column density is consistent with zero in our modelling.

3.2 UVOT data

3.2.1 Filter selection

We are ultimately interested in estimating the integrated continuum energy output of the accretion disc, along with the flux density at rest-frame 2500 Å – the latter is needed for the calculation of α_{ox} as defined in Tananbaum et al. (1979, Section 6.5). Quasar spectra bluewards of rest-frame 1000 Å generally suffer Lyman α forest absorption, and therefore do not represent the intrinsic continuum. We therefore select all UVOT filters that cover rest-frame wavelengths redwards of Lyman α, where we expect the emission to be dominated by the unabsorbed continuum. For the highest redshift objects in our sample, only the UVOT *V* filter samples rest-frame wavelengths longer than 1000 Å. In these cases, we split the observing time between the *U*, *B* and *V* filters, so as to at least partially constrain the UV spectral shape. Quasars selected from SDSS DR7 were originally observed as part of another Danish *Swift* programme, with different filter selection criteria. However, all these observations include the *Swift V*, *B* and *U* filters, which cover the desired spectral regions.

3.2.2 Data processing

We first combine the data from multiple observations to obtain one UVOT image per bandpass filter for each quasar. We then perform aperture photometry to extract the source and background fluxes, respectively. Lastly, we correct the measured fluxes for Galactic reddening.

Each UVOT observation consists of multiple snapshot observations (detector readouts) with exposure times of a few seconds. The imaging data for each filter are delivered as multi-extension FITS[9] files containing all snapshots for that filter. We use the task '*uvotimsum*' once on each 'Level 2' image to produce a combined image for that filter. We visually inspect this image, checking for pointing offsets and other issues (such as satellite trails) with the images. Most of the quasars in our sample were observed by *Swift* multiple times. Aperture photometry was performed on each of the

[9] Flexible Image Transport System (Griesen & Calabretta 2002).

single-observation images in order to check for significant flux variations between observations. For quasars detected in the individual exposures, we do not see flux variations at a 3σ level; however, we are only sensitive to variations of around 0.2 mag or greater, and only for those quasars in our sample with the brightest apparent magnitudes ($m_V \approx 17.5$). Finally, we use the task '*uvotimsum*' to produce a stacked image of all observations of a given quasar in a given filter.

3.2.3 Photometric measurements

We perform aperture photometry using the task '*uvotsource*'. We use a circular source aperture of radius 3 arcsec, which maximizes the signal to noise in the extraction region (Poole 2008; Breeveld et al. 2010), and a circular background aperture with a radius of approximately 30 arcsec. We adjust the background aperture size and positioning on a per-image basis so as to sample the sky background near the quasar's image coordinates while avoiding contaminating sources. Since the UVOT photometric system is calibrated using a 5 arcsec aperture, we apply an aperture correction, again using the '*uvotsource*' task, in order to obtain fully calibrated source apparent magnitudes. The '*uvotsource*' task also provides the background-subtracted flux density at the bandpass pivot wavelength, assuming a Gamma-ray Burst (GRB)-like power-law source spectrum (Poole 2008), also suitable for quasars in the UV–optical. If the quasar is not detected at a significance of 5σ or greater in the combined image, we instead record the 5σ upper limit on the flux density. We correct the observed flux densities for Galactic dust extinction using values of $E(B - V)$ given by Schlafly & Finkbeiner (2011). We present the UVOT extinction-corrected flux densities for our quasar sample in Table 3, and the apparent magnitudes on the UVOT photometric system (similar to the Johnson system; Poole 2008) in Table 4.

3.3 Summary of *Swift* data

We present the number of detections versus non-detections in our XRT and UVOT data in Table 5. Not all objects have XRT detections (21 are undetected), or are detected in all UVOT filters (two objects are undetected in all filters, while seven objects are only detected in two filters). To better establish the shape of the UV continuum, we include additional photometric data in our UV analysis as available, as detailed in Section 4.

4 SUPPLEMENTARY SDSS UV–OPTICAL DATA

As the UVOT bandpasses do not cover rest-frame wavelengths longer than ≈ 2000 Å at $z \approx 2$, we include archival SDSS-III (Eisenstein et al. 2011) photometry in our analysis so as to extend our spectral coverage. Of the present sample of 44 quasars, 35 objects have SDSS photometry; 23 objects also have SDSS spectroscopy. The SDSS data are processed using the latest SDSS photometric pipeline (Data Release 12, Alam et al. 2015).

The SDSS contains observations of the targets at time separations of months to years with respect to the *Swift* observations. As we are interested in the instantaneous SEDs of individual objects, flux variability must be accounted for. We follow the approach of Wu et al. (2012) to create 'pseudo-simultaneous' photometric data points by rescaling the flux levels of the SDSS photometry to match the UVOT flux density, assuming that the spectral shape is constant. We quantify the uncertainty due to possible spectral shape variation in Section 5.1. For the lowest redshift quasars in our sample (z

$\lesssim 1.9$), we prefer to match the observed *Swift* U-band flux (central wavelength 3465 Å) and the SDSS u band (central wavelength 3551 Å), as they sample very similar wavelength ranges. For objects with $z \geq 1.9$ the U and u bands are strongly absorbed by the Lyman α forest, and may not display the same flux variations as the unabsorbed continuum. We therefore match the fluxes to either the *Swift* B or V bands for $z \gtrsim 1.9$ objects, choosing whichever bandpass we infer to be more continuum dominated at a given redshift.

To determine the necessary rescaling, we fit the SDSS broad-band photometry with a power-law model, omitting any SDSS bands that sample strong quasar emission lines (Section 5.1). We use this model to estimate the flux density, as observed by the SDSS, at the pivot wavelength of the *Swift* UVOT bandpass selected for matching. Based thereon, we rescale the SDSS photometric data to the flux level at the time of the UVOT observations.

For the $z = 3.53$ quasar Q1442+101, all of the UVOT bands cover spectral regions absorbed by the Lyman α forest. In these cases, our best option is to scale the SDSS photometry based on the *Swift* V band and the SDSS g band. We consider this particular scaling to be highly uncertain, and therefore regard the subsequent modelling as only a rough estimate of the UV continuum level.

5 DETERMINING THE UV TO X-RAY SPECTRAL ENERGY DISTRIBUTION

For black hole masses of the order of 10^9 M$_\odot$, typical of bright quasars, standard α-disc models predict that the inner accretion disc emission peaks in the far-UV or EUV (e.g. Shakura & Sunyaev 1973). The X-ray emission is commonly thought to be reprocessed UV continuum emission, along with a contribution from the jet for RLQ (Section 1). Thus, by studying the continuum emission on each side of the unobservable EUV region, and assuming a shape for the EUV SED, we can constrain the energy released by the central accretion process (albeit with some uncertainty involved, Section 6.6). In this calculation, we do not include the IR emission in our estimate of the accretion energy, as the IR emission is due to dust outside the central regions, heated by the central continuum emission (e.g. Barvainis 1987; Hughes et al. 1993). In the following, we describe our modelling of the quasar UV continuum using UVOT and SDSS data (Section 5.1), and present the observed SEDs covering the rest-frame UV and X-ray regimes based on our data and modelling (Section 5.2).

5.1 Modelling the UV quasar continuum

Here, we model the UV continuum emission over the rest-frame wavelength interval 1000–3000 Å. The dominant spectral component in the rest-frame UV for these quasars is the continuum emission due to the accretion disc. We expect the host galaxy contamination of the UV continuum to be low: luminous quasars are known to reside in massive elliptical galaxies at $z \lesssim 0.25$ (Dunlop et al. 2003), which are faint emitters below rest-frame 4000 Å (e.g. Kinney et al. 1996). At higher redshift, there is evidence for quasar host galaxies being actively star forming, however, the AGN contribution is still brighter than the host galaxy by ~2 mag in the U band (Floyd et al. 2012). The broad emission lines, on the other hand, can contribute significantly to the broad-band flux if they are covered by the UVOT bandpasses. Absorption features such as the Lyman α forest bluewards of 1200 Å also complicate the measurement of the underlying continuum flux.

For all 42 UVOT-detected quasars, we have broad-band photometry in at least two bandpasses (Section 3.2). For 23 quasars

Table 3. *Swift* UVOT flux measurements.

Object name (1)	$E(B-V)$ (2)	F_λ $UW1$ (3)	F_λ $UW2$ (4)	F_λ $UM2$ (5)	F_λ U (6)	F_λ B (7)	F_λ V (8)	SDSS matching bandpass (9)
J0147−1014[a]	0.0303 ± 0.0009	7.85 ± 1.21	<4.48	<1.48	53.07 ± 3.06	39.73 ± 2.45	30.94 ± 2.95	B
J0823+0611[a]	0.0224 ± 0.0003	–	–	24.92 ± 1.30	28.87 ± 1.25	33.28 ± 1.25	24.11 ± 1.16	B
J0948+0855[a]	0.0258 ± 0.0005	49.25 ± 2.76	10.37 ± 1.87	9.37 ± 1.02	78.18 ± 3.33	60.05 ± 2.57	46.51 ± 2.29	B
J1049−0110[a]	0.0349 ± 0.0013	<6.50	<2.73	<1.37	<8.30	<11.01	<15.81	–
J1106−1731[a]	0.0395 ± 0.0011	–	–	–	28.51 ± 1.16	44.95 ± 1.51	33.52 ± 1.30	V
J1111+0237[a]	0.033 ± 0.0012	52.32 ± 2.75	–	52.38 ± 2.66	65.61 ± 2.83	43.24 ± 1.86	30.32 ± 1.84	B
J1125+0001[a]	0.0258 ± 0.0003	45.14 ± 2.42	–	–	79.27 ± 3.25	46.91 ± 1.77	27.31 ± 1.40	V
J1144+0327[a]	0.0186 ± 0.0005	23.91 ± 1.46	–	3.61 ± 0.56	61.29 ± 2.85	44.61 ± 1.99	36.70 ± 2.12	B
J1318+0111[a]	0.0266 ± 0.0011	55.38 ± 2.88	–	–	58.10 ± 2.43	35.77 ± 1.42	21.63 ± 1.22	B
J1429+0240[a]	0.0252 ± 0.0006	70.34 ± 4.83	66.40 ± 4.67	64.05 ± 4.61	74.90 ± 2.94	64.54 ± 3.75	45.70 ± 4.10	B
J1457+0247[a]	0.041 ± 0.0011	27.89 ± 1.82	9.13 ± 1.40	12.12 ± 1.81	74.91 ± 3.37	56.24 ± 3.85	62.82 ± 5.06	B
J2348+0039[a]	0.0228 ± 0.0009	13.36 ± 1.18	3.62 ± 0.33	<1.86	56.54 ± 2.76	40.11 ± 1.99	24.46 ± 1.99	B
Q0002−008	0.046 ± 0.0079	–	–	–	23.76 ± 1.18	18.60 ± 1.21	13.76 ± 1.42	B
Q0015+026	0.0258 ± 0.0006	–	–	–	4.68 ± 0.51	8.69 ± 0.80	5.31	V
Q0020+022	0.0229 ± 0.0004	16.20 ± 1.12	–	–	21.78 ± 1.35	16.22 ± 1.92	<16.08	B
Q0038−019	0.0196 ± 0.0004	46.19 ± 2.40	–	–	84.42 ± 3.47	54.45 ± 2.27	38.92 ± 2.50	B
Q0040−017	0.0253 ± 0.001	2.96 ± 0.54	–	–	7.11 ± 0.81	8.23 ± 1.47	<14.85	B
Q0106+013	0.0207 ± 0.0008	10.95 ± 0.80	–	–	32.57 ± 1.59	25.11 ± 1.77	20.32 ± 2.73	B
Q0115−011	0.0274 ± 0.001	–	–	–	44.99 ± 1.87	40.02 ± 1.66	24.50 ± 1.33	V
Q0123+257	0.0913 ± 0.0019	18.76 ± 1.08	–	–	33.71 ± 1.41	35.57 ± 1.90	24.74 ± 2.18	B
Q0226−038	0.0261 ± 0.0012	–	–	–	85.72 ± 3.39	55.14 ± 1.97	38.20 ± 1.55	B
Q0238+100	0.2025 ± 0.0385	34.36 ± 0.92	–	–	66.17 ± 1.25	41.52 ± 1.13	29.68 ± 1.42	–
Q0244+017	0.0382 ± 0.0012	–	–	–	21.74 ± 1.10	13.34 ± 1.00	9.74 ± 1.20	V
Q0249−184	0.0247 ± 0.0009	–	–	–	–	7.91 ± 0.59	13.05 ± 0.83	–
Q0252+016	0.0802 ± 0.0034	–	–	–	46.15 ± 1.63	51.37 ± 1.66	36.18 ± 1.56	V
Q0445+097	0.2798 ± 0.0165	–	–	–	8.73 ± 0.45	12.68 ± 0.54	<8.82	–
Q0458−020	0.0638 ± 0.0022	–	–	–	9.51 ± 0.51	18.04 ± 0.73	18.10 ± 0.93	–
Q0504+030	0.0564 ± 0.0012	–	–	–	13.42 ± 0.67	19.38 ± 0.82	12.18 ± 0.85	–
Q0808+289	0.0288 ± 0.0003	–	–	–	49.02 ± 2.16	39.09 ± 1.69	27.38 ± 1.55	V
Q1311−270	0.0655 ± 0.0013	17.74 ± 0.84	–	–	41.02 ± 1.44	39.18 ± 1.43	25.11 ± 1.36	–
Q1402−012	0.0469 ± 0.0008	–	–	–	23.87 ± 0.96	28.98 ± 1.04	19.80 ± 0.89	V
Q1442+101	0.0217 ± 0.0008	–	–	–	–	22.94 ± 0.89	26.63 ± 1.15	V
Q1542+042	0.0746 ± 0.0059	–	–	–	39.34 ± 1.34	30.43 ± 0.99	18.86 ± 0.97	V
Q1614+051	0.0577 ± 0.0016	–	–	–	–	6.00 ± 0.64	9.08 ± 0.86	V
Q1626+115	0.0487 ± 0.0006	21.08 ± 1.30	–	–	26.79 ± 1.37	19.08 ± 1.57	17.11 ± 2.16	V
Q1656+477	0.0177 ± 0.0006	58.85 ± 3.11	–	–	67.22 ± 3.05	43.16 ± 2.35	26.59 ± 2.38	U
Q1726+344	0.0261 ± 0.0005	–	–	–	10.22 ± 0.64	15.35 ± 0.82	8.60 ± 0.86	B
Q2212−299	0.013 ± 0.0003	–	–	–	–	56.52 ± 2.00	37.85 ± 1.44	–
Q2223+210	0.04 ± 0.0017	30.28 ± 1.62	–	–	78.63 ± 3.07	51.88 ± 2.17	33.31 ± 2.22	V
Q2251+244	0.1695 ± 0.0187	–	–	–	28.60 ± 0.88	30.39 ± 0.99	18.13 ± 1.16	B
Q2334+019	0.0477 ± 0.0015	–	–	–	20.71 ± 0.97	–	11.75 ± 1.07	U
Q2341+010	0.032 ± 0.0015	–	–	–	30.54 ± 1.49	19.18 ± 1.32	8.30 ± 1.51	V
Q2350−007	0.0306 ± 0.0014	15.36 ± 1.00	–	–	21.59 ± 1.20	18.49 ± 1.61	16.38 ± 2.61	B
Q2359+002	0.0252 ± 0.002	–	–	–	<4.23	<7.00	<7.06	–

Notes. (1) Object name. (2) The differential extinction $E(B-V)$ is adopted from the work of Schlafly & Finkbeiner (2011), and is the mean value of all measurements within a 2 arcmin aperture centred on the quasar coordinates. (3,4,5,6,7,8) The effective flux density at the pivot wavelength in each UVOT bandpass, in unit of 10^{17} erg s^{-1} Å^{-1}, assuming a power-law source SED over the bandpass (Section 3.2.3). The 1σ uncertainties on F_λ are listed for detected quasars. The 5σ upper limits are listed for non-detections. Filters that were not used for a given observation are marked with '–'. (9) The UVOT filter bandpass used for rescaling of the SDSS photometric fluxes (Section 4). Quasars which lack SDSS photometry, or which are not detected in UVOT imaging, are marked with '–'.
[a]For typographical reasons, we shorten the names of the SDSS quasars in this table. See Table 1 for the full names.

with supplementary SDSS spectroscopy (Section 4), we use these spectra to ascertain which of the available photometric bandpasses suffer absorption- or emission-line contamination. For objects without SDSS spectra, we use the composite quasar spectrum of Selsing et al. (2016) as a guide. This template spectrum is comprised of bright quasars with little host galaxy contribution, as expected for our $z \approx 2$ sample. We perform an initial power-law model fit using all available photometric bands (Fig. 4, left-hand panel). If the flux

density in a given band lies outside the 1σ uncertainty range of this initial model, and we see emission or absorption features in the spectrum at that bandpass, we exclude it from the final model (Fig. 4, right-hand panel). For quasars with little usable photometric data, we exclude data points only if we believe that they introduce a gross error into our estimate of the integrated UV flux. For example, we exclude the UVOT U band for quasar Q0249−184 to avoid fitting an unrealistically red model continuum (Fig. A8).

Table 4. *Swift* UVOT apparent magnitudes.

Object (1)	m_{UW1} (2)	m_{UW2} (3)	m_{UM2} (4)	m_U (5)	m_B (6)	m_V (7)
J014725.50−101439.11	19.26 ± 0.17	<20.19	<21.24	17.05 ± 0.06	18.03 ± 0.07	17.71 ± 0.10
J082328.62+061146.07	–	–	18.18 ± 0.06	17.72 ± 0.05	18.22 ± 0.04	17.98 ± 0.05
J094853.60+085514.40	17.27 ± 0.06	19.28 ± 0.20	19.24 ± 0.12	16.64 ± 0.05	17.58 ± 0.05	17.26 ± 0.05
J104915.44−011038.18	<19.47	<20.73	<21.33	<19.07	<19.42	<18.44
J110607.48−173113.60	–	–	–	17.73 ± 0.04	17.90 ± 0.04	17.62 ± 0.04
J111159.70+023719.76	17.20 ± 0.06	–	17.37 ± 0.06	16.83 ± 0.05	17.94 ± 0.05	17.73 ± 0.07
J112542.30+000101.33	17.36 ± 0.06	–	–	16.62 ± 0.04	17.85 ± 0.04	17.84 ± 0.06
J114449.32+032751.96	18.05 ± 0.07	–	20.27 ± 0.17	16.90 ± 0.05	17.91 ± 0.05	17.52 ± 0.06
J131810.74+011140.86	17.14 ± 0.06	–	– –	16.96 ± 0.05	18.15 ± 0.04	18.10 ± 0.06
J142923.92+024023.14	16.88 ± 0.07	17.27 ± 0.08	17.15 ± 0.08	16.68 ± 0.04	17.50 ± 0.06	17.28 ± 0.10
J145717.86+024747.36	17.89 ± 0.07	19.42 ± 0.17	18.96 ± 0.16	16.68 ± 0.05	17.65 ± 0.07	16.94 ± 0.09
J234830.41+003918.57	18.69 ± 0.10	20.42 ± 0.10	<21.00	16.99 ± 0.05	18.02 ± 0.05	17.96 ± 0.09
Q0002−008	–	–	–	17.93 ± 0.05	18.86 ± 0.07	18.59 ± 0.11
Q0015+026	–	–	–	19.47 ± 0.10	19.50 ± 0.09	19.62 ± 0.17
Q0020+022	18.48 ± 0.08	–	–	18.02 ± 0.07	19.00 ± 0.13	<18.42
Q0038−019	17.34 ± 0.06	–	–	16.55 ± 0.04	17.69 ± 0.05	17.46 ± 0.07
Q0040−017	20.32 ± 0.19	–	–	19.24 ± 0.12	19.74 ± 0.19	<18.50
Q0106+013	18.90 ± 0.08	–	–	17.59 ± 0.05	18.53 ± 0.08	18.16 ± 0.15
Q0115−011	–	–	–	17.24 ± 0.05	18.02 ± 0.05	17.96 ± 0.06
Q0123+257	18.31 ± 0.06	–	–	17.55 ± 0.05	18.15 ± 0.06	17.94 ± 0.10
Q0226−038	–	–	–	16.54 ± 0.04	17.68 ± 0.04	17.48 ± 0.04
Q0238+100	17.66 ± 0.03	–	–	16.82 ± 0.02	17.98 ± 0.03	17.75 ± 0.05
Q0244+017	–	–	–	18.03 ± 0.06	19.22 ± 0.08	18.96 ± 0.13
Q0249−184	–	–	–	–	19.78 ± 0.08	18.64 ± 0.07
Q0252+016	–	–	–	17.21 ± 0.04	17.75 ± 0.04	17.54 ± 0.05
Q0445+097	–	–	–	19.02 ± 0.06	19.27 ± 0.05	<19.07
Q0458−020	–	–	–	18.92 ± 0.06	18.89 ± 0.04	18.29 ± 0.06
Q0504+030	–	–	–	18.55 ± 0.05	18.81 ± 0.05	18.71 ± 0.08
Q0808+289	–	–	–	17.14 ± 0.05	18.04 ± 0.05	17.83 ± 0.06
Q1311−270	18.38 ± 0.05	–	–	17.34 ± 0.04	18.05 ± 0.04	17.93 ± 0.06
Q1402−012	–	–	–	17.92 ± 0.04	18.37 ± 0.04	18.19 ± 0.05
Q1442+101	–	–	–	–	18.63 ± 0.04	17.87 ± 0.05
Q1542+042	–	–	–	17.38 ± 0.04	18.32 ± 0.04	18.24 ± 0.06
Q1614+051	–	–	–	–	20.08 ± 0.12	20.08 ± 0.11
Q1626+115	18.22 ± 0.06	–	–	17.87 ± 0.05	18.82 ± 0.07	18.27 ± 0.11
Q1656+477	17.08 ± 0.06	–	–	16.80 ± 0.05	17.94 ± 0.06	17.87 ± 0.10
Q1726+344	–	–	–	18.84 ± 0.07	19.06 ± 0.06	19.10 ± 0.10
Q2212−299	–	–	–	–	17.65 ± 0.04	17.48 ± 0.04
Q2223+210	17.80 ± 0.06	–	–	16.63 ± 0.04	17.74 ± 0.04	17.63 ± 0.07
Q2251+244	–	–	–	17.73 ± 0.03	18.32 ± 0.04	18.29 ± 0.07
Q2334+019	–	–	–	18.08 ± 0.05	–	18.76 ± 0.10
Q2341+010	–	–	–	17.66 ± 0.05	18.82 ± 0.07	19.13 ± 0.20
Q2350−007	18.53 ± 0.07	–	–	18.03 ± 0.06	18.86 ± 0.09	18.40 ± 0.17
Q2359+002	–	–	–	<19.80	<19.91	<19.31

Notes. (1) Object name. (2,3,4,5,6,7) Apparent magnitudes on the UVOT photometric system. The 1σ uncertainties are listed for detected quasars. The 5σ upper limits are listed for non-detections. Filters that were not used for a given observation are marked with '–'.

Table 5. Summary of *Swift* detections for our sample.

	UVOT non-detection	Detected in 2 UVOT filters	Detected in ≥3 UVOT filters	Sum[a]
XRT non-detection	2	3	16	21
XRT detection	0	4	19	23
Sum[b]	2	7	35	(Sample of 44)

[a]Number of XRT detections and non-detections, irrespective of UVOT detection status.

[b]Number of objects with a given UVOT detection status, irrespective of XRT detection status. All detected objects were detected in two or more bandpasses.

We fit a power-law model,[10] $F_\lambda = A\lambda^{-\beta_{UV}}$, to the measured UVOT and the rescaled SDSS fluxes. Here, F_λ denotes the flux density at wavelength λ, while β_{UV} is the UV spectral index. We perform a non-linear least-squares fit of this model to the available photometric data based on the Levenberg–Marquardt algorithm, using the SCIPY.OPTIMIZE package.[11] Fig. 4 shows a typical case for a quasar with SDSS photometry. The left-hand panel shows a model

[10] Equivalently, some authors fit a power-law model in wavelength space, $F(\lambda) = A_\lambda \lambda^{-\beta}$. Given that $F(\nu) = F\lambda(d\nu/d\lambda)$, the relation between the power-law indices is $\beta = \alpha - 2$.

[11] SCIPY: Open Source Scientific Tools for PYTHON, 2001, http://www.scipy.org/ [Online; accessed 2015 October 27]
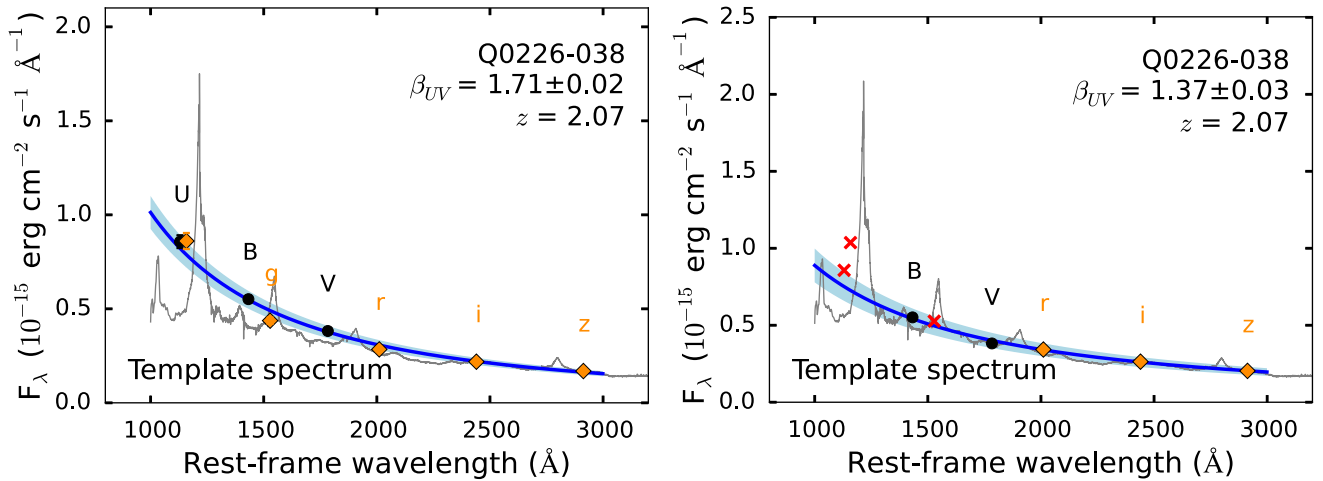
Figure 4. Steps in our modelling of the UV/optical spectrum for quasar Q0226−038. The dark blue curve and light blue shaded area shows our power-law continuum model and its uncertainty, fitted to the UVOT broad-band photometric data (black points) and to the SDSS photometry (gold squares). The composite spectrum of bright $1.1 < z < 2.1$ quasars compiled by Selsing et al. (2016), scaled to match the model flux at 2500 Å, is included for illustrative purposes (grey curves). Left-hand panel: a fit to all available photometric data, including the UVOT U and SDSS u bands, which cover the Lyman α emission line, and the SDSS g filter, which is superimposed on the C IV broad emission line. Right-hand panel: final model after removing the aforementioned emission-line-contaminated bandpasses (red crosses). Note that the rescaling of the SDSS data points changes slightly between the initial and the final model. This is due to the g filter that is no longer being used in the rescaling of SDSS photometry for the final fit.

fitted to all available photometric data, while the right-hand panel shows our final model, for which we reject the UVOT U and SDSS u bands in accordance with the criteria outlined above. We tabulate the model values of β_{UV} and F_ν(2500 Å) in Table 6. The photometric data and best-fitting models for our quasars are shown in the Appendix (Figs A1–A15, right-hand panels).

For three objects, we only have a single usable photometric data point according to the above criteria (namely, Q0249−184, Q0445+097 and Q2212−299). To obtain a guideline estimate of the continuum emission in this case, we adopt a power-law model with a spectral index equal to the canonical value $\beta_{UV} = 1.5$, scaled to this single photometric data point. For three quasars, only two UV photometric measurements are usable (Q0238+100, Q0458−020 and Q0504+030). In these cases, we make a guideline estimate of the UV SED by connecting the two photometry points with a power-law function. We exclude all six of the aforementioned quasars from the analyses of Section 6, as we regard their UV continuum models as very crude guideline estimates, unfit for further analysis.

Our flux rescaling of the SDSS data (Section 4) assumes that the UV spectral index does not vary significantly on time-scales of years. In fact, quasar UV–optical spectral index variations have been observed, of order $\Delta\beta_{UV} \approx 0.2$ (Pu, Bian & Huang 2006; Bian et al. 2012; Schmidt et al. 2012; Zhang 2013). To quantify the 'worst-case' uncertainty due to spectral index variation, we artificially steepen the spectral index of the SDSS photometry by $\Delta\beta_{UV} = 0.2$ for quasar Q0038−019, leaving the UVOT data unchanged, and repeat our UV modelling (including the flux rescaling). This quasar is a fairly typical case for our SDSS sample, with two UVOT bandpasses and four SDSS bandpasses used to model the continuum. We find that the spectral index of the joint continuum model steepens significantly ($\Delta\beta_{UV} = 0.19$), while the integrated UV luminosity changes by less than 1 per cent. Although modelling based on UVOT photometry alone would negate the issue of spectral variability, the resulting SEDs would lack near-UV data for most sample quasars. We therefore prefer to include the SDSS photometry where available. A major advantage of observing with *Swift* is the simultaneity between X-ray and UV–optical observations. We

therefore do not use SDSS data to determine the UV–optical SED in cases where we lack a UVOT detection; in such cases we are ignorant of the appropriate flux rescaling for the SDSS photometry.

5.2 UV to X-ray spectral energy distributions

The rest-frame UV to X-ray SEDs of two quasars are shown in Fig. 5. The remainder of our sample SEDs are presented in the Appendix. In the left-hand panels, we show νL_ν as a function of ν. To represent the observed XRT data in units of physical flux, we show the 'unfolded' XRT spectrum, i.e. the measured number of counts in a given bin, scaled by the ratio of the incident model to the model convolved with the instrumental response function. The X-ray data points are rebinned for clarity. Note that unfolded spectra of this type are model-dependent visualizations of X-ray data; we find them useful for presentation purposes, but they are not suitable for further spectral analyses. We also show the best-fitting X-ray model including Galactic absorption, along with the assumed underlying power-law continuum corrected for Galactic absorption. In the right-hand panels, we show a detailed view of our UV photometry, along with the best-fitting continuum model, and its 1σ uncertainty (indicated by a shaded region). Quasar J082328.62+061146.07 (Fig. 5, top) is securely detected by both the UVOT and the XRT. Quasar J014725.50−101439.11 (Fig. 5, bottom) is an example of an XRT non-detection, for which we present the 3σ limiting X-ray luminosity.

We include the SDSS spectra (rescaled by the same factor as for the SDSS photometric data) in the SED figures (see the Appendix) for comparison purposes. For many objects, our model continua overestimate the true continuum level. This is due to the contributions of emission lines (e.g. the blended Fe II and Balmer emission features redwards of 2000 Å) even in continuum-dominated bandpasses; see Section 6.6.3. Apart from this, we find significant flux offsets between the SDSS spectra and the SDSS photometry for several objects observed by the SDSS-III BOSS campaign (Dawson et al. 2013). In most cases, we are able to mitigate these offsets by applying the flux recalibration given by Margala et al.

Table 6. Integrated luminosities and SED diagnostics.

| Object name (1)	$\beta_{\rm UV}$ (2)	$F_\nu(2500$ Å) (3)	$\alpha_{\rm ox}$ (4)	$L_{\rm X}$ (2–10 keV) (5)	$L_{\rm X}$ (0.3–10 keV) (6)	$L_{\rm X}$ (1–25 keV) (7)	$L_{\rm UV}$ (1000–3000 Å) (8)	$L_{\rm EUV}$ (1000 Å–0.3 keV) (9)	$L_{\rm EUV}$ (1000 Å–1 keV) (10)	$L_{\rm tot}$ (3000 Å–25 keV) (11)
J0147−1014[a]	1.28 ± 0.02	3.90 ± 0.27	≥ 1.94	–	–	–	6.55 ± 0.76	–	–	–
J0823+0611[a]	1.68 ± 0.02	2.69 ± 0.36	1.42 ± 0.08	$0.92^{+0.10}_{-0.07}$	$1.75^{+0.49}_{-0.77}$	$1.89^{+0.08}_{-0.41}$	8.75 ± 1.18	$10.12^{+2.13}_{-2.28}$	$14.60^{+2.51}_{-2.54}$	$25.23^{+3.93}_{-3.96}$
J0948+0855[a]	1.02 ± 0.02	6.45 ± 0.63	1.60 ± 0.10	$0.51^{+0.07}_{-0.07}$	$0.78^{+0.10}_{-0.09}$	$1.13^{+0.22}_{-0.17}$	8.45 ± 0.86	$5.49^{+1.12}_{-1.37}$	$8.50^{+1.40}_{-1.49}$	$18.09^{+2.49}_{-2.57}$
J1049−0110[a]	–	–	–	–	–	–	–	–	–	–
J1106−1731[a]	1.53 ± 0.01	4.18 ± 0.41	≥ 1.65	–	–	–	10.60 ± 1.07	–	–	–
J1111+0237[a]	1.72 ± 0.02	3.09 ± 0.30	≥ 1.61	–	–	–	4.98 ± 0.50	–	–	–
J1125+0001[a]	1.54 ± 0.02	3.01 ± 0.31	1.41 ± 0.08	$0.49^{+0.07}_{-0.08}$	$0.86^{+0.08}_{-0.09}$	$1.04^{+0.17}_{-0.18}$	3.85 ± 0.42	$3.91^{+0.87}_{-0.97}$	$5.88^{+1.02}_{-1.04}$	$10.55^{+1.66}_{-1.64}$
J1144+0327[a]	1.15 ± 0.03	4.85 ± 1.92	≥ 1.72	–	–	–	7.57 ± 0.76	–	–	–
J1318+0111[a]	1.82 ± 0.02	2.65 ± 0.16	≥ 1.66	–	–	–	3.26 ± 0.21	–	–	–
J1429+0240[a]	0.75 ± 0.01	7.06 ± 0.30	≥ 1.80	–	–	–	6.27 ± 0.28	–	–	–
J1457+0247[a]	1.13 ± 0.02	5.70 ± 0.73	≥ 1.93	–	–	–	7.81 ± 1.04	–	–	–
J2348+0039[a]	0.77 ± 0.02	4.86 ± 0.42	1.52 ± 0.07	$0.70^{+0.05}_{-0.07}$	$1.03^{+0.07}_{-0.08}$	$1.61^{+0.20}_{-0.18}$	5.96 ± 0.42	$3.80^{+0.65}_{-0.73}$	$6.15^{+0.85}_{-0.88}$	$13.73^{+1.59}_{-1.62}$
Q0002−008	1.50 ± 0.01	1.33 ± 0.10	≥ 1.68	–	–	–	3.09 ± 0.67	–	–	–
Q0015+026	1.76 ± 0.02	0.57 ± 0.09	≥ 1.27	–	–	–	1.50 ± 0.25	–	–	–
Q0020+022	1.60 ± 0.01	1.25 ± 0.11	≥ 1.69	–	–	–	1.76 ± 0.16	–	–	–
Q0038−019	1.43 ± 0.03	6.91 ± 0.39	1.46 ± 0.05	$0.68^{+0.07}_{-0.06}$	$1.11^{+0.08}_{-0.10}$	$1.47^{+0.17}_{-0.19}$	5.17 ± 0.63	$5.00^{+0.95}_{-1.00}$	$7.69^{+1.17}_{-1.19}$	$14.33^{+1.97}_{-1.97}$
Q0040−017	1.34 ± 0.04	0.83 ± 0.24	≥ 1.33	–	–	–	1.73 ± 0.51	–	–	–
Q0106+013	0.89 ± 0.02	2.84 ± 0.19	1.28 ± 0.06	$1.99^{+0.12}_{-0.19}$	$2.80^{+0.16}_{-0.21}$	$4.79^{+0.64}_{-0.48}$	4.10 ± 0.42	$3.74^{+0.62}_{-0.64}$	$6.52^{+0.88}_{-0.89}$	$15.40^{+1.94}_{-1.95}$
Q0115−011	1.56 ± 0.02	3.01 ± 0.39	≥ 1.61	–	–	–	5.85 ± 0.78	–	–	–
Q0123+257	1.33 ± 0.02	3.07 ± 0.22	1.28 ± 0.09	$2.93^{+0.25}_{-0.33}$	$4.26^{+0.25}_{-0.34}$	$6.87^{+0.86}_{-0.87}$	6.52 ± 0.66	$8.17^{+1.61}_{-1.79}$	$13.65^{+2.19}_{-2.27}$	$27.04^{+3.70}_{-3.70}$
Q0226−038	1.37 ± 0.02	5.31 ± 0.54	1.45 ± 0.07	$1.17^{+0.08}_{-0.15}$	$1.72^{+0.16}_{-0.14}$	$2.70^{+0.31}_{-0.28}$	8.06 ± 1.05	$6.95^{+1.39}_{-1.49}$	$11.17^{+1.87}_{-1.89}$	$21.94^{+3.24}_{-3.24}$
Q0238+100	$1.53\ (1.54^{+0.40}_{-0.51})^{b}$	3.33^{b}	1.46 ± 0.07	$0.46^{+0.04}_{-0.03}$	$0.82^{+0.03}_{-0.05}$	$0.96^{+0.09}_{-0.10}$	4.60^{b}	$4.68^{+0.44}_{-0.57}$	$6.94^{+0.42}_{-0.48}$	12.51
Q0244+017	1.17 ± 0.01	1.19 ± 0.10	≥ 1.36	–	–	–	1.62 ± 0.13	–	–	–
Q0249−184	1.5^{b}	1.8^{b}	≥ 1.44	–	–	–	6.55^{h}	–	–	–
Q0252+016	1.67 ± 0.01	4.13 ± 0.37	≥ 1.62	–	–	–	10.39 ± 0.10	–	–	–
Q0445+097	$1.5\ (1.12 \pm 0.6)^{b}$	1.12^{b}	1.23 ± 0.11	$1.00^{+0.12}_{-0.19}$	$1.47^{+0.15}_{-0.18}$	$2.34^{+0.27}_{-0.21}$	1.93	2.40	4.04	8.24
Q0458−020	$-0.02\ (0.20 \pm 0.18)^{b,\,c}$	$3.80^{b,\,c}$	1.24 ± 0.06	$3.70^{+0.25}_{-0.30}$	$5.83^{+0.23}_{-0.31}$	$8.16^{+0.77}_{0.76}$	$>5.01^{h,\,c}$	$4.46^{+0.57}_{-0.66}$	$7.58^{+0.66}_{-0.49}$	$20.76^{+1.43}_{-1.49}$
Q0504+030	$2.12\ (1.63 \pm 0.33)^{b}$	1.14	1.33 ± 0.16	$0.96^{+0.12}_{-0.16}$	$1.06^{+0.12}_{-0.23}$	$2.52^{0.46}_{-0.53}$	3.51	$3.81^{0.77}_{-1.02}$	$6.58^{0.77}_{1.06}$	$12.61^{+1.23}_{-1.51}$
Q0808+289	1.11 ± 0.02	3.45 ± 0.32	1.46 ± 0.13	$0.55^{+0.10}_{-0.11}$	$1.01^{+0.13}_{-0.18}$	$1.22^{+0.26}_{-0.23}$	4.33 ± 0.42	$3.69^{+0.93}_{-1.20}$	$5.67^{+1.08}_{-1.20}$	$11.21^{+1.77}_{-1.88}$
Q1311−270	0.90 ± 0.03	4.33 ± 1.35	1.48 ± 0.07	$0.64^{+0.05}_{-0.06}$	$1.30^{+0.08}_{-0.07}$	$1.28^{+0.13}_{-0.15}$	6.50 ± 2.1	$5.82^{+2.16}_{-2.17}$	$8.19^{+2.56}_{-2.60}$	$15.98^{+4.80}_{-4.77}$
Q1402−012	1.26 ± 0.01	2.79 ± 0.18	1.63 ± 0.13	$0.42^{+0.06}_{-0.04}$	$0.53^{+0.08}_{-0.09}$	$1.17^{+0.17}_{-0.25}$	5.94 ± 0.41	$3.37^{+0.53}_{-0.70}$	$5.68^{+0.78}_{-0.87}$	$12.79^{+1.57}_{-1.66}$
Q1442+101	1.72 ± 0.01	2.65 ± 0.23	1.43 ± 0.09	$4.36^{+0.32}_{-0.43}$	$5.79^{+0.36}_{-0.59}$	$11.20^{-0.83}_{1.02}$	14.85 ± 2.29	$15.25^{+3.28}_{-3.45}$	$26.18^{+4.96}_{-5.02}$	$52.23^{+8.09}_{-8.14}$
Q1542+042	1.35 ± 0.01	2.93 ± 0.19	1.23 ± 0.06	$1.80^{+0.14}_{-0.14}$	$3.36^{+0.21}_{-0.18}$	$3.72^{+0.36}_{-0.33}$	4.56 ± 0.53	$6.81^{+1.32}_{-1.38}$	$10.08^{+1.50}_{-1.51}$	$18.37^{+2.38}_{-2.39}$
Q1614+051	1.24 ± 0.01	0.90 ± 0.18	1.24 ± 0.15	$1.86^{+0.19}_{-0.36}$	$2.49^{+0.27}_{-0.27}$	$4.72^{+0.43}_{0.95}$	4.08 ± 0.83	$5.10^{+1.64}_{-1.91}$	$8.84^{+2.48}_{-2.59}$	$17.64^{+3.74}_{-3.85}$
Q1626+115	1.31 ± 0.02	1.66 ± 0.14	1.39 ± 0.07	$0.74^{+0.08}_{-0.08}$	$1.09^{+0.11}_{-0.08}$	$1.73^{0.18}_{-0.18}$	2.02 ± 0.18	$2.14^{+0.36}_{-0.40}$	$3.56^{+0.49}_{-0.50}$	$7.31^{+0.87}_{-0.89}$
Q1656+477	1.85 ± 0.01	2.95 ± 0.20	1.32 ± 0.06	$0.86^{+0.10}_{-0.09}$	$1.39^{+0.13}_{-0.10}$	$1.89^{0.31}_{-0.26}$	3.81 ± 0.27	$4.86^{+0.71}_{-0.79}$	$7.55^{+0.81}_{-0.84}$	$13.25^{+1.36}_{-1.39}$
Q1726+344	1.68 ± 0.01	1.21 ± 0.09	≥ 1.34	–	–	–	2.97 ± 0.24	–	–	–
Q2212−299	$1.5\ (2.46 \pm 0.07)^{b}$	4.91^{b}	1.61 ± 0.12	$0.83^{+0.09}_{-0.14}$	$1.11^{+0.13}_{-0.16}$	$2.12^{+0.33}_{-0.33}$	13.43	9.12	14.85	30.43
Q2223+210	1.46 ± 0.03	3.77 ± 3.11	1.19 ± 0.05	$4.31^{+0.17}_{-0.22}$	$5.89^{0.29}_{0.34}$	$10.70^{+0.60}_{-0.77}$	6.03 ± 0.81	$7.27^{+1.28}_{-1.29}$	$12.92^{+1.91}_{-1.91}$	$29.64^{+3.34}_{-3.33}$
Q2251+244	1.08 ± 0.01	4.60 ± 0.39	1.28 ± 0.08	$4.03^{+0.33}_{-0.37}$	$5.01^{0.28}_{-0.48}$	$11.50^{+0.76}_{-1.42}$	6.23 ± 0.72	$5.22^{+1.65}_{-1.09}$	$9.86^{+1.65}_{-1.69}$	$27.57^{+3.13}_{-3.16}$
Q2334+019	1.42 ± 0.02	1.42 ± 0.14	≥ 1.30	–	–	–	2.62 ± 0.27	–	–	–
Q2341+010	1.45 ± 0.02	1.57 ± 0.18	≥ 1.87	–	–	–	2.09 ± 0.29	–	–	–
Q2350−007	1.56 ± 0.05	1.43 ± 0.30	≥ 1.69	–	–	–	1.63 ± 0.36	–	–	–
Q2359+002	–	–	–	–	–	–	–	–	–	–

Notes. (1) Object name. (2) The best-fitting UV–optical quasar continuum slope (Section 5.1). The 1σ uncertainties are derived from the fit covariance matrix. (3) The flux density at 2500 Å, in units of 10^{-27} erg s^{-1} cm^{-2} Hz^{-1}. (4) The X-ray to UV–optical spectral index $\alpha_{\rm ox}$, as defined by Tananbaum et al. (1979). (5,6,7) Integrated luminosities over the rest-frame energy intervals 2–10 keV, 0.3–10 keV, and 1–25 keV. Units of 10^{46} erg s^{-1}. (8) Integrated luminosity over the rest-frame interval 1000–3000 Å, as derived from our UV continuum modelling, in units of 10^{46} erg s^{-1}. (9,10) Guideline estimates of the EUV luminosity (Section 6.6). We interpolate over the rest-frame intervals 1000 Å to 1 keV and 1000 Å to 0.3 keV. Units of 10^{46} erg s^{-1}. (11) Guideline estimate of the integrated luminosity over the rest-frame interval 3000 Å–25 keV. Units of 10^{46} erg s^{-1}.

[a]For typographical reasons, we shorten the names of the SDSS quasars in this table. See Table 1 for the full object names.

[b]Denotes objects with only one or two UV photometric data points suitable for continuum modelling (Section 5.1). Spectral indices as measured by Vestergaard (2003) are listed in parentheses when available.

[c]Quasar Q0458−020 has an intervening damped Lyman α system (Wolfe et al. 1993), and appears severely reddened. The measured $L_{\rm UV}$ should be regarded as a lower limit with respect to the intrinsic luminosity.
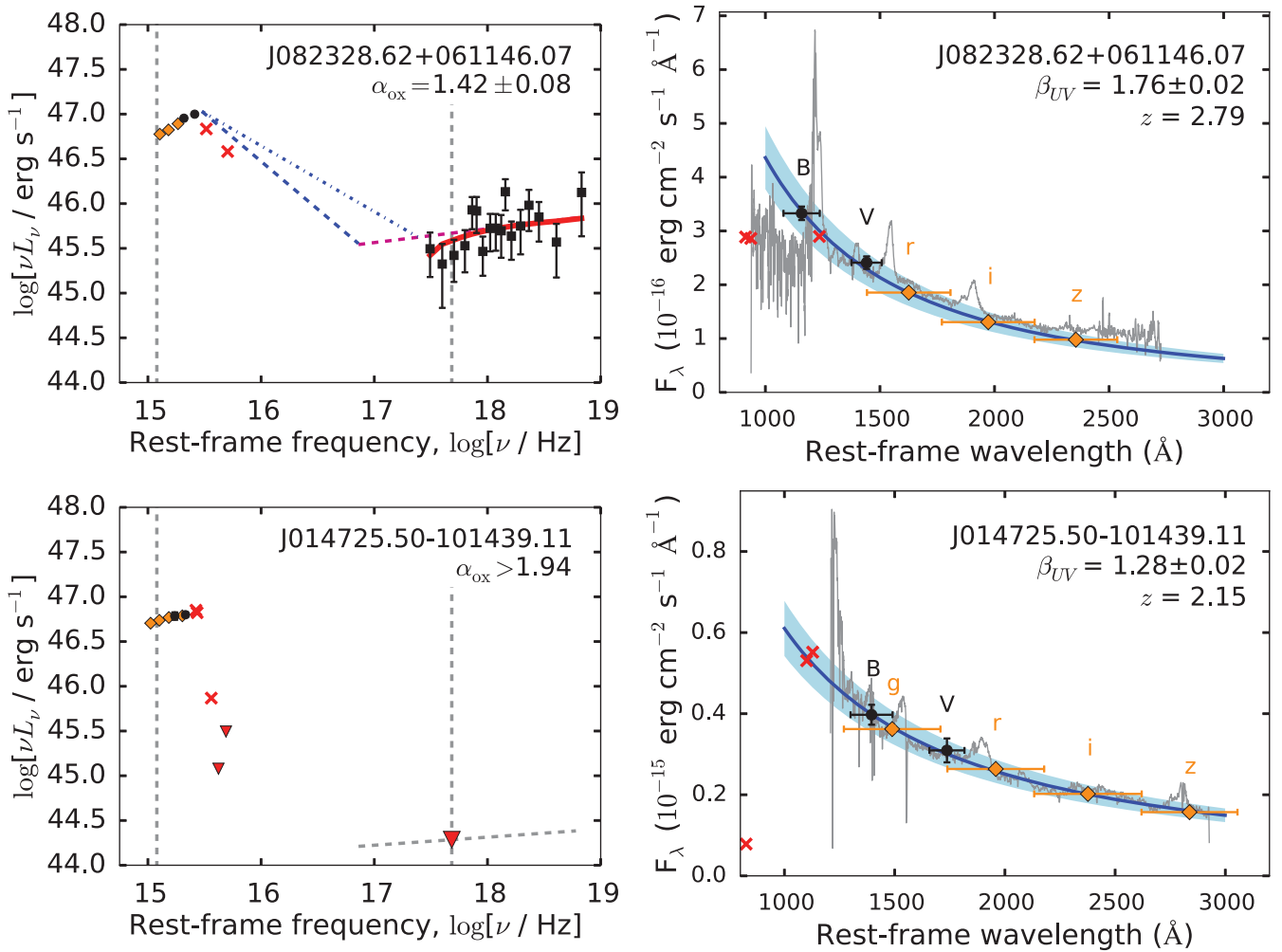
Figure 5. SEDs for two quasars in our sample: one X-ray-detected object (upper panels), and one X-ray non-detection (lower panels). Left-hand panels: rest-frame UV to X-ray SEDs. The leftmost and rightmost vertical dashed lines indicate the frequencies corresponding to 2500 Å and 2 keV, respectively. Right-hand panels: detailed view of the UV data and continuum modelling. Symbols: black squares: 'unfolded' XRT spectrum (Section 5.2) with 1σ uncertainties. Solid red curve: X-ray model including Galactic absorption. Dashed magenta curve: intrinsic, absorption-corrected X-ray model. Red triangles: 3σ upper limit fluxes (for X-ray upper limits, grey dashed line illustrates a $\Gamma = 1.91$ power law). Black dots: Galactic absorption-corrected UVOT photometry. Orange squares: rescaled SDSS broad-band photometry (Section 4). Red crosses: photometric data points excluded from modelling (Section 5.1). Blue dashed and dash–dotted lines: EUV interpolations (Section 6.6), connecting with the X-ray model at 0.3 and 1 keV, respectively. Grey curve: SDSS spectrum, if available – otherwise, composite quasar spectrum of Selsing et al. (2016), scaled to the model flux at 2500 Å. In the right-hand panels, the horizontal bars represent the full-width at half maximum (FWHM) of the filter bandpasses.

(2016); in the Appendix, we discuss the targets for which this is successful.

6 MEASUREMENTS AND ANALYSIS

Here, we present some fundamental measurements of the quasar SEDs that help describe the current subsample, including estimates of the integrated UV to X-ray luminosity (Section 6.6). All X-ray detected objects are radio loud, while all but one of the X-ray non-detections are radio quiet. This is unsurprising, as RLQs tend to be brighter in the X-ray than RQQs at a given optical luminosity (Zamorani et al. 1981). We will address the remainder of the sample in future work, pending completion of the *Swift* observations.

6.1 UV and X-ray luminosities

Our sample spans a full range $1.0 \leq L_\nu(2500\,\text{Å})/(10^{46}\,\text{erg s}^{-1}) \leq 9.8$ (Fig. 6, left-hand panel), with an average monochromatic UV luminosity of $\langle \nu L_\nu(2500\,\text{Å})\rangle = 4.2 \times 10^{46}$ erg s^{-1}. Two quasars

are not detected in any UVOT bands; we make no attempt to determine limiting values of $L_\nu(2500\,\text{Å})$ for these objects, as we lack simultaneous UV data with which to rescale the SDSS photometry. Six quasars are detected in only one or two UV bandpasses, making the determination of $L_\nu(2500\,\text{Å})$ uncertain (Section 5.1). In the X-ray data we detect 23 quasars and present 3σ upper limits for 21 objects (Fig. 6, right-hand panel). The average $\nu L_\nu(2\,\text{keV})$ for detected objects is 8.3×10^{44} erg s^{-1}. All X-ray-detected objects have $\nu L_\nu(2\,\text{keV}) > 10^{44}$ erg s^{-1}. The average integrated rest-frame 0.3–10 keV luminosity for X-ray-detected quasars is 2.0×10^{46} erg s^{-1}. Thus, our sample is comparable in terms of X-ray luminosity to the brightest quasars in the *Swift* sample presented by Wu et al. (2012).

6.2 The X-ray hardness ratio

The X-ray HR is a crude representation of the X-ray spectral slope, useful for observations with few detected X-ray counts, for which the photon index Γ is not well determined. We calculate the HR
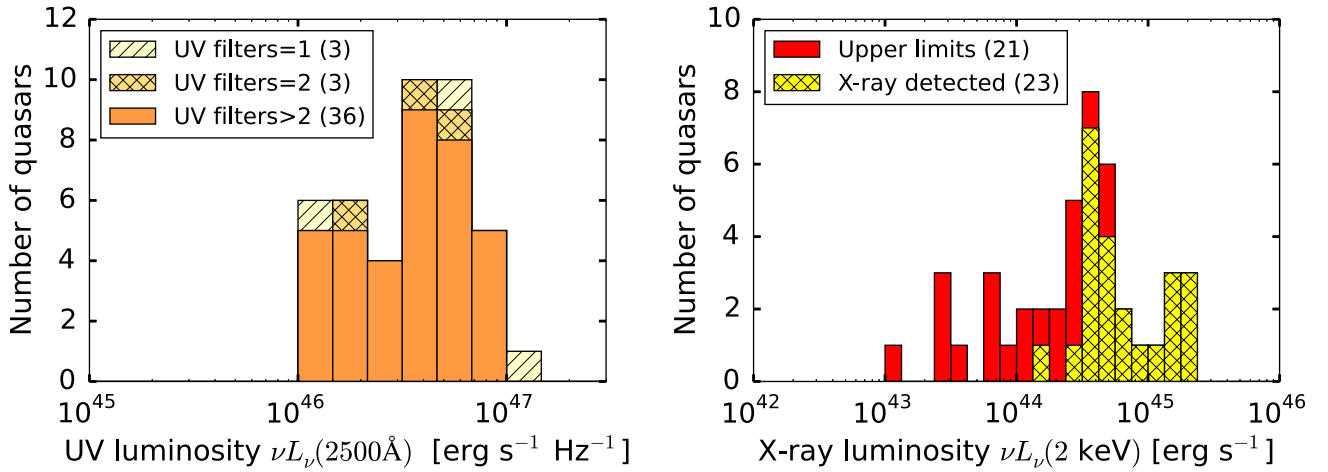
Figure 6. Left: distribution of $\nu L_\nu(2500\,\text{Å})$ for our sample, based on the continuum modelling (Section 5.1). Only quasars detected in three or more UV bandpasses (solid orange histogram) are included in our further analysis (Section 6.5). Right: distribution of $\nu L_\nu(2\,\text{keV})$. Upper limits for non-detections are at the 3σ level (solid yellow histogram). This is a stacked histogram (see caption of Fig. 1)
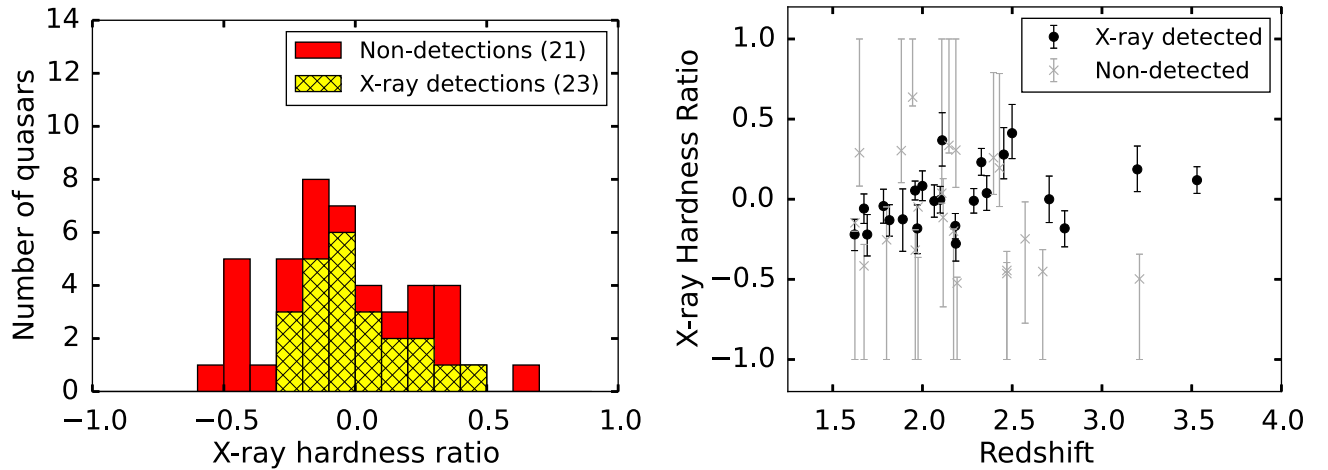
Figure 7. Left: distribution of the X-ray HR for our sample. Here, the soft band is 0.3–1.5 keV, while the hard band is the 1.5–10 keV range. Larger values of HR imply harder X-ray spectra. This is a stacked histogram (see caption of Fig. 1). Right: redshift distribution of the HRs. The mean hardness ratio is $\langle HR \rangle = 0.01$ with a standard deviation of 0.19 for X-ray detections (black points), $\langle HR \rangle = -0.08$ with a standard deviation of 0.34 for non-detections (grey crosses).

for each quasar as $HR = (H - S)/(H + S)$. Here, H and S are the background-subtracted hard-band (observed-frame 1.5–10 keV) and soft-band (0.3–1.5 keV) source aperture counts, respectively. We use the c- and FORTRAN-based software *Bayesian Estimation of Hardness Ratios*[12] (BEHR; Park et al. 2006) to determine the uncertainties on HR, choosing a flat prior distribution. For X-ray detections, we find a mean hardness ratio $\langle HR \rangle = 0.01 \pm 0.01$, with a sample standard deviation $\sigma_{HR} = 0.19$ (Fig. 7, left-hand panel). For non-detections, we find $\langle HR \rangle = -0.08 \pm 0.04$ and $\sigma_{HR} = 0.34$. For the majority of the X-ray non-detections, the HR is poorly determined, with uncertainties consistent with the extreme values ($HR = \pm1$, Fig. 7, right-hand panel). A possible weak tendency for a higher HR at higher redshift (Fig. 7, right-hand panel) is likely due to the soft excess becoming increasingly redshifted outside the *Swift* observable window at higher z. It is difficult to determine how common the soft excess feature is at $z \sim 2$, due to the redshifting of the relevant energies into the unobservable EUV spectral region.

However, if there is a soft excess component, its high-energy tail would contribute to the XRT soft band for quasars at $z \sim 1.5$, but less so for higher redshift objects. Piconcelli et al. (2005) find evidence for a soft excess in 39 (of 40) $M_B \lesssim 23$ AGN, including a few objects at $z \sim 1.5$.

6.3 The X-ray photon index

For X-ray-detected quasars, we find an average value $\langle \Gamma \rangle = 1.46 \pm 0.05$, with a sample standard deviation of 0.23, and a full range $1.08 \leq \Gamma \leq 1.93$. The distribution of Γ is fairly symmetric around the mean (Fig. 8, left-hand panel), in agreement with previous studies of both RLQs and RQQs (e.g. Scott et al. 2011; Wu et al. 2012); we find a median photon index $\Gamma = 1.47$, in agreement with our mean value. We see a weak tendency towards decreasing Γ with increasing redshift (Fig. 8, right-hand panel). While this tendency is not highly significant for the current sample (the Spearman rank correlation $p = 3$ per cent), it is in agreement with the findings of Scott et al. (2011) for a larger sample of $z < 6$ AGN. Similarly to the
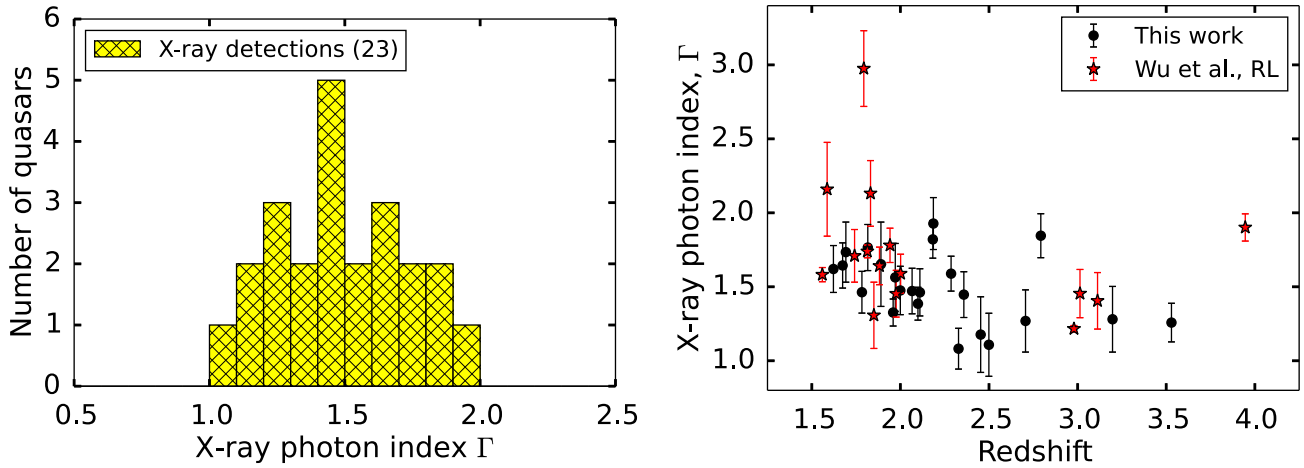
Figure 8. Left-hand panel: distribution of the X-ray photon index Γ for X-ray-detected quasars, measured across the observed frame energy range 0.3–10 keV. The average uncertainty on individual measurements of Γ is 0.15 for observations with $N_{\rm sub} > 50$ (orange dotted area), and 0.23 for observations with $20 < N_{\rm sub} < 50$. This is a stacked histogram (see caption of Fig. 1). Right-hand panel: redshift distribution of Γ for X-ray-detected objects in our sample (black points), and for radio loud $z > 1.5$ quasars in the sample of Wu et al. (2012, red stars).

Table 7. Distributions of Γ in previous studies of RLQ.

Study (1)	Redshift range (2)	Objects in sample (3)	$\langle\Gamma\rangle^a$ (4)	$\sigma_\Gamma{}^b$ (5)	Energy range (keV)^c (6)
This study	$1.5 < z < 3.6$	23	1.46 ± 0.05	0.23	0.3–10, obs.
Wu et al. (2012)^d	$1.5 > z > 5.5$	15	1.74 ± 0.11	0.42	0.3–10, obs.
Wu et al. (2013)	$z \gtrsim 4$	16	1.60 ± 0.06	0.23	2–10, obs.
Scott et al. (2011)	$z < 6$	75	1.86 ± 0.02	0.20	0.5–12
Page et al. (2005)	$2 < z < 7$	16	1.55 ± 0.04	0.28	2–10
Reeves & Turner (2000)	$z \leq 4.3$	35	1.66 ± 0.04	0.22	2–10

^{a}The average value of Γ for the sample indicated in Column 1. For studies including both RLQs and RQQs, we include $\langle\Gamma\rangle$ for the radio-loud subsample only.
^{b}Sample standard deviation of Γ.
^{c}The energy range over which Γ is measured. Rest-frame energies unless noted as 'obs.'.
^{d}In this study, Γ is only modelled as a free parameter for those objects with source X-ray counts $N_{\rm sub} \geq 100$, and for objects with $N_{\rm sub} \geq 50$ and intrinsic absorption consistent with zero. The authors measure Γ for 15 of a total of 46 RLQ. This may bias the average value of Γ for the measured subsample.

weak trend discussed in 6.2, the cause of this trend in our sample may be the redshifting of the soft excess out of the XRT observing window.

We find a smaller $\langle\Gamma\rangle$ than that of any other study of RLQ of which we are aware (Table 7). While the RLQ presented by Scott et al. (2011) are fainter than our sample in terms of the integrated luminosity between 2 and 10 keV, those presented by Wu et al. (2012) have comparable luminosities, and those of Page et al. (2005) are more luminous. Thus, this discrepancy is not purely a luminosity effect. The use of different energy ranges for which Γ is measured for the different studies complicates this issue. However, the discrepancy persists if we limit our X-ray modelling to the rest-frame 2–10 keV energy range to allow a direct comparison with the findings of Page et al. (2005) and Reeves & Turner (2000): for this energy range, we find $\langle\Gamma\rangle = 1.23 \pm 0.12$. Given our moderate sample size (23 detected RLQ), the low $\langle\Gamma\rangle$ may simply be a statistical anomaly. Indeed, the discrepancy between our sample and that of Wu et al. (2012) is driven by just three objects with $\Gamma > 2$ in their sample (Fig. 8). We discuss a possible explanation for this discrepancy, should it be real, in Section 7.

6.4 The UV–optical spectral index

For quasars with at least three photometric data points used in the modelling, we find an average spectral index $\langle\beta_{\rm UV}\rangle = 1.41 \pm 0.05$, with a sample standard deviation of $\sigma_\beta = 0.33$. This is somewhat redder than the $\beta_{\rm UV} = 1.56$ measured for the SDSS composite quasar spectrum (Vanden Berk et al. 2001). It is, however, consistent with the average value $\langle\beta_{\rm UV}\rangle = 1.34 \pm 0.15$ found by Carballo et al. (1999) for RLQ. We note that our UV–optical measurements, and those of Carballo et al. (1999), are based on broad-band photometry. Vestergaard (2003) presents measurements of the UV continuum slope, based on spectroscopic data, for 22 quasars in the current sample. These measurements are on average steeper (bluer) than our $\beta_{\rm UV}$ by 0.32 ± 0.11. This indicates that our modelling is affected by broad emission-line contamination of the photometric bandpasses, despite our strategy of excluding bandpasses with strong broad-line contributions (Section 5.1). In particular, the presence of Balmer continuum emission and of the multitude of Fe II emission lines in the rest-frame near-UV causes a systematic overestimation of the continuum level and a flattening of the measured spectral index. In Section 6.6, we quantify
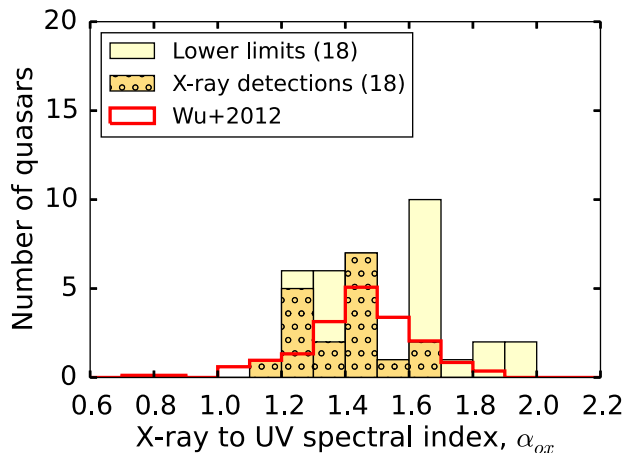
Figure 9. Distribution of α_{ox} (and 3σ upper limits for X-ray non-detections) for all quasars with reliable UV continuum fits (Section 6.5). This is a stacked histogram (see caption of Fig. 1). The red histogram shows the distribution of α_{ox} for objects detected in both UV and X-ray data at $z > 1.5$ in the sample of Wu et al. (2012), comprising both radio quiet and RLQs. This histogram is normalized to have the same total area as that of our X-ray-detected sample.

the resulting systematic uncertainty introduced into our accretion luminosity estimates.

6.5 The X-ray to UV spectral index α_{ox}

We measure the X-ray to UV spectral index α_{ox} as defined by Tananbaum et al. (1979), or its 3σ lower limit, for each quasar for which we have a UVOT detection (Table 6). In the following discussion, we only include quasars for which we have three or more photometry data points suitable for our UV continuum modelling (36 objects, Section 5.1). We find an average value of $\langle\alpha_{ox}\rangle = 1.39 \pm 0.03$ for the X-ray detected objects, with a sample standard deviation of 0.12 (Fig. 9). Assuming that those upper limits with $\alpha_{ox} \approx 2$ are close to the true values, our sample covers a similar range of α_{ox} as the $z > 1.5$ subsample of Wu et al. (2012), comprising both RLQs and RQQs, as shown in Fig. 9. The mean value of α_{ox} for the RLQ subsample is in rough agreement with previous studies of RLQs (Wu et al. 2013, $\langle\alpha_{ox}\rangle = 1.35 \pm 0.05$, Miller et al. 2011, $\langle\alpha_{ox}\rangle = 1.37 \pm 0.03$). Previous studies tend to find a steeper α_{ox} for RQQs than for RLQs. For example, Steffen et al. (2006) find $\langle\alpha_{ox}\rangle = 1.71 \pm 0.02$ for RQQs with comparable UV–optical luminosities to our sample. The upper limits on α_{ox} obtained for RQQs in our sample are consistent with this: we find an average limiting value of $\alpha_{ox} > 1.62$.

At low redshift, α_{ox} correlates with Γ (as measured in the observed XRT band, 0.3–10 keV) in the sense that AGN that are X-ray faint relative to the optical–UV tend to have softer X-ray SEDs (Atlee & Mathur 2009; Grupe et al. 2010). We find no such correlation in our $z \approx 2$ sample, for which we model the SED at rest-frame energies $\gtrsim 0.75$ keV. As suggested by Wu et al. (2012), the observed trend at low redshift is likely driven by the soft X-ray excess component. The soft excess may be due to Compton-upscattered UV emission from the accretion disc, and may therefore be stronger when the accretion disc is brighter relative to the coronal emission (i.e. for higher values of α_{ox}). The lack of this trend in our data is then explained by the redshifting of the soft excess outside our spectral window.

The relationship between α_{ox} and $L_\nu(2500\,\text{Å})$ for RQQs has been studied by several authors (e.g. Tananbaum et al. 1979; Wilkes
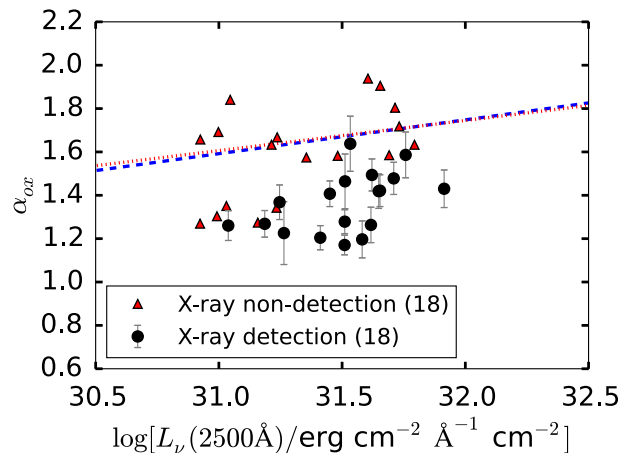
Figure 10. The SED shape, as represented by α_{ox}, as a function of $L_\nu(2500\,\text{Å})$. The dashed blue line shows the $L_\nu(2500\,\text{Å})$–α_{ox} sample of Wu et al. (2012), which contains both RLQs and RQQs, but is predominately radio quiet. The red dotted line shows the $L_\nu(2500\,\text{Å})$–α_{ox} relation found by Strateva et al. (2005) for RQQs. We note that the distribution of our X-ray detections (which are radio loud) is offset from the relations previously established for RQQs.

et al. 1994; Strateva et al. 2005; Wu et al. 2012). These authors find a non-linear relationship between the UV and X-ray luminosities, with more UV-luminous AGN being relatively weaker X-ray emitters. Given the small dynamic range in $L_\nu(2500\,\text{Å})$ for X-ray detections in our current sample, it is unsurprising that this trend does not exist in our data [a generalized Kendall's τ test gives the probability $p = 0.17$ of observing this distribution given no intrinsic relation between $L_\nu(2500\,\text{Å})$ and α_{ox}]. Here, we simply note that our X-ray detections are offset from the previously established relationships between $L_\nu(2500\,\text{Å})$ and α_{ox} for RQQs (Fig. 10), as expected for RLQ as they tend to be X-ray bright (e.g. Zamorani et al. 1981; Miller et al. 2011).

6.6 Integrated luminosities

6.6.1 X-ray and UV luminosities

As a measure of the X-ray luminosity of the quasars, we integrate the power-law model corrected for Galactic absorption over the rest-frame energy range 1–25 keV, $L_X(1\text{–}25\text{ keV})$. We select this energy range as it requires minimal extrapolation from the observed spectrum, given the redshift range of our sample. For ease of comparison with other work, we also provide two alternative estimates of the X-ray luminosity: namely, L_X (0.3–10 keV), integrated from 0.3 to 10 keV in the rest-frame (which implies an extrapolation of our model fit into the soft X-rays, and is therefore systematically underestimated if these quasars have a soft excess component), and L_X (XRT Band), integrated from 0.3 to 10 keV in the observed frame. The latter involves no extrapolation, but is not directly comparable between objects at different redshifts. Similarly, we estimate the quasar's UV luminosity L_{UV} by integrating the UV continuum model over the rest-frame interval 1000–3000 Å. These measurements of L_{UV} and L_X, along with their uncertainties as propagated from the 1σ errors on the respective model parameters, are tabulated in Table 6.

6.6.2 Extreme-UV and total luminosities

The EUV is not directly observable due to strong absorption by the neutral hydrogen and helium in the Milky Way, in the intergalactic

medium, and by gas in the quasar host galaxy. This spectral region may harbour the peak energy output of the accretion disc emission feature (Section 1), and must therefore be included in an estimate of the accretion luminosity. Physically motivated modelling of the EUV energy output generally depends on parameters that are not strongly constrained by broad-band photometric observations. For example, the accretion disc model used by Done et al. (2012) requires a determination of the black hole mass (or spin). It also requires that the thermal emission peak is constrained by the observations, which is not true of $z \approx 2$ quasars observed with *Swift*. Similarly, the truncated power-law model employed by Korista et al. (1997) depends on an inner-disc cutoff temperature that is not constrained by broad-band data. For the low-redshift Seyfert galaxy NGC 5548, Kilerci Eser and coworkers find that a simple linear interpolation between the observed UV and X-ray luminosities yields an integrated luminosity roughly halfway between that predicted by the Done et al. (2012) and the Korista et al. (1997) models. The difference between the interpolated luminosity and either of the model predictions is 23 per cent (Kilerci-Eser 2014; Kilerci-Eser & Vestergaard in preparation). Due to our ignorance of the EUV SED shape, and following Grupe et al. (2010) and Wu et al. (2012), we make guideline estimates of the EUV luminosities, L_{EUV}, by interpolating over the EUV region using a power-law function. Due to Lyman α forest absorption and/or Lyman α emission in the shortest wavelength UVOT bandpass, we do not use this data point directly in the interpolation. Instead we use our UV continuum model (Section 5.1). However, due to emission-line contamination, our UV model systematically overestimates the continuum luminosity. We quantify the resulting systematic uncertainty on the EUV luminosity and on the integrated X-ray to UV luminosity in Section 6.6.3.

Several previous studies find a spectral turnover at roughly 1000 Å (Shang et al. 2005; Barger & Cowie 2010; Shull et al. 2012; Stevans et al. 2014). We therefore interpolate between the 1000 Å model luminosity and the 1 keV unabsorbed X-ray model luminosity (blue dash–dotted curves, Figs 5 and A1–A15). We also interpolate between 1000 Å and 0.3 keV, providing an alternative estimate of L_{EUV} (blue dashed lines). The latter interpolation may be more appropriate for quasars that lack the soft X-ray excess component; for these $z \approx 2$ quasars, we cannot determine whether the soft excess component is present based on the XRT data. In any case, due to our ignorance of the EUV SED, the resulting integrated luminosities are order-of-magnitude estimates. The work of Kilerci-Eser & Vestergaard (in preparation) suggests that the uncertainty on L_{EUV} due to model assumptions is of the order of 25 per cent.

We tabulate L_{EUV}, along with the estimated total UV to X-ray luminosity $L_{tot} = L_{UV} + L_{EUV} + L_{X(1-25)}$, in Table 6. The 1σ uncertainties on L_{EUV} for X-ray-detected quasars are calculated by extrapolating between the 1σ limiting values of the 1000 Å and 1 keV flux densities. The average value of L_{tot} for X-ray-detected objects in our sample is 1.8×10^{47} erg s^{-1}, with a full span between $L_{tot} = 6.3 \times 10^{46}$ erg s^{-1} and $L_{tot} = 4.5 \times 10^{47}$ erg s^{-1} (Fig. 11). Thus, the X-ray-detected objects in our sample are comparable in terms of accretion luminosity with the more luminous objects presented by Wu et al. (2012).

6.6.3 Systematic uncertainty on L_{tot} due to UV emission-line contribution

While we exclude data points that we believe to be strongly contaminated by emission lines from our UV continuum modelling (Section 5.1), the remaining bands also have an emission-line contribution. In particular, the broad, blended Fe II emission lines
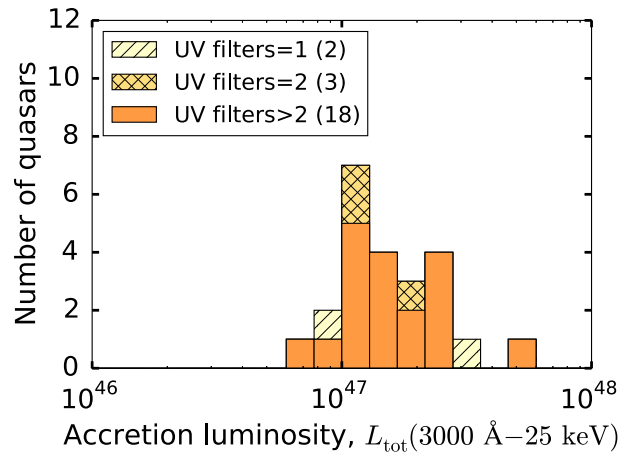
Figure 11. Stacked histogram of L_{tot} (3000 Å–25 keV) for all sample quasars with both XRT and UVOT detections. Quasars with only one or two UV photometric data points suitable for continuum fitting (Section 5.1) are shown as striped and hashed regions, respectively.
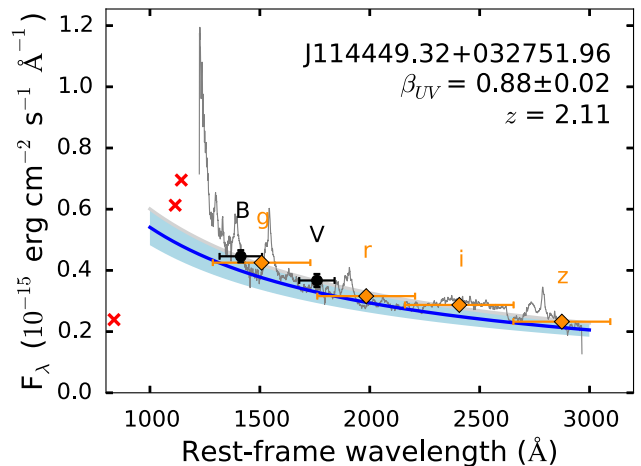
Figure 12. Rescaling of continuum model to match the flux level of the continuum-dominated 'window' near 1450 Å. For this quasar, both the UVOT (black points) and SDSS (orange diamonds) photometry bandpasses suffer some emission-line contamination. The horizontal error bars indicate the width of the photometric bandpasses. We decrease the model flux (blue curve) by 10 per cent, at which point it roughly matches the SDSS spectroscopy (dark grey curve) at 1450 Å. The blue shaded region shows the uncertainty on the rescaled continuum level. The original continuum model fit, before rescaling, is shown as a light grey curve near the upper edge of the blue shaded region.

and Balmer continuum produce a 'pseudo-continuum' feature at rest-frame 2000–4000 Å. We estimate the resulting systematic uncertainty as follows. The narrow spectral region around 1450 Å is thought to be almost free of emission-line flux (e.g. Vanden Berk et al. 2001; Selsing et al. 2016). We therefore adjust the scaling of the UV power-law continuum model until its flux density around 1450 Å roughly matches the continuum flux in this spectral region (Fig. 12). For objects lacking SDSS spectroscopy, we perform this test using the Selsing et al. (2016) quasar template, scaled to the initial continuum model flux at 2500 Å. We find that the systematic overestimation of the UV continuum flux is approximately 25 per cent in the worst cases, and 11 per cent on average. The resulting overestimation of L_{tot} is 18 per cent in the worst cases, and 8 per cent on average. While the main purpose of this exercise

is to obtain an estimate of the *average* systematic uncertainty, we nevertheless provide preliminary corrections to the UV, EUV and total luminosities (Table 8). These corrections are somewhat subjective in nature, and should be used with caution. Note that the UV–optical models shown in the Appendix are the original model fits, before applying this correction.

6.6.4 Bolometric luminosity estimates based on UV data

We make guideline estimates of the bolometric (rest-frame 1 μm–8 keV) luminosities, L_{bol}, of our sample, using the average bolometric correction presented by Runnoe, Brotherton & Shang (2012) for a sample of RLQs and RQQs at $z < 1.4$ with $\log[L_{bol}/\mathrm{erg\,s^{-1}}] < 47.3$ and assuming isotropic emission. We note that, while the sample presented by Richards et al. (2006) is better matched in terms of redshift to our sample, their bolometric corrections include the infrared spectral region (1–100 μm), which we do not wish to include in our estimate of the accretion luminosity (Section 5). We estimate L_{bol} using the specific luminosity at rest-frame 1450 Å, using equation 9 of Runnoe et al. (2012). For X-ray-detected quasars, the integrated accretion luminosity L_{tot} agrees with the estimated L_{bol} to within the 1σ level for all quasars (Fig. 13, black points). However, the L_{bol} (1 μm–8 keV) estimates are on average 26 per cent larger than L_{tot} (3000 Å–25 keV) as inferred from our *Swift* data. This is likely due to the smaller spectral window covered by our L_{tot} measurement. Indeed, if we extrapolate our UV power-law continuum model to 1 μm, we find that L_{bol} is on average only 1 per cent larger than L (1 μm–25 keV) (Fig. 13, red points). We use L_{bol} to make guideline estimates of the Eddington luminosity for the X-ray non-detections in Section 6.8.

6.7 Mass accretion rates

The mass accretion rate, $\dot{M}$, represents the instantaneous growth rate of the black hole. We estimate $\dot{M}$ for a subset of our sample. Namely, those quasars for which we have spectroscopy covering the C IV broad emission line, allowing estimation of the black hole mass, M_{BH}, and for which we have SDSS photometry, allowing a determination of the optical luminosity L_{opt}. Given these requirements, we estimate $\dot{M}$ for a total of 34 quasars, as follows.

Quasar accretion discs are traditionally modelled as geometrically thin, optically thick α-discs (Section 1). For such models, Raimundo et al. (2012, following Davis & Laor 2011) show that $\dot{M}$ depends on M_{BH} and L_{opt} as

$$\dot{M} = 1.53\,\mathrm{M_\odot\,yr^{-1}} \left(\frac{\nu L_\nu(\mathrm{opt})}{10^{45}\cos(i)\,\mathrm{erg\,s^{-1}}} \right)^{3/2}$$
$$\times \left(\frac{M_{BH}}{10^8\,\mathrm{M_\odot}} \right)^{-1} \frac{\lambda(\mathrm{opt})^2}{(4392\,\text{Å})^2}. \quad (4)$$

The optical specific luminosity, $L_\nu(\mathrm{opt})$, can be measured at any optical wavelength $\lambda(\mathrm{opt})$. However, $\dot{M}$ has an additional dependence on the black hole spin, which becomes stronger at wavelengths shorter than 4000 Å (as illustrated by fig. 1 of Davis & Laor 2011). To avoid extrapolation of our continuum model beyond the wavelength coverage of the data, we use νL_ν as measured at the pivot wavelength of the SDSS z bandpass (pivot wavelength ~2000–3500 Å in the rest frame). This bandpass is our reddest photometric data point, and thus minimizes the dependence of $\dot{M}$ on black hole spin, although this dependence is not negligible at these wavelengths; we will quantify this uncertainty in future work, upon completion of

our *Swift* observing programme. We also require estimates of M_{BH} and the accretion disc inclination i, as detailed below.

Black hole mass estimates: we use the scaling relationship presented by Vestergaard & Peterson (2006, their equation 7) to calculate single-epoch spectroscopic black hole mass estimates, based on the C IV FWHM (Vestergaard 2000) and the monochromatic continuum luminosity L_λ (1350 Å). This luminosity is determined by extrapolating the power-law continuum with slope and normalization at 1550 Å, as presented by Vestergaard (2003) for our sample quasars. For the 12 quasars in our SDSS sample (Section 1), we measure L_λ (1350 Å) and the C IV FWHM in the SDSS spectroscopy; if the Mg II broad emission line is also covered by the SDSS spectra, we use a variance-weighted average of M_{BH} calculated using C IV and Mg II (Vestergaard & Osmer 2009, equation 1), with the variance based on the uncertainties of the spectral measurements. Our sample has an average black hole mass of $\langle M_{BH}\rangle = (5.0 \pm 0.7) \times 10^9\,\mathrm{M_\odot}$, with a full range in black hole mass of $0.6 \leq M_{BH}/10^9\,\mathrm{M_\odot} \leq 18.0$, similar to that of $z \approx 2$ quasars in the Large Bright Quasar Survey (Vestergaard & Osmer 2009). Typical uncertainties on M_{BH} are of the order of 0.6 dex, and are dominated by the scatter of the Vestergaard & Peterson (2006) scaling relationship with respect to the M_{BH} determined by reverberation mapping, and by the uncertainty on the normalization of the reverberation-mapping mass scale itself, as determined by Onken et al. (2004).

Inclination angle estimates: equation (4) contains a dependency on the disc inclination, i, as this determines the solid angle subtended by the disc on the sky, and therefore affects the observed luminosity. For the RLQs in our sample, we are able to make a crude estimate of i, as follows. If the radio jet is launched perpendicularly to the disc plane, and the jet does not twist, the radio jet inclination is a proxy for the accretion disc inclination. Here, we use the radio spectral index, α_R, as an indicator of the radio jet inclination (e.g. Jarvis & McLure 2006). Padovani & Urry (1992) apply a radio emission beaming model to the observed luminosity functions of RLQ and radio galaxies. In this scenario, steep-spectrum radio sources (SSS; defined as sources with radio spectral index $\alpha_R < -0.6$) are the unbeamed parent population of flat spectrum radio source (FSS, $\alpha_R > -0.6$), but become obscured in the UV–optical (and are therefore seen as radio galaxies) for the largest inclinations. They find that flat-spectrum radio sources are aligned with the line of sight to within $14°$, while steep-spectrum sources are aligned at $14° \leq i \leq 40°$, with an expectation value of $\langle i\rangle = 28°$. Based thereon, we assume accretion disc inclinations $i = 10°$ for FSS and $i = 28°$ for SSS. We calculate α_R between 408 MHz and 5 GHz if these measurements are available, or between 1400 MHz and 5 GHz otherwise (Table 1). For our SDSS RLQ sample (four objects), we only have single-band radio data, at 1.4 GHz as observed by Faint Images of the Radio Sky at Twenty-Centimeters (FIRST, Becker, White & Helfand 1995), and therefore lack a measurement of α_R. For the RQQs, and for the four SDSS RLQs (for which we only have single-band radio data and therefore lack measurements of α_R), we assume $\langle i\rangle = 28°$, the average value of i for a distribution of random orientations satisfying $0° \leq i \leq 40°$. Likewise, for sources for which the radio spectra are known to peak at GHz frequencies, we assume $i = 28°$, as their radio SED shape is thought to be linked to their environment or youth, and not primarily to inclination (e.g. Fanti et al. 1995; Orienti 2016). In practice the uncertainty on $\dot{M}$ is dominated by the M_{BH} uncertainty, and therefore these guideline estimates of i suffice for the current purpose.

Mass accretion rate estimates: using equation (4), the average mass accretion rate for the 34 quasars examined here is $\langle\dot{M}\rangle = (6.7 \pm 1.3)\,\mathrm{M_\odot\,yr^{-1}}$, with a full range of $1.0 < \dot{M}/(\mathrm{M_\odot\,yr^{-1}}) < 33.1$.

Table 8. Integrated luminosities including preliminary correction for UV emission lines.

Object name (1)	Corr. per cent (2)	$F_\nu(2500\,\text{Å})$ (3)	α_{ox} (4)	L_{UV} (1000–3000 Å) (5)	L_{EUV} (1000 Å–0.3 keV) (6)	L_{EUV} (1000 Å–1 keV) (7)	L_{tot} (3000 Å–25 keV) (8)	ΔL_{tot} per cent (9)	L_{bol} (1 μm–10 keV) (10)
J014725.50−101439.11	10	3.51 ± 0.44	≥ 1.94	5.90 ± 0.76	–	–	–	–	$24.69^{+13.52}_{-12.89}$
J082328.62+061146.07	5	2.47 ± 0.35	1.42 ± 0.08	7.97 ± 1.16	$9.71^{+2.14}_{-2.27}$	$14.00^{+2.53}_{-2.56}$	$23.87^{+3.93}_{-3.96}$	3.8	$36.70^{+19.63}_{-18.00}$
J094853.60+085514.40	10	6.45 ± 0.63	1.59 ± 0.11	7.61 ± 0.86	$5.05^{+1.09}_{-1.37}$	$7.85^{+1.37}_{-1.45}$	$16.58^{+2.47}_{-2.53}$	8.3	$36.70^{+17.07}_{-17.07}$
J104915.44−011038.18	ND	–	–	–	–	–	–	–	–
J110607.48−173113.60	0	3.97 ± 0.41	≥ 1.63	10.08 ± 1.07	–	–	–	–	$44.37^{+23.25}_{-21.59}$
J111159.70+023719.76	NB	–	–	–	–	–	–	–	$18.18^{+9.68}_{-8.90}$
J112542.30+000101.33	20	2.35 ± 0.36	1.37 ± 0.08	2.93 ± 0.46	$3.41^{+0.87}_{-0.95}$	$5.14^{+1.04}_{-1.05}$	$9.11^{+1.66}_{-1.64}$	15.2	$13.06^{+7.16}_{-6.47}$
J114449.32+032751.96	10	4.85 ± 0.53	≥ 1.72	6.80 ± 0.76	–	–	–	–	$25.84^{+14.40}_{-12.89}$
J131810.74+011140.86	5	2.23 ± 0.29	≥ 1.63	3.07 ± 0.40	–	–	–	–	$14.41^{+7.54}_{-7.01}$
J142923.92+024023.14	0	7.06 ± 0.30	≥ 1.80	6.27 ± 0.28	–	–	–	–	$22.88^{+11.53}_{-10.97}$
J145717.86+024747.36	20	5.70 ± 0.73	≥ 1.90	6.25 ± 1.04	–	–	–	–	$25.31^{+14.72}_{-12.85}$
J234830.41+003918.57	15	4.12 ± 0.42	1.49 ± 0.07	5.07 ± 0.42	$3.36^{+0.63}_{-0.69}$	$5.47^{+0.83}_{-0.86}$	$12.15^{+1.57}_{-1.59}$	11.5	$18.70^{+10.42}_{-9.32}$
Q0002−008	15	1.47 ± 0.10	≥ 1.67	2.62 ± 0.67	–	–	–	–	$11.21^{+6.95}_{-5.85}$
Q0015+026	0	0.57 ± 0.09	≥ 1.27	1.50 ± 0.25	–	–	–	–	$6.93^{+3.78}_{-3.43}$
Q0020+022	20	1.00 ± 0.11	≥ 1.66	1.40 ± 0.16	–	–	–	–	$6.29^{+3.29}_{-3.06}$
Q0038−019	15	3.84 ± 0.52	1.41 ± 0.05	4.39 ± 0.63	$4.42^{+1.16}_{-0.97}$	$6.83^{+1.17}_{-1.19}$	$12.69^{+1.96}_{-1.96}$	11.4	$19.00^{+10.39}_{-9.40}$
Q0040−017	15	0.71 ± 0.24	≥ 1.30	1.47 ± 0.51	–	–	–	–	$6.24^{+4.25}_{-3.39}$
Q0106+013	0	2.84 ± 0.19	1.28 ± 0.06	4.10 ± 0.42	$3.74^{+0.62}_{-0.64}$	$6.52^{+0.88}_{-0.89}$	$15.40^{+1.94}_{-1.95}$	0.0	$15.62^{+8.57}_{-7.74}$
Q0115−011	15	2.56 ± 0.39	≥ 1.58	4.97 ± 0.78	–	–	–	–	$22.03^{+12.13}_{-10.93}$
Q0123+257	25	2.12 ± 0.28	1.19 ± 0.09	4.90 ± 0.66	$6.65^{+1.52}_{-1.64}$	$11.25^{+2.11}_{-2.15}$	$23.02^{+3.66}_{-3.62}$	14.9	$29.43^{+15.21}_{-14.24}$
Q0226−038	15	4.20 ± 0.61	1.42 ± 0.07	6.85 ± 1.04	$6.13^{+1.36}_{-1.43}$	$9.91^{+1.84}_{-1.86}$	$19.46^{+3.21}_{-3.21}$	11.3	$29.26^{+16.29}_{-14.59}$
Q0238+100	NS	–	–	–	–	–	–	–	$20.31^{+9.45}_{-9.45}$
Q0244+017	10	1.11 ± 0.10	≥ 1.35	1.51 ± 0.13	–	–	–	–	$6.15^{+3.23}_{-3.00}$
Q0249−184	NS	–	–	–	–	–	–	–	$28.70^{+13.35}_{-13.35}$
Q0252+016	20	3.36 ± 0.37	≥ 1.58	8.43 ± 0.10	–	–	–	–	$38.12^{+19.92}_{-18.53}$
Q0445+097	NS	–	–	–	–	–	–	–	$8.48^{+3.94}_{-3.94}$
Q0458−020	NS	–	–	–	–	–	–	–	$14.47^{+6.73}_{-6.73}$
Q0504+030	NS	–	–	–	–	–	–	–	$17.09^{+7.95}_{-7.95}$
Q0808+289	0	3.45 ± 0.32	1.46 ± 0.13	4.33 ± 0.42	$3.69^{+0.93}_{-1.27}$	$5.67^{+1.08}_{-1.20}$	$11.21^{+1.77}_{-1.88}$	0	$17.75^{+9.45}_{-8.69}$
Q1311−270	NS	–	–	–	–	–	–	–	$24.81^{+18.07}_{-13.95}$
Q1402−012	NB	–	–	–	–	–	–	–	$26.79^{+13.90}_{-12.99}$
Q1442+101	0	2.65 ± 0.23	1.43 ± 0.09	14.85 ± 2.29	$15.25^{+3.28}_{-3.45}$	$26.18^{+4.96}_{-5.02}$	$52.23^{+8.09}_{-8.14}$	0	$68.62^{+37.00}_{-33.77}$
Q1542+042	15	2.18 ± 0.28	1.20 ± 0.06	3.88 ± 0.52	$6.13^{+1.29}_{-1.38}$	$9.09^{+1.48}_{-1.49}$	$16.69^{+2.37}_{-2.37}$	9.1	$16.47^{+9.02}_{-8.16}$
Q1614+051	10	0.82 ± 0.18	1.23 ± 0.15	3.67 ± 0.83	$4.71^{+1.61}_{-1.85}$	$8.21^{+2.45}_{-2.54}$	$16.60^{+3.71}_{-3.79}$	5.9	$17.58^{+9.84}_{-8.79}$
Q1626+115	20	1.33 ± 0.14	1.26 ± 0.07	1.61 ± 0.18	$1.82^{+0.47}_{-0.48}$	$3.06^{+0.47}_{-0.48}$	$6.41^{+0.85}_{-0.86}$	12.4	$6.80^{+3.63}_{-3.33}$
Q1656+477	25	2.21 ± 0.20	1.27 ± 0.06	2.86 ± 0.27	$3.93^{+0.71}_{-0.78}$	$6.16^{+0.85}_{-0.86}$	$10.91^{+1.43}_{-1.44}$	17.7	$13.35^{+6.78}_{-6.42}$
Q1726+344	0	1.21 ± 0.09	≥ 1.34	2.97 ± 0.24	–	–	–	–	$13.48^{+6.83}_{-6.47}$
Q2212−299	NS	–	–	–	–	–	–	–	$58.87^{+27.38}_{-27.38}$
Q2223+210	15	3.32 ± 0.52	1.17 ± 0.05	5.14 ± 0.84	$6.54^{+1.30}_{-1.31}$	$11.72^{+1.97}_{-1.97}$	$27.55^{+3.43}_{-3.42}$	7.5	$22.44^{+12.52}_{-11.19}$
Q2251+244	10	3.13 ± 0.39	1.26 ± 0.08	5.61 ± 0.73	$4.83^{+0.99}_{-1.06}$	$9.18^{+1.62}_{-1.69}$	$26.26^{+3.11}_{-3.13}$	4.7	$22.38^{+12.52}_{-11.18}$
Q2334+019	15	1.42 ± 0.14	≥ 1.27	2.23 ± 0.27	–	–	–	–	$9.61^{+5.15}_{-4.72}$
Q2341+010	15	1.57 ± 0.18	≥ 1.84	1.78 ± 0.29	–	–	–	–	$7.80^{+4.33}_{-3.89}$
Q2350−007	NB	–	–	–	–	–	–	–	$7.25^{+4.21}_{-3.68}$
Q2359+002	ND	–	–	–	–	–	–	–	–

Notes. (1) Object name. (2) Estimate of the necessary emission-line correction (Section 6.6.3), as a percentage of the original model flux. We are unable to make this estimate for quasars without SDSS photometry (denoted with NS), for BOSS spectra without a flux calibration correction (see the Appendix) (NB) and for objects not detected with UVOT (ND). (3) The flux density at 2500 Å, with preliminary emission-line correction, in units of 10^{-27} erg s^{-1} cm^{-2} Hz^{-1}. (4) The corrected X-ray to UV–optical spectral index α_{ox}. (5) The corrected integrated luminosity over the rest-frame interval 1000–3000 Å. Units of 10^{46} erg s^{-1}. (6,7) Guideline estimates of the EUV luminosity (Section 6.6), with preliminary emission-line correction. We interpolate over the rest-frame intervals 1000 Å to 1 keV and 1000 Å to 0.3 keV. Units of 10^{46} erg s^{-1}. (8) Guideline estimate of the integrated luminosity over the rest-frame interval 3000 Å– 25 keV, with preliminary emission-line correction. Units of 10^{46} erg s^{-1}. (9) Reduction in L_{tot} (3000 Å–25 keV) due to the UV emission-line correction, listed as a percentage change in the uncorrected value. (10) The estimated bolometric luminosity (1 μm–10 keV), using the bolometric correction from rest-frame 1450 Å as presented by Runnoe et al. (2012). Units of 10^{46} erg s^{-1}.
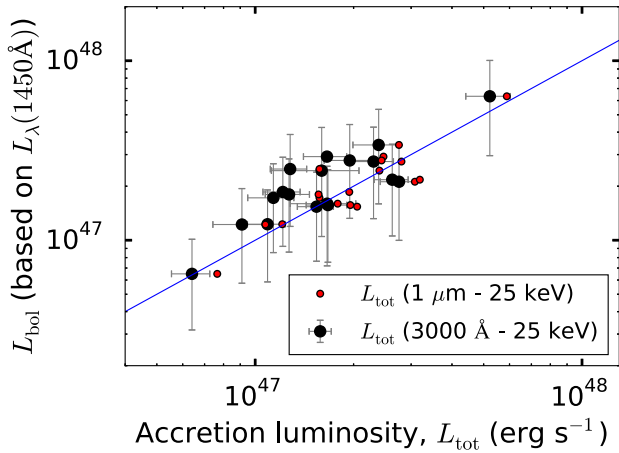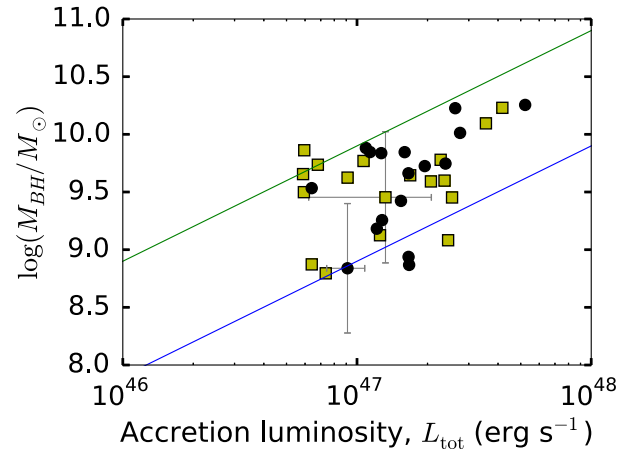
Figure 13. Bolometric luminosity estimates based on $L_\lambda(1450\,\text{Å})$, using the average bolometric correction determined by Runnoe et al. (2012), as a function of the accretion luminosity L_{tot} (3000 Å–25 keV) (black points), as determined using our *Swift* observations, for X-ray-detected quasars in our sample. The blue line illustrates $L_{\text{tot}} = L_{\text{bol}}$. Extrapolating the UV power-law continuum to 1 μm and calculating L_{tot} (1 μm–25 keV) provides a better agreement with L_{bol} (red points).
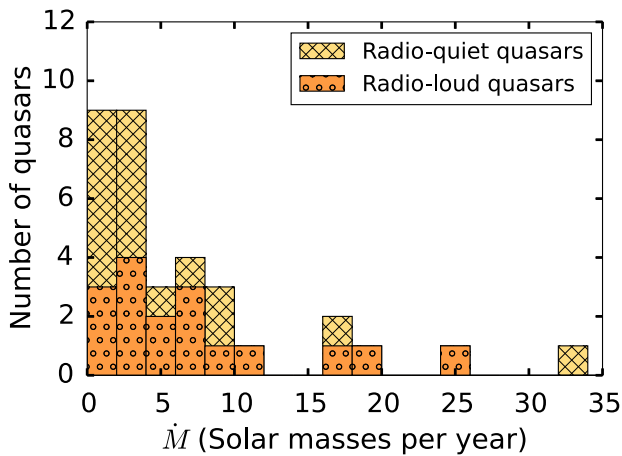
Figure 14. The distribution of $\dot{M}$ for our sample, as estimated using equation (4). The correction for emission-line contamination of L_{opt} (Section 6.7) is not included here. Stacked histogram (as defined in Fig. 1).

We find no significant difference between the distributions of $\dot{M}$ for RLQs ($\langle\dot{M}_{\text{RLQ}}\rangle = (7.3 \pm 1.7)\,\text{M}_\odot\,\text{yr}^{-1}$) and RQQs ($\langle\dot{M}_{\text{RQQ}}\rangle = (5.9 \pm 1.9)\,\text{M}_\odot\,\text{yr}^{-1}$). The distribution is asymmetric, with more than half the sample having $\dot{M} \leq 6\,\text{M}_\odot\,\text{yr}^{-1}$ (Fig. 14); the median $\dot{M}$ is just 3.3 $\text{M}_\odot\,\text{yr}^{-1}$. We note that equation (4) is derived assuming a purely thermal accretion disc spectrum without emission lines. Existing analyses of high-redshift quasar spectroscopy that include decomposition into continuum and emission-line components (Dietrich et al. 2003; Selsing et al. 2016) indicate that the typical emission-line contribution to $L_\nu(\text{opt})$ is of the order of 10–20 per cent, primarily due to the Balmer continuum and Fe II emission; our preliminary analysis of the overestimation of the power-law continuum level indicates a similar emission-line contribution (Section 6.6.3). We calculate alternative estimates of $\dot{M}$ assuming a 20 per cent emission-line contribution to the measured L_{opt}, which decreases the average mass accretion rate to $\langle\dot{M}\rangle = (4.8 \pm 0.9)\,\text{M}_\odot\,\text{yr}^{-1}$. For comparison, Davis & Laor (2011) find $\langle\dot{M}\rangle = 2.4\,\text{M}_\odot\,\text{yr}^{-1}$ for $z \lesssim 2$ Palomar Green quasars

with $M_{\text{BH}} > 10^9\,\text{M}_\odot$, similar to the quasars studied here, while Capellupo et al. (2015) find $\langle\dot{M}\rangle = 5.1\,\text{M}_\odot\,\text{yr}^{-1}$ for quasars with $M_{\text{BH}} > 10^9\,\text{M}_\odot$ in their SDSS-selected $1.45 \leq z \leq 1.65$ sample. In summary, our sample quasars have similar mass accretion rates to previous studies of quasars with comparable M_{BH} values; we note that all of these studies base their estimates on variants of equation (4), and therefore share any systematic uncertainties inherent to the thin-disc approximation.

6.8 Eddington luminosity ratios

For spherically symmetric accretion of ionized hydrogen, the Eddington luminosity, given by $L_{\text{Edd}} = 4\pi G m_{\text{p}} M_{\text{BH}} c \sigma_T^{-1}$, is the limiting luminosity for which radiation pressure balances gravitational attraction;[13] here, m_{p} is the proton mass, σ_T is the cross-section for Thomson scattering, G is the gravitational constant and c is the speed of light. The Eddington luminosity ratio, $\lambda = L_{\text{tot}}/L_{\text{Edd}}$, is thus a measure of how close to the theoretical limiting luminosity a given supermassive black hole is accreting. We use our estimates of L_{tot} (1 μm–25 keV) (Section 6.6) and of M_{BH} (Section 6.7) to calculate λ for X-ray-detected quasars with SDSS photometry (21 objects in total), and find an average $\langle\lambda\rangle = 0.52 \pm 0.10$, with a full range $0.11 \leq \lambda \leq 1.75$. All objects are consistent with sub-Eddington accretion to within the 1σ uncertainties on λ (as indicated by the blue line in Fig. 15). For the X-ray non-detected quasars, we instead calculate the Eddington ratio using the estimated bolometric luminosity, L_{bol} (Section 6.6.4). For these quasars, we find $\langle\lambda\rangle = 0.45 \pm 0.09$, consistent with the average value for X-ray-detected quasars. As our X-ray non-detections are mostly RQQs, we thus find that RQQs and RLQs in our sample are accreting at similar Eddington fractions.

---

[13] The equivalent limit for a thin-disc geometry may in some cases be larger than L_{Edd} by up to a factor ∼5 (Abolmasov & Chashkina 2015). As we do not perform detailed modelling of the accretion discs here, we assume spherical symmetry, as is standard practice when calculating L_{Edd} for large samples of AGN (e.g. Trakhtenbrot & Netzer 2012).

Figure 15. Accretion luminosities, L_{tot} (3000 Å–25 keV) versus black hole masses for our sample. Black points are X-ray-detected quasars, while yellow squares show X-ray non-detections, for which we use bolometric corrections to estimate L_{tot} (Section 6.6.4). The green and blue lines trace Eddington luminosity ratios of $\lambda = 0.1$ and $\lambda = 1$, respectively. For clarity, we only show representative error bars on one X-ray-detected object and one non-detection.

7 DISCUSSION AND SUMMARY

We present the first results of an ongoing observing campaign of redshift ~ 2 quasars with *Swift*. The full sample of quasars will span a large range of redshifts, radio loudnesses, and, for the RLQs, accretion disc orientation angles. All X-ray-detected objects presented here are radio loud. We estimate the accretion luminosity for each X-ray-detected quasar (Section 6.6), finding an average value of $L_{\rm tot}(3000\,\text{Å}-25\,\text{keV}) = 1.8 \times 10^{47}$ erg s^{-1}, similar to the brightest quasars studied by Wu et al. (2012); our RLQs appear to be accreting close to the Eddington limit (Section 6.7). Our UV–optical spectral indices, based on broad-band photometry, are somewhat flatter (redder) than those typically seen for spectroscopically studied SDSS quasars. This is due to emission-line contamination in the photometric bandpasses (Section 6.4), which we will address in detail in future work. We find an average UV–optical to X-ray spectral index $\langle \alpha_{\rm ox} \rangle = 1.39 \pm 0.03$ for the X-ray-detected sources, consistent with that found for RLQs in the literature (Section 6.5). While we do not detect any RQQs in the X-ray in the current sample, the lower limits derived for $\alpha_{\rm ox}$ are consistent with previous studies of RQQs of comparable luminosities. In summary, we find that the quasars in this preliminary sample display broad-band SED shapes typical of quasars at $z \approx 2$.

We do, however, find the RLQs in our sample to have unusually hard X-ray spectra on average, compared to similar quasar samples in the literature (Section 6.3). This is likely due to an overrepresentation of flat-spectrum radio sources (FSS) in the current sample. According to the Padovani & Urry (1992) study discussed in Section 6.7, RLQ are seen as blazars for $\phi < 5°$, as FSS for $5° < \phi < 15°$, and as steep-spectrum sources for $15° < \phi < 40°$. Thus, in a sample of bright, non-blazar-like RLQ with otherwise randomly drawn inclination angles, we would expect only around 13 per cent of the quasars to be FSS. In fact, based on the radio observations listed in Table 1, at least 52 per cent of our X-ray-detected objects are FSS; we lack multiband radio data for two objects. We find $\langle \Gamma \rangle = 1.37 \pm 0.06$ for the FSS, compared to $\langle \Gamma \rangle = 1.60 \pm 0.10$ for the remainder of the sample, although the sample size is currently too small to conclusively show a bimodality in Γ. Similarly, Worrall (1989) find that FSS sources display smaller Γ than do other $z > 0.8$ RLQs. It is well known that RLQs as a class show harder X-ray SEDs than do RQQs at comparable luminosities (e.g. Williams et al. 1992; Page et al. 2005; Scott et al. 2011). This suggests that the X-ray emission due to the radio jet has a harder SED than that of the corona. This is consistent with the jet component possibly being more dominant for FSS relative to other RLQs, due to geometric effects, e.g. relativistic beaming of the jet X-ray emission for these small-angle sources.

Our sample is well suited to the study of the radiative efficiency of quasar accretion due to the simultaneous nature of the *Swift* X-ray and UV observations, the relatively low level of dust obscuration, and to the availability of radio data for RLQs, which allows estimation of the accretion disc inclination angle. We will present a more detailed analysis of these quasars, including an analysis of their radiative efficiencies, in the context of a larger sample of quasars including X-ray-detected RQQs, upon completion of our *Swift* observing programme.
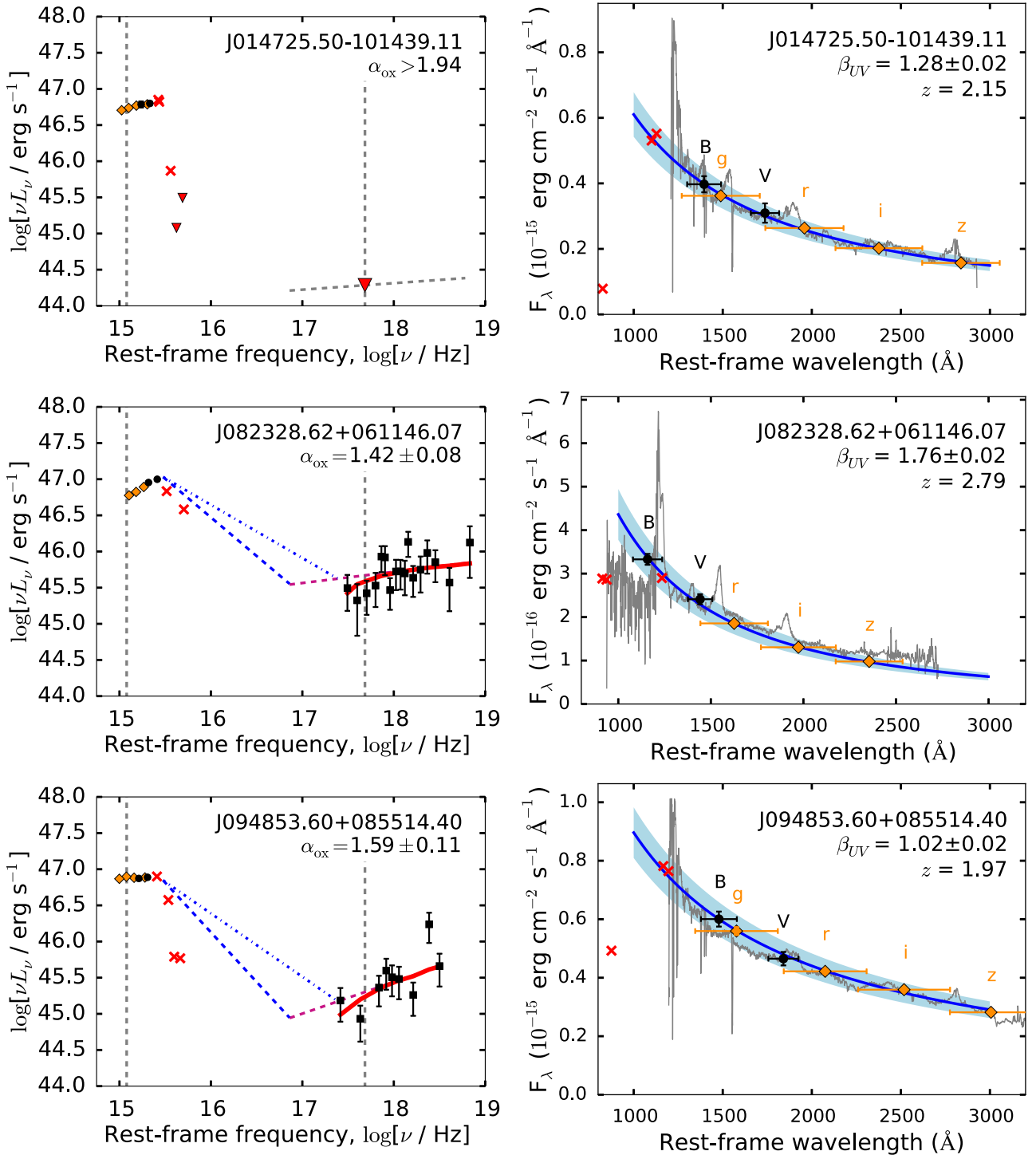
ACKNOWLEDGEMENTS

REFERENCES

Abolmasov P., Chashkina A., 2015, MNRAS, 454, 3432
Alam S. et al., 2015, ApJS, 219, 12
Arnaud K. A., 1996, in Jacoby G. H., Barnes J., eds, ASP Conf. Ser. Vol. 101, Astronomical Data Analysis Software and Systems V. Astron. Soc. Pac., San Francisco, p. 17
Atlee D. W., Mathur S., 2009, ApJ, 703, 1597
Barger A. J., Cowie L. L., 2010, ApJ, 718, 1235
Barthel P. D., 1989, ApJ, 336, 606
Barthel P. D., Miley G. K., Schilizzi R. T., Lonsdale C. J., 1988, A&AS, 73, 515
Barthel P. D., Tytler D. R., Thomson B., 1990, A&AS, 82, 339
Barvainis R., 1987, ApJ, 320, 537
Becker R. H., White R. L., Helfand D. J., 1995, ApJ, 450, 559
Bian W.-H., Zhang L., Green R., Hu C., 2012, ApJ, 759, 88
Breeveld A. A. et al., 2010, MNRAS, 406, 1687
Brenneman L. W. et al., 2014, ApJ, 788, 61
Burrows D. N. et al., 2005, Space Sci. Rev., 120, 165
Capellupo D. M., Netzer H., Lira P., Trakhtenbrot B., Mejía-Restrepo J., 2015, MNRAS, 446, 3427
Capellupo D. M., Netzer H., Lira P., Trakhtenbrot B., Mejía-Restrepo J., 2016, MNRAS, 460, 212
Carballo R., González-Serrano J. I., Benn C. R., Sánchez S. F., Vigotti M., 1999, MNRAS, 306, 137
Cash W., 1979, ApJ, 228, 939
Czerny B., Elvis M., 1987, ApJ, 321, 305
Davis S. W., Laor A., 2011, ApJ, 728, 98
Dawson K. S. et al., 2013, AJ, 145, 10
Dietrich M., Hamann F., Appenzeller I., Vestergaard M., 2003, ApJ, 596, 817
Done C., Davis S. W., Jin C., Blaes O., Ward M., 2012, MNRAS, 420, 1848
Dunlop J. S., McLure R. J., Kukula M. J., Baum S. A., O'Dea C. P., Hughes D. H., 2003, MNRAS, 340, 1095
Eisenstein D. J. et al., 2011, AJ, 142, 72
Elvis M. et al., 1994, ApJS, 95, 1
Elvis M. et al., 2012, ApJ, 759, 6
Emmanoulopoulos D., Papadakis I. E., Dovčiak M., McHardy I. M., 2014, MNRAS, 439, 3931

Fabian A. C., Lohfink A., Kara E., Parker M. L., Vasudevan R., Reynolds C. S., 2015, MNRAS, 451, 4375

Fanti C., Fanti R., Dallacasa D., Schilizzi R. T., Spencer R. E., Stanghellini C., 1995, A&A, 302, 317

Floyd D. J. E., Dunlop J. S., Kukula M. J., Brown M. J. I., McLure R. J., Baum S. A., O'Dea C. P., 2012, MNRAS, p. 340

Gehrels N. et al., 2004, ApJ, 611, 1005

Ghosh R., Dewangan G. C., Raychaudhuri B., 2016, MNRAS, 456, 554

Gibson R. R., Brandt W. N., 2012, ApJ, 746, 54

Greisen E. W., Calabretta M. R., 2002, A&A, 395, 1061

Grupe D., Komossa S., Leighly K. M., Page K. L., 2010, ApJS, 187, 64

Haardt F., Maraschi L., 1991, ApJ, 380, L51

Hewitt A., Burbidge G., 1993, ApJS, 87, 451

Hill J. E. et al., 2004, in Flanagan K. A., Siegmund O. H. W., eds, Proc. SPIEConf. Ser. Vol. 5165, X-Ray and Gamma-Ray Instrumentation for Astronomy XIII. SPIE, Bellingham, p. 217

Hughes D. H., Robson E. I., Dunlop J. S., Gear W. K., 1993, MNRAS, 263, 607

Jansen F. et al., 2001, A&A, 365, L1

Jarvis M. J., McLure R. J., 2006, MNRAS, 369, 182

Jin C., Ward M., Done C., 2012, MNRAS, 422, 3268

Kalberla P. M. W., Burton W. B., Hartmann D., Arnal E. M., Bajaja E., Morras R., Pöppel W. G. L., 2005, A&A, 440, 775

Kaspi S., Smith P. S., Maoz D., Netzer H., Jannuzi B. T., 1996, ApJ, 471, L75

Kaspi S., Brandt W. N., Maoz D., Netzer H., Schneider D. P., Shemmer O., 2007, ApJ, 659, 997

Kilerci-Eser E., 2014, PhD thesis, Available at: http://www.nbi.ku.dk/english/research/phd_theses/phd_theses_2014/ece_kilerci_eser/

Kinney A. L., Calzetti D., Bohlin R. C., McQuade K., Storchi-Bergmann T., Schmitt H. R., 1996, ApJ, 467, 38

Kishimoto M., Antonucci R., Blaes O., Lawrence A., Boisson C., Albrecht M., Leipski C., 2008, Nature, 454, 492

Korista K., Baldwin J., Ferland G., Verner D., 1997, ApJS, 108, 401

Kraft R. P., Burrows D. N., Nousek J. A., 1991, ApJ, 374, 344

Krolik J. H., Kallman T. R., 1988, ApJ, 324, 714

Laor A., Fiore F., Elvis M., Wilkes B. J., McDowell J. C., 1997, ApJ, 477, 93

Lusso E., Risaliti G., 2016, ApJ, 819, 154

Lynden-Bell D., 1978, Phys. Scr, 17, 185

Lynden-Bell D., Rees M. J., 1971, MNRAS, 152, 461

Margala D., Kirkby D., Dawson K., Bailey S., Blanton M., Schneider D. P., 2016, ApJ, 831, 157

Matt G. et al., 2015, MNRAS, 447, 3029

Miller B. P., Brandt W. N., Schneider D. P., Gibson R. R., Steffen A. T., Wu J., 2011, ApJ, 726, 20

Morrison R., McCammon D., 1983, ApJ, 270, 119

Murphy D. W., Browne I. W. A., Perley R. A., 1993, MNRAS, 264, 298

Nandra K., Pounds K. A., 1994, MNRAS, 268, 405

Onken C. A., Ferrarese L., Merritt D., Peterson B. M., Pogge R. W., Vestergaard M., Wandel A., 2004, ApJ, 615, 645

Orienti M., 2016, Astron. Nachr., 337, 9

Padovani P., Urry C. M., 1992, ApJ, 387, 449

Page K. L., Reeves J. N., O'Brien P. T., Turner M. J. L., 2005, MNRAS, 364, 195

Park T., Kashyap V. L., Siemiginowska A., van Dyk D. A., Zezas A., Heinke C., Wargelin B. J., 2006, ApJ, 652, 610

Piconcelli E., Jimenez-Bailón E., Guainazzi M., Schartel N., Rodríguez-Pascual P. M., Santos-Lleó M., 2005, A&A, 432, 15

Planck Collaboration XIII, 2016, A&A, 594, A13

Poole T. S. et al., 2008, MNRAS, 383, 627

Porquet D., Reeves J. N., O'Brien P., Brinkmann W., 2004, A&A, 422, 85

Pu X., Bian W., Huang K., 2006, MNRAS, 372, 246

Raimundo S. I., Fabian A. C., Vasudevan R. V., Gandhi P., Wu J., 2012, MNRAS, 419, 2529

Reeves J. N., Turner M. J. L., 2000, MNRAS, 316, 234

Richards G. T. et al., 2006, ApJS, 166, 470

Roming P. W. A. et al., 2005, Space Sci. Rev., 120, 95

Runnoe J. C., Brotherton M. S., Shang Z., 2012, MNRAS, 422, 478

Schlafly E., Finkbeiner D. P., 2011, ApJ, 737, 103

Schmidt K. B., Rix H.-W., Shields J. C., Knecht M., Hogg D. W., Maoz D., Bovy J., 2012, ApJ, 744, 147

Scott A. E., Stewart G. C., Mateos S., Alexander D. M., Hutton S., Ward M. J., 2011, MNRAS, 417, 992

Selsing J., Fynbo J. P. U., Christensen L., Krogager J.-K., 2016, A&A, 585, A87

Shakura N. I., Sunyaev R. A., 1973, A&A, 24, 337

Shang Z. et al., 2005, ApJ, 619, 41

Shull J. M., Stevans M., Danforth C. W., 2012, ApJ, 752, 162

Siemiginowska A., Kuhn O., Elvis M., Fiore F., McDowell J., Wilkes B. J., 1995, ApJ, 454, 77

Steffen A. T., Strateva I., Brandt W. N., Alexander D. M., Koekemoer A. M., Lehmer B. D., Schneider D. P., Vignali C., 2006, AJ, 131, 2826

Stevans M. L., Shull J. M., Danforth C. W., Tilton E. M., 2014, ApJ, 794, 75

Strateva I. V., Brandt W. N., Schneider D. P., Vanden Berk D. G., Vignali C., 2005, AJ, 130, 387

Tananbaum H. et al., 1979, ApJ, 234, L9

Tananbaum H., Wardle J. F. C., Zamorani G., Avni Y., 1983, ApJ, 268, 60

Trakhtenbrot B., Netzer H., 2012, MNRAS, 427, 3081

Urry C. M., Padovani P., 1995, PASP, 107, 803

Uttley P., Cackett E. M., Fabian A. C., Kara E., Wilkins D. R., 2014, A&AR, 22, 72

Vanden Berk D. E. et al., 2001, AJ, 122, 549

Vanden Berk D. E. et al., 2004, ApJ, 601, 692

Vestergaard M., 2000, PASP, 112, 1504

Vestergaard M., 2003, ApJ, 599, 116

Vestergaard M., Osmer P. S., 2009, ApJ, 699, 800

Vestergaard M., Peterson B. M., 2006, ApJ, 641, 689

Vestergaard M., Wilkes B. J., Barthel P. D., 2000, ApJ, 538, L103

Wilkes B. J., Tananbaum H., Worrall D. M., Avni Y., Oey M. S., Flanagan J., 1994, ApJS, 92, 53

Williams O. R. et al., 1992, ApJ, 389, 157

Wolfe A. M., Turnshek D. A., Lanzetta K. M., Lu L., 1993, ApJ, 404, 480

Worrall D. M., 1989, in Hunt J., Battrick B., eds, ESA SP-296: Two Topics in X-Ray Astronomy, Volume 1: X Ray Binaries. Volume 2: AGN and the X Ray Background. ESA, Noordwijk, p. 719

Worrall D. M., 2009, A&AR, 17, 1

Wu J. et al., 2012, ApJS, 201, 10

Wu J., Brandt W. N., Miller B. P., Garmire G. P., Schneider D. P., Vignali C., 2013, ApJ, 763, 109

Young S., Axon D. J., Robinson A., Capetti A., 2009, ApJ, 698, L121

Zamorani G. et al., 1981, ApJ, 245, 357

Zdziarski A. A., Johnson W. N., Magdziarz P., 1996, MNRAS, 283, 193

Zhang X.-G., 2013, MNRAS, 435, 2141

APPENDIX: SPECTRAL ENERGY DISTRIBUTION FIGURES FOR SAMPLE QUASARS

We present the optical to X-ray SEDs of the quasars in our sample, along with the UV photometry and continuum modelling, in Figs A1 through A15. Where available, we show the SDSS spectra used to guide our selection of UV data (Section 5.1) as grey curves in the right-hand panels. For quasars without SDSS spectroscopy, we show the high-redshift quasar template spectrum produced by Selsing et al. (2016), normalized to the continuum model flux level at 2500 Å. This template is constructed from spectroscopic observations of seven bright ($M_i \approx -29$ mag) quasars at $1 < z < 2$, i.e. objects that overlap our sample in terms of luminosity and redshift distribution, but that are somewhat brighter and reside at lower redshift than the average properties of our quasars. For such bright quasars the host galaxy contribution is expected to be small. Note that we do

Figure A1. Left: rest-frame UV to X-ray SEDs of quasars in our sample. Right: UV photometry and continuum modelling. See Fig. 5 for symbol and colour coding.

not use this template spectrum directly to model the UV continuum (Section 5.1), we merely use it as a rough guide to the amount of emission-line flux in a given UV bandpass for a typical bright quasar.

Spectra of $z \gtrsim 2$ quasars observed as part of the SDSS BOSS campaign suffer flux calibration uncertainties due to alterations in the instrumental setup (Dawson et al. 2013), the intent of which was to maximize throughput at short wavelengths. For the BOSS spectra,

we recalibrate the fluxes using the prescription presented by Margala et al. (2016), in order to better inform our continuum modelling. For quasars Q1402−012 and Q2350−007, Margala et al. (2016) do not provide a recalibration. In these cases, we find significant flux offsets between the SDSS photometry and spectroscopy (see Figs A2, A11 and A15). As we do not use the SDSS spectra directly in our SED modelling, we do not attempt additional corrective steps for these spectra.

Figure A2. Left: rest-frame UV to X-ray SEDs of quasars in our sample. Right: UV photometry and continuum modelling. See Fig. 5 for symbol and colour coding.

COMMENTS ON INDIVIDUAL OBJECTS

J014725.50−101439.11: we find a 3σ lower limit on α_{ox} of $\alpha_{ox} > 1.94$. Combined with the non-detections in the *Swift* far-UV filters, this may suggest strong absorption.

J104915.44−011038.18: this quasar is a non-detection in our *Swift* observations. We find a 3σ limiting apparent *V* magni-

tude of 18.5 mag. The catalogue of Hewitt & Burbidge (1993) lists $m_V = 17.9$ for this object; thus it has dimmed significantly over a period of approximately 30 observed-frame years.

J111159.70+023719.76: the UVOT *B* and *B* bandpasses suffer broad emission line (BEL) contamination. We therefore rescale the
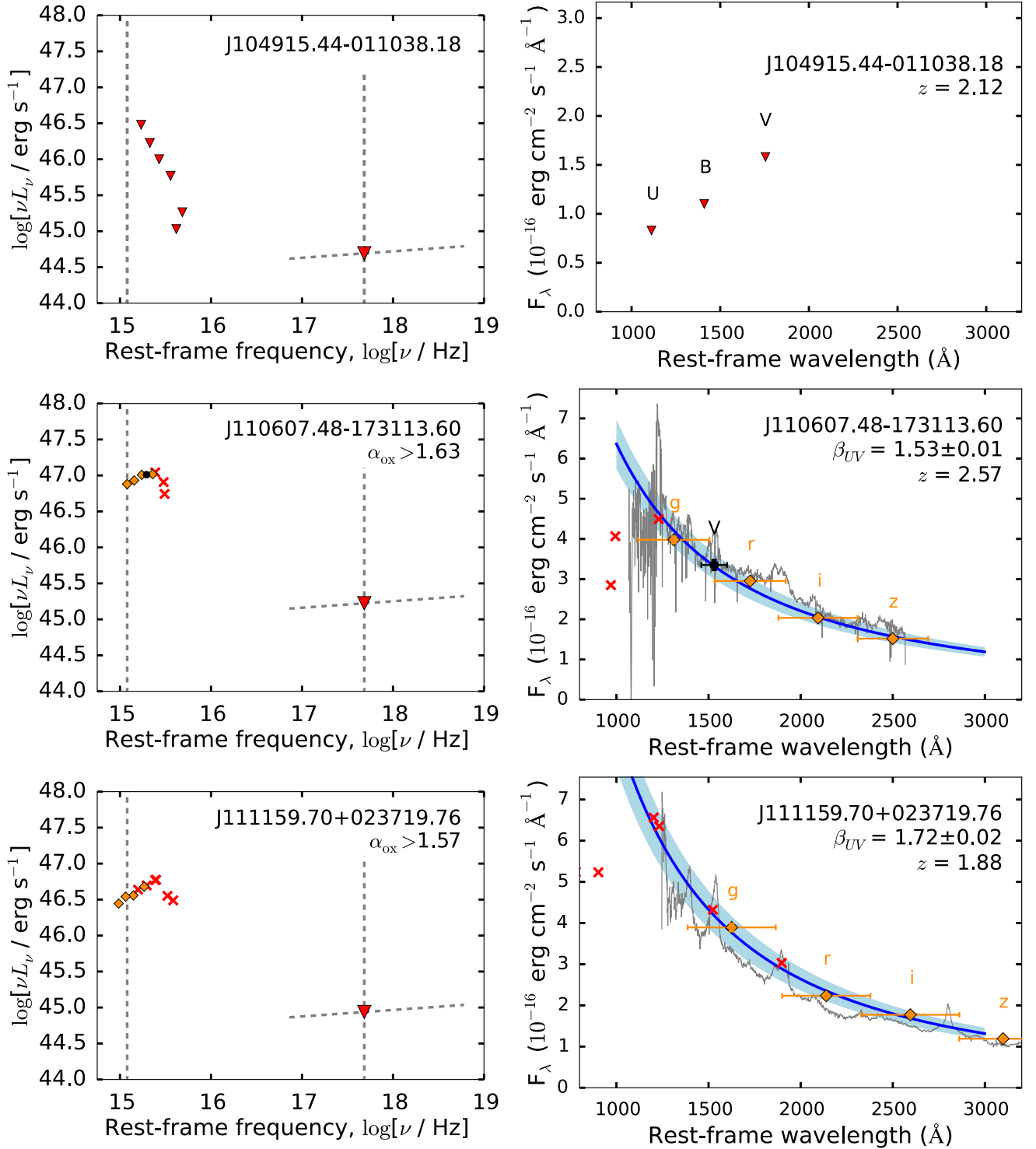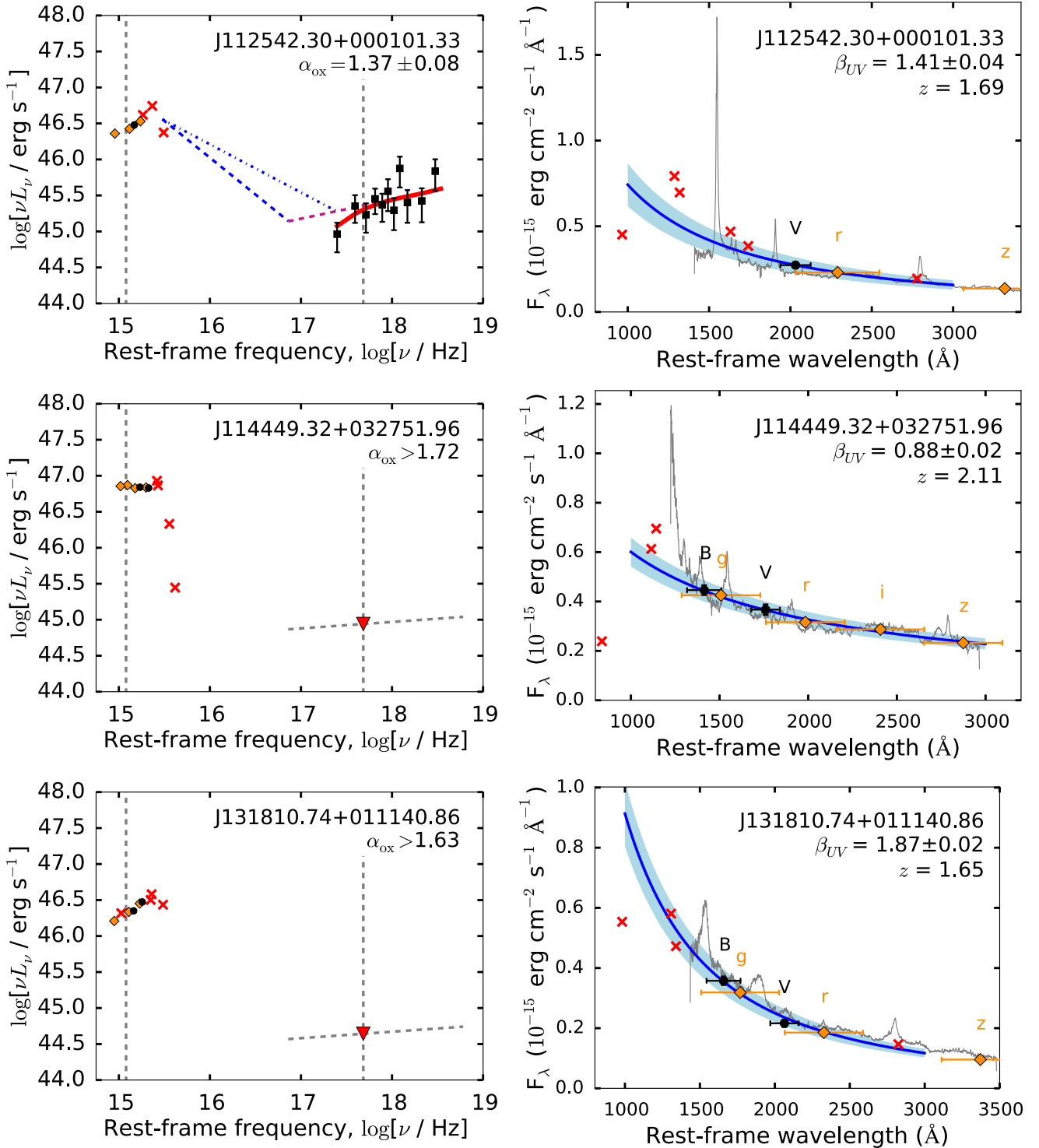
Figure A3. Left: rest-frame UV to X-ray SEDs of quasars in our sample. Right: UV photometry and continuum modelling. See Fig. 5 for symbol and colour coding.

SDSS fluxes based on the UVOT *U* flux, and discard all UVOT data from the final fit. Irrespective of flux rescaling, we find a flux offset between SDSS photometry and spectroscopy. Margala et al. (2016) do not provide a recalibration for this BOSS spectrum.
J145717.86+024747.36: the SDSS spectrum for this quasar shows a flat continuum. Our continuum model based on SDSS and *Swift* photometric data is somewhat steeper – this may be due

to the lack of continuum-dominated photometric data points towards the blue end of the spectrum. The BOSS flux calibration is known to be erroneous for high-redshift quasars (Dawson et al. 2013). While we apply the flux recalibration of Margala et al. (2016), they note that the calibration can be inaccurate for individual observations, especially at the blue end of the spectrum.
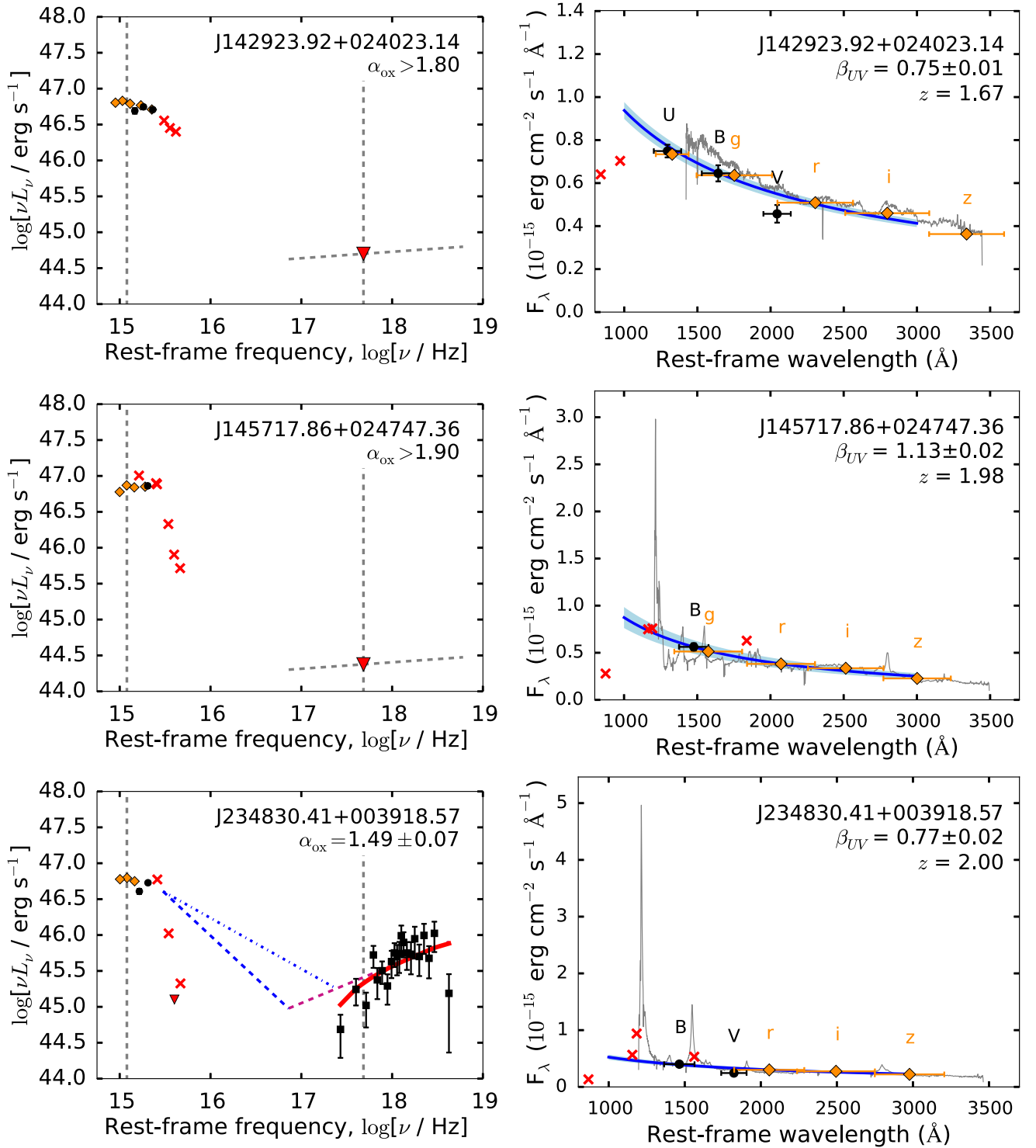
Figure A4. Optical to X-ray SEDs of quasars in our sample. See Fig. 5 for symbol and colour coding.

Q0015+026, Q0020+022, Q0252+016 and Q0504+030: the rescaling of the SDSS fluxes may be erroneously large due to the lack of continuum-dominated UVOT bandpasses.

Q0458−020: this quasar appears very red in our UVOT photometry. Wolfe et al. (1993) find a damped Lyman α absorber at $z = 2.04$ towards this quasar, along with at least three other intervening absorption systems. We therefore believe that the intrinsic UV continuum is likely to be significantly brighter and bluer than that

inferred from photometry, and regard the measured L_{UV} as a lower limit.

Q0504+030: all UVOT bandpasses likely suffer BEL contamination. We therefore regard all quantities derived from the UV-optical modelling as highly uncertain.

Q1402−012: for this object, all UVOT bandpasses suffer strong BEL contamination. The SDSS-III BOSS spectrum displays a significant offset from the SDSS photometry even after applying the
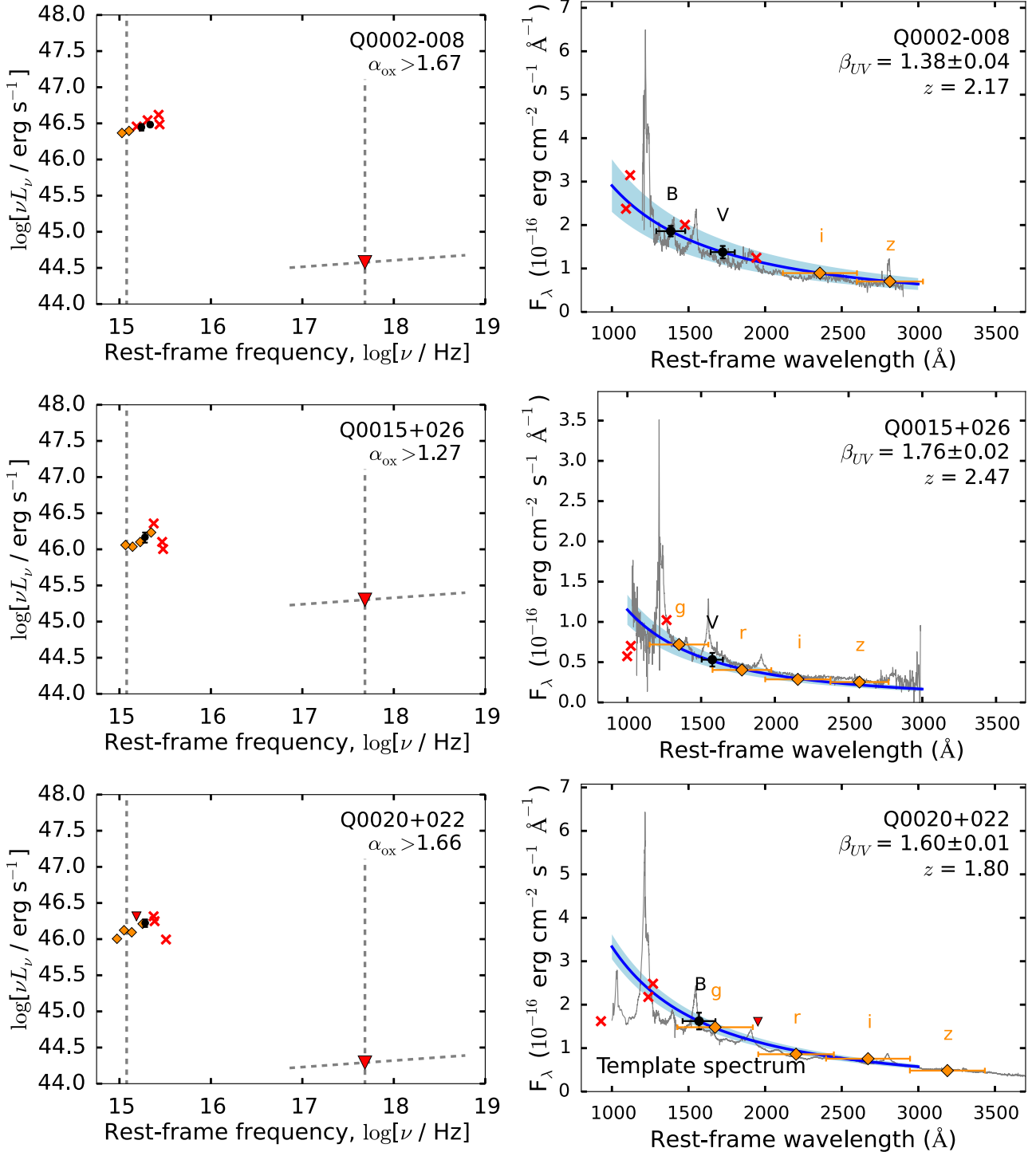
Figure A5. Left: rest-frame UV to X-ray SEDs of quasars in our sample. Right: UV photometry and continuum modelling. See Fig. 5 for symbol and colour coding.

flux recalibration of Margala et al. (2016); this may be due to flux variation between the photometric and spectroscopic SDSS observations, or perhaps the flux recalibration is not accurate for this object. *Q1442+101:* for this $z = 3.53$ quasar, all UVOT photometric bands suffer Lyman α forest absorption. We use the UVOT *V*-band flux to determine a scaling factor between the UVOT and SDSS observations, and model the UV–optical power-law continuum based on the rescaled SDSS *r*, *i* and *z* bands. We

regard the UV–optical continuum modelling for this object as highly uncertain.
Q1626+115: the SDSS-III BOSS spectrum for this object displays a significant offset from the SDSS photometry even after applying the flux recalibration of Margala et al. (2016); this may be due to flux variation between the photometric and spectroscopic SDSS observations, or perhaps the flux recalibration is not accurate for this object.

Figure A6. Left: rest-frame UV to X-ray SEDs of quasars in our sample. Right: UV photometry and continuum modelling. See Fig. 5 for symbol and colour coding.

Figure A7. Left: rest-frame UV to X-ray SEDs of quasars in our sample. Right: UV photometry and continuum modelling. See Fig. 5 for symbol and colour coding.
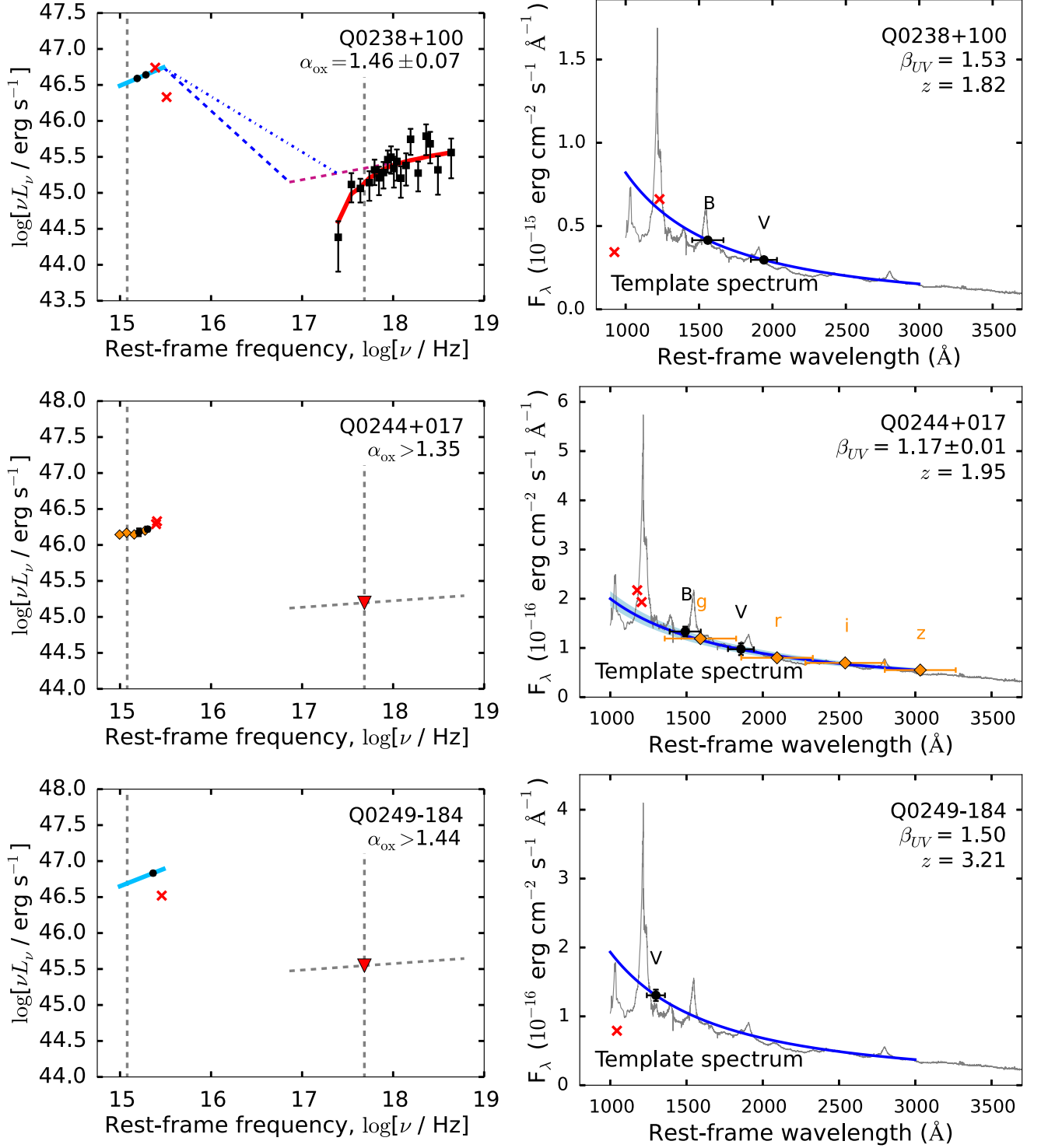
Figure A8. Left: rest-frame UV to X-ray SEDs of quasars in our sample. Right: UV photometry and continuum modelling. See Fig. 5 for symbol and colour coding.
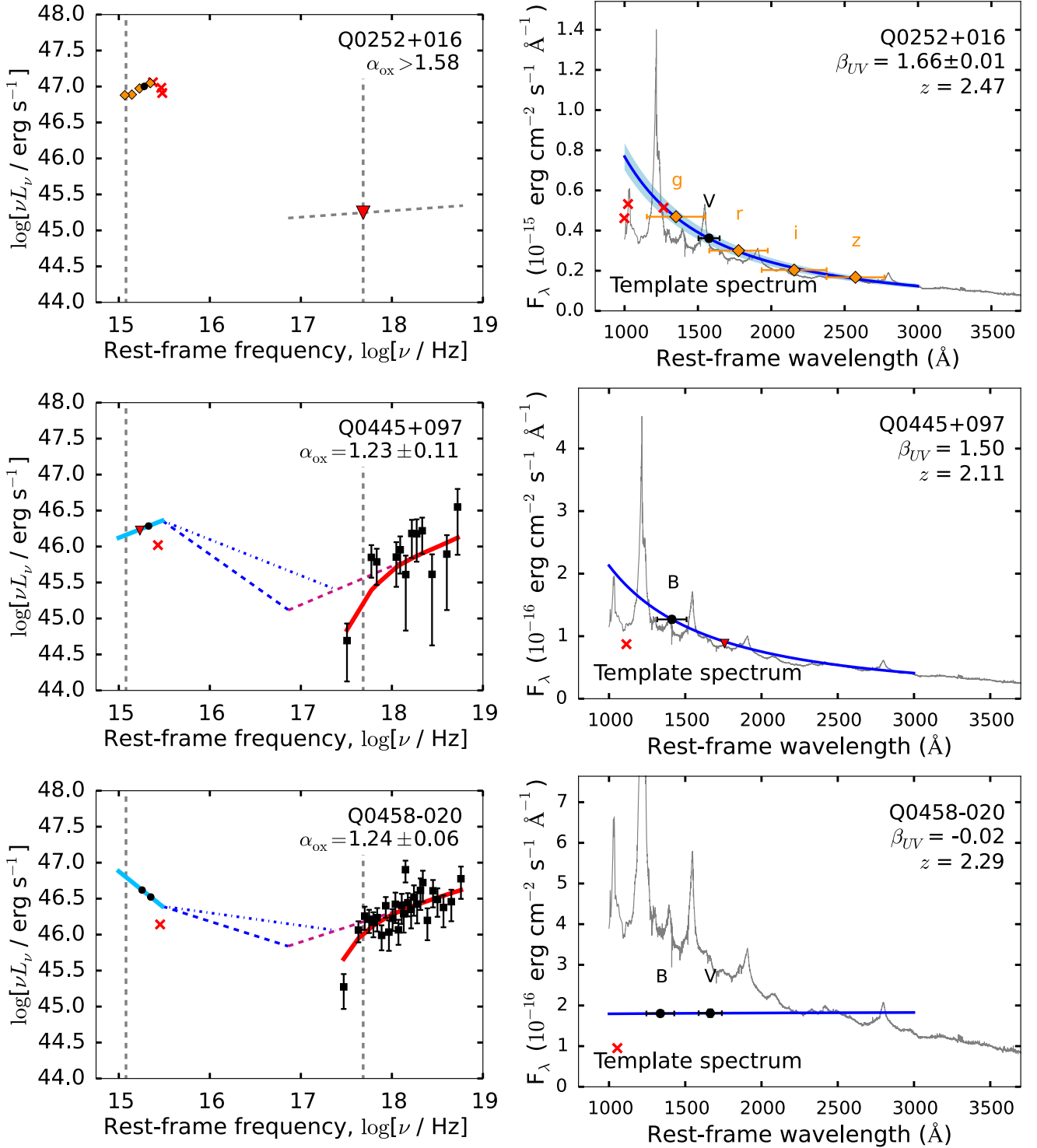
Figure A9. Left: rest-frame UV to X-ray SEDs of quasars in our sample. Right: UV photometry and continuum modelling. See Fig. 5 for symbol and colour coding.
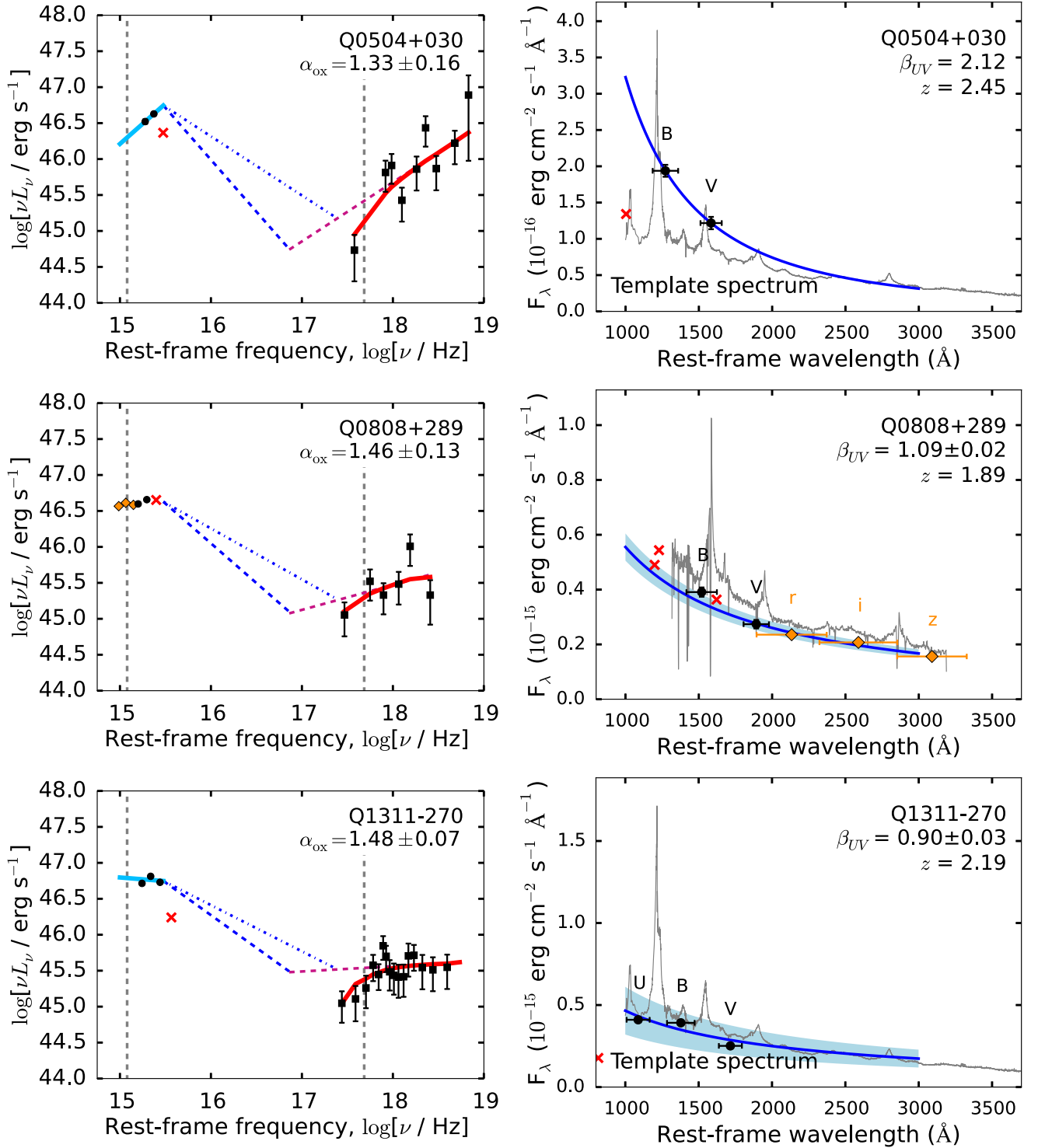
Figure A10. Left: rest-frame UV to X-ray SEDs of quasars in our sample. Right: UV photometry and continuum modelling. See Fig. 5 for symbol and colour coding.
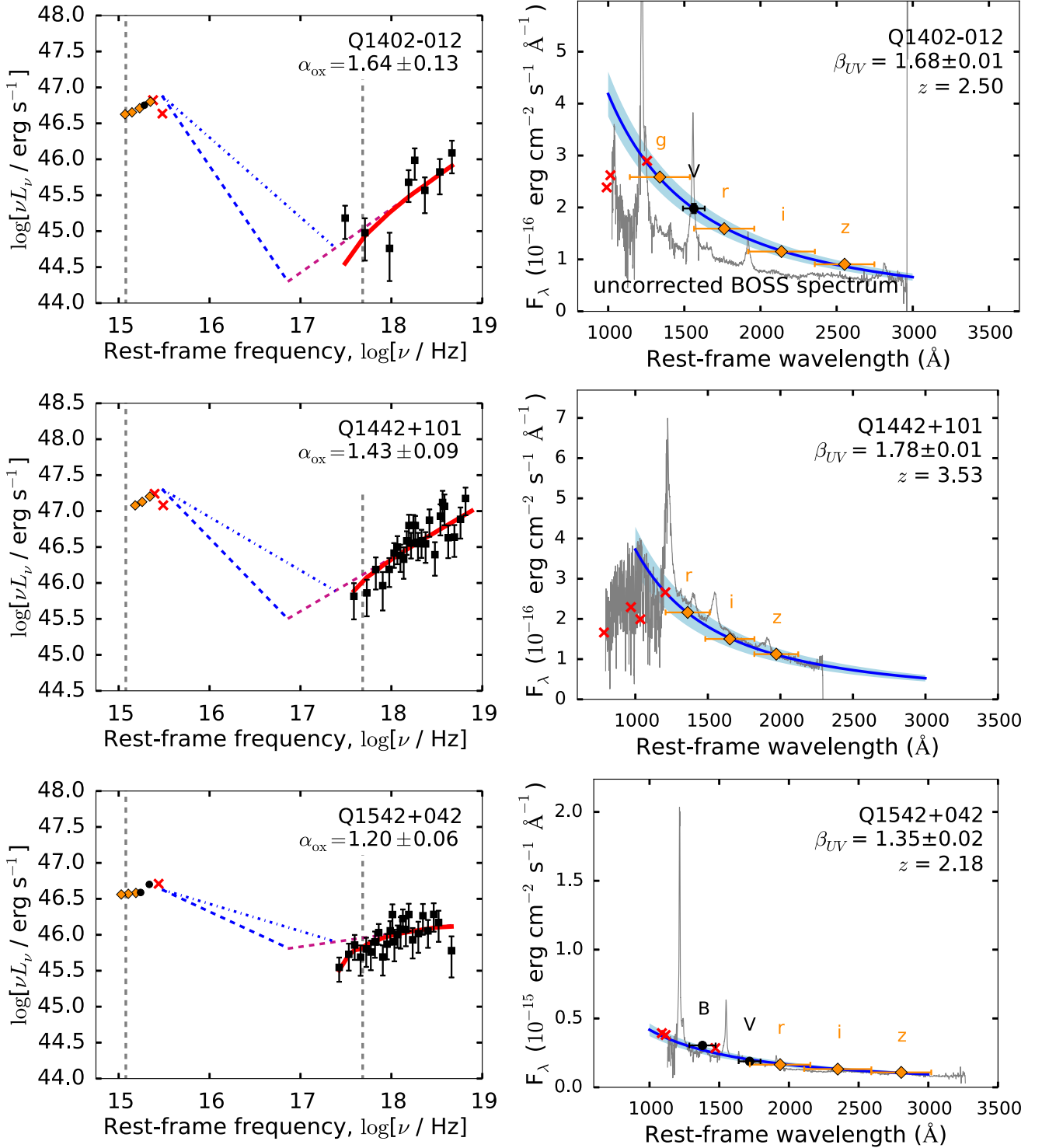
Figure A11. Left: rest-frame UV to X-ray SEDs of quasars in our sample. Right: UV photometry and continuum modelling. See Fig. 5 for symbol and colour coding.
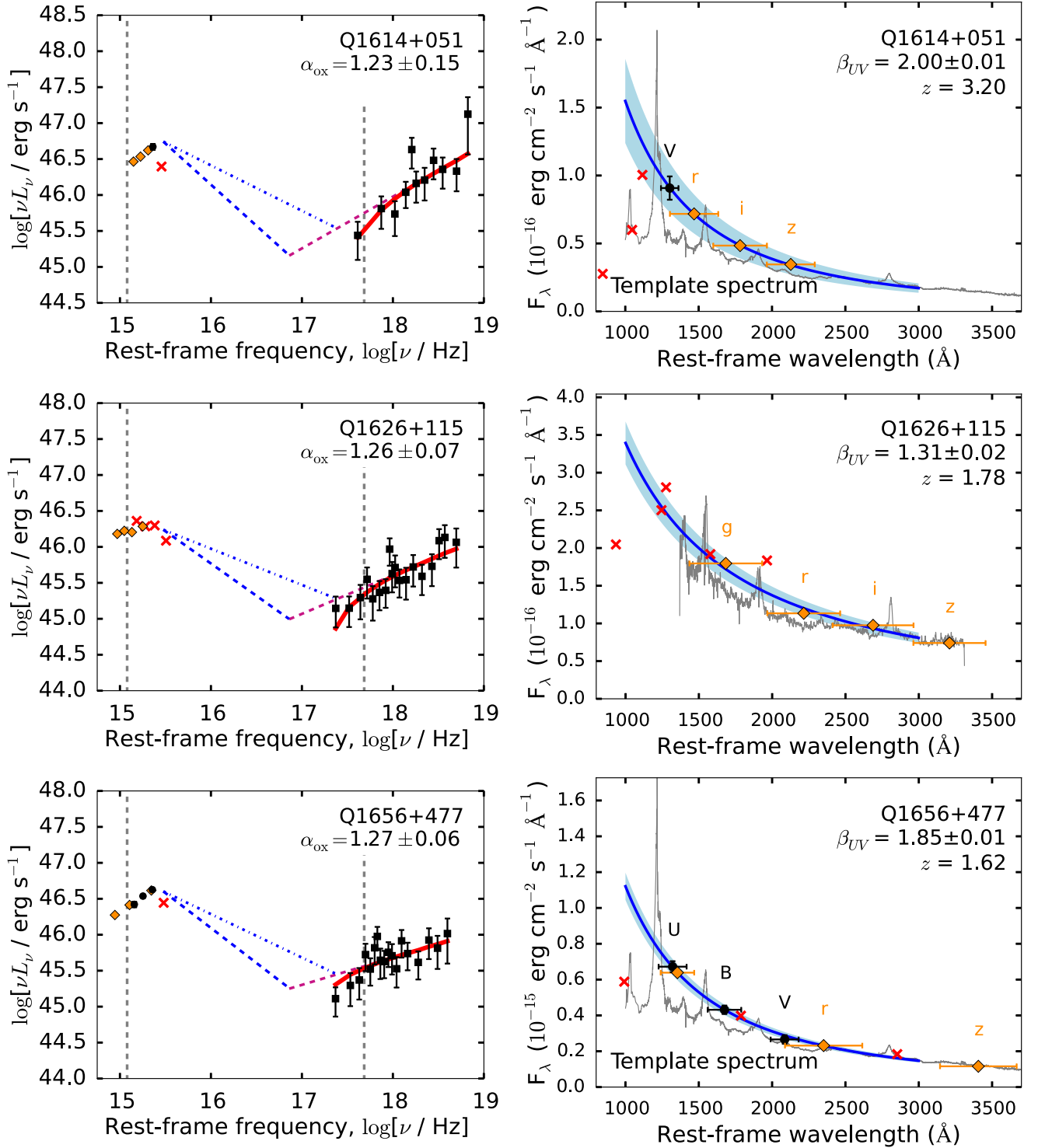
Figure A12. Left: rest-frame UV to X-ray SEDs of quasars in our sample. Right: UV photometry and continuum modelling. See Fig. 5 for symbol and colour coding.
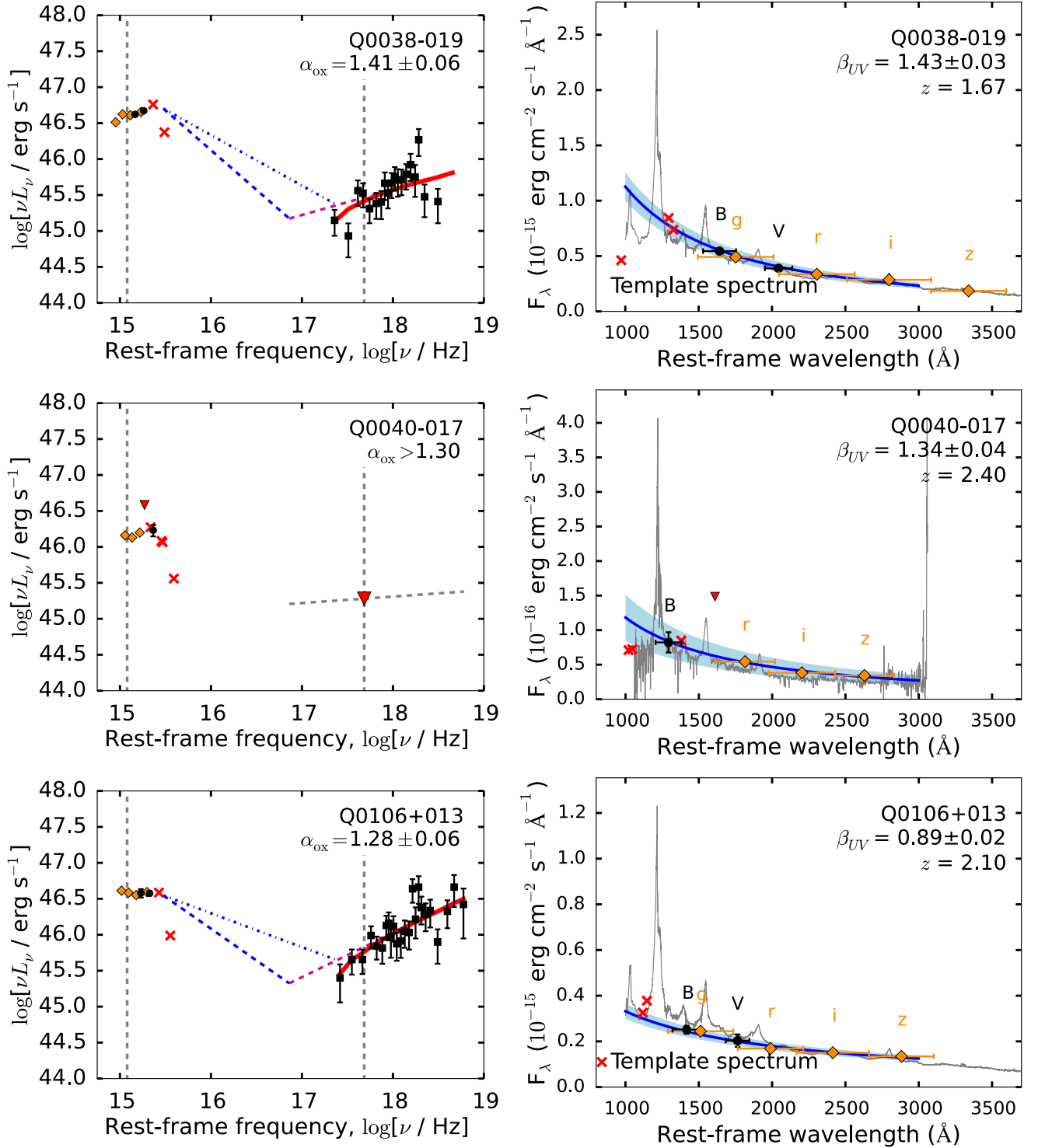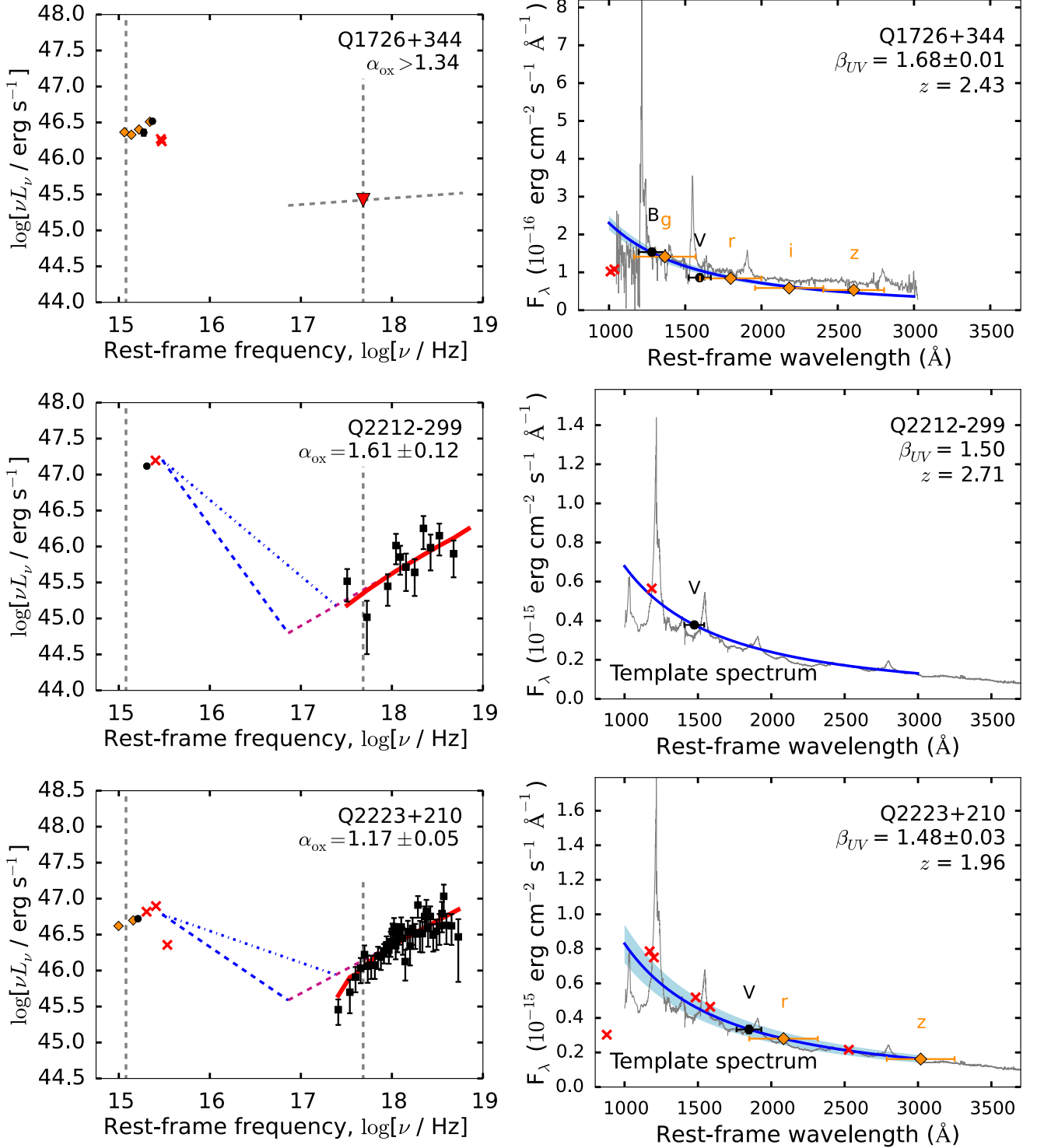
Figure A13. Left: rest-frame UV to X-ray SEDs of quasars in our sample. Right: UV photometry and continuum modelling. See Fig. 5 for symbol and colour coding.
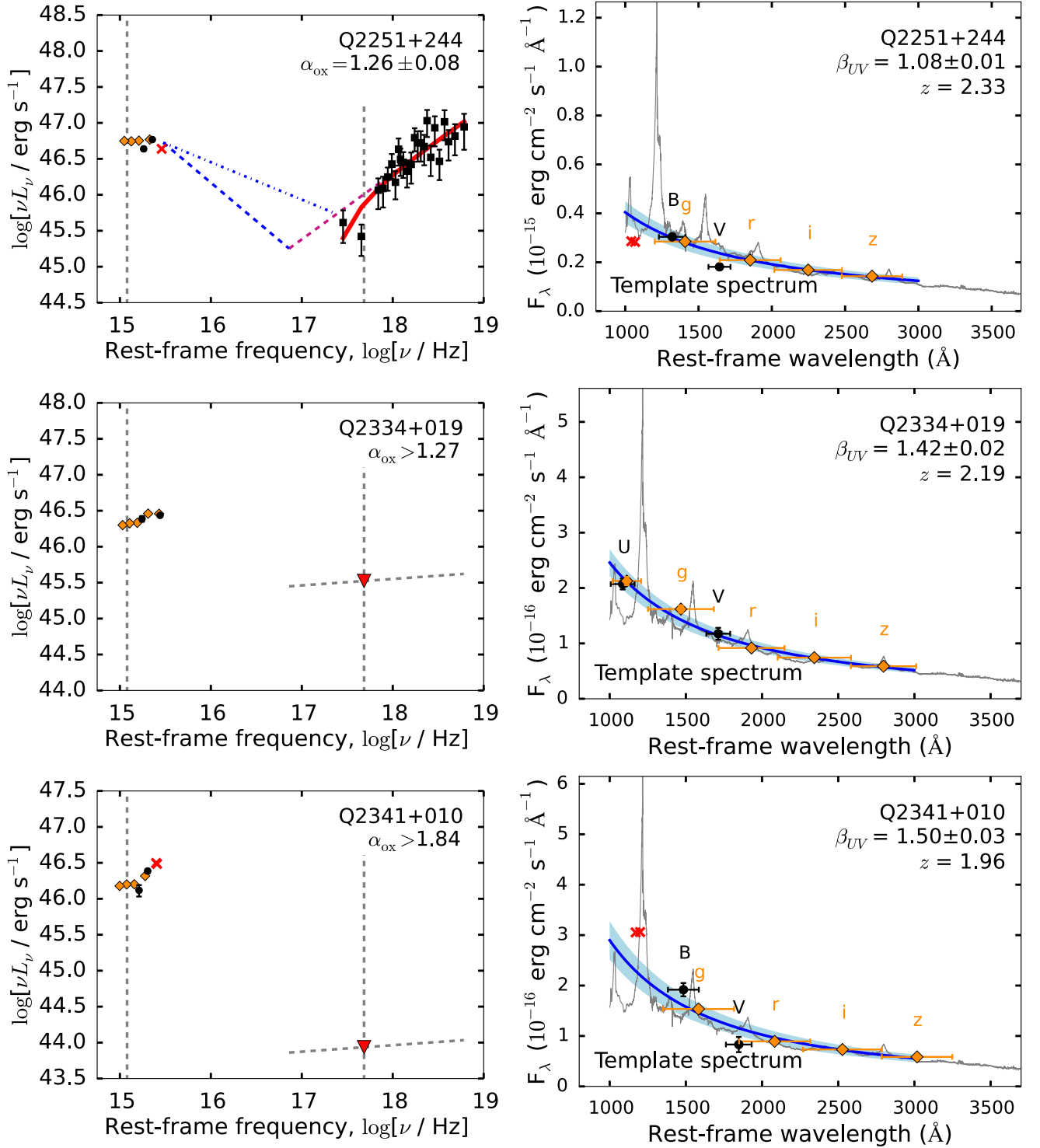
Figure A14. Left: rest-frame UV to X-ray SEDs of quasars in our sample. Right: UV photometry and continuum modelling. See Fig. 5 for symbol and colour coding.
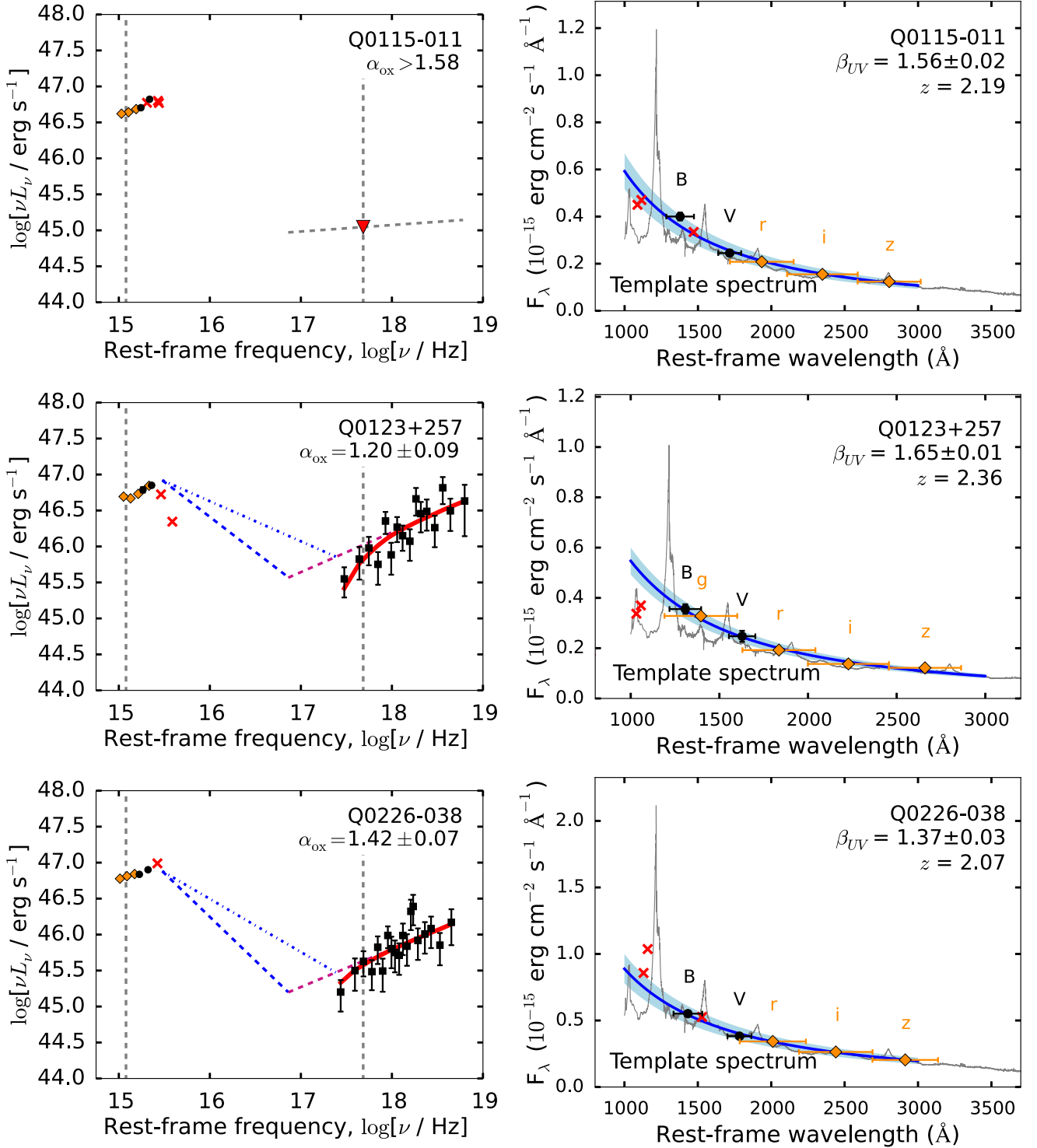
Figure A15. Left: rest-frame UV to X-ray SEDs of quasars in our sample. Right: UV photometry and continuum modelling. See Fig. 5 for symbol and colour coding.

This paper has been typeset from a TEX/LATEX file prepared by the author.

Chapter 6

Swift $z \sim 2$ Quasar Catalog. II: Full Sample

This chapter is comprised of a draft journal paper to be submitted, plus an exploratory accretion disk modeling study based on the data presented in that paper. The authors of the journal article draft are Daniel Lawther, Marianne Vestergaard, and Sandra Raimundo.
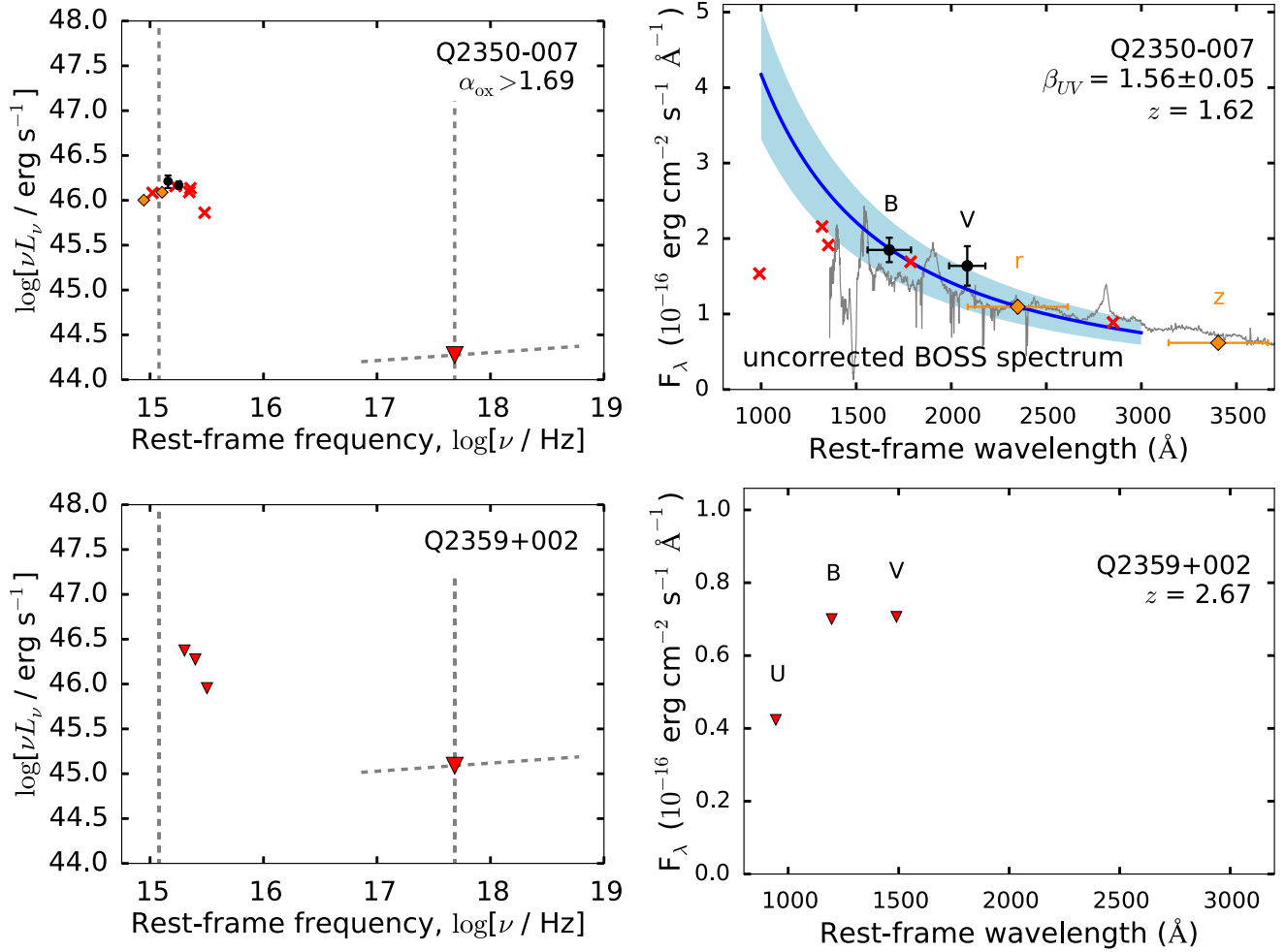
In this Chapter, I characterize the optical-UV–X-ray spectral energy distributions for a sample of 143 quasars at redshifts $1.5 < z < 3.6$, as observed by the *Swift* satellite. The simultaneous *Swift* XRT and UVOT observations provide a 'snapshot' measurement of the spectral energy distribution, in contrast to non-simultaneous SED observations, where quasar variability introduces additional uncertainty to, e.g., measurements of the UV to X-ray spectral shape (e.g., Kilerci Eser et al., 2015). Importantly, this sample contains pairs of radio-loud and radio-quiet quasars that are matched in terms of redshift and V-band apparent magnitude. It may therefore be well-suited to studies of the similarities and differences between radio-loud and radio-quiet sources. Additionally, we have archival UV spectroscopic observations of the broad emission lines for all quasars in this sample, confirming that they are not affected by broad absorption lines (§1.1.6), and enabling single-epoch spectroscopic black hole mass estimates (§1.4.2) for each source. The work presented here is part of a larger, on-going study of the spectral energy distributions and emission line properties for this quasar sample (PI: Vestergaard).

The main objective of my work in this Chapter is to determine to which degree these quasars are typical of the broader quasar population at that redshift range. Our sample was selected by Vestergaard (2000) prior to the release of the first release of the Sloane Digital Sky Survey (SDSS) quasar catalog (Schneider et al., 2002). Subsequent SDSS quasar catalogs have vastly increased the number of spectroscopically identified quasars; the most recent release includes over 500,000 quasars (Pâris et al., 2018; Rakshit et al., 2020). Our understanding of quasar demographics at $z \sim 2$ is thus much improved in the years since this sample was selected. In particular, the SDSS Quasar Catalogs identify many quasars at fainter i-band apparent magnitudes that were not previously known, while many of the sources with bright i-band apparent magnitudes had already been discovered prior to their SDSS identification (e.g., Schneider et al., 2002). Thus, the SDSS Quasar Catalogs extended our sample of spectroscopically identified quasars to lower apparent magnitudes, and correspondingly lower absolute magnitudes at a given redshift. For this reason, it is important to determine to which degree our sample is representative of the broader population of quasars, as revealed by modern wide-field quasar surveys. This characterization will provide context for our

on-going study of these sources, allowing us to harness the unique properties of the sample, i.e., that it contains redshift and apparent magnitude-matched radio-loud and radio-quiet sources, with spectroscopic measurements of the broad emission lines available for the entire sample.

My study of the $z \sim 2$ quasar sample is still at a 'work-in-progress' stage. In particular, my comparison of the UV luminosities of our quasar sample in the current draft is rather simplistic. While it is true that our sample quasars at $z \sim 3$ are much brighter than the typical SDSS $z \sim 3$ quasars, as stated in the current draft, this is also the case for a few individual sources at $z \sim 2$. To improve the usefulness of this sample for future work, it is important to know which *individual* quasars are particularly UV-bright relative to the broader population. Before submission of this work to a journal, I will perform a more comprehensive analysis of the UV luminosities of our sample quasars relative to the SDSS quasars, on a per-object basis. For each quasar, I will calculate which percentage of SDSS quasars at the corresponding redshift (within a narrow redshift bin) it is more UV-luminous than. This will then allow me to highlight individual quasars that are unusually UV-bright relative to the broader population.

The main questions addressed in this Chapter regard the characterization of the UV–optical–X-ray spectral energy distributions of our sample quasars, in the context of the broader $z \sim 2$ quasar population. Specifically, in the draft journal article, I address the following issues:

- Are the 143 quasars in our $z \sim 2$ sample representative of the broader $z \sim 2$ quasar population in terms of their UV and X-ray luminosities?

- Our sample contains redshift and *V*-band luminosity matched radio-loud and radio-quiet subsamples. To which degree are these subsamples representative of the broader populations of radio-loud and radio-quiet quasars, in terms of UV and X-ray luminosities and SED shapes?

- What are the similarities and differences between the spectral energy distributions of radio-loud and radio-quiet quasars at $z \sim 2$? In particular, given the already established difference in X-ray brightness at a given UV luminosity, are there also differences in the UV–optical SED shape? Different UV–optical SED shapes are predicted if radio-loud sources contain more rapidly spinning black holes (e.g., Blandford and Payne, 1982; Schulze et al., 2017).

- Are our *Swift* XRT observations sufficiently deep to provide useful measurements of the UV to X-ray SED shape diagnostic α_{ox}? In particular, given that radio-quiet quasars are more faint in the X-rays, do we achieve sufficiently tight constraints on α_{ox} for the radio-quiet subsample?

- Are our black hole mass estimates for this sample consistent with those for $z \sim 2$ quasars in the SDSS?

- Do our radio-loud and radio-quiet subsamples display significantly different distributions of black hole mass? In order to provide a useful comparison between the SEDs of radio-loud and radio-quiet sources, it is vital to ensure that their black hole masses are well-matched, as the SED shape depends on black hole mass according to thin-disk models (§1.2).

I am also interested in whether our *Swift* spectral energy distributions provide meaningful constraints on the black hole spin and mass accretion rates for our sample quasars. Using VLT

X-Shooter observations of 39 quasars at $z \sim 1.5$, Capellupo et al. (2015) demonstrate that their UV–optical–infrared continua can be modeled satisfactorily as Novikov and Thorne (1973) thin accretion disks. For their sample of quasars at $z \sim 1.5$, these *X-Shooter* observations cover rest-frame wavelengths from ~ 1200 Å to ~ 9000 Å, thus including the low-energy power-law 'tail' of the accretion disk emission and constraining the mass accretion rate (e.g., Davis and Laor, 2011; Raimundo et al., 2012). Our *Swift* UVOT and supplementary SDSS photometry cover a more narrow rest-frame wavelength range, from ~ 1000 Å to ~ 3000 Å. To determine whether we can place any constraints on the nature of the accretion disks using our *Swift* UVOT and supplementary SDSS photometry alone, I present an exploratory study of disk model fits to our UV spectral energy distributions in §6.3. In general, I find that we require additional far-UV and infrared data in order to constrain and test the thin-disk models for our quasar sample. As the results of this analysis are largely inconclusive, I do not include the disk modeling study in the draft journal article itself.

6.1   Statement of Authorship

All data processing and analysis was performed by Daniel Lawther. The initial experimental design is due to Marianne Vestergaard and Dirk Grupe. The V-band apparent magnitudes and radio classifications (Table 1) are provided by Marianne Vestergaard, who also defined the quasar sample. The manuscript is written by Daniel Lawther, who also produced the figures; all co-authors provided feedback during the writing process. Sandra Raimundo provided the code used to generate Novikov-Thorne disk models. I include a signed statement of authorship with this Thesis (Chapter 8).

6.2   Paper to be Submitted

Optical to X-ray spectral energy distributions of $z \approx 2$ quasars observed with *Swift*. II: Full catalog.

Lawther, D.,[1] Vestergaard, M.,[1][2] Raimundo, S.,[1]

[1] *Dark Cosmology Centre, Niels Bohr Institute, University of Copenhagen.*
[2] *Steward Observatory, University of Arizona, 933 N. Cherry Avenue, 85721 Tucson, AZ, USA.*

August 17, 2020

ABSTRACT

We present the *Swift* optical to X-ray Spectral Energy Distributions of 143 quasars at redshifts $z \sim 2$. Our main objective is to determine whether these quasars, comprising 76 radio-loud and 67 radio-quiet sources, are typical of the broader $z \sim 2$ population, for the purpose of follow-up studies of this quasar sample. We also quantify the similarities and differences in the observed SEDs for the radio-loud and radio-quiet subsamples. Due to our selection criteria, this sample is well suited for comparison studies of typical radio loud and radio quiet quasars at $z \sim 2$. We find that the majority of quasars in our sample have UV and X-ray luminosities corresponding to typical luminous quasars in the Sloan Digital Sky Survey. However, the higher-redshift $z \gtrsim 2.8$ quasars in our sample are atypically UV-luminous relative to the broader quasar population. An important result is that the two radio-class subsets of our sample are statistically indistinguishable in terms of observed UV-optical SED diagnostics and black hole masses. A total of 97 quasars are detected in X-rays, of which 70 are radio-loud. Our radio loud quasars have typical X-ray photon index $\Gamma \sim 1.6$, typical of bright $z \sim 2$ quasars; Γ for the radio quiets is not well constrained. The radio loud UV to X-ray SEDs are energetically harder ($\alpha_{\rm ox} \sim 1.4$) than those of our radio quiet quasars, for which the X-ray detected objects typically have $\alpha_{\rm ox} \sim 1.6$, and the undetected have even softer SEDs. The UV to X-ray SED shapes of the radio quiet sources are broadly consistent with the typical SED shapes of Sloan Digital Sky Survey quasars at $z \sim 2$. The radio-quiet sources are accreting at substantial fractions of the Eddington ratio, $L_{\rm acc}/L_{\rm Edd} \sim 0.23$, consistent with measurements for massive $z \sim 2$ quasars in the SDSS. The distribution of Eddington ratio for radio-loud sources is not significantly different from that of the radio-quiet subsample.

1 INTRODUCTION

The only known mechanism which can produce the high luminosities, energetically hard emission, and rapid coherent variability observed for quasars is mass accretion onto a central supermassive black hole (Lynden-Bell & Rees 1971; Lynden-Bell 1978). The detailed physics of the accretion flow are not well-understood. Quasars emit over the entire electromagnetic spectrum, and no single emission component can reproduce the observed radio to X-ray spectral energy distributions (SEDs). Their UV–optical emission is dominated by strong continuum emission (e.g., Malkan & Sargent 1982), approximated by a power-law flux distribution, $F_\lambda \propto \lambda^{-\beta}$, with $\beta \sim 1.5$–1.7 (e.g., Vanden Berk et al. 2001; Xie et al. 2015; Shankar et al. 2016). Far-UV observations reveal a flux turnover at ~ 1000 Å (e.g., Shang et al. 2005; Stevans et al. 2014). This 'big blue bump' is generally identified with thermal emission from an accretion disk. The extreme-UV (EUV) contribution from this disk then provides the ionizing continuum that excites gas at distances of $\sim$ light-days to produce the observed UV and optical broad emission lines, and on pc scales, to produce the narrow emission lines (e.g., Peterson et al. 2013). Standard, analytically tractable models require that the accretion disk is geometrically thin and optically thick (Shakura & Sunyaev 1973; Novikov & Thorne 1973).

It is currently unclear whether thin-disk models accurately capture the accretion physics of real quasars.

For black hole masses typical of luminous quasars, $M_{\rm BH} \gtrsim 10^8 M_\odot$, the standard thin-disk models do not produce strong X-ray emission. Additional emission components must therefore be posited to explain both the observed X-ray power-law continuum (e.g., Nandra & Pounds 1994), and the soft X-ray excess observed at rest-frame energies below ~ 2 keV (e.g., Arnaud et al. 1985; Porquet et al. 2004; Piconcelli et al. 2005; Crummy et al. 2006). We do not address the soft X-ray excess in this work, as it is not observationally accessible for quasars at $z \sim 2$. The hard X-ray continuum may be due to inverse-Compton scattering of UV or soft X-ray photons in a hot ($kT_e \sim 100$ keV) corona (Zdziarski et al. 1996; Ghosh et al. 2016). The detailed physical mechanisms at play are poorly understood. However, a substantial transfer of energy from the disk to the corona is required, given that inverse-Compton scattering of disk photons will efficiently cool the hot plasma in the hard X-ray corona. The relative emission strengths of the UV-optical and X-ray components, often parameterized as $\alpha_{\rm ox}$ (Tananbaum et al. 1979), is an important probe of the X-ray reprocessing mechanism. The $\alpha_{\rm ox}$ parameter is found to correlate with the UV luminosity, in the sense that more UV-luminous quasars reprocess a smaller fraction of their accretion energy into X-rays (Zamorani et al. 1981;

Vignali et al. 2003; Strateva et al. 2005; Wu et al. 2012). In fact, the underlying relationship between UV and X-ray luminosity is sufficiently tight and non-linear (for a carefully selected sample, Lusso & Risaliti 2016) that it may allow the use of AGN as standard candles for cosmological distance measurement (Risaliti & Lusso 2015).

Roughly 10% of quasars are radio-loud (e.g., Kellermann et al. 1989; Padovani 1993). A common definition of radio loudness is $R > 10$, where R is the ratio of flux densities at rest-frame 5 GHz and at 4400 Å. The observed radio-loud fraction depends on redshift and rest-frame UV luminosity (Jiang et al. 2007). The radio-loud quasars (hereafter, RLQs) are ubiquitously associated with large-scale radio jets. They also tend to be stronger X-ray emitters than radio-quiet quasars (RQQs; Zamorani et al. 1981), which may be due to emission from the radio jet (Miller et al. 2011). The radio jets may be launched due to magnetic stresses between an accretion disk and its magnetosphere (e.g., Blandford & Znajek 1977; Blandford & Payne 1982). It is unclear why only ~10% of quasars produce such a jet. Rapidly rotating black holes are likely required for jet production (Maraschi et al. 2012). Supporting this idea, Schulze et al. (2017) find indirect evidence for higher black hole spin in RLQs versus RQQs. They use the [OIII] narrow emission line luminosity as a proxy for the ionizing continuum luminosity, and find an enhancement in ionizing continuum luminosity for their RLQs relative to a sample of RQQs with comparable redshifts, black hole masses, and UV–optical luminosities. On the other hand, interpretations of observed quasar UV–optical SEDs in the context of Novikov-Thorne thin accretion disks do not necessarily support a spin dichotomy. In particular, these models require near-maximal black hole spin for quasars with black hole masses exceeding $\sim 10^9 M_\odot$ in order to reproduce the observed SEDs, irrespective of radio class (e.g., Netzer & Trakhtenbrot 2014; Capellupo et al. 2016). These high spin values are implied by the similarity of observed SED turnover energies for RLQs and RQQs (Shang et al. 2005; Stevans et al. 2014), while according to the thin-disk models, non-spinning massive black holes should display SED turnovers at lower energies than rapidly spinning black holes.

SED studies as probes of accretion physics: The SED atlas presented in the seminal work of Elvis et al. (1994) reveals significant (~ 1 dex) variations in the normalized flux distributions of 47 optically selected quasars at redshifts $0.01 < z < 3.3$. Subsequent SED studies confirm these shape differences, using larger samples and diverse selection techniques (e.g., Richards et al. 2006; Elvis et al. 2012). Some of the differences in observed SED shape are likely due to intrinsic reddening and/or variations in the host galaxy contribution to the SED between objects. However, the thin-disk paradigm also predicts SED shape differences depending on the accretion rate, black hole mass, and black hole spin. Thus, studies of the typical quasar SED and the distribution of SED shapes can potentially provide clues as to the underlying accretion physics. As outlined above, the SED turnover energy and its dependence on black hole mass and spin provides an important test of the thin-disk paradigm.

In this context, it is vital to determine the total energy output of the central engine, which must ultimately be powered by the mass accretion flow. While it is common to estimate the bolometric luminosities of individual objects based on a bolometric correction determined for pre-existing quasar samples (e.g., Runnoe et al. 2012), this approach involves considerable uncertainties. Indeed, Kilerci Eser & Vestergaard (2018) find variations in the bolometric luminosity of up to a factor 2 for repeated broad-band SED observations of individual objects, and this variation may be even larger for highly varying objects and/or longer time separations between observations. This will introduce scatter into the SED shape distribution if individual sources are observed non-simultaneously at different wavelengths, as is often the case due to observational constraints. Thus, simultaneous broad-band observations of a large sample of quasars are necessary in order to constrain the true diversity in their accretion properties. Equally, in order to investigate the physical mechanism underlying the observed dichotomy of radio emission properties, an SED atlas of a well-matched sample of RLQs and RQQs is required.

Outline of this work: This current work harnesses the unique capabilities of the *Swift* satellite (Roming et al. 2005) to obtain simultaneous UV–optical and X-ray observations of 144 quasars at $z \sim 2$, of which 76 are radio-loud. The majority of the RLQs and RQQs in our sample are pair-matched in terms of redshift and V-band absolute magnitude (§2). These observations allow us to isolate the 'big blue bump' feature commonly identified with the accretion disk, and measure the rest-frame ~ 1 keV – 25 keV X-ray continuum, on a per-object basis. We obtain measurements of the UV to X-ray luminosity ratios and estimates of the total accretion luminosities for each quasar, allowing a direct comparison of SED diagnostics between radio types.

As part of an ongoing investigation of this sample, our main objective here is to describe the SEDs of these quasars as observed by *Swift*, and to assess to what degree they represent typical $z \sim 2$ quasars as observed in large surveys (e.g., the SDSS spectroscopic quasar catalog, Schneider et al. 2010; Shen et al. 2011). We explore the possible biases inherent to this sample, relative to the broader population. This will provide important qualifications for the interpretation of future results for this sample. In particular, we are currently obtaining spectroscopic observations for a subset of these quasars, with which we intend to study the dependence of the emission line properties on the broad-band SED diagnostics presented here. In this paper, we present and characterize the broad-band SED properties of each quasar in our sample. We also estimate their black hole masses and Eddington luminosity ratios, and compare these quantities to the broader population of quasars observed in the SDSS. We verify that our RLQ and RQQ subsamples, which are selected to have matching distributions of V-band luminosity and redshift, are also well-matched in terms of black hole mass and Eddington ratio.

We describe our sample selection and the *Swift* observing campaign in §2. In §2.4 we describe supplementary data used to constrain the UV–optical continuum slope and to obtain virial $M_{\rm BH}$ estimates. We present our SED production methodology in §3, and include SEDs for all sample members in Appendices A (for RQQs) and B (for RLQs). The distributions of integrated luminosities and SED shape diagnostics are presented in §4. Finally, we discuss whether our quasars are representative of the broader $z \sim 2$ quasar population (§5). In that Section we also discuss the distributions of monochromatic bolometric corrections and of Eddington ra-

tios for our sample quasars . Throughout this work we assume a spatially flat λCDM cosmology with $H_0 = 67.7$, Ω_{m}=0.307 (Planck Collaboration et al. 2015).

2 SAMPLE SELECTION AND OBSERVATIONS

2.1 Sample Selection

Our full sample comprises 144 quasars in the redshift interval $1.5 < z < 3.6$, of which, 76 are RLQs and 68 are RQQs[1]. Radio imaging data for the RLQs are presented by Barthel et al. (1988), Lonsdale et al. (1993) and Barthel et al. (2000); the majority of the RLQs are members of the 3C and 4C radio source catalogs (Bennett 1962; Pilkington & Scott 1965). Most of our sample (127 objects) are originally selected by Vestergaard (2000) to allow a comparison of emission-line and intrinsic absorption-line properties between RQQs and RLQs (Vestergaard 2003). The majority of these sources are pair-matched in terms of redshift and V-band absolute magnitude, with one RLQ and one RQQ in each pair. The original selection criteria are as follows.

- Apparent V-band magnitude $m_V \lesssim 19.5$ mag, so as to be spectroscopically observable with the Palomar Hale 5-meter telescope (for RLQs), the 4.5-meter MMT in Arizona, USA, or the ESO 3.6-meter telescope in Chile (for RQQs).
- Declination $\delta > -30°$ for RLQs, so as to be observationally accessible for the Very Large Array. For RQQs, sources were selected to be observable from Arizona and/or Chile.
- Redshift $z \geqslant 1.5$, to ensure that the Lyman-α emission line is observable in ground-based spectroscopy.
- Strongly variable objects (e.g., blazars) are excluded, so as to eliminate sources with Doppler-boosted emission.
- Objects identified as broad absorption line quasars as per 1998 are excluded[2].

We also include 16 quasars from the Sloan Digital Sky Survey Data Release 7 (SDSS DR7) that fulfill $z > 1.6$ and $m_V < 18$ mag, in order to cover a wide range of UV emission line properties (as determined via inspection of the SDSS spectra). We refer to objects from the Vestergaard et al. sample using the name convention Q$xxxx \pm xxx$, while J$xxxx \pm xxx$ denote the additional SDSS DR7 quasars. For the SDSS subsample, we extract radio flux densities at 1.4 GHZ from the FIRST survey (Becker et al. 1995). Five objects in the SDSS subsample have $R > 10$, where R is the ratio of flux densities in the B-band and at 5 GHz, assuming a radio spectral index of $\alpha_{\mathrm{r}} = -0.5$ in order to extrapolate from 1.4 GHz. We classify these five sources as radio-loud.

We present coordinates, redshifts and absolute V-band magnitudes for the full sample in Table 1; the redshifts are extracted from the NASA/IPAC Extragalactic Database[3]. We note that our sample is not complete in terms of luminosity or redshift. Rather, its primary advantage is that the RLQ and RQQ subsamples are by construction well-matched in

terms of redshift (Figure 1) and V-band absolute magnitude. This allows a robust comparison of other observed properties between the two radio classes. The RLQ subsample also spans the full range of inclinations expected for unobscured quasars ($5° \lesssim i \lesssim 45°$, Barthel 1989), as estimated based on the radio data (Vestergaard et al. 2000), and excluding Doppler-boosted sources ($i \lesssim 5°$) as outlined above. Previous analyses of the Vestergaard et al. sample reveal a dependence of the C IV broad emission line profile shapes on radio jet orientation for the RLQs Vestergaard et al. (2000), and a similar occurrence of narrow C IV absorption lines for RLQs and RQQs (Vestergaard 2003).

All 44 objects originally presented by Lawther et al. (2017) (hereafter, Paper 1) are re-analyzed here, as we have improved our UV-optical spectral modeling for the current work (§3.1). These improvements affect the measured UV to X-ray spectral index, α_{ox}, and the estimated bolometric luminosities.

2.2 *Swift* Observations

Our sample was observed by the *Swift* Gamma-ray Burst Explorer satellite (Gehrels et al. 2004) between 2010 June – 2017 December; the vast majority of the observations were performed in 2013 – 2017. The ability of the *Swift* satellite to observe simultaneously with the X-Ray Telescope (XRT, Burrows et al. 2005) and the UV-Optical Telescope (UVOT, Roming et al. 2005) is essential for this study, as it avoids introducing uncertainty to the relative UV-optical and X-ray luminosities (and thus the SED shape and α_{ox} measurements) due to source variability (§1). For this project, we were granted a total of 767 ks *Swift* observation time as part of the dedicated Danish time allocation (Instrument center for Danish Astrophysics Cycles 1–4, years 2013–2016, PI: Vestergaard). We were also granted 292 ks *Swift* Guest Observer time as fill-in programs in Cycles 10–13 (Proposal IDs 1013203, 1215240 and 1316208, PI: Vestergaard).

The majority of our targets (excluding several objects in the SDSS subsample) have not been observed in X-rays prior to this study. We initially estimated the appropriate XRT exposure times using on the V-band fluxes compiled by Vestergaard (2000), primarily based on Hewitt & Burbidge (1989) and Veron-Cetty & Veron (1991), and assuming α_{ox} =1.35, the typical value for unobscured quasars (e.g., Laor et al. 1997; Jin et al. 2012). For several quasars that turned out to be X-ray faint, we obtained additional *Swift* observing time in Cycles 12 and 13 so as to obtain a secure detection and/or reduce the uncertainty on the X-ray continuum SED. As a result, we here present a larger fraction of X-ray detected quasars (especially RQQs) relative to the subsample presented in Paper 1. All XRT observations were performed in photon-counting (PC) mode (Hill et al. 2004). The total UVOT exposure time for each object is similar to the XRT exposure time, but is distributed across the UVOT V, B, U and (for higher-redshift objects) $UW1$ bandpasses, so as to determine the UV-optical SED.

The quasars were observed by *Swift* as 'fill-in' observations (i.e., observed while the telescope was not responding to a Gamma-ray Burst trigger or performing other time-critical observations). The total observed on-source time is 980 ks, i.e., 92.6% of the allocated time. The standard procedure for *Swift* is to observe at least 80% of the allocated time. Most of

---

[1] One of the RQQs is not detected by either *Swift* XRT or UVOT (§2.3). This source is not included in any of our analyses.
[2] We note that two sample objects were subsequently found to be broad absorption line quasars (Q1227+120, Vestergaard (2003), and Q2350-007, Reichard et al. (2003)).
[3] Online resource: https://ned.ipac.caltech.edu/
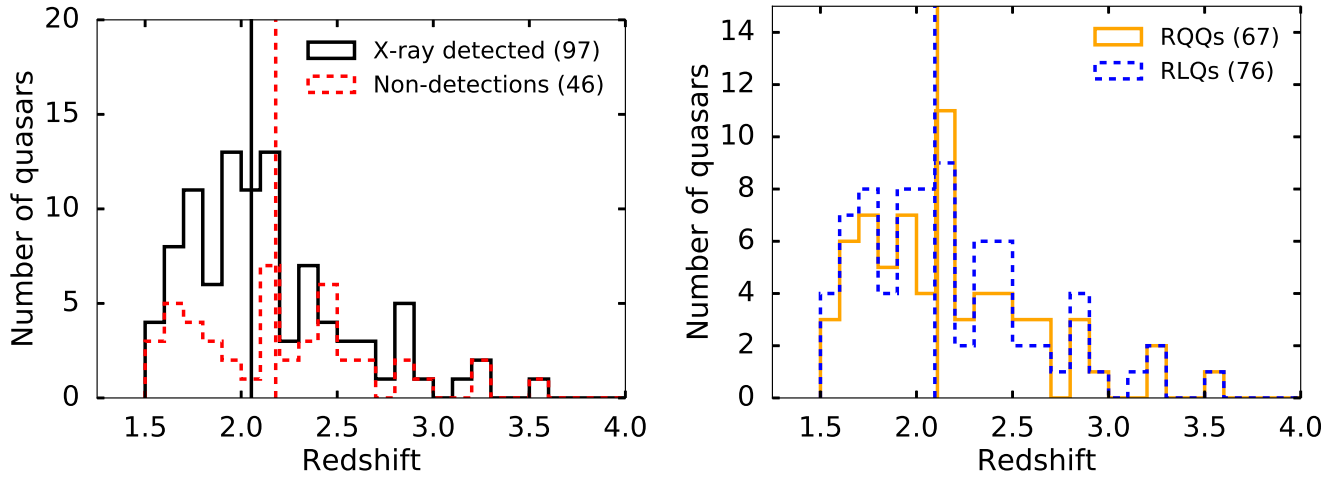
Figure 1. *Left:* Redshift distribution for *Swift* XRT detected quasars (solid black outline) versus non-detected quasars (dashed red outline) in our sample. Of the X-ray non-detections, six are RLQs, while 40 are RQQs. The vertical lines indicate the median redshifts for the detected and non-detected subsamples. *Right:* Redshift distribution for RLQ and RQQ subsamples (§2).
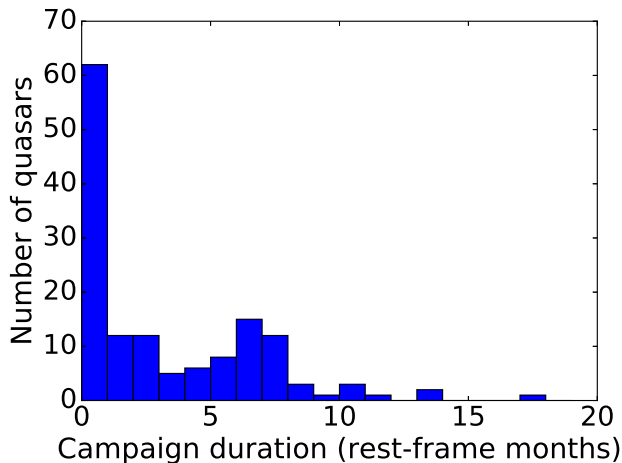
Figure 2. Total campaign duration Δt for each quasar, i.e., time interval between the first and last *Swift* observation utilized in this study, in units of rest-frame months (defined here as 30-day intervals). For 63 quasars, the total duration was less than one rest-frame month. The duration exceeds 6 rest-frame months for 38 quasars; it exceeds 12 months for three objects.

the quasars were observed multiple times so as to fulfill this requirement. The total rest-frame campaign duration Δt (i.e., the time interval between the first and the final *Swift* observation utilized, corrected for cosmological time dilation) is three months or less for most of our sample, and is less than one month for 63 quasars (Figure 2; Table 2). The second broad peak in the distribution of Δt ($\sim$7 rest-frame months, Figure 2) represents those X-ray faint sources for which follow-up observations were obtained. Quasar variability tends to increase for larger values of Δt (up to $\Delta t \sim$ few years) (e.g., Vanden Berk et al. 2004; Wilhite et al. 2005). Therefore, those sample quasars with follow-up observations are more likely to have varied in luminosity during our campaign. For *i*-band luminous SDSS quasars at $z \sim 2$, the typical intrinsic vari-

ability in the rest-frame UV over timescales of $\lesssim$1 rest-frame year is of order 10%–20% (e.g., Vanden Berk et al. 2004; Kaspi et al. 2007; Guo & Gu 2014). Thus, roughly half of our sample may display source variability of order $\sim$ 15% in the rest-frame UV between observations. Because we have simultaneous X-ray and UV-optical observations for all epochs, the SEDs generated using the combined observations for each quasar will correspond to exposure-time weighted averages of the SEDs at each observational epoch. We will therefore not suffer additional uncertainty in the UV to X-ray SED shape due to source variability, except that due to any correlations between SED shape and luminosity for individual quasars. We are not sensitive to variability for individual quasars, as the targets with large Δt (i.e., those for which we requested follow-up observations) are faint and are only detected in the combined data.

We utilize almost all *Swift* observations related to our programs. Observations with near-zero exposure time (generally due to *Swift* responding to a higher-priority transient target at the beginning of an observation), or with problematic UVOT data (e.g. visible 'trails' from point sources, presumably due to spacecraft slewing), are not included. Serendipitous observations, targeted at sky coordinates near to one of our targets, are not included. We inspected several such observations. Their inclusion would in all cases either increase Δt for that quasar, utilize data from near the edge of the XRT detector, or (in the case of Gamma Ray Burst observations) risk contaminating the XRT source and/or background extraction regions with flux from the transient source. We utilize between one and 30 discrete observation IDs per quasar (Table 2).

2.3 Processing of *Swift* XRT and UVOT data

XRT Data: We refer the reader to Paper 1 for a description of our XRT data processing and spectral modeling. We use an identical methodology here. We fit each X-ray detected quasar using a power-law function along with a Galactic absorption component. As demonstrated in Paper 1, our data

generally do not warrant the inclusion of an intrinsic absorption component. We list the background-subtracted XRT photon counts N_{sub}, the detection status, the model parameters and the integrated model fluxes for each quasar in Table 2. For X-ray non-detections we present 3σ upper limits, assuming an X-ray photon index of $\Gamma = 1.91$, a typical value for AGN X-ray spectra (e.g., Young et al. 2009; Jin et al. 2012). As we demonstrate in Paper 1, the best-fit photon index and X-ray continuum normalization are not, in general, statistically independent. For this reason, we do not study any putative relationship between Γ and the X-ray luminosity in this work, and advise caution in using our measurements for such investigations.

UVOT Photometry: The UVOT data processing and source extraction methodology is described Paper 1. We present the UVOT flux densities, corrected for Galactic reddening, for our sample in Table 3; we use the Galactic $E(B-V)$ measurements presented by Schlafly & Finkbeiner (2011), as extracted from the NASA/IPAC Infrared Science Archive[4]. We also list the observed apparent magnitudes on the UVOT photometric system (similar to the Johnson system; Poole 2008) in Table 4.

Detection Summary: We present the number of detections versus non-detections in our XRT and UVOT data in Table 5. The quasar Q2359+002 is not detected in any UVOT bandpasses (or with XRT), and is excluded from the remainder of the analysis. Of the 143 remaining sources, 46 are not detected in XRT. Of these, six are radio-loud. Not all objects are detected in all selected UVOT filters (18 objects are detected in two UVOT filters or fewer; of which, one object is not detected by UVOT at all). Given that we estimated the necessary XRT exposure times assuming a single value of α_{ox} for the entire sample (§2), the higher detection rate for RLQs is expected, as RLQs tend to be brighter than RQQs for a given optical luminosity (Zamorani et al. 1981). Nevertheless, we have X-ray detections for 27 RQQs.

2.4 Supplementary Sloan Digital Sky Survey Data

As the UVOT bandpasses do not cover rest-frame wavelengths longer than ≈ 2000 Å at $z \approx 2$, and given that some objects are only detected in one or two UVOT bandpasses, we extend our spectral coverage by including archival *Sloan Digital Sky Survey* (SDSS-III, Eisenstein et al. 2011) photometry in our analysis. Of the present sample of 143 UVOT-detected quasars, 122 objects have SDSS photometry. The SDSS data are processed using the latest SDSS photometric pipeline (Data Release 12, Alam et al. (2015)). We correct the observed flux densities for Galactic reddening using the values of $E(B-V)$ presented by Schlafly & Finkbeiner (2011). A total of 104 quasars in our sample also have SDSS spectroscopy. In this work, we do not model/decompose the SDSS spectra. We include them in our SED Figures (Appendices A and B) for visualization purposes only. For 12 quasars (four RQQs and eight RLQs), the SDSS spectroscopy is offset in flux from the SDSS photometric data. All but two of these

12 quasars are observed as part of the SDSS BOSS survey (Dawson et al. 2013). The spectroscopic observing procedure was modified for this survey to optimize the throughput at the short-wavelength end of the spectrograph. This modification caused a systematic uncertainty in the flux calibration of SDSS BOSS spectra, which has only been rectified in a statistical sense (Margala et al. 2015). Provided that the photometric fluxes are accurate, this flux offset is not a major issue for our study, given that we only use the SDSS spectra for visualization purposes.

3 DETERMINING THE UV TO X-RAY SPECTRAL ENERGY DISTRIBUTION

3.1 UV-Optical Emission Line Correction

Our UV-optical data consist of extinction-corrected UVOT (§2.3) and SDSS (§2.4) photometry. They sample rest-frame wavelengths of ~ 800 Å to ~ 3200 Å (e.g., Figure 3). In order to study the accretion physics, we need to isolate the emission due to the continuum source. Superimposed on the nuclear continuum emission are the broad emission lines, the narrow emission lines, and the Balmer continuum feature, which are all due to reprocessed nuclear continuum emission. Our broad-band photometry contains the combined flux due to these components. The relative contribution in each bandpass depends on the filter throughput curve, the redshift, and the relative strengths of the emission components in a given quasar.

In order to approximate the emission-line contribution in each bandpass, we use template quasar spectra for which a detailed spectral decomposition is available. For most of our sample we utilize the template presented by Selsing et al. (2016), i.e., an inverse-variance weighted mean spectrum of seven luminous quasars at $1 < z < 2.1$. One advantage of this template is that it covers a rest-frame wavelength range of ~ 1000 Å–9000 Å, allowing a flux correction for bandpasses that sample the rest-frame far-UV. Additionally, the template has negligible host galaxy contamination, as expected for the distant and luminous quasars in our sample. These authors find an underlying power-law continuum that can be parameterized as $F_\lambda \propto \lambda^{-1.70}$. In general, the slope of the UV-optical continuum may vary significantly between quasars residing at $z \sim 1$ and $z \sim 2$ (Xie et al. 2015). However, for SDSS quasars at $z \sim 2$ with bolometric luminosities $L_{\mathrm{bol}} > 10^{47}$, corresponding to the median accretion luminosity for our sample (§4.6), Xie et al. (2015) also find a spectral index $\beta_{\mathrm{UV}} \sim 1.7$. Thus, while our chosen template spectrum is based on sources with a lower median redshift than that of our sample, the overall continuum spectral shape is likely appropriate for our bright $z \sim 2$ quasars.

To obtain an estimate of the continuum flux in each bandpass, we first blue-shift the UVOT or SDSS filter throughput function to the appropriate rest-frame wavelength for a given quasar, and then fold the template spectrum with the throughput function and integrate over the bandpass. We then fold the continuum component (as determined by Selsing et al. (2016) in their spectral decomposition) with the same filter curve. The ratio of these two integrals yields the fractional continuum contribution in each bandpass. We use these ratios to estimate the continuum flux density for each

---

[4] Web resource: http://irsa.ipac.caltech.edu/applications/DUST/
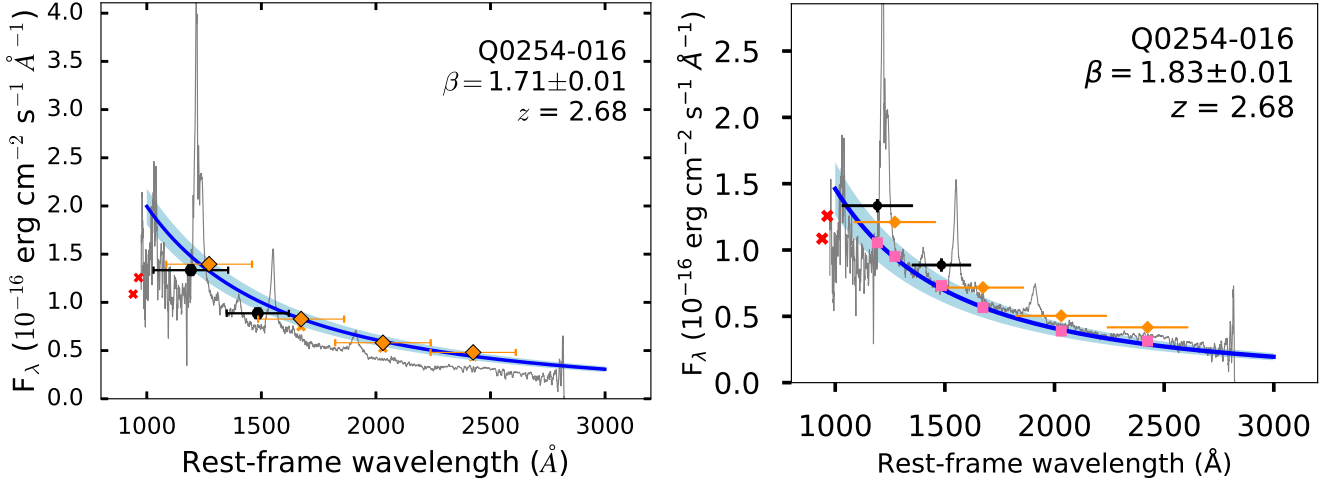
Figure 3. Illustration of UV-optical emission line correction and power-law continuum fit, for quasar Q0254-016. The dark blue curve and light blue shaded area shows our power-law continuum model and its uncertainty. The model is fitted to the *Swift* UVOT broad band photometric data (black circles) and to the rescaled SDSS photometry (gold diamonds). Red crosses denote data points not utilized in the model fit. The SDSS spectrum is included for illustrative purposes (grey curves); it is rescaled by the same factor as is the SDSS photometry. *Left panel:* A fit to the raw data, without emission line correction. *Right panel:* Final model after correcting for emission line contribution using the Selsing et al. (2016) composite bright quasar spectrum, as described in §3.1. Here, we again show the uncorrected UVOT (black circles) and SDSS (gold diamonds) fluxes, but the continuum model is fitted to the corrected fluxes (pink squares).

bandpass, thus correcting them (in a statistical sense) for contamination due to the non-nuclear emission components described above.

For objects with SDSS spectroscopy, we visually compare the photometry (and our fitted UV-optical continuum model, §3.3) with the observed spectrum, paying particular attention to the continuum-dominated spectral windows discussed by Selsing et al. (2016) (their §6). We do this after applying the flux rescaling for the SDSS data, as described in §3.2. For objects where the fluxes appear to be overestimated relative to the observed spectrum in the continuum-dominated regions, or where the fitted continuum seems steep compared to the observed spectrum, we perform an alternative emission line correction using the template presented by Vanden Berk et al. (2001). This template includes lower-luminosity AGN, and has substantial host galaxy contamination at longer wavelengths. We recalculate the SDSS flux rescaling for the alternative emission line correction, and then visually compare the corrected photometry using each template to the observed SDSS spectrum. We prefer the Vanden Berk et al. rescaling for 16 quasars, of a total of 104 for which this comparison is possible (i.e., those with SDSS spectroscopy). We remark on the choice of template on a per-object basis in Appendices A, where we present the SEDs for our RQQ subsample, and B, for RLQs.

3.2 Flux Rescaling for SDSS Photometry

The SDSS observations were performed at time separations of months to years with respect to the *Swift* observations. Flux variability must therefore be accounted for. We follow the approach of Wu et al. (2012), who rescale the SDSS photometry by a constant factor to match the observed UVOT flux level in a given 'matching bandpass' (defined below). To determine the necessary rescaling, we fit the emission-line corrected (§3.1) SDSS photometry with a power-law model, and

calculate the ratio of the power-law flux density to that observed by UVOT at the throughput-weighted centroid wavelength of the matching bandpass. We rescale all SDSS photometric data points (for a given quasar) by this ratio. For the lowest-redshift quasars in our sample ($z \lesssim 1.9$), we match the observed *Swift* U band flux (central wavelength 3465 Å) and the SDSS u band (central wavelength 3551 Å), as they sample very similar wavelength ranges. At higher redshifts, the u and U bands sample the Lyman forest, for which the continuum determination is uncertain. In these cases, we instead match the fluxes in a bandpass sampling the far-UV region between the Lyα and C IV BEL, depending on the available UVOT data. The matching UVOT filter for each object is listed in Table 3. This approach depends on the assumption that only the flux normalization changes between the SDSS and the *Swift* observation, while the spectral shape is constant. We discuss this further in §3.3.

3.3 UV-Optical Continuum Modeling

We model the UV continuum emission over the rest-frame wavelength interval 1000 Å – 3000 Å, based on the emission line-corrected flux densities. Most of our sample (125 objects) are detected in three or more UVOT bandpasses (Table 5). In typical cases, we utilize all available (UVOT and SDSS) photometric data-points in bandpasses redwards of, or roughly superimposed on, the Lyman-α emission line; at higher energies than this, the observed flux is not expected to follow a power-law, due to Lyman forest absorption. We fit a power-law model, $F_\lambda = A\lambda^{-\beta_{\rm UV}}$, to the emission-line corrected flux densities. Here, F_λ denotes the flux density at wavelength λ, while $\beta_{\rm UV}$ is the UV continuum spectral index. We perform a non-linear least-squares fit of this model to the available photometric data based on the Levenberg-Marquardt algo-

rithm, using the *scipy.optimize* package[5]. We show a representative continuum model, and its uncertainties, before and after emission-line correction (§3.1) in Figure 3. We note that the flux rescaling of the SDSS data is performed after the emission line correction. Thus, while we rescale the SDSS data in both the left and right panels for our example spectrum (Figure 3), the rescaled SDSS flux values depend on whether the emission line correction is applied. In the example spectrum shown, the rescaling factor is smaller after applying the emisison line correction, resulting in a steeper UV continuum model fit.

For three objects (Q0249-184, Q1203-111, and Q1557-199) we only have a single photometric data point in the appropriate spectral region. To obtain a guideline estimate of the continuum emission in this case, we adopt a power-law model with a spectral index equal to the canonical value $\beta_{UV} = 1.5$ (e.g., Richards et al. 2006), scaled to this single photometric data point. For 17 quasars, we only have two UV photometric measurements redwards of Lyman-α. In these cases, we make a guideline estimate of the UV SED by connecting the two photometry points with a power law function. We note that some objects for which we only utilized one or two photometric bands in Paper 1 are now modeled using additional bandpasses. This change is due to our implementation of emission-line corrections, allowing the inclusion of data points with strong broad-line emission.

Uncertainties in the UV–optical modeling due to continuum shape variability: Our UVOT data are observed at time separations of months to years with regard to the SDSS observations. Significant variations in quasar UV-optical spectral indices (of up to $\Delta\beta_{UV} \sim 0.2$) are observed over rest-frame timescales of $\sim$months to years (Pu et al. 2006; Bian et al. 2012), with a tendency for quasars to be more blue at brighter epochs (e.g., Schmidt et al. 2012). Even though we correct the SDSS data for variations in overall flux level, the spectral shape variations may introduce additional uncertainty into our UV–optical modeling. We quantify the uncertainty due to spectral shape variation in Paper 1, finding that, in the worst-case scenario, it introduces an uncertainty of $\Delta\beta \sim 0.19$ to the measured spectral index in our joint UVOT+SDSS modeling. The corresponding uncertainty in the integrated UV-optical flux is only of order 1%. We also note that the effect of spectral shape variation on the monochromatic luminosity of the UV–optical continuum model at rest-frame 1000 Å is negligible, as this luminosity is directly constrained by our UVOT observations for most sources. This minimizes the uncertainty introduced into our EUV interpolation (as discussed below) due to UV–optical shape variability.

3.4 EUV Interpolation Strategy

Due to strong absorption by neutral hydrogen and helium in our Galaxy, in the intergalactic medium, and in the host galaxy, the extreme-UV (EUV) spectral region is not directly accessible to electromagnetic observations. We interpolate over this unobservable region using a simple power-law

function. We motivate our interpolation scheme in Paper 1. To summarize, we connect the UV continuum model luminosity at rest-frame 1000 Å with the absorption-corrected X-ray continuum model luminosity at rest-frame 1 keV using a power-law model, and integrate this model between these two extremes to obtain an estimate of the EUV luminosity. We also perform an alternative interpolation between rest-frame 1000 Å and rest-frame 0.3 keV, which in most cases leads to a smaller estimated EUV luminosity; for a few sources with very soft X-ray spectra (e.g., Q1225-017) the opposite is true. We present an example of the two EUV interpolations in Figure 4 (top left).

3.5 Optical–UV–X-ray Spectral Energy Distributions

We present two examples of the rest-frame optical–UV–X-ray continuum SEDs in Figure 4. Quasar Q0003-006 (Figure 4, top) is securely detected by both the UVOT and the XRT. Q0115-011 (Figure 4, bottom) is an example of an XRT non-detection, for which we present the 3σ limiting X-ray luminosity. In the left panels we show νL_ν as a function of ν. To represent the observed XRT data in units of physical flux, we show the 'unfolded' XRT spectrum, i.e., the measured number of counts in a given bin, scaled by the ratio of the incident model to the model convolved with the instrumental response function. That is, the detector response is corrected for. The X-ray data points are rebinned for clarity. We note that unfolded spectra of this type are model-dependent visualizations of X-ray data; we find them useful for presentation purposes, but they are not suitable for further spectral analyses. We also show the best-fit X-ray model including Galactic absorption, along with the assumed underlying power law continuum corrected for Milky Way absorption. The unobserved EUV region is interpolated over using power-law functions anchored to the X-ray model at 1 keV (blue dash-dotted line) and at 0.3 keV (blue dashed line). In the right-hand panels we display the UV-optical photometry in detail, along with our fitted UV-optical continuum model (§3.3) and its 1σ uncertainty (indicated by a shaded region). The SEDs for the remainder of our quasar sample are presented in Appendices A and B for RQQs and RLQs, respectively.

4 CHARACTERISTICS OF THE SED CATALOG

Here we present some fundamental measurements of the quasar SEDs. Our main goal is to determine to which degree the sample and its RLQ and RQQ subsamples are representative of the broader $z \sim 2$ RLQ and RQQ populations, respectively. The measurements presented here also quantify any differences in SED properties between the RLQ and RQQ subsample. We begin by describing some important comparison samples that we use to determine whether our RLQs and RQQs are representative of the broader $z \sim 2$ population (§4.1). Thereafter, we describe the UV–optical (§4.2) and X-ray (§4.3) properties of our sample quasars. We also examine their UV to X-ray SED shapes (§4.4), and determine whether they are consistent with the UV to X-ray luminosity relationship previously found for statistical samples of AGN (§4.5). Finally, we estimate their integrated accretion luminosities (§4.6).
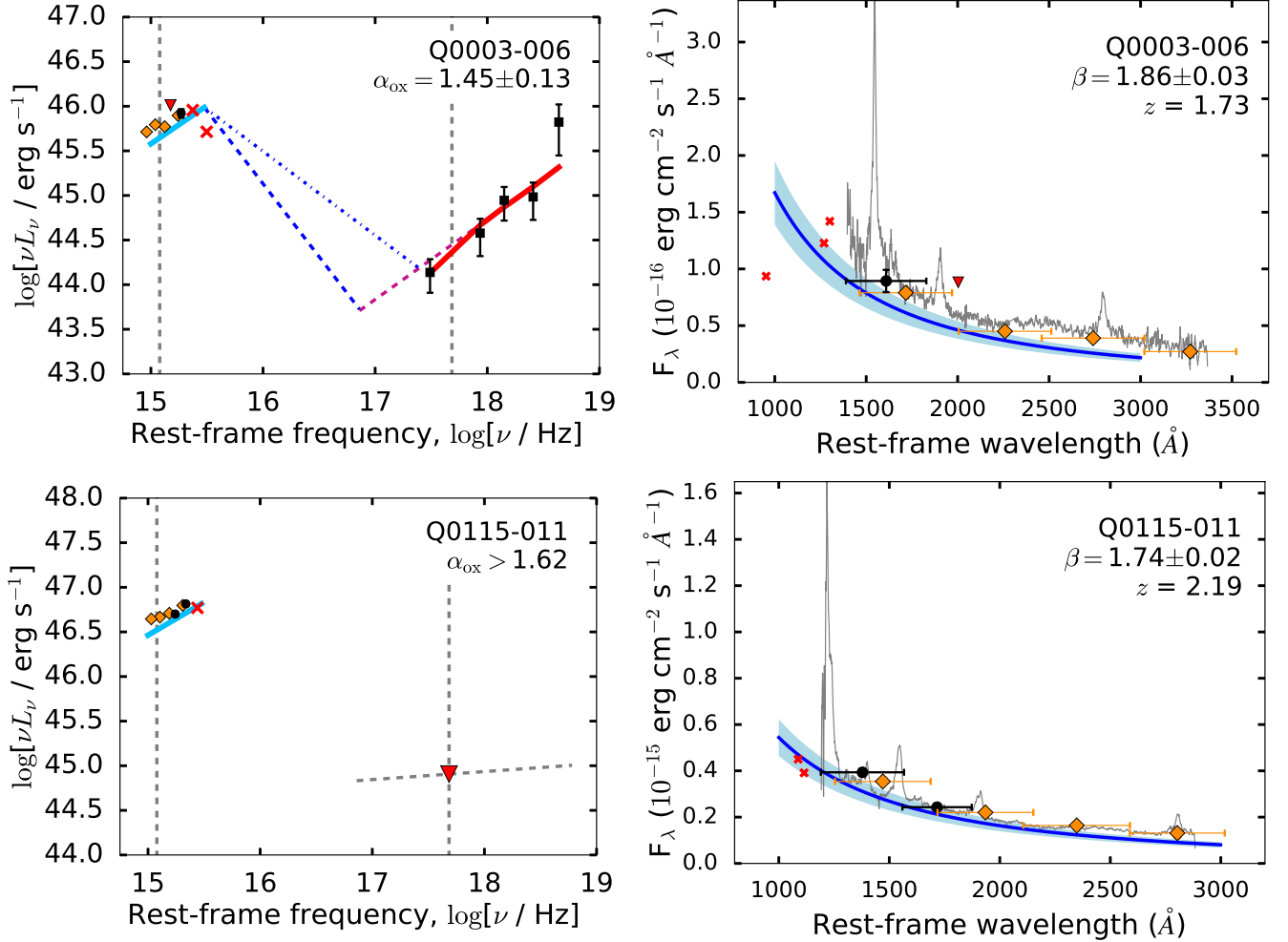
Figure 4. SEDs for two quasars in our sample: one X-ray detected object (upper panels), and one X-ray nondetection (lower panels). **Left panels:** Rest-frame UV to X-ray SEDs. The leftmost and rightmost vertical dashed lines indicate the frequencies corresponding to 2500 Å and 2 keV, respectively. **Right panels:** Detailed view of the UV data and continuum modeling. **Symbols:** Black squares: 'unfolded' XRT spectrum (§3.5) with 1σ uncertainties. Solid red curve: X-ray model including Galactic absorption. Dashed magenta curve: intrinsic, absorption-corrected X-ray model. Red triangles: 3σ upper limit fluxes (for X-ray upper limits, grey dashed line illustrates a $\Gamma = 1.91$ power-law). Black dots: Galactic absorption-corrected UVOT photometry. Orange squares: rescaled SDSS broadband photometry (§2.4). Red crosses: photometric data points excluded from modeling (§3.3). Blue dashed and dash-dotted lines: EUV interpolations (§4.6), connecting with the X-ray model at 0.3 keV and 1 keV, respectively. Grey curve: SDSS spectrum, if available - otherwise, composite quasar spectrum of Selsing et al. (2016), scaled to the model flux at 2500 Å. In the right panels, the horizontal bars represent the Full Width at Half Maximum of the filter bandpasses.

4.1 Main Comparison Samples

The Sloan Digital Sky Survey Quasar Catalog: Shen et al. (2011) (hereafter, S11) present the measured UV–optical SED characteristics for quasars in the SDSS Data Release 7 (Abazajian et al. 2009) spectroscopic quasar catalog (Schneider et al. 2010). This sample contains over 10^5 spectroscopically classified quasars, originally identified as quasar candidates due to their photometric colors. We select a subset of these quasars as a comparison sample. Namely, sources at redshifts $1.5 < z < 3.6$ (i.e., matching the redshift range of our sample), that are not flagged as Broad Absorption Line quasars by S11. As we use this sample to determine how typical the UV luminosities of our sample quasars are, we wish to include all spectroscopically identified quasars in

the relevant redshift range. We therefore do not impose any luminosity cutoff for the SDSS comparison sample.

SED Catalogs: Richards et al. (2006) (hereafter, R06) present the mid-infrared to near-UV SEDs of 259 quasars. These quasars are spectroscopically identified in the SDSS Data Release 3 (Schneider et al. 2005), and are also detected by the *Spitzer* Infrared Array Camera (Fazio et al. 2004). They therefore represent spectroscopically identified quasars; the requirement of an infrared detection does not significantly affect the properties of this sample, as only one quasar in their sample is not detected with *Spitzer*. R06 include available radio, far-UV and/or X-ray data for a subset of these quasars. Of their sample, 113 quasars have redshifts $1.5 < z < 3.5$. While their full sample is on average fainter in the UV than our sample, the mean SED for their 'lumi-
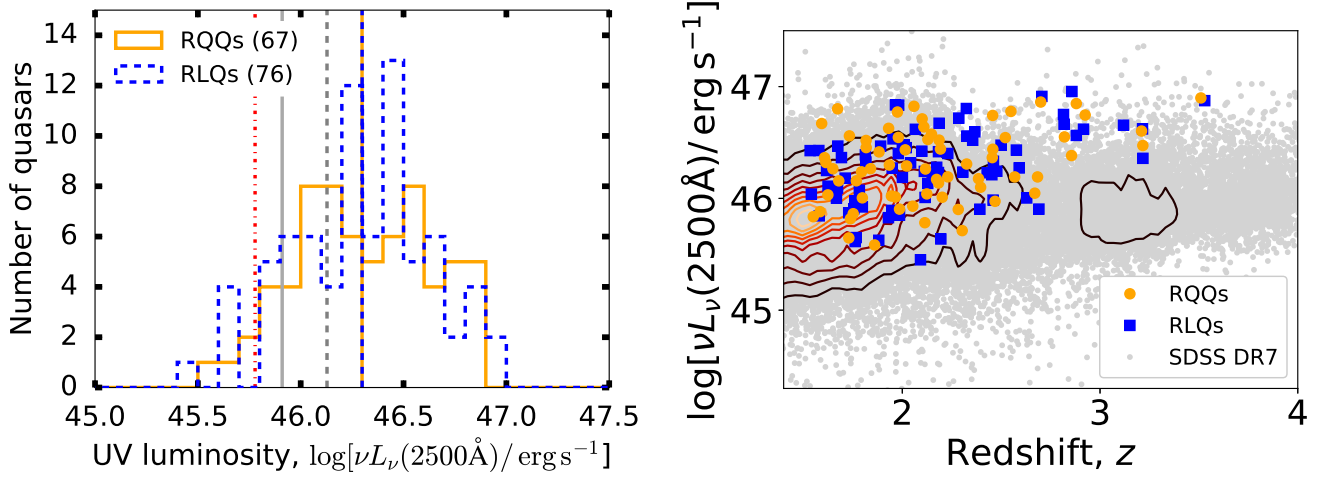
Figure 5. *Left:* Distribution of $\nu L_\nu(2500\,\text{Å})$ for our RQQ (solid orange histogram) and RLQ (dashed blue) samples, based on the UV-optical continuum modeling (§3.3). The median luminosities for the RQQ and RLQ subsamples are almost equal (vertical orange and blue lines, respectively). For comparison purposes, we show the average luminosities of the $1.5 < z < 3.5$ RQQs (solid gray line) and RLQs (dotted gray line) presented by W12. We also show the mean UV luminosity of the E94 sample of $z < 1$ quasars (dash-dot red line). While there is an overlap in UV luminosity between our sample quasars and these earlier quasar SED studies, our quasars are on average UV-brighter than the E94 sample by a factor 3.2. *Right:* Redshift distribution of $\nu L_\nu(2500\,\text{Å})$ for our RQQ and RLQ subsamples. Here, we also show the distribution of z and $\nu L_\nu(2500\,\text{Å})$ for non-BAL quasars in the SDSS Data Release 7 (Shen et al. 2011). For the SDSS sources, we extrapolate to the 2500 Å luminosity using the published values of $\nu L_\nu(3000\,\text{Å})$ for $z < 2.25$, or $\nu L_\nu(1350\,\text{Å})$ for $z > 2.25$, and the sample median local continuum slope measured near the relevant wavelength. The apparent dip in the luminosity distribution for the SDSS quasars at $z \sim 2.25$ is likely due to our extrapolation methods. The contours illustrate iso-density lines for the SDSS quasars in the luminosity-redshift plane. At redshifts below $z \sim 2.8$, our sample quasars are on average brighter than the SDSS sources, but their luminosity distribution overlaps with the most dense regions of the z–$\nu L_\nu(2500\,\text{Å})$ distribution for the SDSS quasars. At redshifts above $z \sim 2.8$, our sample quasars are unusually UV-luminous relative to the luminosity distribution of SDSS quasars. We note that this result may partially be due to the change in UV interpolation strategies at the $z \sim 2.25$ threshold for the SDSS sources.

nous quasar' subsample displays a similar UV luminosity to our sample quasars. We do not use this catalog to compare X-ray SED properties, as it includes only four X-ray detected quasars at redshifts $1.5 < z < 3.5$.

Wu et al. (2012) (hereafter, W12) present an SED catalog for 843 AGN, based on *Swift* UVOT and XRT observations. Their sample is selected by matching spectroscopically identified AGN from the SDSS Data Release 5 with archival *Swift* observations. For comparison purposes, we examine the subsample of sources in the W12 catalog situated at redshifts $1.6 < z < 3.6$ (174 RQQs and 35 RLQs). This sample is in particular useful in order to study the inherent limitations of *Swift* XRT observations of $z \sim 2$ quasars due to instrumental sensitivity.

Among the earliest comprehensive quasar SED catalogs is that presented by Elvis et al. (1994) (hereafter, E94). These authors present the radio to X-ray SEDs of 29 RQQs and 18 RLQs, all at redshifts $z < 1$. They tend to be X-ray bright, as E94 select quasars that have X-ray detections with the *Einstein* satellite. While this catalog does not include sources as luminous as our $z \sim 2$ sample, we include it here as a comparison to lower-redshift sources. It is also the most cited SED catalog in the existing literature, and thus represents a 'canonical' quasar SED catalog with which to compare our higher-redshift sample.

Catalogs with Deep X-ray Observations: Of the SED catalogs described above, only Wu et al. (2012) includes a significant number of X-ray detected sources at $z \sim 2$. However,

due to the inherent limitations of the *Swift* XRT detector, the $z \sim 2$ RQQs in the Wu et al. (2012) sample are mostly only marginally detected. We therefore turn to samples with large numbers of X-ray detected AGN, including deep, wide-field X-ray observations that are able to detect fainter sources. For this purpose, we select two studies of the $L_{\rm UV}$–L_X relationship in AGN. These comparison samples also support our investigations of the UV to X-ray SED shape for our sample quasars (§4.4).

Lusso & Risaliti (2016) (hereafter, L16) study the relationship between rest-frame 2500 Å and 2 keV luminosities for a sample of 2605 radio-quiet AGN, all of which are selected from the spectroscopically confirmed quasar sample presented by S11. These 2605 AGN are observed by *XMM-Newton*, with an X-ray detection rate of $\sim$80%. Their 'full sample' regression result is consistent with several previous studies of the $L_{\rm UV}$–L_X (or $L_{\rm UV}$–$\alpha_{\rm ox}$) relationship for RQQs across a broad range of redshifts and luminosities (e.g., Vignali et al. 2003; Strateva et al. 2005; Steffen et al. 2006; Just et al. 2007). The L16 sample spans a redshift range of $0.06 < z < 4.93$. For comparison purposes, we impose a redshift cutoff $1.5 < z < 3.5$ (881 AGN). For our comparison of 2 keV X-ray luminosities, we also impose a UV luminosity cutoff on their sample, excluding sources with 2500 Å luminosities fainter than 4.7×10^{45} erg s^{-1}, in order to remove quasars that are more UV-faint than any of our sample RQQs. Applying both the luminosity and redshift cutoffs yields a comparison sample of 541 quasars.
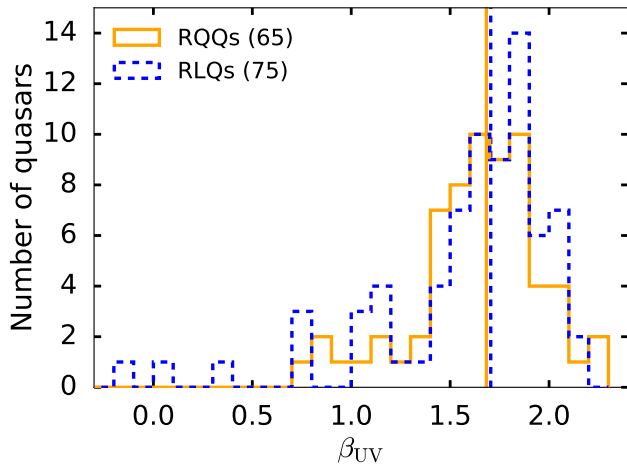
Figure 6. Distribution of the UV-optical spectral index β_{UV}, as measured for the emission line-corrected UVOT and SDSS photometric data. The vertical lines indicate the median spectral indices for the RQQ and RQQ subsamples.

Miller et al. (2011) (hereafter, M11) present a comprehensive study of the L_{UV}–L_X relationship for RLQs. These authors select 654 radio-loud and radio-intermediate SDSS quasars that have X-ray observations with *Chandra, XMM-Newton*, or *ROSAT*. The most X-ray bright sources presented by M11 are designated as a supplementary sample, as they were observed with the *Einstein* satellite by Worrall et al. (1987). Given that our RLQs are also X-ray bright, we select quasars in their full (primary plus supplementary) sample that have redshifts $1.5 < z < 3.5$, and that are classified as radio-loud. This yields a comparison sample comprised of 240 RLQs, of which 33 are taken from their supplementary sample.

4.2 The UV-Optical SED

Here, we present the distributions of UV luminosities and UV–optical spectral indices for our sample. Our measurements are performed on the power-law UV-optical models, $F_\lambda \propto \lambda^{-\beta_{\mathrm{UV}}}$ (§3.3), fitted to the emission line-corrected UVOT and SDSS photometry (§3.1). For comparison with other studies, we note that $\beta_{\mathrm{UV}} = \alpha + 2$, where $F_\nu \propto \nu^\alpha$.

Our main results regarding the UV–optical SEDs of our sample quasars are as follows.

• Our sample quasars are on average UV-luminous. At $z \sim 2$ they correspond to typical bright quasars in the SDSS, while at $z \sim 3$ they are much more UV-luminous than typical SDSS quasars.
• Our RLQ and RQQ subsamples are well-matched in terms of UV luminosities.
• Our quasars display UV–optical spectral indices consistent with those of luminous quasars at $z \geqslant 1$.
• We find no significant difference in the distributions of UV–optical spectral indices for our RLQ and RQQ subsamples.

We describe each of these results in more detail in the remainder of this Section.

Monochromatic luminosities at 2500 Å: Our sample spans the range of 2500 Å luminosities $2.8 < \nu L_\nu (2500\,\text{Å})/10^{45} \text{ erg s}^{-1} < 91.2$ (Figure 5, left panel). Its dynamic range in terms of UV luminosity is ~ 1.5 dex at $1.5 \lesssim z \lesssim 2.5$, but is only ~ 0.8 dex at $z > 2.5$ (Figure 5, right panel). We find average monochromatic luminosities of $\nu L_\nu (2500\,\text{Å}) = 2.6 (\pm 0.2) \times 10^{46} \text{ erg s}^{-1}$ for the RQQs; the quoted uncertainty represents the standard deviation of the mean luminosity, while the sample standard deviation is $\sigma_L = 2.3 \times 10^{45} \text{ erg s}^{-1}$. For the RLQs, we find $\nu L_\nu (2500\,\text{Å}) = 2.5 (\pm 0.2) \times 10^{46} \text{ erg s}^{-1}$, with $\sigma_L = 2.2 \times 10^{45}$. The two radio subsets are statistically similar, as indicated by two-sample KS tests ($p = 0.98$). The UV luminosities of our X-ray detected and non-detected subsamples are also statistically similar($p = 0.66$).

The 'optically luminous' subsample defined by R06 has a mean $L_\nu (2500\,\text{Å}) \sim 2 \times 10^{46} \text{ erg s}^{-1}$, similar to our mean UV luminosities. This suggests that our sample is comprised of UV-luminous quasars. Our sample quasars are also, on average, more luminous than those in the SDSS comparison sample (S11). At $z \sim 2$, our quasars are on average a factor ~ 3 more luminous than the peak of the SDSS luminosity distribution at $z \sim 2$ (Figure 5, right panel). We find that the deviation of the UV luminosities in our sample relative to the SDSS sample is larger at higher redshifts. At redshifts above $z \sim 2.8$, our quasars are roughly an order of magnitude brighter than typical SDSS quasars, and only a few SDSS quasars have comparable luminosities. At $1.5 \leqslant z \leqslant 2.8$, the UV luminosity distribution of our sample overlaps with the most dense regions of the SDSS z–$\nu L_\nu (2500\,\text{Å})$ distribution, although the SDSS distribution extends to much fainter UV luminosities (Figure 5, right panel). Thus, at redshifts $z \sim 2$, our quasars are comparable in terms of UV luminosities to typical *bright* quasars in the SDSS, whereas our $z \sim 3$ quasars are atypically bright relative to the broader quasar population as characterized by the SDSS.

UV-optical spectral indices: We measure the UV–optical spectral slope for 140 quasars, i.e., those which are detected in at least two *Swift* UVOT filters. Of which, 17 quasars have only two usable photometric data points. The statistics of our measured β_{UV} values are not strongly sensitive to the inclusion of these 17 quasars. We find an average spectral index $\langle \beta_{\mathrm{UV}} \rangle = 1.63 \pm 0.04$ for RQQs and $\langle \beta_{\mathrm{UV}} \rangle = 1.62 \pm 0.06$ for RLQs (Figure 6), with sample standard deviations of $\sigma_{\beta,\mathrm{RQQ}} = 0.32$ and $\sigma_{\beta\,\mathrm{RLQ}} = 0.48$, respectively. The median spectral indices are 1.66 and 1.71 for RQQs and RLQs, respectively. Thus, our RLQ and RQQ subsamples have similar UV-optical SED shapes, as also indicated by a two-sample KS test ($p = 0.89$). We find no trend of β_{UV} with either redshift, $L_\nu (2500 \text{ Å})$, or integrated accretion luminosity, L_{acc} (as defined in §4.6). Our distributions of β_{UV} contain outliers with flat spectra ($\beta_{\mathrm{UV}} \lesssim 1$), perhaps due to substantial reddening in the AGN and/or host galaxy. The SEDs for these sources may also be intrinsically red, as is the case for massive black holes with low spin in the context of Shakura & Sunyaev (1973) thin-disk models.

We now examine whether the UV–optical SED spectral indices of our quasar sample are consistent with quasars at comparable redshifts and UV luminosities. Shankar et al. (2016) study the UV–optical SEDs for a sample of SDSS quasars at redshifts $1.0 < z < 1.2$, as a function of UV luminos-
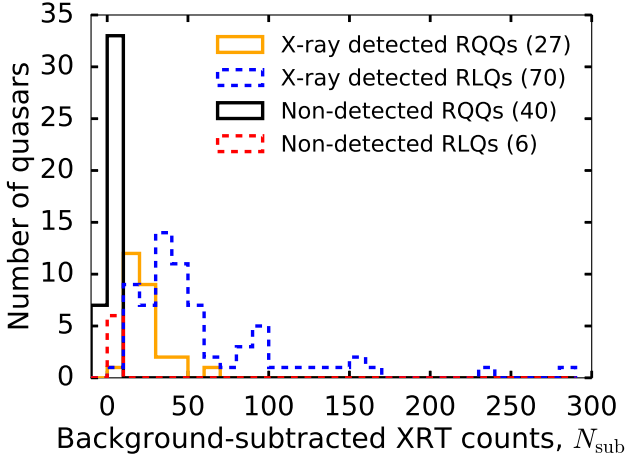
Figure 7. Histogram of the background-subtracted number of X-ray counts, $N_{\rm sub}$, for X-ray detected RQQs (solid orange outline) and RLQs (dashed blue), along with non-detected RQQs (solid black) and RLQs (dashed red). We detect 92% of the RLQs, but only 40% of the RQQ subsample. Seven RQQs have $N_{\rm sub} < 0$; this is attributable to fluctuations in the background levels in the background and/or source aperture, given negligible source flux.

ity and black hole mass. For quasars with $L_{\rm UV} > 10^{45.5}$ erg s^{-1}, corresponding to our UV luminosity range, they find $1.5 \lesssim \beta_{\rm UV} \lesssim 1.7$; they have 2852 RQQs and 146 RLQs in this luminosity range. For quasars with black hole masses exceeding $10^9 M_\odot$ (i.e., the mass range of our sample, §5.3) they find a similar range of spectral indices. We note that the redshift range examined by Shankar et al. (2016) is somewhat lower than for our sample. Xie et al. (2015) present UV–optical spectral index measurements for over 22000 luminous (bolometric luminosities $L_{\rm bol} > 10^{47}$ erg s^{-1}) SDSS quasars at redshifts $z > 1.8$. They find no significant redshift dependence of $\beta_{\rm UV}$. For these luminous AGN, they find $\beta_{\rm UV} \sim 1.7$, again broadly consistent with the spectral indices for our sample. These results confirm that our sample have similar UV–optical spectral indices to *1)* a sample of luminous, high-mass quasars at $1.0 < z < 1.2$, and *2)* that they also have similar spectral indices to luminous quasars in the SDSS at $z > 1.8$. We therefore find that our sample quasars have UV-optical spectra that are representative of the broader population of luminous quasars.

4.3 The X-Ray SED

Here, we present the X-ray detection statistics and X-ray spectral measurements for our sample. Our main results regarding the X-ray observations are as follows.

- Our RQQ subsample is fainter in the X-rays relative to the RLQ subsample, confirming previous results (e.g., Zamorani et al. 1981). Only 40% of our RQQs are detected in X-rays.
- Taking non-detections into account, the intrinsic X-ray luminosity distribution for our RQQ subsample is roughly consistent with that found for UV-luminous RQQs in the sample presented by L16.

- Our RLQ sample spans a more narrow range of X-ray luminosities than does the RLQ sample presented by M11.
- The distributions of X-ray photon indices for our RLQ and RQQ subsamples are statistically indistinguishable. Previous studies find significantly softer X-ray spectra for RQQs. This is likely due to the poor X-ray photon statistics for our X-ray detected RQQs.

We elaborate these results in the remainder of this Section.

X-ray detection completeness: While we detect 92% of the RLQ subsample in X-rays, only 40% of the RQQ subsample are detected. Many of the X-ray detected RQQs have background-subtracted total XRT counts $N_{\rm sub} \sim 20$ (Figure 7), and are close to our 3σ X-ray detection limit (as defined in Paper 1) given the background levels for these data. Thus, the XRT-detected RQQ sample may represent an upper envelope in terms of X-ray luminosities for the entire RQQ sample, as discussed further below.

Monochromatic luminosities at 2 keV: For X-ray detected quasars, our sample spans $2.3 < \nu L_\nu(2\,{\rm keV})/10^{44}$ erg s$^{-1} < 153.7$ (Figure 8, left panel). At these high luminosities, the non-AGN contribution to the X-ray emission should be minimal: the brightest non-transient X-ray sources apart from AGN are the ultra-luminous X-ray binaries, which do not exceed $\nu L_\nu(2\,{\rm keV}) \sim 10^{42}$ erg s^{-1} (Colbert & Ptak 2002). The 3σ upper limits on the X-ray luminosity for our X-ray non-detected quasars have a median value of $\nu L_\nu(2\,{\rm keV}) \approx 9 \times 10^{44}$ erg s^{-1}. Thus, our X-ray non-detections are not necessarily extremely faint; the upper limits overlap with the luminosity distribution of the detected quasars, with an offset of a factor ~ 2.2 between the average luminosities of detected quasars and the upper limits for non-detections (Figure 8, left panel).

We see a significant difference in the distributions of L_ν for the X-ray detected RLQ and RQQ subsamples (Figure 8, right panel). The X-ray detected RQQs have an average X-ray luminosity of $\langle \nu L_\nu \rangle = 1.3(\pm 0.3) \times 10^{45}$ erg s^{-1}, with a sample standard deviation of $\sigma_{\nu L_\nu} = 1.5 \times 10^{45}$ erg s^{-1}. The X-ray detected RLQs are on average a factor ~ 3 brighter, with average luminosities $\langle \nu L_\nu \rangle = 4.0(\pm 0.5) \times 10^{45}$ erg s^{-1}, and a rather large sample standard deviation, $\sigma_{\nu L_\nu} = 3.8 \times 10^{45}$ erg s^{-1}. A two-sample KS test excludes that the X-ray luminosity distributions for detected RLQs and RQQs are drawn from the same parent distribution (with a null hypothesis probability $p < 10^{-5}$), confirming previous findings (e.g., Zamorani et al. 1981).

W12 find comparable average X-ray luminosities to those of our sample, for their *Swift* XRT observations of $z \sim 2$ quasars (Figure 8, right panel). Most of their X-ray detected RQQs at $z > 1.6$ have few background-subtracted XRT counts, and are thus close to their X-ray detection limit, which is also the case for our RQQ subsample. This indicates that *Swift* XRT is only able to detect RQQs at $z \sim 2$ if they are atypically X-ray bright. Indeed, our X-ray detected RQQs are brighter than those presented by L16 at comparable redshifts (Figure 9, left panel). This is a direct consequence of the low X-ray detection rate for RQQs in our sample. The L16 X-ray detected sample extends to much lower 2 keV luminosities than are detectable using *Swift* XRT observations at these redshifts (Figure 9, green dots). Thus, we need to consider the
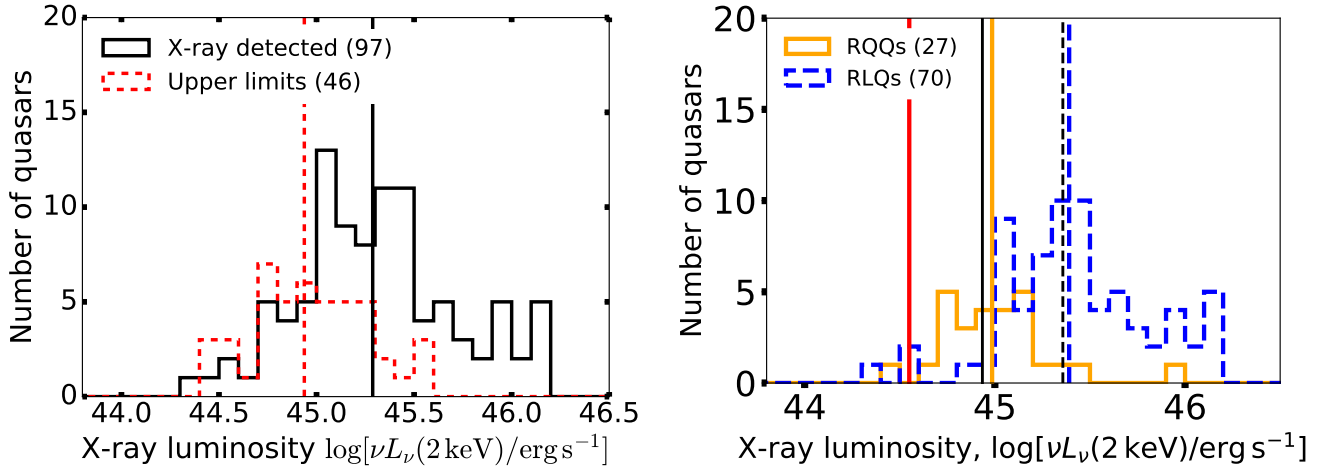
Figure 8. *Left:* Distribution of $\nu L_\nu(2\,\mathrm{keV})$. Upper limits for non-detections are at the 3σ level. We also show the mean 2 keV luminosities for X-ray detected sources (solid black line) and upper limits (dashed red line). *Right:* Distribution of $\nu L_\nu(2\,\mathrm{keV})$ for X-ray detected RQQ and RLQ subsamples. The median X-ray luminosities for the RQQ and RLQ subsamples (vertical orange and blue lines, respectively) differ by a factor ~ 2.2. The X-ray luminosity of the mean SED for the $z < 1$ quasar sample presented by E94 (red vertical line) is a factor ~ 2.5 dimmer than the median values for our X-ray detected RQQs. The median 2 keV luminosities for RQQs (solid black line) and RLQs (dashed black line) for $1.5 < z < 3.5$ quasars presented by W12 are similar to those of our RQQ and RLQ subsamples. Their study is based on serendipitous *Swift* observations, and is therefore indicative of the population of $z \sim 2$ quasars that can be detected in X-rays using *Swift* XRT.
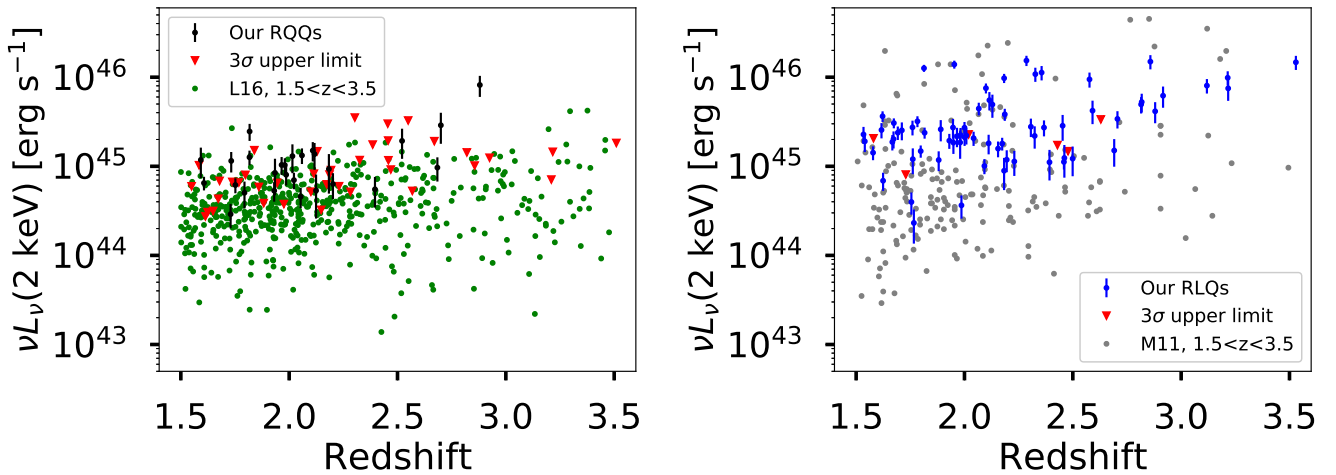
Figure 9. *Left:* Redshift distribution of 2 keV luminosities for our X-ray detected RQQ subsample (black circles). Upper limits for non-detections (red triangles) are at the 3σ level. The radio-quiet, $1.5 < z < 3.5$ sources presented by L16 with similar 2500 Å luminosities to our sample (green dots) extend to lower luminosities than do our X-ray detected RQQs. However, a Kaplan-Meier survival analysis suggests that the luminosity distributions are roughly consistent when accounting for the large number of non-detections in our RQQ subsample (§4.3). *Right:* Redshift distribution of 2 keV luminosities for our RLQ subsample (blue circles). Here, we also show the radio-loud, $1.5 < z < 3.5$, X-ray detected sources presented by M11 (gray circles).

X-ray non-detections in our RQQ subsample in order to perform a robust comparison with the deep X-ray observations presented by L16.

In order to probe the underlying X-ray luminosity distribution for our sample, we utilize the Kaplan-Meier (KM) estimator[6], a survival analysis technique (Feigelson & Nelson 1985; Isobe et al. 1986), which accounts for censored data (here, X-ray non-detections). Including the upper limits for non-detections, the KM estimates of the median luminosity are $\nu L_{\nu,\mathrm{KM}} = 5.3 \times 10^{44}$ erg s^{-1} for our RQQ subsample, and $\nu L_{\nu,\mathrm{KM}} = 2.3 \times 10^{45}$ erg s^{-1} for our RLQs. For our RQQs, the KM estimator of the median luminosity is similar to the

---

[6] We use the implementation of the KM estimator algorithm provided by the *lifelines* package (`https://github.com/CamDavidsonPilon/lifelines/`), a Python interpretation of survival analysis techniques.
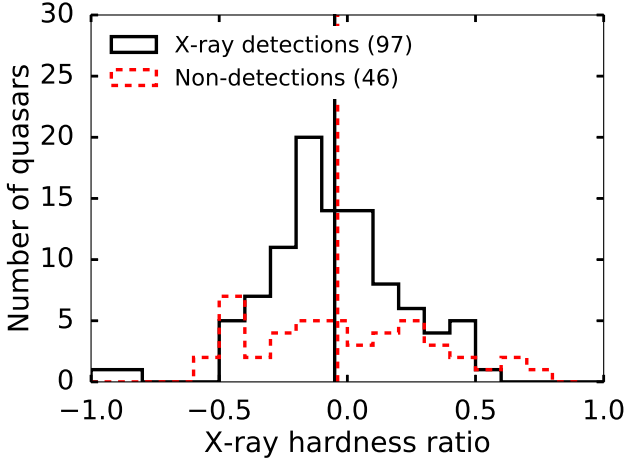
Figure 10. Distribution of the X-ray hardness ratio for our sample. Here, the soft band is 0.3 keV - 1.5 keV, while the hard band is the 1.5 keV - 10 keV range. Larger values of HR imply harder X-ray spectra. The vertical lines indicate the median HR for the detected and non-detected subsamples.

median X-ray luminosity, $\nu L_\nu (2\,\mathrm{keV}) = 4.6 \times 10^{44}$ erg s^{-1}, for X-ray detected RQQs at redshifts $1.5 < z < 3.5$, and with UV luminosities exceeding 4.7×10^{45} erg s^{-1} in the sample presented by L16 (541 quasars). We impose this UV luminosity cutoff on the L16 sample in order to match the UV luminosities of our RQQs. Formally, survival analysis techniques assume that the censoring is random (e.g., Feigelson & Nelson 1985), which is not the case for flux-limited samples. The KM estimator may therefore be biased towards a high median luminosity for the RQQ sample, given the low ($\sim$40%) X-ray detection rate for our RQQs. However, the agreement of our $\nu L_{\nu,\mathrm{KM}}$ with the median X-ray luminosity for the redshift- and UV-luminosity matched quasars presented by L16 supports that the KM estimator is not strongly biased in this case.

The distribution of X-ray luminosities for our RLQ sample overlaps with that of the $1.5 < z < 3.5$ quasars presented by M11. However, their sample quasars display a broader range of X-ray luminosities. In particular, their sample contains sources with X-ray luminosities roughly one order of magnitude fainter than our faintest RLQs (Figure 9, right panel). Given that our RLQ sample only includes six non-detections, this discrepancy is unlikely to be due to non-detected sources. Instead, it is probably due to their sample spanning a larger range of UV luminosities than does ours, given the log-linear relationship that M11 identify between UV and X-ray luminosity for RLQs. Also, our RLQs are 3C sources, and are therefore among the most radio loud RLQs, while M11 also include sources with more moderate radio loudness values. M11 find that the excess X-ray luminosity for RLQs is proportional to their radio loudness, which suggests that our quasars will have a large excess X-ray luminosity. We demonstrate that our RLQs are consistent with the existing $L_{\mathrm{UV}}-L_X$ relationship for RLQs in §4.5.

In summary, our RLQs appear to have intrinsic X-ray luminosities typical of luminous $z \sim 2$ quasars, as further demonstrated in §4.5. We only detect an X-ray bright subpopulation

of RQQs. The Kaplan-Meier estimator of the median 2 keV luminosity for our RQQs, accounting for non-detections, is consistent with the typical 2 keV luminosities for luminous $z \sim 2$ quasars in the sample presented by L16.

X-ray hardness ratios: We calculate the X-ray hardness ratio for each quasar, including XRT non-detections, following the method described in Paper 1. We define the soft and hard bands as observed-frame 0.3 keV − 1.5 keV and 1.5 keV − 10.0 keV, respectively. A positive X-ray hardness ratio corresponds to there being more photon counts in the hard band than in the soft band. This crude measure of the X-ray spectral slope is useful in cases for which the photon index Γ is not well-determined. Quasars with $HR \gtrsim 0$ may be intrinsically absorbed (Wilkes et al. 2013). We present the hardness ratios in Table 2. For X-ray detections we find a mean hardness ratio $\langle HR \rangle = -0.06 \pm 0.03$, with a sample standard deviation $\sigma_{HR} = 0.26$ (Figure 10). For non-detections, $\langle HR \rangle = -0.01 \pm 0.05$ and $\sigma_{HR} = 0.35$. Thus, there is no indication that the non-detected quasars differ in X-ray hardness from the detected objects. However, for the majority of the non-detections, HR is poorly determined, with uncertainties consistent with one of the extreme values ($HR = \pm 1$). The mean hardness ratios for RLQs (including non-detections, $\langle HR \rangle = -0.06 \pm 0.03$) and RQQs (including non-detections, $\langle HR \rangle = -0.02 \pm 0.04$) are consistent. Only eight sources (of which, one is an X-ray detection) have $HR > 0$ at the 2σ confidence level. Thus, while we cannot quantify the intrinsic absorbing column in our XRT modeling (Paper 1), the data are consistent with little intrinsic absorption for most X-ray detected objects. Two XRT-detected RQQs, Q0253-024 and Q1225-017, have anomalously soft X-ray spectra, with $HR < -0.8$. Both objects are consistent with zero photon counts in the hard X-ray band, given the background levels.

The X-ray photon index, Γ: We model the observed-frame 0.3–10 keV X-ray spectrum as a power-law plus Galactic absorption (§2.3). Given the redshift range of our sample, this corresponds to a rest-frame energy range of $\sim$1–30 keV. We therefore do not expect the observed X-ray spectrum to be strongly contaminated by soft X-ray excess, as this emission component is strongest at energies below ~ 1 keV (e.g., Petrucci et al. 2018). However, the observations do cover the iron K complex ~ 6.4 keV and the iron absorption edge at ~ 7 keV − 9 keV (e.g., Nandra & Pounds 1994). For higher-redshift objects, our observations also cover the broad Compton reflection hump (e.g., Lightman & White 1988), which is most prominent at ~ 25 keV. We are not able to discern these features from the X-ray continuum emission in our XRT data. If present, they may introduce a systematic bias of the measured photon index relative to that of the underlying continuum.

For our X-ray detected quasars, we find a full range of photon indices $1.08 \leqslant \Gamma \leqslant 3.54$ (Figure 11, left). For RLQs and RQQs we find average photon indices $\langle \Gamma \rangle = 1.64 \pm 0.03$ and $\langle \Gamma \rangle = 1.71 \pm 0.10$, respectively. The median values of Γ are 1.60 and 1.62 for RQQs and RLQs, respectively. Thus, the measured photon indices are statistically indistinguishable for RQQs and RLQs in our sample. We see no significant trend of Γ with redshift. Two RQQs have very soft X-ray spectra, with $\Gamma > 2.5$; these are the objects with $HR < -0.8$ discussed above. These two quasars have $N_{\mathrm{sub}} < 15$ (Figure
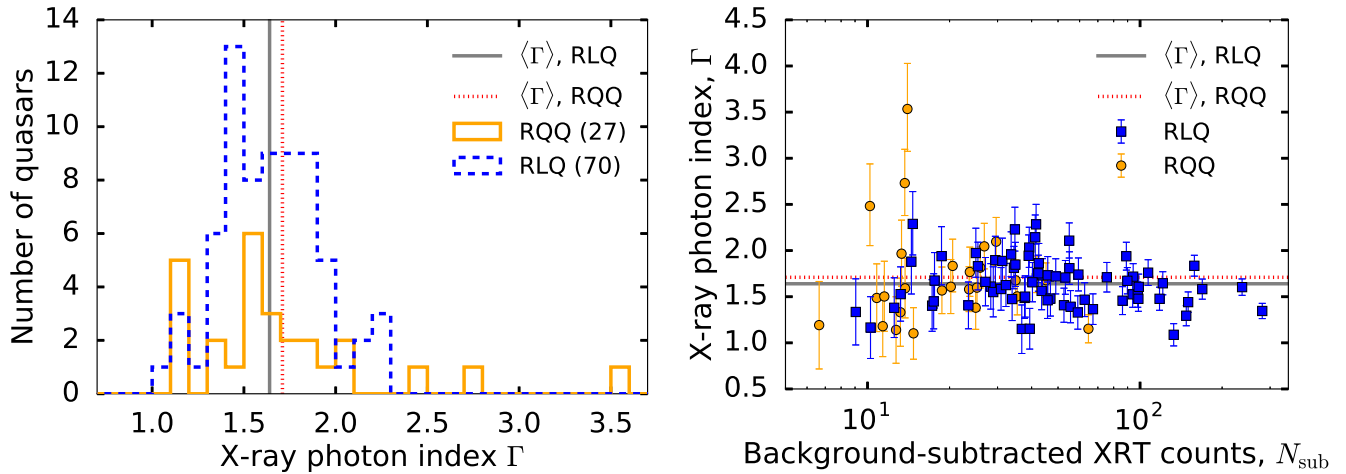
Figure 11. *Left:* Distribution of the X-ray photon index Γ for X-ray detected quasars, measured over the observed-frame energy range 0.3 keV - 10 keV. The 68% confidence intervals on individual measurements of Γ range from $\Delta\Gamma \sim 0.1$ for observations with $N_{\rm sub} \sim 100$, to $\Delta\Gamma \sim 0.4$ for marginal detections. The average values of Γ for RLQs (grey solid line) and RQQs (red dotted line) are consistent to within their 1σ uncertainties. *Right:* The X-ray photon index displayed as a function of the background-subtracted number of XRT counts (0.3–10 keV) for X-ray detected RQQs (orange circles) and RLQs (blue squares). Outliers with $\Gamma \gtrsim 2.5$ have $N_{\rm sub} \lesssim 15$ counts, which results in rather large uncertainties on Γ for these sources.

11, right), with correspondingly large uncertainties on the measured photon index, $\Delta_\Gamma \sim 0.5$.

We firstly compare our RLQ photon indices with previous results. W12 find $\langle\Gamma\rangle = 1.72 \pm 0.12$ for the 13 X-ray detected RLQs at redshifts $1.5 < z < 3.5$ in their sample. These quasars have very similar X-ray luminosities to our RLQ sample (Figure 8), while being on average slightly fainter in terms of UV luminosity (Figure 5). Similarly, Page et al. (2005) find $\langle\Gamma\rangle = 1.55 \pm 0.04$ for the rest-frame energy interval 2–10 keV, with a sample standard deviation $\sigma_\Gamma = 0.28$, for 16 $z > 2$ RLQs that are on average a factor ~ 10 X-ray brighter than our RLQ sample. Scott et al. (2011) present a sample of 75 RLQs spanning a broad range of X-ray luminosities. For RLQs with $L_\nu(2 \text{ keV}) > 3 \times 10^{45}$ erg s^{-1}, they find $\Gamma \sim 1.68$ when modeling the X-ray spectrum as a simple power-law, consistent with our results. Thus, our mean value of Γ for RLQs is consistent with those measured for $z \gtrsim 1.5$ RLQs in previous studies. In Paper 1 we found $\langle\Gamma\rangle = 1.46 \pm 0.05$ for 23 X-ray detected RLQs, all of which are included in the present work. This preliminary result was mildly inconsistent with previous studies of RLQ. We attribute this discrepancy to the smaller sample size in our previous work.

For the RQQ subsample, our measured photon indices are surprisingly small. For the 541 RQQs presented by L16 with $1.5 < z < 3.5$ and UV luminosities exceeding 6.7×10^{45} erg s^{-1}, the average photon index is $\langle\Gamma\rangle = 1.89 \pm 0.02$, with a sample standard deviation of $\sigma_\Gamma = 0.54$. If we instead select quasars from the L16 study with comparable X-ray luminosities to our RQQ sample (437 sources), the average photon index is $\langle\Gamma\rangle = 1.90 \pm 0.02$. The *average* photon index for RQQs in our sample is inconsistent with this result at the $\sim 2\sigma$ level, while our *median* $\Gamma = 1.60$ for RQQs is discrepant at the $\sim 3\sigma$ level. Also, our distributions of photon indices for RLQs and RQQs are statistically indistinguishable. Both Page et al. (2005) and Scott et al. (2011) find that RQQs have, on average, softer X-ray spectra (i.e., larger Γ) than

RLQs. Scott et al. (2011) study 522 RQQs and 75 RLQs. Their RLQ and RQQ subsamples are not significantly different from each other in terms of redshift or absolute i-band magnitude, suggesting that there is an underlying physical difference in the X-ray emission for the two radio classes. As our RLQ and RQQ samples are also well-matched in redshift and luminosity, we might also expect to find larger photon indices for RQQs relative to RLQs.

We suspect that the anomalously small measured Γ values for our RQQs are due to the large modeling uncertainties for sources in our sample with few background-subtracted XRT counts, $N_{\rm sub}$. All but three of our RQQs have $N_{\rm sub} < 30$ (Figure 11). In their *Swift* XRT spectral modeling, W12 include Γ as a modeling parameter only for observations with $N_{\rm sub} \geqslant 30$, and *assume* $\Gamma = 1.9$ otherwise. They find an average $\langle\Gamma\rangle = 2.0 \pm 0.02$ with a sample standard deviation $\sigma_\Gamma = 0.24$ for sources with $N_{\rm sub} > 30$, which is consistent with the deeper X-ray observations presented by Lusso & Risaliti (2016). These results indicate that the photon index is underestimated for our X-ray detected RQQ subsample, due to the poor X-ray photon counting statistics.

In summary, our RLQs display X-ray photon indices consistent with existing $z \sim 2$ RLQ samples, while our RQQs display significantly lower Γ (i.e., harder X-ray SEDs) than found in the literature. Our X-ray spectral modeling is likely biased towards low values of Γ for X-ray detected sources with low total XRT counts, $N_{\rm sub} < 30$. For this reason, we cannot determine whether the RQQs have X-ray spectra typical of the broader $z \sim 2$ population of luminous quasars. In contrast, most of our RLQs have $N_{\rm sub} > 30$. The measured X-ray photon indices for our RLQs are consistent with those found for the broader RLQ population at $1.5 < z < 3.5$.
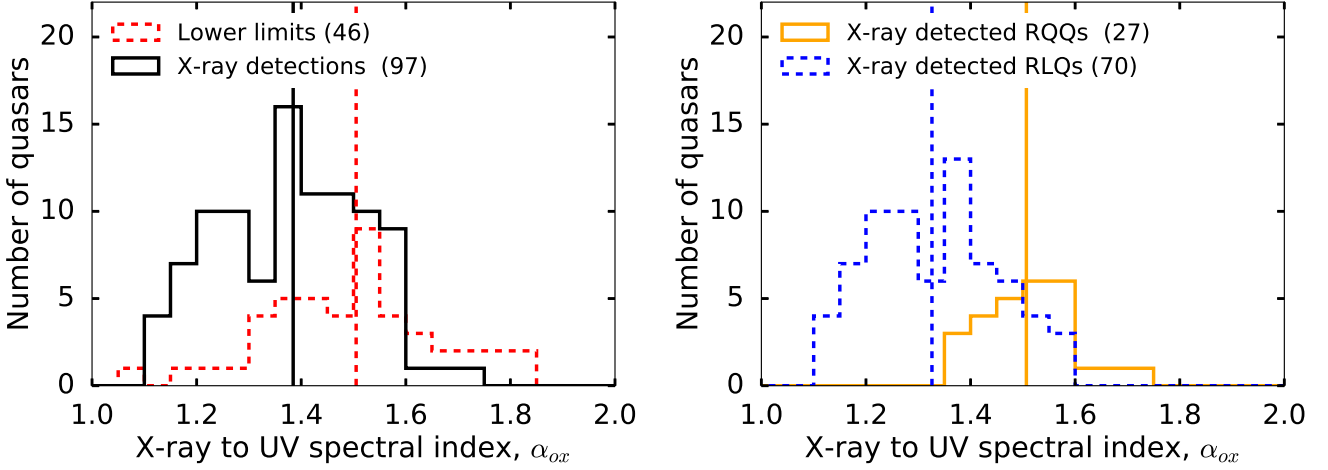
Figure 12. *Left panel:* Distribution of α_{ox} (and 3σ upper limits for X-ray non-detections) for all quasars detected with UVOT; an XRT non-detection corresponds to a lower limit on α_{ox}. *Right panel:* Distribution of α_{ox} between radio types, for X-ray detected quasars. The vertical lines indicate the median α_{ox} for the subsamples.

4.4 The X-ray to UV Spectral Index, α_{ox}

The X-ray to UV-optical spectral index, α_{ox}, is defined by Tananbaum et al. (1979) as

$$\alpha_{ox} = -\frac{\log(F_\nu(2\,\text{keV})/F_\nu(2500\,\text{Å}))}{\log(\nu(2\,\text{keV})/\nu(2500\,\text{Å}))}. \qquad (1)$$

Smaller values of α_{ox} correspond to relatively X-ray brighter sources. We present measurements of α_{ox}, or its 3σ lower limit for XRT non-detections, for each quasar in Table 6. We see no trend of α_{ox} with redshift for our sample.

Given that our RLQ and RQQ subsamples have similar distributions of optical luminosity, the larger median 2 keV luminosities for our RLQ subsample leads to smaller values of α_{ox} for X-ray detected RLQs (Figure 12). The X-ray detected RLQs have a mean value $\langle\alpha_{ox}\rangle = 1.33 \pm 0.01$, with a sample standard deviation of 0.12 (Figure 12). For the 27 X-ray detected RQQs we find $\langle\alpha_{ox}\rangle = 1.51 \pm 0.02$, with a sample standard deviation of 0.08 (Figure 12). However, as discussed in §4.3, we only detect an X-ray luminous subset of our RQQs with *Swift* XRT. It is therefore necessary to account for X-ray non-detections in order to estimate the intrisic median α_{ox} for our RQQs.

Including the six non-detected RLQs, the Kaplan-Meier estimate of the median is $\alpha_{ox,KM} = 1.36$. Thus, the median α_{ox} for our RLQs is not strongly sensitive to the inclusion of non-detected sources.

The KM estimator of the median α_{ox} for the RQQs, including the 41 non-detections, is $\alpha_{ox,KM} = 1.59$. This suggests that our RQQs are, on average, intrinsically fainter in X-rays than our RLQs, at a given UV luminosity. Alternatively, the discrepancy might be a byproduct of the much lower X-ray detection rate for our RQQs. To investigate this possibility, we first compare the distribution of α_{ox}, including lower limits, for the entire sample (RLQs and RQQs). These distributions are significantly offset from each other, as evidenced by two-sample KS tests (Table 7). For the combined sample, the X-ray detections are mostly radio-loud, while the non-detections are radio-quiet. On the other hand, the distributions of α_{ox} measurements for X-ray detections versus

α_{ox} lower limits for non-detections are *not* significantly offset within the individual RLQ and RQQ subsamples. I.e., within each radio class, the intrinsic α_{ox} values for X-ray detections and non-detections are consistent with being drawn from the same underlying sample. This supports that the observed difference in Kaplan Meier estimators for the median α_{ox} in our RLQ and RLQ subsamples is indeed driven by the difference in intrinsic X-ray brightness between RLQs and RQQs.

For RLQs at redshifts $1.5 < z < 3.5$ in the sample presented by M11, the average value of α_{ox} is 1.38 ± 0.01, with a sample standard deviation of 0.14. For those $1.5 < z < 3.5$ RLQs that also have optical luminosities comparable to our sample (96 sources), $\langle\alpha_{ox}\rangle = 1.43 \pm 0.02$. These results are consistent with the KM estimator median, $\alpha_{ox} = 1.36$,for our RLQs. W12 find $\langle\alpha_{ox}\rangle = 1.28 \pm 0.03$ for 41 X-ray detected RLQs at redshifts $1.5 < z < 3.5$. This result is broadly consistent with our median α_{ox} for X-ray detected RLQs.

W12 find $\langle\alpha_{ox}\rangle = 1.41 \pm 0.03$ for 174 X-ray detected RQQs at redshifts $1.5 < z < 3.5$. As discussed in §4.3, given the observing efficiency of *Swift* XRT, the X-ray detected RQQs presented by W12 represent an X-ray bright subset of the general RQQ population, as do ours. The underlying α_{ox} distribution for RQQs extends to larger values (i.e., softer UV to X-ray SEDs) than can be detected with *Swift* XRT. For RQQs at $1.5 < z < 3.5$ in the sample studied by L16 with UV luminosities comparable to our RQQs (541 sources), the average α_{ox} is 1.64 ± 0.01, with a sample standard deviation of 0.14. This is broadly consistent with our KM estimator of the sample median for RQQs, $\alpha_{ox,KM} = 1.59$, although our KM estimator implies a slightly X-ray brighter underlying luminosity distribution. This is probably due to our upper limits on the X-ray luminosity for non-detections being rather bright (e.g., Figure 9) relative to the detected faint X-ray sources in their sample.

In summary, the distribution of α_{ox} for our RLQs is consistent with the broader population of $z \sim 2$ RLQs, as represented by a redshift-matched subsample of the sample presented by M11. As *Swift* XRT only detects an X-ray luminous subset of quasars at $z \sim 2$, it is vital to account for non-
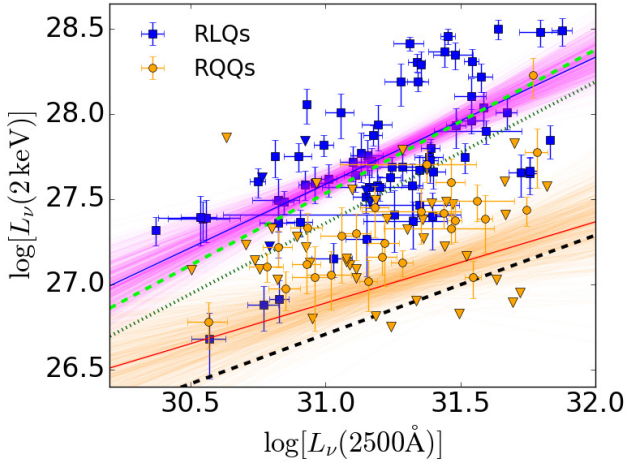
Figure 13. UV versus X-ray luminosities, for all quasars detected in at least one UVOT bandpass. At a given L_ν (2500 Å), X-ray detected RLQs (blue squares) tend to be brighter at 2 keV than do X-ray detected RQQs (orange circles). For X-ray non-detections, downwards-pointing triangles denote 3σ upper limits on L_X. The most likely linear relationships are shown as a solid blue line for RLQs and a solid dark orange line for RQQs. The magenta and orange shaded regions display a randomly-drawn subset of the individual realizations generated by our Bayesian analysis; thus, the shaded region corresponds to the posterior distribution of the model. We show the linear relations found by M11 for all RLQs in their sample (dark green dotted line) and for RLQs with radio loudness parameter $R^* \geqslant 3$ (dashed light green line). Our most likely log-linear relationship for RLQs is most consistent with the relationship presebted by M11 for $R^* \geqslant 3$ sources. For the RQQs, our most likely log-linear relationship lies above the regression line obtained by L16 (black dashed line). This is likely due to us only detecting the X-ray brightest RQQs, and obtaining insufficiently faint limiting X-ray luminosities for non-detections.

detections in order to estimate the underlying distribution of α_{ox}. The KM estimator median α_{ox} for RQQs in our sample is broadly consistent with the average α_{ox} values found for RQQs in previous work.

4.5 The L_{UV}–L_X Relationship

The non-linear relationship between L_{UV} and L_X for RQQs (e.g., L16, and references therein) implies that more UV-luminous AGN transfer less of their available accretion energy into the X-ray corona. Here, we examine to what degree our RLQ and RQQ subsamples display this behavior, and whether they are consistent with the previously established L_{UV}–L_X relationships. We use the L_{UV} values derived from our UV-optical continuum model (§3), which are corrected (in a statistical sense) for broad-line and Balmer continuum emission. As M11 show that the L_{UV}–L_X relationship for RLQs is offset relative to RQQs, we treat the two radio sub-samples individually. We consider a log-linear relationship of the form

$$\log\left[\frac{L_\nu(2\,\text{keV})}{1\,\text{erg s}^{-1}\text{Hz}^{-1}}\right] = A + B\log\left[\frac{L_\nu(2500\,)}{1\,\text{erg s}^{-1}\text{Hz}^{-1}}\right], \quad (2)$$

and use the Linmix_err algorithm (Kelly 2007) to obtain

the best-fit intercept, A, and slope, B. The Linmix_err code applies a Bayesian statistical analysis to the regression problem, via a Monte Carlo Markov Chain (MCMC) algorithm. It allows for an intrinsic scatter in the dependent variable (here, L_X), and accounts for censored data (here, limiting fluxes for X-ray non-detections). This approach is more powerful than survival analysis techniques for linear regression (e.g., Isobe et al. 1986)), as the latter techniques do not account for measurement uncertainties or intrinsic scatter. For high X-ray detection rates, these methods produce very similar results (L16). However, Kelly (2007) demonstrates that only Linmix_err retrieves an unbiased estimate for low X-ray detection rates and large measurement uncertainties, appropriate for our RQQ sample.

The most likely values of the A and B parameters, as determined using Linmix_err, are listed in Table 9. For each of the RLQ and RQQ subsamples, we perform the modeling once using only the X-ray detected objects, and again including the censored data. Due to the limited range of L_{UV} for our sample, the mean values of the intercept A are not well-determined in any of these regressions. However, the distribution of realizations of the L_{UV}–L_X relationship produced by Linmix_err for RLQs and RQQs are distinct in the sense that RLQs have higher X-ray luminosities than RQQs at a given UV luminosity (Figure 13). For comparison purposes, we also list in Table 9 the parameters found by L16 for RQQs, and by M11 for RLQs. We quote the relationships found for the full samples presented in these studies, without imposing redshift or luminosity cutoffs, as the statistical power of their regressions depends on having large dynamic ranges in UV and X-ray luminosities. Thus, we are investigating whether our quasar samples (with limited dynamic ranges in terms of UV and X-ray luminosities) are consistent with the broader AGN populations in terms of the L_{UV}–L_X relationship.

We first discuss our results for the RQQ subsample. The relationship presented by L16 for a sample of 2685 RQQs (Figure 13, dashed black line) is marginally consistent with our Linmix_err regression (solid orange line), at least at $\log[L_\nu(2500\,\text{Å})/\text{erg s}^{-1}\text{Hz}^{-1}] \gtrsim 31.5$. Only one X-ray detected RQQ in our sample lies below the log-linear relationship determined for the entire RQQ sample. This confirms that our XRT observations only detect an X-ray bright subset of the full X-ray luminosity distribution for RQQs, as first discussed in §4.3, and implies that the log-linear relationship we find is highly dependent on the limiting X-ray luminosities for non-detections. Given the large number of X-ray non-detections for our RQQ sample, we cannot exclude that our RQQs follow an underlying L_{UV}–L_X relationship consistent with that found by L16.

Our regression results for RLQs (Figure 13, solid blue line) are consistent with those found by M11 for the most radio-loud sources in their sample (dotted green line). These sources have $R^* \geqslant 3$, where $R^* = \log[L_\nu\,(5\,\text{GHz})] - \log[L_{UV}]$. Their relationship for the full RLQ sample (dotted dark green line) is offset from ours towards lower X-ray luminosities. Given that many of our RQQ sample are originally detected in the Cambridge 3C and 4C radio catalogs (§2), they are among the most radio-luminous sources at $z \sim 2$. Therefore, their radio luminosities correspond to the most radio-loud sources in the M11 sample. Our results are thus consistent with the correlation between radio loudness and X-ray luminosity found by M11.

In summary, the $L_{\rm UV}$–$L_{\rm X}$ relationships found for our RLQ subsample is consistent with previous results for highly radio-loud quasars. Our regression results exclude a 1:1 relationship between $L_{\rm UV}$ and $L_{\rm X}$ at the $\sim 2.5\sigma$ level based on the uncertainties on the slope parameters B (Table 9), suggesting that RLQs become relatively more X-ray faint at higher UV luminosities, as also found by M11 at a higher significance. For RQQs, our $L_{\rm UV}$–$L_{\rm X}$ analysis confirms that we only detect the X-ray brightest sources, as also implied by the low values of $\alpha_{\rm ox}$ for the X-ray detected RQQs (§4.4). Accounting for X-ray non-detections, our RLQ subsample displays a trend in $L_{\rm UV}$–$L_{\rm X}$ that may be consistent with the results presented by L16, although we would require deeper *Swift* XRT observations to obtain sufficiently tight limiting X-ray luminosities in order to confirm this.

4.6 Integrated Luminosities

Here, we use our observed UV–optical-X-ray SEDs to estimate the integrated accretion luminosities of our sample quasars. We use these integrated luminosities to estimate the Eddington ratios for our sample quasars (§5.4).

UV–optical luminosities: We integrate the UV continuum model (§3.3) over the rest-frame interval 1000 Å – 3000 Å to obtain the UV–optical luminosity due to the continuum component, $L_{\rm UV}$. These measurements are tabulated in Table 6. We determine the uncertainties of these integrated luminosities by integrating over the $\pm 1\sigma$ uncertainties on $f_\lambda(\lambda)$, as determined from the uncertainties on $\beta_{\rm UV}$ and the flux normalization using standard error propagation.

X-ray luminosities: The lowest rest-frame energy observed by XRT is 1 keV for a source at $z = 2$. We integrate the luminosity of the absorption-corrected X-ray model (§2.3) over the rest-frame energy range 1 keV – 25 keV, and we denote this quantity L_X(1-25 keV). This range roughly corresponds to the rest-frame energies observed by XRT, given the redshift distribution of our sample. To aid comparison with other AGN samples, we also calculate L_X (0.3-10 keV) and L_X (2-10 keV), both integrated over the respective energy intervals in the rest-frame. All three luminosities are determined based on the same XSPEC model, namely, that fitted to the observed-frame interval 0.3-10 keV. The 1σ uncertainties on the integrated X-ray luminosities are determined using the XSPEC *lumin* task, assuming that the underlying distribution of parameter values is a multivariate Gaussian, with distribution widths calculated from the fit covariance matrix. We list these various measures of X-ray luminosity for each X-ray detected source in Table 6. For X-ray detected quasars, we find $0.08 \lesssim L_X(\text{2-10 keV})/10^{46}$ erg s$^{-1} \lesssim 4.75$.

The measurement of L_X (0.3-10 keV) involves an extrapolation of our model fit into the unobserved soft X-ray regime. Thus, L_X (0.3-10 keV) will be systematically underestimated if these quasars have a significant soft X-ray excess, as the XRT data generally extend to rest-frame $\sim$1 keV (Figure 4). The typical soft excess strength in $z \sim 2$ quasars is currently unknown. However, the physical mechanism producing the soft X-ray excess may be Compton upscattering of UV continuum emission in the accretion disk atmosphere (Czerny & Elvis 1987) or in a warm (0.1 keV $< kT_e <$1 keV) corona

(Done et al. 2012; Jin et al. 2013; Petrucci et al. 2018). In both scenarios, the SED of the resulting soft excess component will depend on the energies of the UV seed photons. In the context of thin-disk models, at a given black hole spin value, the large black hole masses for our sample (§5.3) lead to SED turnovers at lower energies relative to low-mass AGN. In that case, a lack of extreme-UV seed photons may preclude the generation of a soft X-ray emission feature for massive quasars.

EUV and total accretion luminosities: We estimate the unobserved extreme-UV (rest-frame 1000Å–1 keV) luminosity, $L_{\rm EUV}$, as the integrated luminosity of our power-law EUV interpolation (§3.4). This estimate, combined with our X-ray and UV-optical continuum models, provides a rough measure of the integrated luminosity between 3000 Å and 25 keV. Given that we have isolated the contribution of the accretion disk, and the X-ray emission believed to be ultimately powered by the accretion process (§1), we denote this quantity the accretion luminosity, $L_{\rm acc}$. In particular, $L_{\rm acc}$(3000Å–25 keV)$= L_{\rm UV} + L_{\rm EUV} + L_{\rm X}$ represents the integrated luminosity over the energy range covered by *Swift* and by the SDSS photometry for our sample, plus the interpolated luminosity over the unobservable EUV. We present $L_{\rm EUV}$ and $L_{\rm acc}$(3000Å–25 keV) for each X-ray detected quasar in Table 6. The 1σ uncertainties on $L_{\rm EUV}$ for X-ray detected quasars are calculated by extrapolating between the 1σ limiting values of the 1000 Å and 1 keV flux densities, and integrating over these adjusted EUV power-law flux distributions. The mean accretion luminosity for our X-ray detected RLQs ($\langle L_{\rm acc} \rangle = 1.0(\pm 0.2) \times 10^{47}$ erg s^{-1}) is consistent with that of the detected RQQs ($\langle L_{\rm acc} \rangle = 0.8(\pm 0.1) \times 10^{47}$ erg s^{-1}). A two-sample KS test does not exclude that the $L_{\rm acc}$ distributions are drawn from the same parent population ($p = 0.46$). The full ranges of accretion luminosities are similar between RLQs and RQQs (Figure 14, left panel).

For Novikov & Thorne (1973) thin-disk models with black hole masses $M_{\rm BH} \sim 10^9 M_\odot$, a substantial fraction of the total energy output is emitted in the rest-frame optical regime, especially for slowly rotating black holes. We therefore also need to consider the rest-frame optical emission to avoid systematically underestimating the accretion luminosity. While the SDSS photometry does not cover the rest-frame optical for our sample, we make a rough estimate of the accretion luminosity between 1μm–25 keV via extrapolation of our UV continuum model to 1μm using the measured continuum slope. We denote this quantity $L_{\rm acc}$(1μm–25 keV). According to this extrapolation, the energy emitted in the unobserved region 3000 Å – 1 μm accounts on average for 16% of $L_{\rm acc}$(1μm–25 keV). Our extrapolation of the UV continuum beyond the observed energy range (i.e., beyond $\sim$ 3000 Å) introduces an additional uncertainty on the integrated accretion luminosity. This is due to the potentially non-negligible spectral curvature in the rest-frame optical regime. In particular, in the context of Novikov & Thorne (1973) thin-disk models, quasars with massive black holes $M_{\rm BH} \gtrsim 10^9 M_\odot$ and low values of the spin parameter have SED turnovers in the rest-frame UV (as demonstrated in Chapter 6.3 of this Thesis). In that case, the continuum slope in the unobserved rest-frame optical is steeper than that in the rest-frame UV. Our naive power-law extrapolation of the observed continuum SED does not account for this spectral curvature. In addition,
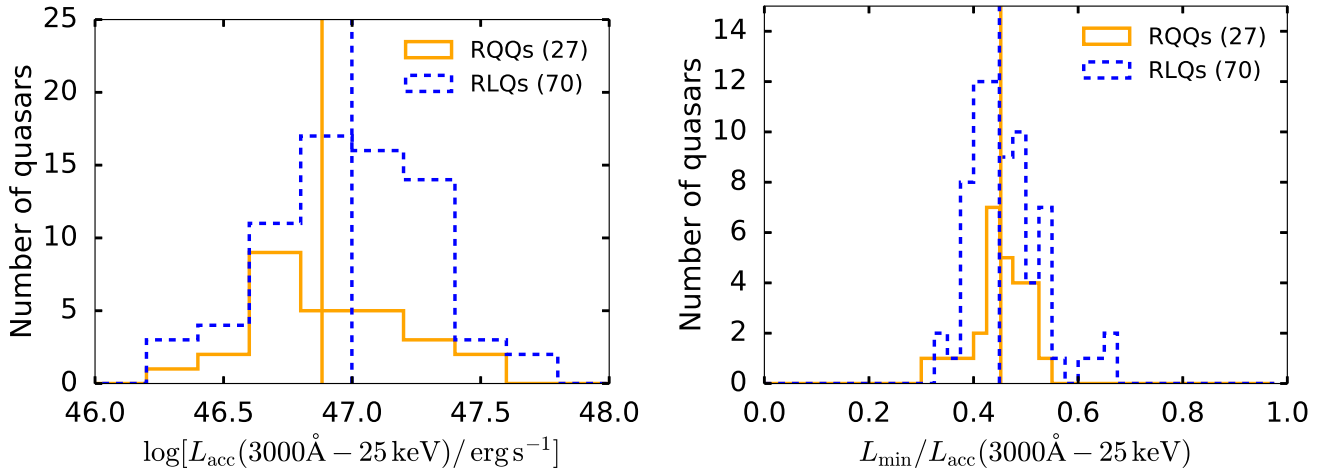
Figure 14. *Left:* Histogram of L_{tot} (3000 Å – 25 keV) for RQQs and RLQs detected with XRT. *Right:* Ratio of the integrated luminosity in the directly observed regions, $L_{min} = L_{int}$ (1000 Å –3000 Å)+ L_{int} (1 keV – 25 keV), to the integrated luminosity including the EUV power-law extrapolation, L_{tot} (3000 Å– 25 keV). The vertical lines indicate the median luminosities (or ratios) for the RQQ and RQQ subsamples.

there may be significant intrinsic reddening for some objects in our sample, which would lead to an underestimation of the continuum slope emitted by the accretion disk. In particular, the RLQs Q0458-020 (Figure B6), Q2222+051 (Figure B24) and Q2338+042 (Figure B25) display shallow UV–optical spectra, with $\beta_{UV} < 1$, which could be due to either an intrinsic SED turnover or intrinsic reddening. Our available *Swift* and SDSS broad-band photometry cannot strongly constrain the amount of intrinsic reddening for individual quasars. On the other hand, the majority of our sample do not show evidence for a spectral turnover in the observed energy range; for these sources, the naive power-law extrapolation may be appropriate. Given these uncertainties, we present our accretion luminosity estimates both in terms of L_{acc}(3000Å–25 keV) and L_{acc}(1μm–25 keV).

Minimum accretion luminosities: The above estimates of the accretion luminosity include significant emission at energies that are not constrained by our data. Both estimates of L_{acc} involve an interpolation over the EUV, while L_{acc}(1μm–25 keV) also includes an extrapolation over the rest-frame optical regime. We therefore also consider a robust minimum accretion luminosity L_{min}, defined as $L_{min} = L_X(1-25\,\text{keV}) + L_{UV}$(3000Å–1000Å). This corresponds to the integrated luminosity across all *observed* energies, assuming zero emission for all unobserved regions of the SED. We find L_{min}/L_{acc}(3000 Å–25 keV)∼ 0.45 for our sample, with no significant difference between RQQs and RLQs (Figure 14, right panel). Thus, according to our chosen interpolation scheme, a substantial fraction of the accretion luminosity is indeed emitted in the EUV.

5 DISCUSSION

5.1 Are Our Quasars Representative of the Broader Population at $z \sim 2$?

The main objective of this work is to ascertain to which degree the quasars included in our SED catalog are representative of the broader $z \sim 2$ quasar population.

The UV Luminosity Distribution: The distributions of UV luminosities for these quasars (§4.2, Figure 5) reveal that the majority of our $z \sim 2$ quasars have 2500 Å luminosities consistent with typical bright spectroscopically confirmed quasars in the SDSS at $z \sim 2$, as presented by S11. However, those quasars in our sample with redshifts $z \gtrsim 2.8$ are atypically bright relative to the SDSS quasar sample. In terms of UV luminosities, we therefore find that only the lower-redshift ($z \lesssim 2.8$) members of our sample can be regarded as representative of the broader population of bright quasars, whereas our $z \sim 3$ quasars are unusually bright.

The UV–optical SED Shapes: Our quasars have UV–optical continuum slopes that are consistent with previous results for quasars within the same redshift range (§4.2).

The X-ray Emission: For the RLQ subsample, the distributions of X-ray photon indices (§4.3) and of the UV to X-ray spectral index, α_{ox} (§4.4) are consistent with previous studies of $z \sim 2$ RLQs. The X-ray luminosity distributions for RLQs and RQQs are significantly different, with our RLQs generally being X-ray brighter, consistent with previous results (e.g., Zamorani et al. 1981; Miller et al. 2011). The brighter X-ray emission for RLQs is not well understood at present, but may be due to emission from the radio jet (e.g., Miller et al. 2011). Our RLQ sample displays a trend in which UV-brighter sources are relatively X-ray fainter, as seen for the broader RLQ population (M11).

Our analysis of the α_X distribution and the $L_{UV}-L_X$ relationship for RQQs demonstrates that we only detect an X-ray

bright subset of the underlying RQQ population with XRT. This is an unavoidable consequence of using *Swift* XRT for X-ray studies of $z \sim 2$ quasar populations, given the fainter X-ray emission of RQQs. Indeed, our distributions of α_{ox} and 2 keV luminosities for RQQs are consistent with those found by W12 using *Swift* XRT, but are inconsistent with the results of deeper X-ray studies using *Chandra* and/or *XMM-Newton*, for which much X-ray fainter RQQs are detected (e.g., L16, $\langle \alpha_{ox} \rangle \sim 1.8$). For RQQs, the small number of X-ray photons received even for detected sources also impairs our ability to measure the X-ray spectral slope accurately (§4.3). We find similar X-ray photon indices for RLQs and RQQs, whereas comparison studies based on deep *XMM-Newton* observations reveal that RQQs tend to have softer X-ray spectra.

In summary, the majority of our sample have luminosities and SED diagnostics that are consistent with other bright sources at $z \sim 2$, with the caveat that the X-ray properties of the RQQ sample are not strongly constrained. However, a subset of our quasars residing at $z \gtrsim 2.8$ have unusually bright UV luminosities, and are therefore not representative of the broader population of $z \sim 3$ quasars.

5.2 Our RQQs and RLQs have Indistinguishable UV–optical SEDs

Our radio-quiet and radio-loud subsets are selected to have similar distributions of redshift and V-band absolute magnitude (§2). However, we did not select them based on broadband UV–optical SED characteristics. Our *Swift* UVOT observations (and supplementary SDSS photometry) reveal that the RQQs and RLQs have statistically indistinguishable UV-optical SEDs. This suggests that the SED shape produced by the thermal disk component for typical RLQs and RQQs is similar, at least for those energy regimes that are accessible using *Swift* and SDSS photometry. Given the similarity between the UV–optical broadband SEDs for the two radio classes, our sample appears well-suited for future investigations of the radio loudness dichotomy for quasars.

5.3 The RLQs and RQQs Have Similar Black Hole Masses

In order to further investigate whether our sample quasars are representative of the broader population at $z \sim 2$, and to probe whether the RLQs and RQQs in our sample might have differences in black hole mass (M_{BH}), we now estimate the distributions of M_{BH}, for each radio subsample. We utilize single-epoch M_{BH} estimates (e.g., Vestergaard 2002),

$$M_{BH} = \frac{V_{vir}^2 R_{BLR}}{G} \approx f \frac{FWHM^2 (\lambda L_\lambda)^\alpha}{G}. \qquad (3)$$

Here, V_{vir} is the virial velocity of the gas emitting a given broad emission line, which is proportional to the emission line Full Width at Half-Maximum if the BLR is fully virialized or moves in Keplerian orbits. The factor f depends on the detailed geometry and source inclination of the BLR, and is usually determined in a statistical sense for ensembles of AGN. The $R_{BLR} \propto L_\lambda^\alpha$ relationship is determined via reverberation mapping of statistical samples of AGN, and is con-

sistent with $\alpha = 0.5$ when the reverberation mapping sample is corrected for host galaxy emission (Bentz et al. 2006, 2013).

We use the scaling relationship presented by Vestergaard & Peterson (2006) for the C IV broad emission line (their Equation 7). This relationship is calibrated for $L_\lambda(1350 \text{ Å})$. For quasars from the Vestergaard (2000) sample, we derive L_λ using the power-law UV continuum model presented by Vestergaard (2003), and use the C IV FWHM measured using the same spectra by Vestergaard (2000). For the 16 quasars in our SDSS sample, we measure both the FWHM and L_λ using the SDSS spectroscopy. For these objects, we use a variance-weighted average of M_{BH} calculated using C IV and Mg II. The Mg II scaling relation is presented by Vestergaard & Osmer (2009). We exclude 13 quasars from this analysis, as they lack rest-frame UV spectroscopy. Namely, Q0123+257, Q0249-184, Q0447-395, Q0518-350, Q1008-055, Q1151-004, Q1203-111, Q1225-017, Q1226-111, Q1318+113, Q1354+258, Q1557-199, and Q2338+042.

The sample spans black hole masses of $0.5 \leqslant M_{BH}/10^9 M_\odot \leqslant 32.3$ (Figure 15, left panel). This mass range is similar to that of the $z \approx 2$ quasars in the Large Bright Quasar Survey (Vestergaard & Osmer 2009), and that found for SDSS quasars at $z \approx 2$ (Shen & Kelly 2012). We see a trend for quasars with higher accretion luminosities to have more massive black holes (Figure 15, right panel), as noted in previous work (e.g., Peterson et al. 2004) and expected if quasars have similar mass-normalized accretion rates (i.e., Eddington ratios, §5.4). The uncertainties on M_{BH} for individual objects are of order 0.56 dex (Vestergaard & Peterson 2006). These uncertainties are due to the scatter of the mass scaling relationship with respect to the M_{BH} determined by reverberation mapping (0.36 dex), and the uncertainty on the normalization of the reverberation-mapping mass scale itself (0.46 dex, Onken et al. 2004). We find nine quasars for which $1 \times 10^{10} < M_{BH}/M_\odot < 6 \times 10^{10}$. However, given the large 1σ statistical uncertainties for our measurements, our M_{BH} distribution is consistent with true masses of $M_{BH} \lesssim 10^{10} M_\odot$ for all sample objects (Figure 15). Based on the Bayesian statistical analysis presented by Kelly et al. (2010), we might expect to find one or two quasars with true masses exceeding $10^{10} M_\odot$ in our sample of 130 quasars with mass estimates.

We find a similar average mass for RQQs and RLQs, namely, $\langle M_{BH} \rangle = (4.6\pm0.6)\times10^9 M_\odot$ for RQQs and $\langle M_{BH} \rangle = (3.9 \pm 0.5) \times 10^9 M_\odot$ for RLQs. Two-sample KM tests do not exclude that the M_{BH} for either the RLQ and RLQ subsamples ($p = 0.39$) or the XRT detections and non-detections ($p = 0.93$) are drawn from the same parent distribution. Thus, for a well-matched (in terms of optical luminosity and redshift, §2) sample of high-mass quasars, there is no significant difference in the M_{BH} distribution of RQQs and RLQs. In contrast, McLure & Jarvis (2004) do find a significant offset in single-epoch M_{BH} estimates for a sample of 6099 RQQs and 436 RLQs at $0.1 < z < 2.1$, selected from the SDSS. Phenomenologically, this offset is driven by the paucity of RLQs with $M_{BH} < 10^8 M_\odot$ in their sample (as evidenced by their Figures 1 and 2). Given that neither our RQQ nor our RLQ subsamples contain $M_{BH} < 10^8 M_\odot$ quasars, we cannot test the purported lack of low-mass RLQs. Here, we simply note that for bright RLQs and RQQs with matched V-band absolute magnitudes, there is no difference in black hole mass distributions. We conclude that our RLQ and RQQ subsamples
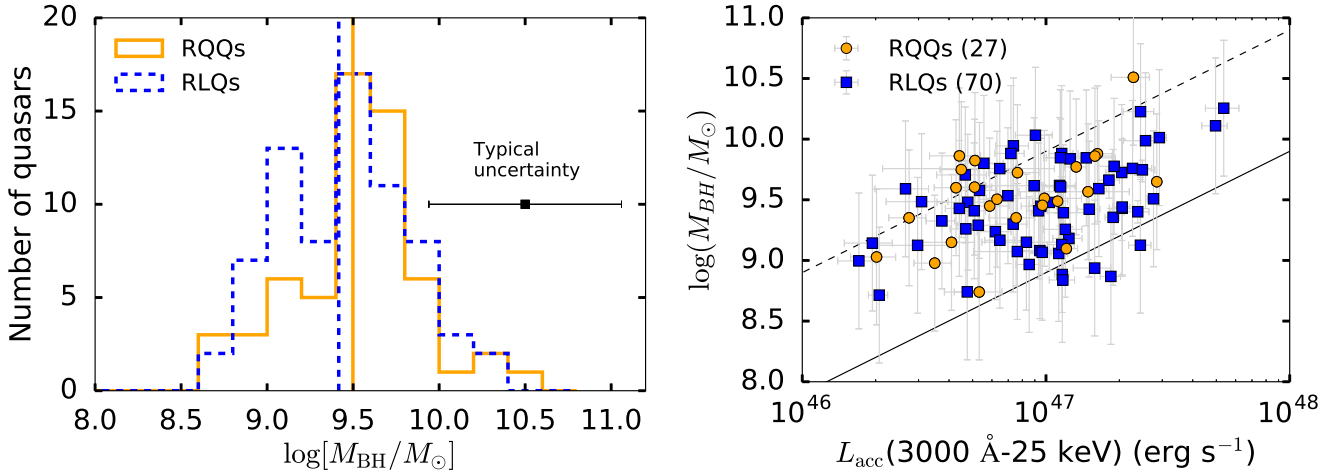
Figure 15. *Left:* The distribution of single-epoch M_{BH} estimates for our sample. The vertical lines indicate the median black hole masses for the RQQ and RQQ subsamples. *Right:* M_{BH} as a function of integrated accretion luminosity L_{tot} for our sample. The solid and dashed lines denote Eddington luminosity ratios L_{tot}/L_{Edd} of unity and 0.1, respectively. The uncertainties on M_{BH} are dominated by the scatter of the Vestergaard & Peterson (2006) scaling relationship with respect to the M_{BH} determined by reverberation mapping, and by the uncertainty on the normalization of the reverberation-mapping mass scale itself, as determined by Onken et al. (2004).

are well-suited to investigations of the differences in accretion properties between RLQs and RQQs.

5.4 The RLQs and RQQs Have Similar Eddington Ratios

Our sample RQQs and RLQs have similar distributions of accretion luminosity (§4.6) and of black hole mass (§5.3). Thus, they must have broadly similar accretion properties. In order to quantify this, we now calculate the distribution of Eddington ratios for these subsamples. This analysis also provides an important diagnostic of whether these quasars are accreting in the thin-disk regime (§1). For spherically symmetric accretion of ionized hydrogen, the Eddington luminosity, given by

$$L_{Edd} = 4\pi G m_p M_{BH} c \sigma_T^{-1}, \qquad (4)$$

is the limiting luminosity for which radiation pressure balances gravitational attraction. Here, m_p is the proton mass, σ_T is the cross-section for Thomson scattering, G is the gravitational constant, and c is the speed of light. The Eddington luminosity is not a strict upper limit for the energy output of quasars, as the accretion flow is not spherically symmetric and may be advective at high mass accretion rates. The Eddington ratio, L_{bol}/L_{Edd}, is therefore mainly useful in the context of AGN studies as an expression of the accretion luminosity normalized by black hole mass.

In this work we define the Eddington ratio as $\lambda_{acc} = L_{acc}(3000 - 25\,\text{keV})/L_{Edd}$, i.e., the ratio of our estimated accretion luminosity to the Eddington luminosity. We calculate this quantity for each X-ray detected quasar for which we also have an estimated black hole mass (§5.4), i.e., for 24 RQQs and 66 RLQs. For radio-quiet objects we find an average $\langle \lambda_{Edd} \rangle = 0.23 \pm 0.04$, with a full range $0.05 \leqslant \lambda_{Edd} \leqslant 0.77$ (Figure 16, left panel; Table 8). For RLQs we find a slightly higher average Eddington ratio, $\langle \lambda_{Edd} \rangle = 0.40 \pm 0.05$, with a

range of $0.05 \leqslant \lambda_{Edd} \leqslant 1.99$. While the RLQ sample appears to extend to higher Eddington ratios, a two-sample KS test yields $p = 0.09$, indicating that the distributions are not significantly different. For $z \sim 2.15$ quasars in the SDSS Data Release 7 (S11) with black hole masses of $M_{BH} \approx 5 \times 10^9 M_\odot$, Kelly & Shen (2013) find that the most common Eddington ratio is ~ 0.2, while sources emitting at Eddington ratios of ~ 1 are more rare by one or two orders of magnitude, consistent with our results. For 28 $z \sim 3$ quasars with black hole masses $M_{BH} \gtrsim 10^9 M_\odot$ Saito et al. (2016) find Eddington ratios of between ~ 0.05 and ~ 2, with most objects having Eddington ratios of around 0.3, again consistent with our findings. While there is an apparent anti-correlation between black hole mass and λ_{acc} (Figure 16, right panel), this is at least partially due to the uncertainties on M_{BH}. Quasars for which M_{BH} is underestimated will have overestimated Eddington ratios, and vice versa. *We would like to to investigate via Monte Carlo methods whether the observed anti-correlation is fully explained by the statistical scatter on M_{BH} before journal submission of this work.*

Uncertainties on λ_{acc}: The main uncertainties affecting our estimated λ_{acc} are the scatter of the black hole mass scaling relationship, and the modeling uncertainty on the integrated accretion luminosities. We first quantify the uncertainty due to the black hole mass estimates. We denote the Eddington ratios calculated using the 1σ upper and lower limits on the black hole masses as $L_{Edd,minM}$ and $L_{Edd,maxM}$, respectively. We remind the reader that using the maximum black hole mass value leads to the *minimum* estimate of λ_{acc}, and vice versa. Both $L_{Edd,minM}$ and $L_{Edd,maxM}$ are calculated using $L_{acc}(3000\,\text{Å}-25\,\text{keV})$. We present the resulting Eddington ratio distributions in Figure 17, top panels. One RQQ and six RLQs have $\lambda_{minM} > 0.3$. The distribution of λ_{maxM} demonstrates that the majority of our sample quasars have Eddington ratios of below one, even assuming that the black hole mass is underestimated at the 1σ level.
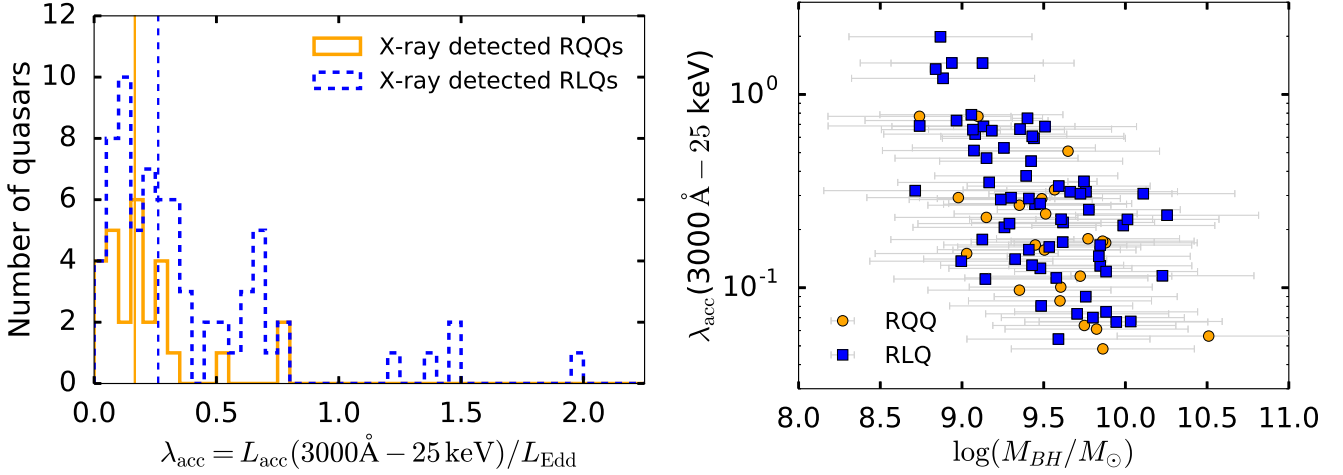
Figure 16. *Left:* The distribution of Eddington ratios, $\lambda_{\mathrm{acc}} = L_{\mathrm{acc}}/L_{\mathrm{Edd}}$, for our sample. Here, we use L_{tot} integrated between 3000 Å and 25 keV in the rest frame. The vertical lines indicate the median Eddington ratios for the RQQ and RQQ subsamples. *Right:* The Eddington ratio, λ_{acc}, as a function of black hole mass. The apparent anti-correlation is at least partially due to the large uncertainty in black hole mass: quasars with underestimated M_{BH} have overestimated λ_{acc}.

As our estimated EUV luminosities are model-dependent and may lead to overestimation of the true accretion luminosity, we calculate an alternative Eddington ratio, λ_{minL}, based on L_{min} as defined in §4.6. This quantity provides a robust lower limit on the Eddington ratio distribution, in a statistical sense; the uncertainties on M_{BH} still introduce scatter to the distribution of λ_{minL} for individual objects. All quasars in our sample are radiating below the Eddington limit based on this conservative estimate. Similarly, we calculate the Eddington ratio λ_{maxL} using the accretion luminosity integrated between 1 μm and 25 keV in order to include the rest-frame optical emission. In this case, the highest Eddington ratio in our sample is $\lambda_{\mathrm{maxL}} = 2.18$ (Figure 17, bottom right panel). We note that, even based on λ_{maxL}, all the RQQs in our sample are radiating at sub-Eddington rates. Thus, our RQQs do not tend to be super-Eddington accreters, although we cannot exclude that a handful of our RQQs may do so, given the uncertainties on their black hole masses.

In summary, our quasars have distributions of Eddington ratios consistent with those found for high-mass SDSS quasars at $z \sim 2$. There is no statistically significant evidence that any of our sample are super-Eddington accreters, given the uncertainties on M_{BH} and on L_{acc}. However, it seems likely that at least six sources are accreting in the 'slim-disk' regime, with $\lambda_{\mathrm{acc}} \gtrsim 0.3$ (Abramowicz et al. 1988; Sądowski et al. 2011), even accounting for these uncertainties.

6 SUMMARY AND CONCLUSIONS

We present *Swift* UVOT and XRT observations of a sample of 144 quasars residing at $1.5 < z < 3.5$. Of this sample, 143 are detected with UVOT (rest-frame UV), while 97 are detected with XRT (rest-frame $\sim$ 1–25 keV). We present X-ray–UV–optical SEDs of each sample quasar in Appendices A and B. The UV luminosities for those of our quasars that reside at redshifts $z \sim 2$ are consistent with those of the broader population of UV-luminous quasars, as observed with the SDSS. In contrast, those quasars in our sample that reside

at $z > 2.8$ are atypically UV-luminous relative to quasars in the SDSS, and are therefore not representative of the broader population of quasars at that redshift range.

All X-ray detected quasars in our sample are accreting at moderate to high Eddington luminosity ratios, $0.01 > L/L_{\mathrm{Edd}} \lesssim 2$, as also observed for the broader population of luminous $z \sim 2$ quasars. A handful of sources are robustly established to have Eddington ratios above 0.3; these quasars may harbor 'slim disks' (e.g., Abramowicz et al. 1988).

Our full sample is comprised of 76 RLQs and 67 RQQs. These radio-class subsamples are well-matched in terms of UV-optical luminosity and redshift. The majority (70) of our X-ray detected objects are RLQs. We confirm that our RLQs are on average more X-ray luminous than the RQQs, confirming previous results (e.g., Zamorani et al. 1981), and demonstrate that they are consistent with the UV–X-ray luminosity relationship for radio-loud sources presented by Miller et al. (2011). The RLQs have X-ray photon indices $\Gamma \sim 1.6$, and UV to X-ray spectral indices $\alpha_{\mathrm{ox}} \sim 1.4$, that are consistent with the broader population of $z \sim 2$ RLQs.

As the *Swift* XRT instrument is not sufficiently sensitive to detect a typical RQQ in X-rays at $z \sim 2$, our X-ray detected RQQs represent an X-ray luminous subset of the broader RQQ population. Accounting for the upper limits on X-ray luminosity for our non-detected sources, we find that the intrinsic distributions of X-ray luminosities and UV to X-ray SED shapes for our RQQ sample are likely also consistent with those of SDSS quasars within the same UV luminosity regime.

Our sample is not selected based on black hole mass. Nevertheless, the RQQs and RLQs show a similar distribution of single-epoch M_{BH} estimates, and have similar distributions of integrated accretion luminosity. For this reason, and given our careful pair-matching of RLQs and RQQs in redshift and V-band absolute magnitude, our sample is well-suited to comparison studies of accretion properties between the two radio classes. We will investigate this further in a follow-up study.

In conclusion, the quasars in this sample with redshifts
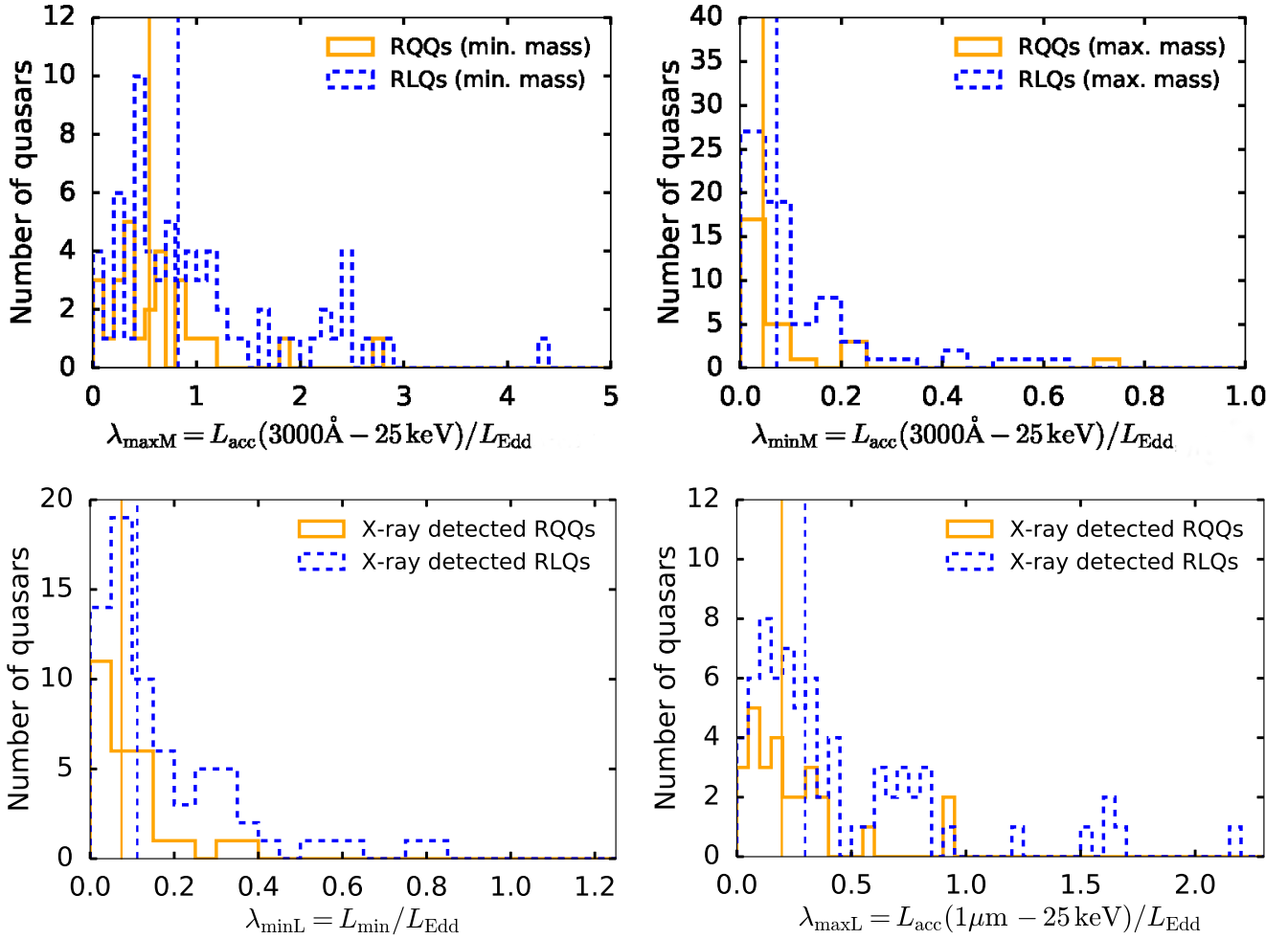
Figure 17. Sensitivity of Eddington ratio distributions to the uncertainties on black hole mass and to the choice of SED model. To illustrate the mass dependency, we recalculate the Eddington luminosity for each quasar using the 1σ lower-limit *(top left)* and 1σ upper-limit M_{BH} *top right*. To illustrate the SED model dependency, we recalculate the Eddington ratios using the minimum integrated luminosity, $L_{\mathrm{min}} = L_{\mathrm{UV}} + L_{\mathrm{X}}$ *(bottom left)*, and again using the $1\mu\mathrm{m} - 25$ keV integrated accretion luminosity *(bottom right)*. At least one RQQ and six RLQs are likely to have Eddington ratios $\lambda_{\mathrm{acc}} \gtrsim 0.3$, even accounting for the uncertainties in our analysis. However, no quasars in our sample are likely to have $\lambda_{\mathrm{acc}} > 5$. The vertical lines indicate the median ratios for the RQQ and RQQ subsamples.

below $z \sim 2.8$ have optical–UV–X-ray properties typical of luminous quasars in the SDSS. They are therefore representative of the broader population of bright quasars. However, the quasars in our sample with redshifts $z \gtrsim 2.8$ tend to be atypically bright relative to SDSS quasars at those redshifts, and are therefore not representative of the broader quasar population.

References

Abazajian K. N., Adelman-McCarthy J. K., Agüeros M. A., Allam S. S., Allende Prieto C., An D., Anderson K. S. J., Anderson S. F., 2009, The Astrophysical Journal Supplement Series, 182, 543

Abramowicz M. A., Czerny B., Lasota J. P., Szuszkiewicz E., 1988, ApJ, 332, 646

Alam S., et al., 2015, ApJS, 219, 12

Arnaud K. A., et al., 1985, MNRAS, 217, 105

Barthel P. D., 1989, ApJ, 336, 606

Barthel P. D., Miley G. K., Schilizzi R. T., Lonsdale C. J., 1988, Astronomy and Astrophysics Supplement Series, 73, 515

Barthel P. D., Vestergaard M., Lonsdale C. J., 2000, A&A, 354, 7

Becker R. H., White R. L., Helfand D. J., 1995, ApJ, 450, 559

Bennett A. S., 1962, MNRAS, 125, 75

Bentz M. C., Peterson B. M., Pogge R. W., Vestergaard M., Onken C. A., 2006, ApJ, 644, 133

Bentz M. C., et al., 2013, ApJ, 767, 149

Bian W.-H., Zhang L., Green R., Hu C., 2012, ApJ, 759, 88

Blandford R. D., Payne D. G., 1982, MNRAS, 199, 883

Blandford R. D., Znajek R. L., 1977, MNRAS, 179, 433

Burrows D. N., et al., 2005, Space Sci. Rev., 120, 165

Capellupo D. M., Netzer H., Lira P., Trakhtenbrot B., Mejía-Restrepo J., 2016, MNRAS, 460, 212

Colbert E. J. M., Ptak A. F., 2002, ApJS, 143, 25

Crummy J., Fabian A. C., Gallo L., Ross R. R., 2006, MNRAS, 365, 1067

Czerny B., Elvis M., 1987, ApJ, 321, 305

Dawson K. S., Schlegel D. J., Ahn C. P., Anderson S. F., Aubourg É., Bailey S., Barkhouser R. H., et al. 2013, AJ, 145, 10

Done C., Davis S. W., Jin C., Blaes O., Ward M., 2012, MNRAS, 420, 1848

Eisenstein D. J., et al., 2011, AJ, 142, 72

Elvis M., et al., 1994, ApJS, 95, 1

Elvis M., et al., 2012, ApJ, 759, 6

Fazio G. G., et al., 2004, ApJS, 154, 10

Feigelson E. D., Nelson P. I., 1985, ApJ, 293, 192

Gehrels N., et al., 2004, ApJ, 611, 1005

Ghosh R., Dewangan G. C., Raychaudhuri B., 2016, MNRAS, 456, 554

Guo H., Gu M., 2014, ApJ, 792, 33

Hewitt A., Burbidge G., 1989, The Astrophysical Journal Supplement Series, 69, 1

Hewitt A., Burbidge G., 1993, ApJS, 87, 451

Hill J. E., et al., 2004, in Flanagan K. A., Siegmund O. H. W., eds, Proc. SPIE Vol. 5165, X-Ray and Gamma-Ray Instrumentation for Astronomy XIII. pp 217–231, doi:10.1117/12.505728

Isobe T., Feigelson E. D., Nelson P. I., 1986, ApJ, 306, 490

Jiang L., Fan X., Ivezić Ž., Richards G. T., Schneider D. P., Strauss M. A., Kelly B. C., 2007, ApJ, 656, 680

Jin C., Ward M., Done C., 2012, MNRAS, 422, 3268

Jin C., Done C., Middleton M., Ward M., 2013, MNRAS, 436, 3173

Just D. W., Brandt W. N., Shemmer O., Steffen A. T., Schneider D. P., Chartas G., Garmire G. P., 2007, ApJ, 665, 1004

Kalberla P. M. W., Burton W. B., Hartmann D., Arnal E. M., Bajaja E., Morras R., Pöppel W. G. L., 2005, A&A, 440, 775

Kaspi S., Brandt W. N., Maoz D., Netzer H., Schneider D. P., Shemmer O., 2007, ApJ, 659, 997

Kellermann K. I., Sramek R., Schmidt M., Shaffer D. B., Green R., 1989, AJ, 98, 1195

Kelly B. C., 2007, ApJ, 665, 1489

Kelly B. C., Shen Y., 2013, ApJ, 764, 45

Kelly B. C., Vestergaard M., Fan X., Hopkins P., Hernquist L., Siemiginowska A., 2010, ApJ, 719, 1315

Kilerci Eser E., Vestergaard M., 2018, MNRAS, 474, 1590

Laor A., Fiore F., Elvis M., Wilkes B. J., McDowell J. C., 1997, ApJ, 477, 93

Lawther D., Vestergaard M., Raimundo S., Grupe D., 2017, MNRAS, 467, 4674

Lightman A. P., White T. R., 1988, ApJ, 335, 57

Lonsdale C. J., Barthel P. D., Miley G. K., 1993, The Astrophysical Journal Supplement Series, 87, 63

Lusso E., Risaliti G., 2016, ApJ, 819, 154

Lynden-Bell D., 1978, Phys. Scr., 17, 185

Lynden-Bell D., Rees M. J., 1971, MNRAS, 152, 461

Malkan M. A., Sargent W. L. W., 1982, ApJ, 254, 22

Maraschi L., Colpi M., Ghisellini G., Perego A., Tavecchio F., 2012, in Journal of Physics: Conference Series, Volume 355, Issue 1, id. 012016 (2012).. , doi:10.1088/1742-6596/355/1/012016

Margala D., Kirkby D., Dawson K., Bailey S., Blanton M., Schneider D. P., 2015, preprint, (arXiv:1506.04790)

McLure R. J., Jarvis M. J., 2004, MNRAS, 353, L45

Miller B. P., Brandt W. N., Schneider D. P., Gibson R. R., Steffen A. T., Wu J., 2011, ApJ, 726, 20

Nandra K., Pounds K. A., 1994, MNRAS, 268, 405

Netzer H., Trakhtenbrot B., 2014, MNRAS, 438, 672

Novikov I. D., Thorne K. S., 1973, in Dewitt C., Dewitt B. S., eds, Black Holes (Les Astres Occlus). pp 343–450

Onken C. A., Ferrarese L., Merritt D., Peterson B. M., Pogge R. W., Vestergaard M., Wandel A., 2004, ApJ, 615, 645

Padovani P., 1993, MNRAS, 263, 461

Page K. L., Reeves J. N., O'Brien P. T., Turner M. J. L., 2005, MNRAS, 364, 195

Park T., Kashyap V. L., Siemiginowska A., van Dyk D. A., Zezas A., Heinke C., Wargelin B. J., 2006, ApJ, 652, 610

Peterson B. M., et al., 2004, ApJ, 613, 682

Peterson B. M., et al., 2013, ApJ, 779, 109

Petrucci P. O., Ursini F., De Rosa A., Bianchi S., Cappi M., Matt G., Dadina M., Malzac J., 2018, A&A, 611

Piconcelli E., Jimenez-Bailón E., Guainazzi M., Schartel N., Rodríguez-Pascual P. M., Santos-Lleó M., 2005, A&A, 432, 15

Pilkington J. D. H., Scott J. F., 1965, Memoirs of the Royal Astronomical Society, 69, 183

Planck Collaboration et al., 2015, preprint, (arXiv:1502.01589)

Poole T. S. e. a., 2008, MNRAS, 383, 627

Porquet D., Reeves J. N., O'Brien P., Brinkmann W., 2004, A&A, 422, 85

Pu X., Bian W., Huang K., 2006, MNRAS, 372, 246

Reichard T. A., et al., 2003, AJ, 126, 2594

Richards G. T., et al., 2006, ApJS, 166, 470

Risaliti G., Lusso E., 2015, ApJ, 815, 33

Roming P. W. A., et al., 2005, Space Sci. Rev., 120, 95

Runnoe J. C., Brotherton M. S., Shang Z., 2012, MNRAS, 422, 478

Saito Y., et al., 2016, PASJ, 68, 1

Schlafly E., Finkbeiner D. P., 2011, in American Astronomical Society Meeting Abstracts #218. p. 318.03

Schmidt K. B., Rix H.-W., Shields J. C., Knecht M., Hogg D. W., Maoz D., Bovy J., 2012, ApJ, 744, 147

Schneider D. P., et al., 2005, AJ, 130, 367

Schneider D. P., et al., 2010, AJ, 139, 2360

Schulze A., Done C., Lu Y., Zhang F., Inoue Y., 2017, ApJ, 849

Scott A. E., Stewart G. C., Mateos S., Alexander D. M., Hutton S., Ward M. J., 2011, MNRAS, 417, 992

Selsing J., Fynbo J. P. U., Christensen L., Krogager J.-K., 2016, A&A, 585, A87

Shakura N. I., Sunyaev R. A., 1973, A&A, 24, 337

Shang Z., et al., 2005, ApJ, 619, 41

Shankar F., et al., 2016, ApJ, 818, L1

Shen Y., Kelly B. C., 2012, ApJ, 746, 169

Shen Y., et al., 2011, ApJS, 194, 45

Sądowski A., Bursa M., Abramowicz M., Kluźniak W., Lasota J. P., Moderski R., Safarzadeh M., 2011, A&A, 532

Steffen A. T., Strateva I., Brandt W. N., Alexander D. M., Koekemoer A. M., Lehmer B. D., Schneider D. P., Vignali C., 2006, AJ, 131, 2826

Stevans M. L., Shull J. M., Danforth C. W., Tilton E. M., 2014, ApJ, 794, 75

Strateva I. V., Brandt W. N., Schneider D. P., Vanden Berk D. G., Vignali C., 2005, AJ, 130, 387

Tananbaum H., et al., 1979, ApJ, 234, L9

Vanden Berk D. E., et al., 2001, AJ, 122, 549

Vanden Berk D. E., et al., 2004, ApJ, 601, 692

Veron-Cetty M. P., Veron P., 1991, European Southern Observatory Scientific Report, 10, 1

Vestergaard M., 2000, PASP, 112, 1504

Vestergaard M., 2002, ApJ, 571, 733

Vestergaard M., 2003, ApJ, 599, 116

Vestergaard M., Osmer P. S., 2009, ApJ, 699, 800

Vestergaard M., Peterson B. M., 2006, ApJ, 641, 689

Vestergaard M., Wilkes B. J., Barthel P. D., 2000, ApJ, 538, L103

Vignali C., Brandt W. N., Schneider D. P., 2003, AJ, 125, 433

Wilhite B. C., Vanden Berk D. E., Kron R. G., Schneider D. P., Pereyra N., Brunner R. J., Richards G. T., Brinkmann J. V., 2005, ApJ, 633, 638

Wilkes B. J., et al., 2013, ApJ, 773, 15

Wolfe A. M., Turnshek D. A., Lanzetta K. M., Lu L., 1993, ApJ, 404, 480

Worrall D. M., Giommi P., Tananbaum H., Zamorani G., 1987, ApJ, 313, 596

Wu J., et al., 2012, ApJS, 201, 10

Xie X., Shen S., Shao Z., Yin J., 2015, ApJ, 802, L16

Young S., Axon D. J., Robinson A., Capetti A., 2009, ApJ, 698, L121

Zamorani G., et al., 1981, ApJ, 245, 357

Zdziarski A. A., Johnson W. N., Magdziarz P., 1996, MNRAS, 283, 193

Table 1.   Quasars in our sample.

Object name (1)	RA [deg] (2)	Dec. [deg] (3)	Redshift (4)	$M_V{}^c$ [mag] (5)	SDSS data? (6)
Radio-Quiet Quasars					
J014725.50-101439.11	26.8562	-10.2442	2.14777	17.4	spec
J104915.44-011038.18	162.312	-1.1772	2.12943	17.9	bad
J110607.48-173113.60	166.531	-17.5204	2.54925	17.8	spec
J111159.70+023719.76	167.999	2.62215	1.88247	17.8	spec
J114449.32+032751.96	176.206	3.46443	2.10035	17.7	spec
J123034.21+073305.32	187.643	7.55148	1.81691		spec
J125140.83+080718.46	192.92	8.1218	1.60686		spec
J131810.74+011140.86	199.545	1.19468	1.64897	17.9	spec
J142923.92+024023.14	217.35	2.67309	1.67283	17.4	spec
J145717.86+024747.36	224.324	2.79649	1.97551	17.0	spec
J215543.09-073902.05	328.93	-7.65057	1.930819		spec
Q0000-001	0.87579863	0.13700795	2.56844	19.8	spec
Q0002-008	1.25177212	-0.56341528	2.17329	18.0	spec
Q0003-006	1.44369895	-0.40388145	1.72966	19.6	spec
Q0008-008	2.71231475	-0.5259068	2.05299	19.4	spec
Q0015+026	4.547375	2.944119444	2.469	18.7	spec
Q0020+022	5.853541667	2.565997222	1.798	18.6	phot
Q0040-017	10.730416667	-1.426733333	2.396	18.0	spec
Q0107-005	17.60211763	-0.2621962	1.75176	18.0	spec
Q0115-011	19.61663334	-0.87772392	2.18606	18.3	spec
Q0244+017	41.739916667	1.986558333	1.945	19.3	phot
Q0249-184	42.950075	-18.24143	3.21	18.6	
Q0252+016	43.812916667	1.807816667	2.457	18.2	
Q0253-024	43.916875	-2.231722222	1.986	19.3	spec
Q0254-016	44.168291667	-1.429505556	2.684	19.3	spec
Q0258+021	45.191666667	2.378983333	2.521	18.0	phot
Q0348+061	57.818791667	6.320616667	2.059	17.6	
Q0447-395	72.286125	-39.483758333	1.980	18.1	
Q0518-350	79.99666666	-34.962511111	2.23	18.2	
Q1008-055	152.655083333	-5.833258333	2.109	18.3	
Q1016-006	154.74984455	-0.90563639	2.18333	18.7	spec
Q1020+014	155.69770928	1.18147344	1.61347	18.1	spec
Q1043+071	161.431666667	6.923263889	2.114	19.3	phot
Q1045+052	161.94619051	4.9440704	2.12403	19.2	spec
Q1046+058	162.16701961	5.59759022	1.96516	18.7	spec
Q1137+305	175.0975182	30.28098015	1.59232	16.9	spec
Q1138+002	175.18197374	-0.02398411	1.7676	18.6	spec
Q1146+111	177.00132129	10.7098328	1.93451	18.9	spec
Q1151-004	178.44913494	-0.77376204	1.54971	18.0	spec
Q1203-111	181.413625	-11.384047222	2.283	19.6	
Q1208+105	182.867833333	10.247897222	1.86	18.5	phot
Q1219+491	185.58010054	48.86688058	2.32543	18.9	spec
Q1223+178	186.52997106	17.61385846	2.92484	18.1	bad
Q1225-017	186.996583333	-2.050961111	2.88	18.0	spec
Q1226-111	187.256208333	-11.388369444	2.455	19.3	
Q1227+120	187.422375	11.822011111	2.458	19.2	spec
Q1230+164	188.293458333	16.181513889	2.7	17.8	spec
Q1232-004	188.8748207	-0.69471666	1.58405	19.1	spec
Q1237+134	190.05503261	13.15778312	1.73254	17.8	spec
Q1246-022	192.35360875	-2.56104425	2.11697	18.1	spec
Q1259+344	195.524791667	34.160816667	2.82	19.1	phot
Q1330+011	203.22675	0.880775	3.51	18.2	spec
Q1409+095	213.071375	9.273886111	2.856	18.6	spec
Q1434-009	219.20907802	-1.2078048	1.67873	18.2	spec
Q1440-004	220.74962529	-0.62358948	1.81742	17.8	bad

Table 1   (cont'd)

Object name (1)	RA [deg] (2)	Dec. [deg] (3)	Redshift (4)	M_V^c [mag] (5)	SDSS data? (6)
Q1443-010	221.4981042	-1.22156759	1.79372	18.3	spec
Q1517+239	229.80564334	23.78267275	1.83929	18.4	spec
Q1634+406	248.93929082	40.50464465	1.7376	18.6	spec
Q1638+390	249.97436784	38.91365027	2.38541	18.5	spec
Q1704+710	256.108166667	70.959608333	2.015	17.5	
Q2233+136	339.11283443	13.9538915	3.21649	20.0	spec
Q2239+007	340.516208333	0.987605556	2.202	19.8	spec
Q2334+019	354.232875	2.203530556	2.193	19.0	bad
Q2341+010	356.118875	1.295155556	2.303	19.5	spec
Q2350-007	358.22298758	-0.48067585	1.62361	18.6	spec
Q2351+022	358.6265	2.569616667	2.022	18.6	spec
Q2359+002	0.550125	0.547847222	2.67	19.8	
Radio-Loud Quasars					
J082328.62+061146.07	125.869	6.19613	2.81524	18.0	spec
J094853.60+085514.40	147.223	8.92067	1.98179	17.3	spec
J112542.30+000101.33	171.426	0.017037	1.6923	17.6	spec
J215954.45-002150.17	329.977	-0.363937	1.965415		spec
J234830.41+003918.57	357.127	0.655158	2.00007	17.8	spec
Q0017+154	5.10508474	15.68186469	2.00873	18.2	spec
Q0038-019	10.358333	-1.720833	1.674	18.5	phot
Q0106+013	17.1615458	1.5834214	2.099	18.4	phot
Q0109+176	17.957625	17.897588889	2.155	18.7	spec
Q0123+257	21.678333333	25.983772222	2.356	17.5	
Q0206+293	32.286083333	29.546016667	2.195	19.0	phot
Q0225-014	37.032541667	-1.261044444	2.042	18.6	spec
Q0226-038	37.2217133	-3.6269792	2.066	17.0	phot
Q0238+100	40.342429	10.313098	1.816	18.0	
Q0317-023	50.119708333	-2.143925	2.092	19.5	
Q0352+123	58.939875	12.529386111	1.617	19.3	spec
Q0445+097	72.090875	9.847530556	2.115	19.6	
Q0458-020	75.303083333	-1.987330556	2.286	19.5	
Q0504+030	76.901833333	3.131030556	2.453	19.0	
Q0730+257	113.286541667	25.606866667	2.691	20.0	spec
Q0751+298	118.74304127	29.69841314	2.11148	18.5	spec
Q0758+120	120.25200809	11.88988182	2.62923	20.0	spec
Q0802+103	121.19986125	10.25659704	1.94889	18.3	spec
Q0805+046	121.989541667	4.542761111	2.88	18.3	spec
Q0808+289	122.90372798	28.75099895	1.89043	18.3	spec
Q0831+101	128.66922926	9.96525396	1.76146	19.6	spec
Q0835+580	129.77720918	57.90473216	1.53397	17.6	spec
Q0856+124	134.89075417	12.27593627	1.7664	19.4	spec
Q0926+117	142.1805	11.573419444	1.755	19.1	spec
Q0941+261	146.17632108	25.91203766	2.91649	18.0	spec
Q1023+067	156.633162	6.4591675	1.71091	18.5	spec
Q1055+499	164.55435889	49.66002987	2.39237	20.0	spec
Q1116+128	169.73874831	12.5782562	2.12883	19.3	spec
Q1158+122	180.2333067	11.95511912	2.01906	17.6	spec
Q1214+106	184.25572443	10.33137252	1.88099	18.5	spec
Q1221+113	186.08257512	11.12309603	1.76009	18.8	spec
Q1226+105	187.15368534	10.31165636	2.30641	18.5	spec
Q1258+404	195.13876692	40.15213796	1.67254	19.4	spec
Q1311-270	198.447323	-27.280352	2.186	17.4	
Q1313+200	199.102166667	19.784222222	2.461	17.4	bad
Q1318+113	200.32848474	11.11388098	2.18285	19.1	spec
Q1323+655	201.37380809	65.25369965	1.62434	17.7	spec
Q1354+258	209.27722638	25.62346685	2.00053	18.5	spec

Table 1 (cont'd)

Object name (1)	RA [deg] (2)	Dec. [deg] (3)	Redshift (4)	M_V^{c} [mag] (5)	SDSS data? (6)
Q1402+044	211.25467341	4.25994756	3.21486	18.8	spec
Q1402-012	211.1912308	-1.5060964	2.49924	18.2	spec
Q1442+101	221.318605	9.9766869	3.52952	17.3	spec
Q1540+180	235.58140846	17.93549729	1.66705	18.0	spec
Q1542+042	236.2476137	4.1295436	2.18294	18.0	spec
Q1554-203	239.338166667	-20.4865	1.947	19.2	
Q1556-245	239.922666667	-24.710825	2.818	19.2	
Q1557-199	240.045458333	-20.128125	1.58	19.5	
Q1602+576	240.982291667	57.514930556	2.858	18.3	spec
Q1606+289	242.046625	28.817219444	1.986	19.0	spec
Q1607+183	242.52203713	18.19540881	3.11884	18.5	phot
Q1614+051	244.15675	4.992288889	3.217	19.5	phot
Q1629+120	247.9385871	11.9341647	1.78288	18.5	spec
Q1629+680	247.46525	67.954152778	2.478	19.0	
Q1633+382	248.81456471	38.13458044	1.81313	18.1	spec
Q1656+477	254.51125	47.630202778	1.622	18.0	phot
Q1658+575	254.940416667	57.525041667	2.174	18.2	
Q1701+379	255.783166667	37.857277778	2.459	19.0	spec
Q1702+298	256.029625	29.782975	1.93	19.1	phot
Q1705+018	256.893458333	1.812319444	2.577	18.9	
Q1726+344	261.957291667	34.377738889	2.429	18.5	spec
Q1816+475	274.581083333	47.612227778	2.23	18.2	
Q1857+566	284.611791667	56.765747222	1.578	17.3	
Q2048+196	312.803125	19.835102778	2.367	18.5	
Q2150+053	328.351875	5.605227778	1.98	17.9	spec
Q2158+101	330.319333333	10.396494444	1.729	17.7	phot
Q2212-299	333.8168104	-29.7398142	2.706	17.3	
Q2222+051	336.311208333	5.452494444	2.324	18.5	phot
Q2223+210	336.408291667	21.301775	1.953	17.8	phot
Q2248+192	342.636583333	19.522244444	1.798	18.5	phot
Q2251+244	343.538375	24.756766667	2.327	18.2	phot
Q2338+042	355.241375	4.520977778	2.591	19.5	spec
Q2345+061	357.132166667	6.416502778	1.54	17.8	spec

Note. — (1) We list RQQs and RLQs separately in all tables. Quasars denoted *Qxxx.xxx* are selected by Vestergaard et al. (2000), while those denoted *Jxxx.xxx* are selected from SDSS DR7. The quasar denoted 'Q1626+115' in Paper 1 is included here as 'Q1629+120', so as to correspond to the J2000 naming convention used for the remainder of the sample. (2,3) Coordinates in decimal degrees for the standard epoch J2000. (4) Spectroscopic redshifts as retrieved from the NASA Extragalactic Database (https://ned.ipac.caltech.edu/). (5) V-band apparent magnitudes, compiled by Hewitt & Burbidge (1993). (6) Availability of SDSS broadband photometry and spectroscopy (§2.4). All objects with spectroscopy also have SDSS photometry. Quasars for which the photometric calibration is problematic according to the SDSS data quality flags are marked 'bad'; for these objects, we do not include the SDSS photometry in our UV-optical modeling.

Table 2. *Swift* XRT observation log and X-ray modeling.

Object name (1)	N_{obs} (2)	Δt [month] (3)	XRT exp. time [s] (4)	XRT detect? (5)	$F_{0.3-10}$ (6)	$F_\nu(2\,\mathrm{keV})$ (7)	Γ (8)	N_H [10^{22} cm^{-2}] (9)	N_{sub} (10)	HR (11)
Radio-Quiet Quasars										
J014725.50-101439.11	1	0.4	6650		<0.49	<0.58	—	0.0268	-0.4	—
J104915.44-011038.18	2	2.1	11001		<1.60	<2.70	—	0.0363	5.1	$-0.12^{+0.24}_{-0.56}$
J110607.48-173113.60	1	—	5769		<2.32	<4.37	—	0.0439	5.3	$-0.06^{+0.60}_{-0.60}$
J111159.70+023719.76	2	0.3	5711		<0.74	<0.88	—	0.0367	2.3	$0.31^{+0.20}_{-0.70}$
J114449.32+032751.96	2	0.3	5507		<0.81	<0.97	—	0.0199	2.7	$0.06^{+0.46}_{-0.16}$
J123034.21+073305.32	6	1.8	9894	✓	$2.40^{+0.49}_{-0.21}$	3.06 ± 0.57	$1.74^{+0.20}_{-0.21}$	0.016	41.8	$-0.16^{+0.16}_{-0.17}$
J125140.83+080718.46	8	1.6	15014	✓	$1.75^{+0.27}_{-0.23}$	1.97 ± 0.34	$1.68^{+0.19}_{-0.19}$	0.0189	45.2	$-0.14^{+0.17}_{-0.17}$
J131810.74+011140.86	1	—	5676		<0.76	<0.91	—	0.0206	2.0	$0.29^{+0.20}_{-0.71}$
J142923.92+024023.14	1	—	5020		<1.02	<1.22	—	0.0244	2.7	$-0.41^{+0.13}_{-0.59}$
J145717.86+024747.36	2	0.3	4885		<0.66	<0.79	—	0.0402	-1.3	—
J215543.09-073902.05	8	13.6	14020	✓	$1.44^{+0.30}_{-0.22}$	1.16 ± 0.29	$1.38^{+0.24}_{-0.23}$	0.0312	24.9	$-0.02^{+0.23}_{-0.24}$
Q0000-001	12	5.0	9560		<0.59	<0.70	—	0.0291	2.5	$0.05^{+0.95}_{-0.03}$
Q0002-008	6	2.5	3936		<0.93	<1.11	—	0.0303	-1.8	—
Q0003-006	13	7.3	10926	✓	$1.52^{+0.37}_{-0.38}$	0.77 ± 0.23	$1.10^{+0.28}_{-0.28}$	0.030	14.7	$0.48^{+0.33}_{-0.26}$
Q0008-008	20	6.6	20015	✓	$0.83^{+0.15}_{-0.19}$	0.89 ± 0.23	$1.57^{+0.25}_{-0.25}$	0.032	18.7	$-0.16^{+0.32}_{-0.31}$
Q0015+026	3	0.9	3481		<1.09	<1.30	—	0.0308	0.8	—
Q0020+022	2	0.4	3446		<1.66	<1.98	—	0.0324	2.8	$-0.26^{+0.20}_{-0.74}$
Q0040-017	16	7.7	8423	✓	$1.37^{+0.42}_{-0.40}$	0.82 ± 0.31	$1.18^{+0.33}_{-0.33}$	0.025	11.4	$0.58^{+0.23}_{-0.14}$
Q0107-005	9	4.4	16003	✓	$0.95^{+0.21}_{-0.14}$	1.60 ± 0.31	$2.05^{+0.25}_{-0.24}$	0.0309	26.8	$-0.41^{+0.21}_{-0.23}$
Q0115-011	4	1.9	5946		<1.18	<1.41	—	0.0389	4.7	$0.31^{+0.69}_{-0.36}$
Q0244+017	7	2.7	3963		<1.17	<1.40	—	0.0432	1.9	$0.64^{+0.36}_{-0.05}$
Q0249-184	7	5.2	11680		<0.54	<0.65	—	0.03	4.8	$-0.19^{+0.23}_{-0.81}$
Q0252+016	3	0.1	2987		<2.32	<2.77	—	0.0743	1.6	$-0.25^{+0.23}_{-0.75}$
Q0253-024	16	6.0	15765	✓	$0.61^{+0.09}_{-0.09}$	1.66 ± 0.40	$2.73^{+0.37}_{-0.35}$	0.0545	13.7	$-0.82^{+0.04}_{-0.19}$
Q0254-016	21	6.5	18508	✓	$0.97^{+0.28}_{-0.15}$	1.19 ± 0.36	$1.58^{+0.24}_{-0.24}$	0.0609	23.6	$0.18^{+0.25}_{-0.25}$
Q0258+021	10	6.0	8106	✓	$2.15^{+0.56}_{-0.61}$	2.63 ± 0.98	$1.60^{+0.25}_{-0.25}$	0.0685	25.2	$0.32^{+0.23}_{-0.22}$
Q0348+061	8	6.2	12559	✓	$4.59^{+0.50}_{-0.55}$	2.57 ± 0.51	$1.15^{+0.15}_{-0.15}$	0.1190	64.6	$0.09^{+0.14}_{-0.14}$
Q0447-395	10	5.4	11535	✓	$1.48^{+0.21}_{-0.21}$	2.15 ± 0.41	$1.81^{+0.22}_{-0.22}$	0.0207	25.9	$0.20^{+0.24}_{-0.30}$
Q0518-350	10	3.7	9005		<0.84	<1.01	—	0.0372	3.7	$0.60^{+0.40}_{-0.09}$
Q1008-055	7	6.8	6346	✓	$1.97^{+0.36}_{-0.42}$	2.79 ± 0.68	$1.77^{+0.27}_{-0.26}$	0.0366	23.7	$-0.03^{+0.22}_{-0.23}$
Q1016-006	2	6.6	4443	✓	$1.63^{+0.51}_{-0.50}$	1.63 ± 0.77	$1.50^{+0.38}_{-0.38}$	0.0456	11.5	$0.44^{+0.34}_{-0.28}$
Q1020+014	2	0.1	3571		<0.69	<0.82	—	0.0403	-1.3	—
Q1043+071	1	—	4213		<1.28	<1.53	—	0.0252	2.4	$0.73^{+0.27}_{-0.01}$
Q1045+052	1	—	3816	✓	$1.63^{+0.67}_{-0.64}$	0.98 ± 0.50	$1.19^{+0.47}_{-0.48}$	0.0269	6.6	$-0.15^{+0.43}_{-0.49}$
Q1046+058	5	7.1	11038	✓	$1.78^{+0.35}_{-0.25}$	2.18 ± 0.49	$1.68^{+0.22}_{-0.22}$	0.0238	34.9	$-0.23^{+0.17}_{-0.19}$
Q1137+305	2	0.4	1443	✓	$5.10^{+1.91}_{-1.77}$	3.64 ± 1.36	$1.33^{+0.37}_{-0.37}$	0.0193	13.2	$0.17^{+0.29}_{-0.26}$
Q1138+002	2	0.4	3948		<1.40	<1.68	—	0.0219	2.5	$-0.46^{+0.11}_{-0.54}$
Q1146+111	2	0.3	3434	✓	$3.36^{+0.65}_{-1.29}$	1.83 ± 0.80	$1.14^{+0.36}_{-0.36}$	0.0377	12.7	$0.08^{+0.31}_{-0.30}$
Q1151-004	5	0.4	3664		<1.62	<1.93	—	0.0202	3.3	$-0.01^{+0.48}_{-0.51}$

Table 2 (cont'd)

Object name (1)	N_{obs} (2)	Δt [month] (3)	XRT exp. time [s] (4)	XRT detect? (5)	$F_{0.3-10}$ (6)	$F_\nu(2\ keV)$ (7)	Γ (8)	N_H [10^{22} cm^{-2}] (9)	N_{sub} (10)	HR (11)
Q1203-111	4	0.3	5075		<0.70	<0.84	—	0.047	-2.2	—
Q1208+105	2	0.1	3276		<1.14	<1.36	—	0.0171	0.3	$0.08^{+0.92}_{-0.14}$
Q1219+491	3	0.1	3716		<1.54	<1.84	—	0.0125	3.8	$0.26^{+0.53}_{-0.23}$
Q1223+178	5	0.1	5409		<1.11	<1.33	—	0.022	2.2	$0.59^{+0.41}_{-0.05}$
Q1225-017	1	—	3052	✓	$1.67^{+0.40}_{-0.26}$	8.92 ± 2.37	$3.53^{+0.49}_{-0.46}$	0.0216	14.0	$-0.88^{+0.01}_{-0.12}$
Q1226-111	4	0.1	5154		<2.33	<4.29	—	0.0319	5.7	$-0.35^{+0.18}_{-0.43}$
Q1227+120	8	0.2	9370		<1.39	<1.66	—	0.0202	4.5	
Q1230+164	6	0.2	5811	✓	$1.99^{+0.85}_{-0.41}$	3.51 ± 1.34	$1.83^{+0.29}_{-0.28}$	0.0211	20.5	$-0.20^{+0.23}_{-0.24}$
Q1232-004	5	1.5	7439		<2.26	<3.20	—	0.0185	5.3	$0.17^{+0.53}_{-0.31}$
Q1237+134	2	10.2	3034	✓	$2.86^{+0.97}_{-0.69}$	3.04 ± 0.79	$1.61^{+0.30}_{-0.29}$	0.0269	20.2	$-0.04^{+0.28}_{-0.27}$
Q1246-022	6	0.6	4674	✓	$0.96^{+0.18}_{-0.26}$	2.53 ± 0.84	$2.48^{+0.46}_{-0.43}$	0.0171	10.2	$-0.43^{+0.27}_{-0.37}$
Q1259-344	7	1.3	3659		<1.35	<1.62	—	0.0111	2.6	$0.28^{+0.72}_{-0.21}$
Q1330-011	5	0.7	4458		<1.21	<1.44	—	0.0178	1.2	$-0.17^{+0.08}_{-0.83}$
Q1409+095	6	1.8	3689		<0.94	<1.13	—	0.0188	-3.0	—
Q1434-009	5	3.0	5427		<1.61	<1.92	—	0.0316	4.4	$0.29^{+0.71}_{-0.22}$
Q1440-004	6	3.2	3811	✓	$3.30^{+0.60}_{-0.75}$	5.97 ± 1.29	$2.10^{+0.26}_{-0.27}$	0.0326	29.6	$-0.36^{+0.17}_{-0.19}$
Q1443-010	8	6.1	4602	✓	$1.37^{+0.52}_{-0.39}$	1.25 ± 0.42	$1.49^{+0.37}_{-0.36}$	0.0377	10.8	$0.33^{+0.50}_{-0.25}$
Q1517+239	8	7.0	4378		<2.84	<3.59	—	0.0382	8.7	$-0.30^{+0.20}_{-0.70}$
Q1634+406	6	2.2	4405		<1.47	<1.76	—	0.0097	2.9	$-0.47^{+0.14}_{-0.53}$
Q1638+390	8	1.8	3366		<2.20	<2.63	—	0.0119	3.9	$0.43^{+0.57}_{-0.16}$
Q1704+710	9	3.0	5342	✓	$1.35^{+0.71}_{-0.32}$	2.62 ± 0.93	$1.97^{+0.36}_{-0.35}$	0.0414	13.3	$-0.05^{+0.31}_{-0.32}$
Q2233+136	6	0.2	4635		<1.11	<1.32	—	0.0455	1.1	$-0.34^{+0.12}_{-0.66}$
Q2239+007	12	7.2	11428	✓	$0.95^{+0.29}_{-0.24}$	1.09 ± 0.35	$1.59^{+0.32}_{-0.32}$	0.0537	13.7	$0.05^{+0.34}_{-0.35}$
Q2334+019	7	0.6	3923		<1.32	<1.57	—	0.0498	0.9	—
Q2341+010	3	1.5	3369		<3.19	<5.61	—	0.0372	5.6	$-0.58^{+0.12}_{-0.42}$
Q2350-007	5	2.7	4375		<0.76	<0.91	—	0.0323	-0.3	—
Q2351+022	13	6.0	17224	✓	$1.44^{+0.19}_{-0.23}$	1.40 ± 0.29	$1.50^{+0.20}_{-0.20}$	0.0312	35.4	$-0.03^{+0.20}_{-0.20}$
Q2359+002	3	2.5	3649	✓	<1.98	<2.37	—	0.0289	3.6	$-0.46^{+0.13}_{-0.54}$
Radio-Loud Quasars										
J082328.62+061146.07	2	0.1	7157	✓	$3.68^{+0.54}_{-0.46}$	5.61 ± 1.17	$1.71^{+0.18}_{-0.18}$	0.0229	53.2	$-0.22^{+0.13}_{-0.14}$
J094853.60+085514.40	5	2.0	5941	✓	$3.55^{+0.57}_{-0.51}$	4.65 ± 0.93	$1.73^{+0.20}_{-0.20}$	0.0252	45.8	$0.14^{+0.14}_{-0.15}$
J112542.30+000101.33	1	—	5364	✓	$5.34^{+0.65}_{-0.74}$	6.58 ± 1.13	$1.74^{+0.18}_{-0.18}$	0.0297	59.4	$-0.22^{+0.12}_{-0.13}$
J215954.45-002150.17	5	6.7	5834	✓	$2.72^{+0.66}_{-0.40}$	4.57 ± 1.12	$1.96^{+0.25}_{-0.24}$	0.0435	33.6	$-0.19^{+0.17}_{-0.18}$
J234830.41+003918.57	3	0.1	11585	✓	$5.91^{+0.84}_{-0.73}$	5.54 ± 0.88	$1.48^{+0.13}_{-0.12}$	0.0337	117.9	$0.08^{+0.09}_{-0.09}$
Q0017+154	10	6.0	7310	✓	$2.08^{+0.28}_{-0.22}$	4.49 ± 0.93	$2.23^{+0.24}_{-0.23}$	0.0357	34.7	$-0.48^{+0.15}_{-0.18}$
Q0038-019	4	0.2	8109	✓	$7.84^{+0.72}_{-1.03}$	8.61 ± 1.10	$1.65^{+0.13}_{-0.12}$	0.0256	121.2	$-0.05^{+0.09}_{-0.09}$
Q0106-013	3	0.3	5090	✓	$15.71^{+1.52}_{-1.98}$	14.13 ± 1.81	$1.44^{+0.11}_{-0.11}$	0.0242	150.1	$-0.01^{+0.08}_{-0.08}$
Q0109+176	11	5.4	10234	✓	$2.93^{+0.60}_{-0.45}$	2.83 ± 0.57	$1.48^{+0.19}_{-0.15}$	0.0418	46.9	$0.03^{+0.15}_{-0.15}$
Q0123+257	4	0.9	2814	✓	$18.07^{+2.78}_{-1.89}$	17.28 ± 3.17	$1.46^{+0.15}_{-0.15}$	0.0687	86.2	$0.04^{+0.11}_{-0.11}$

Table 2 (cont'd)

Object name (1)	N_{obs} (2)	Δt [month] (3)	XRT exp. time [s] (4)	XRT detect? (5)	$F_{0.3-10}$ (6)	$F_\nu(2\,\mathrm{keV})$ (7)	Γ (8)	N_H [10^{22} cm^{-2}] (9)	N_{sub} (10)	HR (11)
Q0206+293	13	7.2	11692	✓	$1.32^{+0.28}_{-0.29}$	2.06 ± 0.57	$1.83^{+0.26}_{-0.26}$	0.0587	25.4	$-0.38^{+0.20}_{-0.23}$
Q0225−014	11	4.3	8296	✓	$3.10^{+0.30}_{-0.32}$	4.07 ± 0.74	$1.72^{+0.19}_{-0.19}$	0.0262	49.1	$-0.14^{+0.15}_{-0.15}$
Q0226−038	3	0.2	5859	✓	$9.06^{+1.00}_{-1.11}$	8.58 ± 1.39	$1.48^{+0.14}_{-0.14}$	0.0221	98.6	$-0.01^{+0.10}_{-0.10}$
Q0238+100	12	2.1	14190	✓	$4.45^{+0.43}_{-0.38}$	5.78 ± 0.82	$1.76^{+0.14}_{-0.14}$	0.0935	107.1	$-0.13^{+0.10}_{-0.10}$
Q0317−023	19	6.5	19020	✓	$1.37^{+0.22}_{-0.21}$	1.90 ± 0.37	$1.75^{+0.20}_{-0.19}$	0.055	42.3	$-0.07^{+0.17}_{-0.18}$
Q0352+123	8	1.5	5105	✓	$4.45^{+0.51}_{-0.43}$	7.67 ± 1.50	$2.14^{+0.24}_{-0.24}$	0.132	41.2	$-0.25^{+0.15}_{-0.16}$
Q0445+097	7	0.6	3758	✓	$10.87^{+1.77}_{-1.90}$	10.22 ± 2.38	$1.47^{+0.18}_{-0.18}$	0.131	62.6	$0.31^{+0.13}_{-0.13}$
Q0458−020	5	0.2	4235	✓	$21.65^{+2.35}_{-1.95}$	24.82 ± 3.27	$1.58^{+0.11}_{-0.11}$	0.0602	169.2	$-0.02^{+0.08}_{-0.08}$
Q0504+030	5	0.3	4258	✓	$7.14^{+0.91}_{-0.91}$	4.08 ± 1.32	$1.15^{+0.22}_{-0.22}$	0.0894	39.4	$0.28^{+0.17}_{-0.15}$
Q0730+257	16	3.8	8673	✓	$1.30^{+0.37}_{-0.38}$	1.84 ± 0.63	$1.68^{+0.30}_{-0.30}$	0.0504	17.6	$0.12^{+0.27}_{-0.27}$
Q0751+298	8	10.6	4812	✓	$2.91^{+0.55}_{-0.56}$	3.36 ± 0.83	$1.61^{+0.25}_{-0.25}$	0.0377	25.7	$-0.12^{+0.20}_{-0.22}$
Q0758+120	12	2.6	7325	✓	<2.22	<4.27	–	0.0254	5.7	$-0.05^{+0.44}_{-0.59}$
Q0802+103	9	8.8	4720	✓	$3.46^{+0.79}_{-0.72}$	3.94 ± 1.00	$1.63^{+0.24}_{-0.23}$	0.0245	32.2	$0.13^{+0.19}_{-0.18}$
Q0805+046	9	4.9	6243	✓	$2.29^{+0.60}_{-0.42}$	4.52 ± 1.20	$1.89^{+0.25}_{-0.24}$	0.0338	31.2	$-0.15^{+0.18}_{-0.19}$
Q0808+289	5	0.7	2897	✓	$4.99^{+1.42}_{-0.79}$	5.87 ± 1.57	$1.66^{+0.26}_{-0.26}$	0.0295	27.1	$-0.13^{+0.19}_{-0.20}$
Q0831+101	8	4.3	4902	✓	$3.10^{+0.97}_{-0.77}$	3.08 ± 0.99	$1.55^{+0.27}_{-0.27}$	0.0403	28.9	$0.08^{+0.19}_{-0.19}$
Q0835+580	4	1.6	2450	✓	$8.44^{+1.66}_{-1.55}$	7.53 ± 1.63	$1.50^{+0.23}_{-0.22}$	0.0448	37.9	$-0.02^{+0.16}_{-0.16}$
Q0856+124	8	8.0	8805	✓	$1.05^{+0.45}_{-0.30}$	0.59 ± 0.24	$1.17^{+0.33}_{-0.34}$	0.0299	10.3	$0.56^{+0.44}_{-0.44}$
Q0926+117	8	7.3	11375	✓	$1.27^{+0.33}_{-0.33}$	1.03 ± 0.29	$1.40^{+0.28}_{-0.28}$	0.03	17.3	$0.10^{+0.30}_{-0.31}$
Q0941+261	5	5.4	4992	✓	$3.68^{+0.61}_{-0.57}$	6.62 ± 1.77	$1.81^{+0.23}_{-0.23}$	0.017	18.8	$-0.40^{+0.15}_{-0.18}$
Q1023+067	1	–	3491	✓	$6.10^{+0.66}_{-1.15}$	6.85 ± 1.56	$1.66^{+0.21}_{-0.21}$	0.0205	40.3	$-0.11^{+0.16}_{-0.16}$
Q1055+499	3	7.4	4857	✓	$1.75^{+0.50}_{-0.48}$	1.66 ± 0.62	$1.45^{+0.30}_{-0.30}$	0.0131	17.5	$0.02^{+0.25}_{-0.24}$
Q1116+128	1	–	2884	✓	$5.19^{+1.51}_{-1.16}$	9.03 ± 2.62	$1.94^{+0.32}_{-0.31}$	0.0192	18.7	$-0.36^{+0.21}_{-0.25}$
Q1158+122	4	7.6	3624	✓	<2.81	<4.57	–	0.0172	6.3	$-0.50^{+0.16}_{-0.50}$
Q1214+106	6	7.3	6086	✓	$1.26^{+0.26}_{-0.20}$	2.68 ± 0.67	$2.29^{+0.35}_{-0.34}$	0.0191	14.7	$-0.50^{+0.25}_{-0.31}$
Q1221+113	1	–	3758	✓	$4.53^{+0.76}_{-0.63}$	7.03 ± 1.32	$1.94^{+0.23}_{-0.22}$	0.0245	39.0	$-0.20^{+0.15}_{-0.17}$
Q1226+105	5	6.4	3946	✓	$2.32^{+0.42}_{-0.36}$	4.42 ± 1.03	$1.97^{+0.27}_{-0.26}$	0.0194	25.0	$-0.38^{+0.19}_{-0.22}$
Q1258+404	3	0.1	3554	✓	$6.57^{+1.56}_{-1.15}$	5.70 ± 1.24	$1.46^{+0.20}_{-0.20}$	0.0153	45.8	$0.00^{+0.15}_{-0.15}$
Q1311−270	6	0.9	10966	✓	$3.80^{+0.48}_{-0.37}$	6.69 ± 1.03	$1.94^{+0.15}_{-0.15}$	0.0589	89.1	$-0.28^{+0.10}_{-0.11}$
Q1313+200	5	0.1	3526	✓	$2.23^{+0.70}_{-0.66}$	1.76 ± 0.70	$1.33^{+0.36}_{-0.36}$	0.019	9.1	$0.48^{+0.18}_{-0.26}$
Q1318+113	5	2.8	5085	✓	$1.88^{+0.49}_{-0.53}$	1.56 ± 0.62	$1.38^{+0.32}_{-0.32}$	0.0172	12.5	$0.37^{+0.33}_{-0.34}$
Q1323+655	4	10.3	3112	✓	$2.03^{+0.44}_{-0.43}$	2.05 ± 0.47	$1.58^{+0.23}_{-0.23}$	0.0191	30.9	$-0.19^{+0.30}_{-0.32}$
Q1354+258	2	0.1	7467	✓	$2.38^{+0.59}_{-0.28}$	4.33 ± 0.87	$2.03^{+0.22}_{-0.21}$	0.0147	39.2	$-0.34^{+0.15}_{-0.17}$
Q1402−012	7	2.9	4800	✓	$2.97^{+0.63}_{-0.70}$	1.69 ± 0.62	$1.15^{+0.26}_{-0.27}$	0.0423	42.0	$0.40^{+0.18}_{-0.16}$
Q1402+044	3	0.1	8581	✓	$5.41^{+0.83}_{-0.62}$	8.98 ± 1.63	$1.72^{+0.14}_{-0.14}$	0.0216	94.3	$-0.14^{+0.10}_{-0.11}$
Q1442+101	3	0.1	6980	✓	$14.44^{+1.47}_{-1.87}$	11.51 ± 2.07	$1.29^{+0.11}_{-0.11}$	0.018	113.3	$0.12^{+0.08}_{-0.08}$
Q1540+180	3	0.1	4694	✓	$5.32^{+1.04}_{-0.88}$	5.31 ± 1.04	$1.56^{+0.21}_{-0.20}$	0.0249	43.5	$0.18^{+0.16}_{-0.15}$
Q1542+042	8	0.1	7102	✓	$10.88^{+0.96}_{-0.83}$	17.06 ± 2.01	$1.84^{+0.11}_{-0.11}$	0.0455	158.2	$-0.17^{+0.08}_{-0.08}$
Q1554−203	4	0.1	4633	✓	$3.72^{+0.66}_{-0.52}$	5.83 ± 1.44	$1.90^{+0.26}_{-0.25}$	0.104	29.5	$-0.20^{+0.18}_{-0.20}$
Q1556−245	9	1.3	5749	✓	$7.36^{+1.21}_{-1.21}$	5.96 ± 1.42	$1.33^{+0.18}_{-0.18}$	0.0897	59.1	$0.20^{+0.14}_{-0.13}$

Table 2 (cont'd)

Object name (1)	N_{obs} (2)	Δt [month] (3)	XRT exp. time [s] (4)	XRT detect? (5)	$F_{0.3-10}$ (6)	$F_\nu(2\,\mathrm{keV})$ (7)	Γ (8)	N_H [10^{22} cm^{-2}] (9)	N_{sub} (10)	HR (11)
Q1557-199	5	1.6	4056		<4.59	<6.45	—	0.104	6.4	$0.13^{+0.51}_{-0.48}$
Q1602+576	5	0.3	3366	✓	$14.49^{+2.11}_{-1.60}$	16.54 ± 3.00	$1.52^{+0.14}_{-0.14}$	0.0202	70.8	$-0.04^{+0.10}_{-0.10}$
Q1606+289	23	8.0	15299	✓	$0.75^{+0.19}_{-0.13}$	0.75 ± 0.22	$1.53^{+0.30}_{-0.29}$	0.0332	13.2	$0.27^{+0.39}_{-0.38}$
Q1607+183	8	4.4	6011	✓	$5.09^{+0.64}_{-0.64}$	7.69 ± 1.42	$1.67^{+0.14}_{-0.14}$	0.0358	89.8	$-0.03^{+0.12}_{-0.12}$
Q1614+051	1	—	4415	✓	$7.02^{+1.29}_{-1.31}$	6.82 ± 1.88	$1.41^{+0.19}_{-0.18}$	0.049	52.6	$0.19^{+0.15}_{-0.14}$
Q1629+120	8	2.9	6501	✓	$8.30^{+1.10}_{-1.03}$	8.02 ± 1.12	$1.53^{+0.14}_{-0.14}$	0.0474	93.9	$-0.04^{+0.10}_{-0.11}$
Q1629+680	5	0.1	4008		<1.74	<2.08	—	0.0431	3.6	$-0.48^{+0.15}_{-0.52}$
Q1633+382	5	0.4	4028	✓	$28.58^{+2.69}_{-2.10}$	30.73 ± 2.78	$1.60^{+0.09}_{-0.09}$	0.011	193.2	$-0.17^{+0.06}_{-0.06}$
Q1656+477	3	0.3	4220	✓	$10.49^{+1.57}_{-1.16}$	10.86 ± 1.49	$1.61^{+0.14}_{-0.14}$	0.0172	98.8	$-0.22^{+0.09}_{-0.10}$
Q1658+575	13	7.6	12726	✓	$2.10^{+0.28}_{-0.24}$	3.17 ± 0.52	$1.81^{+0.18}_{-0.17}$	0.0204	55.1	$-0.16^{+0.14}_{-0.15}$
Q1701+379	30	17.3	24821	✓	$1.09^{+0.15}_{-0.14}$	1.60 ± 0.28	$1.73^{+0.18}_{-0.17}$	0.0242	43.8	$-0.16^{+0.17}_{-0.18}$
Q1702+298	5	6.5	3996	✓	$5.39^{+0.74}_{-0.72}$	4.22 ± 0.81	$1.36^{+0.17}_{-0.17}$	0.0454	67.2	$0.42^{+0.17}_{-0.20}$
Q1705+018	9	2.0	5132	✓	$8.52^{+0.87}_{-0.99}$	12.44 ± 2.39	$1.71^{+0.16}_{-0.16}$	0.0661	75.5	$0.04^{+0.12}_{-0.12}$
Q1726+344	3	0.1	3339		<2.11	<2.51	—	0.028	4.5	$0.21^{+0.58}_{-0.24}$
Q1816+475	9	6.5	4558	✓	$2.20^{+0.43}_{-0.57}$	1.91 ± 0.60	$1.41^{+0.25}_{-0.25}$	0.031	23.5	$-0.27^{+0.33}_{-0.37}$
Q1857+566	5	8.5	4981	✓	$3.32^{+0.60}_{-0.51}$	4.46 ± 0.79	$1.86^{+0.21}_{-0.21}$	0.0459	42.5	$-0.11^{+0.17}_{-0.19}$
Q2048+196	13	9.5	13825	✓	$1.60^{+0.19}_{-0.18}$	4.14 ± 0.84	$2.28^{+0.22}_{-0.21}$	0.071	41.5	$-0.47^{+0.15}_{-0.17}$
Q2150+053	5	4.0	3247	✓	$2.48^{+0.98}_{-0.65}$	3.85 ± 1.32	$1.88^{+0.36}_{-0.35}$	0.0436	14.5	$-0.17^{+0.26}_{-0.29}$
Q2158+101	2	0.1	2952		<1.79	<2.14	—	0.0434	1.9	$0.16^{+0.84}_{-0.21}$
Q2212-299	5	0.2	6765	✓	$4.60^{+0.98}_{-0.77}$	4.12 ± 0.91	$1.39^{+0.18}_{-0.17}$	0.0105	55.6	$0.00^{+0.14}_{-0.14}$
Q2222+051	6	3.6	5649	✓	$3.52^{+0.72}_{-0.75}$	3.44 ± 0.97	$1.47^{+0.23}_{-0.23}$	0.0591	33.9	$-0.26^{+0.16}_{-0.18}$
Q2223+210	2	0.1	4248	✓	$38.86^{+2.34}_{-3.68}$	29.63 ± 3.05	$1.35^{+0.08}_{-0.08}$	0.0388	280.8	$0.05^{+0.06}_{-0.06}$
Q2248+192	11	6.4	13148	✓	$2.02^{+0.18}_{-0.22}$	3.66 ± 0.57	$2.11^{+0.19}_{-0.19}$	0.0531	55.0	$-0.31^{+0.13}_{-0.14}$
Q2251+244	2	0.1	2919	✓	$33.71^{+4.26}_{-4.08}$	16.95 ± 3.06	$1.09^{+0.12}_{-0.12}$	0.0488	132.8	$0.23^{+0.09}_{-0.08}$
Q2338+042	8	1.4	4463	✓	$5.30^{+0.52}_{-0.93}$	5.49 ± 1.62	$1.49^{+0.22}_{-0.22}$	0.0572	37.7	$0.21^{+0.17}_{-0.16}$
Q2345+061	5	6.7	3918	✓	$4.77^{+1.08}_{-0.76}$	6.26 ± 1.51	$1.85^{+0.24}_{-0.24}$	0.0693	34.9	$-0.11^{+0.17}_{-0.18}$

Note. — (1) Object name. (2) Number of discrete *Swift* observations utilized, i.e., number of observation IDs associated with this target. See §2 for details of which observation IDs are utilized for each quasar. (3) Total campaign duration for each quasar, in rest-frame months (defined here as 30-day intervals). (4) Total XRT exposure time used in X-ray modeling. (5) A checkmark indicates an X-ray detection as defined in §2.3. (6) *Swift* XRT integrated flux, observed-frame energy interval 0.3 keV - 10.0 keV, units of 10^{-13} erg s^{-1} cm^{-1}. The 3σ limiting flux is given for non-detections (§2.3). (7) Flux density F_ν at rest-frame energy of 2 keV, units of 10^{-31} erg s^{-1} cm^{-1} Hz^{-1}. (8) X-ray photon index, model fit to observed-frame energy interval 0.3 keV - 10 keV. For non-detections we assume $\Gamma = 1.91$ (not tabulated). (9) The Galactic column density of neutral hydrogen towards the quasar, adopted from the work of Kalberla et al. (2005). (10) The background-subtracted number of X-ray counts collected in the source aperture over all observations for this quasar. For quasars with $N_{sub} < 5$, we use the HEASARC PIMMS tool to estimate the 3σ upper limit on the flux, assuming $\Gamma = 1.91$. (11) The X-ray hardness ratio (§4.3), calculated using the BEHR software (Park et al. 2006) using the 'quadrature' algorithm. Uncertainties shown are based on 68% posterior intervals.

Table 3. *Swift* UVOT flux measurements.

Object name (1)	E(B-V) (2)	F_λ UW1 (3)	F_λ UW2 (4)	F_λ UM2 (5)	F_λ U (6)	F_λ B (7)	F_λ V (8)	UVOT–SDSS matching bandpass (9)
Radio-Quiet Quasars								
J014725.50-101439.11	0.0303	6.98 ± 1.21	-4.01 ± 0.62	-1.31 ± 0.21	46.22 ± 3.07	35.43 ± 2.45	28.46 ± 2.95	B
J104915.44-011038.18	0.0349	5.70 ± 1.17	<2.34	<1.20	26.10 ± 2.17	20.35 ± 2.28	<14.34	V
J110607.48-173113.60	0.0395	—	—	—	24.16 ± 1.17	39.08 ± 1.52	30.53 ± 1.32	U
J111159.70+023719.76	0.033	47.21 ± 2.80	—	47.51 ± 2.72	57.73 ± 2.89	38.69 ± 1.87	27.79 ± 1.84	B
J114449.32+032751.96	0.0186	24.11 ± 1.56	—	3.58 ± 0.57	60.79 ± 3.04	44.27 ± 2.08	36.45 ± 2.17	U
J123034.21+073305.32	0.016	56.93 ± 3.17	—	—	78.07 ± 3.49	50.81 ± 1.95	31.38 ± 1.44	U
J125140.83+080718.46	0.0214	91.84 ± 4.96	—	—	85.75 ± 3.77	51.89 ± 1.93	33.09 ± 1.38	U
J131810.74+011140.86	0.0266	51.05 ± 2.94	—	—	52.18 ± 2.47	33.05 ± 1.44	20.36 ± 1.24	U
J142923.92+024023.14	0.0252	65.18 ± 4.90	61.70 ± 4.76	58.62 ± 4.62	67.95 ± 3.00	60.26 ± 3.80	43.76 ± 4.14	U
J145717.86+024747.36	0.041	27.81 ± 1.81	9.06 ± 1.40	12.03 ± 1.80	74.42 ± 3.35	55.97 ± 3.84	62.12 ± 5.04	U
J215543.09-073902.05	0.0295	23.60 ± 1.42	4.79 ± 0.43	<6.18	56.95 ± 2.62	46.13 ± 1.93	39.77 ± 2.02	U
Q0000-001	0.025	—	—	—	5.74 ± 0.47	10.82 ± 0.75	7.94 ± 0.76	U
Q0002-008	0.0303	—	—	—	19.08 ± 1.17	15.51 ± 1.20	13.06 ± 1.43	B
Q0003-006	0.0302	7.59 ± 0.56	—	—	9.50 ± 0.66	7.25 ± 0.98	<7.53	V
Q0008-008	0.0438	—	—	—	18.02 ± 0.86	11.17 ± 0.59	6.99 ± 0.66	B
Q0015+026	0.0258	—	—	—	4.84 ± 0.53	8.92 ± 0.82	4.68 ± 0.84	B
Q0020+022	0.0229	16.35 ± 1.20	—	—	21.12 ± 1.40	16.13 ± 1.94	<15.06	B
Q0040-017	0.0253	2.90 ± 0.55	—	—	7.72 ± 0.54	10.24 ± 0.72	8.33 ± 0.85	B
Q0107-005	0.0275	7.54 ± 0.51	—	—	12.95 ± 0.72	10.75 ± 0.91	7.01 ± 1.28	V
Q0115-011	0.0274	—	—	—	39.67 ± 1.87	35.49 ± 1.65	22.47 ± 1.32	B
Q0244+017	0.0382	—	—	—	18.66 ± 1.12	11.37 ± 1.00	8.63 ± 1.20	U
Q0249-184	0.0247	—	—	—	—	9.40 ± 0.46	13.65 ± 0.61	
Q0252+016	0.0802	11.98 ± 0.99	—	—	31.90 ± 1.63	37.94 ± 1.66	28.87 ± 1.56	
Q0253-024	0.0488	—	—	—	14.42 ± 0.70	10.08 ± 0.53	7.11 ± 0.55	U
Q0254-016	0.0541	—	—	—	8.45 ± 0.44	10.87 ± 0.50	7.59 ± 0.50	B
Q0258+021	0.0804	13.59 ± 0.94	—	—	29.58 ± 1.42	30.36 ± 1.42	23.21 ± 1.36	B
Q0348+061	0.2331	13.70 ± 0.92	—	—	52.30 ± 2.32	40.80 ± 1.92	34.10 ± 1.41	
Q0447-395	0.0283	29.72 ± 1.67	—	—	50.57 ± 2.28	32.09 ± 1.37	25.15 ± 1.25	
Q0518-350	0.0306	—	—	—	20.30 ± 0.97	18.59 ± 0.77	11.91 ± 0.68	
Q1008-055	0.0306	—	—	—	59.14 ± 2.67	43.15 ± 1.77	28.67 ± 1.40	
Q1016-006	0.0444	—	—	—	18.45 ± 1.06	14.18 ± 1.18	10.32 ± 1.20	B
Q1020+014	0.0523	36.74 ± 2.27	—	—	52.20 ± 2.66	34.83 ± 2.48	24.34 ± 3.76	U
Q1043+071	0.0227	—	—	—	8.96 ± 0.83	7.33 ± 1.27	<6.94	B
Q1045+052	0.0233	—	—	—	17.77 ± 1.15	11.40 ± 1.52	<7.12	B
Q1046+058	0.0236	11.16 ± 0.74	—	—	21.24 ± 1.10	14.51 ± 1.27	10.69 ± 2.14	V
Q1137+305	0.0183	115.97 ± 7.40	—	—	140.73 ± 7.52	87.30 ± 6.03	<57.94	B
Q1138+002	0.023	36.65 ± 2.21	—	—	35.68 ± 1.96	24.49 ± 2.11	21.46 ± 3.26	U
Q1146+111	0.0354	33.64 ± 2.10	—	—	44.47 ± 2.33	26.88 ± 2.15	22.31 ± 3.23	B

Table 3 (cont'd)

Object name (1)	E(B−V) (2)	F_λ UW1 (3)	F_λ UW2 (4)	F_λ UM2 (5)	F_λ U (6)	F_λ B (7)	F_λ V (8)	UVOT–SDSS matching bandpass (9)
Q1151-004	0.0174	20.11 ± 1.37	—	—	20.12 ± 1.47	12.90 ± 2.12	<21.37	U
Q1203-111	0.0635	—	—	—	5.63 ± 0.62	5.96 ± 0.76	<5.46	U
Q1208+105	0.0196	5.05 ± 0.74	—	—	<4.93	<11.86	<19.41	B
Q1219+491	0.0123	—	—	—	16.59 ± 0.99	22.49 ± 1.10	12.99 ± 1.21	V
Q1223+178	0.0228	—	—	—	5.39 ± 0.52	20.33 ± 1.11	19.64 ± 1.17	
Q1225-017	0.0201	—	—	—	20.11 ± 1.21	36.96 ± 1.75	23.27 ± 1.75	
Q1226-111	0.0443	—	—	—	7.01 ± 0.62	11.02 ± 0.83	9.53 ± 1.13	
Q1227+120	0.0262	—	—	—	6.48 ± 0.49	12.47 ± 0.77	11.05 ± 0.84	
Q1230+164	0.025	—	—	—	27.37 ± 1.36	38.58 ± 1.61	31.34 ± 1.46	B
Q1232-004	0.0197	21.38 ± 1.31	—	—	22.05 ± 1.21	12.70 ± 1.33	<10.36	B
Q1237+134	0.0329	80.61 ± 4.55	—	—	91.20 ± 4.24	59.44 ± 2.91	46.54 ± 3.19	U
Q1246-022	0.0219	—	—	—	25.58 ± 1.34	19.29 ± 1.19	14.30 ± 1.35	B
Q1259-344	0.0093	—	—	—	9.71 ± 0.73	20.32 ± 1.07	16.44 ± 1.22	B
Q1330-011	0.0239	—	—	—	<2.50	10.13 ± 0.87	20.81 ± 1.38	V
Q1409+095	0.0211	—	—	—	5.60 ± 0.58	18.47 ± 1.05	10.57 ± 1.10	V
Q1434-009	0.0338	31.38 ± 1.88	—	—	32.41 ± 1.69	23.10 ± 1.68	17.24 ± 2.20	U
Q1440-004	0.0328	61.69 ± 3.53	—	—	71.09 ± 3.43	46.71 ± 2.59	32.32 ± 2.99	
Q1443-010	0.0406	22.01 ± 1.38	—	—	29.89 ± 1.55	21.61 ± 1.54	19.44 ± 2.10	
Q1517-239	0.0343	32.79 ± 1.87	—	—	37.62 ± 1.79	25.70 ± 1.32	17.76 ± 1.52	U
Q1634+406	0.0055	18.22 ± 1.23	—	—	22.87 ± 1.32	13.84 ± 1.30	9.11 ± 1.26	U
Q1638+390	0.0102	—	—	—	12.13 ± 0.83	15.92 ± 0.94	9.73 ± 1.04	B
Q1704+710	0.0315	—	—	—	44.92 ± 2.10	30.37 ± 1.31	21.55 ± 1.09	
Q2233-136	0.0481	—	—	—	<2.04	8.26 ± 0.70	12.99 ± 1.05	V
Q2239+007	0.0631	—	—	—	9.00 ± 0.51	9.53 ± 0.56	7.58 ± 0.65	B
Q2334+019	0.0477	—	—	—	22.12 ± 1.19	—	15.33 ± 1.17	
Q2341+010	0.0326	13.80 ± 1.01	—	—	5.92 ± 0.79	5.48 ± 1.09	<7.31	B
Q2350-007	0.0254	—	—	—	18.97 ± 1.21	16.57 ± 1.62	15.35 ± 2.61	V
Q2351+022	0.0238	—	—	—	24.37 ± 1.11	19.38 ± 0.81	15.63 ± 0.74	B
Q2359-002	0.0252	—	—	—	<3.77	<6.38	<6.56	
Radio-Loud Quasars								
J082328.62+061146.07	0.0224	—	—	—	27.39 ± 1.31	32.36 ± 1.31	23.54 ± 1.18	B
J094853.60+085514.40	0.0258	50.15 ± 3.04	12.42 ± 1.28	9.29 ± 1.06	80.10 ± 3.83	61.20 ± 2.79	52.37 ± 2.65	B
J112542.30+000101.33	0.0258	42.30 ± 2.49	—	—	72.69 ± 3.35	43.87 ± 1.81	26.12 ± 1.42	U
J215954.45-002150.17	0.0501	76.73 ± 4.37	3.26 ± 0.32	62.57 ± 3.50	113.25 ± 5.22	74.65 ± 3.24	59.62 ± 2.85	B
J234830.41+003918.57	0.0228	12.10 ± 1.17	—	<1.70	50.63 ± 2.75	36.58 ± 1.99	23.09 ± 1.99	B
Q0017+154	0.0465	10.99 ± 0.75	—	—	37.37 ± 1.80	29.29 ± 1.61	23.73 ± 1.97	B
Q0038-019	0.0196	42.13 ± 2.36	—	—	76.05 ± 3.43	50.71 ± 2.28	36.00 ± 2.49	U
Q0106+013	0.0207	10.07 ± 0.80	—	—	29.58 ± 1.59	23.11 ± 1.77	19.22 ± 2.73	U
Q0109+176	0.0732	—	—	—	12.27 ± 0.68	12.84 ± 0.73	9.92 ± 0.80	B

Table 3 (cont'd)

Object name (1)	E(B-V) (2)	F_λ UW1 (3)	F_λ UW2 (4)	F_λ UM2 (5)	F_λ U (6)	F_λ B (7)	F_λ V (8)	UVOT–SDSS matching bandpass (9)
Q0123+257	0.0913	13.78 ± 1.10	—	—	22.84 ± 1.43	26.37 ± 1.92	20.60 ± 2.19	B
Q0206+293	0.06	—	—	—	5.01 ± 0.37	4.63 ± 0.42	<2.48	B
Q0225-014	0.0311	—	—	—	45.03 ± 2.03	29.08 ± 1.15	17.55 ± 0.88	V
Q0226-038	0.0261	—	—	—	75.80 ± 3.38	49.98 ± 1.97	35.22 ± 1.54	U
Q0238+100	0.2025	16.08 ± 0.92	—	—	25.74 ± 1.24	18.86 ± 1.12	15.72 ± 1.41	
Q0317-023	0.0751	—	—	—	3.39 ± 0.26	2.71 ± 0.30	2.03 ± 0.40	
Q0352+123	0.2169	11.80 ± 0.87	—	—	21.55 ± 1.21	15.76 ± 1.28	12.79 ± 1.61	U
Q0445+097	0.2798	—	—	—	2.37 ± 0.45	4.43 ± 0.54	3.94 ± 0.80	
Q0458-020	0.0638	—	—	—	7.08 ± 0.51	14.06 ± 0.73	15.08 ± 0.93	
Q0504+030	0.0564	—	—	—	10.41 ± 0.67	15.84 ± 0.83	10.83 ± 0.86	
Q0730+257	0.04	—	—	—	2.95 ± 0.30	5.83 ± 0.43	4.72 ± 0.56	B
Q0751+298	0.0371	—	—	—	34.17 ± 1.65	21.93 ± 1.17	15.60 ± 1.06	U
Q0758+120	0.0218	—	—	—	8.16 ± 0.53	7.86 ± 0.55	6.10 ± 0.72	B
Q0802+103	0.0189	8.65 ± 1.09	—	—	28.68 ± 1.44	20.79 ± 1.07	16.32 ± 1.09	U
Q0805+046	0.0247	—	—	—	9.01 ± 0.83	20.38 ± 0.89	14.80 ± 0.81	V
Q0808+289	0.0288	—	—	—	42.96 ± 2.16	35.00 ± 1.69	25.13 ± 1.55	B
Q0831+101	0.0368	2.89 ± 0.43	—	—	7.40 ± 0.63	6.19 ± 0.91	<6.17	B
Q0835+580	0.0665	27.74 ± 1.88	—	—	37.46 ± 2.08	33.77 ± 2.24	30.03 ± 2.35	U
Q0856+124	0.0204	11.17 ± 0.74	—	—	12.27 ± 0.78	7.42 ± 1.05	8.02 ± 1.57	U
Q0926+117	0.0263	22.03 ± 1.28	—	—	25.35 ± 1.28	14.93 ± 1.21	10.66 ± 1.62	U
Q0941+261	0.0169	—	—	—	18.31 ± 1.07	20.67 ± 1.19	16.22 ± 1.33	V
Q1023+067	0.019	15.01 ± 1.18	—	—	23.23 ± 1.55	16.80 ± 2.17	<18.18	B
Q1055+499	0.0112	—	—	—	8.80 ± 0.71	9.47 ± 0.76	7.25 ± 1.00	B
Q1116+128	0.0214	—	—	—	17.27 ± 1.18	14.74 ± 1.59	9.57 ± 1.49	B
Q1158+122	0.0219	—	—	—	35.98 ± 1.83	25.72 ± 1.42	24.04 ± 1.66	U
Q1214+106	0.0274	7.24 ± 0.65	—	—	10.17 ± 0.84	<6.46	<11.48	(U)
Q1221+113	0.0247	18.31 ± 1.29	—	—	23.53 ± 1.53	15.90 ± 2.07	<13.39	U
Q1226+105	0.0244	—	—	—	14.94 ± 0.89	17.80 ± 0.99	11.84 ± 1.14	B
Q1258+404	0.014	22.04 ± 1.43	—	—	33.61 ± 1.77	22.72 ± 1.75	11.16 ± 2.01	B
Q1311-270	0.0655	14.00 ± 0.85	—	—	30.60 ± 1.46	30.70 ± 1.44	21.62 ± 1.38	U
Q1313-200	0.0167	—	—	—	10.21 ± 0.94	7.96 ± 1.15	12.29 ± 1.43	
Q1318+113	0.0208	—	—	—	14.74 ± 0.86	14.75 ± 0.84	10.18 ± 1.06	B
Q1323+655	0.0148	27.15 ± 1.56	—	—	42.23 ± 1.96	27.69 ± 1.31	17.09 ± 1.24	B
Q1354+258	0.0153	—	—	—	25.24 ± 1.21	18.30 ± 0.81	12.64 ± 0.84	B
Q1402+044	0.0228	—	—	—	—	6.19 ± 0.44	11.58 ± 0.74	V
Q1402-012	0.0469	—	—	—	19.30 ± 0.96	24.31 ± 1.04	17.31 ± 0.89	B
Q1442+101	0.0217	—	—	—	—	20.95 ± 0.88	24.99 ± 1.15	V
Q1540+180	0.0296	10.98 ± 0.83	—	—	14.96 ± 0.94	17.13 ± 1.26	12.11 ± 1.39	B
Q1542+042	0.0746	—	—	—	27.75 ± 1.33	22.93 ± 0.99	15.20 ± 0.97	U

Table 3 (cont'd)

Object name (1)	E(B-V) (2)	F_λ UW1 (3)	F_λ UW2 (4)	F_λ UM2 (5)	F_λ U (6)	F_λ B (7)	F_λ V (8)	UVOT–SDSS matching bandpass (9)
Q1554-203	0.2436	6.89 ± 0.80	—	—	13.30 ± 1.11	7.77 ± 1.59	<9.56	
Q1556-245	0.0871	—	—	—	8.84 ± 1.54	14.15 ± 2.09	10.76 ± 0.76	
Q1557-199	0.1935	4.74 ± 0.88	—	—	8.40 ± 1.07	<9.01	<11.07	
Q1602+576	0.0183	—	—	—	47.76 ± 2.26	55.58 ± 2.27	35.40 ± 1.62	B
Q1606+289	0.0323	—	—	—	5.40 ± 0.33	5.05 ± 0.35	4.19 ± 0.38	B
Q1607+183	0.0419	—	—	—	6.20 ± 0.50	13.94 ± 0.65	13.49 ± 0.77	V
Q1614+051	0.0577	—	—	—	—	4.42 ± 0.64	7.36 ± 0.85	V
Q1629+120	0.0487	16.97 ± 1.06	—	—	20.15 ± 1.12	15.50 ± 1.30	15.69 ± 1.83	U
Q1629+680	0.0354	—	—	—	11.77 ± 0.77	15.06 ± 0.86	10.67 ± 0.87	
Q1633+382	0.0101	39.92 ± 2.40	—	—	53.68 ± 2.63	38.65 ± 2.12	31.57 ± 2.03	B
Q1656+477	0.0177	55.19 ± 3.12	—	—	61.58 ± 3.03	40.23 ± 2.35	25.47 ± 2.39	U
Q1658+575	0.0179	—	—	—	23.82 ± 1.10	18.90 ± 0.77	12.43 ± 0.64	
Q1701+379	0.0244	—	—	—	6.62 ± 0.34	8.63 ± 0.40	6.27 ± 0.36	B
Q1702+298	0.0465	4.47 ± 0.40	—	—	10.03 ± 0.61	8.43 ± 0.78	<4.61	B
Q1705+018	0.1544	—	—	—	9.59 ± 0.64	14.97 ± 0.82	11.20 ± 0.91	
Q1726+344	0.0261	—	—	—	9.08 ± 0.65	13.88 ± 0.83	7.96 ± 0.87	B
Q1816+475	0.0321	—	—	—	21.92 ± 1.06	22.09 ± 0.93	15.07 ± 0.78	
Q1857+566	0.049	42.28 ± 2.42	—	—	60.19 ± 2.80	44.15 ± 2.10	33.42 ± 2.08	
Q2048+196	0.0866	—	—	—	11.86 ± 0.59	18.46 ± 0.75	16.44 ± 0.76	
Q2150+053	0.0535	12.44 ± 0.98	—	—	37.98 ± 2.08	29.36 ± 2.09	16.41 ± 2.55	B
Q2158+101	0.0479	14.55 ± 1.12	—	—	17.25 ± 1.22	11.88 ± 1.71	<16.07	U
Q2212-299	0.013	—	—	—	—	53.16 ± 1.98	36.38 ± 1.44	
Q2222+051	0.1319	—	—	—	5.91 ± 0.53	15.24 ± 0.88	16.17 ± 1.14	V
Q2223+210	0.0399	25.38 ± 1.58	—	—	63.16 ± 2.98	43.48 ± 2.13	28.31 ± 2.17	U
Q2248+192	0.0541	8.88 ± 0.57	—	—	14.84 ± 0.76	11.45 ± 0.76	8.23 ± 1.05	U
Q2251+244	0.1695	—	—	—	12.62 ± 0.86	15.25 ± 0.97	11.10 ± 1.17	B
Q2338+042	0.0686	—	—	—	-2.74 ± 0.54	4.62 ± 0.82	<5.39	B
Q2345+061	0.1031	18.47 ± 1.27	—	—	21.55 ± 1.40	13.57 ± 2.12	<24.71	B

Note. — (1) Object name. (2) The differential extinction E(B-V) is adopted from the work of Schlafly & Finkbeiner (2011), and is the mean value of all measurements within a 2 arcminute aperture centered on the quasar coordinates. (3–8) The effective flux density at the bandpass pivot wavelength, in unit of 10^{17} ergs s^{-1} Å^{-1}, assuming a power law source SED over the bandpass (§2.3). The 1σ uncertainties on F_λ are listed for detected quasars. The 5σ upper limits are listed for non-detections. Filters that were not used for a given observation are marked with "—". Here we tabulate the observed fluxes; a correction for Galactic reddening is applied prior to fitting the UV-optical continuum model. (9) The UVOT filter bandpass used for rescaling of the SDSS photometric fluxes, for quasars with SDSS data (§2.4). Parentheses indicate that the matching bandpass was not suitable for inclusion in the subsequent UV-optical continuum fit.

Table 4. *Swift* UVOT apparent magnitudes.

Object (1)	m_{UW1} (2)	m_{UW1} (3)	m_{UM2} (4)	m_U (5)	m_B (6)	m_V (7)
Radio–Quiet Quasars						
J014725.50-101439.11	19.39 ± 0.17	-20.31 ± -0.16	-21.37 ± -0.16	17.21 ± 0.07	18.16 ± 0.07	17.80 ± 0.10
J104915.44-011038.18	19.61 ± 0.21	>20.90	>21.47	17.83 ± 0.08	18.76 ± 0.11	>18.54
J110607.48-173113.60	—	—	—	17.91 ± 0.05	18.05 ± 0.04	17.72 ± 0.04
J111159.70+023719.76	17.32 ± 0.06	—	17.47 ± 0.06	16.97 ± 0.05	18.06 ± 0.05	17.82 ± 0.07
J114449.32+032751.96	18.05 ± 0.06	—	20.28 ± 0.16	16.91 ± 0.05	17.91 ± 0.05	17.53 ± 0.06
J123034.21+073305.32	17.11 ± 0.06	—	—	16.64 ± 0.04	17.76 ± 0.04	17.69 ± 0.05
J125140.83+080718.46	16.59 ± 0.05	—	—	16.54 ± 0.04	17.74 ± 0.04	17.63 ± 0.04
J131810.74+011140.86	17.23 ± 0.06	—	—	17.08 ± 0.05	18.23 ± 0.04	18.16 ± 0.06
J142923.92+024023.14	16.97 ± 0.08	17.35 ± 0.08	17.25 ± 0.08	16.79 ± 0.04	17.58 ± 0.06	17.33 ± 0.09
J145717.86+024747.36	17.89 ± 0.07	19.43 ± 0.15	18.97 ± 0.15	16.69 ± 0.04	17.66 ± 0.07	16.95 ± 0.08
J215543.09-073902.05	18.07 ± 0.06	20.12 ± 0.09	>19.69	16.98 ± 0.05	17.87 ± 0.04	17.43 ± 0.05
Q0000-001	—	—	—	19.47 ± 0.08	19.44 ± 0.07	19.18 ± 0.10
Q0002-008	—	—	—	18.17 ± 0.06	19.05 ± 0.08	18.64 ± 0.11
Q0003-006	19.30 ± 0.07	—	—	18.92 ± 0.07	19.88 ± 0.14	>19.24
Q0008-008	—	—	—	18.23 ± 0.05	19.41 ± 0.05	19.32 ± 0.09
Q0015+026	—	—	—	19.66 ± 0.11	19.65 ± 0.09	19.76 ± 0.18
Q0020+022	18.47 ± 0.07	—	—	18.06 ± 0.07	19.01 ± 0.12	>18.49
Q0040-017	20.35 ± 0.19	—	—	19.15 ± 0.07	19.50 ± 0.07	19.13 ± 0.10
Q0107-005	19.31 ± 0.07	—	—	18.59 ± 0.06	19.45 ± 0.08	19.32 ± 0.18
Q0115-011	—	—	—	17.37 ± 0.05	18.15 ± 0.05	18.05 ± 0.06
Q0244+017	—	—	—	18.19 ± 0.06	19.39 ± 0.09	19.09 ± 0.14
Q0249-184	—	—	—	—	19.60 ± 0.05	18.60 ± 0.04
Q0252+016	—	—	—	17.61 ± 0.05	18.08 ± 0.04	17.78 ± 0.05
Q0253-024	18.80 ± 0.08	—	—	18.47 ± 0.05	19.52 ± 0.05	19.30 ± 0.08
Q0254-016	—	—	—	19.05 ± 0.05	19.44 ± 0.05	19.23 ± 0.07
Q0258+021	18.67 ± 0.07	—	—	17.69 ± 0.05	18.32 ± 0.05	18.02 ± 0.06
Q0348+061	18.66 ± 0.07	—	—	17.07 ± 0.04	18.00 ± 0.05	17.60 ± 0.04
Q0447-395	17.82 ± 0.06	—	—	17.11 ± 0.04	18.26 ± 0.04	17.93 ± 0.05
Q0518-350	—	—	—	18.10 ± 0.05	18.86 ± 0.04	18.74 ± 0.06
Q1008-055	—	—	—	16.94 ± 0.05	17.94 ± 0.04	17.79 ± 0.05
Q1016-006	—	—	—	18.20 ± 0.06	19.15 ± 0.08	18.90 ± 0.12
Q1020+014	17.59 ± 0.06	—	—	17.07 ± 0.05	18.17 ± 0.07	17.97 ± 0.15
Q1043+071	—	—	—	18.99 ± 0.09	19.87 ± 0.17	>19.33
Q1045+052	—	—	—	18.25 ± 0.06	19.39 ± 0.13	>19.30
Q1046+058	18.88 ± 0.07	—	—	18.05 ± 0.05	19.12 ± 0.09	18.86 ± 0.20
Q1137+305	16.34 ± 0.06	—	—	16.00 ± 0.05	17.18 ± 0.07	>17.03
Q1138+002	17.59 ± 0.06	—	—	17.49 ± 0.06	18.56 ± 0.09	18.10 ± 0.15
Q1146+111	17.68 ± 0.06	—	—	17.25 ± 0.05	18.46 ± 0.08	18.06 ± 0.14
Q1151-004	18.24 ± 0.07	—	—	18.11 ± 0.07	19.25 ± 0.16	>18.11
Q1203-111	—	—	—	19.49 ± 0.11	20.09 ± 0.13	>19.59

Table 4 (cont'd)

Object (1)	m_{UW1} (2)	m_{UW1} (3)	m_{UM2} (4)	m_U (5)	m_B (6)	m_V (7)
Q1208+105	19.74 ± 0.15	—	—	>19.64	>19.34	>18.21
Q1219+491	—	—	—	18.32 ± 0.06	18.65 ± 0.05	18.65 ± 0.09
Q1223+178	—	—	—	19.54 ± 0.10	18.76 ± 0.05	18.20 ± 0.06
Q1225-017	—	—	—	18.11 ± 0.06	18.11 ± 0.05	18.02 ± 0.08
Q1226-111	—	—	—	19.25 ± 0.09	19.42 ± 0.08	18.98 ± 0.12
Q1227+120	—	—	—	19.34 ± 0.08	19.29 ± 0.06	18.82 ± 0.08
Q1230+164	—	—	—	17.78 ± 0.05	18.06 ± 0.04	17.69 ± 0.05
Q1232-004	18.18 ± 0.06	—	—	18.01 ± 0.05	19.27 ± 0.10	>18.89
Q1237+134	16.73 ± 0.06	—	—	16.47 ± 0.05	17.59 ± 0.05	17.26 ± 0.07
Q1246-022	—	—	—	17.85 ± 0.05	18.82 ± 0.06	18.54 ± 0.09
Q1259+344	—	—	—	18.90 ± 0.07	18.76 ± 0.05	18.39 ± 0.07
Q1330+011	—	—	—	>20.37	19.51 ± 0.09	18.14 ± 0.07
Q1409+095	—	—	—	19.50 ± 0.10	18.86 ± 0.06	18.87 ± 0.10
Q1434-009	17.76 ± 0.06	—	—	17.59 ± 0.05	18.62 ± 0.07	18.34 ± 0.13
Q1440-004	17.02 ± 0.06	—	—	16.74 ± 0.05	17.86 ± 0.06	17.66 ± 0.09
Q1443-010	18.14 ± 0.06	—	—	17.68 ± 0.05	18.69 ± 0.07	18.21 ± 0.11
Q1517+239	17.71 ± 0.06	—	—	17.43 ± 0.05	18.50 ± 0.05	18.31 ± 0.09
Q1634+406	18.35 ± 0.07	—	—	17.97 ± 0.06	19.18 ± 0.09	19.03 ± 0.14
Q1638+390	—	—	—	18.66 ± 0.07	19.02 ± 0.06	18.96 ± 0.11
Q1704+710	—	—	—	17.24 ± 0.05	18.32 ± 0.04	18.10 ± 0.05
Q2233+136	—	—	—	>20.59	19.74 ± 0.08	18.65 ± 0.08
Q2239+007	—	—	—	18.98 ± 0.06	19.58 ± 0.06	19.23 ± 0.09
Q2334+019	—	—	—	18.01 ± 0.05	—	18.47 ± 0.08
Q2341+010	—	—	—	19.44 ± 0.13	20.18 ± 0.20	>19.27
Q2350-007	18.65 ± 0.07	—	—	18.17 ± 0.06	18.98 ± 0.10	18.47 ± 0.17
Q2351+022	—	—	—	17.90 ± 0.05	18.81 ± 0.04	18.45 ± 0.05
Q2359+002	—	—	—	>19.93	>20.02	>19.39
Radio-Loud Quasars						
J082328.62+061146.07	—	—	—	17.78 ± 0.05	18.25 ± 0.04	18.00 ± 0.05
J094853.60+085514.40	17.25 ± 0.06	19.09 ± 0.10	19.25 ± 0.11	16.61 ± 0.05	17.56 ± 0.05	17.14 ± 0.05
J112542.30+000101.33	17.43 ± 0.06	—	—	16.72 ± 0.05	17.92 ± 0.04	17.89 ± 0.05
J215954.45-002150.17	16.79 ± 0.06	—	17.18 ± 0.06	16.23 ± 0.05	17.35 ± 0.04	16.99 ± 0.09
J234830.41+003918.57	18.79 ± 0.10	20.54 ± 0.10	>21.09	17.11 ± 0.05	18.12 ± 0.05	18.02 ± 0.09
Q0017+154	18.90 ± 0.07	—	—	17.44 ± 0.05	18.36 ± 0.06	17.99 ± 0.08
Q0038-019	17.44 ± 0.06	—	—	16.67 ± 0.05	17.77 ± 0.04	17.54 ± 0.07
Q0106+013	18.99 ± 0.08	—	—	17.69 ± 0.05	18.62 ± 0.08	18.22 ± 0.14
Q0109+176	—	—	—	18.65 ± 0.06	19.26 ± 0.06	18.94 ± 0.08
Q0123+257	18.65 ± 0.08	—	—	17.97 ± 0.06	18.48 ± 0.07	18.15 ± 0.11
Q0206+293	—	—	—	19.62 ± 0.07	20.37 ± 0.09	>20.45
Q0225-014	—	—	—	17.24 ± 0.05	18.37 ± 0.04	18.32 ± 0.05
Q0226-038	—	—	—	16.67 ± 0.04	17.78 ± 0.04	17.57 ± 0.04

Table 4 (cont'd)

Object (1)	m_{UW2} (2)	m_{UW1} (3)	m_{UM2} (4)	m_U (5)	m_B (6)	m_V (7)
Q0238+100	18.48 ± 0.06	—	—	17.84 ± 0.05	18.84 ± 0.06	18.44 ± 0.09
Q0317-023	—	—	—	20.04 ± 0.08	20.95 ± 0.11	20.67 ± 0.20
Q0352+123	18.82 ± 0.07	—	—	18.04 ± 0.06	19.04 ± 0.08	18.67 ± 0.13
Q0445+097	—	—	—	20.43 ± 0.19	20.41 ± 0.12	19.94 ± 0.20
Q0458-020	—	—	—	19.24 ± 0.07	19.16 ± 0.05	18.49 ± 0.06
Q0504+030	—	—	—	18.83 ± 0.06	19.03 ± 0.05	18.85 ± 0.08
Q0730+257	—	—	—	20.20 ± 0.10	20.12 ± 0.07	19.75 ± 0.12
Q0751+298	—	—	—	17.54 ± 0.05	18.68 ± 0.05	18.45 ± 0.07
Q0758+120	—	—	—	19.09 ± 0.07	19.79 ± 0.07	19.47 ± 0.12
Q0802+103	19.16 ± 0.13	—	—	17.73 ± 0.05	18.73 ± 0.05	18.40 ± 0.07
Q0805+046	—	—	—	18.98 ± 0.09	18.76 ± 0.04	18.51 ± 0.05
Q0808+289	—	—	—	17.29 ± 0.05	18.17 ± 0.05	17.93 ± 0.06
Q0831+101	20.35 ± 0.15	—	—	19.20 ± 0.08	20.05 ± 0.15	>19.46
Q0835+580	17.89 ± 0.07	—	—	17.44 ± 0.06	18.21 ± 0.07	17.74 ± 0.08
Q0856+124	18.88 ± 0.07	—	—	18.65 ± 0.06	19.85 ± 0.14	19.17 ± 0.20
Q0926+117	18.14 ± 0.06	—	—	17.86 ± 0.05	19.09 ± 0.08	18.86 ± 0.15
Q0941+261	—	—	—	18.21 ± 0.06	18.74 ± 0.06	18.41 ± 0.08
Q1023+067	18.56 ± 0.08	—	—	17.95 ± 0.07	18.97 ± 0.13	>18.28
Q1055+499	—	—	—	19.01 ± 0.08	19.59 ± 0.08	19.28 ± 0.14
Q1116+128	—	—	—	18.28 ± 0.07	19.11 ± 0.11	18.98 ± 0.16
Q1158+122	—	—	—	17.48 ± 0.05	18.50 ± 0.06	17.98 ± 0.07
Q1214+106	19.35 ± 0.09	—	—	18.85 ± 0.08	>20.00	>18.78
Q1221+113	18.34 ± 0.07	—	—	17.94 ± 0.06	19.03 ± 0.13	>18.62
Q1226+105	—	—	—	18.43 ± 0.06	18.90 ± 0.06	18.75 ± 0.10
Q1258+404	18.14 ± 0.06	—	—	17.55 ± 0.05	18.64 ± 0.08	18.81 ± 0.18
Q1311-270	18.63 ± 0.06	—	—	17.65 ± 0.05	18.31 ± 0.05	18.10 ± 0.06
Q1313+200	—	—	—	18.85 ± 0.09	19.78 ± 0.14	18.71 ± 0.12
Q1318+113	—	—	—	18.45 ± 0.06	19.11 ± 0.06	18.91 ± 0.10
Q1323+655	17.92 ± 0.06	—	—	17.31 ± 0.05	18.42 ± 0.05	18.35 ± 0.07
Q1354+258	—	—	—	17.86 ± 0.05	18.87 ± 0.04	18.68 ± 0.07
Q1402+044	—	—	—	—	20.05 ± 0.07	18.77 ± 0.06
Q1402-012	—	—	—	18.16 ± 0.05	18.56 ± 0.04	18.34 ± 0.05
Q1442+101	—	—	—	—	18.73 ± 0.04	17.94 ± 0.05
Q1540+180	18.90 ± 0.08	—	—	18.43 ± 0.06	18.94 ± 0.07	18.72 ± 0.11
Q1542+042	—	—	—	17.76 ± 0.05	18.63 ± 0.04	18.48 ± 0.06
Q1554-203	19.40 ± 0.12	—	—	18.56 ± 0.08	19.80 ± 0.20	>18.98
Q1556-245	—	—	—	19.00 ± 0.17	19.15 ± 0.15	18.85 ± 0.07
Q1557-199	19.81 ± 0.19	—	—	19.06 ± 0.13	>19.64	>18.82
Q1602+576	—	—	—	17.17 ± 0.05	17.67 ± 0.04	17.56 ± 0.05
Q1606+289	—	—	—	19.54 ± 0.06	20.27 ± 0.07	19.88 ± 0.09
Q1607+183	—	—	—	19.39 ± 0.08	19.17 ± 0.05	18.61 ± 0.06

Table 4 (cont'd)

Object (1)	m_{UW1} (2)	m_{UW1} (3)	m_{UM2} (4)	m_U (5)	m_B (6)	m_V (7)
Q1614+051	—	—	—	—	20.41 ± 0.14	19.27 ± 0.12
Q1629+120	18.43 ± 0.06	—	—	18.11 ± 0.06	19.05 ± 0.08	18.44 ± 0.12
Q1629+680	—	—	—	18.69 ± 0.07	19.08 ± 0.06	18.86 ± 0.08
Q1633+382	17.50 ± 0.06	—	—	17.04 ± 0.05	18.06 ± 0.05	17.68 ± 0.06
Q1656+477	17.15 ± 0.06	—	—	16.90 ± 0.05	18.02 ± 0.06	17.92 ± 0.09
Q1658+575	—	—	—	17.93 ± 0.05	18.84 ± 0.04	18.70 ± 0.05
Q1701+379	—	—	—	19.32 ± 0.05	19.69 ± 0.05	19.44 ± 0.06
Q1702+298	19.87 ± 0.09	—	—	18.87 ± 0.06	19.71 ± 0.09	>19.77
Q1705+018	—	—	—	18.92 ± 0.07	19.09 ± 0.05	18.81 ± 0.08
Q1726+344	—	—	—	18.97 ± 0.07	19.17 ± 0.06	19.18 ± 0.11
Q1816+475	—	—	—	18.02 ± 0.05	18.67 ± 0.04	18.49 ± 0.05
Q1857+566	17.43 ± 0.06	—	—	16.92 ± 0.05	17.92 ± 0.05	17.62 ± 0.06
Q2048+196	—	—	—	18.68 ± 0.05	18.86 ± 0.04	18.39 ± 0.05
Q2150+053	18.76 ± 0.08	—	—	17.42 ± 0.05	18.36 ± 0.07	18.39 ± 0.16
Q2158+101	18.59 ± 0.08	—	—	18.28 ± 0.07	19.34 ± 0.14	>18.42
Q2212-299	—	—	—	—	17.72 ± 0.04	17.53 ± 0.04
Q2222+051	—	—	—	19.44 ± 0.09	19.07 ± 0.06	18.41 ± 0.07
Q2223+210	17.99 ± 0.06	—	—	16.87 ± 0.05	17.93 ± 0.05	17.80 ± 0.08
Q2248+192	19.13 ± 0.06	—	—	18.44 ± 0.05	19.38 ± 0.07	19.14 ± 0.13
Q2251+244	—	—	—	18.62 ± 0.07	19.07 ± 0.06	18.82 ± 0.10
Q2338+042	—	—	—	>20.28	20.37 ± 0.18	>19.60
Q2345+061	18.33 ± 0.07	—	—	18.04 ± 0.07	19.20 ± 0.16	>17.95

Note. — (1) Object name. (2) Apparent magnitudes on the UVOT photometric system. The 1σ uncertainties are listed for detected quasars. The 5σ upper limits are listed for non-detections. Filters that were not used for a given observation are marked with "– – –".

Table 5.   Summary of *Swift* detections for our sample.

	UVOT non-detection	Detected in 1 UVOT filter	Detected in 2 UVOT filters	Detected in $\geqslant 3$ UVOT filters	Sum[a]
XRT non-detection	1	1	8	36	46
XRT detection	0	1	7	89	97
Sum[b]	1	2	15	125	(sample of 143)

[a]Number of XRT detections and non-detections, irrespective of UVOT detection status.

[b]Number of objects with a given UVOT detection status, irrespective of XRT detection status.

Table 6. Integrated luminosities and SED diagnostics.

Object name (1)	β_{UV} (2)	F_ν(2500 Å) (3)	α_{ox} (4)	L_X (0.3-10 keV) (5)	L_X (2-10 keV) (6)	L_X (1-25 keV) (7)	L_{UV} (1000-3000Å) (8)	L_{EUV} (1000Å-0.3 keV) (9)	L_{EUV} (1000Å-1 keV) (10)
Radio-Quiet Quasars									
J014725.50-101439.11	1.45 ± 0.02	2.72 ± 0.43	>1.79	—	—	—	4.90 ± 0.77	—	—
J104915.44-011038.18	0.83 ± 0.00	2.48 ± 0.00	>1.52	—	—	—	3.48 ± 0.00	—	—
J110607.48-173113.60	1.67 ± 0.01	2.98 ± 0.36	>1.47	—	—	—	7.92 ± 0.94	—	—
J111159.70-023719.76	1.93 ± 0.01	2.39 ± 0.19	>1.70	—	—	—	4.21 ± 0.33	—	—
J114449.32-032751.96	1.16 ± 0.02	3.89 ± 0.50	>1.77	—	—	—	6.00 ± 0.77	—	—
J123034.21+073305.32	1.72 ± 0.02	3.23 ± 0.27	1.54 ± 0.08	$0.47^{+0.05}_{-0.05}$	$0.27^{+0.04}_{-0.04}$	$0.56^{+0.08}_{-0.09}$	4.84 ± 0.41	$4.54^{+0.42}_{-0.42}$	$6.72^{+0.87}_{-0.91}$
J125140.83+080718.46	2.03 ± 0.02	2.83 ± 0.27	1.60 ± 0.08	$0.24^{+0.04}_{-0.03}$	$0.14^{+0.02}_{-0.02}$	$0.31^{+0.05}_{-0.05}$	3.90 ± 0.37	$3.66^{+0.37}_{-0.37}$	$5.46^{+0.71}_{-0.74}$
J131810.74+011140.86	1.73 ± 0.01	2.15 ± 0.16	>1.68	—	—	—	2.72 ± 0.20	—	—
J142923.92+024023.14	0.75 ± 0.01	7.19 ± 0.30	>1.83	—	—	—	6.35 ± 0.26	—	—
J145717.86+024747.36	1.34 ± 0.01	4.99 ± 0.49	>1.84	—	—	—	7.40 ± 0.73	—	—
J215543.09-073902.05	1.43 ± 0.01	3.71 ± 0.26	1.73 ± 0.11	$0.22^{+0.03}_{-0.03}$	$0.16^{+0.02}_{-0.02}$	$0.38^{+0.10}_{-0.07}$	5.50 ± 0.38	$3.37^{+0.32}_{-0.33}$	$5.29^{+0.63}_{-0.69}$
Q0000-001	1.55 ± 0.01	0.83 ± 0.12	>1.56	—	—	—	2.12 ± 0.30	—	—
Q0002-008	1.84 ± 0.02	1.05 ± 0.14	>1.53	—	—	—	2.29 ± 0.31	—	—
Q0003-006	1.86 ± 0.03	0.47 ± 0.08	1.45 ± 0.13	$0.14^{+0.02}_{-0.02}$	$0.11^{+0.02}_{-0.03}$	$0.31^{+0.05}_{-0.08}$	0.69 ± 0.12	$0.59^{+0.12}_{-0.13}$	$1.02^{+0.23}_{-0.24}$
Q0008-008	1.81 ± 0.02	0.67 ± 0.09	1.49 ± 0.11	$0.18^{+0.03}_{-0.03}$	$0.11^{+0.02}_{-0.02}$	$0.25^{+0.05}_{-0.06}$	1.30 ± 0.18	$1.26^{+0.19}_{-0.19}$	$1.94^{+0.37}_{-0.39}$
Q0015+026	1.91 ± 0.02	0.54 ± 0.09	>1.39	—	—	—	1.50 ± 0.24	—	—
Q0020+022	1.79 ± 0.01	1.01 ± 0.09	>1.26	—	—	—	1.53 ± 0.13	—	—
Q0040-017	1.56 ± 0.02	0.76 ± 0.14	1.52 ± 0.16	$0.25^{+0.05}_{-0.05}$	$0.20^{+0.04}_{-0.04}$	$0.53^{+0.11}_{-0.13}$	1.72 ± 0.32	$1.28^{+0.29}_{-0.30}$	$2.16^{+0.55}_{-0.59}$
Q0107-005	1.44 ± 0.03	0.76 ± 0.11	1.41 ± 0.08	$0.23^{+0.07}_{-0.07}$	$0.10^{+0.02}_{-0.02}$	$0.20^{+0.03}_{-0.04}$	0.95 ± 0.14	$1.18^{+0.15}_{-0.15}$	$1.59^{+0.29}_{-0.30}$
Q0115-011	1.74 ± 0.02	2.34 ± 0.34	>1.62	—	—	—	4.91 ± 0.72	—	—
Q0244+017	1.53 ± 0.01	0.91 ± 0.07	>1.46	—	—	—	1.42 ± 0.10	—	—
Q0249-184	1.50 ± 0.00	1.47 ± 0.00	>1.67	—	—	—	7.35 ± 0.00	—	—
Q0252+016	1.72 ± 0.00	3.18 ± 0.00	>1.56	—	—	—	8.08 ± 0.00	—	—
Q0253-024	1.89 ± 0.02	0.67 ± 0.08	1.38 ± 0.10	$0.43^{+0.03}_{-0.03}$	$0.08^{+0.01}_{-0.01}$	$0.17^{+0.04}_{-0.02}$	1.27 ± 0.16	$2.71^{+0.26}_{-0.27}$	$2.83^{+0.58}_{-0.62}$
Q0254-016	1.84 ± 0.02	0.65 ± 0.11	1.43 ± 0.13	$0.37^{+0.04}_{-0.04}$	$0.24^{+0.03}_{-0.03}$	$0.53^{+0.09}_{-0.09}$	2.04 ± 0.33	$2.13^{+0.37}_{-0.37}$	$3.31^{+0.76}_{-0.76}$
Q0258+021	1.98 ± 0.02	1.93 ± 0.24	1.48 ± 0.16	$0.74^{+0.07}_{-0.10}$	$0.47^{+0.04}_{-0.04}$	$1.03^{+0.11}_{-0.11}$	5.76 ± 0.71	$5.91^{+0.92}_{-0.94}$	$9.09^{+1.97}_{-2.27}$
Q0348+061	2.08	5.21	1.65 ± 0.08	$0.78^{+0.05}_{-0.05}$	$0.56^{+0.05}_{-0.04}$	$1.37^{+0.11}_{-0.20}$	11.5	$9.86^{+0.30}_{-0.35}$	$15.6^{+0.82}_{-1.00}$
Q0447-395	1.11 ± 0.03	2.94 ± 1.30	1.59 ± 0.08	$0.38^{+0.04}_{-0.05}$	$0.21^{+0.03}_{-0.03}$	$0.43^{+0.09}_{-0.06}$	4.01 ± 1.76	$3.04^{+1.08}_{-1.13}$	$4.42^{+1.77}_{-1.78}$
Q0518-350	2.02 ± 0.00	1.06 ± 0.00	>1.54	—	—	—	2.61 ± 0.00	—	—
Q1008-055	1.49 ± 0.03	3.27 ± 1.24	1.56 ± 0.11	$0.56^{+0.06}_{-0.07}$	$0.31^{+0.06}_{-0.07}$	$0.65^{+0.14}_{-0.13}$	5.80 ± 2.20	$5.04^{+1.64}_{-1.68}$	$7.41^{+2.77}_{-2.77}$
Q1016-006	1.60 ± 0.03	0.97 ± 0.16	1.45 ± 0.20	$0.37^{+0.07}_{-0.06}$	$0.25^{+0.04}_{-0.05}$	$0.56^{+0.17}_{-0.17}$	1.92 ± 0.32	$1.79^{+0.38}_{-0.40}$	$2.84^{+0.83}_{-1.00}$
Q1020-014	1.66 ± 0.01	2.54 ± 0.17	>1.72	—	—	—	2.99 ± 0.20	—	—
Q1043+071	1.91 ± 0.02	0.45 ± 0.09	>1.33	—	—	—	0.97 ± 0.20	—	—
Q1045+052	1.64 ± 0.03	0.81 ± 0.14	1.50 ± 0.22	$0.24^{+0.07}_{-0.06}$	$0.19^{+0.06}_{-0.05}$	$0.50^{+0.14}_{-0.11}$	1.55 ± 0.27	$1.21^{+0.30}_{-0.33}$	$2.04^{+0.59}_{-0.71}$
Q1046-058	1.90 ± 0.02	0.87 ± 0.12	1.38 ± 0.10	$0.39^{+0.04}_{-0.04}$	$0.23^{+0.03}_{-0.04}$	$0.50^{+0.11}_{-0.09}$	1.63 ± 0.22	$1.95^{+0.27}_{-0.27}$	$2.96^{+0.58}_{-0.56}$
Q1137+305	1.57 ± 0.03	6.58 ± 0.64	1.63 ± 0.16	$0.50^{+0.13}_{-0.12}$	$0.36^{+0.09}_{-0.08}$	$0.89^{+0.37}_{-0.30}$	7.26 ± 0.70	$5.05^{+0.72}_{-0.77}$	$8.10^{+1.45}_{-1.71}$
Q1138+002	1.86 ± 0.01	1.48 ± 0.08	>1.51	—	—	—	2.25 ± 0.13	—	—
Q1146-111	1.72 ± 0.02	1.74 ± 0.22	1.53 ± 0.19	$0.40^{+0.08}_{-0.09}$	$0.31^{+0.06}_{-0.10}$	$0.86^{+0.22}_{-0.32}$	2.91 ± 0.37	$2.23^{+0.44}_{-0.49}$	$3.77^{+0.86}_{-1.02}$
Q1151-004	1.58 ± 0.03	0.90 ± 0.10	>1.41	—	—	—	0.95 ± 0.11	—	—

Table 6 (cont'd)

Object name (1)	β_{UV} (2)	F_ν(2500 Å) (3)	α_{ox} (4)	L_X (0.3-10 keV) (5)	L_X (2-10 keV) (6)	L_X (1-25 keV) (7)	L_{UV} (1000-3000 Å) (8)	L_{EUV} (1000Å-0.3 keV) (9)	L_{EUV} (1000Å-1 keV) (10)
Q1203-111	1.50 ± 0.00	0.52 ± 0.00	>1.46	—	—	—	1.36 ± 0.00	—	—
Q1208+105	1.05 ± 0.03	0.36 ± 0.06	>1.31	—	—	—	0.43 ± 0.07	—	—
Q1219+491	1.77 ± 0.02	1.28 ± 0.15	>1.48	—	—	—	3.04 ± 0.36	—	—
Q1223+178	1.33 ± 0.02	2.39 ± 0.48	>1.63	—	—	—	6.92 ± 1.38	—	—
Q1225-017	2.23 ± 0.01	1.65 ± 0.20	1.25 ± 0.12	$10.60^{+0.49}_{-0.36}$	$0.53^{+0.10}_{-0.12}$	$1.66^{+0.33}_{-0.32}$	6.95 ± 0.84	$42.25^{+2.93}_{-3.00}$	$25.58^{+6.55}_{-7.25}$
Q1226-111	0.96 ± 0.00	1.33 ± 0.00	>1.34	—	—	—	2.51 ± 0.00	—	—
Q1227+120	0.80 ± 0.00	1.58 ± 0.00	>1.53	—	—	—	2.81 ± 0.00	—	—
Q1230+164	1.42 ± 0.01	3.57 ± 0.34	1.54 ± 0.17	$1.08^{+0.19}_{-0.22}$	$0.57^{+0.09}_{-0.16}$	$1.18^{+0.25}_{-0.30}$	9.39 ± 0.90	$8.47^{+1.06}_{-1.08}$	$12.27^{+2.56}_{-3.12}$
Q1232-004	0.96 ± 0.00	1.33 ± 0.00	>1.34	—	—	—	2.51 ± 0.00	—	—
Q1237+134	1.78 ± 0.01	3.86 ± 0.22	1.58 ± 0.11	$0.44^{+0.07}_{-0.04}$	$0.27^{+0.07}_{-0.04}$	$0.60^{+0.16}_{-0.13}$	5.46 ± 0.31	$4.79^{+0.38}_{-0.39}$	$7.24^{+0.86}_{-0.96}$
Q1246-022	1.63 ± 0.02	1.35 ± 0.19	1.43 ± 0.14	$0.62^{+0.11}_{-0.09}$	$0.16^{+0.05}_{-0.05}$	$0.33^{+0.11}_{-0.07}$	2.57 ± 0.36	$4.09^{+0.52}_{-0.52}$	$4.73^{+1.23}_{-1.40}$
Q1259+344	1.56 ± 0.02	1.62 ± 0.27	>1.54	—	—	—	4.85 ± 0.80	—	—
Q1330+011	1.68 ± 0.01	2.52 ± 0.45	>1.63	—	—	—	11.42 ± 2.05	—	—
Q1409+095	2.20 ± 0.01	1.08 ± 0.12	>1.53	—	—	—	4.43 ± 0.48	—	—
Q1434-009	1.62 ± 0.02	1.62 ± 0.13	>1.51	—	—	—	2.02 ± 0.16	—	—
Q1440-004	2.03 ± 0.04	2.78 ± 1.45	1.41 ± 0.09	$0.93^{+0.11}_{-0.09}$	$0.39^{+0.08}_{-0.07}$	$0.77^{+0.14}_{-0.14}$	4.80 ± 2.51	$6.93^{+2.76}_{-2.96}$	$9.31^{+4.44}_{-4.48}$
Q1443-010	1.42 ± 0.01	1.73 ± 0.13	1.59 ± 0.15	$0.20^{+0.04}_{-0.03}$	$0.13^{+0.02}_{-0.04}$	$0.31^{+0.18}_{-0.09}$	2.23 ± 0.17	$1.64^{+0.18}_{-0.19}$	$2.57^{+0.40}_{-0.46}$
Q1517+239	1.76 ± 0.02	1.76 ± 0.15	>1.42	—	—	—	2.75 ± 0.24	—	—
Q1634+406	2.11 ± 0.03	0.70 ± 0.10	>1.38	—	—	—	1.15 ± 0.16	—	—
Q1638+390	1.85 ± 0.02	0.91 ± 0.15	>1.36	—	—	—	2.33 ± 0.40	—	—
Q1704+710	1.61 ± 0.03	2.21 ± 0.88	1.51 ± 0.15	$0.48^{+0.07}_{-0.07}$	$0.23^{+0.07}_{-0.05}$	$0.46^{+0.14}_{-0.12}$	3.80 ± 1.51	$4.04^{+1.38}_{-1.41}$	$5.59^{+2.49}_{-2.53}$
Q2223+136	2.22 ± 0.01	1.09 ± 0.27	>1.50	—	—	—	5.48 ± 1.33	—	—
Q2239+007	1.89 ± 0.01	0.71 ± 0.09	1.46 ± 0.14	$0.24^{+0.03}_{-0.03}$	$0.15^{+0.03}_{-0.03}$	$0.34^{+0.12}_{-0.07}$	1.61 ± 0.19	$1.66^{+0.24}_{-0.24}$	$2.55^{+0.50}_{-0.55}$
Q2334+019	1.24 ± 0.00	1.94 ± 0.00	>1.57	—	—	—	3.33 ± 0.00	—	—
Q2341+010	1.85 ± 0.03	0.33 ± 0.07	>1.06	—	—	—	0.80 ± 0.17	—	—
Q2350-007	1.60 ± 0.03	1.29 ± 0.18	>1.59	—	—	—	1.49 ± 0.20	—	—
Q2351+022	1.51 ± 0.02	1.58 ± 0.21	1.55 ± 0.09	$0.28^{+0.03}_{-0.03}$	$0.18^{+0.03}_{-0.03}$	$0.42^{+0.07}_{-0.05}$	2.62 ± 0.34	$2.08^{+0.29}_{-0.29}$	$3.26^{+0.55}_{-0.57}$
Q2359+002	—	—	—	—	—	—	—	—	—
Radio-Loud Quasars									
J082328.62+061146.07	1.74 ± 0.01	2.57 ± 0.23	1.41 ± 0.09	$1.86^{+0.16}_{-0.15}$	$1.09^{+0.11}_{-0.12}$	$2.31^{+0.33}_{-0.34}$	8.35 ± 0.74	$9.45^{+0.93}_{-0.93}$	$14.20^{+2.04}_{-2.14}$
J094853.60-085514.40	1.17 ± 0.01	5.72 ± 0.38	1.57 ± 0.09	$0.84^{+0.07}_{-0.07}$	$0.48^{+0.04}_{-0.04}$	$1.01^{+0.25}_{-0.25}$	8.00 ± 0.53	$6.12^{+0.49}_{-0.49}$	$9.12^{+1.11}_{-1.19}$
J112542.30+000101.33	1.93 ± 0.02	2.58 ± 0.21	1.38 ± 0.07	$0.88^{+0.09}_{-0.09}$	$0.50^{+0.07}_{-0.07}$	$1.06^{+0.16}_{-0.16}$	3.73 ± 0.30	$4.64^{+0.41}_{-0.41}$	$6.94^{+0.91}_{-0.95}$
J215954.45-002150.17	1.66 ± 0.01	5.83 ± 0.39	1.58 ± 0.11	$0.80^{+0.07}_{-0.11}$	$0.38^{+0.05}_{-0.05}$	$0.77^{+0.15}_{-0.13}$	9.79 ± 0.65	$9.47^{+0.77}_{-0.77}$	$13.23^{+1.85}_{-2.08}$
J234830.41+003918.57	1.63 ± 0.02	2.40 ± 0.29	1.40 ± 0.07	$1.08^{+0.05}_{-0.05}$	$0.73^{+0.05}_{-0.05}$	$1.68^{+0.12}_{-0.13}$	4.11 ± 0.49	$4.13^{+0.51}_{-0.51}$	$6.64^{+1.02}_{-1.04}$
Q0017+154	1.51 ± 0.02	2.47 ± 0.26	1.44 ± 0.09	$0.87^{+0.05}_{-0.05}$	$0.32^{+0.05}_{-0.05}$	$0.63^{+0.09}_{-0.09}$	4.04 ± 0.42	$5.41^{+0.52}_{-0.52}$	$6.82^{+1.18}_{-1.25}$
Q0038-019	1.60 ± 0.01	3.33 ± 0.26	1.38 ± 0.06	$1.15^{+0.09}_{-0.09}$	$0.70^{+0.06}_{-0.05}$	$1.52^{+0.24}_{-0.17}$	4.08 ± 0.32	$4.50^{+0.37}_{-0.37}$	$6.95^{+0.79}_{-0.81}$
Q0106+013	1.31 ± 0.02	2.00 ± 0.18	1.21 ± 0.06	$3.04^{+0.26}_{-0.20}$	$2.10^{+0.16}_{-0.17}$	$4.93^{+0.45}_{-0.45}$	3.27 ± 0.30	$3.98^{+0.39}_{-0.39}$	$6.84^{+0.86}_{-0.87}$
Q0109+176	1.62 ± 0.02	1.23 ± 0.13	1.40 ± 0.09	$0.63^{+0.06}_{-0.05}$	$0.42^{+0.07}_{-0.05}$	$0.98^{+0.16}_{-0.12}$	2.38 ± 0.25	$2.37^{+0.28}_{-0.28}$	$3.82^{+0.58}_{-0.60}$
Q0123+257	1.80 ± 0.02	2.05 ± 0.27	1.18 ± 0.08	$4.53^{+0.27}_{-0.46}$	$3.10^{+0.37}_{-0.29}$	$7.23^{+0.63}_{-0.83}$	5.03 ± 0.66	$7.31^{+1.01}_{-1.01}$	$12.30^{+2.17}_{-2.21}$
Q0206+293	1.95 ± 0.04	0.30 ± 0.10	1.11 ± 0.00	$0.44^{+0.04}_{-0.06}$	$0.23^{+0.03}_{-0.04}$	$0.48^{+0.11}_{-0.07}$	0.70 ± 0.24	$1.22^{+0.34}_{-0.35}$	$1.79^{+0.66}_{-0.66}$

Table 6 (cont'd)

Object name (1)	β_{UV} (2)	$F_\nu(2500\ \text{Å})$ (3)	α_{ox} (4)	L_X (0.3-10 keV) (5)	L_X (2-10 keV) (6)	L_X (1-25 keV) (7)	L_{UV} (1000-3000Å) (8)	L_{EUV} (1000Å-0.3 keV) (9)	L_{EUV} (1000Å-1 keV) (10)
Q0225−014	2.12 ± 0.01	1.65 ± 0.16	1.38 ± 0.08	$0.77^{+0.07}_{-0.07}$	$0.45^{+0.05}_{-0.05}$	$0.95^{+0.15}_{-0.16}$	3.66 ± 0.34	$4.69^{+0.46}_{-0.46}$	$7.01^{+0.96}_{-0.99}$
Q0226−038	1.84 ± 0.02	3.23 ± 0.36	1.37 ± 0.07	$1.77^{+0.17}_{-0.17}$	$1.20^{+0.13}_{-0.13}$	$2.76^{+0.36}_{-0.36}$	6.42 ± 0.71	$7.02^{+0.83}_{-0.83}$	$11.28^{+1.65}_{-1.69}$
Q0238+100	2.06 ± 0.02	2.07 ± 0.60	1.36 ± 0.06	$0.88^{+0.05}_{-0.04}$	$0.50^{+0.05}_{-0.05}$	$1.04^{+0.10}_{-0.11}$	3.62 ± 1.05	$4.80^{+1.14}_{-1.16}$	$7.12^{+1.94}_{-1.93}$
Q0317−023	1.86 ± 0.00	0.21 ± 0.00	1.17 ± 0.08	$0.38^{+0.02}_{-0.02}$	$0.21^{+0.03}_{-0.03}$	$0.45^{+0.06}_{-0.07}$	0.44 ± 0.00	$0.78^{+0.03}_{-0.03}$	$1.18^{+0.11}_{-0.13}$
Q0352+123	1.64 ± 0.01	2.15 ± 0.13	1.32 ± 0.08	$0.98^{+0.05}_{-0.04}$	$0.39^{+0.05}_{-0.05}$	$0.77^{+0.11}_{-0.09}$	2.51 ± 0.15	$4.06^{+0.27}_{-0.27}$	$5.25^{+0.71}_{-0.76}$
Q0445+097	1.85 ± 0.00	0.76 ± 0.00	1.10 ± 0.10	$2.20^{+0.13}_{-0.13}$	$1.50^{+0.12}_{-0.12}$	$3.48^{+0.31}_{-0.47}$	1.58 ± 0.00	$2.68^{+0.16}_{-0.16}$	$4.58^{+0.54}_{-0.54}$
Q0458−020	-0.13 ± 0.00	3.41 ± 0.00	1.20 ± 0.06	$5.91^{+0.25}_{-0.25}$	$3.76^{+0.29}_{-0.24}$	$8.34^{+0.61}_{-0.74}$	4.04 ± 0.00	$3.75^{+0.16}_{-0.16}$	$6.47^{+0.58}_{-0.58}$
Q0504+030	2.08 ± 0.00	0.94 ± 0.00	1.29 ± 0.14	$1.33^{+0.13}_{-0.13}$	$1.05^{+0.11}_{-0.11}$	$2.86^{+0.59}_{-0.38}$	2.82 ± 0.00	$3.18^{+0.24}_{-0.31}$	$5.60^{+0.62}_{-0.62}$
Q0730+257	1.88 ± 0.02	0.40 ± 0.08	1.28 ± 0.15	$0.57^{+0.07}_{-0.07}$	$0.34^{+0.04}_{-0.04}$	$0.73^{+0.16}_{-0.14}$	1.29 ± 0.25	$1.79^{+0.36}_{-0.36}$	$2.76^{+0.77}_{-0.82}$
Q0751+298	2.06 ± 0.02	1.31 ± 0.15	1.38 ± 0.11	$0.69^{+0.08}_{-0.08}$	$0.43^{+0.07}_{-0.07}$	$0.95^{+0.20}_{-0.21}$	2.98 ± 0.35	$3.61^{+0.47}_{-0.48}$	$5.59^{+0.99}_{-1.04}$
Q0758+120	1.86 ± 0.02	0.52 ± 0.09	>1.18	—	—	—	1.57 ± 0.27	—	—
Q0802+103	1.45 ± 0.01	1.61 ± 0.11	1.39 ± 0.11	$0.70^{+0.09}_{-0.09}$	$0.43^{+0.06}_{-0.06}$	$0.94^{+0.23}_{-0.20}$	2.44 ± 0.17	$2.53^{+0.25}_{-0.26}$	$3.94^{+0.62}_{-0.69}$
Q0805+046	1.92 ± 0.01	1.61 ± 0.13	1.36 ± 0.12	$1.55^{+0.17}_{-0.16}$	$0.79^{+0.11}_{-0.15}$	$1.60^{+0.26}_{-0.23}$	5.88 ± 0.48	$8.07^{+0.78}_{-0.78}$	$11.55^{+1.89}_{-2.07}$
Q0808+289	1.51 ± 0.01	2.67 ± 0.18	1.40 ± 0.12	$0.98^{+0.15}_{-0.15}$	$0.59^{+0.07}_{-0.07}$	$1.28^{+0.30}_{-0.29}$	3.92 ± 0.27	$4.09^{+0.40}_{-0.41}$	$6.26^{+0.11}_{-2.99}$
Q0831+101	1.69 ± 0.03	0.43 ± 0.06	1.20 ± 0.14	$0.46^{+0.06}_{-0.06}$	$0.30^{+0.05}_{-0.05}$	$0.67^{+0.19}_{-0.17}$	0.59 ± 0.09	$0.85^{+0.16}_{-0.16}$	$1.38^{+0.37}_{-0.41}$
Q0835+580	0.74 ± 0.02	3.57 ± 0.37	1.41 ± 0.09	$0.89^{+0.12}_{-0.12}$	$0.59^{+0.09}_{-0.09}$	$1.36^{+0.28}_{-0.28}$	2.68 ± 0.28	$2.02^{+0.35}_{-0.35}$	$3.32^{+0.47}_{-0.57}$
Q0856+124	2.00 ± 0.03	0.42 ± 0.06	1.48 ± 0.18	$0.11^{+0.02}_{-0.02}$	$0.08^{+0.02}_{-0.02}$	$0.23^{+0.08}_{-0.06}$	0.68 ± 0.10	$0.61^{+0.13}_{-0.13}$	$1.02^{+0.29}_{-0.35}$
Q0926+117	2.05 ± 0.02	0.84 ± 0.07	1.50 ± 0.12	$0.16^{+0.03}_{-0.03}$	$0.11^{+0.02}_{-0.02}$	$0.27^{+0.06}_{-0.06}$	1.38 ± 0.11	$1.31^{+0.15}_{-0.15}$	$2.09^{+0.31}_{-0.34}$
Q0941+261	1.97 ± 0.02	1.79 ± 0.24	1.32 ± 0.12	$2.32^{+0.25}_{-0.25}$	$1.25^{+0.22}_{-0.20}$	$1.40^{+0.54}_{-0.50}$	6.84 ± 0.93	$9.82^{+1.38}_{-1.38}$	$14.41^{+3.00}_{-3.17}$
Q1023+067	0.77 ± 0.02	1.66 ± 0.18	1.30 ± 0.10	$0.95^{+0.13}_{-0.13}$	$0.58^{+0.06}_{-0.06}$	$1.25^{+0.34}_{-0.26}$	1.54 ± 0.17	$1.56^{+0.20}_{-0.20}$	$2.49^{+0.53}_{-0.50}$
Q1055+499	2.01 ± 0.02	0.48 ± 0.07	1.33 ± 0.16	$0.45^{+0.11}_{-0.11}$	$0.31^{+0.06}_{-0.06}$	$0.72^{+0.18}_{-0.17}$	1.34 ± 0.20	$1.60^{+0.30}_{-0.31}$	$2.61^{+0.65}_{-0.73}$
Q1116+128	1.75 ± 0.02	1.00 ± 0.12	1.17 ± 0.13	$1.83^{+0.29}_{-0.31}$	$0.89^{+0.17}_{-0.18}$	$1.79^{+0.47}_{-0.41}$	2.02 ± 0.25	$3.95^{+0.52}_{-0.52}$	$5.63^{+1.33}_{-1.43}$
Q1158+122	1.24 ± 0.02	2.30 ± 0.29	>1.42	—	—	—	3.42 ± 0.43	—	—
Q1214+106	2.04 ± 0.04	0.39 ± 0.10	1.21 ± 0.11	$0.48^{+0.07}_{-0.07}$	$0.16^{+0.04}_{-0.04}$	$0.32^{+0.07}_{-0.07}$	0.72 ± 0.18	$1.70^{+0.32}_{-0.33}$	$2.05^{+0.61}_{-0.62}$
Q1221+113	1.81 ± 0.02	0.99 ± 0.11	1.21 ± 0.08	$1.01^{+0.11}_{-0.11}$	$0.49^{+0.08}_{-0.08}$	$0.98^{+0.16}_{-0.14}$	1.45 ± 0.17	$2.68^{+0.29}_{-0.29}$	$3.76^{+0.65}_{-0.67}$
Q1226+105	1.64 ± 0.02	1.20 ± 0.15	1.32 ± 0.10	$1.03^{+0.13}_{-0.13}$	$0.49^{+0.10}_{-0.06}$	$0.98^{+0.19}_{-0.15}$	2.66 ± 0.33	$3.87^{+0.47}_{-0.47}$	$5.42^{+1.03}_{-1.03}$
Q1258+404	1.69 ± 0.01	1.40 ± 0.09	1.30 ± 0.09	$0.80^{+0.10}_{-0.10}$	$0.55^{+0.09}_{-0.07}$	$1.28^{+0.36}_{-0.22}$	1.79 ± 0.12	$2.07^{+0.21}_{-0.21}$	$3.41^{+0.49}_{-0.48}$
Q1311−270	1.09 ± 0.04	3.31 ± 1.18	1.42 ± 0.07	$1.42^{+0.09}_{-0.09}$	$0.69^{+0.07}_{-0.06}$	$1.39^{+0.13}_{-0.13}$	5.33 ± 1.90	$5.63^{+1.58}_{-1.52}$	$7.91^{+2.55}_{-2.57}$
Q1313+200	1.14 ± 0.12	1.23 ± 0.95	1.48 ± 0.17	$0.52^{+0.11}_{-0.11}$	$0.38^{+0.08}_{-0.08}$	$0.94^{+0.31}_{-0.24}$	2.49 ± 1.91	$1.81^{+1.27}_{-1.22}$	$3.03^{+2.18}_{-2.15}$
Q1318+113	1.18 ± 0.03	1.20 ± 0.20	1.49 ± 0.17	$0.37^{+0.07}_{-0.07}$	$0.26^{+0.05}_{-0.05}$	$0.63^{+0.19}_{-0.16}$	2.00 ± 0.33	$1.48^{+0.31}_{-0.31}$	$2.42^{+0.64}_{-0.71}$
Q1323+655	1.91 ± 0.04	1.54 ± 0.27	1.49 ± 0.10	$0.26^{+0.04}_{-0.04}$	$0.17^{+0.03}_{-0.03}$	$0.37^{+0.07}_{-0.07}$	2.05 ± 0.35	$2.05^{+0.36}_{-0.36}$	$3.14^{+0.68}_{-0.69}$
Q1354+258	1.67 ± 0.01	1.27 ± 0.11	1.33 ± 0.09	$0.80^{+0.08}_{-0.08}$	$0.35^{+0.06}_{-0.06}$	$0.71^{+0.16}_{-0.11}$	2.21 ± 0.20	$3.32^{+0.30}_{-0.30}$	$4.48^{+0.73}_{-0.78}$
Q1402−012	1.84 ± 0.01	1.67 ± 0.21	1.53 ± 0.16	$0.57^{+0.08}_{-0.08}$	$0.45^{+0.19}_{-0.19}$	$1.23^{+0.20}_{-0.27}$	4.63 ± 0.58	$3.67^{+0.70}_{-0.65}$	$6.15^{+1.24}_{-1.39}$
Q1402+044	1.70 ± 0.01	1.53 ± 0.10	1.24 ± 0.08	$3.71^{+0.26}_{-0.26}$	$2.16^{+0.19}_{-0.19}$	$4.57^{+0.42}_{-0.36}$	6.09 ± 0.38	$8.93^{+0.70}_{-0.70}$	$13.74^{+1.75}_{-1.84}$
Q1442+101	2.14 ± 0.01	2.36 ± 0.38	1.27 ± 0.08	$6.41^{+0.42}_{-0.42}$	$4.75^{+0.49}_{-0.49}$	$11.99^{+0.85}_{-1.03}$	13.32 ± 2.15	$16.59^{+2.75}_{-2.75}$	$28.31^{+5.29}_{-5.32}$
Q1540+180	1.60 ± 0.01	1.15 ± 0.06	1.28 ± 0.09	$0.66^{+0.11}_{-0.08}$	$0.45^{+0.06}_{-0.06}$	$1.03^{+0.17}_{-0.16}$	1.40 ± 0.08	$1.61^{+0.13}_{-0.14}$	$2.65^{+0.35}_{-0.35}$
Q1542+042	1.75 ± 0.01	1.85 ± 0.13	1.16 ± 0.05	$3.60^{+0.24}_{-0.16}$	$1.91^{+0.14}_{-0.14}$	$3.93^{+0.31}_{-0.30}$	3.89 ± 0.27	$7.23^{+0.50}_{-0.50}$	$10.65^{+1.18}_{-1.20}$
Q1554−203	2.86 ± 0.00	0.67 ± 0.00	1.18 ± 0.11	$1.00^{+0.06}_{-0.06}$	$0.51^{+0.05}_{-0.05}$	$1.03^{+0.20}_{-0.19}$	2.01 ± 0.00	$4.39^{+0.16}_{-0.17}$	$6.29^{+0.65}_{-0.79}$
Q1556−245	1.04 ± 0.00	2.10 ± 0.00	1.36 ± 0.10	$2.24^{+0.19}_{-0.21}$	$1.64^{+0.14}_{-0.23}$	$4.06^{+0.55}_{-0.45}$	5.13 ± 0.00	$4.24^{+0.23}_{-0.26}$	$7.30^{+0.69}_{-0.82}$
Q1557−199	1.50 ± 0.00	0.88 ± 0.00	>1.20	—	—	—	1.19 ± 0.00	—	—

Table 6 (cont'd)

Object name (1)	β_{UV} (2)	$F_\nu(2500\,\text{Å})$ (3)	α_{ox} (4)	L_X (0.3-10 keV) (5)	L_X (2-10 keV) (6)	L_X (1-25 keV) (7)	L_{UV} (1000-3000Å) (8)	L_{EUV} (1000Å-0.3 keV) (9)	L_{EUV} (1000Å-1 keV) (10)
Q1602+576	1.79 ± 0.01	4.03 ± 0.35	1.30 ± 0.08	$5.89^{+0.45}_{-0.50}$	$3.89^{+0.33}_{-0.50}$	$8.81^{+0.85}_{-0.99}$	13.69 ± 1.19	$16.81^{+1.71}_{-1.71}$	$27.12^{+3.74}_{-3.88}$
Q1606+289	0.77 ± 0.02	0.59 ± 0.08	1.49 ± 0.13	$0.14^{+0.03}_{-0.03}$	$0.09^{+0.01}_{-0.02}$	$0.21^{+0.04}_{-0.04}$	0.72 ± 0.09	$0.49^{+0.07}_{-0.08}$	$0.78^{+0.16}_{-0.17}$
Q1607+183	2.07 ± 0.01	1.54 ± 0.28	1.23 ± 0.09	$3.85^{+0.23}_{-0.23}$	$2.25^{+0.28}_{-0.32}$	$4.77^{+0.45}_{-0.39}$	6.84 ± 1.26	$11.04^{+1.85}_{-1.85}$	$16.86^{+3.72}_{-3.76}$
Q1614+051	1.63 ± 0.01	0.84 ± 0.11	1.19 ± 0.12	$3.09^{+0.30}_{-0.32}$	$2.17^{+0.18}_{-0.44}$	$5.17^{+0.81}_{-0.59}$	3.22 ± 0.41	$4.32^{+0.70}_{-0.70}$	$7.45^{+1.59}_{-1.68}$
Q1629+120	1.54 ± 0.02	1.20 ± 0.10	1.22 ± 0.06	$1.24^{+0.10}_{-0.07}$	$0.82^{+0.08}_{-0.08}$	$1.85^{+0.31}_{-0.18}$	1.61 ± 0.13	$2.13^{+0.19}_{-0.19}$	$3.52^{+0.44}_{-0.45}$
Q1629+680	1.82 ± 0.00	0.99 ± 0.00	>1.41	—	—	—	2.68 ± 0.00	—	—
Q1633+382	1.71 ± 0.02	2.41 ± 0.30	1.11 ± 0.04	$4.81^{+0.21}_{-0.33}$	$3.02^{+0.17}_{-0.18}$	$6.64^{+0.62}_{-0.58}$	3.59 ± 0.44	$6.33^{+0.66}_{-0.67}$	$10.34^{+1.35}_{-1.35}$
Q1656+477	2.01 ± 0.02	2.17 ± 0.17	1.27 ± 0.06	$1.38^{+0.13}_{-0.13}$	$0.87^{+0.09}_{-0.07}$	$1.90^{+0.28}_{-0.24}$	3.01 ± 0.24	$4.27^{+0.37}_{-0.37}$	$6.69^{+0.80}_{-0.82}$
Q1658+575	1.53 ± 0.03	1.35 ± 0.52	1.39 ± 0.07	$0.67^{+0.05}_{-0.05}$	$0.36^{+0.04}_{-0.05}$	$0.75^{+0.10}_{-0.09}$	2.57 ± 0.99	$2.96^{+0.89}_{-0.93}$	$4.31^{+1.49}_{-1.50}$
Q1701+379	1.79 ± 0.01	0.55 ± 0.06	1.36 ± 0.08	$0.42^{+0.05}_{-0.03}$	$0.24^{+0.02}_{-0.04}$	$0.51^{+0.06}_{-0.06}$	1.46 ± 0.16	$1.81^{+0.20}_{-0.20}$	$2.72^{+0.41}_{-0.42}$
Q1702+298	1.81 ± 0.01	0.59 ± 0.04	1.21 ± 0.08	$0.81^{+0.09}_{-0.09}$	$0.58^{+0.06}_{-0.06}$	$1.41^{+0.19}_{-0.15}$	1.02 ± 0.07	$1.35^{+0.13}_{-0.14}$	$2.32^{+0.31}_{-0.33}$
Q1705+018	1.95 ± 0.00	1.44 ± 0.00	1.18 ± 0.08	$3.55^{+0.24}_{-0.26}$	$2.07^{+0.20}_{-0.24}$	$4.40^{+0.45}_{-0.55}$	4.39 ± 0.00	$7.63^{+0.28}_{-0.30}$	$11.75^{+1.08}_{-1.24}$
Q1726+344	1.74 ± 0.01	0.99 ± 0.10	>1.38	—	—	—	2.51 ± 0.24	—	—
Q1816+475	1.46 ± 0.04	1.72 ± 0.58	1.52 ± 0.14	$0.46^{+0.08}_{-0.07}$	$0.33^{+0.04}_{-0.04}$	$0.78^{+0.16}_{-0.15}$	3.32 ± 1.13	$2.62^{+0.86}_{-0.86}$	$4.22^{+1.56}_{-1.57}$
Q1857+566	1.42 ± 0.03	3.39 ± 1.35	1.49 ± 0.08	$0.52^{+0.06}_{-0.06}$	$0.27^{+0.04}_{-0.04}$	$0.55^{+0.10}_{-0.08}$	3.47 ± 1.38	$3.41^{+1.08}_{-1.13}$	$4.91^{+1.79}_{-1.80}$
Q2048+196	1.04 ± 0.00	2.41 ± 0.00	1.45 ± 0.09	$1.10^{+0.05}_{-0.05}$	$0.37^{+0.05}_{-0.04}$	$0.74^{+0.09}_{-0.08}$	4.38 ± 0.00	$5.34^{+0.12}_{-0.12}$	$6.54^{+0.63}_{-0.63}$
Q2150+053	1.85 ± 0.01	2.11 ± 0.19	1.44 ± 0.15	$0.68^{+0.12}_{-0.09}$	$0.35^{+0.10}_{-0.08}$	$0.71^{+0.22}_{-0.15}$	3.92 ± 0.34	$4.70^{+0.53}_{-0.54}$	$6.73^{+1.31}_{-1.55}$
Q2158+101	1.82 ± 0.02	0.80 ± 0.11	>1.37	—	—	—	1.14 ± 0.15	—	—
Q2212-299	1.54 ± 0.00	3.99 ± 0.00	1.53 ± 0.10	$1.41^{+0.16}_{-0.20}$	$1.00^{+0.12}_{-0.07}$	$2.39^{+0.22}_{-0.44}$	11.09 ± 0.00	$8.76^{+0.33}_{-0.38}$	$14.13^{+0.95}_{-1.15}$
Q2222+051	0.03 ± 0.01	4.03 ± 0.40	1.56 ± 0.12	$0.87^{+0.09}_{-0.09}$	$0.59^{+0.07}_{-0.07}$	$1.37^{+0.26}_{-0.23}$	5.13 ± 0.51	$2.32^{+0.31}_{-0.32}$	$3.80^{+0.71}_{-0.77}$
Q2223+210	1.85 ± 0.01	2.93 ± 0.19	1.15 ± 0.04	$5.83^{+0.25}_{-0.34}$	$4.22^{+0.35}_{-0.20}$	$10.37^{+0.42}_{-0.84}$	5.30 ± 0.34	$7.68^{+0.58}_{-0.58}$	$13.53^{+1.28}_{-1.30}$
Q2248+192	1.70 ± 0.02	0.84 ± 0.08	1.29 ± 0.07	$0.56^{+0.05}_{-0.04}$	$0.23^{+0.03}_{-0.02}$	$0.46^{+0.06}_{-0.04}$	1.22 ± 0.11	$2.07^{+0.17}_{-0.17}$	$2.73^{+0.38}_{-0.39}$
Q2251+244	1.19 ± 0.02	2.28 ± 0.38	1.20 ± 0.08	$5.28^{+0.41}_{-0.33}$	$4.24^{+0.32}_{-0.34}$	$12.03^{+0.88}_{-1.36}$	4.27 ± 0.71	$4.21^{+0.79}_{-0.79}$	$8.14^{+1.64}_{-1.63}$
Q2338+042	0.40 ± 0.01	0.98 ± 0.12	1.25 ± 0.13	$1.68^{+0.21}_{-0.15}$	$1.13^{+0.14}_{-0.17}$	$2.60^{+0.37}_{-0.35}$	1.68 ± 0.21	$1.53^{+0.26}_{-0.26}$	$2.66^{+0.65}_{-0.69}$
Q2345+061	1.56 ± 0.02	1.45 ± 0.14	1.29 ± 0.10	$0.70^{+0.08}_{-0.07}$	$0.37^{+0.07}_{-0.06}$	$0.75^{+0.16}_{-0.14}$	1.50 ± 0.15	$2.11^{+0.24}_{-0.24}$	$3.08^{+0.60}_{-0.66}$

Note. — (1) Object name. (2) The best-fitting UV-optical quasar continuum slope (§3.3). The 1σ uncertainties are derived from the fit covariance matrix. (3) The flux density at 2500 Å, in units of 10^{-27} ergs s^{-1} cm^{-2} Hz^{-1}. (4) The X-ray to UV-optical spectral index α_{ox}, as defined by Tananbaum et al. (1979). (5,6,7) Integrated luminosities over the rest-frame energy intervals 0.3 keV - 10 keV and 1 keV - 25 keV, units of 10^{46} ergs s^{-1}. (8) Integrated luminosity over the rest-frame interval 1000 Å - 3000 Å, as derived from our UV continuum modeling, in units of 10^{46} ergs s^{-1}. (9,10) Guideline estimates of the extreme-UV luminosity (§4.6). We interpolate over the rest-frame intervals 1000 Å to 1 keV and 1000 Å to 0.3 keV. Units of 10^{46} ergs s^{-1}.

Table 7.   Summary of Kolmogorov-Smirnov tests.

Variable (1)	Distributions (2)	p-value (3)
Redshift, z	XRT det.	0.28
Redshift, z	RQQs,RLQs	>0.99
λL_λ (2500Å)	XRT det.	0.66
λL_λ (2500Å)	RQQs,RLQs	0.98
UV–optical continuum spectral index $\beta_{\rm UV}$	RQQs,RLQs	0.89
νL_ν (2 keV)	RQQs,RLQs	$<10^{-6}$
X-ray Hardness Ratio	XRT det.	0.21
X-ray Hardness Ratio	RQQs,RLQs	0.22
X-ray Photon Index, Γ	RQQs,RLQs	0.83
UV to X-ray Spectral Index, $\alpha_{\rm ox}$	XRT det.	0.004
UV to X-ray Spectral Index, $\alpha_{\rm ox}$	RQQs,RLQs	$<10^{-6}$
Single-epoch Mass Estimate, $M_{\rm BH}$	XRT det.	0.93
Single-epoch Mass Estimate, $M_{\rm BH}$	RQQs,RLQs	0.39
Accretion Luminosity, $L_{\rm acc}(3000-25\,{\rm keV})$	RQQs,RLQs	0.46
Eddington Ratio, $\lambda_{\rm acc} = L_{\rm acc}/L_{\rm Edd}$	RQQs,RLQs	0.09

Note. — The p-values derived from 2-sample Kolmogorov-Smirnov tests for the distributions of several measured quantities, for radio-type subsamples and XRT detection status subsamples of our catalog. Column (1): The measured parameter under consideration. (2): The subsamples for which we perform the KS test. We test for similarity either between X-ray detected and non-detected quasars, or between RLQ and RQQ subsamples. (3): The derived p-value, for the null hypothesis that the subsamples are drawn from the same parent distribution.

Table 8.   Accretion luminosities, single-epoch spectroscopic $M_{\rm BH}$ estimates, and Eddington ratios.

Object name (1)	$L_{\rm acc}$ (3000Å-25 keV) (2)	$L_{\rm acc}$ (1μm-25 keV) (3)	$L_{\rm min}$ (4)	$\log[M_{\rm BH}/M_{\odot}]$ (5)	$\lambda_{\rm acc}$ (6)	$\lambda_{\rm maxL}$ (7)	$\lambda_{\rm minL}$ (8)
Radio-Quiet Quasars							
J014725.50-101439.11				9.60 ± 0.19			
J104915.44-011038.18				9.69 ± 0.087			
J110607.48-173113.60				$10.23^{+0.16}_{-0.26}$			
J111159.70+023719.76				9.64 ± 0.12			
J114449.32+032751.96				9.45 ± 0.08			
J123034.21+073305.32	$12.12^{+1.36}_{-1.41}$	14.45	5.40	9.10 ± 0.03	0.77 ± 0.13	0.92	0.34
J125140.83+080718.46	$9.67^{+1.14}_{-1.16}$	11.00	4.21	9.45 ± 0.05	0.27 ± 0.12	0.31	0.12
J131810.74+011140.86				9.45 ± 0.10			
J142923.92+024023.14				$9.78^{+0.32}_{-9.78}$			
J145717.86+024747.36				9.08 ± 0.04			
J215543.09-073902.05	$11.16^{+1.11}_{-1.14}$	14.83	5.88	$9.49^{+0.08}_{-0.10}$	0.29 ± 0.12	0.38	0.15
Q0000-001				9.43 ± 0.59			
Q0002-008				9.77 ± 0.59			
Q0003-006	$2.02^{+0.40}_{-0.44}$	2.30	1.00	9.03 ± 0.57	$0.15^{+0.4}_{-0.11}$	0.17	0.07
Q0008-008	$3.49^{+0.59}_{-0.62}$	4.06	1.55	8.98 ± 0.57	$0.29^{+0.77}_{-0.21}$	0.34	0.13
Q0015+026				8.87 ± 0.61			
Q0020+022				9.66 ± 0.57			
Q0040-017	$4.41^{+0.98}_{-1.08}$	5.41	2.25	9.86 ± 0.58	$0.05^{+0.13}_{-0.03}$	0.06	0.02
Q0107-005	$2.74^{+0.47}_{-0.48}$	3.37	1.15	9.35 ± 0.58	$0.1^{+0.26}_{-0.07}$	0.12	0.04
Q0115-011				9.59 ± 0.58			
Q0244+017				9.5 ± 0.58			
Q0249-184	—	—	—				
Q0252+016				10.1 ± 0.58			
Q0253-024	$4.27^{+0.77}_{-0.80}$	4.78	1.44	9.6 ± 0.58	$0.09^{+0.22}_{-0.06}$	0.10	0.03
Q0254-016	$5.87^{+1.17}_{-1.22}$	6.73	2.56	9.45 ± 0.58	$0.17^{+0.44}_{-0.12}$	0.19	0.07
Q0258+021	$15.88^{+2.80}_{-3.15}$	17.95	6.79	9.86 ± 0.57	$0.17^{+0.46}_{-0.13}$	0.2	0.07
Q0348+061	$28.49^{+0.93}_{-1.20}$	32.18	12.88	9.65 ± 0.58	$0.51^{+1.34}_{-0.37}$	0.57	0.23
Q0447-395	$8.86^{+3.62}_{-3.61}$	12.74	4.44	—			
Q0518-350	—	—	—				
Q1008-055	$13.87^{+5.12}_{-5.09}$	17.48	6.46	—			
Q1016-006	$5.32^{+1.28}_{-1.49}$	6.37	2.48	8.74 ± 0.56	$0.77^{+2.03}_{-0.56}$	0.92	0.36
Q1020+014				9.83 ± 0.6			
Q1043+071				8.77 ± 0.58			
Q1045+052	$4.10^{+1.00}_{-1.24}$	4.92	2.05	9.15 ± 0.57	$0.23^{+0.61}_{-0.17}$	0.28	0.12
Q1046+058	$5.09^{+0.89}_{-0.89}$	5.74	2.13	9.6 ± 0.57	$0.1^{+0.26}_{-0.07}$	0.11	0.04
Q1137+305	$16.26^{+2.52}_{-2.71}$	20.41	8.16	9.88 ± 0.57	$0.17^{+0.45}_{-0.12}$	0.21	0.09
Q1138+002				9.53 ± 0.58			
Q1146+111	$7.54^{+1.45}_{-1.71}$	8.95	3.77	9.35 ± 0.57	$0.27^{+0.7}_{-0.19}$	0.32	0.13
Q1151-004	—	—	—				
Q1203-111	—	—	—				
Q1208+105				9.24 ± 0.61			
Q1219+491				8.93 ± 0.57			
Q1223+178				10.32 ± 0.59			
Q1225-017	$34.20^{+7.72}_{-8.40}$	41.23	10.89	—			
Q1226-111	—	—	—				
Q1227+120				9.67 ± 0.63			
Q1230+164	$22.84^{+3.71}_{-4.31}$	29.21	10.57	10.51 ± 0.6	$0.06^{+0.15}_{-0.04}$	0.07	0.03
Q1232-004				9.12 ± 0.59			
Q1237+134	$13.30^{+1.34}_{-1.40}$	15.75	6.06	9.77 ± 0.57	$0.18^{+0.47}_{-0.13}$	0.21	0.08
Q1246-022	$7.64^{+1.71}_{-1.83}$	9.00	2.90	9.72 ± 0.58	$0.11^{+0.3}_{-0.08}$	0.14	0.04
Q1259+344				9.84 ± 0.59			
Q1330+011				9.33 ± 0.59			
Q1409+095				9.42 ± 0.58			
Q1434-009				9.39 ± 0.57			
Q1440-004	$14.88^{+7.09}_{-7.13}$	16.51	5.57	9.57 ± 0.57	$0.32^{+0.84}_{-0.23}$	0.36	0.12

Table 8 (cont'd)

Object name (1)	$L_{\rm acc}$ (3000Å-25 keV) (2)	$L_{\rm acc}$ (1μm-25 keV) (3)	$L_{\rm min}$ (4)	$\log[M_{\rm BH}/M_\odot]$ (5)	$\lambda_{\rm acc}$ (6)	$\lambda_{\rm maxL}$ (7)	$\lambda_{\rm minL}$ (8)
Q1443-010	$5.11^{+0.65}_{-0.71}$	6.62	2.54	9.82 ± 0.58	$0.06^{+0.16}_{-0.04}$	0.08	0.03
Q1517+239				9.54 ± 0.59			
Q1634+406				9.4 ± 0.61			
Q1638+390				9.62 ± 0.58			
Q1704+710	$9.85^{+4.14}_{-4.16}$	11.93	4.26	9.51 ± 0.58	$0.24^{+0.63}_{-0.17}$	0.29	0.1
Q2233+136				9.2 ± 0.59			
Q2239+007	$4.49^{+0.81}_{-0.82}$	5.13	1.95	9.75 ± 0.59	$0.06^{+0.17}_{-0.05}$	0.07	0.03
Q2334+019				9.62 ± 0.58			
Q2341+010				8.8 ± 0.6			
Q2350-007				9.74 ± 0.76			
Q2351+022	$6.29^{+0.96}_{-0.96}$	7.89	3.04	9.5 ± 0.58	$0.16^{+0.41}_{-0.11}$	0.2	0.08
Q2359+002				9.68 ± 0.58			
Radio-Loud Quasars							
J082328.62+061146.07	$24.86^{+3.11}_{-3.22}$	28.77	10.66	$9.75^{+0.08}_{-0.10}$	$0.35^{+0.09}_{-0.06}$	0.41	0.15
J094853.60+085514.40	$18.13^{+1.88}_{-1.86}$	25.33	9.01	$9.66^{+0.11}_{-0.15}$	$0.31^{+0.13}_{-0.07}$	0.44	0.16
J112542.30+000101.33	$11.73^{+1.37}_{-1.41}$	13.15	4.79	8.84 ± 0.03	$1.35^{+0.11}_{-0.1}$	0.70	0.35
J215954.45-002150.17	$23.80^{+2.65}_{-2.86}$	28.86	10.56	9.40 ± 0.09	$0.75^{+0.18}_{-0.14}$	0.91	0.33
J234830.41+003918.57	$12.43^{+1.63}_{-1.76}$	14.61	5.79	9.18 ± 0.05	$0.65^{+0.08}_{-0.07}$	0.76	0.30
Q0017+154	$11.48^{+1.70}_{-1.76}$	13.96	4.66	9.61 ± 0.58	$0.23^{+0.59}_{-0.16}$	0.27	0.09
Q0038-019	$12.56^{+1.35}_{-1.30}$	14.82	5.61	9.84 ± 0.57	$0.15^{+0.38}_{-0.11}$	0.17	0.06
Q0106+013	$15.04^{+1.60}_{-1.62}$	17.55	8.19	9.42 ± 0.57	$0.45^{+1.19}_{-0.33}$	0.53	0.25
Q0109+176	$7.18^{+0.95}_{-1.01}$	8.47	3.36	9.88 ± 0.6	$0.07^{+0.2}_{-0.05}$	0.09	0.04
Q0123+257	$24.56^{+3.46}_{-3.71}$	26.77	12.26	—			
Q0206+293	$2.97^{+1.01}_{-0.96}$	3.23	1.19	9.12 ± 0.57	$0.18^{+0.47}_{-0.13}$	0.19	0.07
Q0225-014	$11.62^{+1.45}_{-1.50}$	12.74	4.61	9.13 ± 0.57	$0.68^{+1.8}_{-0.49}$	0.75	0.27
Q0226-038	$20.46^{+2.73}_{-2.85}$	23.16	9.18	9.72 ± 0.58	$0.31^{+0.81}_{-0.22}$	0.35	0.14
Q0238+100	$11.79^{+3.07}_{-3.09}$	12.97	4.66	9.39 ± 0.59	$0.38^{+1.0}_{-0.27}$	0.42	0.15
Q0317-023	$2.07^{+0.17}_{-0.20}$	2.25	0.89	8.71 ± 0.58	$0.32^{+0.84}_{-0.23}$	0.35	0.14
Q0352+123	$8.53^{+0.97}_{-1.00}$	9.86	3.28	8.97 ± 0.58	$0.73^{+1.93}_{-0.53}$	0.85	0.28
Q0445+097	$9.65^{+0.85}_{-1.10}$	10.30	5.06	9.07 ± 0.6	$0.66^{+1.73}_{-0.48}$	0.70	0.35
Q0458-020	$18.85^{+1.19}_{-1.36}$	35.37	12.37	9.36 ± 0.59	$0.66^{+1.74}_{-0.48}$	1.24	0.43
Q0504+030	$11.28^{+1.00}_{-1.40}$	12.18	5.68	9.06 ± 0.59	$0.79^{+2.07}_{-0.57}$	0.85	0.4
Q0730+257	$4.78^{+1.18}_{-1.21}$	5.29	2.02	9.48 ± 0.57	$0.13^{+0.33}_{-0.09}$	0.14	0.05
Q0751+298	$9.52^{+1.54}_{-1.60}$	10.50	3.93	9.45 ± 0.58	$0.27^{+0.71}_{-0.2}$	0.30	0.11
Q0758+120				9.78 ± 0.6	—		
Q0802+103	$7.33^{+1.02}_{-1.06}$	8.93	3.39	9.3 ± 0.57	$0.29^{+0.77}_{-0.21}$	0.36	0.14
Q0805+046	$19.03^{+2.62}_{-2.78}$	21.28	7.48	9.78 ± 0.57	$0.25^{+0.67}_{-0.18}$	0.28	0.1
Q0808+289	$11.46^{+1.56}_{-1.67}$	13.86	5.20	9.85 ± 0.6	$0.13^{+0.34}_{-0.09}$	0.16	0.06
Q0831+101	$2.65^{+0.64}_{-0.67}$	2.95	1.27	9.59 ± 0.59	$0.05^{+0.14}_{-0.04}$	0.06	0.03
Q0835+580	$7.35^{+1.12}_{-1.14}$	11.33	4.03	9.94 ± 0.6	$0.07^{+0.17}_{-0.05}$	0.10	0.04
Q0856+124	$1.93^{+0.41}_{-0.46}$	2.22	0.93	9.14 ± 0.61	$0.11^{+0.29}_{-0.08}$	0.13	0.05
Q0926+117	$3.74^{+0.49}_{-0.52}$	4.20	1.65	9.33 ± 0.6	$0.14^{+0.37}_{-0.1}$	0.16	0.06
Q0941+261	$22.65^{+4.47}_{-4.60}$	25.13	8.24	9.76 ± 0.59	$0.31^{+0.83}_{-0.23}$	0.35	0.11
Q1023+067	$5.27^{+1.01}_{-0.95}$	7.47	2.78	9.29 ± 0.6	$0.21^{+0.56}_{-0.16}$	0.30	0.11
Q1055+499	$4.67^{+1.03}_{-1.11}$	5.13	2.06	9.7 ± 0.59	$0.07^{+0.19}_{-0.05}$	0.08	0.03
Q1116+128	$9.45^{+2.04}_{-2.09}$	10.39	3.81	9.08 ± 0.57	$0.62^{+1.64}_{-0.45}$	0.69	0.25
Q1158+122				9.54 ± 0.59	—		
Q1214+106	$3.09^{+0.87}_{-0.88}$	3.33	1.03	9.48 ± 0.61	$0.08^{+0.21}_{-0.06}$	0.09	0.03
Q1221+113	$6.20^{+0.99}_{-0.98}$	6.83	2.44	9.24 ± 0.58	$0.29^{+0.75}_{-0.21}$	0.31	0.11
Q1226+105	$9.05^{+1.56}_{-1.56}$	10.45	3.64	10.03 ± 0.59	$0.07^{+0.18}_{-0.05}$	0.08	0.03
Q1258+404	$6.47^{+0.97}_{-0.86}$	7.36	3.06	9.17 ± 0.62	$0.35^{+0.92}_{-0.25}$	0.40	0.17
Q1311-270	$14.64^{+4.59}_{-4.60}$	19.91	6.73	9.85 ± 0.59	$0.17^{+0.44}_{-0.12}$	0.18	0.08
Q1313+200	$6.46^{+4.37}_{-4.32}$	8.78	3.43	9.76 ± 0.57	$0.09^{+0.24}_{-0.07}$	0.12	0.05
Q1318+113	$5.06^{+1.15}_{-1.21}$	6.84	2.64	—			
Q1323+655	$5.56^{+1.10}_{-1.12}$	6.36	2.42	9.8 ± 0.6	$0.07^{+0.18}_{-0.05}$	0.08	0.03
Q1354+258	$7.40^{+1.09}_{-1.08}$	8.53	2.92	—			

Table 8   (cont'd)

Object name (1)	L_{acc} (3000Å-25 keV) (2)	L_{acc} (1μm-25 keV) (3)	L_{min} (4)	$\log[M_{BH}/M_\odot]$ (5)	λ_{acc} (6)	λ_{maxL} (7)	λ_{minL} (8)
Q1402+044	$12.00^{+2.03}_{-2.24}$	13.95	10.65	9.13 ± 0.57	$1.45^{+3.82}_{-1.05}$	1.63	0.63
Q1402-012	$24.39^{+2.55}_{-2.58}$	27.38	5.85	9.26 ± 0.58	$0.53^{+1.39}_{-0.38}$	0.61	0.26
Q1442+101	$53.61^{+8.29}_{-8.50}$	57.59	25.31	10.26 ± 0.59	$0.24^{+0.62}_{-0.17}$	0.25	0.11
Q1540+180	$5.08^{+0.57}_{-0.58}$	5.85	2.43	9.41 ± 0.58	$0.16^{+0.41}_{-0.11}$	0.18	0.08
Q1542+042	$18.47^{+1.76}_{-1.78}$	20.28	7.82	8.87 ± 0.57	$1.99^{+5.23}_{-1.44}$	2.18	0.84
Q1554-203	$9.33^{+0.84}_{-0.99}$	9.59	3.04	9.41 ± 0.58	$0.29^{+0.76}_{-0.21}$	0.30	0.09
Q1556-245	$16.48^{+1.24}_{-1.27}$	21.88	9.19	9.59 ± 0.59	$0.34^{+0.88}_{-0.24}$	0.45	0.19
Q1557-199	—	—	—				
Q1602+576	$49.63^{+5.77}_{-6.05}$	55.69	22.51	10.11 ± 0.59	$0.31^{+0.81}_{-0.22}$	0.34	0.14
Q1606+289	$1.71^{+0.29}_{-0.31}$	2.74	0.93	9.0 ± 0.65	$0.14^{+0.36}_{-0.1}$	0.22	0.07
Q1607+183	$25.61^{+5.37}_{-5.47}$	27.81	10.54	9.99 ± 0.63	$0.21^{+0.55}_{-0.15}$	0.23	0.09
Q1614+051	$15.84^{+2.60}_{-2.91}$	17.56	8.39	8.94 ± 0.57	$1.46^{+3.83}_{-1.05}$ 1.61	0.77	
Q1629+120	$6.98^{+0.88}_{-0.76}$	7.93	3.46	9.53 ± 0.58	$0.16^{+0.43}_{-0.12}$	0.18	0.08
Q1629+680				9.19 ± 0.57	—		
Q1633+382	$20.56^{+2.41}_{-2.38}$	22.30	10.22	9.43 ± 0.57	$0.61^{+1.6}_{-0.44}$	0.66	0.30
Q1656+477	$11.60^{+1.32}_{-1.30}$	12.65	4.91	9.88 ± 0.58	$0.12^{+0.32}_{-0.09}$	0.13	0.05
Q1658+575	$7.63^{+2.57}_{-2.59}$	9.16	3.31	9.07 ± 0.57	$0.51^{+1.35}_{-0.37}$	0.62	0.22
Q1701+379	$4.69^{+0.64}_{-0.65}$	5.34	1.97	9.26 ± 0.59	$0.21^{+0.54}_{-0.15}$	0.23	0.09
Q1702+298	$4.75^{+0.57}_{-0.55}$	5.20	2.43	8.74 ± 0.61	$0.69^{+1.81}_{-0.5}$	0.75	0.35
Q1705+018	$20.54^{+1.53}_{-1.79}$	22.18	8.79	9.44 ± 0.6	$0.59^{+1.56}_{-0.43}$	0.23	0.09
Q1726+344				9.13 ± 0.57	—		
Q1816+475	$8.31^{+2.85}_{-2.85}$	10.45	4.09	9.15 ± 0.59	$0.47^{+1.23}_{-0.34}$	0.59	0.23
Q1857+566	$8.94^{+3.26}_{-3.26}$	11.28	4.02	9.62 ± 0.57	$0.17^{+0.45}_{-0.12}$	0.22	0.08
Q2048+196	$11.66^{+0.72}_{-0.82}$	16.26	5.13	8.88 ± 0.57	$1.21^{+3.19}_{-0.88}$	1.69	0.53
Q2150+053	$11.36^{+1.88}_{-2.05}$	12.99	4.63	9.62 ± 0.58	$0.22^{+0.57}_{-0.16}$	0.25	0.09
Q2158+101				8.96 ± 0.58	—		
Q2212-299	$27.62^{+1.16}_{-1.59}$	34.18	13.49	9.51 ± 0.57	$0.68^{+1.79}_{-0.49}$	0.84	0.33
Q2222+051	$10.31^{+1.48}_{-1.51}$	(27.67)	6.51	9.48 ± 0.64	$0.27^{+0.72}_{-0.2}$	0.73	0.17
Q2223+210	$29.20^{+2.04}_{-2.48}$	31.40	15.67	10.01 ± 0.59	$0.23^{+0.59}_{-0.16}$	0.23	0.12
Q2248+192	$4.41^{+0.55}_{-0.55}$	5.01	1.68	9.43 ± 0.58	$0.13^{+0.34}_{-0.09}$	0.15	0.05
Q2251+244	$24.43^{+3.23}_{-3.71}$	28.18	16.29	10.23 ± 0.63	$0.12^{+0.3}_{-0.08}$	0.13	0.08
Q2338+042	$6.93^{+1.23}_{-1.26}$	10.62	4.28	—	—		
Q2345+061	$5.34^{+0.91}_{-0.94}$	6.20	2.25	9.58 ± 0.57	$0.11^{+0.3}_{-0.08}$	0.13	0.05

Note. — (2,3) Guideline estimates of the integrated luminosity over the rest-frame intervals 3000 Å– 25 keV and 1 μm – 25 keV; the latter interval may be a better representation of the bolometric luminosity, but involves an uncertain extrapolation into the rest-frame optical. Units of 10^{46} ergs s^{-1}. We do not attempt to quantify the uncertainty of the extrapolation beyond 3000 Å; the remaining uncertainties are identical for the two measures. (4) The minimum accretion luminosity, i.e., the sum of the integrated luminosities of our UV–optical and X-ray models. Units of 10^{46} ergs s^{-1}. (5) The single-epoch spectroscopic black hole mass estiamtes. (6,7,8) Estiamted Eddington ratios based on L_{acc}(3000Å–25 keV), L_{min}, and L_{acc}(1μm–25 keV).

Table 9. Posterior medians of the intercept (A) and slope (B) obtained from Linmix_err modeling of the log-linear $L_{\mathrm{UV}}-L_{\mathrm{X}}$ relationship (Equation 2). We model the radio classes seperately, and for each class we investigate the X-ray detected and the full (censored) sample. In the lower part of the table, we list some previous results from the literature (as derived by the original authors, using heterogenous linear regression methods). Here, S06 denotes Steffen et al. (2006), J07:Just et al. (2007), L16:Lusso & Risaliti (2016).

Sample	Intercept, A	Slope, B
RLQs, detected	4.16 ± 3.66	0.76 ± 0.11
RLQs, all	4.47 ± 3.48	0.75 ± 0.11
RQQs, detected	6.95 ± 4.54	0.65 ± 0.15
RQQs, all	11.87 ± 6.07	0.48 ± 0.19
RQQs, S06	6.873 ± 0.625	0.642 ± 0.021
RQQs, J07	7.055 ± 0.553	0.636 ± 0.018
RQQs, L16	8.664 ± 0.417	0.582 ± 0.014
RLQs, M11	3.557 ± 0.017	$0.831^{+0.026}_{-0.025}$

APPENDIX A: SPECTRAL ENERGY DISTRIBUTIONS FOR RADIO-QUIET SAMPLE

We present the optical to X-ray spectral energy distributions (SEDs) of the radio-quiet quasars in our sample, along with the UV photometry and continuum modeling, in Figures A1 through A23; we present the SEDs of radio-loud objects in Appendix B. Where available, we show the SDSS spectra used to guide our selection of photometric data (§3.3) as gray curves in the right-hand panels. For quasars without SDSS spectroscopy, we show the high-redshift quasar template spectrum produced by Selsing et al. (2016), normalized to the continuum model flux level at 2500 Å. This template is constructed from spectroscopic observations of seven bright ($M_i \approx -29$ mag) quasars at $1 < z < 2$, i.e., objects that overlap our sample in terms of luminosity and redshift distribution, but that are somewhat brighter and reside at lower redshift than the average properties of our quasars. For such bright quasars the host galaxy contribution is expected to be small. Note that we do not use this template spectrum directly to model the UV continuum (§3.3), we merely use it as a rough guide to the amount of emission line flux in a given UV bandpass for a typical bright quasar.

Due to an unfortunate oversight, we do not show the emission-line corrected fluxes in the UV–optical SEDs shown here, but only the observed fluxes. We will update these figures to also show the emission-line corrected fluxes before submitting this work to a journal.
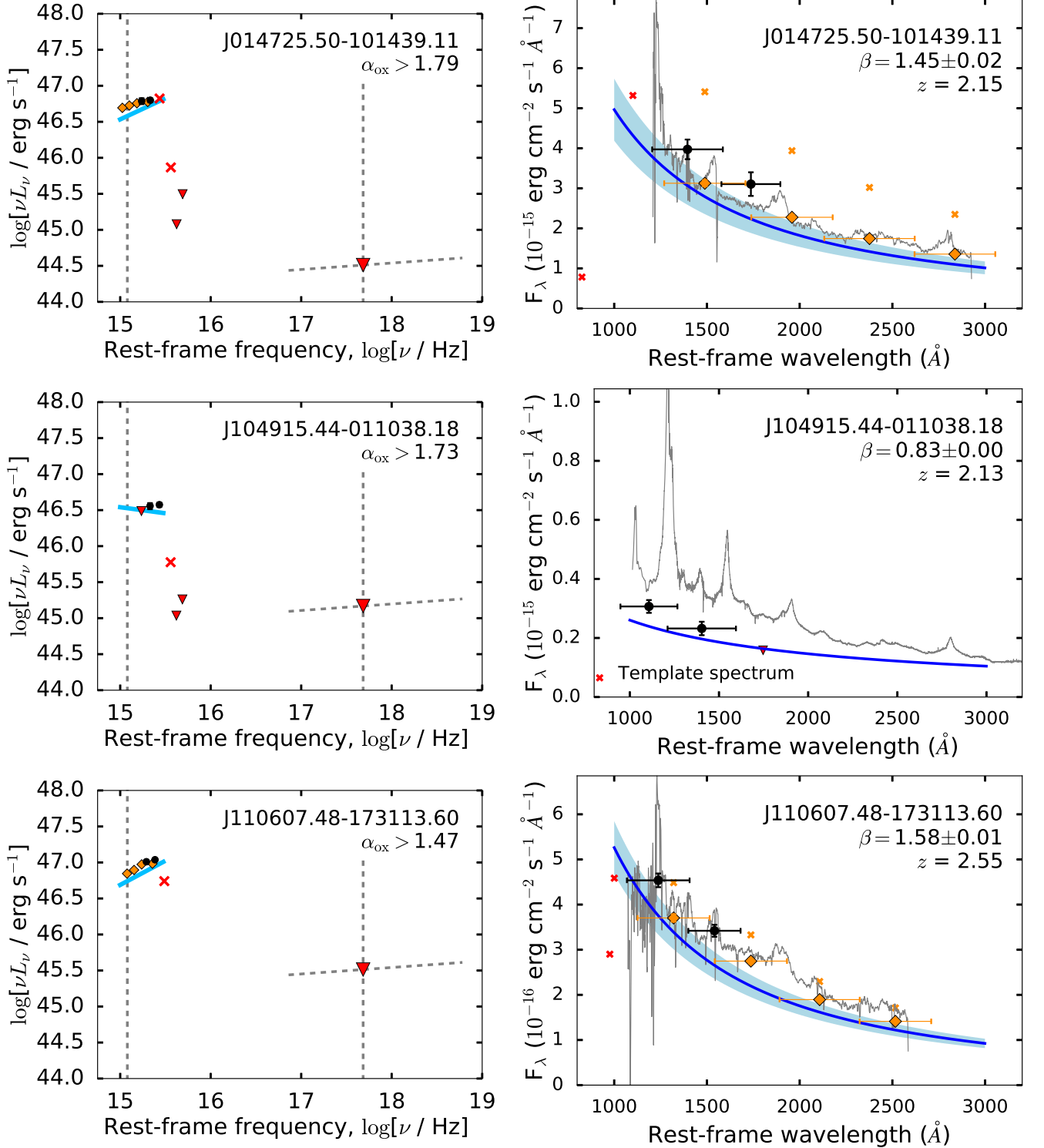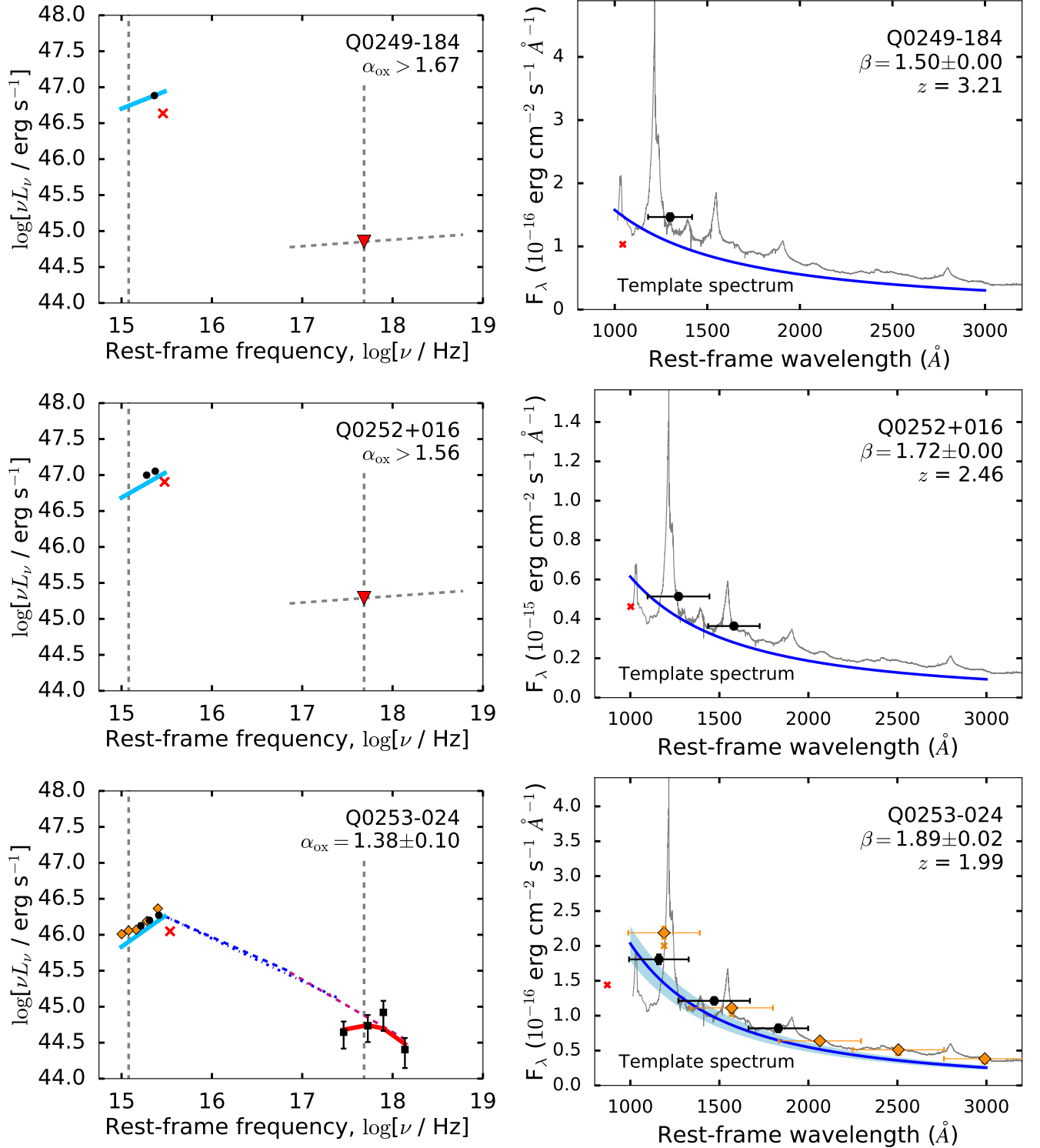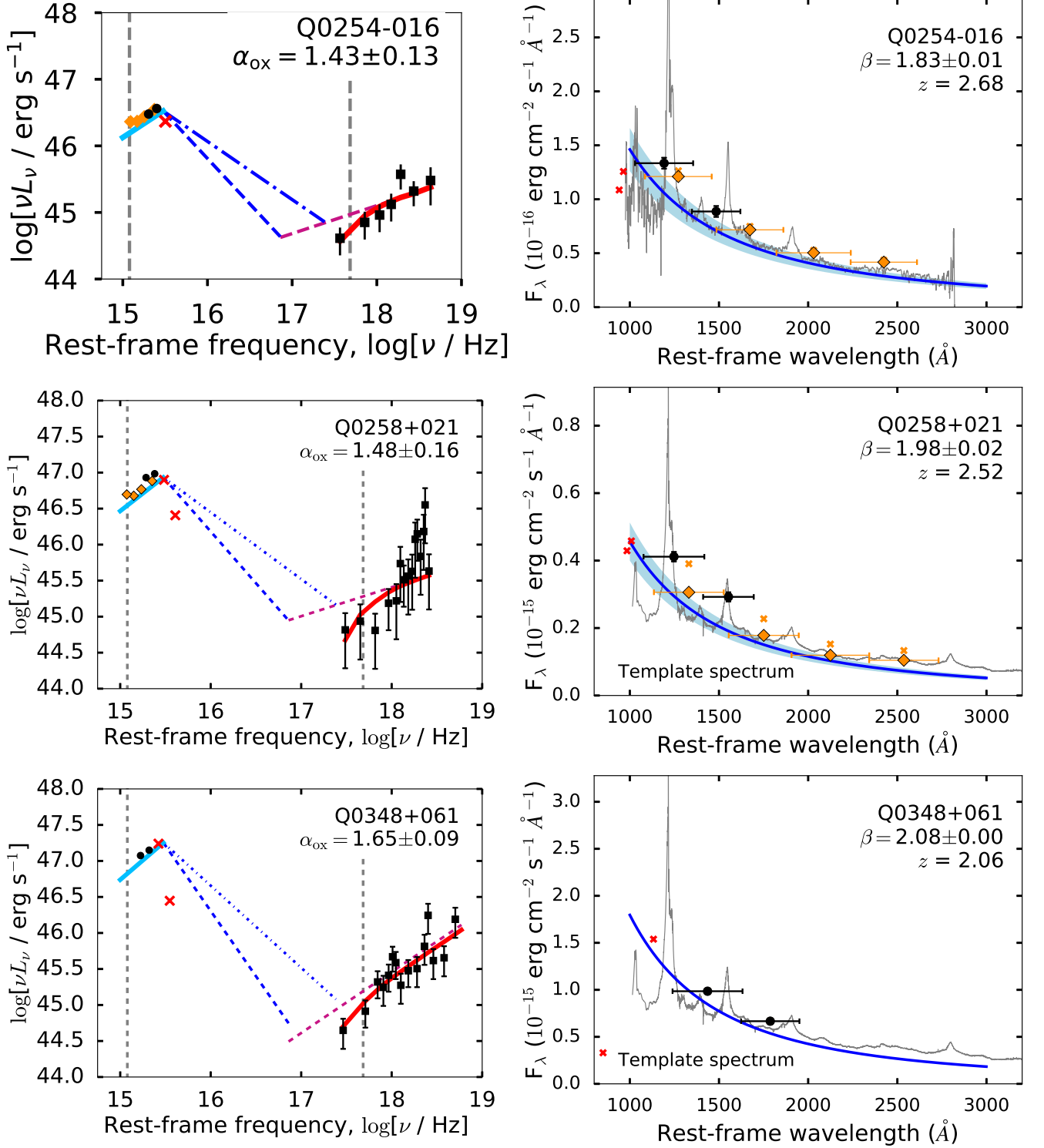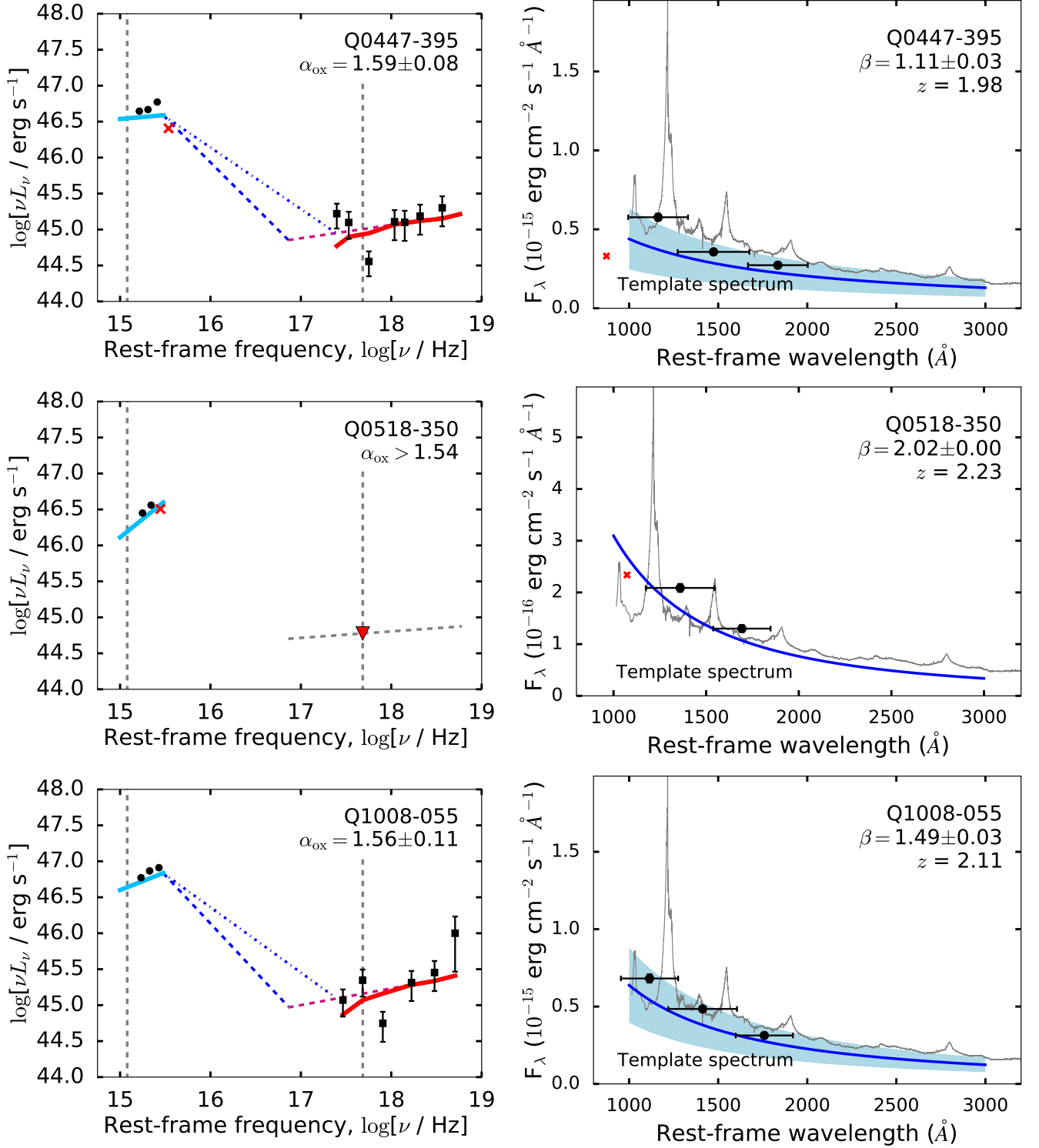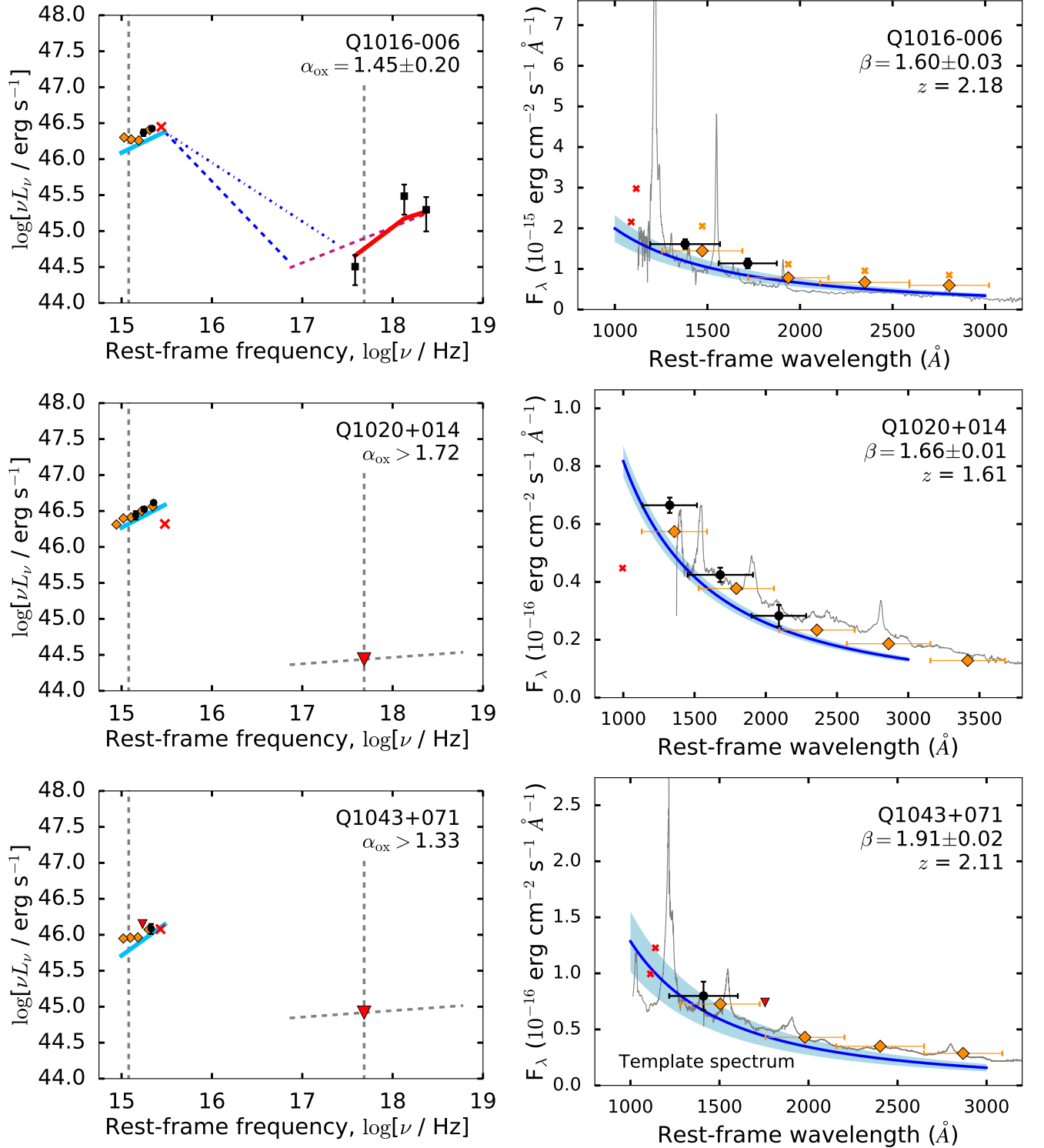
Figure A1. *Left:* Rest-frame UV to X-ray spectral energy distributions (SEDs) of quasars in our sample. *Right*: UV photometry and continuum modeling. See Figure 4 for symbol and color coding. *Notes on individual objects:* For J10491544-01103818, while SDSS photometric data are available, we exclude them based on the DQ flags (deblending issues). For J01472550-10143911 and J11060748-17311360, we use the VB quasar template to estimate the BEL contribution.
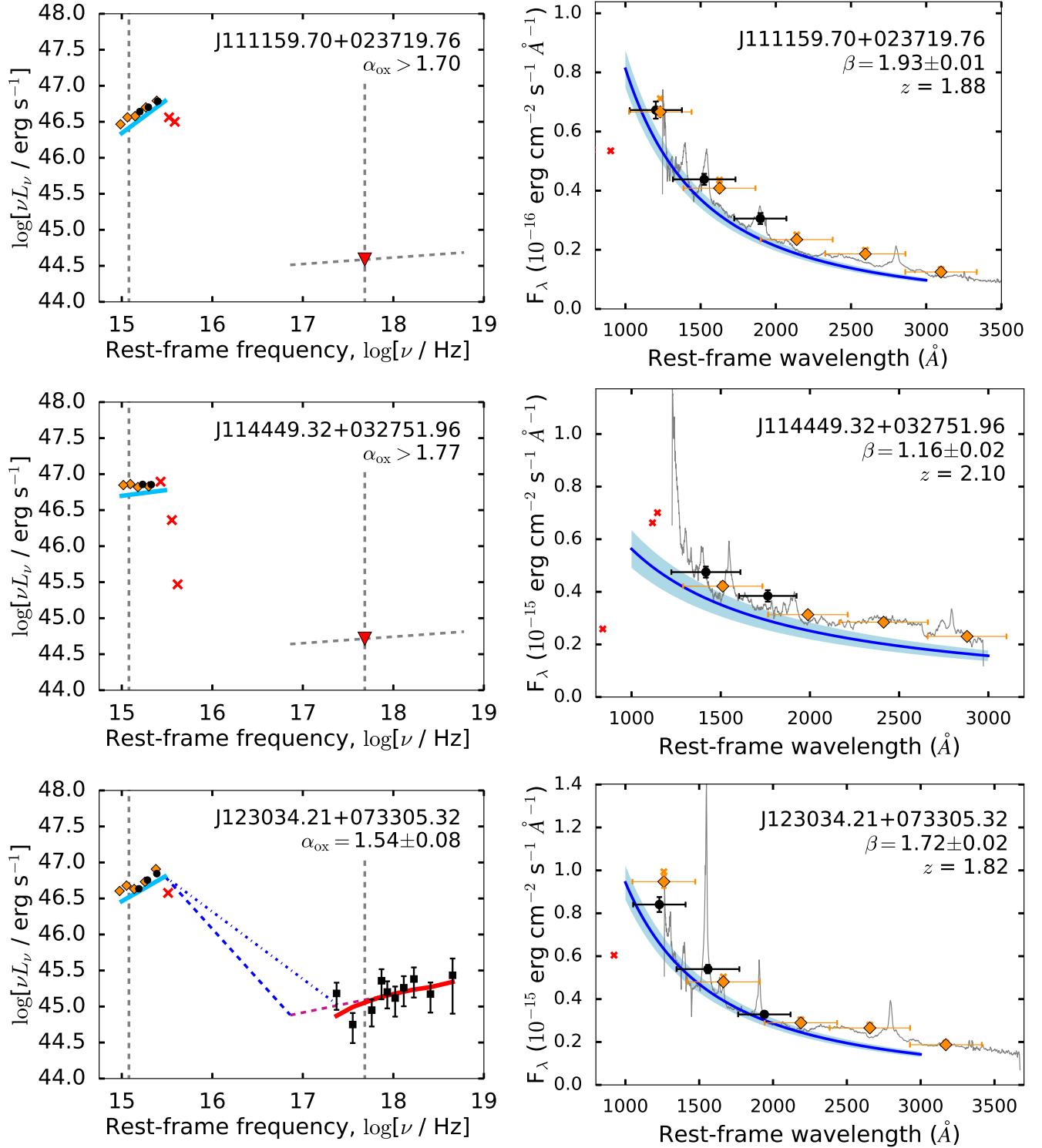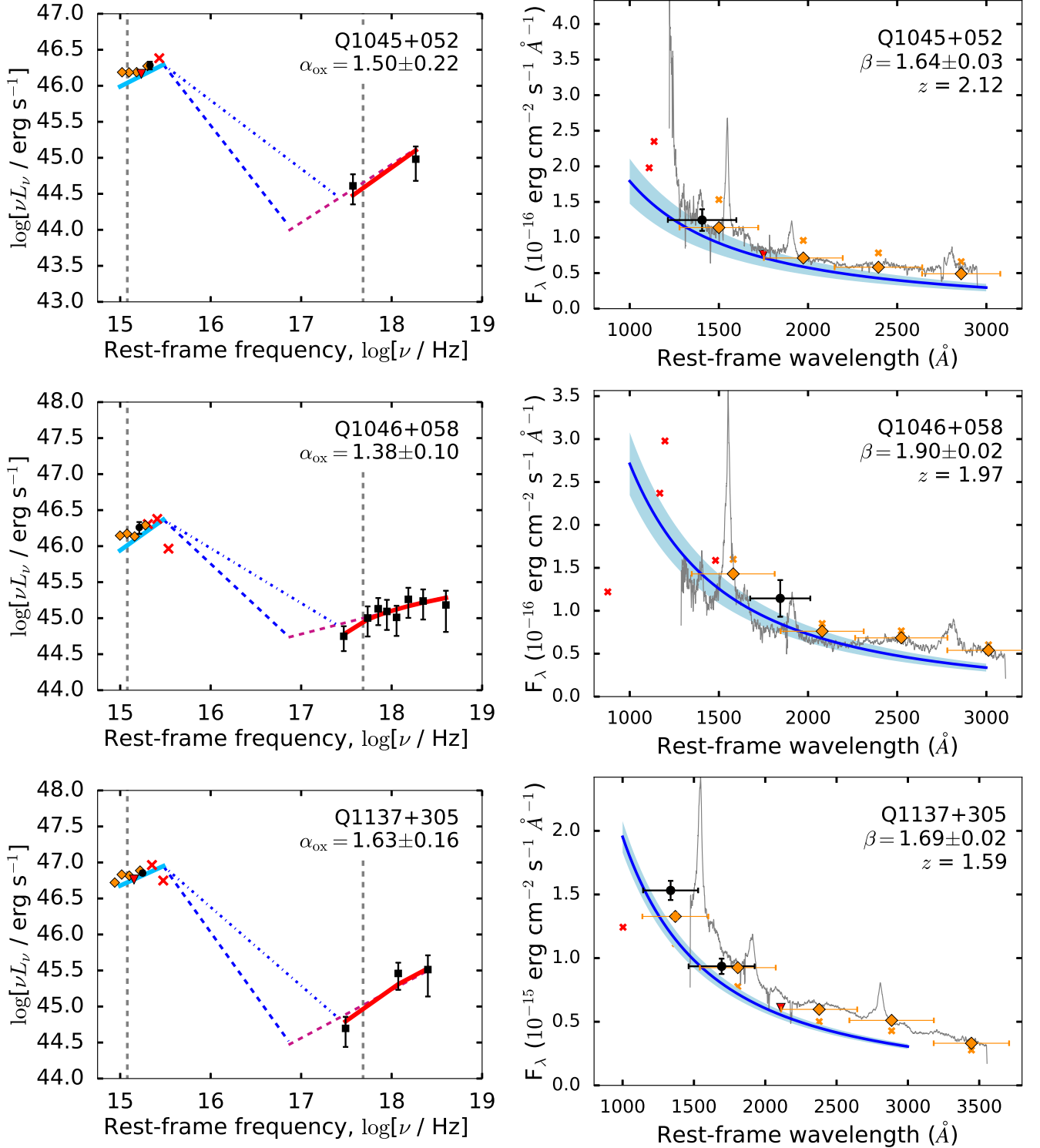
Figure A2. *Left:* Rest-frame UV to X-ray spectral energy distributions (SEDs) of quasars in our sample. *Right*: UV photometry and continuum modeling. See Figure 4 for symbol and color coding. *Notes on individual objects:* None.
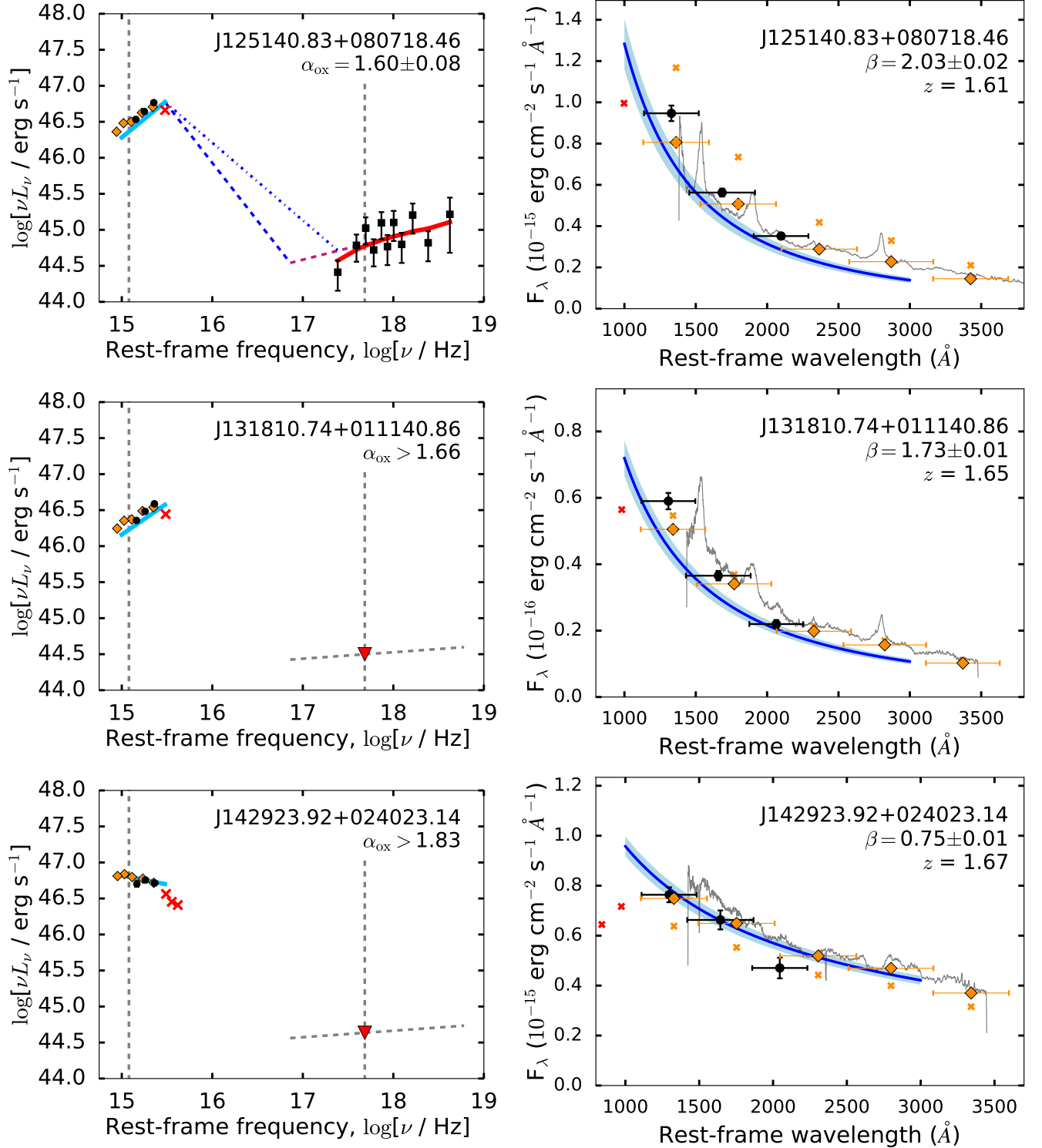
Figure A3. *Left:* Rest-frame UV to X-ray spectral energy distributions (SEDs) of quasars in our sample. *Right:* UV photometry and continuum modeling. See Figure 4 for symbol and color coding. *Notes on individual objects:* For J13181074+01114086, we use the VB quasar template to estimate the BEL contribution.
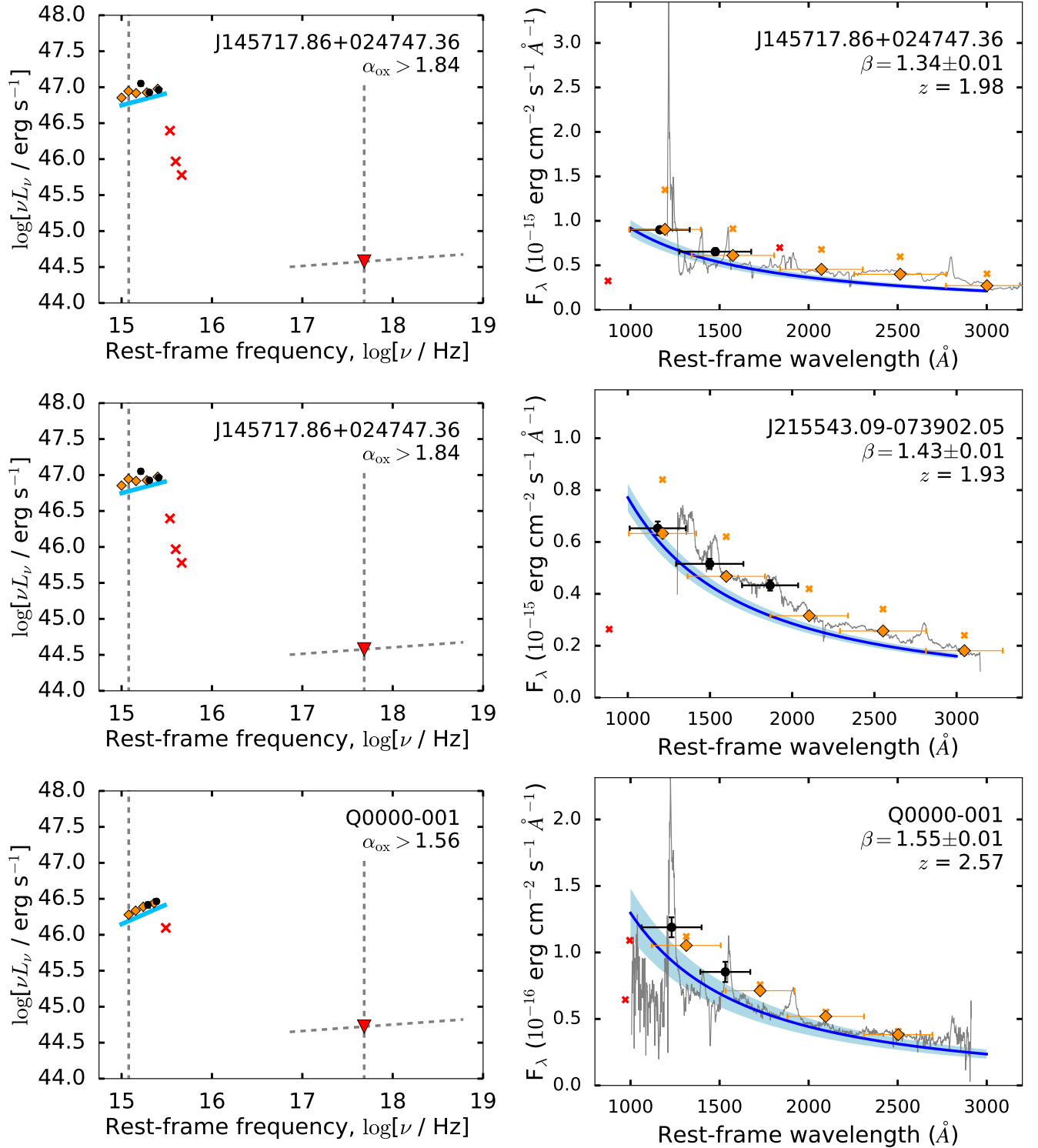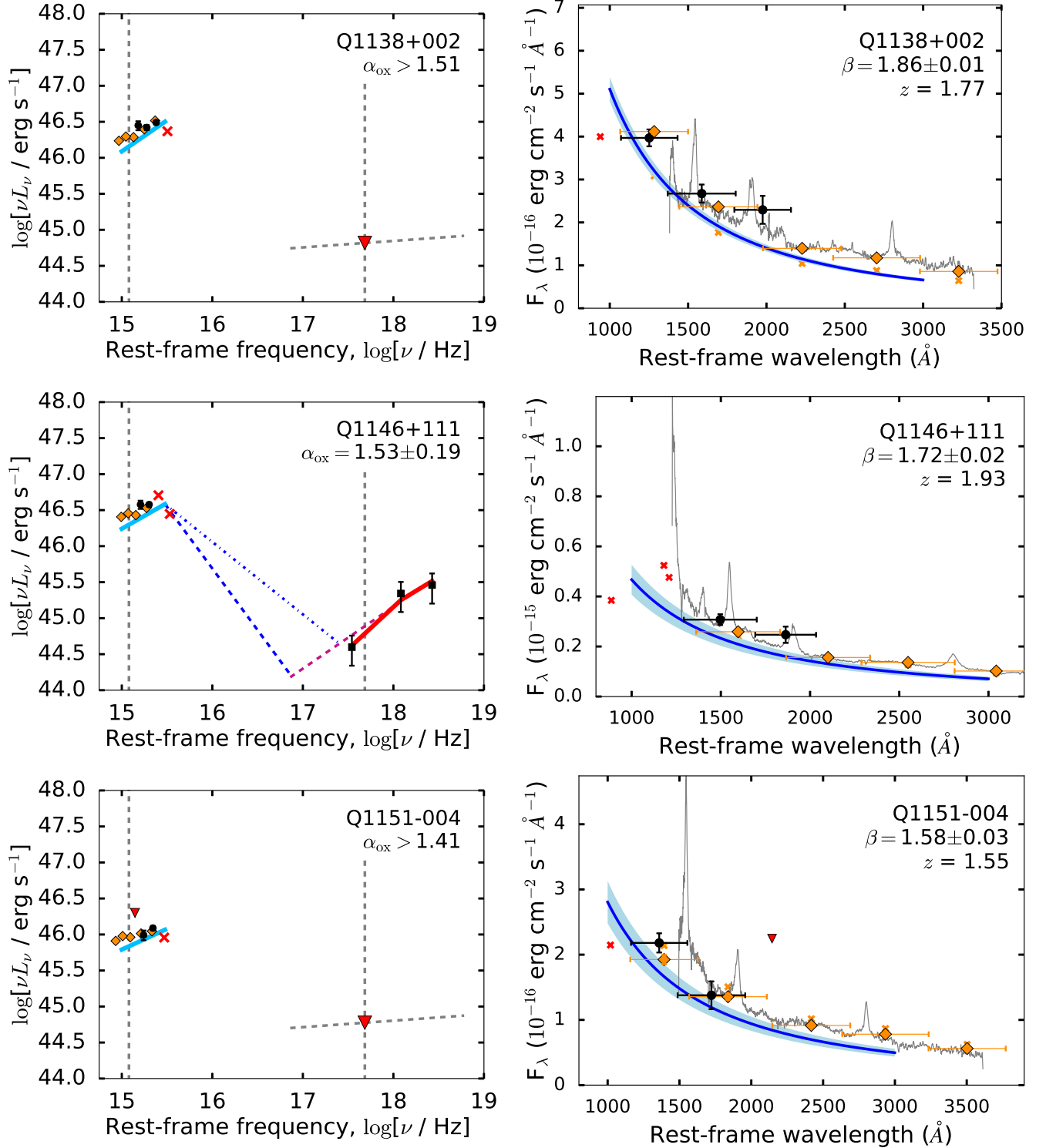
Figure A4. *Left:* Rest-frame UV to X-ray spectral energy distributions (SEDs) of quasars in our sample. *Right*: UV photometry and continuum modeling. See Figure 4 for symbol and color coding. *Notes on individual objects:* For J14571786+02474736, we exclude the UVOT *V* filter from the UV-optical model fit, as its emission-line correction seems underestimated based on visual comparison with the SDSS spectrum. The UV-optical model is only weakly dependent on this choice (i.e., β changes by less than 0.02 when including *V*). For J14571786+02474736, we use the VB quasar template to estimate the BEL contribution.
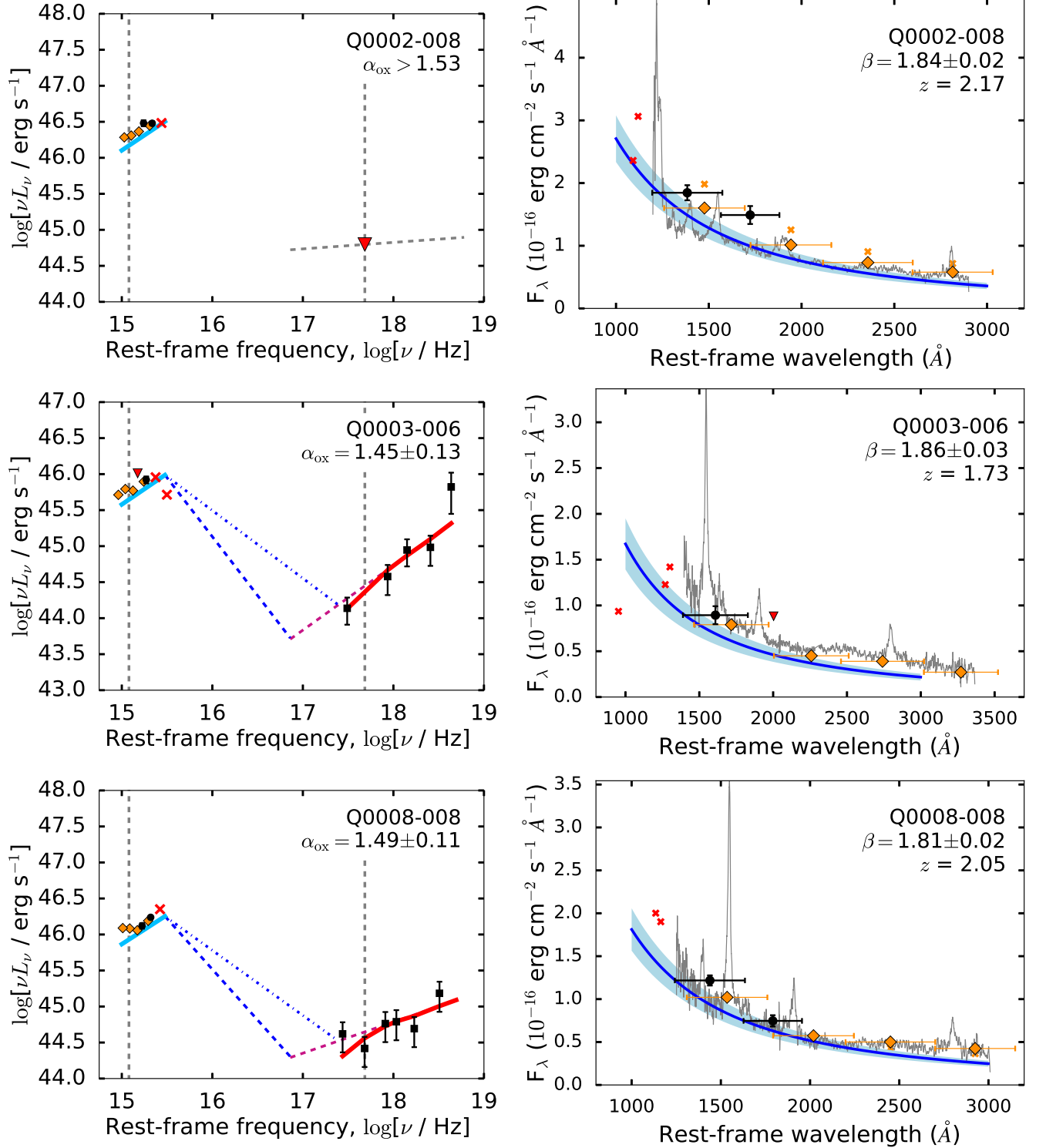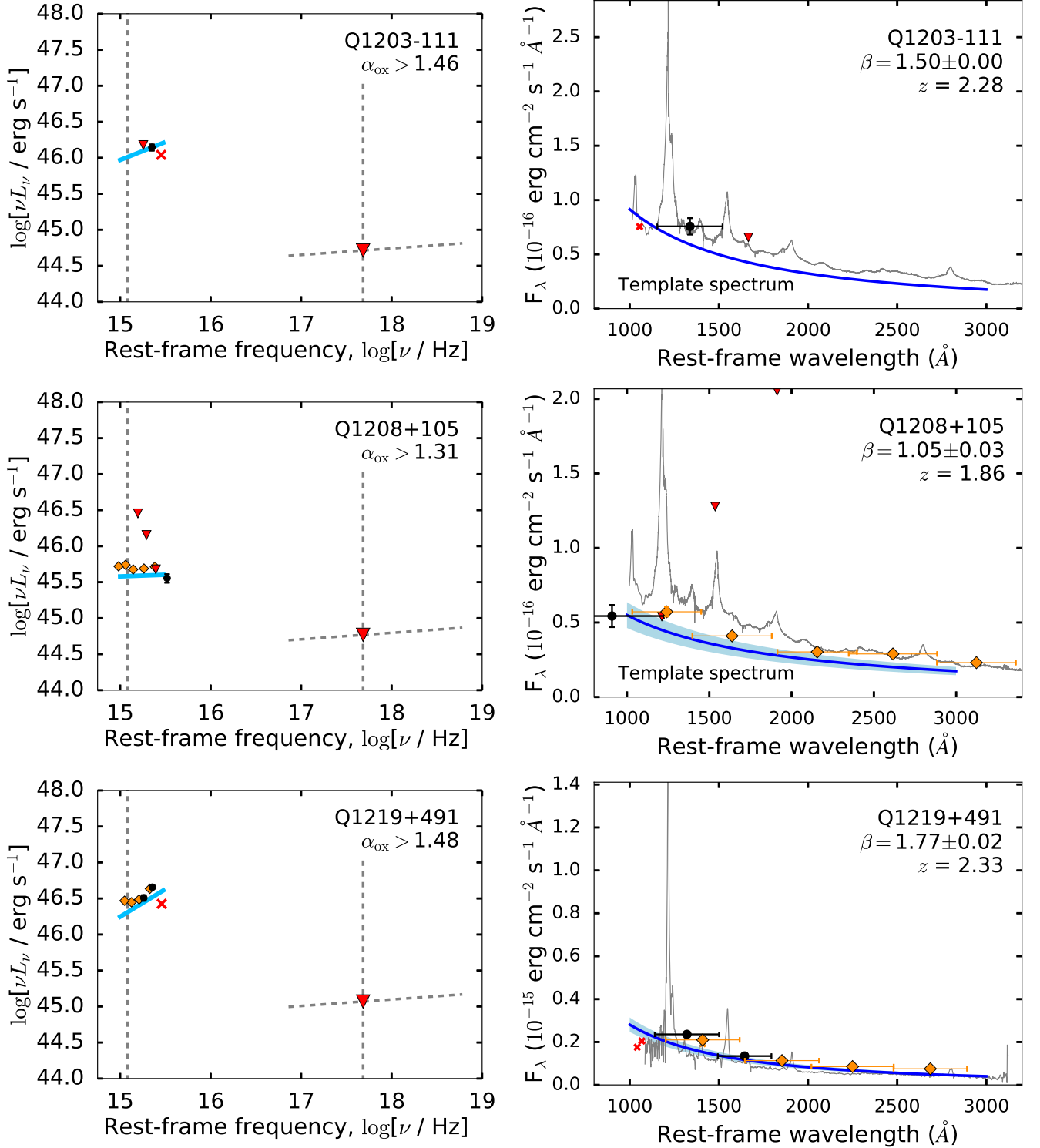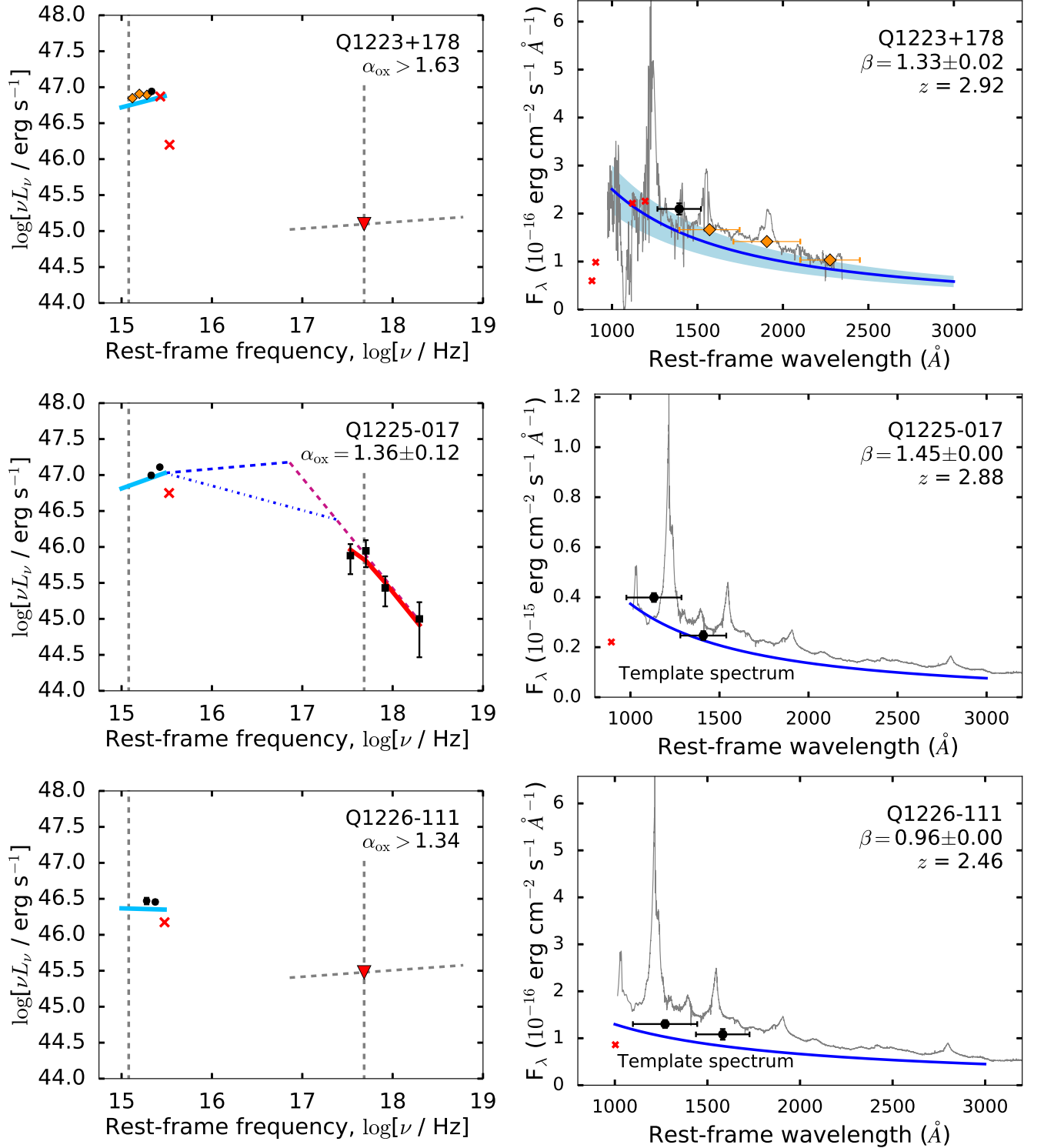
Figure A5. *Left:* Rest-frame UV to X-ray spectral energy distributions (SEDs) of quasars in our sample. *Right*: UV photometry and continuum modeling. See Figure 4 for symbol and color coding. *Notes on individual objects:* None.
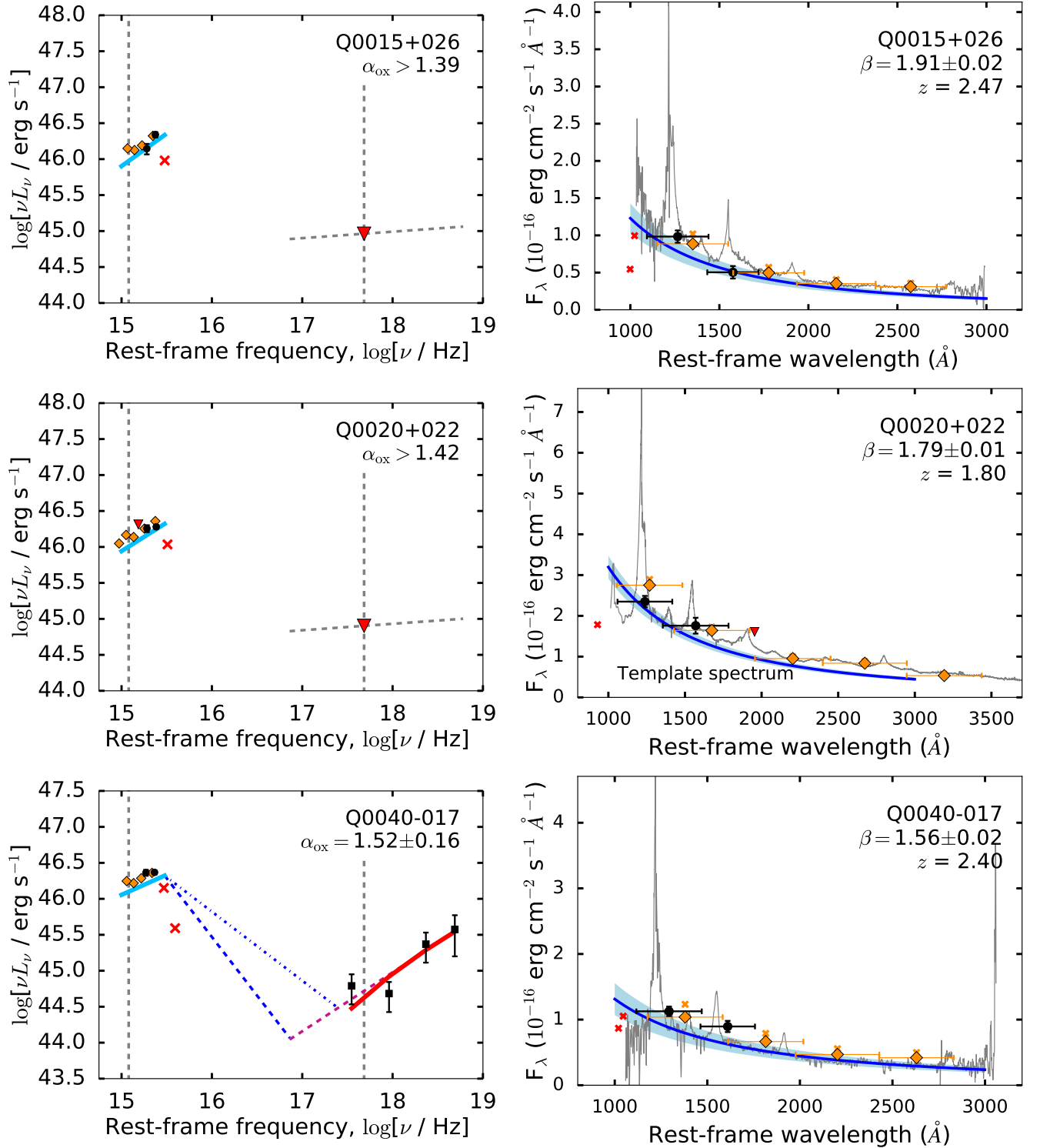
Figure A6. *Left:* Rest-frame UV to X-ray spectral energy distributions (SEDs) of quasars in our sample. *Right*: UV photometry and continuum modeling. See Figure 4 for symbol and color coding. *Notes on individual objects:* None.
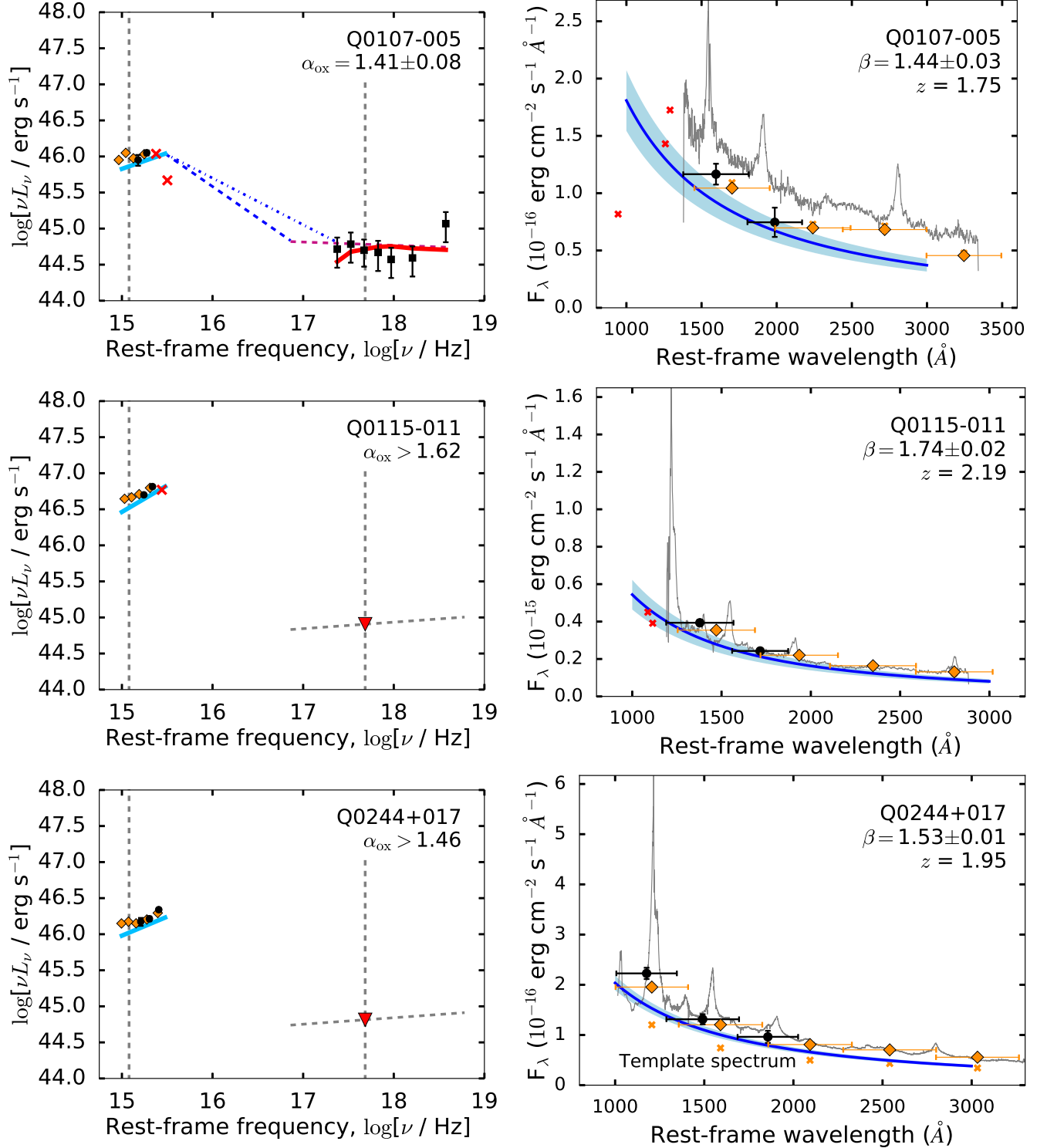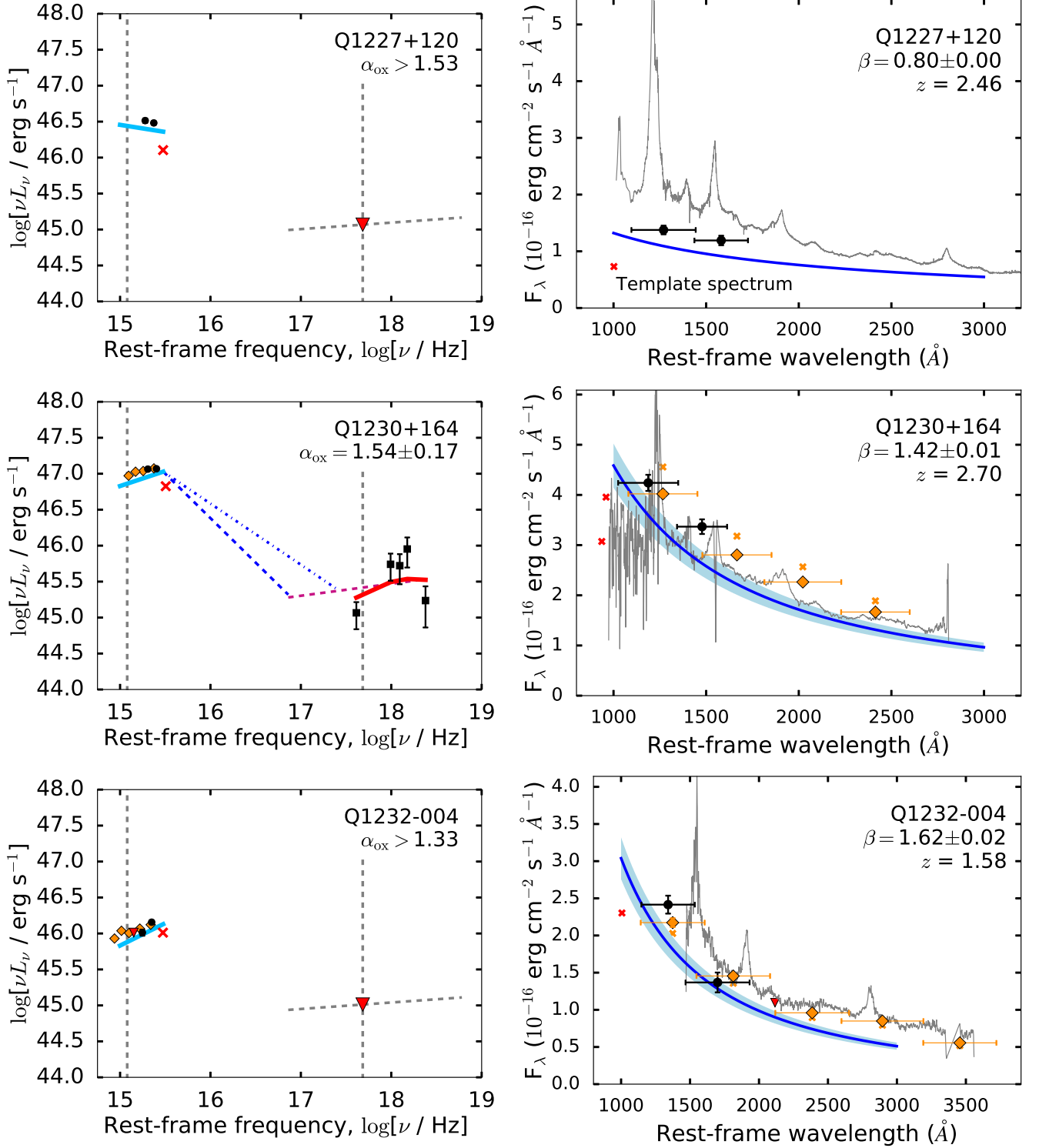
Figure A7. *Left:* Rest-frame UV to X-ray spectral energy distributions (SEDs) of quasars in our sample. *Right:* UV photometry and continuum modeling. See Figure 4 for symbol and color coding. *Notes on individual objects:* For Q0107-005, the SDSS photometric data (used for the UV-optical model fit) are offset in flux from the SDSS spectrum (used only for visualization purposes).
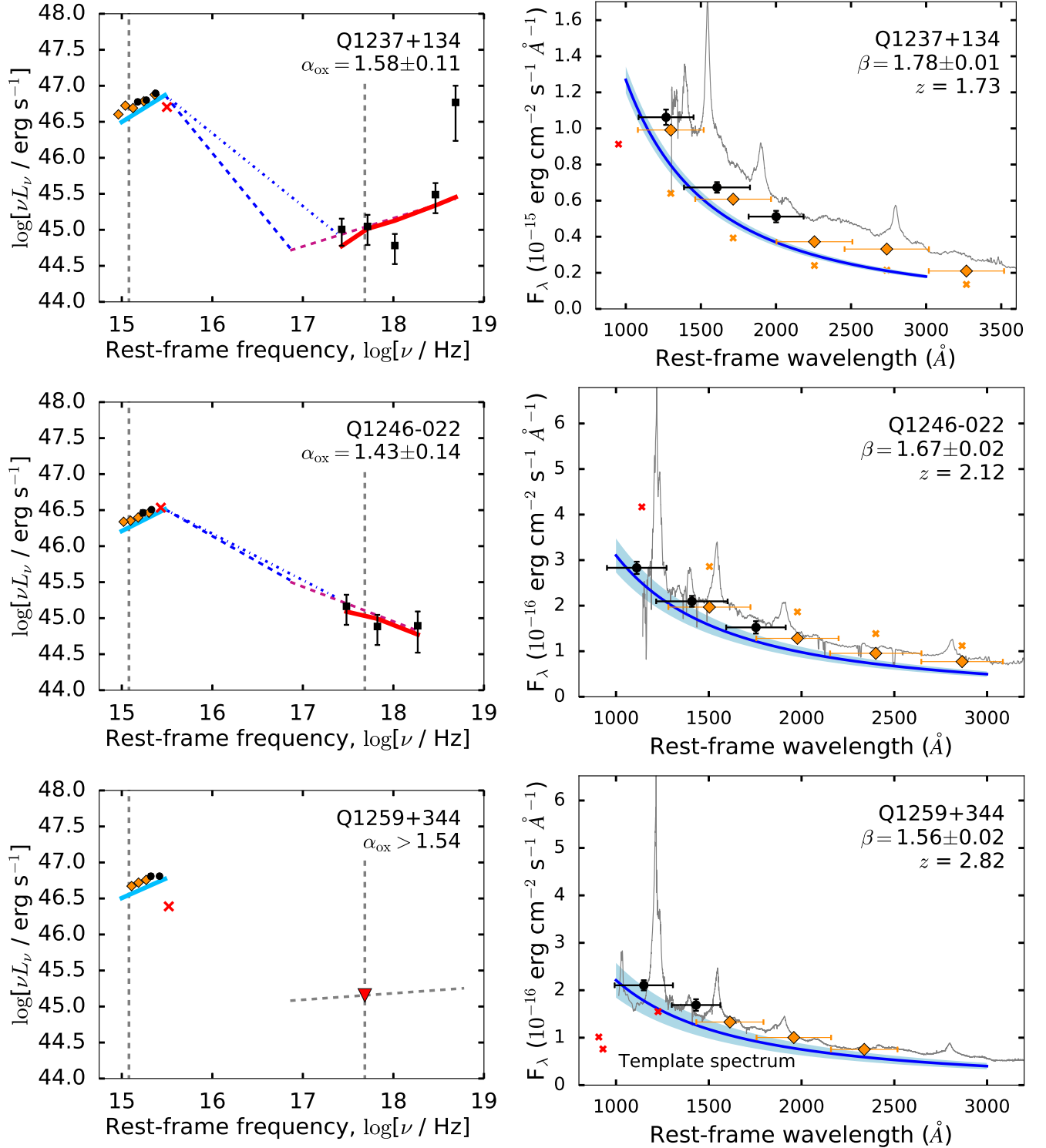
Figure A8. *Left:* Rest-frame UV to X-ray spectral energy distributions (SEDs) of quasars in our sample. *Right*: UV photometry and continuum modeling. See Figure 4 for symbol and color coding. *Notes on individual objects:*

Figure A9. *Left:* Rest-frame UV to X-ray spectral energy distributions (SEDs) of quasars in our sample. *Right*: UV photometry and continuum modeling. See Figure 4 for symbol and color coding. *Notes on individual objects:* None.

Figure A10. *Left:* Rest-frame UV to X-ray spectral energy distributions (SEDs) of quasars in our sample. *Right*: UV photometry and continuum modeling. See Figure 4 for symbol and color coding. *Notes on individual objects:* None.
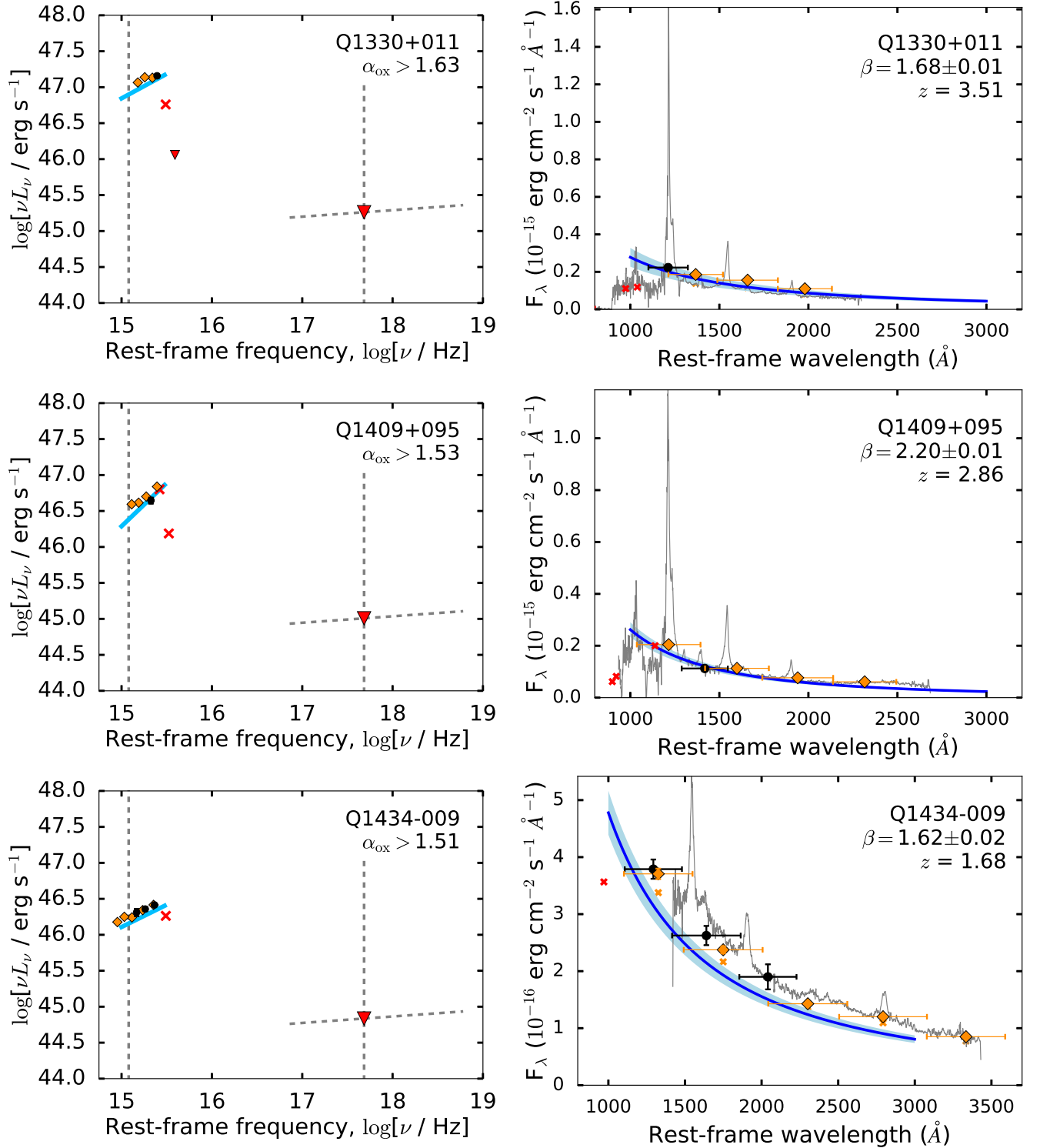
Figure A11. *Left:* Rest-frame UV to X-ray spectral energy distributions (SEDs) of quasars in our sample. *Right*: UV photometry and continuum modeling. See Figure 4 for symbol and color coding. *Notes on individual objects:* For Q1016-006 there is significant offset between the SDSS photometry (used for the UV-optical model fit) and SDSS spectroscopy (used only for visualization purposes). For Q1020+014, we use the VB quasar template to estimate the BEL contribution.

Figure A12. *Left:* Rest-frame UV to X-ray spectral energy distributions (SEDs) of quasars in our sample. *Right:* UV photometry and continuum modeling. See Figure 4 for symbol and color coding. *Notes on individual objects:* For Q1137+305, we use the VB quasar template to estimate the BEL contribution.

Figure A13. *Left:* Rest-frame UV to X-ray spectral energy distributions (SEDs) of quasars in our sample. *Right*: UV photometry and continuum modeling. See Figure 4 for symbol and color coding. *Notes on individual objects:* None.
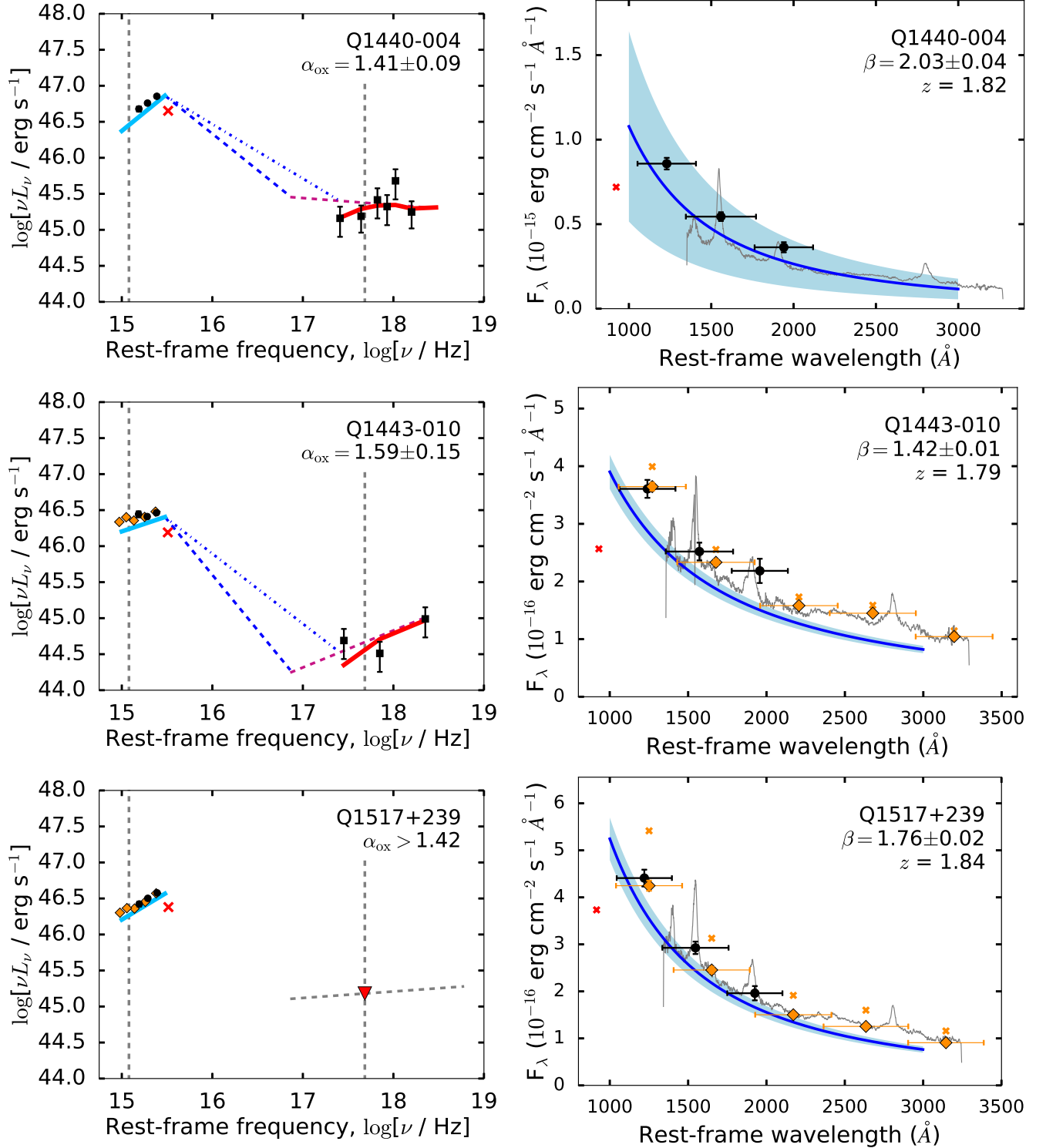
Figure A14. *Left:* Rest-frame UV to X-ray spectral energy distributions (SEDs) of quasars in our sample. *Right:* UV photometry and continuum modeling. See Figure 4 for symbol and color coding. *Notes on individual objects:* For Q1208+105 we do not rescale the SDSS photometric fluxes to match the UVOT data, due to the difficulty of determining the correct rescaling given a single detected UVOT data point outside the SDSS spectral window.
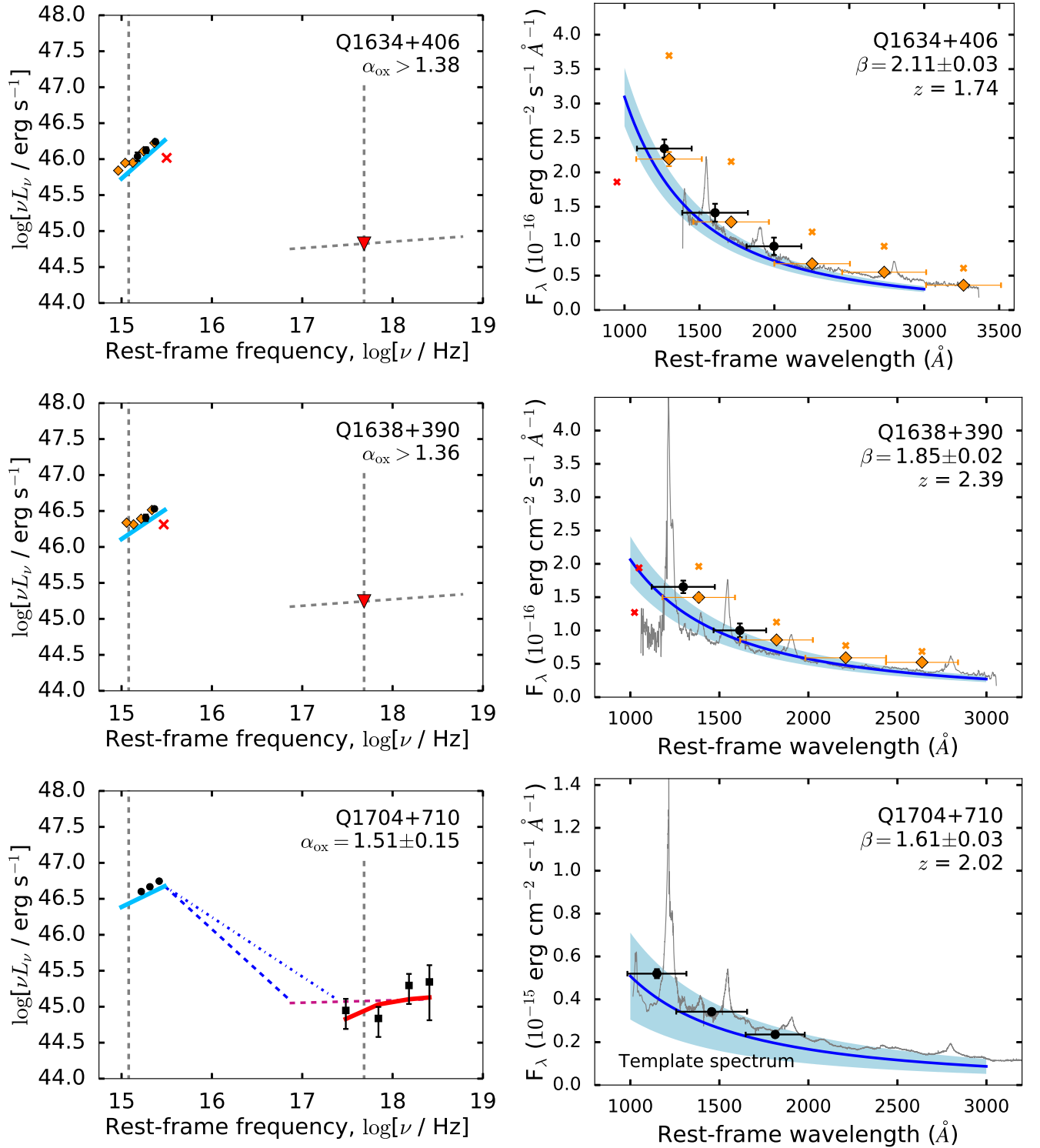
Figure A15. *Left:* Rest-frame UV to X-ray spectral energy distributions (SEDs) of quasars in our sample. *Right*: UV photometry and continuum modeling. See Figure 4 for symbol and color coding. *Notes on individual objects:* For Q1223+178, we exclude the UVOT *U,B* bands along with SDSS *u,g* due to the absorption feature visible in the SDSS spectrum. We measure an extremely soft X-ray spectrum for Q1225-017; this quasar is thus an outlier in terms of the X-ray photon index distribution for our sample.
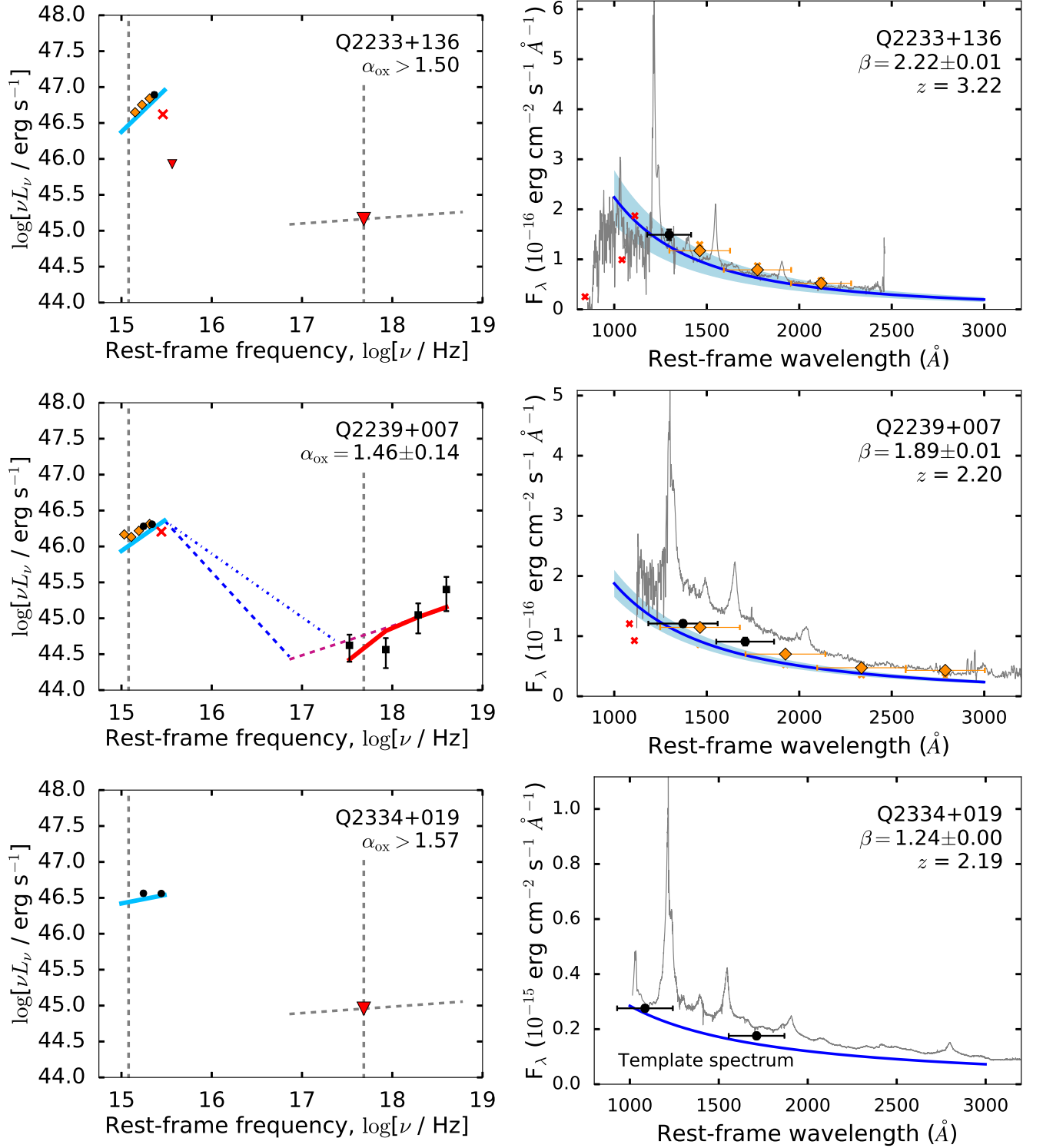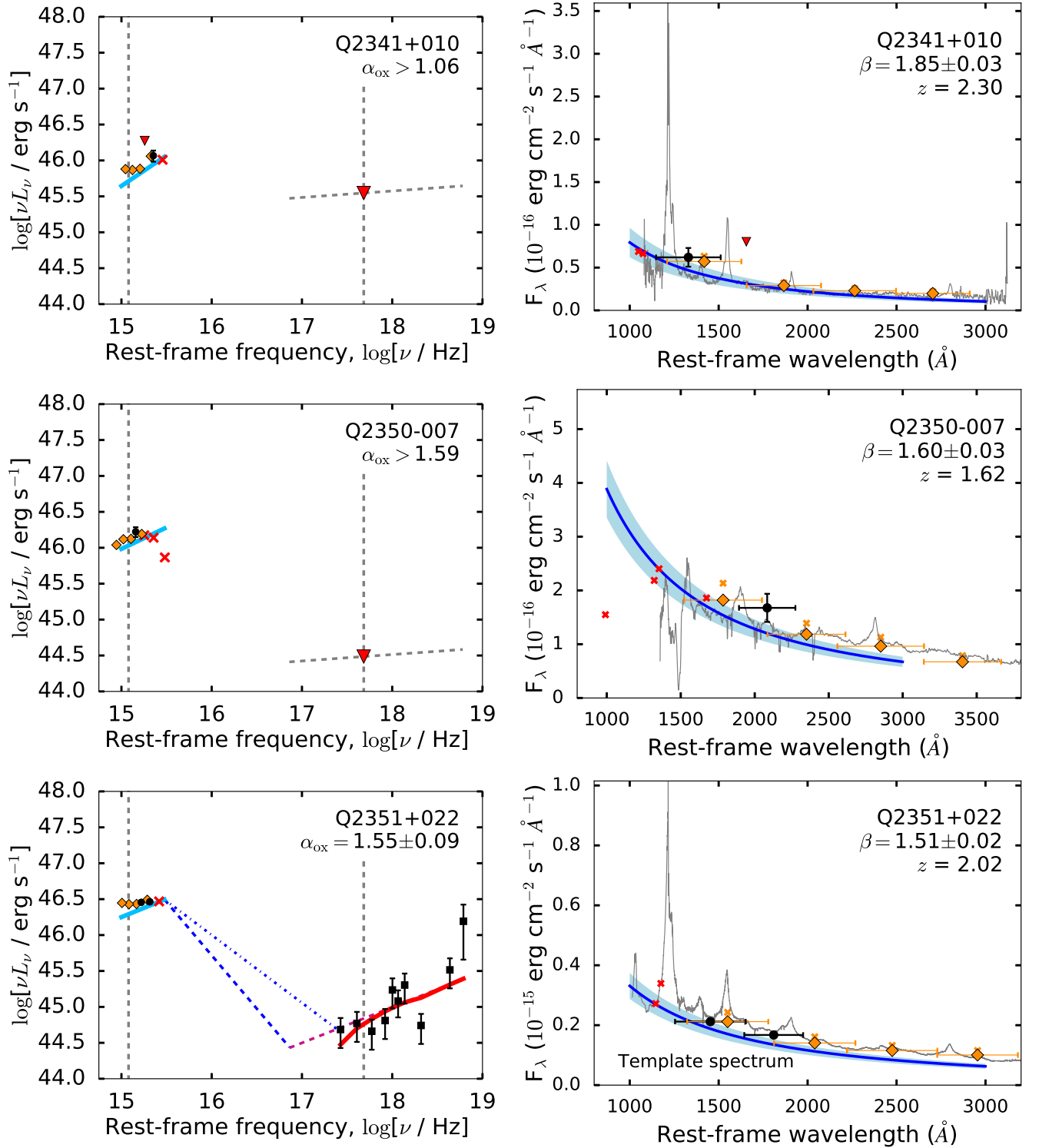
Figure A16. *Left:* Rest-frame UV to X-ray spectral energy distributions (SEDs) of quasars in our sample. *Right*: UV photometry and continuum modeling. See Figure 4 for symbol and color coding. *Notes on individual objects:*

Figure A17. *Left:* Rest-frame UV to X-ray spectral energy distributions (SEDs) of quasars in our sample. *Right:* UV photometry and continuum modeling. See Figure 4 for symbol and color coding. *Notes on individual objects:* For Q1237+134, there is significant offset between the SDSS photometry (used for the UV-optical model fit) and SDSS spectroscopy (used only for visualization purposes). For Q1246-022, we use the VB quasar template to estimate the BEL contribution.
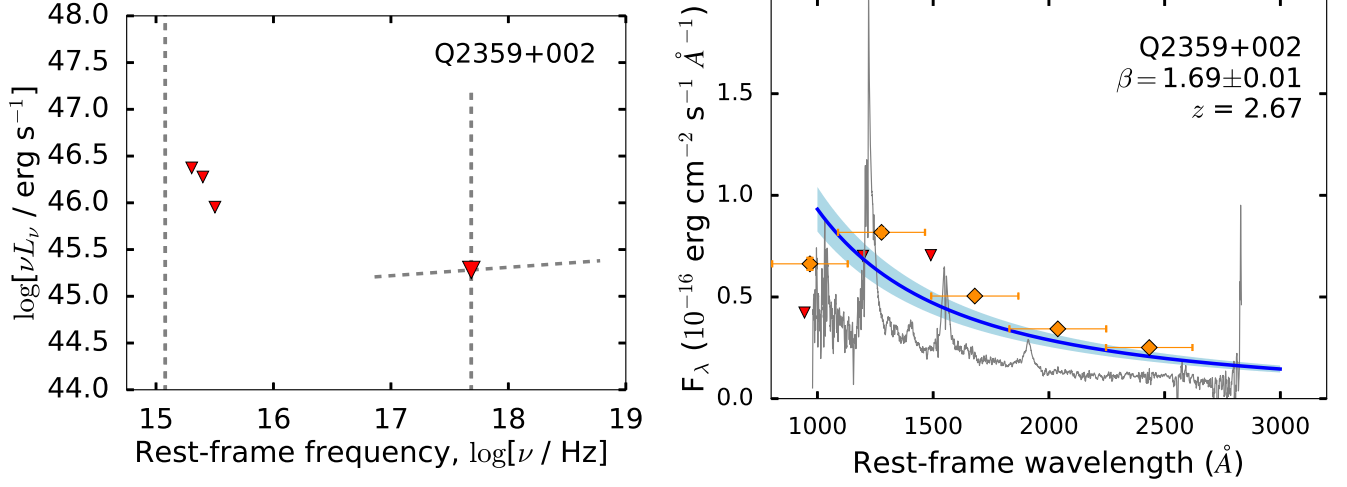
Figure A18. *Left:* Rest-frame UV to X-ray spectral energy distributions (SEDs) of quasars in our sample. *Right:* UV photometry and continuum modeling. See Figure 4 for symbol and color coding. *Notes on individual objects:* For Q1434-009, we use the VB quasar template to estimate the BEL contribution.

Figure A19. *Left:* Rest-frame UV to X-ray spectral energy distributions (SEDs) of quasars in our sample. *Right:* UV photometry and continuum modeling. See Figure 4 for symbol and color coding. *Notes on individual objects:* For Q1440-004, the SDSS photometry is corrupted (all *ugriz* magnitudes are set to -9999 in the *photoObj* file). We rely on the UVOT data for our model fit, and include the SDSS spectrum here for visualization purposes only. For Q1517+239, we use the VB quasar template to estimate the BEL contribution.

Figure A20. *Left:* Rest-frame UV to X-ray spectral energy distributions (SEDs) of quasars in our sample. *Right:* UV photometry and continuum modeling. See Figure 4 for symbol and color coding. *Notes on individual objects:* For Q1638+390, there is significant offset between the SDSS photometry (used for the UV-optical model fit) and SDSS spectroscopy (used only for visualization purposes).

Figure A21. *Left:* Rest-frame UV to X-ray spectral energy distributions (SEDs) of quasars in our sample. *Right:* UV photometry and continuum modeling. See Figure 4 for symbol and color coding. *Notes on individual objects:* For Q2239+007, there is significant offset between the SDSS photometry (used for the UV-optical model fit) and SDSS spectroscopy (used only for visualization purposes).

Figure A22. *Left:* Rest-frame UV to X-ray spectral energy distributions (SEDs) of quasars in our sample. *Right:* UV photometry and continuum modeling. See Figure 4 for symbol and color coding. *Notes on individual objects:* For Q2350-007, we exclude UVOT *B* due to the C IV absorption feature visible in the SDSS spectrum.
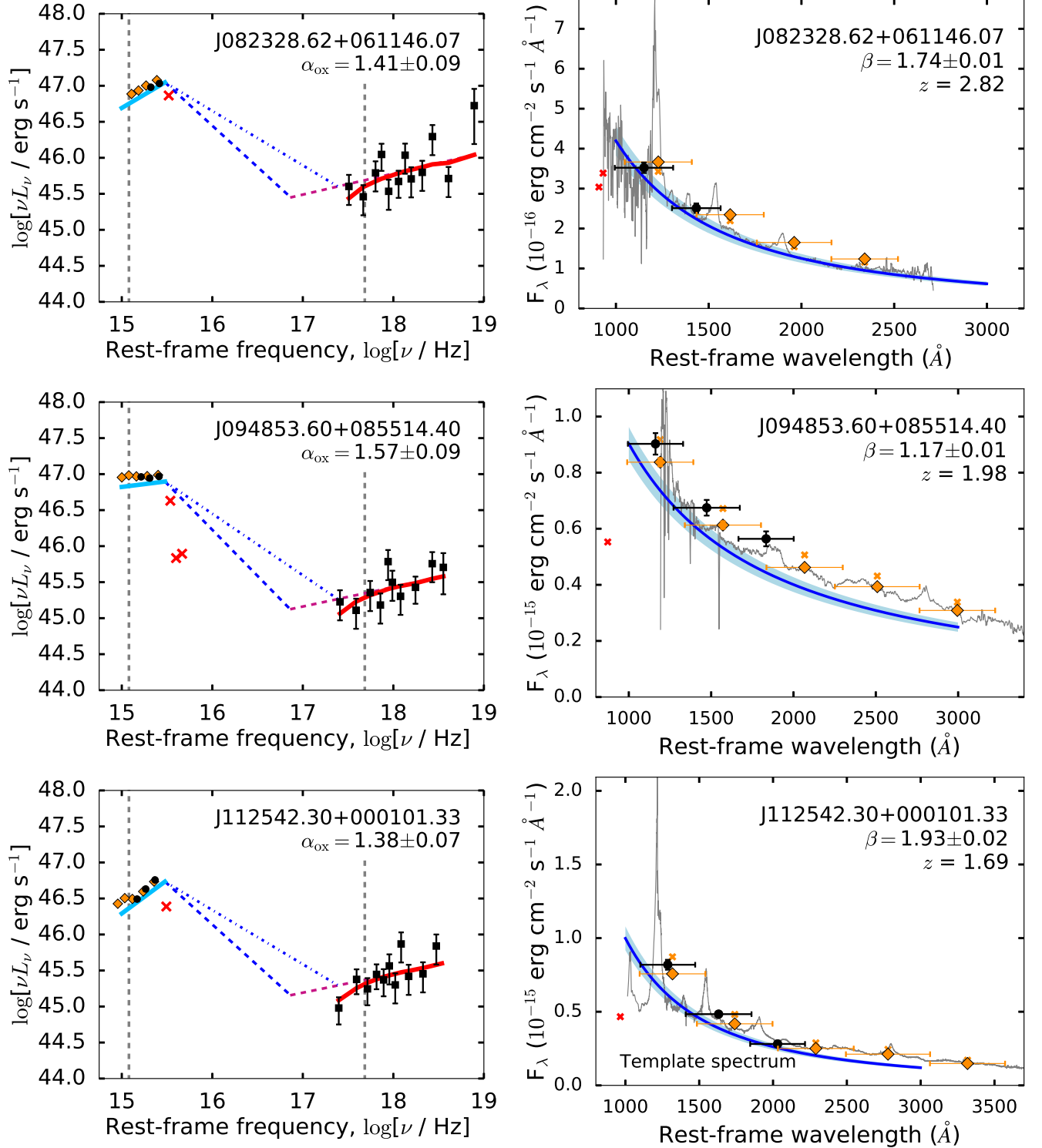
Figure A23. *Left:* Rest-frame UV to X-ray spectral energy distributions (SEDs) of quasars in our sample. *Right*: UV photometry and continuum modeling. See Figure 4 for symbol and color coding. *Notes on individual objects:* This quasar is not detected by *Swift* in either XRT or UVOT imaging. We show the SDSS spectrum and photometry for reference only; there are significant offsets between the SDSS photometric data and the SDSS spectrum.

APPENDIX B: SPECTRAL ENERGY DISTRIBUTIONS FOR RADIO-LOUD SAMPLE

Here, we present the optical to X-ray spectral energy distributions (SEDs) of the radio-loud quasars in our sample, along with the UV photometry and continuum modeling, in Figures B1 through B26.

Due to an unfortunate oversight, we do not show the emission-line corrected fluxes in the UV–optical SEDs shown here, but only the observed fluxes. We will update these figures to also show the emission-line corrected fluxes before submitting this work to a journal.
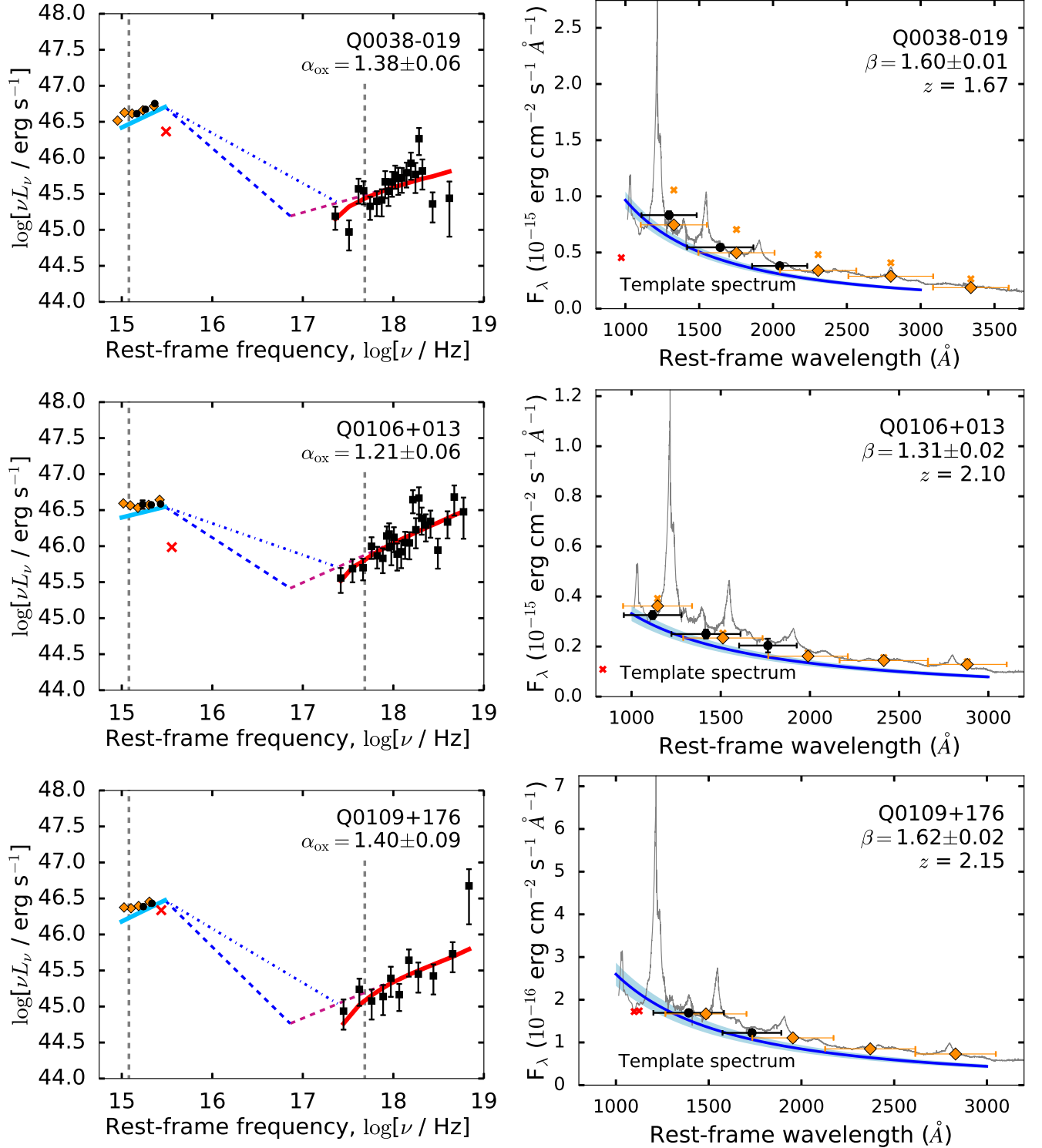
Figure B1. *Left:* Rest-frame UV to X-ray spectral energy distributions (SEDs) of quasars in our sample. *Right:* UV photometry and continuum modeling. See Figure 4 for symbol and color coding. *Notes on individual objects:* For J094853.60+085514.40, we use the VB quasar template to estimate the BEL contribution.
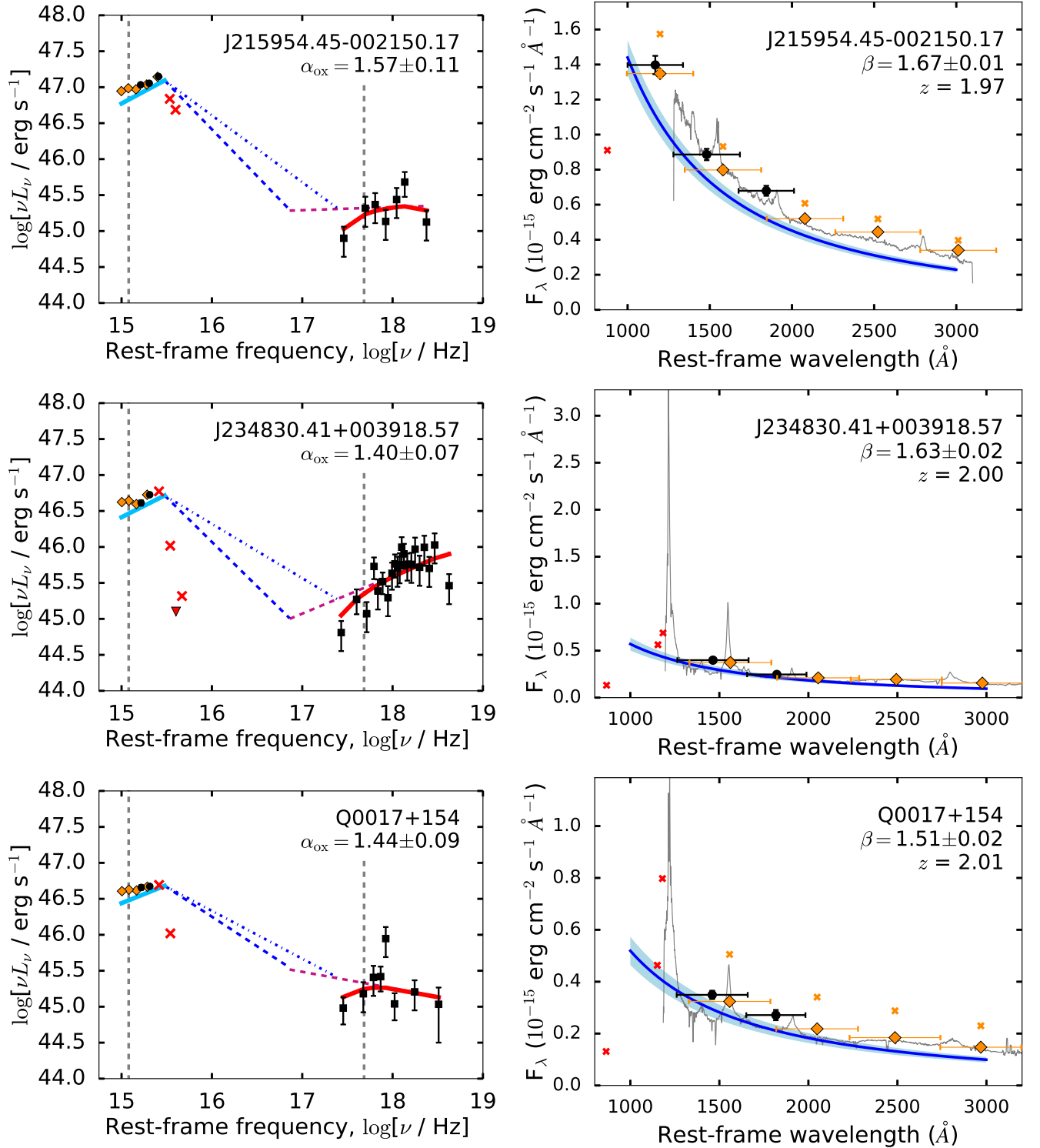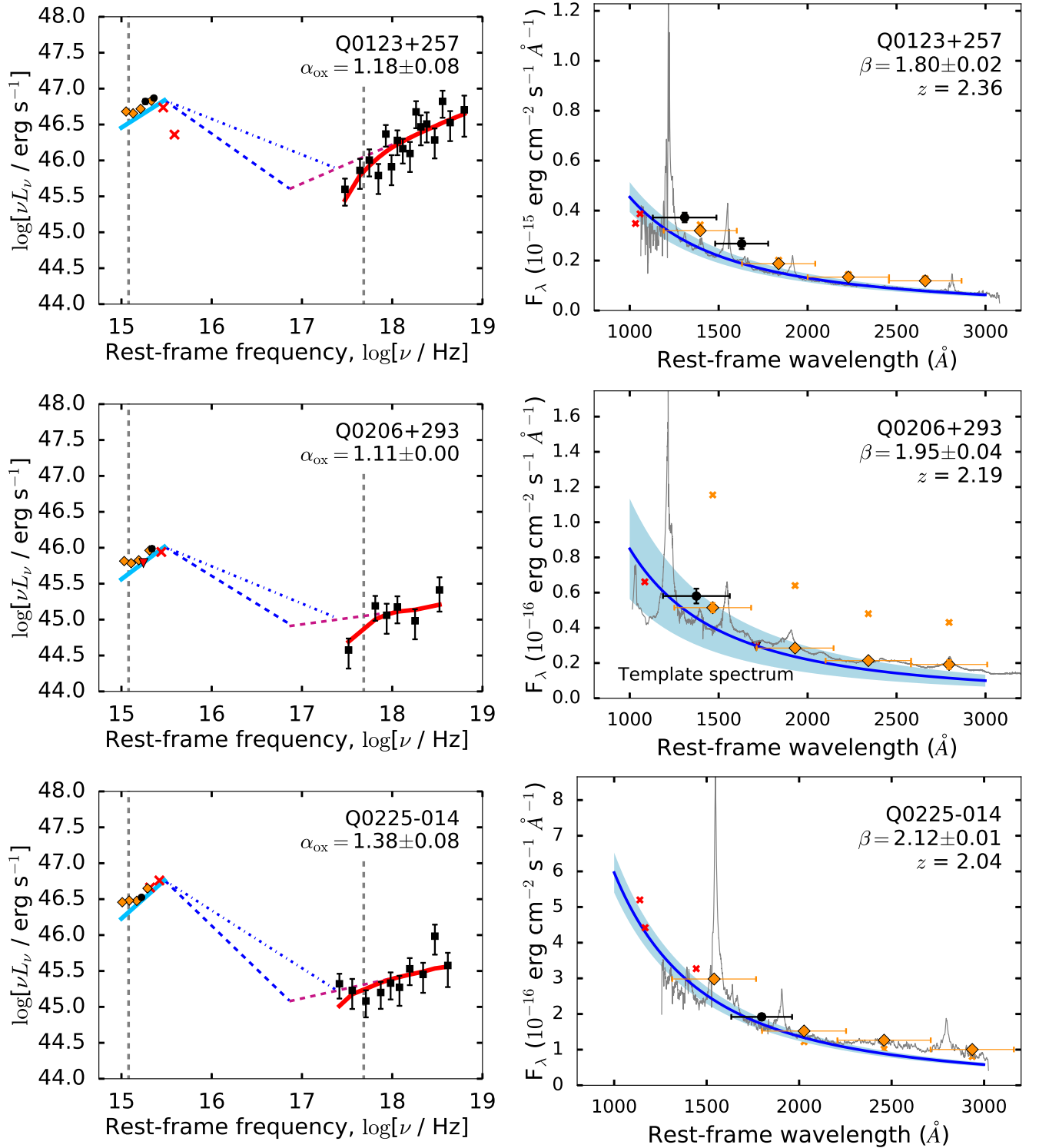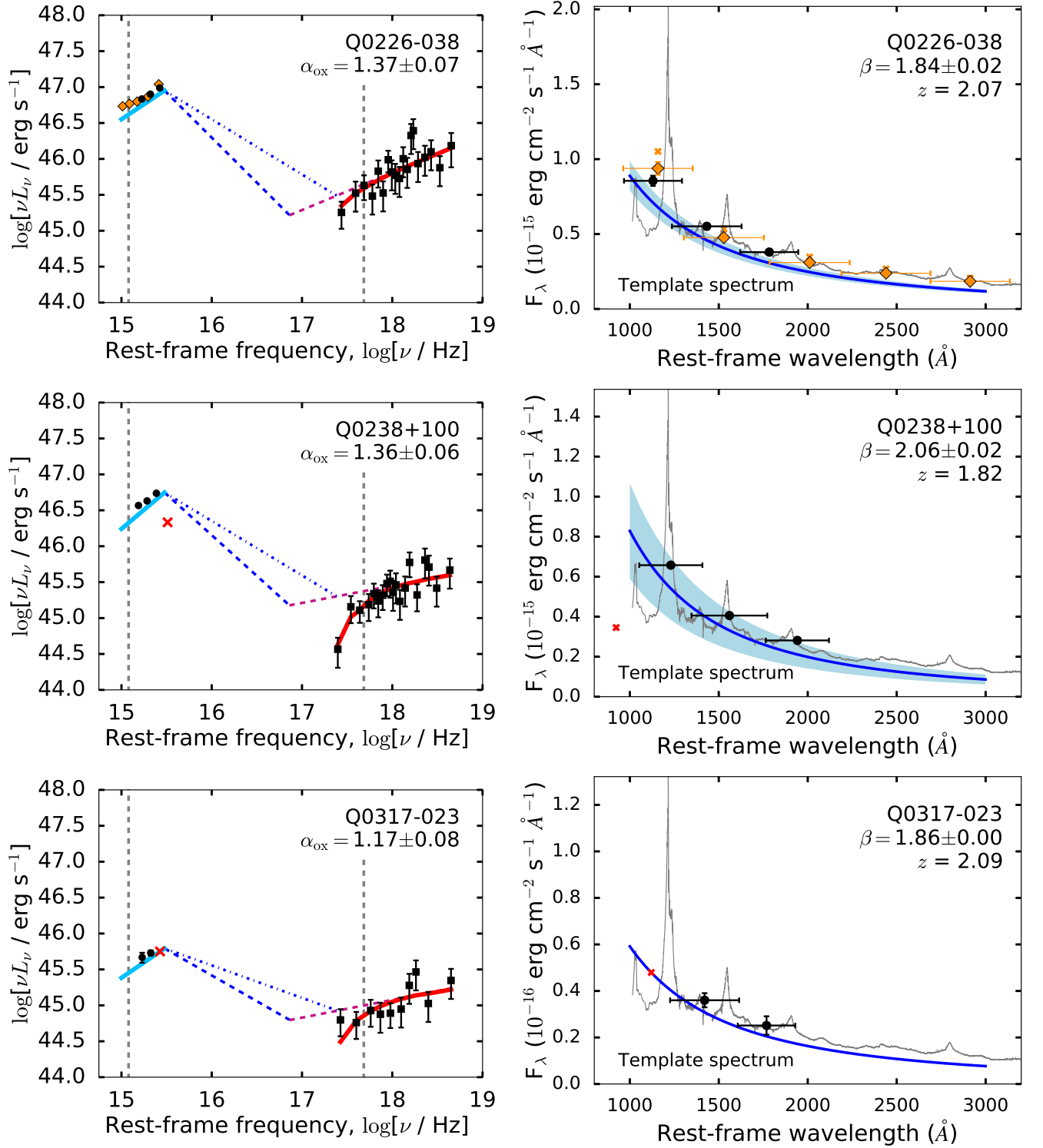
Figure B2. *Left:* Rest-frame UV to X-ray spectral energy distributions (SEDs) of quasars in our sample. *Right*: UV photometry and continuum modeling. See Figure 4 for symbol and color coding. *Notes on individual objects:* For J21595445-00215017, we use the VB quasar template to estimate the BEL contribution.
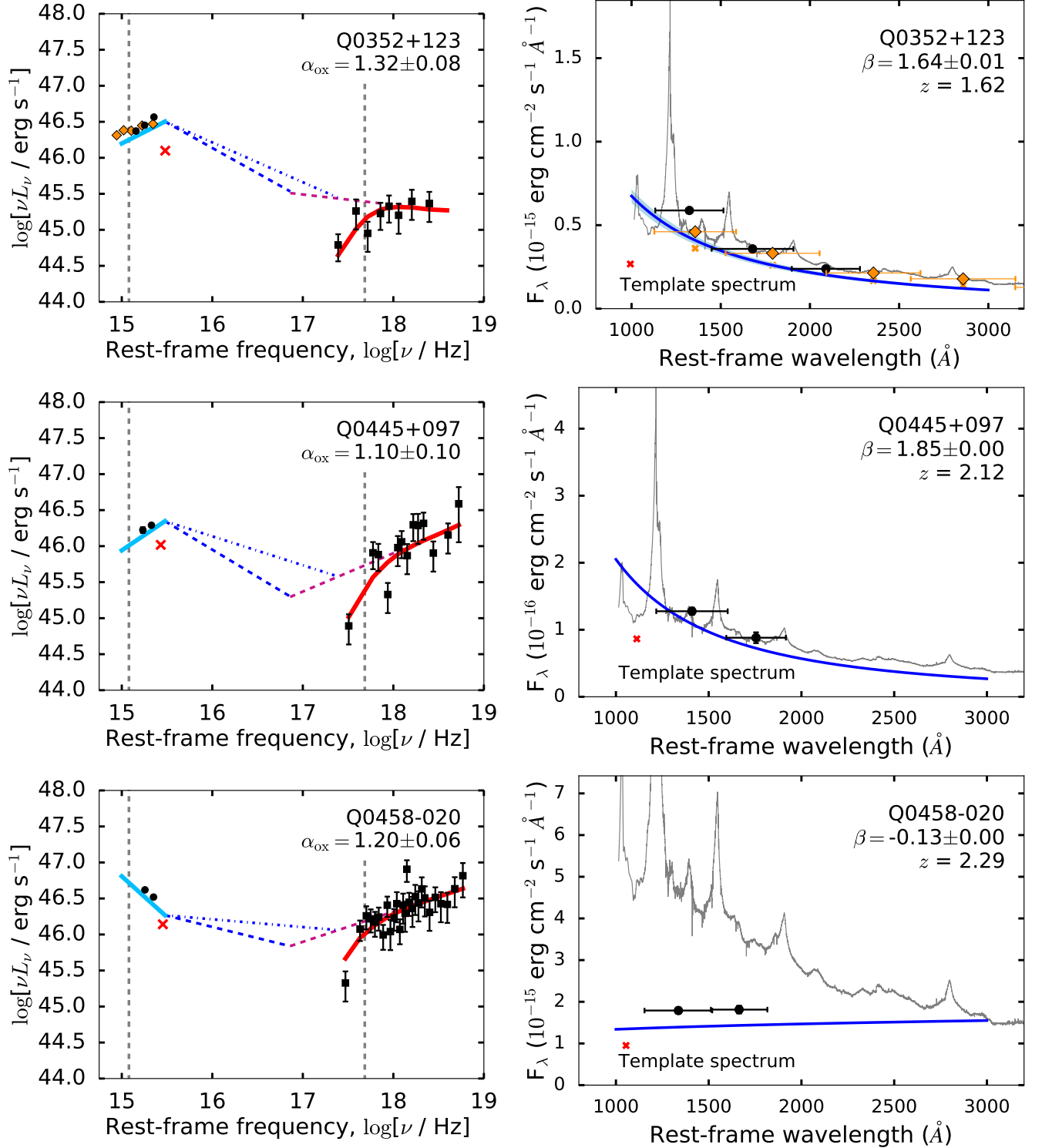
Figure B3. *Left:* Rest-frame UV to X-ray spectral energy distributions (SEDs) of quasars in our sample. *Right*: UV photometry and continuum modeling. See Figure 4 for symbol and color coding. *Notes on individual objects:* None.

Figure B4. *Left:* Rest-frame UV to X-ray spectral energy distributions (SEDs) of quasars in our sample. *Right*: UV photometry and continuum modeling. See Figure 4 for symbol and color coding. *Notes on individual objects:* None.

Figure B5. *Left:* Rest-frame UV to X-ray spectral energy distributions (SEDs) of quasars in our sample. *Right*: UV photometry and continuum modeling. See Figure 4 for symbol and color coding. *Notes on individual objects:*None.
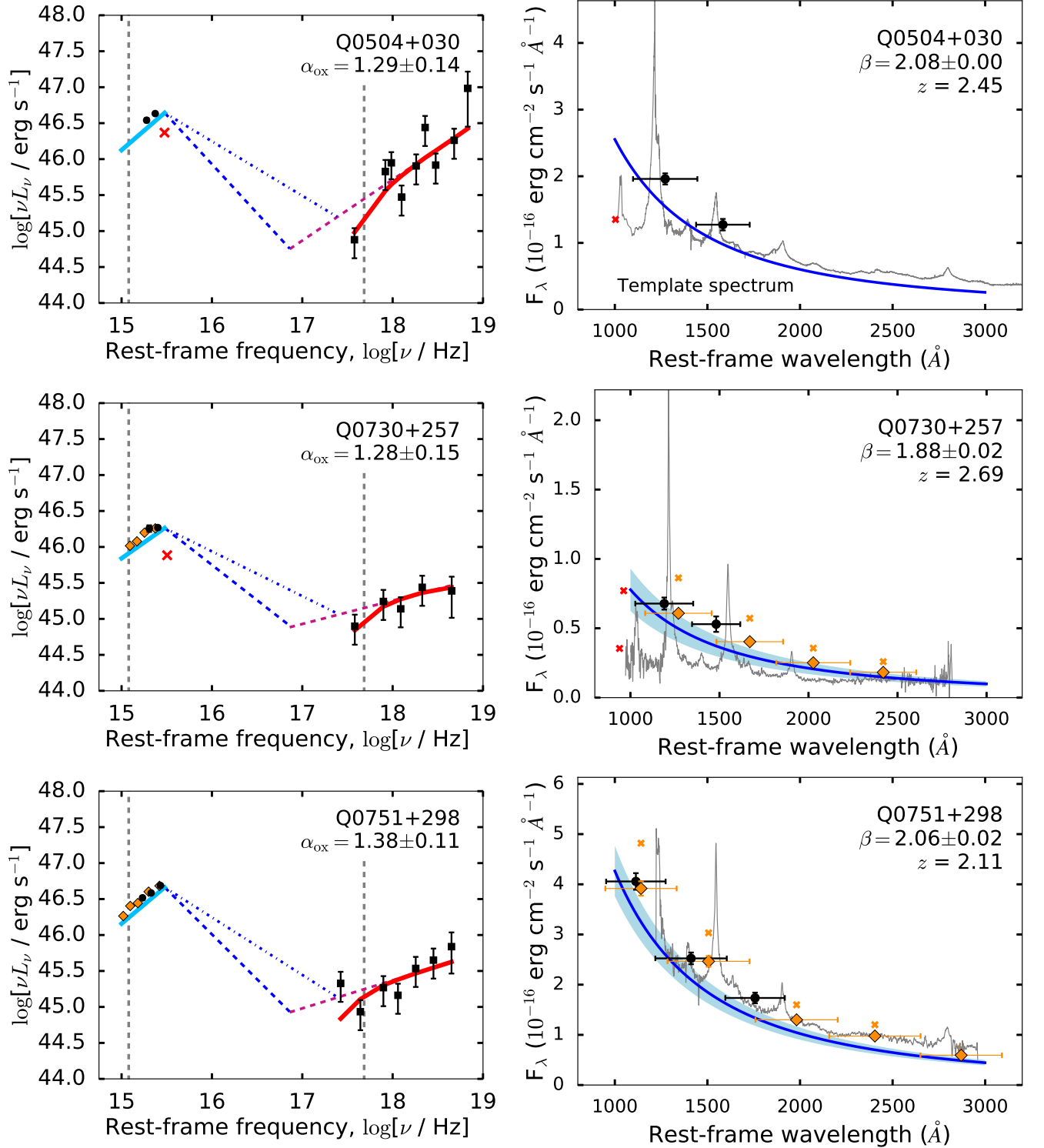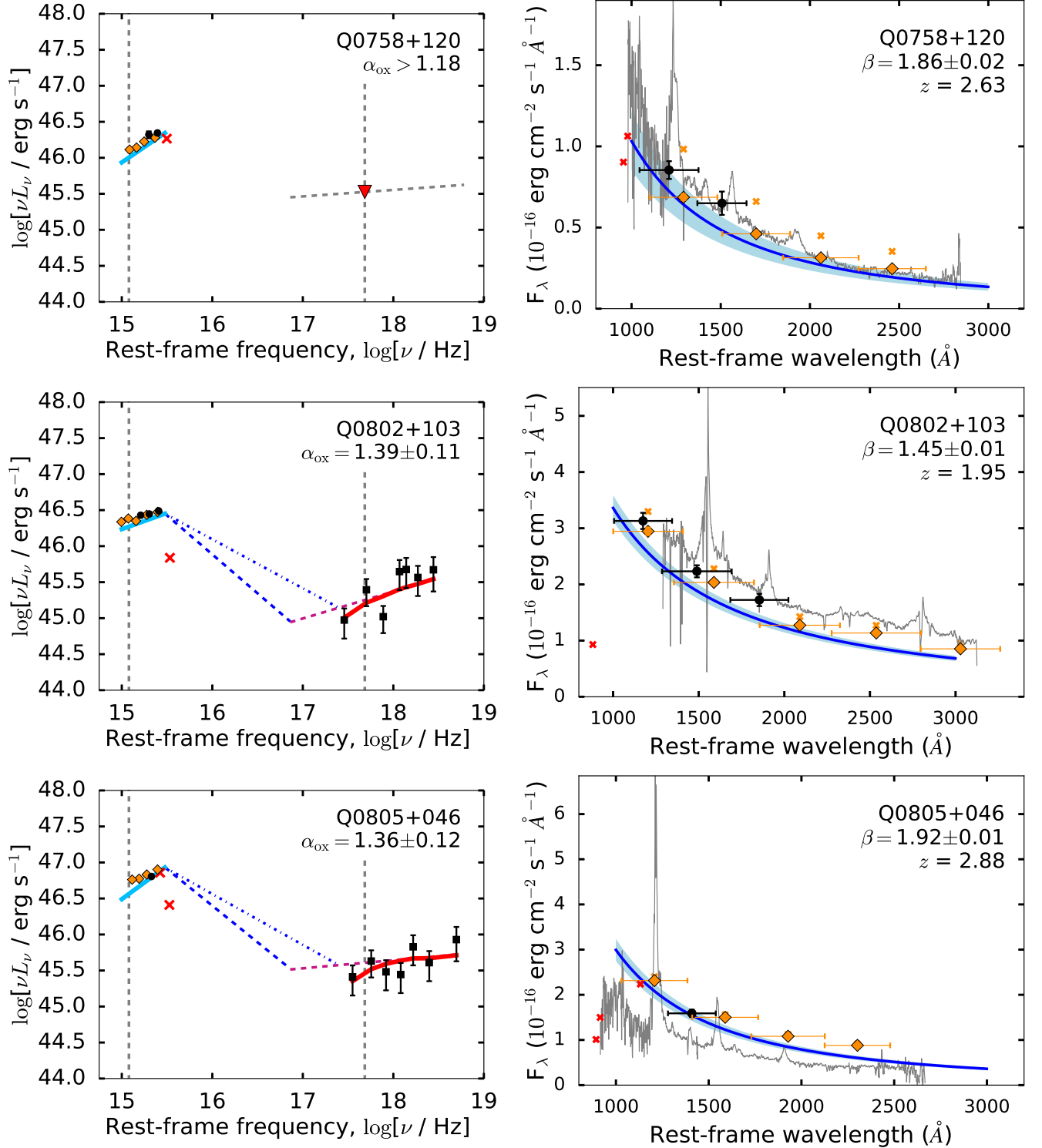
Figure B6. *Left:* Rest-frame UV to X-ray spectral energy distributions (SEDs) of quasars in our sample. *Right*: UV photometry and continuum modeling. See Figure 4 for symbol and color coding. *Notes on individual objects:* Based on detections in three UVOT bandpasses (of which we exclude the *U* band from our model), Quasar Q0458-020 appears to have a heavily reddened UV-optical SED. This object has an intervening damped Lyman-α system (Wolfe et al. 1993), which likely explains the reddening.
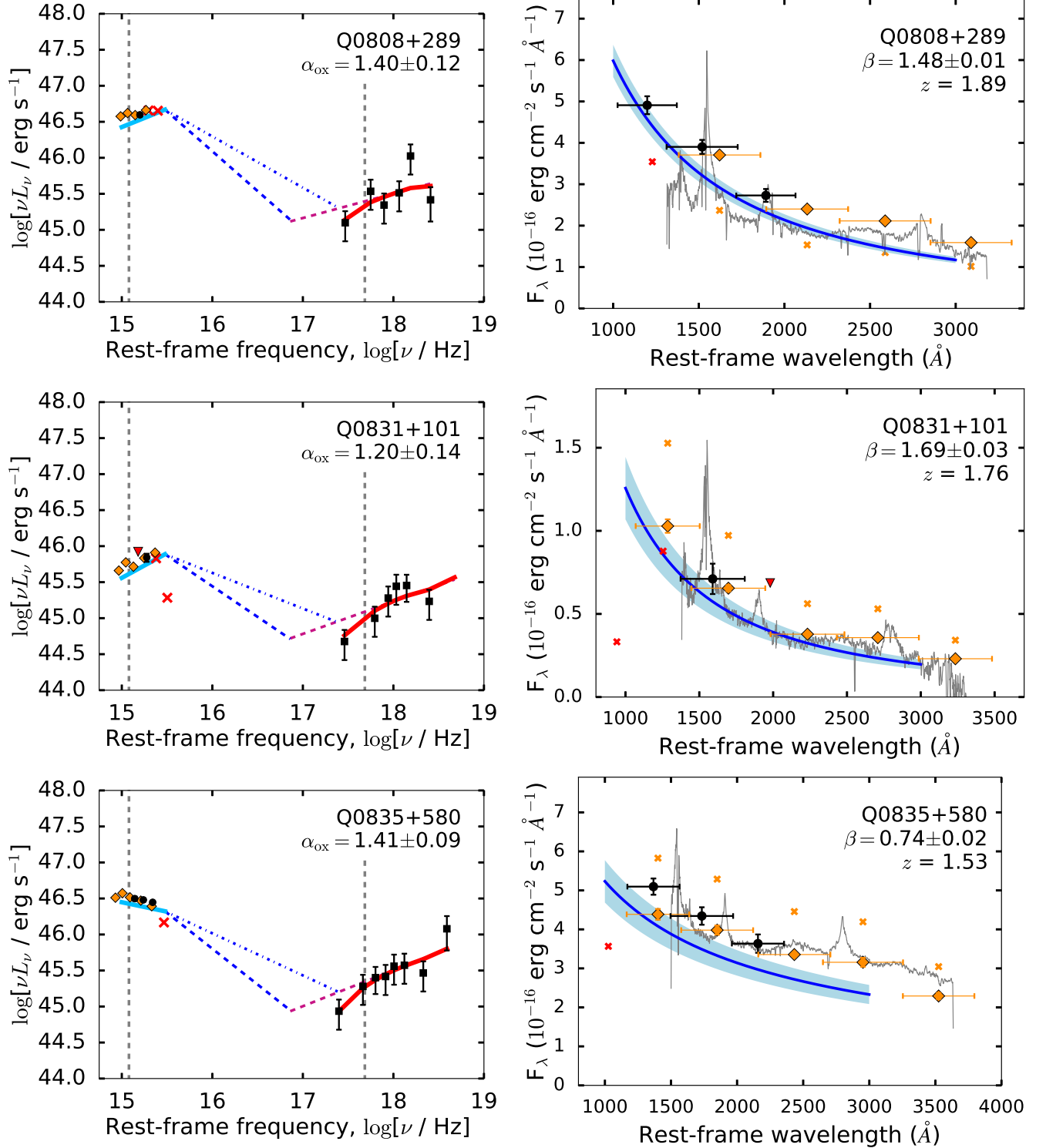
Figure B7. *Left:* Rest-frame UV to X-ray spectral energy distributions (SEDs) of quasars in our sample. *Right*: UV photometry and continuum modeling. See Figure 4 for symbol and color coding. *Notes on individual objects:* For Q0730+257, there may be significant offset between the SDSS spectrum and the SDSS photometric data points; alternatively, this object may simply show unusually strong BEL, such that our BEL contamination correction underestimates the required rescaling.

Figure B8. *Left:* Rest-frame UV to X-ray spectral energy distributions (SEDs) of quasars in our sample. *Right*: UV photometry and continuum modeling. See Figure 4 for symbol and color coding. *Notes on individual objects:* For Q0758+120, we use the VB quasar template to estimate the BEL contribution. For Q802+103 and Q0805+046, the SDSS photometric data (used for the UV-optical model fit) are offset in flux from the SDSS spectrum (used only for visualization purposes).

Figure B9. *Left:* Rest-frame UV to X-ray spectral energy distributions (SEDs) of quasars in our sample. *Right*: UV photometry and continuum modeling. See Figure 4 for symbol and color coding. *Notes on individual objects:* For Q0835+580, we use the VB quasar template to estimate the BEL contribution.
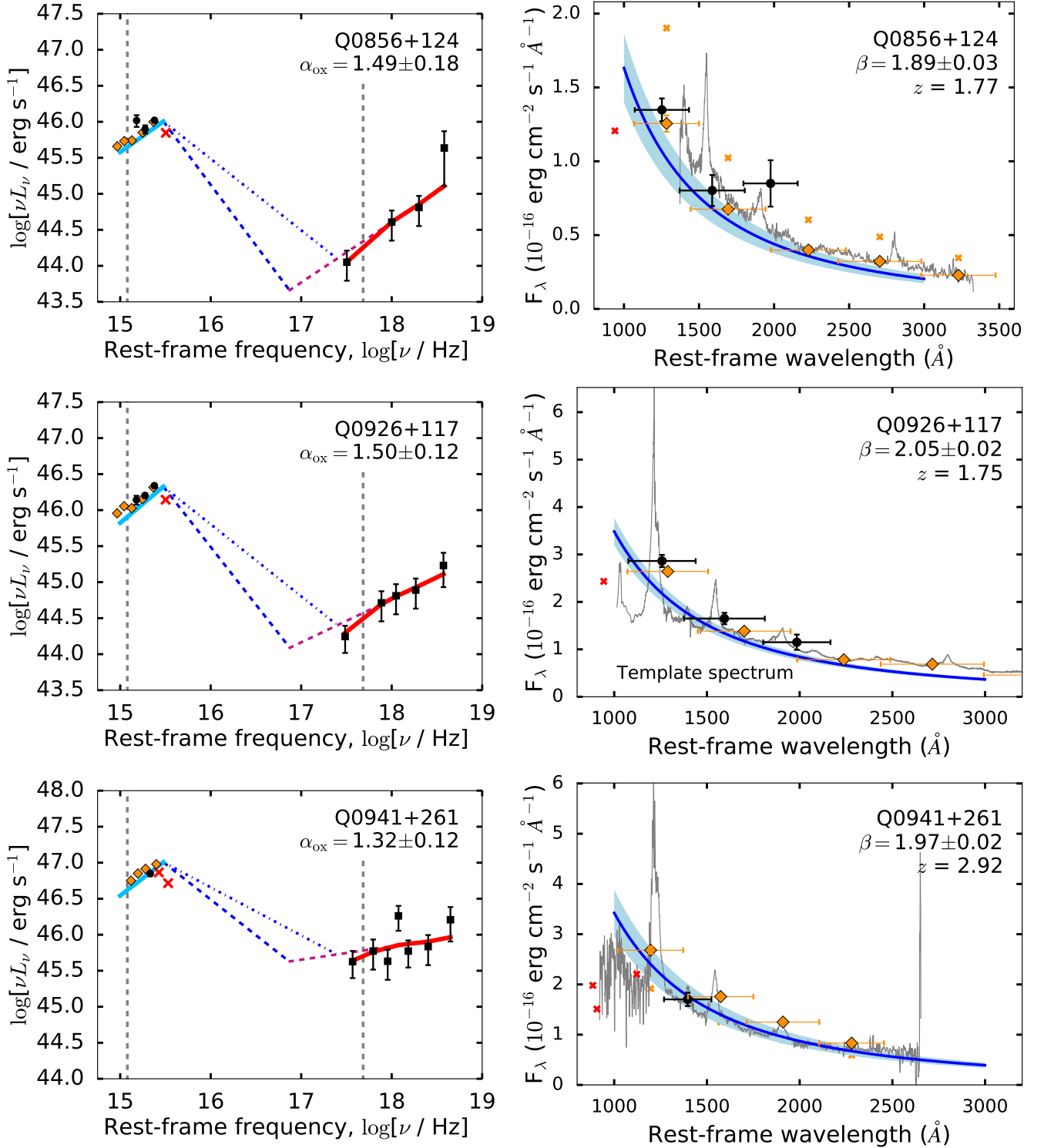
Figure B10. *Left:* Rest-frame UV to X-ray spectral energy distributions (SEDs) of quasars in our sample. *Right:* UV photometry and continuum modeling. See Figure 4 for symbol and color coding. *Notes on individual objects:* For Q0856+124, we use the VB quasar template to estimate the BEL contribution.
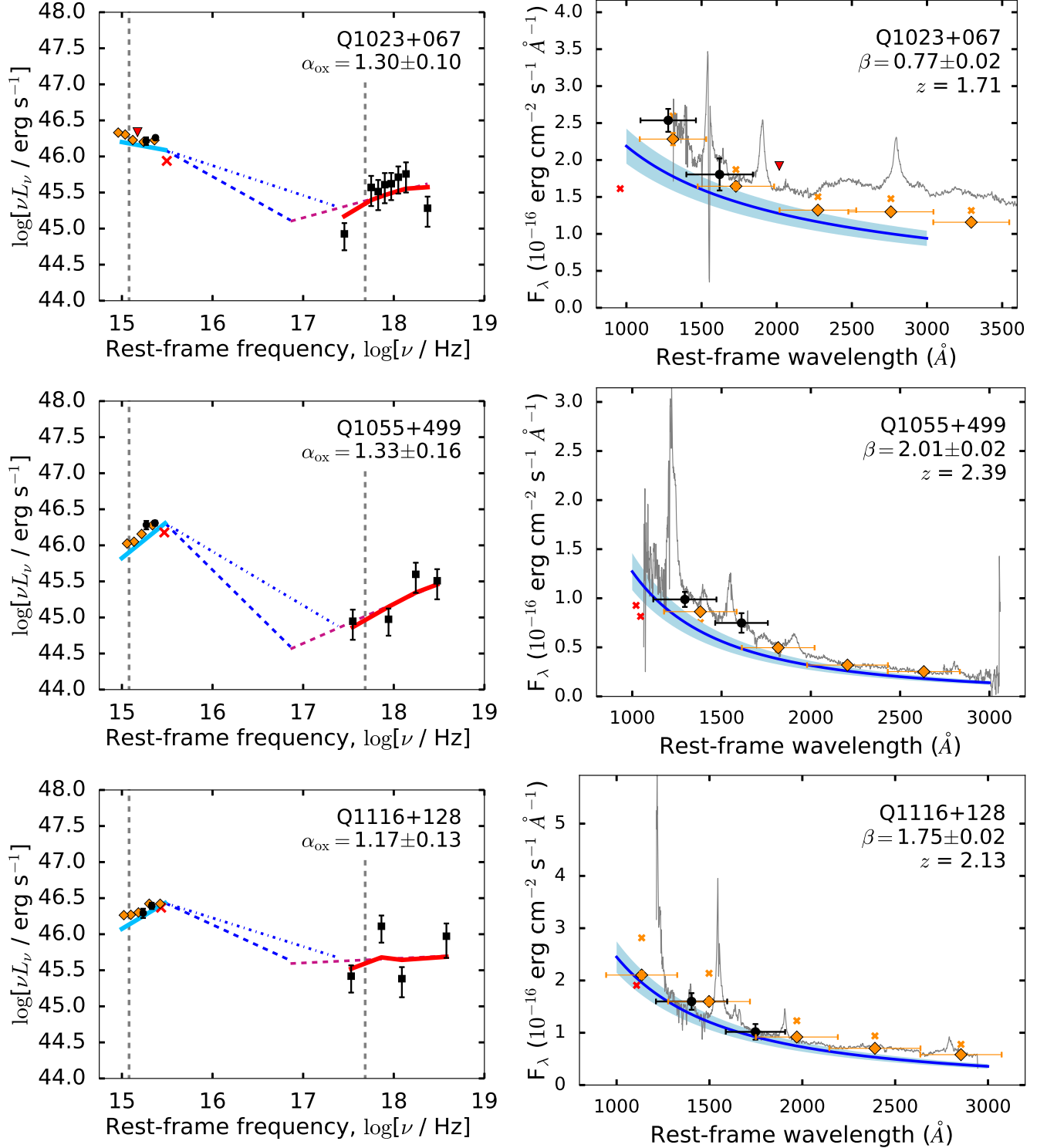
Figure B11. *Left:* Rest-frame UV to X-ray spectral energy distributions (SEDs) of quasars in our sample. *Right*: UV photometry and continuum modeling. See Figure 4 for symbol and color coding. *Notes on individual objects:* For Q1023+067, we use the VB quasar template to estimate the BEL contribution. For this quasar, the SDSS spectroscopy displats a flux offset relative to the SDSS photometry.
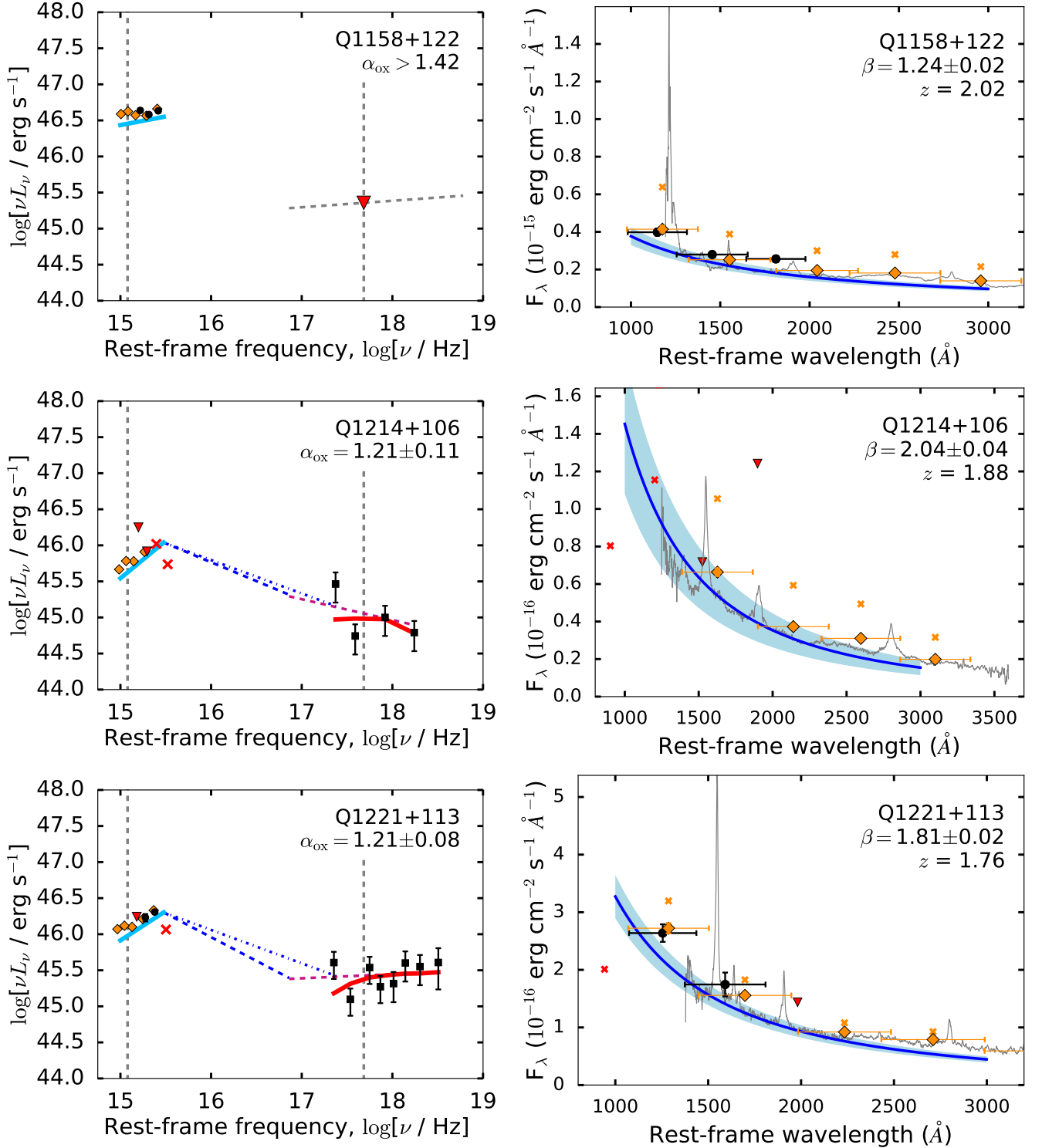
Figure B12. *Left:* Rest-frame UV to X-ray spectral energy distributions (SEDs) of quasars in our sample. *Right:* UV photometry and continuum modeling. See Figure 4 for symbol and color coding. *Notes on individual objects:* For Q1214+106, we only detect UVOT emission in the UVOT *U* filter. We use this filter to rescale the SDSS data, but do not include it in the UV-optical model fit.
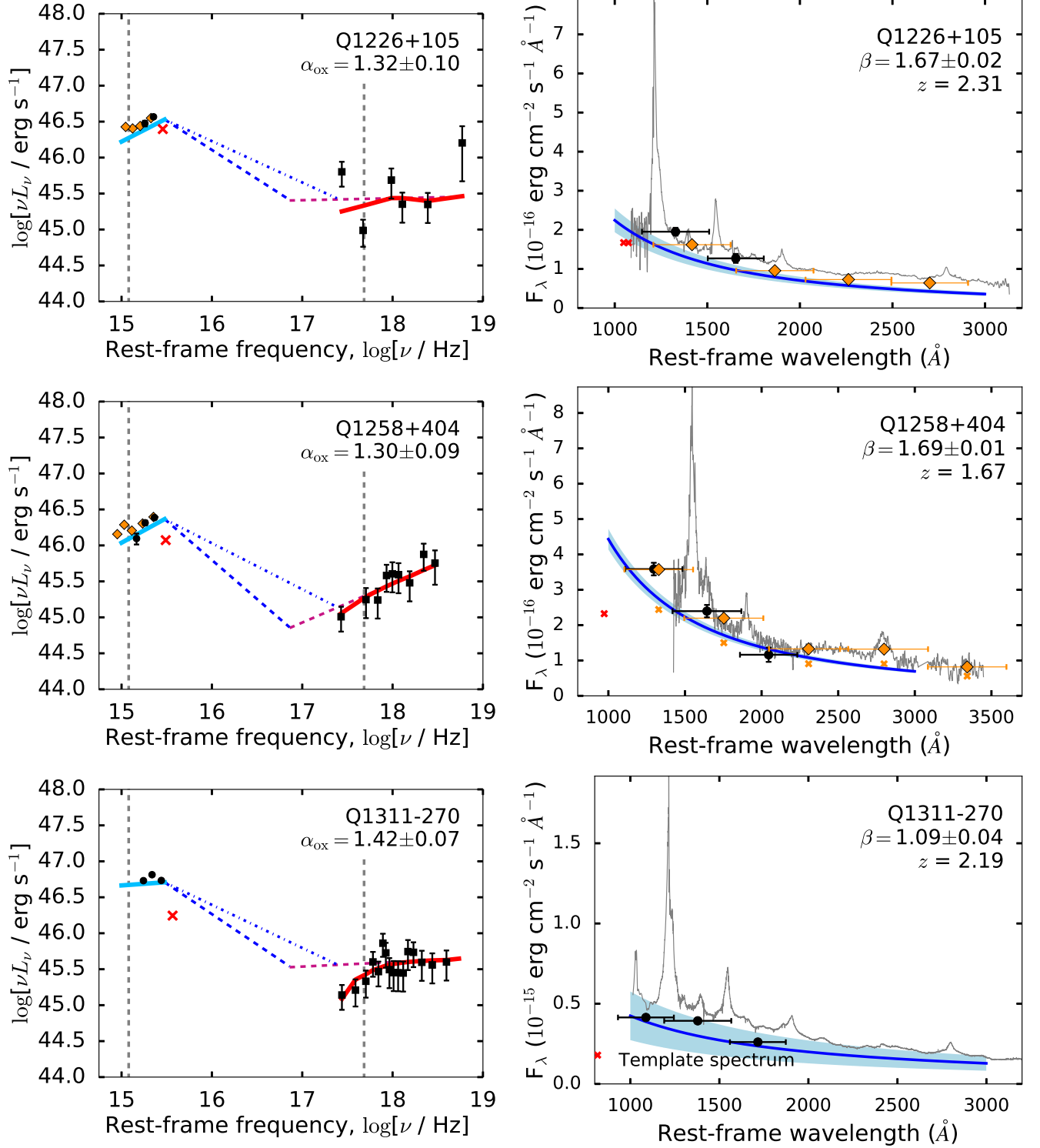
Figure B13. *Left:* Rest-frame UV to X-ray spectral energy distributions (SEDs) of quasars in our sample. *Right*: UV photometry and continuum modeling. See Figure 4 for symbol and color coding. *Notes on individual objects:* None.
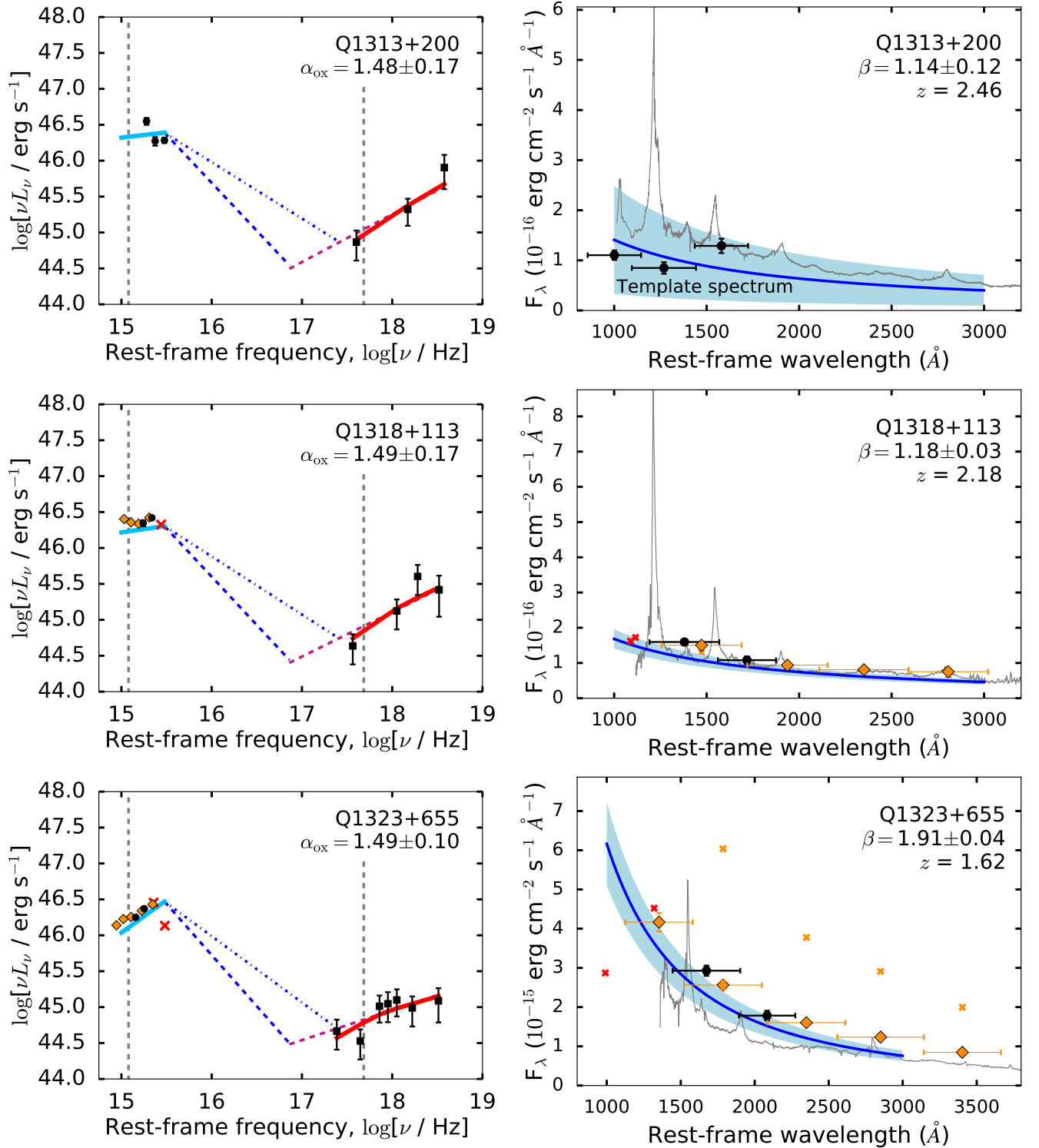
Figure B14. *Left:* Rest-frame UV to X-ray spectral energy distributions (SEDs) of quasars in our sample. *Right:* UV photometry and continuum modeling. See Figure 4 for symbol and color coding. *Notes on individual objects:* For Q1323+655, the SDSS photometric data (used for the UV-optical model fit) are offset in flux from the SDSS spectrum (used only for visualization purposes). Also, this quasar appears to have decreased in flux by a factor ∼ 2.5 since the SDSS observation (2013 June).

Figure B15. *Left:* Rest-frame UV to X-ray spectral energy distributions (SEDs) of quasars in our sample. *Right:* UV photometry and continuum modeling. See Figure 4 for symbol and color coding. *Notes on individual objects:* For Q1402-012, the SDSS photometric data (used for the UV-optical model fit) are offset in flux from the SDSS spectrum (used only for visualization purposes).
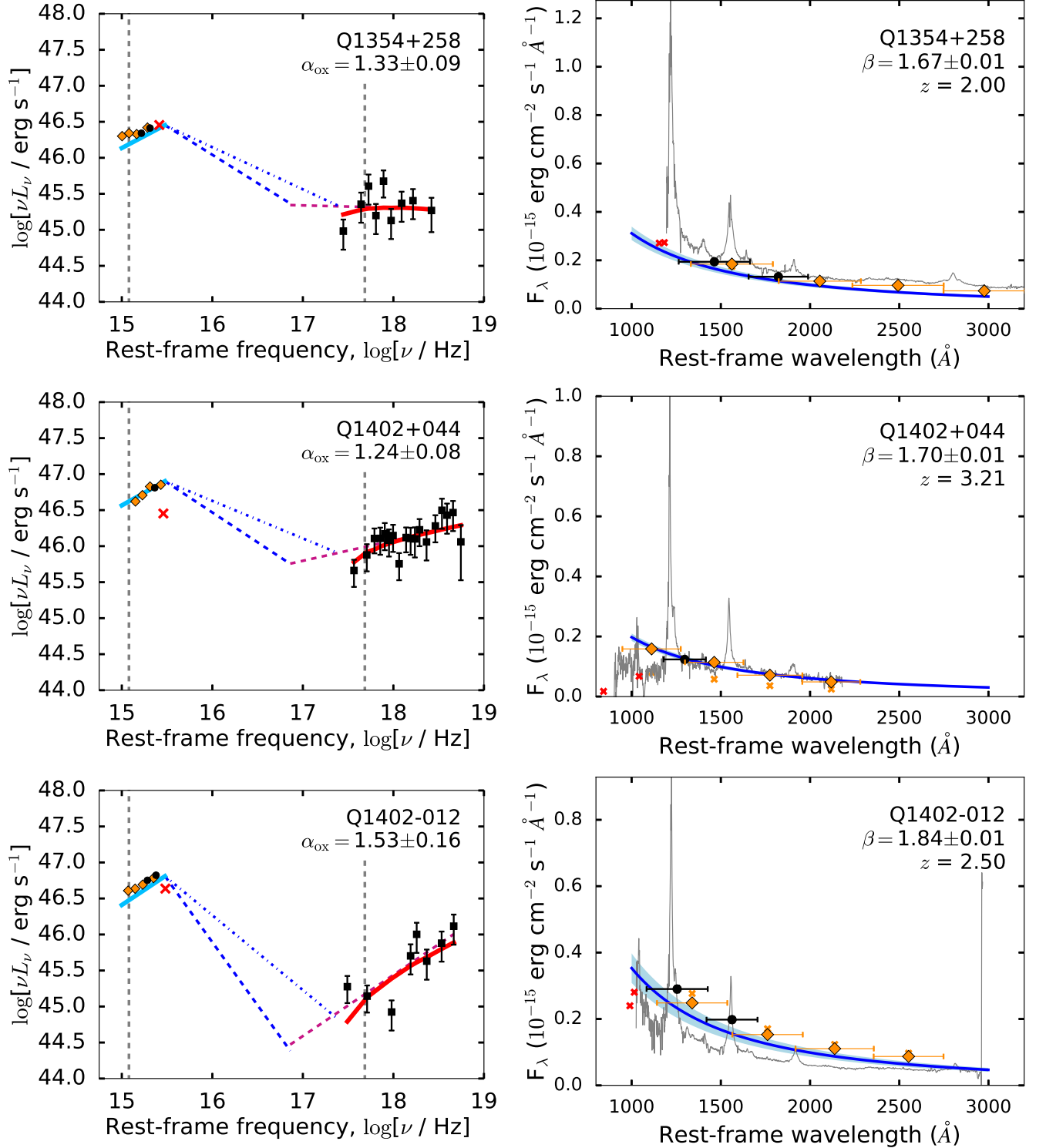
Figure B16. *Left:* Rest-frame UV to X-ray spectral energy distributions (SEDs) of quasars in our sample. *Right*: UV photometry and continuum modeling. See Figure 4 for symbol and color coding. *Notes on individual objects:* None.

Figure B17. *Left:* Rest-frame UV to X-ray spectral energy distributions (SEDs) of quasars in our sample. *Right*: UV photometry and continuum modeling. See Figure 4 for symbol and color coding. *Notes on individual objects:* Quasar Q1554-203 is an outlier in terms of the UV-optical spectral index β. Given only two usable photometric data points, and lacking SDSS spectroscopy, we can only guess that this might be due to extremely strong Ly-α emission, or to broad C IV absorption.
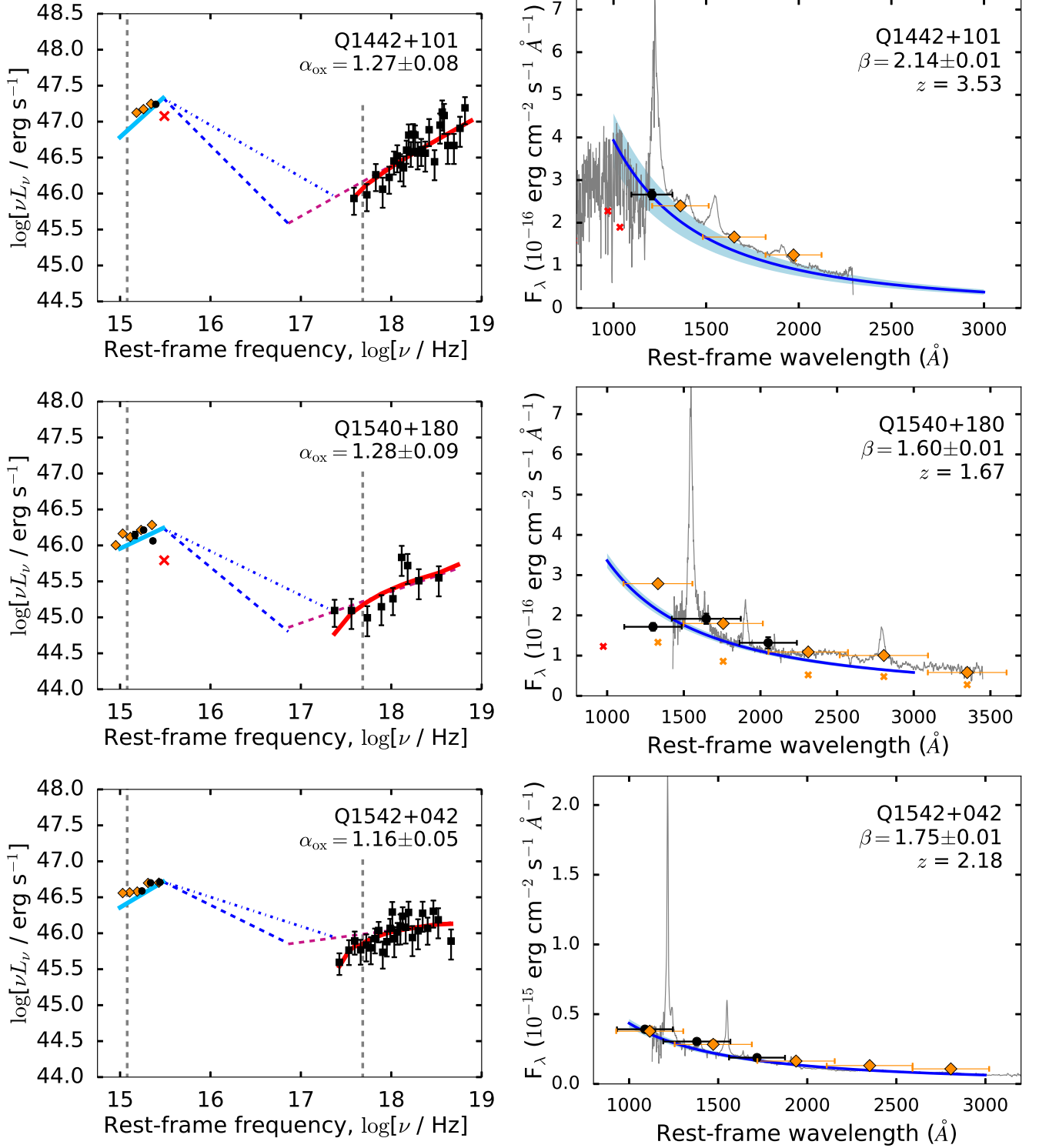
Figure B18. *Left:* Rest-frame UV to X-ray spectral energy distributions (SEDs) of quasars in our sample. *Right:* UV photometry and continuum modeling. See Figure 4 for symbol and color coding. *Notes on individual objects:* For Q1607+183, the SDSS photometric data (used for the UV-optical model fit) are offset in flux from the SDSS spectrum (used only for visualization purposes)

Figure B19. *Left:* Rest-frame UV to X-ray spectral energy distributions (SEDs) of quasars in our sample. *Right*: UV photometry and continuum modeling. See Figure 4 for symbol and color coding. *Notes on individual objects:* None.
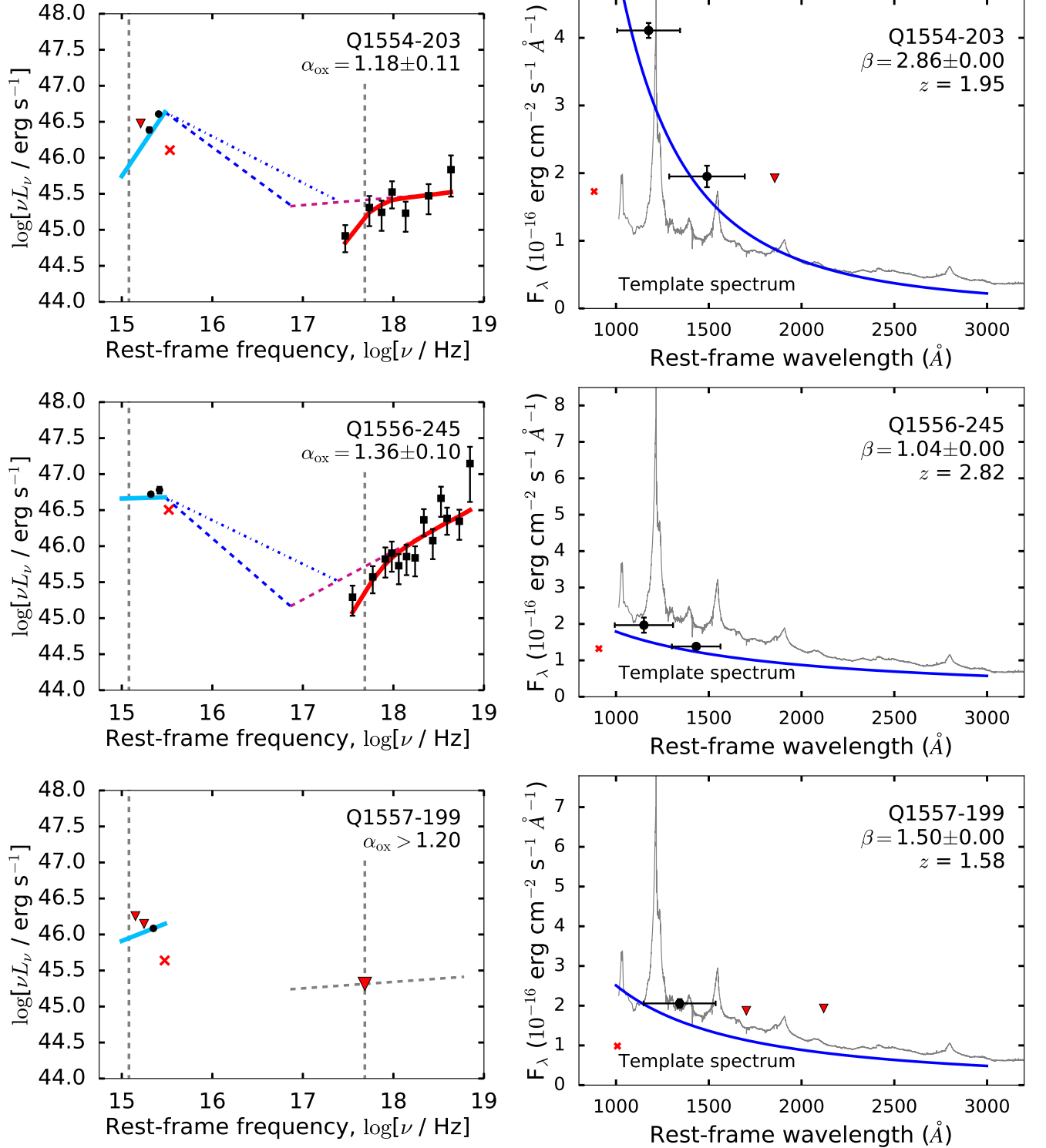
Figure B20. *Left:* Rest-frame UV to X-ray spectral energy distributions (SEDs) of quasars in our sample. *Right*: UV photometry and continuum modeling. See Figure 4 for symbol and color coding. *Notes on individual objects:* None.

Figure B21. *Left:* Rest-frame UV to X-ray spectral energy distributions (SEDs) of quasars in our sample. *Right*: UV photometry and continuum modeling. See Figure 4 for symbol and color coding. *Notes on individual objects:* None.
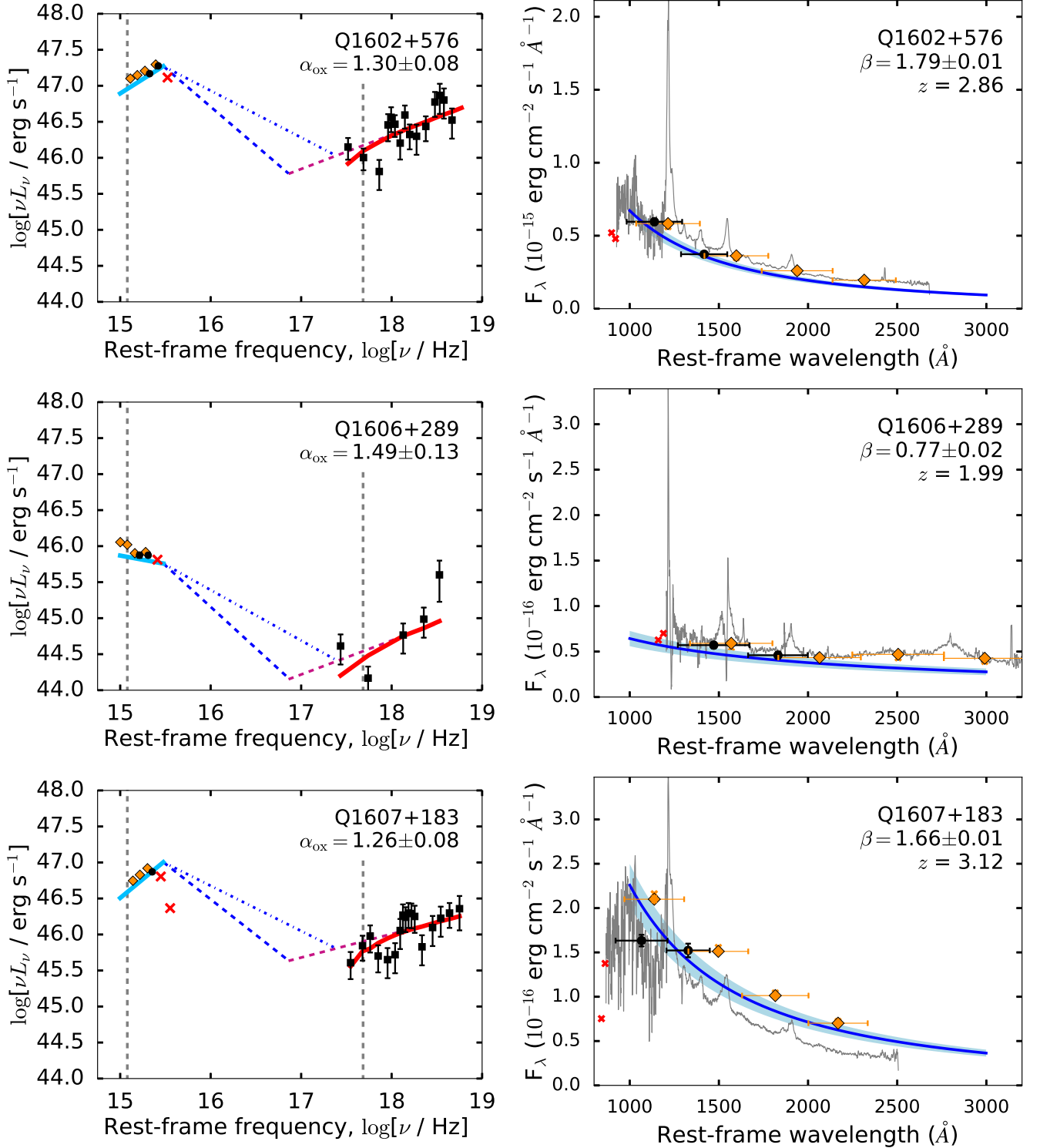
Figure B22. *Left:* Rest-frame UV to X-ray spectral energy distributions (SEDs) of quasars in our sample. *Right*: UV photometry and continuum modeling. See Figure 4 for symbol and color coding. *Notes on individual objects:* None.
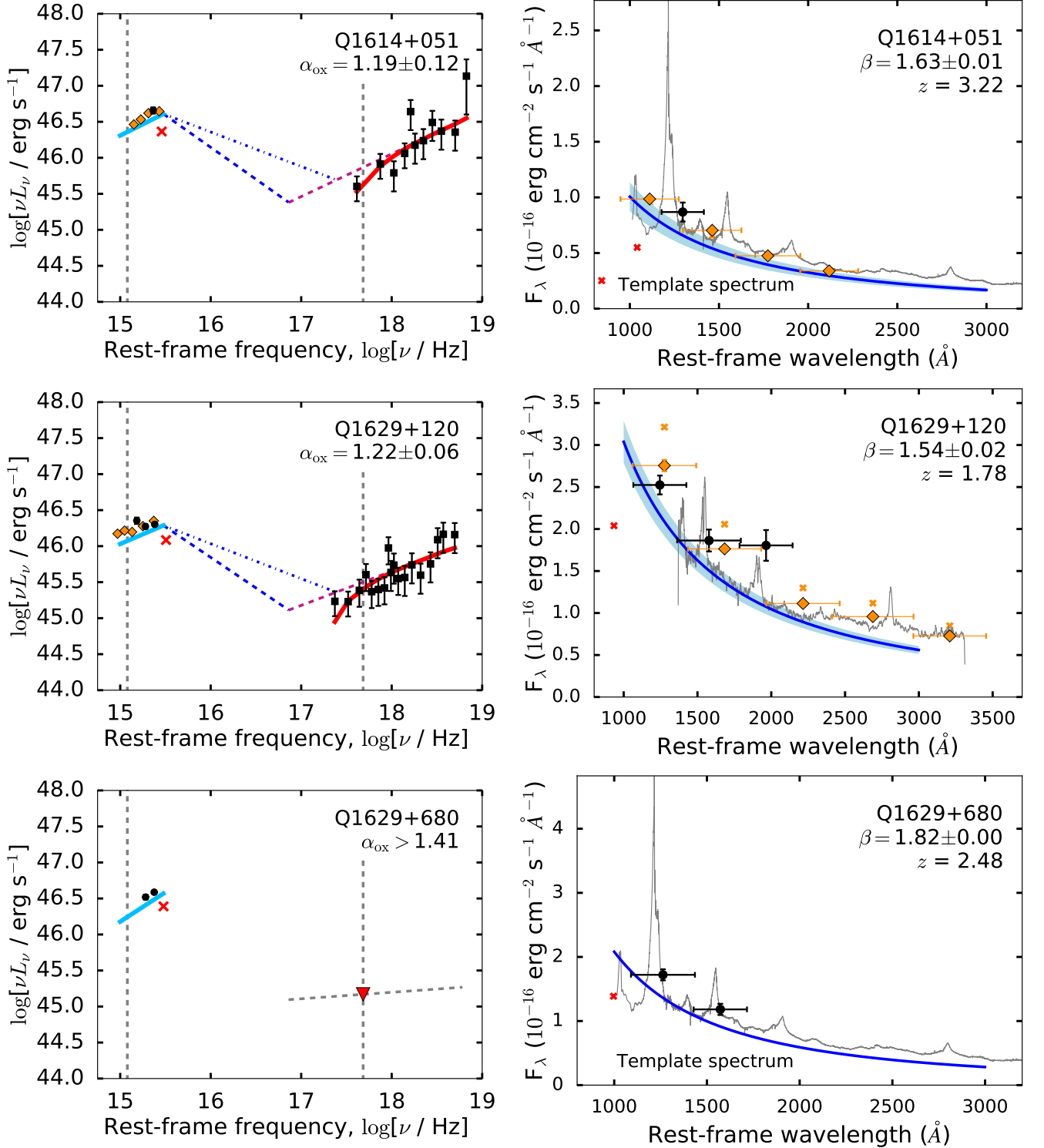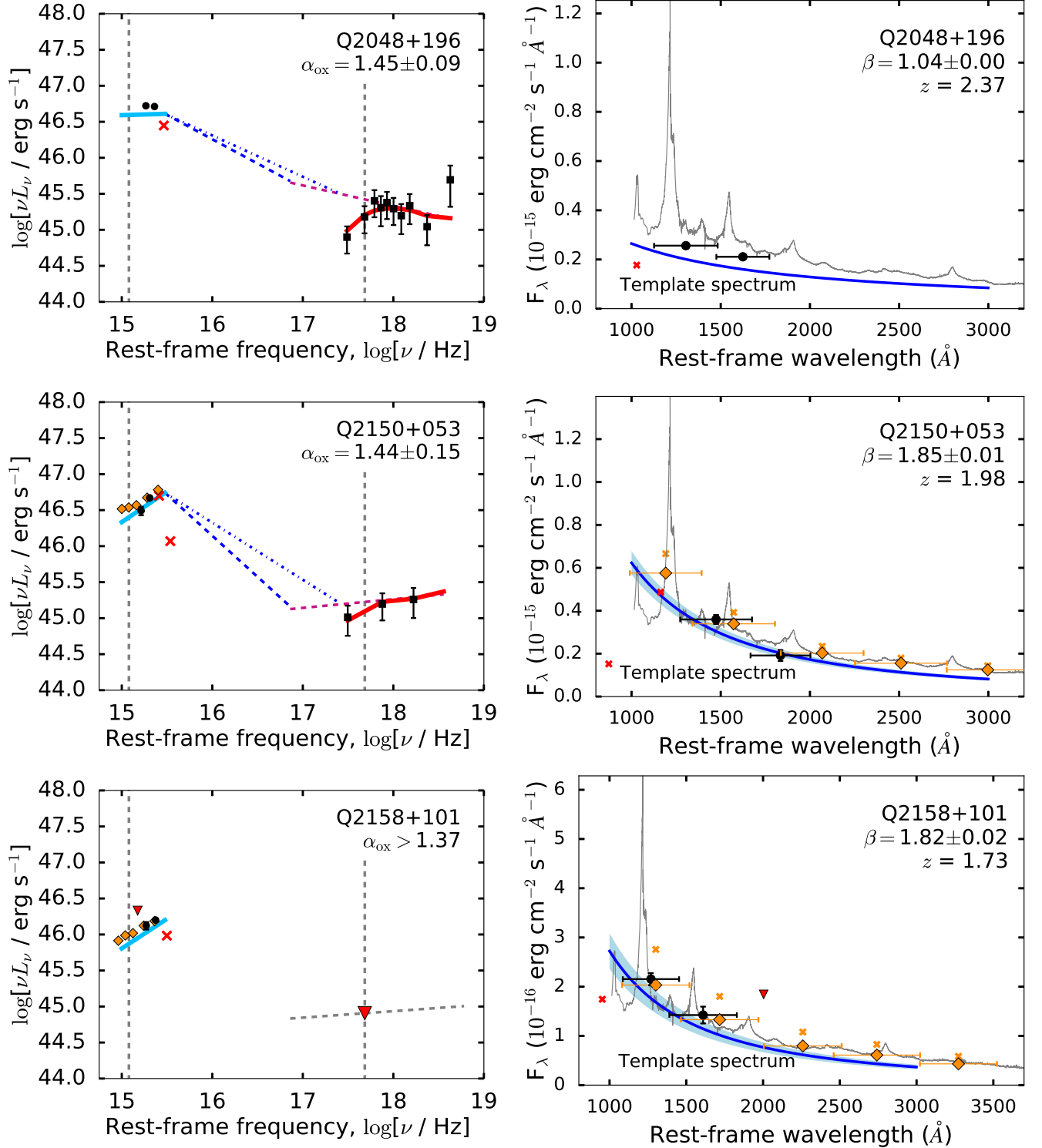
Figure B23. *Left:* Rest-frame UV to X-ray spectral energy distributions (SEDs) of quasars in our sample. *Right*: UV photometry and continuum modeling. See Figure 4 for symbol and color coding. *Notes on individual objects:* None.
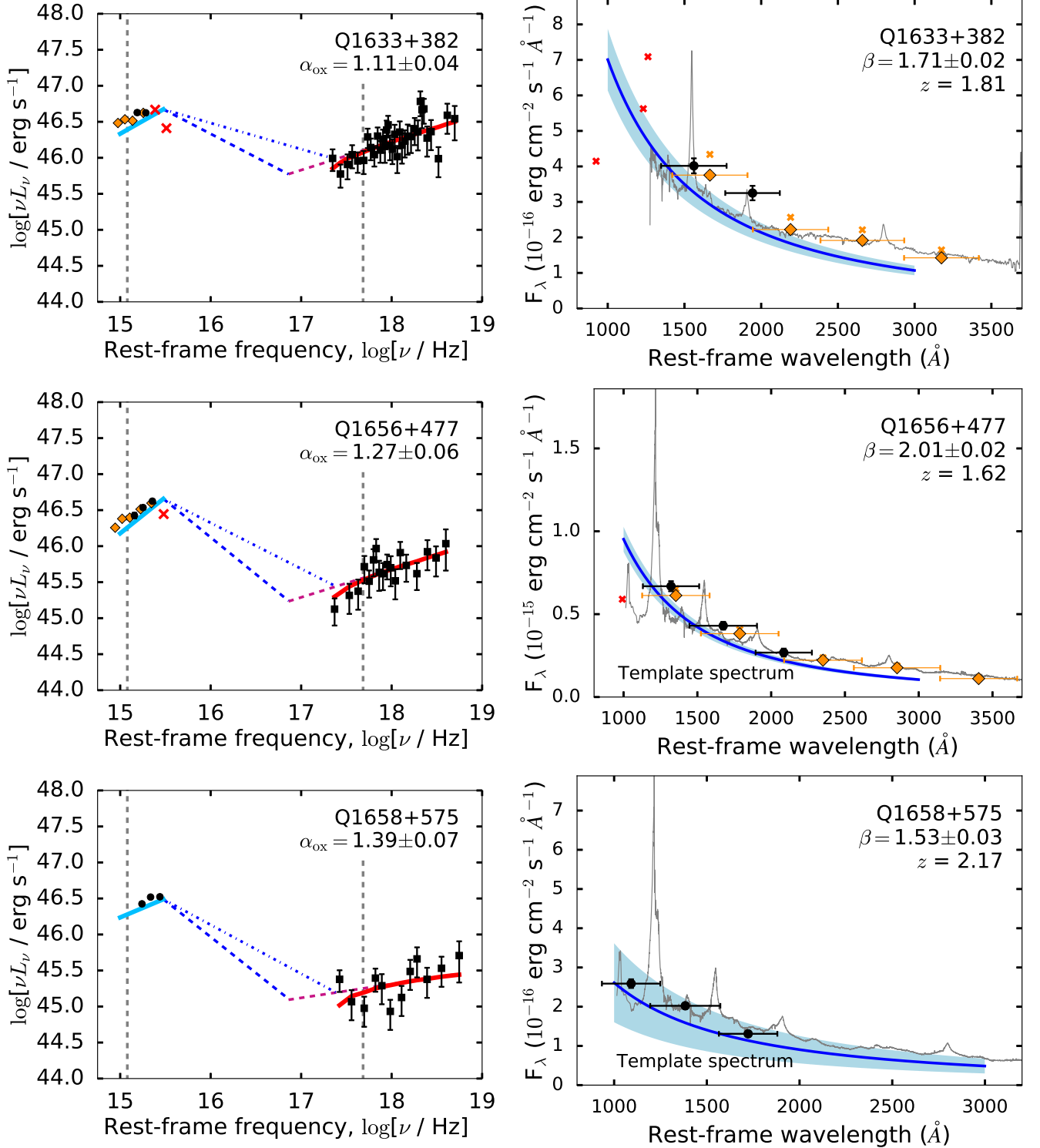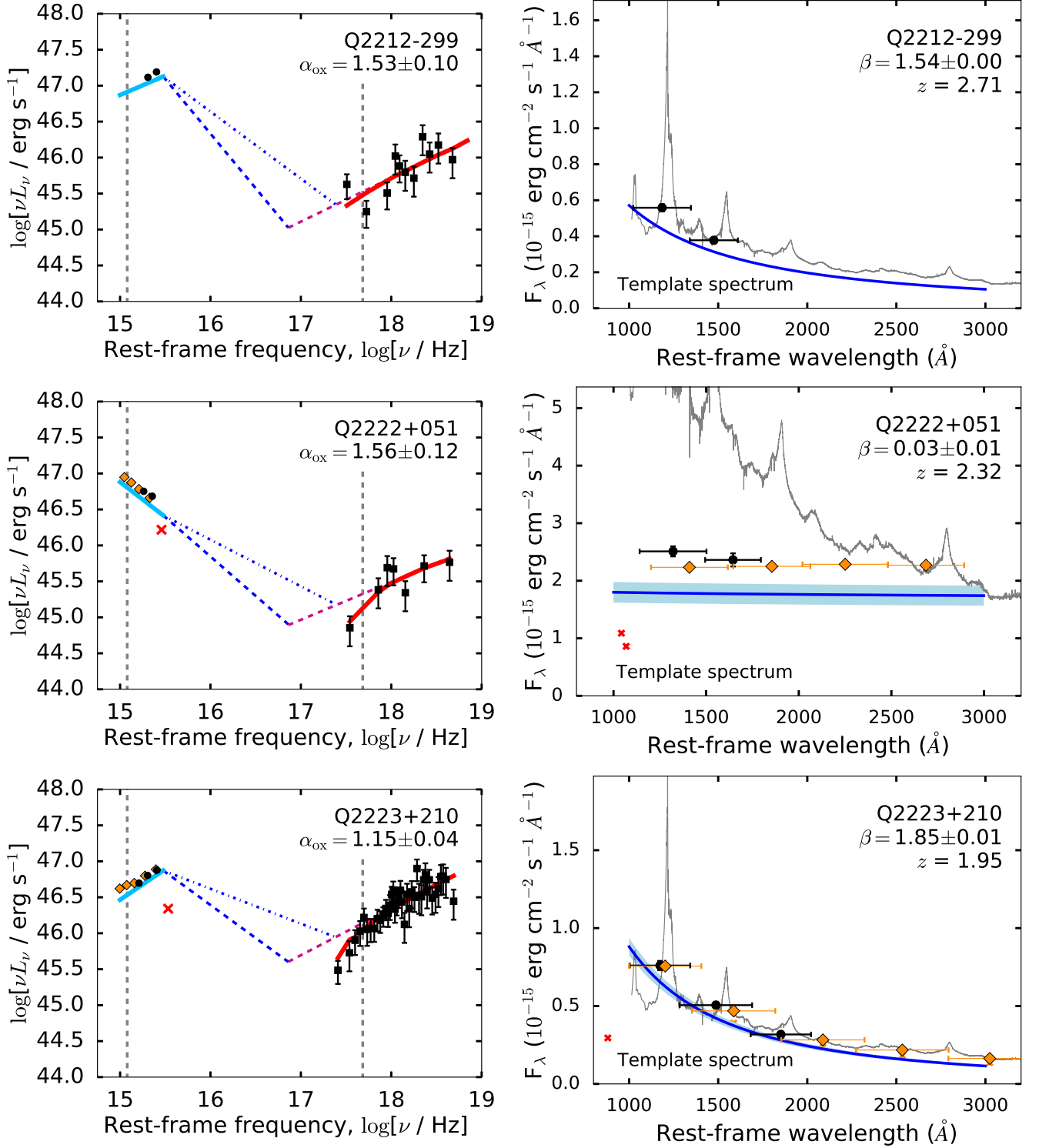
Figure B24. *Left:* Rest-frame UV to X-ray spectral energy distributions (SEDs) of quasars in our sample. *Right:* UV photometry and continuum modeling. See Figure 4 for symbol and color coding. *Notes on individual objects:* The UV-optical SED of Q2222+051 appears to be heavily reddened.
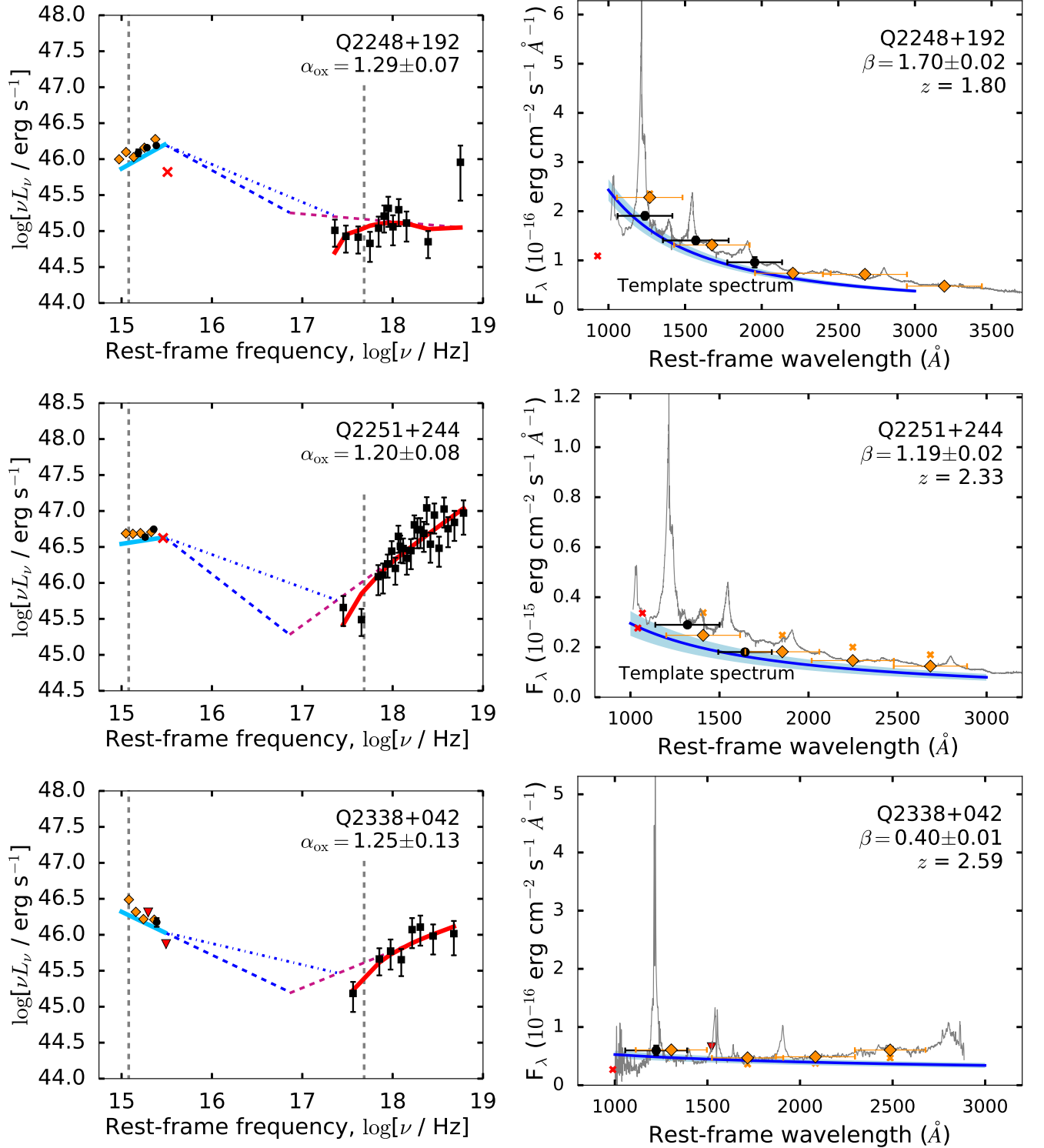
Figure B25. *Left:* Rest-frame UV to X-ray spectral energy distributions (SEDs) of quasars in our sample. *Right:* UV photometry and continuum modeling. See Figure 4 for symbol and color coding. *Notes on individual objects:* For Q2338+042, the BEL and especially the Balmer / Fe II pseudo-continuum emission appear unusually strong in the SDSS spectrum. This impairs our continuum slope determination, as we do not perform spectral decomposition for individual quasars, which may explain the outlying value of $\beta_{\rm UV}$ for this object.
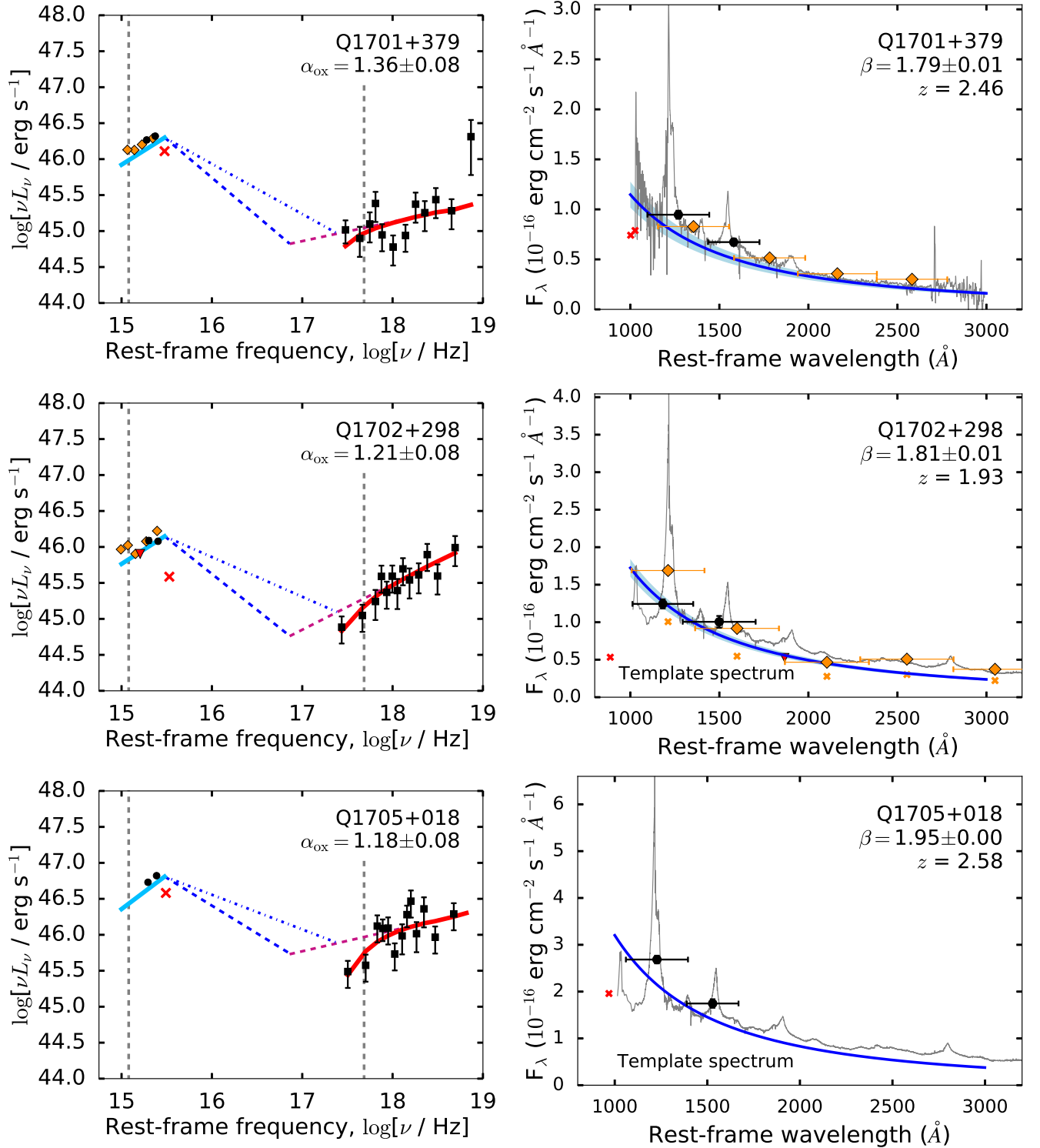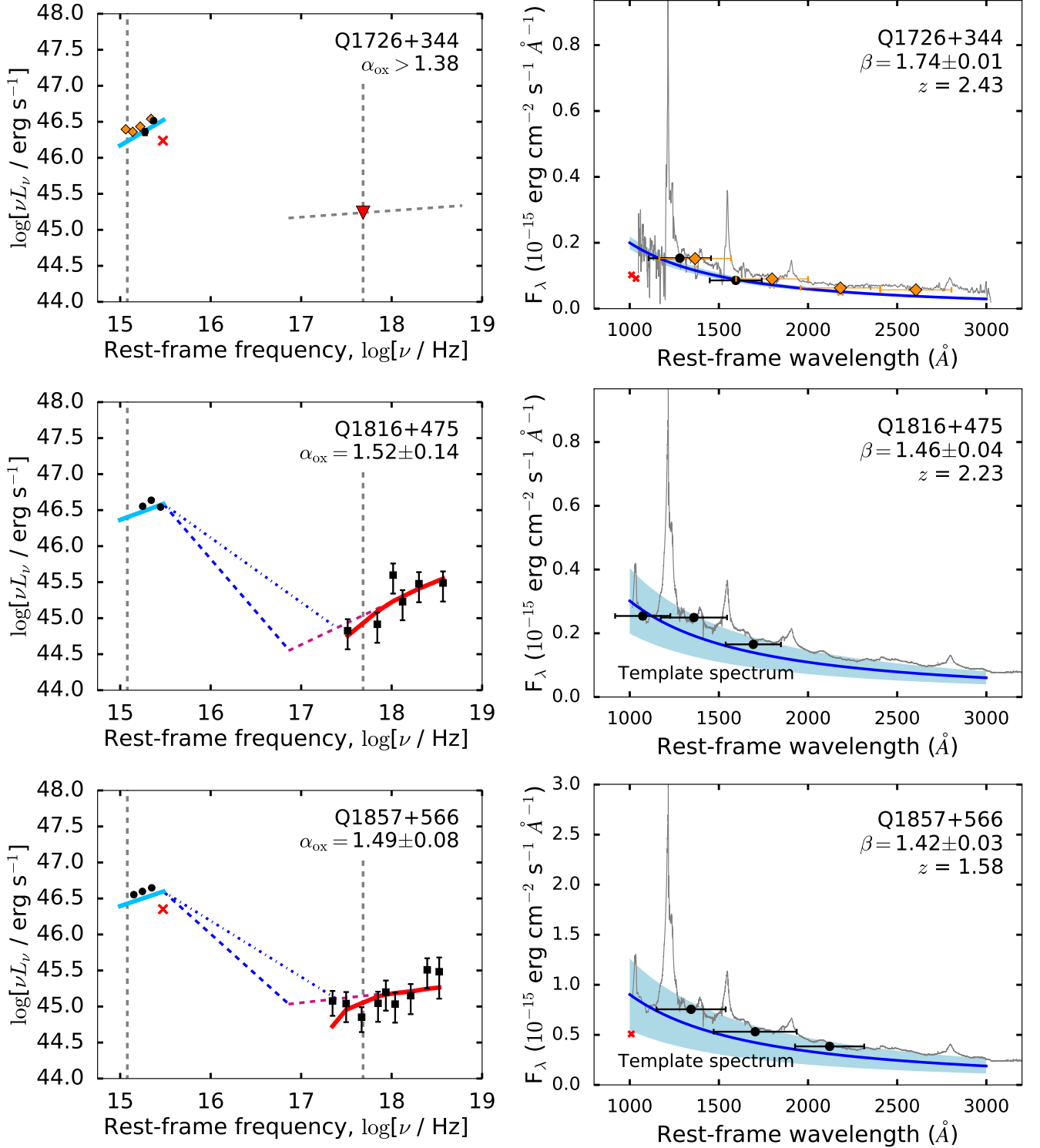
Figure B26. *Left:* Rest-frame UV to X-ray spectral energy distributions (SEDs) of quasars in our sample. *Right*: UV photometry and continuum modeling. See Figure 4 for symbol and color coding. *Notes on individual objects:* None.
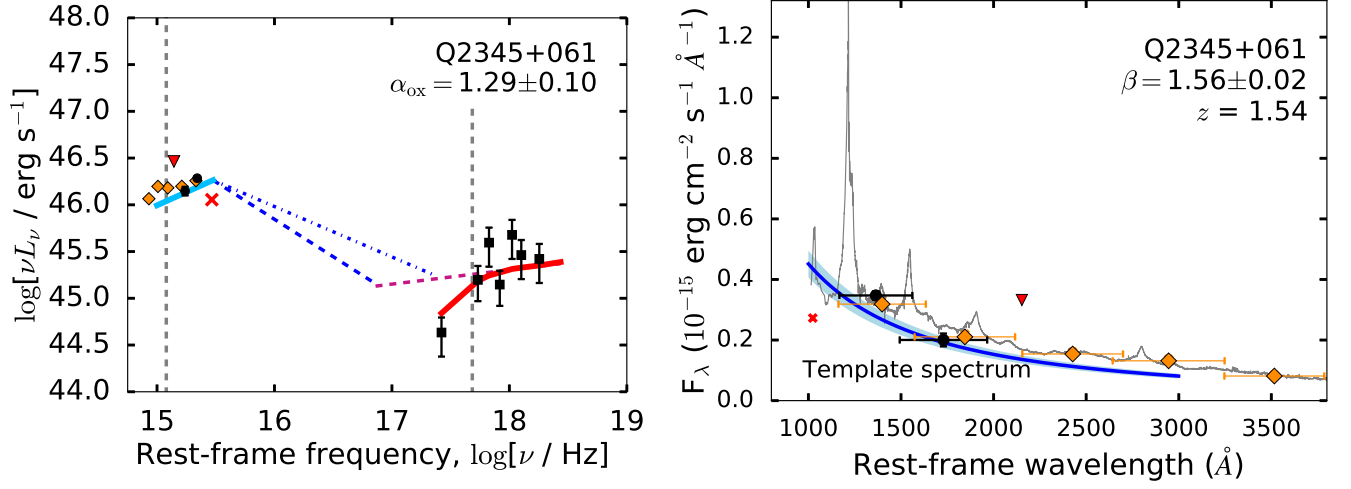
6.3   Prospects for Determining Thin-Disk Accretion Parameters

In this Section, I explore whether the *Swift* UVOT broad-band photometric spectral energy distributions (SEDs) for the quasar sample presented in our draft journal article (§6.2) can constrain the model parameters of the standard geometrically thin, optically thick accretion disk models originally developed by Shakura and Sunyaev (1973) and by Novikov and Thorne (1973). I address two related questions here. Firstly, are the observed SEDs for our sample quasars *consistent* with the thin-disk models? And secondly, if the SEDs can be satisfactorily modeled as thin disks, can we provide useful *constraints* on the black hole spin and mass accretion rate for these quasars, given the currently available data?

In general, I find that our *Swift* observations do not either definitively rule out the thin-disk models, or display convincing evidence that our quasars harbor thin accretion disks. If the thin disk models are in fact correct, my modeling indicates that high-mass ($M_{\mathrm{BH}} \gtrsim 5 \times 10^9 M_\odot$) quasars in our sample must have near-maximally spinning black holes, while quasars with black hole masses $M_{\mathrm{BH}} \approx 1 \times 10^9 M_\odot$ may instead have intermediate black hole spins. However, I do not consider this preliminary result to be robust, for the following reasons:

- Our observations do not cover sufficiently long wavelengths to provide useful constraints on the mass accretion rate of these $z \sim 2$ quasars.

- Only two quasars in our sample display clear evidence of an SED turnover within the energy range observed by UVOT. Of these two, only one quasar is reasonably well modeled by the thin-disk spectrum. For the other quasars in our sample, the disk models are not well-constrained, except for sources with large black hole masses, for which the *lack* of an SED turnover requires a near-maximal black hole spin. It is not clear (based on our data) whether the black hole spins are uniformly high for the high-mass quasars, or whether the models are wrong.

- The thin-disk models often provide a poor approximation to our observed SED shapes. This may in part be due to an inadequate correction for broad emission line contamination in our *Swift* UVOT photometry.

- A major source of uncertainty in this exploratory investigation is the factor ~ 3 statistical uncertainty on our black hole mass estimates. In particular, for quasars with overestimated black hole masses and very blue SEDs, the thin-disk models will overestimate the black hole spin. This uncertainty must be explicitly included in our modeling to facilitate a more robust test of the thin-disk models in future work.

Very Large Telescope *X-Shooter* spectroscopic observations would solve two major uncertainties inherent to my modeling. Firstly, they would allow the continuum component to be isolated on a per-object basis. Secondly, they would provide better constraints on the mass accretion rate, because they cover the power-law low-energy tail of the disk emission component. Based on this exploratory study, I find that rest-frame UV to near-IR spectroscopic observations are required in order to robustly test the thin-disk models; *X-Shooter* spectra would be ideal!

In the rest of this Section, I describe my attempts to perform accretion disk modeling using the *Swift* UVOT SEDs.

6.3.1 Motivation

Many of our sample quasars have Eddington ratios consistent with the thin-disk regime: The thin-disk models are not the only available theoretical models for accretion disks around black holes. More advanced models include advective 'slim accretion disks' that are thought to be required at high mass accretion rates (Abramowicz et al., 1988), and advection-dominated 'ADAF' disks that are required at very low mass accretion rates (Narayan et al., 1998, 2014). Additionally, several authors suggest modifications to the thin-disk model that modify the resulting UV–optical emission, including the effects of atmospheric reprocessing (e.g., Czerny and Elvis, 1987; Hall et al., 2018) and outflowing winds that serve to decrease the mass accretion rate in the inner regions (Laor and Davis, 2014; Slone and Netzer, 2012). In §6.2, I demonstrate that our sample quasars have Eddington luminosity ratios greater than $L/L_{\rm Edd} \approx 0.01$. Thus, they are unlikely to harbor ADAF disks, which do not emit efficiently in the ultraviolet and optical regimes, and for which we would not detect significant UV–optical emission from the accretion disk at $z \sim 2$. However, I also find that a few of our sample quasars have Eddington ratios above ~ 0.3 (even if we underestimate their black hole masses at the 1σ level). This luminosity regime is consistent with them harboring 'slim accretion disks'. It is not my goal in this exploratory study to investigate the more advanced accretion disk models, but rather, to determine whether our available data are consistent with the simple thin-disk models.

Do all quasars have rapidly spinning black holes?: The standard thin-disk models predict a spectral turnover in the UV–optical for quasars with massive black holes, $M_{\rm BH} \gtrsim 10^9 M_\odot$, unless the black hole is spinning rapidly. Our SEDs for individual sources (Appendices A and B of §6.2) show evidence of an SED turnover in the UV–optical in only a few cases; most of the UV–optical SEDs are consistent with a power-law continuum that extends to rest-frame ~ 1200 Å, beyond which our photometric data are affected by Galactic and extra-galactic Hydrogen absorption. Observationally, this result is consistent with previous quasar studies that find SED turnovers near rest-frame 1000 Å irrespective of $M_{\rm BH}$ (e.g., Shang et al., 2005; Stevans et al., 2014). However, according to thin-disk models, for high-mass black holes, near-maximal black hole spins are required in order to produce a spectral turnover at such a high energy Capellupo et al. (e..g., 2015). If the thin-disk models are correct, the roughly constant observed spectral turnover energies for quasars require a scenario where higher-mass quasars have increasingly high black hole spins. It is intriguing that we seldom observe high-mass quasars with low inferred black hole spins. My main motivation for this preliminary study is to examine to which degree our sample quasars require rapidly spinning black holes in order to explain their observed SEDs in the context of thin-disk models.

Do radio-loud quasars have more rapidly spinning black holes than radio-quiets?: A scenario where all quasars have high black hole spins also has implications for our understanding of

the radio-loud fraction of quasars. The reason that $\sim 10\%$ of quasars are radio-loud, and are able to launch kpc-scale radio jets, is currently poorly understood (§1.1.8). Radio-loud sources may require rapidly spinning black holes (e.g., Blandford and Payne, 1982; Maraschi et al., 2012). If a rapidly spinning black hole is a sufficient condition for a quasar to appear as radio-loud, we would expect that radio-loud quasars have more rapid black hole spins than do radio-quiet quasars. This is because the black hole spin determines the radius of the innermost stable circular orbit (§1.1.1), and (for thin-disk models) modifies the temperature profile of the disk emission (§1.2). On the contrary, if both radio-quiet and radio-loud quasars have rapidly spinning black holes, there must be some other physical difference between their central engines.

Schulze et al. (2017) find indirect evidence that radio-loud quasars have higher black hole spins than do a sample of radio-quiet quasars with matching black hole masses and accretion rates. In their study, the accretion rates are inferred from the luminosity of the low-energy power-law 'tail' of the accretion disk emission. Instead of modeling the accretion disk SEDs directly, they estimate the ionizing extreme-UV continuum based on the narrow emission line luminosities for their sample. They find that radio-loud sources have a stronger ionizing continuum than do the matched radio-quiet sources, as expected if their accretion disks have smaller innermost circular stable orbits, due to higher black hole spins. I speculate that the inner jet in radio-loud quasars might also produce ionizing radiation, causing this result. It would therefore be useful to independently study the purported difference in black hole spins directly using SED modeling.

Can we constrain thin-disk models using our currently available data?:   While our quasar sample selection and *Swift* observations were not explicitly designed to study accretion disk models, I demonstrate in §6.2 that they have luminosities and SED shapes consistent with those found for the broader population of luminous quasars at $z \sim 2$. It would therefore be interesting to study whether their rest-frame UV–optical emission is consistent with the predictions of thin-disk models, and to study their distributions of black hole spins. In particular, do we see evidence for the elusive UV–optical spectral turnover predicted for high-mass, low-spin black holes? Additionally, our RQQ and RLQ subsamples are selected to have similar distributions of redshift and *V*-band absolute magnitude. I demonstrate in §6.2 that they also have similar distributions of black hole mass. Our *sample* is therefore well-suited to study differences in accretion properties between radio-loud and radio-quiet quasars, as suggested if radio-loud sources require rapidly spinning black holes in order to launch radio jets. In order to further investigate these issues, we need to determine how sensitive our photometric SEDs are to the underlying accretion disk properties. I.e., might a wide range of accretion disk properties produce similar SEDs as observed with *Swift* UVOT? If that is the case, we would require more data in order to determine whether our radio-loud and radio-quiet sources indeed have similar accretion rates and black hole spins.

In the following subsections, I demonstrate that our available data do *not* strongly constrain the black hole spins for typical quasars in our sample. This is partly due to the dependence of the spectral turnover energy on the mass accretion rate - it is difficult to constrain both parameters independently with only a few photometric data points - but also due to the uncertainty in black hole masses for single-epoch spectroscopic measurements. In §6.3.2 I illustrate the broad range

of accretion disk SEDs that the thin-disk models can produce for the energy range observed by *Swift* UVOT. In §6.3.3 I discuss whether it is appropriate to estimate the mass accretion rate using a monochromatic luminosity at the longest wavelengths probed by our observations. Finally, in §6.3.4 I present some examples of thin-disk model fits to our *Swift* UVOT data, and demonstrate the limitations of this approach.

6.3.2   Thin-Disk Model SEDs for $\sim 10^9 M_\odot$ Black Holes

Here, I generate a range of thin-disk models with different model parameters, in order to examine the resulting range of SED shapes as observed by *Swift* UVOT and SDSS. These models are calculated using the updated relativistic correction factors presented by Riffert and Herold (1995). Locally, these models are fully determined by the black hole mass M_{BH}, the mass accretion rate $\dot{M}$, and the black hole spin, as parameterized by the dimensionless spin coefficient a_*. The observed SED also depends on the disk inclination i and on the source redshift. The numerical code used to produce these models is provided by Sandra Raimundo.

Choice of parameter ranges: The quasars in our sample have virial black hole mass estimates spanning $8.5 \lesssim \log[M_{BH}/M_\odot] \lesssim 10.6$ (§6.2). In order to explore the mass dependence of the thin-disk emission, I generate models at four different black hole masses, roughly corresponding to the observed range of masses (Figure 6.1, upper panels). For these models, the mass accretion rate is held constant.

Our sample quasars are accreting at substantial fractions of the Eddington luminosity ratio (§6.2). Assuming that the radiative efficiency does not depend on accretion rate, the Eddington luminosity ratio is equal to $\dot{M}/\dot{M}_{Edd}$ for thin-disk models, where $\dot{M}_{Edd}$ is the mass accretion rate at the Eddington limit. I therefore assume that our sample quasars have a range of accretion rates $0.01 \lesssim \dot{M}/\dot{M}_{Edd} \lesssim 1$, corresponding to the observed range of Eddington luminosity ratios. I illustrate the effects of varying $\dot{M}$, for a constant M_{BH}, in Figure 6.1 (lower panels); the mass accretion rates are sub-Eddington for all models shown.

I calculate disk SEDs for a non-rotating black hole (Figure 6.1, left panels), and a maximally rotating black hole (Figure 6.1, right panels), for a range of black hole masses and accretion rates. At constant accretion rate, increasing the spin parameter a_* shifts the SED turnover energy towards shorter wavelengths, while increasing M_{BH} shifts the SED turnover towards longer wavelengths. At constant black hole mass, increasing either $\dot{M}$ or a_* shifts the SED turnover towards higher energies, although the effect of $\dot{M}$ on the turnover frequency is weaker than that of a_* for the parameter ranges investigated.

Thin-disk model SEDs in the rest-frame UV: Our UV–optical data cover rest-frame wavelengths of $1000\,\text{Å} \lesssim \lambda \lesssim 3000\,\text{Å}$ for these $z \sim 2$ quasars. For the range of black hole masses and accretion rates relevant to our quasar sample, it is evident that the thin-disk models can either produce a blue spectrum (i.e., increasing in flux towards short wavelengths), a flat spectrum, or a red spectrum. For black holes with masses $M_{BH} \gtrsim 10^9 M_\odot$, the thin-disk models do provide an interesting constraint
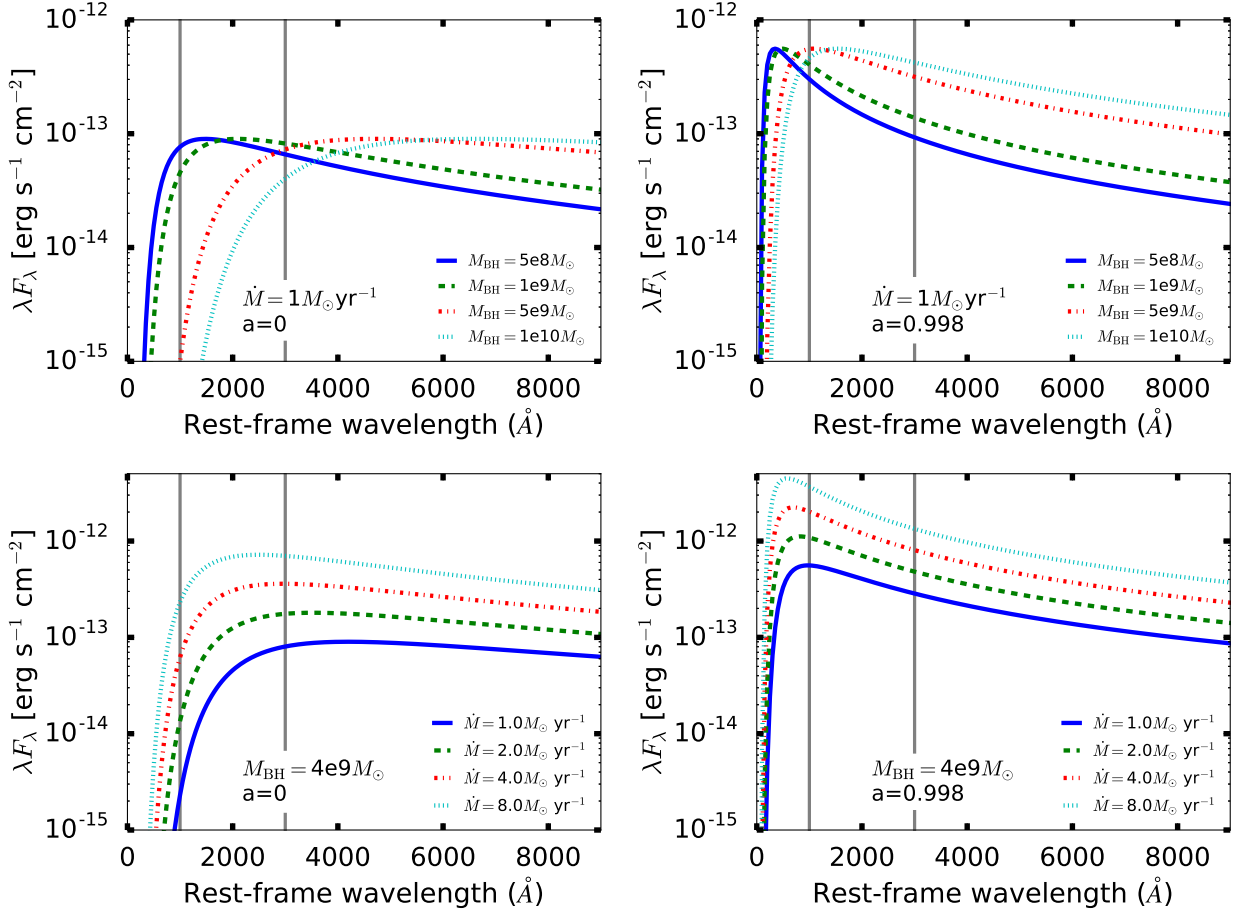
Fig. 6.1 Exploring the parameter space relevant for Novikov-Thorne thin-disk models with black hole masses and Eddington ratios relevant to our quasar sample. All models in this figure have a disk inclination angle of $i = 30°$ (where $i = 0$ corresponds to viewing along the disk rotation axis). Observed fluxes are calculated for sources at $z = 2$, assuming no reddening. Vertical gray lines indicate the approximate rest-frame wavelength range observed by UVOT and SDSS for our $z \sim 2$ sample. *Top panels:* The effect of M_{BH}, shown for the zero-spin case (left) and for a maximally spinning SMBH (right). All models have $\dot{M} = 1 M_\odot$ yr^{-1}. For this accretion rate, $L_{bol}/L_{Edd} < 0.3$ for the range of M_{BH} shown, and I therefore expect the thin-disk approximation to be valid. *Bottom panels:* The effect of the accretion rate, $\dot{M}$, at fixed $M_{BH} = 4 \times 10^9 M_\odot$, which is approximately the average black hole mass estimated for our sample.

on the SED shape I would observe. For thin-disk models at sub-Eddington accretion rates, the UVOT data should reveal an SED turnover for quasars harboring slowly-rotating black holes with $M_{\rm BH} \gtrsim 10^9 M_\odot$. For maximally spinning black holes ($a_* \approx 0.998$, Novikov and Thorne, 1973), only the most massive SMBH will display a spectral turnover in the UV–optical. Only two quasars in our sample (J142923.92+024023.14 and Q0835+580) display clear evidence of a SED turnover in their UV SEDs. Thus, if the thin-disk models are correct, the majority of quasars with *true* black hole masses $M_{\rm BH} \gtrsim 10^9 M_\odot$ in our sample have rapidly spinning black holes.

Increasing $\dot{M}$ (or a_*) also increases the overall flux level. However, increasing the disk inclination, i, produces a lower overall observed flux, as the projected area of the disk is decreased. Therefore, $\dot{M}$ and i are near-degenerate for the observed wavelength range, especially in cases where the SED turnover is not constrained. Thus, while the non-detection of a SED turnover in the UV–optical regime does require near-maximal black hole spin for the most massive quasars in our sample (irrespective of the inclination angles and accretion rates), we do not observe a sufficiently broad wavelength range to constrain i, $\dot{M}$ and a_* independently. This precludes precise measurement of the black hole spin using our broad-band SEDs. I tested this by fitting thin-disk models to all quasars in our sample that have black hole mass estimates, as described in §6.3.4. While the models require near-maximal black hole spins for quasars with $M_{\rm BH} \gtrsim 10^9 M_\odot$ that do not display an SED turnover, the mass accretion rate is not well-constrained for any sources. In §6.3.3 I outline an alternative approach towards constraining the mass accretion rate, and ascertain whether it is useful given our available data.

6.3.3   Feasibility of Monochromatic $\dot{M}$ Estimates

At sufficiently low energies, in the rest-frame optical or NIR depending on the black hole mass, the thin-disk model SEDs can be approximated by power-laws with similar slopes irrespective of the other model parameters. This is illustrated in Figure 6.1: at wavelengths exceeding ~ 8000 Å the thin-disk SEDs display little spectral curvature, and the luminosity depends only weakly on the black hole spin. This behavior allows $\dot{M}$ to be estimated using a single observed monochromatic luminosity, if estimates of $M_{\rm BH}$ and the inclination i are available (e.g., Davis and Laor, 2011; Raimundo et al., 2012).

In Lawther et al. (2017) (Chapter 5) we performed a preliminary analysis of $\dot{M}$ for our initial quasar sample, based on the longest-wavelength photometric data available for each quasar. I now realize that this was a 'beginner's mistake'! Regrettably, Figure 6.1 demonstrates that we cannot expect the SDSS data to sample the power-law tail of the disk SED in all cases, given the range of $M_{\rm BH}$ for our sample, as the longest rest-frame wavelength observed by the SDSS is ~ 3000 Å for these $z \sim 2$ quasars. The luminosity at ~ 3000 Å is highly sensitive to black hole spin for quasars with high $M_{\rm BH}$. While the measurements of $\dot{M}$ presented in Lawther et al. (2017) can be regarded as order-of-magnitude estimations of the accretion rates, they may be systematically biased (e.g., if most of our quasars are rapidly spinning). On the other hand, if the sample contains a wide range of black hole spins, the accretion rate estimates presented by Lawther et al. (2017) will suffer an additional statistical scatter. For these reasons, we do not use the monochromatic z-band luminosities

to estimate $\dot{M}$ for the full sample. Photometry extending out to a wavelength of $\sim 2\mu$m in the observed frame is required for such estimates to be reliable for $z \sim 2$ quasars, absent prior constraints on a_*. Alternatively, VLT *X-Shooter* spectroscopic observations would provide strong constraints on the long-wavelegth 'tail' of the thin-disk emission, in which case, the thin-disk models can simultaneously constrain the accretion rate and the black hole spin (e.g., Capellupo et al., 2015).

6.3.4   Examples of Thin-disk Model Fits to Our Sample Quasars

In order to investigate whether our observed SEDs can be satisfactorily described by the standard thin-disk models, I model the *Swift* UVOT photometry for each quasar as a relativistic (Novikov-Thorne) thin-disk. I model the mass accretion rate $\dot{M}$ and the black hole spin M_{BH} as free parameters. The disk inclination angle i is somewhat degenerate with $\dot{M}$, especially in cases where we do not observe an SED turnover. Instead of modeling i as a free parameter, I model each quasar for three different inclinations: $i = 5°$ (an almost face-on accretion disk), $i = 30°$, and $i = 70°$ (almost edge-on). My intention is not to infer the inclination angle by comparing the model fits, but simply to demonstrate the wide range of $\dot{M}$ values that are consistent with the overall SED shapes when the inclination is unknown.

To minimize the contribution of the broad emission lines, I use the broad emission line-corrected *Swift* UVOT photometry. As these data are only corrected in a statistical sense for the emission line flux (using a quasar template spectrum; Section 3.2 in the draft journal article presented in §6.2), they may over- or underestimate the continuum level in each *Swift* UVOT bandpass. It is perhaps unsurprising that I do not in general obtain very good fits to the observed SEDs (in terms of the reduced-χ^2 goodness of fit statistic), as many of our photometric bandpasses are likely to contain a significant broad-line contribution. While the contamination due to broad emission lines does not strongly bias our determinations of the integrated luminosities (§6.2; Kilerci Eser and Vestergaard (as demonstrated by 2018)), an over- or undersubtracted broad-line contribution in an individual *Swift* UVOT bandpass will cause it to deviate from the true continuum level. For these broad-band photometric data, my goal is only to study the overall shape of the UV continuum and compare to that of the thin-disk models.

I find that the thin-disk models are generally poorly constrained by our data. For that reason, I do not discuss the individual model fits in detail in this Thesis. Instead, I present notable examples of model fits that, *taken at face value*, suggest that our sample contains *1)* several quasars with rapidly spinning black holes; and *2)* just two massive quasars with low inferred spin values. For each of these cases, I discuss the limitations of my modeling, and the additional observations that would be required in order to robustly test the 'face-value' interpretations.

Quasars with no SED turnover in the UV–optical: For all but two of our sample quasars, our *Swift* UVOT photometry do not display strong evidence of an SED turnover in the UV–optical. For thin accretion disks, this behavior is consistent with non-spinning or intermediate-spin black holes only for quasars with masses $M_{\text{BH}} \approx 5 \times 10^8 M_{\odot}$ (§6.3.2). For black holes with masses

$M_{\rm BH} \gtrsim 5 \times 10^9 M_\odot$, the lack of an SED turnover in the rest-frame near-UV requires maximally spinning black holes.

In Figure 6.2 I present four examples of SEDs for which we do not observe an SED turnover, but for which our modeling does not demand maximal black hole spin. The best-fitting thin-disk models display an SED turnover at energies roughly corresponding to those covered by the shortest-wavelength available *Swift* UVOT filter. The observed SED shapes are roughly *consistent* with such a turnover, but do not strongly constrain it. For these quasars, far-UV photometric observations (with an appropriate correction for Galactic and extragalactic Hydrogen absorption) might provide a more robust test of whether the SED indeed displays a spectral turnover, as predicted by the thin-disk models. Unfortunately, as our *Swift* UVOT observations were not originally designed to constrain the spectral turnover (but rather, to measure the UV to X-ray spectral shape), we did not obtain photometry in the UVOT far-UV bands for most of our sample quasars. While it may be useful to obtain far-UV observations to constrain the spectral turnover for quasars displaying this kind of SED, an approximate correction for extragalactic Hydrogen absorption would be required, and I am not sure whether such a correction would be sufficiently robust that a measurement of the SED turnover energy based on such a correction would be reliable. Capellupo et al. (2016) obtain reasonable thin-disk model fits to combined *X-Shooter* and rest-frame extreme-UV *GALEX* data only for around half of their sample, although they argue that variability between the *X-Shooter* and *GALEX* observations is likely the main reason why the modeling fails. I also note that the inclination angles and mass accretion rates for the thin-disk models are highly degenerate for the four sources presented in Figure 6.2.

More interestingly, for quasars in our sample with black hole masses $\log(M_{\rm BH}/M_\odot) \gtrsim 9.75$, our thin-disk models *require* near-maximal black hole spin in order to reproduce the observed lack of UV–optical turnover. For these extreme black hole spins, I find that thin-disk models with a large inclination angle i provide a better approximation of the UV spectral shape (Figure 6.3). Taken at face value, these results would imply that the high-mass quasars in our sample must have near-maximal black hole spins. However, I find this result unconvincing given the currently available data, for a few reasons. Most importantly, my modeling results depend critically on the assumption that our estimated black hole masses are correct. The single-epoch black hole mass estimates I use here are based on the C IV emission line, and have a 1σ statistical uncertainty of approximately 0.56 dex (Vestergaard and Peterson, 2006). As a preliminary test of how severely the black hole mass uncertainty affects the best-fit spin parameter, I re-fit the thin disk model for the quasar Q0040-017, which has black hole mass $M_{\rm BH} = 7.3 \times 10^9 M_\odot$ according to our single-epoch mass estimates, and which requires near-maximal spin for this value of $M_{\rm BH}$. In this fit, I set the black hole mass to $M_{\rm BH} = 2.0 \times 10^9 M_\odot$, as is appropriate if we overestimate the true black hole mass at the 1σ level. In that case, the spin parameter ranges between $a_* = 0.88$ for $i = 5°$, and $a_* = 0.6$ for $i = 70°$. This test demonstrates that even our high-mass black holes do not *require* near-maximal spin, given the uncertainties on their masses. To determine in a statistical sense whether our non-detections of the SED turnover actually require near-maximally spinning black holes for some objects would require e.g. Monte Carlo modeling of the underlying mass distribution. Alternatively, Capellupo et al. (2016) present a Bayesian statistical approach to thin-disk modeling, using a grid of model
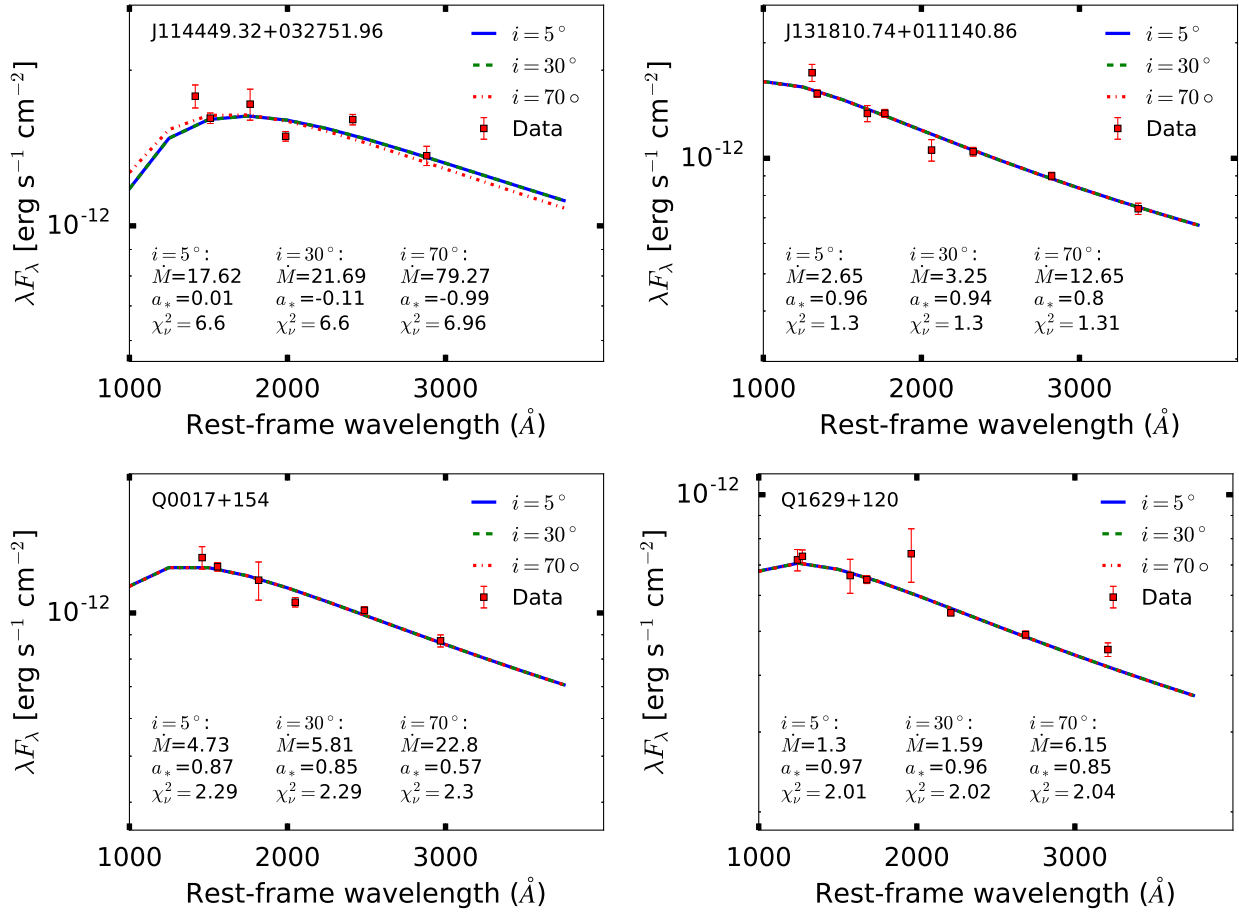
Fig. 6.2 Examples of thin-disk model fits to quasars for which we do not see clear evidence of an SED turnover. I show the emission line-corrected *Swift* UVOT and Swift flux densities *(red squares)* along with the best-fitting thin-disk models for three different inclination angles, *i*. The accretion rate $\dot{M}$ and the spin parameter a_* for the best-fitting models are listed for each quasar, along with the reduced χ^2 of the model fit. The overall shape of our observed SEDs (i.e., a power-law in λF_λ) is in some cases roughly *consistent* with the thin-disk models, but do not strongly constrain their parameters. All four quasars shown here have rather high black hole masses, $\log(M_{\mathrm{BH}}/M_\odot) \approx 9.5$. For J11444932+03275196, for which our observed SED is almost flat, the best-fit model displays a spectral turnover at ~ 1500 Å, which is consistent with a slowly spinning black hole with a high mass accretion rate. However, the photometric data do not provide strong evidence that this turnover is real. For J13181074+01114086, the best-fit thin-disk models have spectral turnovers in the unobserved far-UV. For a black hole mass of $\log(M_{\mathrm{BH}}/M_\odot) \approx 9.45$, this requires a rather high black hole spin, irrespective of inclination angle. For Q0017+154 and Q1629+020, the best-fit models again display a flattening of the spectrum at high energies, yet the observed photometry does not strongly constrain such a turnover. In general, these types of SEDs require far-UV observations to constrain the SED turnover, and/or long-wavelength observations to constrain the accretion rate, in order to robustly test the thin-disk models.
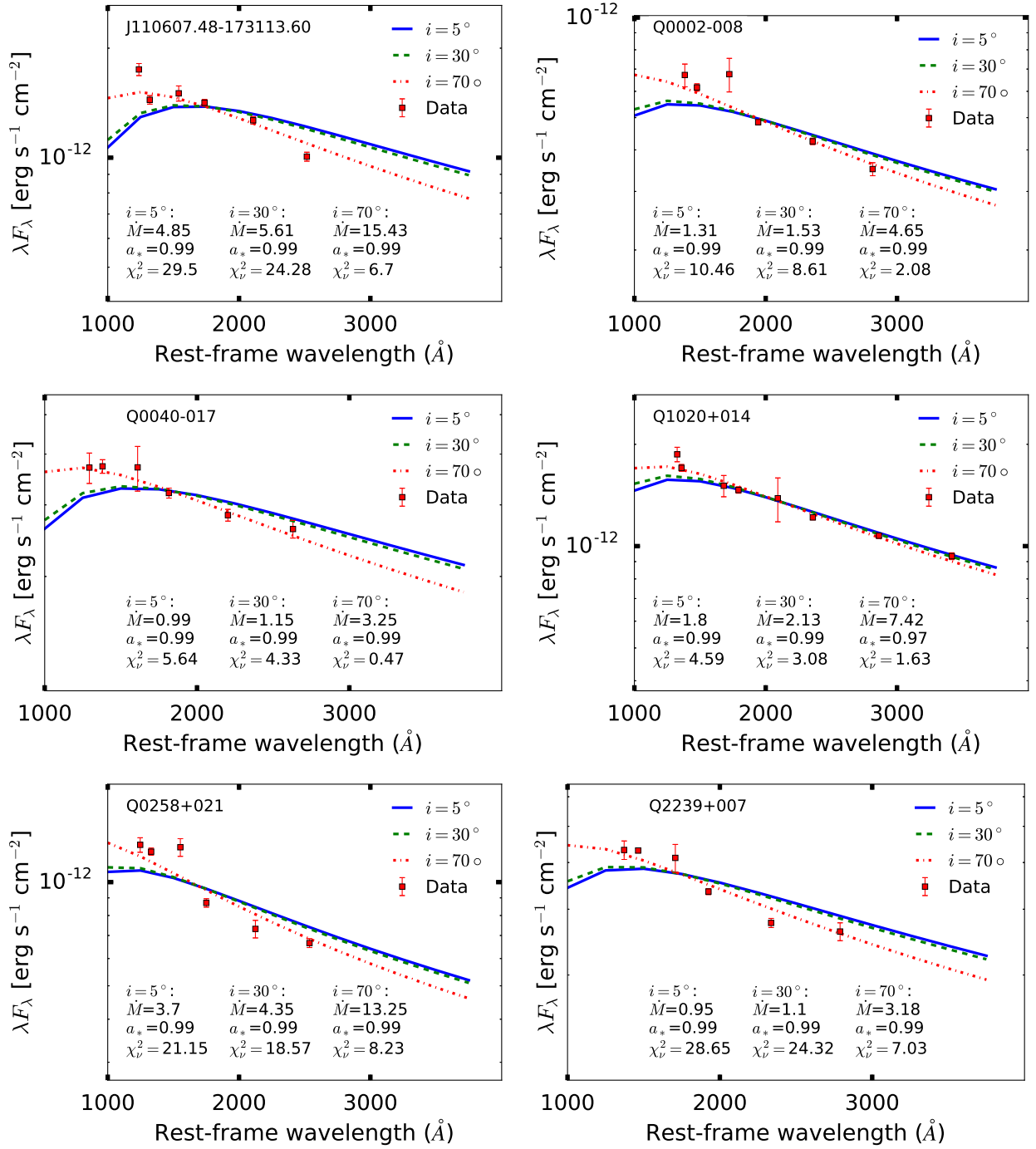
Fig. 6.3 Examples of high-mass quasars for which we observe no spectral turnover in the UV, and for which the thin-disk model requires a very large inclination angle to approximately reproduce the SED shape. Similar to figure 6.2, we observe no SED turnover for these spectra. However, due to their large black hole masses ($9.75 \lesssim \log(M_{\mathrm{BH}}/M_\odot) \lesssim 10.23$), these quasars additionally require a large inclination angle i in order to explain the lack of a spectral turnover in the context of thin-disk models. All of these high-mass sources require near-maximal black hole spins for thin-disk models, in order to explain the lack of a spectral turnover.
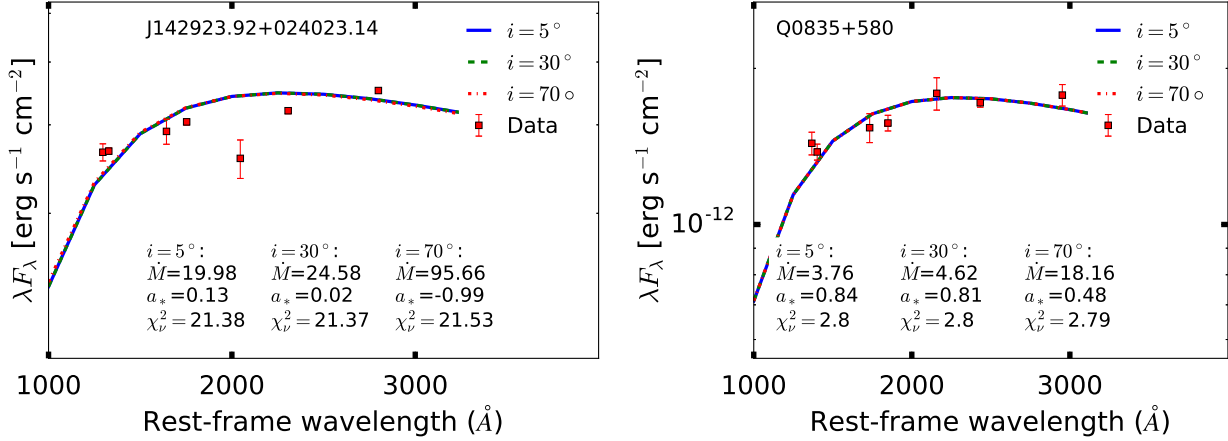
Fig. 6.4 Here, we display the SEDs of the two quasars in our sample for which we see clear evidence of a spectral turnover. For J14292392+02402314, the thin-disk models describe the observed spectral shape very poorly, irrespective of inclination angle. I obtain a better fit for Q0835+580; however, due to its very high black hole mass ($\log(M_{\mathrm{BH}}/M_\odot) \approx 9.94$), our modeling allows for intermediate spin values for this source.

parameters including the black hole mass, and adopting the single-epoch mass estimate and its statistical uncertainty as a prior probability distribution for M_{BH}. As it also seems clear (based on the preliminary results presented here) that we require observations covering a longer range of rest-frame wavelengths in order to adequately constrain the disk model parameters, I defer a comprehensive statistical treatment of the M_{BH} uncertainties to future work.

Secondly, it seems unrealistic that *all* high-mass quasars demand large inclination angles (i.e., that the model fits are better for the $i = 70°$ models for the high-mass quasars in Figure 6.3). It seems more likely to me that these high inclinations are an artifact of our lack of constraints on the SED turnover. If the black hole masses for our sample are roughly correct, I suspect that the high inferred inclination angles are indicative of a problem with the simple thin-disk models themselves. Laor and Davis (2014) present a model in which the spectral turnovers in AGN spectra do not depend strongly on black hole mass or spin, but instead is governed by line-driven winds from the accretion disk surface. For this model, the SED turnover occurs at wavelengths of ~ 1000 Å irrespective of black hole mass. Thin-disk models fitted to such an SED would require rapidly spinning black holes for high-mass sources, irrespective of the true black hole spin.

I finally emphasize that the thin-disk models depend on four parameters. Namely, the black hole mass M_{BH}, the accretion rate $\dot{M}$, the black hole spin parameter, and the disk inclination i. Given that we constrain the black hole masses independently using our single-epoch mass estimates, the model fits have three unconstrained parameters, for only 5–7 data points per quasar (i.e., the available *Swift* UVOT and SDSS photometric measurements). In order to robustly test whether the continuum SEDs correspond to the model spectra, we would require more observational data. In particular, longer-wavelength data that capture the power-law tail of the accretion disk emission would provide better constraints on the mass accretion rate. I therefore suggest that, e.g., VLT *X-Shooter* spectroscopic observations of our sample are required in order to robustly test the thin-disk models and derive accretion disk parameters for these quasars. *X-Shooter* spectra will also allow us

to isolate the continuum emission on a per-object basis, instead of the statistical correction I apply, which is based on composite quasar templates. Happily, we have already obtained *X-Shooter* data for a few of these quasars, which will allow us to more robustly model the accretion disk emission and test the thin-disk models in future work.

Two quasars with observed SED turnovers: I see clear evidence for an SED turnover for only two quasars in our sample, namely, J142923.92+024023.14 and Q0835+580 (Figure 6.4). For J14292392+02402314, the thin-disk models describe the observed spectral shape poorly. The photometric data appear inconsistent with a spectral turnover at ~ 2000 Å as required by the best-fitting thin-disk model. The unusual SED shape for this quasar may be due to substantial reddening and absorption, either intrinsic to the AGN central engine, and/or in its host galaxy. Of our sample quasars, Q0835+580 is the only mildly convincing example of a thin-disk like spectral turnover in the near-UV. Even in this case, the photometric data do not strongly constrain the turnover energy: the observed SED is fairly flat at wavelengths ~ 2000 Å –3000 Å. While this quasar would be an interesting source to follow up on, longer-wavelength observations are required in order to verify that the turnover suggested by the thin-disk model is real.

6.3.5 Summary of the thin-disk analysis

In summary, while the observed UV–optical SEDs are broadly consistent with thin-disk models with (in most cases) substantial black hole spins, due to the fact that the observed SEDs approximately follow power-laws, the spin and accretion rate parameters are poorly constrained given the available data. The blue SEDs for the majority of high-mass quasars in our sample would indicate near-maximal black hole spins, if the inferred M_{BH} are roughly correct. However, a more thorough analysis is required in order to determine whether the high spin values instead are due to overestimated black hole masses. More generally, I find that the rest-frame wavelength coverage of our *Swift* UVOT and SDSS photometry is too narrow to obtain tight constraints on the thin-disk model parameters. Rest-frame near-infrared observations with, e.g., *X-Shooter* will provide much better constraints on the thin-disk models for these quasars. *X-Shooter* observations have the additional advantage that they allow isolation of the AGN continuum component on a per-object basis.

Chapter 7

Conclusion and Future Prospects

During my PhD, I have worked on four separate projects, all of which involve the enigmatic central engines of AGN. Here, I offer a few concluding remarks regarding the implications of my results, and ideas on how to pursue these issues in future work.

The diffuse continuum contribution to inter-band continuum delays: In Chapter 2, I demonstrate that the tension between AGN accretion disk sizes derived from inter-band continuum reverberation mapping and those predicted by standard thin-disk theoretical models is at least partially due to the diffuse continuum emission produced in the BLR. This emission is ultimately powered by the central ionizing continuum source, but it responds to continuum variations on significantly longer timescales than the accretion disk itself does. At the same time, it contributes significantly to the UV–optical continuum luminosity. This causes the reverberation signal of the accretion disk to be 'diluted' by the diffuse continuum reverberation, such that the *observed* continuum delays are longer than the underlying disk delays. According to my pressure-law BLR models, the entire UV–optical continuum suffers this 'dilution' effect.

The first comprehensive *Swift* monitoring campaigns recognized that the anomalously long time delay in the U band was likely due to the Balmer continuum response, and excluded the U-band data from their lamp-post model fits (e.g., Edelson et al., 2015). However, the inferred disk sizes are still larger than theoretical predictions by a factor $\sim$ 2–3. In their spectroscopic inter-band continuum reverberation mapping observations, Cackett et al. (2018) find 'smoking-gun' evidence of additional time delays induced by the Balmer continuum. Korista and Goad (2019) extend the work presented in Chapter 2 to include the 'locally optimally-emitting cloud' BLR model Baldwin et al. (1995); they also find a substantial diffuse continuum contribution to the total continuum luminosity at all UV–optical wavelengths. It is now commonly accepted that the diffuse continuum emission is an significant contaminant at all UV–optical wavelengths, and that this effect may account for much of the observed disk size discrepancy (e.g., Cackett et al., 2020; Edelson et al., 2019; Hernández Santisteban et al., 2020). In particular, Hernández Santisteban et al. (2020) find that they are able to correct for the relatively weak diffuse continuum emission in the Seyfert 1 source Fairall 9, and obtain time delays that are consistent with thin-disk predictions. As also suggested by Edelson et al. (2019), it would be useful to study the diffuse continuum emission at near-infrared wavelengths, in order to determine whether it will strongly influence disk reverberation mapping in the outer

accretion disk. It may also be necessary to extend the diffuse continuum modeling to other BLR density distributions than pressure-laws (e.g., Lawther et al., 2018b) and LOC models (Korista and Goad, 2019), and to other BLR geometries than the simple spherically-symmetric case. In fact, the latter issue may be less important: Korista and Goad (2019) find that the diffuse continuum emission and delay spectra are similar for spherical and 'bowl-like' geometries. As several 2-dimensional reverberation mapping studies find that AGN broad line region kinematics are consistent with rotation in a thick disk (§1.1.4), a 'bowl-like' geometry is likely a reasonable assumption.

Mrk 590 and changing-look AGN: In Chapter 3, I demonstrate that the changing-look AGN Mrk 590 has displayed a typical UV to X-ray spectral shape since its re-ignition in 2017. In contrast, Mrk 590 was very faint in the UV–optical in 2013. (Denney et al., 2014) find that the optical spectrum in 2013 is consistent with only host galaxy emission, while the UV emission lines displayed only a very faint broad component. My estimates of the integrated optical–UV–X-ray accretion luminosity suggest that, between 2014 and 2017, the Eddington luminosity ratio increased from $L/L_{\mathrm{Edd}} \sim 0.003$ to $L/L_{\mathrm{Edd}} \sim 0.03$ as the UV emission component reappeared. Accretion state transitions between advection-dominated (ADAF) disks and standard thin accretion disks are predicted to occur at $L/L_{\mathrm{Edd}} \sim 0.01$. Given our *Swift* UVOT and XRT observations, along with any available supplementary observations in the low-flux and high-flux states, I wonder whether it would be possible to determine whether such an accretion state change actually occurred.

An important step towards understanding the re-ignition of Mrk 590 is to develop an improved model for the host galaxy emission, particularly in the UV regime. In Chapter 3, I model the host galaxy emission in a rather crude fashion, by assuming that the 2013 *Swift* UVOT observations are entirely due to host galaxy emission. While this treatment is sufficient in order to measure large changes in the Eddington luminosity ratio, it is unlikely to be entirely correct. In particular, given that there appears to be some residual UV broad emission lines in 2013, I likely underestimate the luminosity of the AGN component in the UV. A better model for the host galaxy UV emission would help constrain whether the AGN emission in 2013-2014 is consistent with the faint UV emission from an ADAF disk.

Our monitoring of Mrk 590 is on-going. At the time of writing, we still observe intermittent flaring activity in the X-rays and UV, and it is always exciting to examine the latest observations and try to guess whether it is flaring up again! Given that we have now documented its extreme variability behavior for several years, it would be appropriate to quantify the timescales on which the flare-ups occur, and compare with theoretical models. In particular, Jiang and Blaes (2020) present magneto-hydrodynamical simulations of extreme AGN variability that is driven by Iron absorption fronts. Qualitatively, the evolution of the Eddington luminosity ratio for their model bears some resemblance to our Eddington luminosity 'light-curve', with significant flare-ups on timescales of ∼years. It would be interesting to investigate whether this similarity holds up to detailed scrutiny.

More generally, the extreme variability of changing-look AGN challenges our understanding of AGN accretion. Lawrence (2018) refers to this issue as the 'quasar viscosity crisis': while reprocessing of X-ray emission may explain the UV–optical continuum variability of 'ordinary' AGN, it does not explain how the UV–optical continuum can entirely disappear (or reappear) on

such short timescales. It is interesting that the X-ray and UV components display such coherent large-scale variations. Might it be possible, as suggested by Lawrence (2018), that the UV–optical emission is entirely due to reprocessing of X-ray (or extreme-UV) emission? In fact, Mahmoud and Done (2020) find that the UV-optical emission and X-ray to UV time delays for NGC 4151 in a low-flux state can be fully explained by reprocessing of X-ray emission in broad line region clouds (i.e., diffuse BLR continuum emission). In their model, no standard thermal accretion disk is necessary in order to reproduce the observed UV–optical continuum. While it is difficult to see how this scenario would explain the broader population of AGN, for which it is well-established that the broad emission lines lag the UV continuum, Mahmoud and Done (2020) argue that it is possible that this effect may be produced by anisotropic BLR cloud emission. In any case, it is certainly notable that the changing-look AGN phenomenon might point towards such unorthodox accretion disk models. With new changing-look sources being discovered at increasing rates, it will be interesting to see which developments in accretion disk theory they inspire.

The evolutionary scenario for FeLoBAL quasars: In Chapter 4 I study the host galaxies of four Iron Low-ionization Broad Absorption Line quasars (FeLoBALs). Our rest-frame UV and rest-frame optical imaging is consistent with either unobscured, moderately star-forming host galaxies, similar to those found for non-BAL quasars, or with obscured galaxies with intense star formation. The latter possibility is expected if FeLoBALs are young, merger-triggered quasars (§1.1.6). Thus, our *Hubble Space Telescope* study does not exclude the young-quasar interpretation. One way to settle this issue is to obtain Atacama Large Millimeter Array observations of the FeLoBALs. If the observed (sub)-millimeter spectral energy distribution is consistent with only hot dust ionized by the AGN, it would confirm the lack of intense star formation in the FeLoBAL hosts. On the other hand, copious extended emission from cooler dust would reveal that the FeLoBALs have on-going, obscured starburst activity. Violino et al. (2016) present a study of FeLoBAL infrared SEDs using the SCUBA-2 telescope; while they do not detect starburst emission, their upper limits on the starburst component for the overlapping-trough FeLoBALs studied in Chapter 4 still allow for significant starburst activity. The higher sensitivity and spatial resolution offered by ALMA would place much stronger constraints on any starburst activity. In particular, the relative timescales of the onset of FeLoBAL activity and star formation in the evolutionary scenario are unknown. It may be that the starburst component is quite faint at the time when the quasar activity transitions from an entirely obscured to a FeLoBAL state. To test this latter scenario, it would be useful to obtain ALMA observations for a large number of FeLoBALs and quantify their potentially faint starburst components, similar to the study performed by Violino et al. (2016), but with a greater sensitivity to star formation activity.

Our $z \sim 2$ quasar sample: In Chapter 6 I characterize the UV to X-ray SEDs for a sample of quasars at redshifts $1.5 < z < 3.6$. I find that the majority of the quasars in this sample at $z \sim 2$ are representative of the broader population of luminous quasars, while the $z \sim 3$ quasars in our sample are extremely bright relative to typical $z \sim 3$ quasars in the SDSS. Before submission of this work, I would like to perform a more thorough comparison of the UV luminosities of our sample quasars

with the SDSS quasars at a given redshift. This will allow us to define subsamples with more typical and with extreme UV luminosities, for use in our on-going study of this quasar sample.

I also found that the radio-loud and radio-quiet quasars in this sample have similar rest-frame UV SEDs, while confirming that the radio-loud sources are brighter in the X-rays. The similarity of their UV continuum shapes is interesting in the context of the AGN radio loudness dichotomy. Radio-loud quasars are expected to have rapidly spinning black holes (e.g., Blandford and Payne, 1982; Maraschi et al., 2012). However, it is unclear whether high black hole spins are a sufficient or merely a necessary condition for radio loudness. As the radio-loud and radio-quiet sources in our sample have similar black hole mass distributions and UV spectral energy distributions, they are well-suited for comparisons of the accretion disk properties of radio-loud and radio-quiet quasars. In my exploratory thin-disk modeling for these quasars (§6.3, I find that the overall SED shapes for many of our quasars require near-maximally spinning black holes if they are produced by thin accretion disks. Unfortunately, given the currently available data, the disk models are not well-constrained. The VLT *X-Shooter* observations that we have obtained for a subset of these quasars will allow (among other things) more robust accretion disk modeling for these quasars, which will hopefully shed some light on the issue of radio-loud versus radio-quiet black hole spins.

Chapter 8

Signed Statements of Authorship

I include signed statements of authorship for each of the five published or draft journal papers included in this Thesis.

References

Abbott, B. P., Abbott, R., Abbott, T. D., Abernathy, M. R., Acernese, F., Ackley, K., Adams, C., Adams, T., Addesso, P., Adhikari, R. X., Adya, V. B., Affeldt, C., Agathos, M., Agatsuma, K., Aggarwal, N., Aguiar, O. D., Aiello, L., Ain, A., Ajith, P., Allen, B., Allocca, A., Altin, P. A., Anderson, S. B., Anderson, W. G., Arai, K., Arain, M. A., Araya, M. C., Arceneaux, C. C., Areeda, J. S., Arnaud, N., Arun, K. G., Ascenzi, S., Ashton, G., Ast, M., Aston, S. M., and et al. (2016). Observation of gravitational waves from a binary black hole merger. *Phys. Rev. Lett.*, 116:061102.

Abramowicz, M. A., Czerny, B., Lasota, J. P., and Szuszkiewicz, E. (1988). Slim Accretion Disks. *ApJ*, 332:646.

Abramowicz, M. A., Lanza, A., and Percival, M. J. (1997). Accretion Disks around Kerr Black Holes: Vertical Equilibrium Revisited. *ApJ*, 479(1):179–183.

Agol, E. and Krolik, J. H. (2000). Magnetic Stress at the Marginally Stable Orbit: Altered Disk Structure, Radiation, and Black Hole Spin Evolution. *ApJ*, 528(1):161–170.

Allen, J. T., Hewett, P. C., Maddox, N., Richards, G. T., and Belokurov, V. (2011). A strong redshift dependence of the broad absorption line quasar fraction. *MNRAS*, 410(2):860–884.

Alonso-Herrero, A., Pereira-Santaella, M., García-Burillo, S., Davies, R. I., Combes, F., Asmus, D., Bunker, A., Díaz-Santos, T., Gand hi, P., González-Martín, O., Hernán-Caballero, A., Hicks, E., Hönig, S., Labiano, A., Levenson, N. A., Packham, C., Ramos Almeida, C., Ricci, C., Rigopoulou, D., Rosario, D., Sani, E., and Ward, M. J. (2018). Resolving the Nuclear Obscuring Disk in the Compton-thick Seyfert Galaxy NGC 5643 with ALMA. *ApJ*, 859(2):144.

Angioni, R., Ros, E., Kadler, M., Ojha, R., Müller, C., Edwards, P. G., Burd, P. R., Carpenter, B., Dutka, M. S., Gulyaev, S., Hase, H., Horiuchi, S., Krauß, F., Lovell, J. E. J., Natusch, T., Phillips, C., Plötz, C., Quick, J. F. H., Rösch, F., Schulz, R., Stevens, J., Tzioumis, A. K., Weston, S., Wilms, J., and Zensus, J. A. (2019). Gamma-ray emission in radio galaxies under the VLBI scope. I. Parsec-scale jet kinematics and high-energy properties of γ-ray-detected TANAMI radio galaxies. *A&A*, 627:A148.

Antonucci, R. (1993). Unified models for active galactic nuclei and quasars. *ARA&A*, 31:473–521.

Antonucci, R. (2012). A panchromatic review of thermal and nonthermal active galactic nuclei. *Astronomical and Astrophysical Transactions*, 27:557–602.

Antonucci, R. R. J. and Miller, J. S. (1985). Spectropolarimetry and the nature of NGC 1068. *ApJ*, 297:621–632.

Ardaneh, K., Luo, Y., Shlosman, I., Nagamine, K., Wise, J. H., and Begelman, M. C. (2018). Direct collapse to supermassive black hole seeds with radiation transfer: cosmological haloes. *MNRAS*, 479(2):2277–2293.

Bañados, E., Venemans, B. P., Decarli, R., Farina, E. P., Mazzucchelli, C., Walter, F., Fan, X., Stern, D., Schlafly, E., Chambers, K. C., Rix, H. W., Jiang, L., McGreer, I., Simcoe, R., Wang, F., Yang,

J., Morganson, E., De Rosa, G., Greiner, J., Baloković, M., Burgett, W. S., Cooper, T., Draper, P. W., Flewelling, H., Hodapp, K. W., Jun, H. D., Kaiser, N., Kudritzki, R. P., Magnier, E. A., Metcalfe, N., Miller, D., Schindler, J. T., Tonry, J. L., Wainscoat, R. J., Waters, C., and Yang, Q. (2016). The Pan-STARRS1 Distant z > 5.6 Quasar Survey: More than 100 Quasars within the First Gyr of the Universe. *ApJS*, 227(1):11.

Bañados, E., Venemans, B. P., Mazzucchelli, C., Farina, E. P., Walter, F., Wang, F., Decarli, R., Stern, D., Fan, X., Davies, F. B., Hennawi, J. F., Simcoe, R. A., Turner, M. L., Rix, H.-W., Yang, J., Kelson, D. D., Rudie, G. C., and Winters, J. M. (2018). An 800-million-solar-mass black hole in a significantly neutral Universe at a redshift of 7.5. *Nature*, 553(7689):473–476.

Balbus, S. A. and Hawley, J. F. (1991). A powerful local shear instability in weakly magnetized disks. I - Linear analysis. II - Nonlinear evolution. *ApJ*, 376:214–233.

Baldassare, V. F., Dickey, C., Geha, M., and Reines, A. E. (2020). Populating the Low-mass End of the $M_{BH} - \sigma$ Relation. *ApJ*, 898(1):L3.

Baldassare, V. F., Reines, A. E., Gallo, E., and Greene, J. E. (2015). A 50000 Solar Mass Black Hole in the Nucleus of RGG 118. *ApJ*, 809(1):L14.

Baldwin, J., Ferland, G., Korista, K., and Verner, D. (1995). Locally Optimally Emitting Clouds and the Origin of Quasar Emission Lines. *ApJ*, 455:L119.

Barai, P., Viel, M., Murante, G., Gaspari, M., and Borgani, S. (2014). Kinetic or thermal AGN feedback in simulations of isolated and merging disc galaxies calibrated by the M-σ relation. *MNRAS*, 437(2):1456–1475.

Bardeen, J. M., Press, W. H., and Teukolsky, S. A. (1972). Rotating Black Holes: Locally Nonrotating Frames, Energy Extraction, and Scalar Synchrotron Radiation. *ApJ*, 178:347–370.

Barnes, J. E. and Hernquist, L. E. (1991). Fueling starburst galaxies with gas-rich mergers. *ApJ*, 370:L65–L68.

Barr, P. (1986). EXOSAT observations of the Seyfert galaxy NGC 7469; rapid hard X-rayvariability and a soft X-ray excess. *MNRAS*, 223:29P–35.

Barthel, P. D. (1989). Is every quasar beamed? *ApJ*, 336:606–611.

Barvainis, R. (1987). Hot dust and the near-infrared bump in the continuum spectra of quasars and active galactic nuclei. *ApJ*, 320:537–544.

Baskin, A. and Laor, A. (2018). Dust inflated accretion disc as the origin of the broad line region in active galactic nuclei. *MNRAS*, 474(2):1970–1994.

Becker, R. H., Fan, X., White, R. L., Strauss, M. A., Narayanan, V. K., Lupton, R. H., Gunn, J. E., Annis, J., Bahcall, N. A., Brinkmann, J., Connolly, A. J., Csabai, I., Czarapata, P. C., Doi, M., Heckman, T. M., Hennessy, G. S., Ivezić, Ž., Knapp, G. R., Lamb, D. Q., McKay, T. A., Munn, J. A., Nash, T., Nichol, R., Pier, J. R., Richards, G. T., Schneider, D. P., Stoughton, C., Szalay, A. S., Thakar, A. R., and York, D. G. (2001). Evidence for Reionization at z~6: Detection of a Gunn-Peterson Trough in a z=6.28 Quasar. *AJ*, 122:2850–2857.

Begelman, M. C. and Nath, B. B. (2005). Self-regulated black hole accretion, the M-σ relation and the growth of bulges in galaxies. *MNRAS*, 361(4):1387–1392.

Bentz, M. C., Denney, K. D., Grier, C. J., Barth, A. J., Peterson, B. M., Vestergaard, M., Bennert, V. N., Canalizo, G., De Rosa, G., Filippenko, A. V., Gates, E. L., Greene, J. E., Li, W., Malkan, M. A., Pogge, R. W., Stern, D., Treu, T., and Woo, J.-H. (2013). The Low-luminosity End of the Radius-Luminosity Relationship for Active Galactic Nuclei. *ApJ*, 767:149.

Bentz, M. C., Walsh, J. L., Barth, A. J., Yoshii, Y., Woo, J.-H., Wang, X., Treu, T., Thornton, C. E., Street, R. A., Steele, T. N., Silverman, J. M., Serduke, F. J. D., Sakata, Y., Minezaki, T., Malkan, M. A., Li, W., Lee, N., Hiner, K. D., Hidas, M. G., Greene, J. E., Gates, E. L., Ganeshalingam, M., Filippenko, A. V., Canalizo, G., Bennert, V. N., and Baliber, N. (2010a). The Lick AGN Monitoring Project: Reverberation Mapping of Optical Hydrogen and Helium Recombination Lines. *ApJ*, 716:993–1011.

Bentz, M. C., Walsh, J. L., Barth, A. J., Yoshii, Y., Woo, J.-H., Wang, X., Treu, T., Thornton, C. E., Street, R. A., Steele, T. N., Silverman, J. M., Serduke, F. J. D., Sakata, Y., Minezaki, T., Malkan, M. A., Li, W., Lee, N., Hiner, K. D., Hidas, M. G., Greene, J. E., Gates, E. L., Ganeshalingam, M., Filippenko, A. V., Canalizo, G., Bennert, V. N., and Baliber, N. (2010b). The Lick AGN Monitoring Project: Reverberation Mapping of Optical Hydrogen and Helium Recombination Lines. *ApJ*, 716(2):993–1011.

Berg, T. A. M., Ellison, S. L., Sánchez-Ramírez, R., Prochaska, J. X., Lopez, S., D'Odorico, V., Becker, G., Christensen, L., Cupani, G., Denney, K., and Worseck, G. (2016). Chemical abundances of the damped Lyman α systems in the XQ-100 survey. *MNRAS*, 463(3):3021–3037.

Blandford, R. D. and Payne, D. G. (1982). Hydromagnetic flows from accretion disks and the production of radio jets. *MNRAS*, 199:883–903.

Blandford, R. D. and Znajek, R. L. (1977). Electromagnetic extraction of energy from Kerr black holes. *MNRAS*, 179:433–456.

Boehle, A., Ghez, A. M., Schödel, R., Meyer, L., Yelda, S., Albers, S., Martinez, G. D., Becklin, E. E., Do, T., Lu, J. R., Matthews, K., Morris, M. R., Sitarski, B., and Witzel, G. (2016). An Improved Distance and Mass Estimate for Sgr A* from a Multistar Orbit Analysis. *ApJ*, 830:17.

Bondi, H. (1952). On spherically symmetrical accretion. *MNRAS*, 112:195.

Brenneman, L. W., Madejski, G., Fuerst, F., Matt, G., Elvis, M., Harrison, F. A., Ballantyne, D. R., Boggs, S. E., Christensen, F. E., Craig, W. W., Fabian, A. C., Grefenstette, B. W., Hailey, C. J., Madsen, K. K., Marinucci, A., Rivers, E., Stern, D., Walton, D. J., and Zhang, W. W. (2014). The Broad-band X-Ray Spectrum of IC 4329A from a Joint NuSTAR/Suzaku Observation. *ApJ*, 788:61.

Brenneman, L. W. and Reynolds, C. S. (2006). Constraining Black Hole Spin via X-Ray Spectroscopy. *ApJ*, 652(2):1028–1043.

Brenneman, L. W., Reynolds, C. S., Nowak, M. A., Reis, R. C., Trippe, M., Fabian, A. C., Iwasawa, K., Lee, J. C., Miller, J. M., Mushotzky, R. F., Nand ra, K., and Volonteri, M. (2011). The Spin of the Supermassive Black Hole in NGC 3783. *ApJ*, 736(2):103.

Bromm, V. and Loeb, A. (2003). Formation of the First Supermassive Black Holes. *ApJ*, 596(1):34–46.

Burtscher, L., Hönig, S., Jaffe, W., Kishimoto, M., Lopez-Gonzaga, N., Meisenheimer, K., and Tristam, K. R. W. (2016). Infrared interferometry and AGNs: Parsec-scale disks and dusty outflows. In *Proc. SPIE*, volume 9907 of *Society of Photo-Optical Instrumentation Engineers (SPIE) Conference Series*, page 99070R.

Cackett, E. M., Chiang, C.-Y., McHardy, I., Edelson, R., Goad, M. R., Horne, K., and Korista, K. T. (2018). Accretion Disk Reverberation with Hubble Space Telescope Observations of NGC 4593: Evidence for Diffuse Continuum Lags. *ApJ*, 857.

Cackett, E. M., Gelbord, J., Li, Y.-R., Horne, K., Wang, J.-M., Barth, A. J., Bai, J.-M., Bian, W.-H., Carroll, R. W., Du, P., Edelson, R., Goad, M. R., Ho, L. C., Hu, C., Khatu, V. C., Luo, B., Miller, J., and Yuan, Y.-F. (2020). Supermassive Black Holes with High Accretion Rates in Active Galactic Nuclei. XI. Accretion Disk Reverberation Mapping of Mrk 142. *ApJ*, 896(1):1.

Cackett, E. M., Gültekin, K., Bentz, M. C., Fausnaugh, M. M., Peterson, B. M., Troyer, J., and Vestergaard, M. (2015). Swift/UVOT Grism Monitoring of NGC 5548 in 2013: An Attempt at MgII Reverberation Mapping. *ApJ*, 810.

Cackett, E. M., Horne, K., and Winkler, H. (2007). Testing thermal reprocessing in active galactic nuclei accretion discs. *MNRAS*, 380:669–682.

Cai, H.-B., Shu, X.-W., Zheng, Z.-Y., and Wang, J.-X. (2010). The study of Seyfert 2 galaxies with and without infrared broad lines. *Research in Astronomy and Astrophysics*, 10(5):427–437.

Cao, X. (2016). On the Radio Dichotomy of Active Galactic Nuclei. *ApJ*, 833(1):30.

Capellupo, D. M., Netzer, H., Lira, P., Trakhtenbrot, B., and Mejía-Restrepo, J. (2015). Active galactic nuclei at z ̃1.5 - I. Spectral energy distribution and accretion discs. *MNRAS*, 446:3427–3446.

Capellupo, D. M., Netzer, H., Lira, P., Trakhtenbrot, B., and Mejía-Restrepo, J. (2016). Active galactic nuclei at z ̃1.5 - III. Accretion discs and black hole spin. *MNRAS*, 460:212–226.

Chainakun, P., Watcharangkool, A., Young, A. J., and Hancock, S. (2019). X-ray time lags in AGN: inverse-Compton scattering and spherical corona model. *MNRAS*, 487(1):667–680.

Chartas, G., Rhea, C., Kochanek, C., Dai, X., Morgan, C., Blackburne, J., Chen, B., Mosquera, A., and MacLeod, C. (2016). Gravitational lensing size scales for quasars. *Astronomische Nachrichten*, 337(4-5):356.

Cheng, H., Yuan, W., Liu, H.-Y., Breeveld, A. A., Jin, C., and Liu, B. (2019). Modelling accretion disc emission with generalized temperature profile and its effect on AGN spectral energy distribution. *MNRAS*, 487(3):3884–3903.

Choudhuri, A. R. (1998). *The physics of fluids and plasmas : an introduction for astrophysicists /.*

Ciotti, L. and Ostriker, J. P. (2001). Cooling Flows and Quasars. II. Detailed Models of Feedback-modulated Accretion Flows. *ApJ*, 551(1):131–152.

Ciotti, L., Ostriker, J. P., and Proga, D. (2010). Feedback from Central Black Holes in Elliptical Galaxies. III. Models with Both Radiative and Mechanical Feedback. *ApJ*, 717(2):708–723.

Clavel, J., Reichert, G. A., Alloin, D., Crenshaw, D. M., Kriss, G., Krolik, J. H., Malkan, M. A., Netzer, H., Peterson, B. M., Wamsteker, W., Altamore, A., Baribaud, T., Barr, P., Beck, S., Binette, L., Bromage, G. E., Brosch, N., Diaz, A. I., Filippenko, A. V., Fricke, K., Gaskell, C. M., Giommi, P., Glass, I. S., Gondhalekar, P., Hackney, R. L., Halpern, J. P., Hutter, D. J., Joersaeter, S., Kinney, A. L., Kollatschny, W., Koratkar, A., Korista, K. T., Laor, A., Lasota, J. P., Leibowitz, E., Maoz, D., Martin, P. G., Mazeh, T., Meurs, E. J. A., Nair, A. D., O'Brien, P., Pelat, D., Perez, E., Perola, G. C., Ptak, R. L., Rodriguez-Pascual, P., Rosenblatt, E. I., Sadun, A. C., Santos-Lleo, M., Shaw, R. A., Smith, P. S., Stirpe, G. M., Stoner, R., Sun, W. H., Ulrich, M. H., van Groningen, E., and Zheng, W. (1991). Steps toward Determination of the Size and Structure of the Broad-Line Region in Active Galactic Nuclei. I. an 8 Month Campaign of Monitoring NGC 5548 with IUE. *ApJ*, 366:64.

Collin, S. and Kawaguchi, T. (2004). Super-Eddington accretion rates in Narrow Line Seyfert 1 galaxies. *A&A*, 426:797–808.

Crummy, J., Fabian, A. C., Gallo, L., and Ross, R. R. (2006). An explanation for the soft X-ray excess in active galactic nuclei. *MNRAS*, 365:1067–1081.

Czerny, B. and Elvis, M. (1987). Constraints on Quasar Accretion Disks from the Optical/Ultraviolet/Soft X-Ray Big Bump. *ApJ*, 321:305.

Czerny, B., Li, Y.-R., Hryniewicz, K., Panda, S., Wildy, C., Sniegowska, M., Wang, J. M., Sredzinska, J., and Karas, V. (2017). Failed Radiatively Accelerated Dusty Outflow Model of the Broad Line Region in Active Galactic Nuclei. I. Analytical Solution. *ApJ*, 846(2):154.

Dai, X., Kochanek, C. S., Chartas, G., Kozłowski, S., Morgan, C. W., Garmire, G., and Agol, E. (2010). The Sizes of the X-ray and Optical Emission Regions of RXJ 1131-1231. *ApJ*, 709(1):278–285.

Davis, S. W. and Laor, A. (2011). The Radiative Efficiency of Accretion Flows in Individual Active Galactic Nuclei. *ApJ*, 728:98.

Davis, S. W., Woo, J.-H., and Blaes, O. M. (2007). The UV Continuum of Quasars: Models and SDSS Spectral Slopes. *ApJ*, 668:682–698.

De Cicco, D., Brandt, W. N., Grier, C. J., Paolillo, M., Filiz Ak, N., Schneider, D. P., and Trump, J. R. (2018). C IV broad absorption line disappearance in a large SDSS QSO sample. *A&A*, 616:A114.

De Rosa, G., Fausnaugh, M. M., Grier, C. J., Peterson, B. M., Denney, K. D., Horne, K., Bentz, M. C., Ciroi, S., Dalla Bontà, E., Joner, M. D., Kaspi, S., Kochanek, C. S., Pogge, R. W., Sergeev, S. G., Vestergaard, M., Adams, S. M., Antognini, J., Araya Salvo, C., Armstrong, E., Bae, J., Barth, A. J., Beatty, T. G., Bhattacharjee, A., Borman, G. A., Boroson, T. A., Bottorff, M. C., Brown, J. E., Brown, J. S., Brotherton, M. S., Coker, C. T., Clanton, C., Cracco, V., Crawford, S. M., Croxall, K. V., Eftekharzadeh, S., Eracleous, M., Fiorenza, S. L., Frassati, A., Hawkins, K., Henderson, C. B., Holoien, T. W. S., Hutchison, T., Kellar, J., Kilerci-Eser, E., Kim, S., King, A. L., La Mura, G., Laney, C. D., Li, M., Lochhaas, C., Ma, Z., MacInnis, F., Manne-Nicholas, E. R., Mason, M., McGraw, S. M., Mogren, K., Montouri, C., Moody, J. W., Mosquera, A. M., Mudd, D., Musso, R., Nazarov, S. V., Nguyen, M. L., Ochner, P., Okhmat, D. N., Onken, C. A., Ou-Yang, B., Pancoast, A., Pei, L., Penny, M., Poleski, R., Portaluri, E., Prieto, J. L., Price-Whelan, A. M., Pulatova, N. G., Rafter, S., Roettenbacher, R. M., Romero-Colmenero, E., Runnoe, J., Schimoia, J. S., Shappee, B. J., Sherf, N., Simonian, G. V., Siviero, A., Skowron, D. M., Skowron, J., Somers, G., Spencer, M., Starkey, D. A., Stevens, D. J., Stoll, R., Tamajo, E., Tayar, J., van Saders, J. L., Valenti, S., Villanueva, S., J., Villforth, C., Weiss, Y., Winkler, H., Zastrow, J., Zhu, W., and Zu, Y. (2018). Velocity-resolved Reverberation Mapping of Five Bright Seyfert 1 Galaxies. *ApJ*, 866(2):133.

Dehghanian, M., Ferland, G. J., Kriss, G. A., Peterson, B. M., Korista, K. T., Goad, M. R., Chatzikos, M., Guzman, F., de Rosa, G., Mehdipour, M., Kaastra, J., Mathur, S., Vestergaard, M., Proga, D., Waters, T., Bentz, M. C., Bisogni, S., Brandt, W. N., Dalla Bont'a, E., Fausnaugh, M. M., Gelbord, J. M., Horne, K., McHardy, I. M., Pogge, R. W., and Starkey, D. A. (2020). Space Telescope and Optical Reverberation Mapping Project. XI. Disk-wind characteristics and contributions to the very broad emission lines of NGC 5548. *arXiv e-prints*, page arXiv:2006.06615.

Denney, K. D. (2012). Are Outflows Biasing Single-epoch C IV Black Hole Mass Estimates? *ApJ*, 759:44.

Denney, K. D., De Rosa, G., Croxall, K., Gupta, A., Bentz, M. C., Fausnaugh, M. M., Grier, C. J., Martini, P., Mathur, S., Peterson, B. M., Pogge, R. W., and Shappee, B. J. (2014). The Typecasting of Active Galactic Nuclei: Mrk 590 no Longer Fits the Role. *ApJ*, 796.

Denney, K. D., Peterson, B. M., Pogge, R. W., Adair, A., Atlee, D. W., Au-Yong, K., Bentz, M. C., Bird, J. C., Brokofsky, D. J., Chisholm, E., Comins, M. L., Dietrich, M., Doroshenko, V. T., Eastman, J. D., Efimov, Y. S., Ewald, S., Ferbey, S., Gaskell, C. M., Hedrick, C. H., Jackson, K., Klimanov, S. A., Klimek, E. S., Kruse, A. K., Ladéroute, A., Lamb, J. B., Leighly, K., Minezaki, T., Nazarov, S. V., Onken, C. A., Petersen, E. A., Peterson, P., Poindexter, S., Sakata, Y., Schlesinger, K. J., Sergeev, S. G., Skolski, N., Stieglitz, L., Tobin, J. J., Unterborn, C., Vestergaard, M., Watkins, A. E., Watson, L. C., and Yoshii, Y. (2009). Diverse Kinematic Signatures from Reverberation Mapping of the Broad-Line Region in AGNs. *ApJ*, 704(2):L80–L84.

Dexter, J. and Begelman, M. C. (2019). Extreme AGN variability: evidence of magnetically elevated accretion? *MNRAS*, 483(1):L17–L21.

Dietrich, M., Hamann, F., Shields, J. C., Constantin, A., Vestergaard, M., Chaffee, F., Foltz, C. B., and Junkkarinen, V. T. (2002). Continuum and Emission-Line Strength Relations for a Large Active Galactic Nuclei Sample. *ApJ*, 581(2):912–924.

Done, C., Davis, S. W., Jin, C., Blaes, O., and Ward, M. (2012). Intrinsic disc emission and the soft X-ray excess in active galactic nuclei. *MNRAS*, 420:1848–1860.

Dunlop, J. S., McLure, R. J., Kukula, M. J., Baum, S. A., O'Dea, C. P., and Hughes, D. H. (2003). Quasars, their host galaxies and their central black holes. *MNRAS*, 340(4):1095–1135.

eBOSS Collaboration, Alam, S., Aubert, M., Avila, S., Balland, C., Bautista, J. E., Bershady, M. A., Bizyaev, D., Blanton, M. R., Bolton, A. S., Bovy, J., Brinkmann, J., Brownstein, J. R., Burtin, E., Chabanier, S., Chapman, M. J., Choi, P. D., Chuang, C.-H., Comparat, J., Cuceu, A., Dawson, K. S., de la Macorra, A., de la Torre, S., de Mattia, A., de Sainte Agathe, V., du Mas des Bourboux, H., Escoffier, S., Etourneau, T., Farr, J., Font-Ribera, A., Frinchaboy, P. M., Fromenteau, S., Gil-Marín, H., Gonzalez-Morales, A. X., Gonzalez-Perez, V., Grabowski, K., Guy, J., Hawken, A. J., Hou, J., Kong, H., Klaene, M., Kneib, J.-P., Le Goff, J.-M., Lin, S., Long, D., Lyke, B. W., Cousinou, M.-C., Martini, P., Masters, K., Mohammad, F. G., Moon, J., Mueller, E.-M., Munõz-Gutieŕrez, A., Myers, A. D., Nadathur, S., Neveux, R., Newman, J. A., Noterdaeme, P., Oravetz, A., Oravetz, D., Palanque-Delabrouille, N., Pan, K., Parker, James, I., Paviot, R., Percival, W. J., Peŕez-Rafols, I., Petitjean, P., Pieri, M. M., Prakash, A., Raichoor, A., Ravoux, C., Rezaie, M., Rich, J., Ross, A. J., Rossi, G., Ruggeri, R., Ruhlmann-Kleider, V., Sańchez, A. G., Sańchez, F. J., Sańchez-Gallego, J. R., Sayres, C., Schneider, D. P., Seo, H.-J., Shafieloo, A., Slosar, A., Smith, A., Stermer, J., Tamone, A., Tinker, J. L., Tojeiro, R., Vargas-Magaña, M., Variu, A., Wang, Y., Weaver, B. A., Weijmans, A.-M., Yeche, C., Zarrouk, P., Zhao, C., Zhao, G.-B., and Zheng, Z. (2020). The Completed SDSS-IV extended Baryon Oscillation Spectroscopic Survey: Cosmological Implications from two Decades of Spectroscopic Surveys at the Apache Point observatory. *arXiv e-prints*, page arXiv:2007.08991.

Eddington, A. S. (1917). On the radiative equilibrium of the stars. *MNRAS*, 77:596–612.

Edelson, R., Gelbord, J., Cackett, E., Connolly, S., Done, C., Fausnaugh, M., Gardner, E., Gehrels, N., Goad, M., Horne, K., McHardy, I., Peterson, B. M., Vaughan, S., Vestergaard, M., Breeveld, A., Barth, A. J., Bentz, M., Bottorff, M., Brandt, W. N., Crawford, S. M., Dalla Bontà, E., Emmanoulopoulos, D., Evans, P., Figuera Jaimes, R., Filippenko, A. V., Ferland, G., Grupe, D., Joner, M., Kennea, J., Korista, K. T., Krimm, H. A., Kriss, G., Leonard, D. C., Mathur, S., Netzer, H., Nousek, J., Page, K., Romero-Colmenero, E., Siegel, M., Starkey, D. A., Treu, T., Vogler, H. A., Winkler, H., and Zheng, W. (2017). Swift Monitoring of NGC 4151: Evidence for a Second X-Ray/UV Reprocessing. *ApJ*, 840:41.

Edelson, R., Gelbord, J., Cackett, E., Peterson, B. M., Horne, K., Barth, A. J., Starkey, D. A., Bentz, M., Brandt, W. N., Goad, M., Joner, M., Korista, K., Netzer, H., Page, K., Uttley, P., Vaughan, S., Breeveld, A., Cenko, S. B., Done, C., Evans, P., Fausnaugh, M., Ferland, G., Gonzalez-Buitrago, D., Gropp, J., Grupe, D., Kaastra, J., Kennea, J., Kriss, G., Mathur, S., Mehdipour, M., Mudd, D., Nousek, J., Schmidt, T., Vestergaard, M., and Villforth, C. (2019). The First Swift Intensive AGN Accretion Disk Reverberation Mapping Survey. *ApJ*, 870(2):123.

Edelson, R., Gelbord, J. M., Horne, K., McHardy, I. M., Peterson, B. M., Arévalo, P., Breeveld, A. A., De Rosa, G., Evans, P. A., Goad, M. R., Kriss, G. A., Brandt, W. N., Gehrels, N., Grupe, D., Kennea, J. A., Kochanek, C. S., Nousek, J. A., Papadakis, I., Siegel, M., Starkey, D., Uttley, P., Vaughan, S., Young, S., Barth, A. J., Bentz, M. C., Brewer, B. J., Crenshaw, D. M., Dalla Bontà, E., De Lorenzo-Cáceres, A., Denney, K. D., Dietrich, M., Ely, J., Fausnaugh, M. M., Grier, C. J., Hall, P. B., Kaastra, J., Kelly, B. C., Korista, K. T., Lira, P., Mathur, S., Netzer, H., Pancoast, A., Pei, L., Pogge, R. W., Schimoia, J. S., Treu, T., Vestergaard, M., Villforth, C., Yan, H., and

Zu, Y. (2015). Space Telescope and Optical Reverberation Mapping Project. II. Swift and HST Reverberation Mapping of the Accretion Disk of NGC 5548. *ApJ*, 806.

Einstein, A. (1916). Die Grundlage der allgemeinen Relativitätstheorie. *Annalen der Physik*, 354(7):769–822.

Eisenstein, D. J., Zehavi, I., Hogg, D. W., Scoccimarro, R., Blanton, M. R., Nichol, R. C., Scranton, R., Seo, H.-J., Tegmark, M., Zheng, Z., Anderson, S. F., Annis, J., Bahcall, N., Brinkmann, J., Burles, S., Castand er, F. J., Connolly, A., Csabai, I., Doi, M., Fukugita, M., Frieman, J. A., Glazebrook, K., Gunn, J. E., Hendry, J. S., Hennessy, G., Ivezić, Z., Kent, S., Knapp, G. R., Lin, H., Loh, Y.-S., Lupton, R. H., Margon, B., McKay, T. A., Meiksin, A., Munn, J. A., Pope, A., Richmond, M. W., Schlegel, D., Schneider, D. P., Shimasaku, K., Stoughton, C., Strauss, M. A., SubbaRao, M., Szalay, A. S., Szapudi, I., Tucker, D. L., Yanny, B., and York, D. G. (2005). Detection of the Baryon Acoustic Peak in the Large-Scale Correlation Function of SDSS Luminous Red Galaxies. *ApJ*, 633(2):560–574.

Elitzur, M. (2012). On the Unification of Active Galactic Nuclei. *ApJ*, 747:L33.

Elitzur, M. and Netzer, H. (2016). Disc outflows and high-luminosity true type 2 AGN. *MNRAS*, 459:585–594.

Elvis, M. (2000). A Structure for Quasars. *ApJ*, 545:63–76.

Elvis, M. (2017). Quasar Rain: The Broad Emission Line Region as Condensations in the Warm Accretion Disk Wind. *ApJ*, 847(1):56.

Elvis, M., Wilkes, B. J., McDowell, J. C., Green, R. F., Bechtold, J., Willner, S. P., Oey, M. S., Polomski, E., and Cutri, R. (1994). Atlas of quasar energy distributions. *ApJS*, 95:1–68.

Event Horizon Telescope Collaboration (2019). First M87 Event Horizon Telescope Results. I. The Shadow of the Supermassive Black Hole. *ApJ*, 875(1):L1.

Fabian, A. C., Lohfink, A., Kara, E., Parker, M. L., Vasudevan, R., and Reynolds, C. S. (2015). Properties of AGN coronae in the NuSTAR era. *MNRAS*, 451:4375–4383.

Falcke, H., Wilson, A. S., and Simpson, C. (1998). Hubble Space Telescope and VLA Observations of Seyfert 2 Galaxies: The Relationship between Radio Ejecta and the Narrow-Line Region. *ApJ*, 502(1):199–217.

Fan, X., Wang, F., Yang, J., Keeton, C. R., Yue, M., Zabludoff, A., Bian, F., Bonaglia, M., Georgiev, I. Y., Hennawi, J. F., Li, J., McGreer, I. D., Naidu, R., Pacucci, F., Rabien, S., Thompson, D., Venemans, B., Walter, F., Wang, R., and Wu, X.-B. (2019). The Discovery of a Gravitationally Lensed Quasar at z = 6.51. *ApJ*, 870(2):L11.

Farrah, D., Lacy, M., Priddey, R., Borys, C., and Afonso, J. (2007). Evidence that FeLoBALs May Signify the Transition between an Ultraluminous Infrared Galaxy and a Quasar. *ApJ*, 662(2):L59–L62.

Farrah, D., Urrutia, T., Lacy, M., Efstathiou, A., Afonso, J., Coppin, K., Hall, P. B., Lonsdale, C., Jarrett, T., Bridge, C., Borys, C., and Petty, S. (2012). Direct Evidence for Termination of Obscured Star Formation by Radiatively Driven Outflows in Reddened QSOs. *ApJ*, 745:178.

Fausnaugh, M. M., Denney, K. D., Barth, A. J., Bentz, M. C., Bottorff, M. C., Carini, M. T., Croxall, K. V., De Rosa, G., Goad, M. R., Horne, K., Joner, M. D., Kaspi, S., Kim, M., Klimanov, S. A., Kochanek, C. S., Leonard, D. C., Netzer, H., Peterson, B. M., Schnülle, K., Sergeev, S. G., Vestergaard, M., Zheng, W.-K., Zu, Y., Anderson, M. D., Arévalo, P., Bazhaw, C., and et al. (2016). Space Telescope and Optical Reverberation Mapping Project. III. Optical Continuum Emission and Broadband Time Delays in NGC 5548. *ApJ*, 821:56.

Fausnaugh, M. M., Grier, C. J., Bentz, M. C., Denney, K. D., De Rosa, G., Peterson, B. M., Kochanek, C. S., Pogge, R. W., Adams, S. M., Barth, A. J., Beatty, T. G., Bhattacharjee, A., Borman, G. A., Boroson, T. A., Bottorff, M. C., Brown, J. E., Brown, J. S., Brotherton, M. S., Coker, C. T., Crawford, S. M., Croxall, K. V., Eftekharzadeh, S., Eracleous, M., Joner, M. D., Henderson, C. B., Holoien, T. W. S., Horne, K., Hutchison, T., Kaspi, S., Kim, S., King, A. L., Li, M., Lochhaas, C., Ma, Z., MacInnis, F., Manne-Nicholas, E. R., Mason, M., Montuori, C., Mosquera, A., Mudd, D., Musso, R., Nazarov, S. V., Nguyen, M. L., Okhmat, D. N., Onken, C. A., Ou-Yang, B., Pancoast, A., Pei, L., Penny, M. T., Poleski, R., Rafter, S., Romero-Colmenero, E., Runnoe, J., Sand, D. J., Schimoia, J. S., Sergeev, S. G., Shappee, B. J., Simonian, G. V., Somers, G., Spencer, M., Starkey, D. A., Stevens, D. J., Tayar, J., Treu, T., Valenti, S., Van Saders, J., Villanueva, S., J., Villforth, C., Weiss, Y., Winkler, H., and Zhu, W. (2017). Reverberation Mapping of Optical Emission Lines in Five Active Galaxies. *ApJ*, 840(2):97.

Fausnaugh, M. M., Starkey, D. A., Horne, K., Kochanek, C. S., Peterson, B. M., Bentz, M. C., Denney, K. D., Grier, C. J., Grupe, D., Pogge, R. W., De Rosa, G., Adams, S. M., Barth, A. J., Beatty, T. G., Bhattacharjee, A., Borman, G. A., Boroson, T. A., Bottorff, M. C., Brown, J. E., Brown, J. S., Brotherton, M. S., Coker, C. T., Crawford, S. M., Croxall, K. V., Eftekharzadeh, S., Eracleous, M., Joner, M. D., Henderson, C. B., Holoien, T. W. S., Hutchison, T., Kaspi, S., Kim, S., King, A. L., Li, M., Lochhaas, C., and Ma, Z. (2018). Continuum Reverberation Mapping of the Accretion Disks in Two Seyfert 1 Galaxies. *ApJ*, 854.

Feng, J., Cao, X., Gu, W.-M., and Ma, R.-Y. (2019). A Global Solution to a Slim Accretion Disk with Radiation-driven Outflows. *ApJ*, 885(1):93.

Ferland, G. J., Porter, R. L., van Hoof, P. A. M., Williams, R. J. R., Abel, N. P., Lykins, M. L., Shaw, G., Henney, W. J., and Stancil, P. C. (2013). The 2013 Release of Cloudy. *Rev. Mex. Astron. Astrofis.*, 49:137–163.

Ferrarese, L. and Ford, H. (2005). Supermassive Black Holes in Galactic Nuclei: Past, Present and Future Research. *Space Sci. Rev.*, 116(3-4):523–624.

Ferrarese, L. and Merritt, D. (2000). A Fundamental Relation between Supermassive Black Holes and Their Host Galaxies. *ApJ*, 539:L9–L12.

Fiore, F., Elvis, M., Siemiginowska, A., Wilkes, B. J., McDowell, J. C., and Mathur, S. (1995). The Complex Optical to Soft X-Ray Spectrum of Low-Redshift Radio-quiet Quasars. II. Comparison with Free-Free and Accretion Disk Models. *ApJ*, 449:74.

Fischer, T. C., Crenshaw, D. M., Kraemer, S. B., and Schmitt, H. R. (2013). Determining Inclinations of Active Galactic Nuclei via their Narrow-line Region Kinematics. I. Observational Results. *ApJS*, 209(1):1.

Fynbo, J. P. U., Geier, S. J., Christensen, L., Gallazzi, A., Krogager, J. K., Krühler, T., Ledoux, C., Maund, J. R., Møller, P., Noterdaeme, P., Rivera-Thorsen, T., and Vestergaard, M. (2013). On the two high-metallicity DLAs at z = 2.412 and 2.583 towards Q 0918+1636. *MNRAS*, 436(1):361–370.

Gallagher, S. C., Hines, D. C., Blaylock, M., Priddey, R. S., Brandt, W. N., and Egami, E. E. (2007). Radio through X-Ray Spectral Energy Distributions of 38 Broad Absorption Line Quasars. *ApJ*, 665:157–173.

Gallimore, J. F., Elitzur, M., Maiolino, R., Marconi, A., O'Dea, C. P., Lutz, D., Baum, S. A., Nikutta, R., Impellizzeri, C. M. V., Davies, R., Kimball, A. E., and Sani, E. (2016). High-velocity Bipolar Molecular Emission from an AGN Torus. *ApJ*, 829(1):L7.

García-Burillo, S., Combes, F., Ramos Almeida, C., Usero, A., Alonso-Herrero, A., Hunt, L. K., Rouan, D., Aalto, S., Querejeta, M., Viti, S., van der Werf, P. P., Vives-Arias, H., Fuente, A.,

Colina, L., Martín-Pintado, J., Henkel, C., Martín, S., Krips, M., Gratadour, D., Neri, R., and Tacconi, L. J. (2019). ALMA images the many faces of the <ASTROBJ>NGC 1068</ASTROBJ> torus and its surroundings. *A&A*, 632:A61.

Gardner, E. and Done, C. (2017). The origin of the UV/optical lags in NGC 5548. *MNRAS*, 470:3591–3605.

Gebhardt, K., Bender, R., Bower, G., Dressler, A., Faber, S. M., Filippenko, A. V., Green, R., Grillmair, C., Ho, L. C., Kormendy, J., Lauer, T. R., Magorrian, J., Pinkney, J., Richstone, D., and Tremaine, S. (2000). A Relationship between Nuclear Black Hole Mass and Galaxy Velocity Dispersion. *ApJ*, 539(1):L13–L16.

Ghosh, R., Dewangan, G. C., and Raychaudhuri, B. (2016). Accretion disc/corona emission from a radio-loud narrow-line Seyfert 1 galaxy PKS 0558-504. *MNRAS*, 456:554–564.

Gibson, R. R., Brandt, W. N., Gallagher, S. C., Hewett, P. C., and Schneider, D. P. (2010). The Evolution of Quasar C IV and Si IV Broad Absorption Lines over Multi-year Timescales. *ApJ*, 713(1):220–231.

Gibson, R. R., Brandt, W. N., and Schneider, D. P. (2008). Are Optically Selected Quasars Universally X-Ray Luminous? X-Ray-UV Relations in Sloan Digital Sky Survey Quasars. *ApJ*, 685:773–786.

Gierliński, M. and Done, C. (2004). Is the soft excess in active galactic nuclei real? *MNRAS*, 349:L7–L11.

Glikman, E., Lacy, M., LaMassa, S., Stern, D., Djorgovski, S. G., Graham, M. J., Urrutia, T., Lovdal, L., Crnogorcevic, M., Daniels-Koch, H., Hundal, C. B., Urry, M., Gates, E. L., and Murray, S. (2018). Luminous WISE-selected Obscured, Unobscured, and Red Quasars in Stripe 82. *ApJ*, 861(1):37.

Glikman, E., Urrutia, T., Lacy, M., Djorgovski, S. G., Mahabal, A., Myers, A. D., Ross, N. P., Petitjean, P., Ge, J., Schneider, D. P., and York, D. G. (2012). FIRST-2MASS Red Quasars: Transitional Objects Emerging from the Dust. *ApJ*, 757(1):51.

Goad, M. R., O'Brien, P. T., and Gondhalekar, P. M. (1993). Response functions as diagnostics of the broad-line region in active galactic nuclei. *MNRAS*, 263:149–167.

Gravity Collaboration, Sturm, E., Dexter, J., Pfuhl, O., Stock, M. R., Davies, R. I., Lutz, D., Clénet, Y., Eckart, A., Eisenhauer, F., Genzel, R., Gratadour, D., Hönig, S. F., Kishimoto, M., Lacour, S., Millour, F., Netzer, H., Perrin, G., Peterson, B. M., Petrucci, P. O., Rouan, D., Waisberg, I., Woillez, J., Amorim, A., Brandner, W., Förster Schreiber, N. M., Garcia, P. J. V., Gillessen, S., Ott, T., Paumard, T., Perraut, K., Scheithauer, S., Straubmeier, C., Tacconi, L. J., and Widmann, F. (2018). Spatially resolved rotation of the broad-line region of a quasar at sub-parsec scale. *Nature*, 563(7733):657–660.

Green, P. J., Aldcroft, T. L., Mathur, S., Wilkes, B. J., and Elvis, M. (2001). A Chandra Survey of Broad Absorption Line Quasars. *ApJ*, 558(1):109–118.

Greig, B., Mesinger, A., and Bañados, E. (2019). Constraints on reionization from the z = 7.5 QSO ULASJ1342+0928. *MNRAS*, 484(4):5094–5101.

Grier, C. J., Pancoast, A., Barth, A. J., Fausnaugh, M. M., Brewer, B. J., Treu, T., and Peterson, B. M. (2017). The Structure of the Broad-line Region in Active Galactic Nuclei. II. Dynamical Modeling of Data From the AGN10 Reverberation Mapping Campaign. *ApJ*, 849(2):146.

Grier, C. J., Peterson, B. M., Horne, K., Bentz, M. C., Pogge, R. W., Denney, K. D., De Rosa, G., Martini, P., Kochanek, C. S., Zu, Y., Shappee, B., Siverd, R., Beatty, T. G., Sergeev, S. G., Kaspi, S., Araya Salvo, C., Bird, J. C., Bord, D. J., Borman, G. A., Che, X., Chen, C., Cohen, S. A., Dietrich, M., Doroshenko, V. T., Efimov, Y. S., Free, N., Ginsburg, I., Henderson, C. B., King, A. L., Mogren, K., Molina, M., Mosquera, A. M., Nazarov, S. V., Okhmat, D. N., Pejcha, O., Rafter, S., Shields, J. C., Skowron, J., Szczygiel, D. M., Valluri, M., and van Saders, J. L. (2013). The Structure of the Broad-line Region in Active Galactic Nuclei. I. Reconstructed Velocity-delay Maps. *ApJ*, 764(1):47.

Gültekin, K., Richstone, D. O., Gebhardt, K., Lauer, T. R., Tremaine, S., Aller, M. C., Bender, R., Dressler, A., Faber, S. M., Filippenko, A. V., Green, R., Ho, L. C., Kormendy, J., Magorrian, J., Pinkney, J., and Siopis, C. (2009). The M-σ and M-L Relations in Galactic Bulges, and Determinations of Their Intrinsic Scatter. *ApJ*, 698(1):198–221.

Guo, Z. and Martini, P. (2019). Classification of Broad Absorption Line Quasars with a Convolutional Neural Network. *ApJ*, 879(2):72.

Haardt, F. and Maraschi, L. (1993). X-Ray Spectra from Two-Phase Accretion Disks. *ApJ*, 413:507.

Hall, P. B., Sarrouh, G. T., and Horne, K. (2018). Non-blackbody Disks Can Help Explain Inferred AGN Accretion Disk Sizes. *ApJ*, 854(2):93.

Haniff, C. A., Wilson, A. S., and Ward, M. J. (1988). High-Resolution Emission-Line Imaging of Seyfert Galaxies. I - Observations. *ApJ*, 334:104.

Hao, L., Strauss, M. A., Tremonti, C. A., Schlegel, D. J., Heckman, T. M., Kauffmann, G., Blanton, M. R., Fan, X., Gunn, J. E., Hall, P. B., Ivezić, Ž., Knapp, G. R., Krolik, J. H., Lupton, R. H., Richards, G. T., Schneider, D. P., Strateva, I. V., Zakamska, N. L., Brinkmann, J., Brunner, R. J., and Szokoly, G. P. (2005). Active Galactic Nuclei in the Sloan Digital Sky Survey. I. Sample Selection. *AJ*, 129(4):1783–1794.

Hawley, J. F. and Balbus, S. A. (1991). A Powerful Local Shear Instability in Weakly Magnetized Disks. II. Nonlinear Evolution. *ApJ*, 376:223.

He, Z., Sun, A.-L., Zakamska, N. L., Wylezalek, D., Kelly, M., Greene, J. E., Rembold, S. B., Riffel, R., and Riffel, R. A. (2018). Morphology of AGN emission-line regions in SDSS-IV MaNGA survey. *MNRAS*, 478(3):3614–3626.

Hernández Santisteban, J. V., Edelson, R., Horne, K., Gelbord, J. M., Barth, A. J., Cackett, E. M., Goad, M. R., Netzer, H., Starkey, D., Uttley, P., Brandt, W. N., Korista, K., Lohfink, A. M., Onken, C. A., Page, K. L., Siegel, M., Vestergaard, M., Bisogni, S., Breeveld, A. A., Cenko, S. B., Dalla Bontà, E., Evans, P. A., Ferland , G., Gonzalez-Buitrago, D. H., Grupe, D., Joner, M. D., Kriss, G., LaPorte, S. J., Mathur, S., Marshall, F., Mehdipour, M., Mudd, D., Peterson, B. M., Schmidt, T., Vaughan, S., and Valenti, S. (2020). Intensive disc-reverberation mapping of Fairall 9: 1st year of Swift & LCO monitoring. *arXiv e-prints*, page arXiv:2008.02134.

Hirschmann, M., Khochfar, S., Burkert, A., Naab, T., Genel, S., and Somerville, R. S. (2010). On the evolution of the intrinsic scatter in black hole versus galaxy mass relations. *MNRAS*, 407:1016–1032.

Hogg, J. D. and Reynolds, C. S. (2018). The Dynamics of Truncated Black Hole Accretion Disks II: Magnetohydrodynamic Case. *ArXiv e-prints*.

Hönig, S. F. and Kishimoto, M. (2017). Dusty Winds in Active Galactic Nuclei: Reconciling Observations with Models. *ApJ*, 838(2):L20.

Hönig, S. F., Watson, D., Kishimoto, M., Gandhi, P., Goad, M., Horne, K., Shankar, F., Banerji, M., Boulderstone, B., Jarvis, M., Smith, M., and Sullivan, M. (2017). Cosmology with AGN dust time lags-simulating the new VEILS survey. *MNRAS*, 464:1693–1703.

Hoormann, J. K., Martini, P., Davis, T. M., King, A., Lidman, C., Mudd, D., Sharp, R., Sommer, N. E., Tucker, B. E., Yu, Z., Allam, S., Asorey, J., Avila, S., Banerji, M., Brooks, D., Buckley-Geer, E., Burke, D. L., Calcino, J., Carnero Rosell, A., Carollo, D., Carrasco Kind, M., Carretero, J., Castand er, F. J., Childress, M., De Vicente, J., Desai, S., Diehl, H. T., Doel, P., Flaugher, B., Fosalba, P., Frieman, J., García-Bellido, J., Gerdes, D. W., Gruen, D., Gutierrez, G., Hartley, W. G., Hinton, S. R., Hollowood, D. L., Honscheid, K., Hoyle, B., James, D. J., Krause, E., Kuehn, K., Kuropatkin, N., Lewis, G. F., Lima, M., Macaulay, E., Maia, M. A. G., Menanteau, F., Miller, C. J., Miquel, R., Möller, A., Plazas, A. A., Romer, A. K., Roodman, A., Sanchez, E., Scarpine, V., Schubnell, M., Serrano, S., Sevilla-Noarbe, I., Smith, M., Smith, R. C., Soares-Santos, M., Sobreira, F., Suchyta, E., Swann, E., Swanson, M. E. C., Tarle, G., Uddin, S. A., and DES Collaboration (2019). C IV black hole mass measurements with the Australian Dark Energy Survey (OzDES). *MNRAS*, 487(3):3650–3663.

Hopkins, P. F., Hernquist, L., Cox, T. J., Di Matteo, T., Martini, P., Robertson, B., and Springel, V. (2005). Black Holes in Galaxy Mergers: Evolution of Quasars. *ApJ*, 630:705–715.

Horne, K. (1994). Echo Mapping Problems Maximum Entropy solutions. In Gondhalekar, P. M., Horne, K., and Peterson, B. M., editors, *Reverberation Mapping of the Broad-Line Region in Active Galactic Nuclei*, volume 69 of *Astronomical Society of the Pacific Conference Series*, page 23.

Horne, K., De Rosa, G., Peterson, B. M., Barth, A. J., Ely, J., Fausnaugh, M. M., Kriss, G. A., Pei, L., Adams, S. M., Anderson, M. D., Arevalo, P., Beatty, T. G., Bennert, V. N., Bentz, M. C., Bigley, A., Bisogni, S., Borman, G. A., Boroson, T. A., Bottorff, M. C., Brandt, W. N., Breeveld, A. A., Brotherton, M., Brown, J. E., Brown, J. S., Cackett, E. M., Canalizo, G., Carini, M. T., Clubb, K. I., Comerford, J. M., Corsini, E. M., Crenshaw, D. M., Croft, S., Croxall, K. V., Dalla Bonta, E., Deason, A. J., Dehghanian, M., De Lorenzo-Caceres, A., Denney, K. D., Dietrich, M., Done, C., Edelson, R., Efimova, N. V., Eracleous, M., Evans, P. A., Ferland, G. J., Filippenko, A. V., Flatland, K., Fox, O. D., Gardner, E., Gates, E. L., Gehrels, N., Geier, S., Gelbord, J. M., Goad, M. R., Gonzalez, L., Gorjian, V., Greene, J. E., Grier, C. J., Grupe, D., Gupta, A., Hall, P. B., Henderson, C. B., Hicks, S., Holmbeck, E., Holoien, T. W. S., Hutchison, T., Im, M., Jensen, J. J., Johnson, C. A., Joner, M. D., Jones, J., Kaastra, J., Kaspi, S., Kelly, P. L., Kennea, J. A., Kim, M., Kim, S., Kim, S. C., King, A., Klimanov, S. A., Kochanek, C. S., Korista, K. T., Krongold, Y., Lau, M. W., Lee, J. C., Leonard, D. C., Li, M., Lira, P., Lochhaas, C., Ma, Z., MacInnis, F., Malkan, M. A., Manne-Nicholas, E. R., Mathur, S., Mauerhan, J. C., McGurk, R., Mc Hardy, I. M., Montuori, C., Morelli, L., Mosquera, A., Mudd, D., Mueller-Sanchez, F., Nazarov, S. V., Netzer, H., Norris, R. P., Nousek, J. A., Nguyen, M. L., Ochner, P., Okhmat, D. N., Pancoast, A., Papadakis, I., Parks, J. R., Penny, M. T., Pizzella, A., Pogge, R. W., Poleski, R., Pott, J. U., Proga, D., Rafter, S. E., Rix, H. W., Runnoe, J., Saylor, D. A., Schimoia, J. S., Schnuelle, K., Scott, B., Sergeev, S. G., Shappee, B. J., Shivvers, I., Siegel, M., Simonian, G. V., Siviero, A., Skielboe, A., Somers, G., Spencer, M., Starkey, D., Stevens, D. J., Strauss, M. A., Sung, H. I., Tayar, J., Teems, K. G., Tejos, N., Treu, T., Turner, C. S., Uttley, P., . Van Saders, J., Vestergaard, M., Vican, L., Villanueva, S., J., Villforth, C., Weiss, Y., Woo, J. H., Yan, H., Young, S., Yuk, H., Zakamska, N. L., Zheng, W., Zhu, W., and Zu, Y. (2020). Space Telescope and Optical Reverberation Mapping Project. IX. Velocity-Delay Maps for Broad Emission Lines in NGC 5548. *arXiv e-prints*, page arXiv:2003.01448.

Hubeny, I. and Hubeny, V. (1997). Non-LTE Models and Theoretical Spectra of Accretion Disks in Active Galactic Nuclei. *ApJ*, 484:L37–L40.

Hughes, D. H., Robson, E. I., Dunlop, J. S., and Gear, W. K. (1993). Thermal Dust Emission from Quasars - Part One - Submillimetre Spectral Indices of Radio Quiet Quasars. *MNRAS*, 263:607.

Inglis, M. D., Young, S., Hough, J. H., Gledhill, T., Axon, D. J., Bailey, J. A., and Ward, M. J. (1995). Spatially resolved spectropolarimetry of the galaxy NGC 1068. *MNRAS*, 275(2):398–416.

Jahnke, K. and Macciò, A. V. (2011). The Non-causal Origin of the Black-hole-galaxy Scaling Relations. *ApJ*, 734:92.

Jiang, L., Fan, X., Ivezić, Ž., Richards, G. T., Schneider, D. P., Strauss, M. A., and Kelly, B. C. (2007). The Radio-Loud Fraction of Quasars is a Strong Function of Redshift and Optical Luminosity. *ApJ*, 656(2):680–690.

Jiang, Y.-F. and Blaes, O. (2020). Opacity Driven Convection and Variability in Accretion Disks around Supermassive Black Holes. *arXiv e-prints*, page arXiv:2006.08657.

Jin, C., Ward, M., and Done, C. (2012). A combined optical and X-ray study of unobscured type 1 active galactic nuclei - II. Relation between X-ray emission and optical spectra. *MNRAS*, 422:3268–3284.

Jones, M. L., Hickox, R. C., Black, C. S., Hainline, K. N., DiPompeo, M. A., and Goulding, A. D. (2016). The Intrinsic Eddington Ratio Distribution of Active Galactic Nuclei in Star-forming Galaxies from the Sloan Digital Sky Survey. *ApJ*, 826(1):12.

Kaspi, S., Brandt, W. N., Maoz, D., Netzer, H., Schneider, D. P., and Shemmer, O. (2007). Reverberation Mapping of High-Luminosity Quasars: First Results. *ApJ*, 659(2):997–1007.

Kellermann, K. I., Condon, J. J., Kimball, A. E., Perley, R. A., and Ivezić, Ž. (2016). Radio-loud and Radio-quiet QSOs. *ApJ*, 831(2):168.

Kellermann, K. I., Sramek, R., Schmidt, M., Shaffer, D. B., and Green, R. (1989). VLA observations of objects in the Palomar Bright Quasar Survey. *AJ*, 98:1195–1207.

Kelly, B. C., Vestergaard, M., Fan, X., Hopkins, P., Hernquist, L., and Siemiginowska, A. (2010). Constraints on Black Hole Growth, Quasar Lifetimes, and Eddington Ratio Distributions from the SDSS Broad-line Quasar Black Hole Mass Function. *ApJ*, 719(2):1315–1334.

Kerr, R. P. (1963). Gravitational Field of a Spinning Mass as an Example of Algebraically Special Metrics. *Phys. Rev. Lett.*, 11(5):237–238.

Kilerci Eser, E. and Vestergaard, M. (2018). Spectral energy distribution variations of nearby Seyfert galaxies during AGN watch monitoring programs. *MNRAS*, 474:1590–1628.

Kilerci Eser, E., Vestergaard, M., Peterson, B. M., Denney, K. D., and Bentz, M. C. (2015). On the Scatter in the Radius-Luminosity Relationship for Active Galactic Nuclei. *ApJ*, 801:8.

King, A. (2008). Disc accretion in active galactic nuclei. *New Astron. Rev.*, 52(6):253–256.

King, A. (2016). How big can a black hole grow? *MNRAS*, 456(1):L109–L112.

King, A. L., Davis, T. M., Denney, K. D., Vestergaard, M., and Watson, D. (2014). High-redshift standard candles: predicted cosmological constraints. *MNRAS*, 441:3454–3476.

Kitaki, T., Mineshige, S., Ohsuga, K., and Kawashima, T. (2018). Systematic two-dimensional radiation-hydrodynamic simulations of super-Eddington accretion flow and outflow: Comparison with the slim disk model. *PASJ*, 70(6):108.

Koay, J. Y., Vestergaard, M., Bignall, H. E., Reynolds, C., and Peterson, B. M. (2016). Parsec-scale radio morphology and variability of a changing-look AGN: the case of Mrk 590. *MNRAS*, 460:304–316.

Kollmeier, J. A., Onken, C. A., Kochanek, C. S., Gould, A., Weinberg, D. H., Dietrich, M., Cool, R., Dey, A., Eisenstein, D. J., Jannuzi, B. T., Le Floc'h, E., and Stern, D. (2006). Black Hole Masses and Eddington Ratios at $0.3 < z < 4$. *ApJ*, 648(1):128–139.

Koratkar, A. P. and Gaskell, C. M. (1991). Radius-Luminosity and Mass-Luminosity Relationships for Active Galactic Nuclei. *ApJ*, 370:L61.

Korista, K., Baldwin, J., Ferland, G., and Verner, D. (1997). An Atlas of Computed Equivalent Widths of Quasar Broad Emission Lines. *ApJS*, 108:401–415.

Korista, K. T. and Goad, M. R. (2019). Quantifying the impact of variable BLR diffuse continuum contributions on measured continuum interband delays. *MNRAS*, 489(4):5284–5300.

Kormendy, J. and Ho, L. C. (2013). Coevolution (Or Not) of Supermassive Black Holes and Host Galaxies. *ARA&A*, 51(1):511–653.

Kozłowski, S. (2017). Limitations on the recovery of the true AGN variability parameters using damped random walk modeling. *A&A*, 597:A128.

Kutkin, A. M., Pashchenko, I. N., Sokolovsky, K. V., Kovalev, Y. Y., Aller, M. F., and Aller, H. D. (2019). Opacity, variability, and kinematics of AGN jets. *MNRAS*, 486(1):430–439.

LaMassa, S. M., Cales, S., Moran, E. C., Myers, A. D., Richards, G. T., Eracleous, M., Heckman, T. M., Gallo, L., and Urry, C. M. (2015). The Discovery of the First "Changing Look" Quasar: New Insights Into the Physics and Phenomenology of Active Galactic Nucleus. *ApJ*, 800:144.

Lansbury, G. B., Banerji, M., Fabian, A. C., and Temple, M. J. (2020). X-ray observations of luminous dusty quasars at z > 2. *MNRAS*, 495(3):2652–2663.

Laor, A. (2004). What is the Broad Line Region? In Richards, G. T. and Hall, P. B., editors, *AGN Physics with the Sloan Digital Sky Survey*, volume 311, page 169.

Laor, A. and Davis, S. W. (2014). Line-driven winds and the UV turnover in AGN accretion discs. *MNRAS*, 438:3024–3038.

Laor, A. and Draine, B. T. (1993). Spectroscopic Constraints on the Properties of Dust in Active Galactic Nuclei. *ApJ*, 402:441.

Lawrence, A. (2018). Quasar viscosity crisis. *Nature Astronomy*, 2:102–103.

Lawther, D., Goad, M. R., Korista, K. T., Ulrich, O., and Vestergaard, M. (2018a). Quantifying the Diffuse Continuum Contribution of BLR Clouds to AGN Continuum Inter-band Delays. *ArXiv e-prints*, page arXiv:1808.04798.

Lawther, D., Vestergaard, M., and Fan, X. (2018b). A Hubble Space Telescope imaging study of four FeLoBAL quasar host galaxies. *MNRAS*, 475:3213–3239.

Lawther, D., Vestergaard, M., Raimundo, S., and Grupe, D. (2017). A catalogue of optical to X-ray spectral energy distributions of z ≈ 2 quasars observed with Swift - I. First results. *MNRAS*, 467:4674–4710.

Lister, M. L., Aller, M. F., Aller, H. D., Homan, D. C., Kellermann, K. I., Kovalev, Y. Y., Pushkarev, A. B., Richards, J. L., Ros, E., and Savolainen, T. (2016). MOJAVE: XIII. Parsec-scale AGN Jet Kinematics Analysis Based on 19 years of VLBA Observations at 15 GHz. *AJ*, 152(1):12.

Lohfink, A. M., Reynolds, C. S., Miller, J. M., Brenneman, L. W., Mushotzky, R. F., Nowak, M. A., and Fabian, A. C. (2012). The Black Hole Spin and Soft X-Ray Excess of the Luminous Seyfert Galaxy Fairall 9. *ApJ*, 758(1):67.

Loli Martínez-Aldama, M., Czerny, B., Kawka, D., Karas, V., Zajaček, M., and Życki, P. T. (2019). Can reverberation-measured quasars be used for cosmology? *arXiv e-prints*, page arXiv:1903.09687.

Lusso, E., Piedipalumbo, E., Risaliti, G., Paolillo, M., Bisogni, S., Nardini, E., and Amati, L. (2019). Tension with the flat ΛCDM model from a high-redshift Hubble diagram of supernovae, quasars, and gamma-ray bursts. *A&A*, 628:L4.

Lusso, E. and Risaliti, G. (2016). The Tight Relation between X-Ray and Ultraviolet Luminosity of Quasars. *ApJ*, 819:154.

Lusso, E. and Risaliti, G. (2017). Quasars as standard candles. I. The physical relation between disc and coronal emission. *A&A*, 602:A79.

Lynden-Bell, D. (1978). Gravity power. *Phys. Scr.*, 17:185–191.

Lynden-Bell, D. and Rees, M. J. (1971). On quasars, dust and the galactic centre. *MNRAS*, 152:461.

Mackenzie, R., Fumagalli, M., Theuns, T., Hatton, D. J., Garel, T., Cantalupo, S., Christensen, L., Fynbo, J. P. U., Kanekar, N., Møller, P., O'Meara, J., Prochaska, J. X., Rafelski, M., Shanks, T., and Trayford, J. (2019). Linking gas and galaxies at high redshift: MUSE surveys the environments of six damped Lyα systems at z ≈ 3. *MNRAS*, page 1435.

Magorrian, J., Tremaine, S., Richstone, D., Bender, R., Bower, G., Dressler, A., Faber, S. M., Gebhardt, K., Green, R., Grillmair, C., Kormendy, J., and Lauer, T. (1998). The Demography of Massive Dark Objects in Galaxy Centers. *AJ*, 115:2285–2305.

Mahmoud, R. D. and Done, C. (2020). Discarding the disc in a changing-state AGN: the UV/X-ray relation in NGC 4151. *MNRAS*, 491(4):5126–5139.

Maraschi, L., Colpi, M., Ghisellini, G., Perego, A., and Tavecchio, F. (2012). On the role of black hole spin and accretion in powering relativistic jets in AGN. In *Journal of Physics Conference Series*, volume 355, page 012016.

Marconi, A. and Hunt, L. K. (2003). The Relation between Black Hole Mass, Bulge Mass, and Near-Infrared Luminosity. *ApJ*, 589(1):L21–L24.

Markoff, S., Nowak, M. A., and Wilms, J. (2005). Going with the Flow: Can the Base of Jets Subsume the Role of Compact Accretion Disk Coronae? *ApJ*, 635(2):1203–1216.

Marshall, H. L., Gelbord, J. M., Worrall, D. M., Birkinshaw, M., Schwartz, D. A., Jauncey, D. L., Griffiths, G., Murphy, D. W., Lovell, J. E. J., Perlman, E. S., and Godfrey, L. (2018). An X-Ray Imaging Survey of Quasar Jets: The Complete Survey. *ApJ*, 856:66.

Martocchia, S., Piconcelli, E., Zappacosta, L., Duras, F., Vietri, G., Vignali, C., Bianchi, S., Bischetti, M., Bongiorno, A., Brusa, M., Lanzuisi, G., Marconi, A., Mathur, S., Miniutti, G., Nicastro, F., Bruni, G., and Fiore, F. (2017). The WISSH quasars project. III. X-ray properties of hyperluminous quasars. *A&A*, 608:A51.

Mathur, S. (2000). Narrow-line Seyfert 1 galaxies and the evolution of galaxies and active galaxies. *MNRAS*, 314(4):L17–L20.

Matthews, J. H., Knigge, C., Higginbottom, N., Long, K. S., Sim, S. A., Mangham, S. W., Parkinson, E. J., and Hewitt, H. A. (2020). Stratified disc wind models for the AGN broad-line region: ultraviolet, optical, and X-ray properties. *MNRAS*, 492(4):5540–5560.

Matthews, J. H., Knigge, C., Long, K. S., Sim, S. A., Higginbottom, N., and Mangham, S. W. (2016). Testing quasar unification: radiative transfer in clumpy winds. *MNRAS*, 458(1):293–305.

McConnell, N. J. and Ma, C.-P. (2013). Revisiting the Scaling Relations of Black Hole Masses and Host Galaxy Properties. *ApJ*, 764(2):184.

McGreer, I. D., Mesinger, A., and D'Odorico, V. (2015). Model-independent evidence in favour of an end to reionization by z ≈ 6. *MNRAS*, 447(1):499–505.

McHardy, I. M., Cameron, D. T., Dwelly, T., Connolly, S., Lira, P., Emmanoulopoulos, D., Gelbord, J., Breedt, E., Arevalo, P., and Uttley, P. (2014). Swift monitoring of NGC 5548: X-ray reprocessing and short-term UV/optical variability. *MNRAS*, 444:1469–1474.

McHardy, I. M., Connolly, S. D., Cackett, K. H. E. M., Gelbord, J., Peterson, B. M., Pahari, M., Gehrels, N., Edelson, R., Goad, M., Lira, P., Arevalo, P., Baldi, R. D., Brandt, N., Breedt, E., Chand, H., Dewangan, G., Done, C., Elvis, M., Emmanoulopoulos, D., Fausnaugh, M. M., Kaspi, S., Kochanek, C. S., Korista, K., Papadakis, I. E., Rao, A. R., Uttley, P., Vestergaard, M., and Ward, M. J. (2017). X-ray/UV/optical variability of NGC 4593 with Swift: Reprocessing of X-rays by an extended reprocessor. *ArXiv e-prints*.

McLeod, K. K. and Bechtold, J. (2009). Host Galaxies of z = 4 Quasars. *ApJ*, 704:415–438.

McLeod, K. K. and McLeod, B. A. (2001). NICMOS Observations of Low-Redshift Quasar Host Galaxies. *ApJ*, 546(2):782–794.

McLure, R. J. and Dunlop, J. S. (2004). The cosmological evolution of quasar black hole masses. *MNRAS*, 352(4):1390–1404.

Michell, J. (1784). On the Means of Discovering the Distance, Magnitude, and c. of the Fixed Stars, in Consequence of the Diminution of the Velocity of Their Light, in Case Such a Diminution Should be Found to Take Place in any of Them, and Such Other Data Should be Procured from Observations, as Would be Farther Necessary for That Purpose. By the Rev. John Michell, B. D. F. R. S. In a Letter to Henry Cavendish, Esq. F. R. S. and A. S. *Philosophical Transactions of the Royal Society of London Series I*, 74:35–57.

Miller, B. P., Brandt, W. N., Schneider, D. P., Gibson, R. R., Steffen, A. T., and Wu, J. (2011). X-ray Emission from Optically Selected Radio-intermediate and Radio-loud Quasars. *ApJ*, 726:20.

Miniutti, G., Ponti, G., Greene, J. E., Ho, L. C., Fabian, A. C., and Iwasawa, K. (2009). The XMM -Newton view of AGN with intermediate-mass black holes. *MNRAS*, 394(1):443–453.

Miniutti, G., Saxton, R. D., Rodríguez-Pascual, P. M., Read, A. M., Esquej, P., Colless, M., Dobbie, P., and Spolaor, M. (2013). A high Eddington-ratio, true Seyfert 2 galaxy candidate: implications for broad-line region models. *MNRAS*, 433:1764–1777.

Moloney, J. and Shull, J. M. (2014). Constraining UV Continuum Slopes of Active Galactic Nuclei with CLOUDY Models of Broad-line Region Extreme-ultraviolet Emission Lines. *ApJ*, 793(2):100.

Morales, A. M., Miller, J. M., Cackett, E. M., Reynolds, M. T., and Zoghbi, A. (2019). X-Ray and UV Monitoring of the Seyfert 1.5 Galaxy Markarian 817. *ApJ*, 870(1):54.

Moran, E. C., Barth, A. J., Kay, L. E., and Filippenko, A. V. (2000). The Frequency of Polarized Broad Emission Lines in Type 2 Seyfert Galaxies. *ApJ*, 540(2):L73–L77.

Mosquera, A. M., Kochanek, C. S., Chen, B., Dai, X., Blackburne, J. A., and Chartas, G. (2013). The Structure of the X-Ray and Optical Emitting Regions of the Lensed Quasar Q 2237+0305. *ApJ*, 769:53.

Mullaney, J. R., Alexander, D. M., Fine, S., Goulding, A. D., Harrison, C. M., and Hickox, R. C. (2013). Narrow-line region gas kinematics of 24 264 optically selected AGN: the radio connection. *MNRAS*, 433(1):622–638.

Murray, N. and Chiang, J. (1995). Active Galactic Nuclei Disk Winds, Absorption Lines, and Warm Absorbers. *ApJ*, 454:L105.

Nagar, N. M., Wilson, A. S., Mulchaey, J. S., and Gallimore, J. F. (1999). Radio Structures of Seyfert Galaxies. VIII. A Distance- and Magnitude-Limited Sample of Early-Type Galaxies. *ApJS*, 120(2):209–245.

Nandra, K., O'Neill, P. M., George, I. M., and Reeves, J. N. (2007). An XMM-Newton survey of broad iron lines in Seyfert galaxies. *MNRAS*, 382(1):194–228.

Nandra, K. and Pounds, K. A. (1994). GINGA Observations of the X-Ray Spectra of Seyfert Galaxies. *MNRAS*, 268:405.

Narayan, R., Mahadevan, R., and Quataert, E. (1998). Advection-dominated accretion around black holes. In Abramowicz, M. A., Björnsson, G., and Pringle, J. E., editors, *Theory of Black Hole Accretion Disks*, pages 148–182.

Narayan, R., McClintock, J. E., and Tchekhovskoy, A. e. (2014). *Energy Extraction from Spinning Black Holes Via Relativistic Jets*, volume 177, page 523.

Narayan, R. and Yi, I. (1994). Advection-dominated Accretion: A Self-similar Solution. *ApJ*, 428:L13.

Netzer, H. (2013). *The Physics and Evolution of Active Galactic Nuclei*.

Netzer, H. (2020). Testing broad-line region models with reverberation mapping. *MNRAS*, 494(2):1611–1621.

Noda, H. and Done, C. (2018). Explaining changing-look AGN with state transition triggered by rapid mass accretion rate drop. *MNRAS*, 480(3):3898–3906.

Novikov, I. D. and Thorne, K. S. (1973). Astrophysics of black holes. In Dewitt, C. and Dewitt, B. S., editors, *Black Holes (Les Astres Occlus)*, pages 343–450.

Onken, C. A., Ferrarese, L., Merritt, D., Peterson, B. M., Pogge, R. W., Vestergaard, M., and Wandel, A. (2004). Supermassive Black Holes in Active Galactic Nuclei. II. Calibration of the Black Hole Mass-Velocity Dispersion Relationship for Active Galactic Nuclei. *ApJ*, 615:645–651.

Osterbrock, D. E. and Pogge, R. W. (1985). The spectra of narrow-line Seyfert 1 galaxies. *ApJ*, 297:166–176.

Pacucci, F., Natarajan, P., Volonteri, M., Cappelluti, N., and Urry, C. M. (2017). Conditions for Optimal Growth of Black Hole Seeds. *ApJ*, 850(2):L42.

Padmanabhan, H. and Refregier, A. (2017). Constraining a halo model for cosmological neutral hydrogen. *MNRAS*, 464(4):4008–4017.

Pâris, I., Petitjean, P., Aubourg, É., Myers, A. D., Streblyanska, A., Lyke, B. W., Anderson, S. F., Armengaud, É., Bautista, J., Blanton, M. R., Blomqvist, M., Brinkmann, J., Brownstein, J. R., Brand t, W. N., Burtin, É., Dawson, K., de la Torre, S., Georgakakis, A., Gil-Marín, H., Green, P. J., Hall, P. B., Kneib, J.-P., LaMassa, S. M., Le Goff, J.-M., MacLeod, C., Mariappan, V., McGreer, I. D., Merloni, A., Noterdaeme, P., Palanque-Delabrouille, N., Percival, W. J., Ross, A. J., Rossi, G., Schneider, D. P., Seo, H.-J., Tojeiro, R., Weaver, B. A., Weijmans, A.-M., Yèche, C., Zarrouk, P., and Zhao, G.-B. (2018). The Sloan Digital Sky Survey Quasar Catalog: Fourteenth data release. *A&A*, 613:A51.

Parker, M. L., Schartel, N., Komossa, S., Grupe, D., Santos-Lleó, M., Fabian, A. C., and Mathur, S. (2014). A partial eclipse of the heart: the absorbed X-ray low state in Mrk 1048. *MNRAS*, 445(1):1039–1047.

Peng, C. Y. (2007). How Mergers May Affect the Mass Scaling Relation between Gravitationally Bound Systems. *ApJ*, 671:1098–1107.

Pêrez, E., Robinson, A., and de La Fuente, L. (1992). The response of the broad emission line region to ionizing continuum variations. II - Numerical simulations. *MNRAS*, 255:502–520.

Perlmutter, S., Aldering, G., Goldhaber, G., Knop, R. A., Nugent, P., Castro, P. G., Deustua, S., Fabbro, S., Goobar, A., Groom, D. E., Hook, I. M., Kim, A. G., Kim, M. Y., Lee, J. C., Nunes, N. J., Pain, R., Pennypacker, C. R., Quimby, R., Lidman, C., Ellis, R. S., Irwin, M., McMahon, R. G., Ruiz-Lapuente, P., Walton, N., Schaefer, B., Boyle, B. J., Filippenko, A. V., Matheson, T., Fruchter, A. S., Panagia, N., Newberg, H. J. M., Couch, W. J., and Project, T. S. C. (1999). Measurements of Ω and Λ from 42 High-Redshift Supernovae. *ApJ*, 517(2):565–586.

Peterson, B. M. (1993). Reverberation Mapping of Active Galactic Nuclei. *PASP*, 105:247.

Peterson, B. M. (2001). Variability of Active Galactic Nuclei. In Aretxaga, I., Kunth, D., and Mújica, R., editors, *Advanced Lectures on the Starburst-AGN*, page 3.

Peterson, B. M., Ferrarese, L., Gilbert, K. M., Kaspi, S., Malkan, M. A., Maoz, D., Merritt, D., Netzer, H., Onken, C. A., Pogge, R. W., Vestergaard, M., and Wandel, A. (2004). Central Masses and Broad-Line Region Sizes of Active Galactic Nuclei. II. A Homogeneous Analysis of a Large Reverberation-Mapping Database. *ApJ*, 613:682–699.

Peterson, B. M., Wanders, I., Horne, K., Collier, S., Alexander, T., Kaspi, S., and Maoz, D. (1998). On Uncertainties in Cross-Correlation Lags and the Reality of Wavelength-dependent Continuum Lags in Active Galactic Nuclei. *PASP*, 110(748):660–670.

Petrucci, P. O., Ursini, F., De Rosa, A., Bianchi, S., Cappi, M., Matt, G., Dadina, M., and Malzac, J. (2018). Testing warm Comptonization models for the origin of the soft X-ray excess in AGNs. *A&A*, 611.

Pitchford, L. K., Farrah, D., Alatalo, K., Afonso, J., Efstathiou, A., Hatziminaoglou, E., Lacy, M., Urrutia, T., and Violino, G. (2019). The mid-infrared and CO gas properties of an extreme star-forming FeLoBAL quasar. *MNRAS*, 487(3):3130–3139.

Pogge, R. W. (1988a). An Extended Ionizing Radiation Cone from the Nucleus of the Seyfert 2 Galaxy NGC 1068. *ApJ*, 328:519.

Pogge, R. W. (1988b). Extended Ionized Gas in the Seyfert 2 Galaxy NGC 4388. *ApJ*, 332:702.

Porquet, D., Done, C., Reeves, J. N., Grosso, N., Marinucci, A., Matt, G., Lobban, A., Nardini, E., Braito, V., Marin, F., Kubota, A., Ricci, C., Koss, M., Stern, D., Ballantyne, D., and Farrah, D. (2019). A deep X-ray view of the bare AGN Ark 120. V. Spin determination from disc-Comptonisation efficiency method. *A&A*, 623:A11.

Porquet, D., Reeves, J. N., O'Brien, P., and Brinkmann, W. (2004). XMM-Newton EPIC observations of 21 low-redshift PG quasars. *A&A*, 422:85–95.

Proga, D. and Kallman, T. R. (2004). Dynamics of Line-driven Disk Winds in Active Galactic Nuclei. II. Effects of Disk Radiation. *ApJ*, 616(2):688–695.

Rafelski, M., Gardner, J. P., Fumagalli, M., Neeleman, M., Teplitz, H. I., Grogin, N., Koekemoer, A. M., and Scarlata, C. (2016). The Star Formation Rate Efficiency of Neutral Atomic-dominated Hydrogen Gas in the Outskirts of Star-forming Galaxies from z ∼1 to z ∼3. *ApJ*, 825(2):87.

Raimundo, S. I., Fabian, A. C., Vasudevan, R. V., Gandhi, P., and Wu, J. (2012). Can we measure the accretion efficiency of active galactic nuclei? *MNRAS*, 419:2529–2544.

Raimundo, S. I., Vestergaard, M., Koay, J. Y., Lawther, D., Casasola, V., and Peterson, B. M. (2019). MUSE observations of a changing-look AGN - I. The reappearance of the broad emission lines. *MNRAS*, 486(1):123–140.

Rakshit, S., Stalin, C. S., and Kotilainen, J. (2020). Spectral Properties of Quasars from Sloan Digital Sky Survey Data Release 14: The Catalog. *ApJS*, 249(1):17.

Readhead, A. C. S., Cohen, M. H., and Blandford, R. D. (1978). A jet in the nucleus of NGC6251. *Nature*, 272(5649):131–134.

Rees, M. J. (1987). Magnetic confinement of broad-line clouds in active galactic nuclei. *MNRAS*, 228:47P–50.

Reid, M. J. and Brunthaler, A. (2004). The Proper Motion of Sagittarius A*. II. The Mass of Sagittarius A*. *ApJ*, 616:872–884.

Reis, R. C. and Miller, J. M. (2013). On the Size and Location of the X-Ray Emitting Coronae around Black Holes. *ApJ*, 769.

Ricci, C., Kara, E., Loewenstein, M., Trakhtenbrot, B., Arcavi, I., Remillard, R., Fabian, A. C., Gendreau, K. C., Arzoumanian, Z., Li, R., Ho, L. C., MacLeod, C. L., Cackett, E., Altamirano, D., Gand hi, P., Kosec, P., Pasham, D., Steiner, J., and Chan, C. H. (2020). The Destruction and Recreation of the X-Ray Corona in a Changing-look Active Galactic Nucleus. *ApJ*, 898(1):L1.

Richards, G. T., Lacy, M., Storrie-Lombardi, L. J., Hall, P. B., Gallagher, S. C., Hines, D. C., Fan, X., Papovich, C., Vanden Berk, D. E., Trammell, G. B., Schneider, D. P., Vestergaard, M., York, D. G., Jester, S., Anderson, S. F., Budavári, T., and Szalay, A. S. (2006). Spectral Energy Distributions and Multiwavelength Selection of Type 1 Quasars. *ApJS*, 166:470–497.

Riess, A. G., Filippenko, A. V., Challis, P., Clocchiatti, A., Diercks, A., Garnavich, P. M., Gilliland, R. L., Hogan, C. J., Jha, S., Kirshner, R. P., Leibundgut, B., Phillips, M. M., Reiss, D., Schmidt, B. P., Schommer, R. A., Smith, R. C., Spyromilio, J., Stubbs, C., Suntzeff, N. B., and Tonry, J. (1998). Observational Evidence from Supernovae for an Accelerating Universe and a Cosmological Constant. *AJ*, 116(3):1009–1038.

Riffert, H. and Herold, H. (1995). Relativistic Accretion Disk Structure Revisited. *ApJ*, 450:508.

Risaliti, G. and Lusso, E. (2015). A Hubble Diagram for Quasars. *ApJ*, 815:33.

Rivers, E., Markowitz, A., Duro, R., and Rothschild, R. (2012). A Suzaku Observation of Mkn 590 Reveals a Vanishing Soft Excess. *ApJ*, 759.

Roming, P. W. A., Kennedy, T. E., Mason, K. O., Nousek, J. A., Ahr, L., Bingham, R. E., Broos, P. S., Carter, M. J., Hancock, B. K., Huckle, H. E., Hunsberger, S. D., Kawakami, H., Killough, R., Koch, T. S., McLelland, M. K., Smith, K., Smith, P. J., Soto, J. C., Boyd, P. T., Breeveld, A. A., Holland, S. T., Ivanushkina, M., Pryzby, M. S., Still, M. D., and Stock, J. (2005). The Swift Ultra-Violet/Optical Telescope. *Space Sci. Rev.*, 120:95–142.

Ross, N. P., Ford, K. E. S., Graham, M., McKernan, B., Stern, D., Meisner, A. M., Assef, R. J., Dey, A., Drake, A. J., Jun, H. D., and Lang, D. (2018). A new physical interpretation of optical and infrared variability in quasars. *MNRAS*, 480(4):4468–4479.

Ross, R. R. and Fabian, A. C. (2005). A comprehensive range of X-ray ionized-reflection models. *MNRAS*, 358(1):211–216.

Ruan, J. J., Anderson, S. F., Eracleous, M., Green, P. J., Haggard, D., MacLeod, C. L., Runnoe, J. C., and Sobolewska, M. A. (2019). The Analogous Structure of Accretion Flows in Supermassive and Stellar Mass Black Holes: New Insights from Faded Changing-look Quasars. *ApJ*, 883(1):76.

Runnoe, J. C., Brotherton, M. S., and Shang, Z. (2012). Updating quasar bolometric luminosity corrections. *MNRAS*, 422:478–493.

Runnoe, J. C., Cales, S., Ruan, J. J., Eracleous, M., Anderson, S. F., Shen, Y., Green, P. J., Morganson, E., LaMassa, S., Greene, J. E., Dwelly, T., Schneider, D. P., Merloni, A., Georgakakis, A., and Roman-Lopes, A. (2016). Now you see it, now you don't: the disappearing central engine of the quasar J1011+5442. *MNRAS*, 455(2):1691–1701.

Sánchez-Sáez, P., Lira, P., Cartier, R., Mirand a, N., Ho, L. C., Arévalo, P., Bauer, F. E., Coppi, P., and Yovaniniz, C. (2019). The QUEST-La Silla AGN Variability Survey: Selection of AGN Candidates through Optical Variability. *ApJS*, 242(1):10.

Sandage, A. (1965). The Existence of a Major New Constituent of the Universe: the Quasistellar Galaxies. *ApJ*, 141:1560.

Sanders, D. B., Soifer, B. T., Elias, J. H., Madore, B. F., Matthews, K., Neugebauer, G., and Scoville, N. Z. (1988). Ultraluminous Infrared Galaxies and the Origin of Quasars. *ApJ*, 325:74.

Schmitt, H. R., Donley, J. L., Antonucci, R. R. J., Hutchings, J. B., Kinney, A. L., and Pringle, J. E. (2003). A Hubble Space Telescope Survey of Extended [O III] $\lambda 5007$ Å Emission in a Far-Infrared-Selected Sample of Seyfert Galaxies: Results. *ApJ*, 597(2):768–779.

Schneider, D. P., Hall, P. B., Richards, G. T., Vanden Berk, D. E., Anderson, S. F., Fan, X., Jester, S., Stoughton, C., Strauss, M. A., SubbaRao, M., Brandt, W. N., Gunn, J. E., Yanny, B., Bahcall, N. A., Barentine, J. C., Blanton, M. R., Boroski, W. N., Brewington, H. J., Brinkmann, J., Brunner, R., Csabai, I., Doi, M., Eisenstein, D. J., Frieman, J. A., Fukugita, M., Gray, J., Harvanek, M., Heckman, T. M., Ivezić, Ž., Kent, S., Kleinman, S. J., Knapp, G. R., Kron, R. G., Krzesinski, J., Long, D. C., Loveday, J., Lupton, R. H., Margon, B., Munn, J. A., Neilsen, E. H., Newberg, H. J., Newman, P. R., Nichol, R. C., Nitta, A., Pier, J. R., Rockosi, C. M., Saxe, D. H., Schlegel, D. J., Snedden, S. A., Szalay, A. S., Thakar, A. R., Uomoto, A., Voges, W., and York, D. G. (2005). The Sloan Digital Sky Survey Quasar Catalog. III. Third Data Release. *AJ*, 130(2):367–380.

Schneider, D. P., Richards, G. T., Fan, X., Hall, P. B., Strauss, M. A., Vanden Berk, D. E., Gunn, J. E., Newberg, H. J., Reichard, T. A., and et al. (2002). The Sloan Digital Sky Survey Quasar Catalog. I. Early Data Release. *AJ*, 123:567–577.

Schulze, A., Done, C., Lu, Y., Zhang, F., and Inoue, Y. (2017). Evidence for Higher Black Hole Spin in Radio-loud Quasars. *ApJ*, 849.

Schwarzschild, K. (1916). On the Gravitational Field of a Mass Point According to Einstein's Theory. *Abh. Konigl. Preuss. Akad. Wissenschaften Jahre 1906,92, Berlin,1907*, 1916:189–196.

Seyfert, C. K. (1943). Nuclear Emission in Spiral Nebulae. *ApJ*, 97:28.

Shakura, N. I. and Sunyaev, R. A. (1973). Black holes in binary systems. Observational appearance. *A&A*, 24:337–355.

Shang, Z., Brotherton, M. S., Green, R. F., Kriss, G. A., Scott, J., Quijano, J. K., Blaes, O., Hubeny, I., Hutchings, J., Kaiser, M. E., Koratkar, A., Oegerle, W., and Zheng, W. (2005). Quasars and the Big Blue Bump. *ApJ*, 619(1):41–59.

Shappee, B. J., Prieto, J. L., Grupe, D., Kochanek, C. S., Stanek, K. Z., De Rosa, G., Mathur, S., Zu, Y., Peterson, B. M., Pogge, R. W., Komossa, S., Im, M., Jencson, J., Holoien, T. W. S., Basu, U., Beacom, J. F., Szczygieł, D. M., Brimacombe, J., Adams, S., Campillay, A., Choi, C., Contreras, C., Dietrich, M., Dubberley, M., Elphick, M., Foale, S., Giustini, M., Gonzalez, C., Hawkins, E., Howell, D. A., Hsiao, E. Y., Koss, M., Leighly, K. M., Morrell, N., Mudd, D., Mullins, D., Nugent, J. M., Parrent, J., Phillips, M. M., Pojmanski, G., Rosing, W., Ross, R., Sand, D., Terndrup, D. M., Valenti, S., Walker, Z., and Yoon, Y. (2014). The Man behind the Curtain: X-Rays Drive the UV through NIR Variability in the 2013 Active Galactic Nucleus Outburst in NGC 2617. *ApJ*, 788.

Shen, Y., Richards, G. T., Strauss, M. A., Hall, P. B., Schneider, D. P., Snedden, S., Bizyaev, D., Brewington, H., Malanushenko, V., Malanushenko, E., Oravetz, D., Pan, K., and Simmons, A. (2011). A Catalog of Quasar Properties from Sloan Digital Sky Survey Data Release 7. *ApJS*, 194:45.

Silverman, J. D., Kovač, K., Knobel, C., Lilly, S., Bolzonella, M., Lamareille, F., Mainieri, V., Brusa, M., Cappelluti, N., Peng, Y., Hasinger, G., Zamorani, G., Scodeggio, M., Contini, T., Carollo, C. M., Jahnke, K., Kneib, J. P., Le Fevre, O., Bardelli, S., Bongiorno, A., Brunner, H., Caputi, K., Civano, F., Comastri, A., Coppa, G., Cucciati, O., de la Torre, S., de Ravel, L., Elvis, M., Finoguenov, A., Fiore, F., Franzetti, P., Garilli, B., Gilli, R., Griffiths, R., Iovino, A., Kampczyk, P., Koekemoer, A., Le Borgne, J. F., Le Brun, V., Maier, C., Mignoli, M., Pello, R., Perez Montero, E., Ricciardelli, E., Tanaka, M., Tasca, L., Tresse, L., Vergani, D., Vignali, C., Zucca, E., Bottini, D., Cappi, A., Cassata, P., Marinoni, C., McCracken, H. J., Memeo, P., Meneux, B., Oesch, P., Porciani, C., and Salvato, M. (2009). The Environments of Active Galactic Nuclei within the zCOSMOS Density Field. *ApJ*, 695(1):171–182.

Slone, O. and Netzer, H. (2012). The effects of disc winds on the spectrum and black hole growth rate of active galactic nuclei. *MNRAS*, 426(1):656–664.

Soltan, A. (1982). Masses of quasars. *MNRAS*, 200:115–122.

Starkey, D., Horne, K., Fausnaugh, M. M., Peterson, B. M., Bentz, M. C., Kochanek, C. S., Denney, K. D., Edelson, R., Goad, M. R., De Rosa, G., Anderson, M. D., Arévalo, P., Barth, A. J., Bazhaw, C., Borman, G. A., Boroson, T. A., Bottorff, M. C., Brandt, W. N., Breeveld, A. A., Cackett, E. M., Carini, M. T., Croxall, K. V., Crenshaw, D. M., Dalla Bontà, E., De Lorenzo-Cáceres, A., Dietrich, M., Efimova, N. V., Ely, J., Evans, P. A., Filippenko, A. V., Flatland , K., Gehrels, N., Geier, S., Gelbord, J. M., Gonzalez, L., Gorjian, V., Grier, C. J., Grupe, D., Hall, P. B., Hicks, S., Horenstein, D., Hutchison, T., Im, M., Jensen, J. J., Joner, M. D., Jones, J., Kaastra, J., Kaspi, S., Kelly, B. C., Kennea, J. A., Kim, S. C., Kim, M., Klimanov, S. A., Korista, K. T., Kriss, G. A., Lee, J. C., Leonard, D. C., Lira, P., MacInnis, F., Manne-Nicholas, E. R., Mathur, S., McHardy, I. M., Montouri, C., Musso, R., Nazarov, S. V., Norris, R. P., Nousek, J. A., Okhmat, D. N., Pancoast, A., Parks, J. R., Pei, L., Pogge, R. W., Pott, J. U., Rafter, S. E., Rix, H. W., Saylor, D. A., Schimoia, J. S., Schnülle, K., Sergeev, S. G., Siegel, M. H., Spencer, M., Sung, H. I., Teems, K. G., Turner, C. S., Uttley, P., Vestergaard, M., Villforth, C., Weiss, Y., Woo, J. H., Yan, H., Young, S., Zheng, W., and Zu, Y. (2017). Space Telescope and Optical Reverberation Mapping Project.VI. Reverberating Disk Models for NGC 5548. *ApJ*, 835(1):65.

Steffen, A. T., Strateva, I., Brandt, W. N., Alexander, D. M., Koekemoer, A. M., Lehmer, B. D., Schneider, D. P., and Vignali, C. (2006). The X-Ray-to-Optical Properties of Optically Selected Active Galaxies over Wide Luminosity and Redshift Ranges. *AJ*, 131:2826–2842.

Stevans, M. L., Shull, J. M., Danforth, C. W., and Tilton, E. M. (2014). HST-COS Observations of AGNs. II. Extended Survey of Ultraviolet Composite Spectra from 159 Active Galactic Nuclei. *ApJ*, 794:75.

Strateva, I. V., Brandt, W. N., Schneider, D. P., Vanden Berk, D. G., and Vignali, C. (2005). Soft X-Ray and Ultraviolet Emission Relations in Optically Selected AGN Samples. *AJ*, 130:387–405.

Suganuma, M., Yoshii, Y., Kobayashi, Y., Minezaki, T., Enya, K., Tomita, H., Aoki, T., Koshida, S., and Peterson, B. A. (2006). Reverberation Measurements of the Inner Radius of the Dust Torus in Nearby Seyfert 1 Galaxies. *ApJ*, 639(1):46–63.

Sugimura, K., Hosokawa, T., Yajima, H., Inayoshi, K., and Omukai, K. (2018). Stunted accretion growth of black holes by combined effect of the flow angular momentum and radiation feedback. *MNRAS*, 478(3):3961–3975.

Tanaka, Y., Nandra, K., Fabian, A. C., Inoue, H., Otani, C., Dotani, T., Hayashida, K., Iwasawa, K., Kii, T., Kunieda, H., Makino, F., and Matsuoka, M. (1995). Gravitationally redshifted emission implying an accretion disk and massive black hole in the active galaxy MCG-6-30-15. *Nature*, 375:659–661.

Targett, T. A., Dunlop, J. S., and McLure, R. J. (2012). The host galaxies and black hole-to-galaxy mass ratios of luminous quasars at z∼4. *MNRAS*, 420(4):3621–3631.

Tran, H. D. (2003). The Unified Model and Evolution of Active Galaxies: Implications from a Spectropolarimetric Study. *ApJ*, 583(2):632–648.

Treister, E., Schawinski, K., Urry, C. M., and Simmons, B. D. (2012). Major Galaxy Mergers Only Trigger the Most Luminous Active Galactic Nuclei. *ApJ*, 758(2):L39.

Tremaine, S., Gebhardt, K., Bender, R., Bower, G., Dressler, A., Faber, S. M., Filippenko, A. V., Green, R., Grillmair, C., Ho, L. C., Kormendy, J., Lauer, T. R., Magorrian, J., Pinkney, J., and Richstone, D. (2002). The Slope of the Black Hole Mass versus Velocity Dispersion Correlation. *ApJ*, 574:740–753.

Urry, C. M. and Padovani, P. (1995). Unified Schemes for Radio-Loud Active Galactic Nuclei. *PASP*, 107:803.

Vanden Berk, D. E., Richards, G. T., Bauer, A., Strauss, M. A., Schneider, D. P., Heckman, T. M., York, D. G., Hall, P. B., Fan, X., Knapp, G. R., Anderson, S. F., Annis, J., Bahcall, N. A., Bernardi, M., Briggs, J. W., Brinkmann, J., Brunner, R., and et al. (2001). Composite Quasar Spectra from the Sloan Digital Sky Survey. *AJ*, 122:549–564.

Vestergaard, M. (2000). Are Radio-loud Quasars Rebellious or Are Radio-quiets Just Plain Untalented? A Study of the Ultraviolet Broad Emission Line Profiles in High-Redshift Radio-loud and Radio-quiet Quasars. *PASP*, 112:1504–1505.

Vestergaard, M. and Osmer, P. S. (2009). Mass Functions of the Active Black Holes in Distant Quasars from the Large Bright Quasar Survey, the Bright Quasar Survey, and the Color-selected Sample of the SDSS Fall Equatorial Stripe. *ApJ*, 699:800–816.

Vestergaard, M. and Peterson, B. M. (2006). Determining Central Black Hole Masses in Distant Active Galaxies and Quasars. II. Improved Optical and UV Scaling Relationships. *ApJ*, 641:689–709.

Vignali, C., Brandt, W. N., and Schneider, D. P. (2003). X-Ray Emission from Radio-Quiet Quasars in the Sloan Digital Sky Survey Early Data Release: The α_{ox} Dependence upon Ultraviolet Luminosity. *AJ*, 125(2):433–443.

Villforth, C., Herbst, H., Hamann, F., Hamilton, T., Bertemes, C., Efthymiadou, A., and Hewlett, T. (2019). The host galaxies of FeLoBAL quasars at z ∼ 0.9 are not dominated by recent major mergers. *MNRAS*, 483(2):2441–2452.

Violino, G., Coppin, K. E. K., Stevens, J. A., Farrah, D., Geach, J. E., Alexander, D. M., Hickox, R., Smith, D. J. B., and Wardlow, J. L. (2016). A SCUBA-2 survey of FeLoBAL QSOs. Are FeLoBALs in a 'transition phase' between ULIRGs and QSOs? *MNRAS*, 457(2):1371–1384.

Viswanath, G., Stalin, C. S., Rakshit, S., Kurian, K. S., Ujjwal, K., Gudennavar, S. B., and Kartha, S. S. (2019). Are Narrow-line Seyfert 1 Galaxies Powered by Low-mass Black Holes? *ApJ*, 881(1):L24.

Vivek, M., Srianand, R., Petitjean, P., Mohan, V., Mahabal, A., and Samui, S. (2014). Variability in Low Ionization Broad Absorption Line outflows. *MNRAS*, 440(1):799–820.

Voit, G. M., Weymann, R. J., and Korista, K. T. (1993). Low-ionization broad absorption lines in quasars. *ApJ*, 413:95–109.

Walter, R. and Fink, H. H. (1993). The ultraviolet to soft X-ray bump of Seyfert 1 type active galactic nuclei. *A&A*, 274:105.

Walton, D. J., Nardini, E., Fabian, A. C., Gallo, L. C., and Reis, R. C. (2013). Suzaku observations of 'bare' active galactic nuclei. *MNRAS*, 428(4):2901–2920.

Wandel, A., Peterson, B. M., and Malkan, M. A. (1999). Central Masses and Broad-Line Region Sizes of Active Galactic Nuclei. I. Comparing the Photoionization and Reverberation Techniques. *ApJ*, 526(2):579–591.

Wang, F., Wu, X.-B., Fan, X., Yang, J., Bian, F., McGreer, I. D., Green, R. F., Yang, Q., Jiang, L., Wang, R., DECaLS Team, and UHS Team (2017). Quasars at Cosmic Dawn: Discoveries and Probes of the Early Universe. In *American Astronomical Society Meeting Abstracts #229*, volume 229 of *American Astronomical Society Meeting Abstracts*, page 220.01.

Wang, T., Yang, C., Wang, H., and Ferland , G. (2015). Evidence for Photoionization-driven Broad Absorption Line Variability. *ApJ*, 814(2):150.

Watson, D., Denney, K. D., Vestergaard, M., and Davis, T. M. (2011). A New Cosmological Distance Measure Using Active Galactic Nuclei. *ApJ*, 740:L49.

Wethers, C. F., Kotilainen, J., Schramm, M., and Schulze, A. (2020). Star Formation in Luminous LoBAL Quasars at 2.0 < z < 2.5. *MNRAS*.

Weymann, R. J., Morris, S. L., Foltz, C. B., and Hewett, P. C. (1991). Comparisons of the Emission-Line and Continuum Properties of Broad Absorption Line and Normal Quasi-stellar Objects. *ApJ*, 373:23.

White, R. J. and Peterson, B. M. (1994). Comments on Cross-Correlation Methodology in Variability Studies of Active Galactic Nuclei. *Publications of the Astronomical Society of the Pacific*, 106:879.

Williams, J. K., Gliozzi, M., and Rudzinsky, R. V. (2018). Are narrow-line Seyfert 1 galaxies highly accreting low-M_{BH} AGNs? *MNRAS*, 480(1):96–107.

Yi, W., Brandt, W. N., Hall, P. B., Vivek, M., Grier, C. J., Filiz Ak, N., Schneider, D. P., and McGraw, S. M. (2019). Variability of Low-ionization Broad Absorption-line Quasars Based on Multi-epoch Spectra from the Sloan Digital Sky Survey. *ApJS*, 242(2):28.

Young, A. J., McHardy, I., Emmanoulopoulos, D., and Connolly, S. (2018). The absence of a thin disc in M81*. *MNRAS*, 476(4):5698–5703.

Young, A. J., Nowak, M. A., Markoff, S., Marshall, H. L., and Canizares, C. R. (2007). High-Resolution X-Ray Spectroscopy of a Low-Luminosity Active Galactic Nucleus: The Structure and Dynamics of M81*. *ApJ*, 669(2):830–840.

Young, S., Hough, J. H., Axon, D. J., Fabian, A. C., and Ward, M. J. (1998). The obscured BLR in the radio galaxy 3C234. *MNRAS*, 294(3):478–484.

Yu, Z., Kochanek, C. S., Peterson, B. M., Zu, Y., Brandt, W. N., Cackett, E. M., Fausnaugh, M. M., and McHardy, I. M. (2020). On reverberation mapping lag uncertainties. *MNRAS*, 491(4):6045–6064.

Zamorani, G., Giommi, P., Maccacaro, T., and Tananbaum, H. (1984). X-ray variability of quasars. *ApJ*, 278:28–36.

Zamorani, G., Henry, J. P., Maccacaro, T., Tananbaum, H., Soltan, A., Avni, Y., Liebert, J., Stocke, J., Strittmatter, P. A., Weymann, R. J., Smith, M. G., and Condon, J. J. (1981). X-ray studies of quasars with the Einstein Observatory II. *ApJ*, 245:357–374.

Zdziarski, A. A., Johnson, W. N., and Magdziarz, P. (1996). Broad-band γ-ray and X-ray spectra of NGC 4151 and their implications for physical processes and geometry. *MNRAS*, 283:193–206.

Zhang, S., Zhou, H., Wang, T., Wang, H., Shi, X., Liu, B., Liu, W., Li, Z., and Wang, S. (2015). Strong Variability of Overlapping Iron Broad Absorption Lines in Five Radio-selected Quasars. *ApJ*, 803(2):58.

Zhao, D., Ho, L. C., Zhao, Y., Shangguan, J., and Kim, M. (2019). The Role of Major Mergers and Nuclear Star Formation in Nearby Obscured Quasars. *ApJ*, 877(1):52.

Zhu, S. F., Brandt, W. N., Wu, J., Garmire, G. P., and Miller, B. P. (2019). Investigating the X-ray enhancements of highly radio-loud quasars at z > 4. *MNRAS*, 482(2):2016–2038.

Zu, Y., Kochanek, C. S., Kozłowski, S., and Udalski, A. (2013). Is Quasar Optical Variability a Damped Random Walk? *ApJ*, 765.

Zu, Y., Kochanek, C. S., and Peterson, B. M. (2011). An Alternative Approach to Measuring Reverberation Lags in Active Galactic Nuclei. *ApJ*, 735.